Climate and Hydrology in Mountain Areas

Climate and Hydrology in Mountain Areas. Edited by C. de Jong, D. Collins and R. Ranzi
© 2005 John Wiley & Sons, Ltd. ISBN: 0-470-85814-1

Climate and Hydrology in Mountain Areas

Editors

Carmen de Jong
University of Bonn, Germany

David Collins
University of Salford, UK

Roberto Ranzi
University of Brescia, Italy



John Wiley & Sons, Ltd

Copyright © 2005

John Wiley & Sons Ltd, The Atrium, Southern Gate, Chichester,
West Sussex PO19 8SQ, England

Telephone (+44) 1243 779777

Email (for orders and customer service enquiries): cs-books@wiley.co.uk
Visit our Home Page on www.wiley.com

All Rights Reserved. No part of this publication may be reproduced, stored in a retrieval system or transmitted in any form or by any means, electronic, mechanical, photocopying, recording, scanning or otherwise, except under the terms of the Copyright, Designs and Patents Act 1988 or under the terms of a licence issued by the Copyright Licensing Agency Ltd, 90 Tottenham Court Road, London W1T 4LP, UK, without the permission in writing of the Publisher. Requests to the Publisher should be addressed to the Permissions Department, John Wiley & Sons Ltd, The Atrium, Southern Gate, Chichester, West Sussex PO19 8SQ, England, or emailed to permreq@wiley.co.uk, or faxed to (+44) 1243 770620.

This publication is designed to provide accurate and authoritative information in regard to the subject matter covered. It is sold on the understanding that the Publisher is not engaged in rendering professional services. If professional advice or other expert assistance is required, the services of a competent professional should be sought.

Other Wiley Editorial Offices

John Wiley & Sons Inc., 111 River Street, Hoboken, NJ 07030, USA

Jossey-Bass, 989 Market Street, San Francisco, CA 94103-1741, USA

Wiley-VCH Verlag GmbH, Boschstr. 12, D-69469 Weinheim, Germany

John Wiley & Sons Australia Ltd, 33 Park Road, Milton, Queensland 4064, Australia

John Wiley & Sons (Asia) Pte Ltd, 2 Clementi Loop #02-01, Jin Xing Distripark, Singapore 129809

John Wiley & Sons Canada Ltd, 22 Worcester Road, Etobicoke, Ontario, Canada M9W 1L1

Wiley also publishes its books in a variety of electronic formats. Some content that appears in print may not be available in electronic books.

British Library Cataloguing in Publication Data

A catalogue record for this book is available from the British Library

ISBN-13 978-0-470-85814-1 (HB)
ISBN-10 0-470-85814-1 (HB)

Typeset in 9/11pt Times by Laserwords Private Limited, Chennai, India
Printed and bound in Great Britain by Antony Rowe Ltd, Chippenham, Wiltshire
This book is printed on acid-free paper responsibly manufactured from sustainable forestry in which at least two trees are planted for each one used for paper production.

Contents

List of contributors *vii*

List of symbols *xi*

Abbreviations *xvii*

Introduction: Climate and Hydrology in Mountain Areas xix
Carmen de Jong, Roberto Ranzi and David Collins

1 Alpine Climate Change and Cryospheric Responses: An Introduction 1
Roger G. Barry

PART I SNOW AND ICE MELT **5**

2 Use of Positive Degree-Day Methods for Calculating Snow and Ice Melting and Discharge in Glacierized Basins in the Langtang Valley, Central Nepal 7
Rijan B. Kayastha, Yutaka Ageta and Koji Fujita

3 Surface Energy Balance of High Altitude Glaciers in the Central Andes: The Effect of Snow Penitentes 15
Javier G. Corripio and Ross S. Purves

4 Using Subgrid Parameterisation and a Forest Canopy Climate Model for Improving Forecasts of Snowmelt Runoff 29
Ulrich Strasser and Pierre Etchevers

5 Assessment of Snow-covered Areas Using Air Temperatures During Melt in a Mountainous Basin 45
Pratap Singh and Lars Bengtsson

PART II SOIL WATER AND PERMAFROST **57**

6 Permafrost Monitoring in High Mountain Areas Using a Coupled Geophysical and Meteorological Approach 59
Christian Hauck, Daniel Vonder Mühll and Martin Hoelzle

7 Effects of Frozen Soil on the Groundwater Recharge in Alpine Areas 73
Daniel Bayard and Manfred Stähli

8 Water Balance in Surface Soil: Analytical Solutions of Flow Equations and Measurements in the Alpine Toce Valley 85
Marilena Menziani, Sergio Pugnaghi, Sergio Vincenzi and Renato Santangelo

9 Saturated Hydraulic Conductivity and Water Retention Relationships for Alpine Mountain Soils 101
Stefano Barontini, Alberto Clerici, Roberto Ranzi and Baldassare Bacchi

PART III EVAPOTRANSPIRATION AND WATER BALANCE 123

10 Water Balance Modeling with Fuzzy Parameterizations: Application to an Alpine Catchment 125
Gerald Eder, Hans-Peter Nachtnebel and Murugesu Sivapalan

11 Water Relations of an Old-growth Douglas Fir Stand 147
Timothy E. Link, Gerald N. Flerchinger, Mike Unsworth and Danny Marks

12 Comparison of Evapotranspiration and Condensation Measurements between the Giant Mountains and the Alps 161
Carmen de Jong, Marco Mundelius and Krzysztof Migała

13 Climatologic and Hydrologic Coupling in the Ecology of Norwegian High Mountain Catchments 185
Jörg Löffler and Ole Rößler

PART IV COUPLING METEOROLOGY AND HYDROLOGY 215

14 Runoff and Floods in the Alps: An Overview 217
Baldassare Bacchi and Vigilio Villi

15 The Use of Coupled Meteorological and Hydrological Models for Flash Flood Simulation 221
Charles A. Lin, Lei Wen, Diane Chaumont and Michel Béland

16 Operational Weather Radar Assessment of Convective Precipitation as an Input to Flood Modelling in Mountainous Basins 233
Stefan Uhlenbrook and Doerthe Tetzlaff

17 Geomorphological Zoning: An Improvement to Coupling Alpine Hydrology and Meteorology? 247
Carmen de Jong, Peter Ergenzinger, Martin Borufka, Arne Köcher and Martin Dresen

PART V CLIMATE CHANGE IMPACT AND MOUNTAIN HYDROLOGY 261

18 The Influence of Glacier Retreat on Water Yield from High Mountain Areas: Comparison of Alps and Central Asia 263
Wilfried Hagg and Ludwig Braun

19 Snowmelt Under Different Temperature Increase Scenarios in the Swiss Alps 277
Franziska Keller and Stéphane Goyette

20 Climate Variability, Water Resources, and Hydrologic Extremes – Modeling the Water and Energy Budgets 291
Osman Yildiz and Ana P. Barros

Index 307

List of Contributors

Yutaka Ageta, Department of Hydrospheric-Atmospheric Science, Graduate School of Environmental Studies, Nagoya University, Japan

Baldassare Bacchi, Department of Civil Engineering, University of Brescia, Brescia, Italy

Stefano Barontini, Department of Civil Engineering, University of Brescia, Italy

Ana P. Barros, Pratt School of Engineering, Duke University, USA

Roger G. Barry, NSIDC/CIRES, University of Colorado, USA

Daniel Bayard, EPF Lausanne, GEOLEP, ENAC, Switzerland

Michel Béland, Réseau québécois de calcul de haute performance, Université de Montréal, Canada

Lars Bengtsson, Department of Water Resources Engineering, Lund University, Sweden

Martin Borufka, Institute of Geographic Sciences, Free University of Berlin, Germany

Ludwig Braun, Bavarian Academy of Sciences, Commission for Glaciology, Germany

Diane Chaumont, Ouranos Consortium sur la climatologie régionale et l'adaptation aux changements climatiques, Canada

Alberto Clerici, Department of Civil Engineering, University of Brescia, Italy

David N. Collins, Division of Geography, School of Environmental and Life Sciences, University of Salford, UK

Javier G. Corripio, Institute of Hydromechanics and Water Resources Management, ETH – Zürich

Carmen de Jong, Geographisches Institut, Universität Bonn, Germany

Martin Dresen, geoSYS, Berlin, Germany

Gerald Eder, Institute of Water Management, Hydrology and Hydraulic Engineering, University of Natural Resources and Applied Life, Austria

Peter Ergenzinger, Berlin-Bonn Environmental Research Group, Bornheim-Uedorf, Germany

Pierre Etchevers, Centre National de Recherches Météorologiques, Centre d'Études de la Neige, METEO-France, France

Gerald N. Flerchinger, USDA Agricultural Research Service, USA

Koji Fujita, Department of Hydrospheric-Atmospheric Science, Graduate School of Environmental Studies, Nagoya University, Japan

Stéphane Goyette, Département de Géosciences, Géographie, Université de Fribourg, Switzerland

Wilfried Hagg, Bavarian Academy of Sciences, Commission for Glaciology, Germany

Christian Hauck, Institute for Meteorology and Climate Research, University of Karlsruhe/Forschungszentrum Karlsruhe, Germany

Martin Hoelzle, Physical Geography Division, Department of Geography, University of Zurich, Switzerland

Rijan B. Kayastha, Department of Hydrospheric-Atmospheric Science, Graduate School of Environmental Studies, Nagoya University, Japan

Franziska Keller, Département de Géosciences, Géographie, Université de Fribourg, Switzerland

Arne Köcher, Institute of Geographic Sciences, Free University of Berlin, Germany

Charles A. Lin, Department of Atmospheric and Oceanic Sciences, and Global Environmental and Climate Change Centre, McGill University, Canada

Timothy E. Link, Department of Forest Resources, University of Idaho, USA

Jörg Löffler, University of Oldenburg, Institute of Biology & Environmental Sciences, Germany

Danny Marks, USDA Agricultural Research Service, USA

Marilena Menziani, Dipartimento di Ingegneria dei Materiali e dell'Ambiente – Osservatorio Geofisico, Università di Modena e Reggio Emilia, Italy

Krzysztof Migała, Institute of Geography, Department of Meteorology and Climatology, University of Wroclaw, Poland

Marco Mundelius, Institut für Gewässerkunde und Binnenfischerei, Berlin, Germany

Hans-Peter Nachtnebel, Institute of Water Management, Hydrology and Hydraulic Engineering, University of Natural Resources and Applied Life, Austria

Sergio Pugnaghi, Dipartimento di Ingegneria dei Materiali e dell'Ambiente – Osservatorio Geofisico, Università di Modena e Reggio Emilia, Italy

Ross S. Purves, Department of Geography, University of Zürich, Switzerland

Roberto Ranzi, Department of Civil Engineering, University of Brescia, Italy

Ole Rößler, Institut für Biologie und Umweltwissenschaften, Universität Oldenburg, Germany

Renato Santangelo, Dipartimento di Ingegneria dei Materiali e dell'Ambiente – Osservatorio Geofisico, Università di Modena e Reggio Emilia, Italy

Pratap Singh, National Institute of Hydrology, India

Murugesu Sivapalan, Centre for Water Research, University of Western Australia, Australia

Manfred Stähli, Swiss Federal Research Institute WSL, Switzerland

Ulrich Strasser, Department of Earth & Environmental Sciences, Section Geography, University of Munich, Germany

Doerthe Tetzlaff, Department of Geography and Environment, University of Aberdeen, UK

Stefan Uhlenbrook, UNESCO-IHE, Department of Water Engineering, Westvest 7, 2611 AX Delft

Mike Unsworth, Oregon State University, College of Oceanic and Atmospheric Sciences, USA

Vigilio Villi, CNR – Research Institute for Hydrogeological Risk Prevention, Italy

Sergio Vincenzi, ISMAR, Grandi Masse, CNR, Italy

Daniel Vonder Mühll, Physical Geography Division, Department of Geography, University of Zurich, Switzerland

Lei Wen, Department of Atmospheric and Oceanic Sciences, and Global Environmental and Climate Change Centre, McGill University, Canada

Osman Yildiz, Faculty of Engineering, Kirikkale University, Turkey

List of Symbols

$\widehat{A}$	Fuzzy number of variable or parameter A
a	coefficient or empirical parameter
a_r	ratio
a^l, a^c & a^r	Characteristic left, center and right values, respectively, of a triangular fuzzy number $\widehat{A}$
$[a^l(\alpha), a^r(\alpha)]$	$a^l(\alpha)$ and $a^r(\alpha)$ indicate the lower and upper bounds of the interval $\widehat{A}(\alpha)$ at any α-level in the interval [0,1]
b	coefficient or empirical parameter
C_*	effective heat capacity of the surface ($\mathrm{J\,m^{-2}\,K^{-1}}$)
$C_{*,\mathrm{snow}}$	effective heat capacity of snow ($\mathrm{J\,m^{-2}\,K^{-1}}$)
C_e	bulk moisture transfer coefficient
$\widehat{C}_\mathrm{fc}$	Soil moisture capacity until field capacity of the soil profile (mm)
C_h	bulk heat transfer coefficient
$\widehat{C}_\mathrm{tp}$	Total capacity of the soil profile. The maximum storage capacity of the bucket model (mm)
c	velocity of the electromagnetic waves in the void ($\mathrm{m\,s^{-1}}$)
c_p	specific heat content of air at constant pressure ($\mathrm{J\,kg^{-1}\,K^{-1}}$)
D	hydraulic diffusivity ($\mathrm{m^2\,s^{-1}}$)
$D(\theta)$	Hydraulic diffusivity in the porous medium ($\mathrm{L^2T^{-1}}$, $\mathrm{m^2\,s^{-1}}$)
D_0	constant with the dimensions of the hydraulic diffusivity ($\mathrm{m^2\,s^{-1}}$)
D_f	density of the forest canopy
$\widehat{D}_\mathrm{tp}$	Total depth of the soil profile to an impervious layer (mm)
d	displacement height (m)
E	evaporation (kg)
E_cum	cumulative evaporation (m)
E_F	frozen soil moisture content ($\mathrm{kg\,m^{-2}}$)
E_g	ground evaporation ($\mathrm{kg\,m^{-2}\,s^{-1}}$)
E_i	istantaneous evaporation ($\mathrm{m\,s^{-1}}$)
E_L	liquid soil moisture content ($\mathrm{kg\,m^{-2}}$)
E_s	snow evaporation rate ($\mathrm{kg\,m^{-2}\,s^{-1}}$)
E_TOT	total evaporation rate ($\mathrm{kg\,m^{-2}\,s^{-1}}$)
E_v	evaporation flux ($\mathrm{m\,s^{-1}}$)
EL_e	latent turbulent heat flux ($\mathrm{W\,m^{-2}}$)
ET	evaporation and transpiration ($\mathrm{mm\,day^{-1}}$)
$\widehat{E}$	Daily potential ($\widehat{E}_p$) or actual evapotranspiration ($\widehat{E}_a$) ($\mathrm{mm\,d^{-1}}$)
e_0	vapour pressure (hPa)
e_s	saturated vapour pressure (Pa)
F	Fractional Vegetation Cover
F_{ms}	correction term for diffuse radiation due to multiple scattering between ground and sky (dimensionless)
F_{sk}	correction term for diffuse radiation from the sky (dimensionless)

F_t	correction term for the angle of incidence of sun on the slope (dimensionless)
f_v	skyview factor (dimensionless)
G_e	Shape parameter (Reynolds and Elrick, 1991) (−, −)
H	Hydraulic head (L, m)
H_c	soil column depth (m)
H_{geo}	Geodetic head (L, m)
$h, h(t), h^*$	Water level inside the infiltrometer (L, m)
h_{sun}	theoretical maximum duration of subshine hours (h)
I	interception (mm)
$I_{\max}$	storage capacity (mm)
I_p	interception of liquid precipitation (mm)
I_s	interception of solid precipitation (mm)
I_{sc}	solar constant ($\mathrm{W\,m^{-2}}$)
$I(t)$	Cumulated drawdown of the water inside the infiltrometer (L, m)
IDW	inverse distance weighting method
K, $K(\theta)$	Hydraulic conductivity ($\mathrm{LT^{-1}}$, $\mathrm{m\,s^{-1}}$)
K	the value of k such that probability function of T_k becomes zero
K_a	apparent dielectric constant (−)
K_{HI}	horizontal hydraulic conductivity
K_s	Saturated hydraulic conductivity ($\mathrm{LT^{-1}}$, $\mathrm{m\,s^{-1}}$)
K_{VI}	vertical hydraulic conductivity
K^*	short-wave radiation budget ($\mathrm{W\,m^{-2}}$)
$K\downarrow$	incoming solar radiation ($\mathrm{W\,m^{-2}}$)
$K\downarrow_{\text{snow}}$	solar flux penetrating the snowpack ($\mathrm{W\,m^{-2}}$)
k'	z-axis unitary vector, positive upward (−, −)
k_b	degree-day factor for ice ablation ($\mathrm{mm\,d^{-1}\,^\circ C^{-1}}$)
k_d	degree-day factor for ice ablation under debris ($\mathrm{mm\,d^{-1}\,^\circ C^{-1}}$)
L	wave guide length (m)
$L(t)$	Length of the saturated soil depth (L, m)
L^*	long-wave radiation budget ($\mathrm{W\,m^{-2}}$)
$L\downarrow$	long-wave downward radiative flux ($\mathrm{W\,m^{-2}}$)
$L\uparrow$	long-wave upward radiative flux ($\mathrm{W\,m^{-2}}$)
$L'\downarrow$	long-wave radiative flux reflected from surrounding slopes ($\mathrm{W\,m^{-2}}$)
L_e	latent heat of evaporation/sublimation ($\mathrm{J\,kg^{-1}}$)
L_{f}	latent heat of fusion of water ($\mathrm{J\,kg^{-1}}$)
L_H	cumulative loss/gain in the soil volumetric water content storage (m)
L_{inf}	Soil length inside the infiltrometer (L, 0.10 m)
L_s	latent heat of sublimation ($\mathrm{J\,kg^{-1}}$)
M	number of observations in a day
M_a	moleculary mass of dry air
M_{F}	frozen soil moisture ($\mathrm{kg\,m^{-2}}$)
M_{S}	melting rate of snow ($\mathrm{kg\,m^{-2}\,s^{-1}}$)
M_{snow}	snow mass ($\mathrm{kg\,m^{-2}}$)
M_t	snowmelt from the trees (mm)
m	Archie exponent; describes the effect of porosity on resistivity change for different materials (−)
$\widehat{m}_f$	Melt factor for snowmelt processes at thaw conditions ($\mathrm{mm\,K^{-1}\,\Delta t^{-1}}$)
N	number of days
n	saturation exponent; describes the effect of saturation on resistivity change (−)
n'	Surface unitary vector, positive outward (−, −)
P	precipitation (mm)
P_0	threshold precipitation (mm)
P_a	atmospheric pressure (Pa)

P_{BH}	precipitation observed at the base house (mm)
P_c	snow falling from the trees (mm)
P_{cum}	cumulative precipitation (m)
P_f	ground precipitation inside a forest canopy (mm)
P_h	precipitation in a single time step (mm)
P_i	instantaneous precipitation ($\mathrm{m\,s^{-1}}$)
P_{L}	liquid precipitation rate ($\mathrm{kg\,m^{-2}\,s^{-1}}$)
P_r	precipitation rate ($\mathrm{mm\,s^{-1}}$)
P_{S}	solid precipitation rate ($\mathrm{kg\,m^{-2}\,s^{-1}}$)
P_{snow}	cumulative precipitation of the snowfall event (mm)
P_Z	precipitation at altitude Z (mm)
P^*	Orographic Precipitation
$\widehat{P}$	Daily precipitation falling as rain ($\widehat{P}_{\mathrm{r}}$) or snow ($\widehat{P}_{\mathrm{s}}$) ($\mathrm{mm\,d^{-1}}$)
p	Pressure ($\mathrm{ML^{-1}T^{-1}}$, kPa)
p_{sfc}	surface pressure (hPa)
Q	Streamflow (Total Runoff) ($\mathrm{m^3\,s^{-1}}$)
Q^*	all-wave surface radiation budget ($\mathrm{W\,m^{-2}}$)
Q_{diff}	diffuse solar radiation ($\mathrm{W\,m^{-2}}$)
$Q_{\mathrm{diff},f}$	diffuse solar radiation in the forest canopy ($\mathrm{W\,m^{-2}}$)
Q_{dir}	direct solar radiation ($\mathrm{W\,m^{-2}}$)
$Q_{\mathrm{dir},f}$	direct solar radiation in the forest canopy ($\mathrm{W\,m^{-2}}$)
Q_{e}	latent heat flux ($\mathrm{W\,m^{-2}}$)
Q_H	sensible turbulent flux per unit area ($\mathrm{W\,m^{-2}}$)
Q_{h}	sensible heat flux ($\mathrm{W\,m^{-2}}$)
Q_l	incoming infrared radiation ($\mathrm{W\,m^{-2}}$)
$Q_{l,f}$	incoming infrared radiation in the forest canopy ($\mathrm{W\,m^{-2}}$)
Q_o	Observed discharge at closure section (crisp value) ($\mathrm{mm\,d^{-1}}$)
Q_{s}	Subsurface Flow ($\mathrm{m^3\,s^{-1}}$)
Q_{sfc}	heat storage term ($\mathrm{W\,m^{-2}}$)
Q_{snow}	heat flux through the snowpack ($\mathrm{W\,m^{-2}}$)
$\widehat{Q}_{\mathrm{bf}}$	Daily baseflow ($\mathrm{mm\,d^{-1}}$)
$\widehat{Q}_{\mathrm{in}}$	Daily interflow ($\mathrm{mm\,d^{-1}}$)
$\widehat{Q}_N$	Daily snowmelt at thawing conditions ($\mathrm{mm\,d^{-1}}$)
$\widehat{Q}_p$	Modeled discharge at closure section ($\mathrm{mm\,d^{-1}}$)
$\widehat{Q}_{\mathrm{se}}$	Daily saturation excess runoff ($\mathrm{mm\,d^{-1}}$)
$\widehat{Q}_{\mathrm{ss}}$	Daily sub-surface runoff ($\mathrm{mm\,d^{-1}}$)
q	Apparent velocity of the fluid in the porous medium ($\mathrm{LT^{-1}}$, $\mathrm{m\,s^{-1}}$)
q_{air}	specific humidity at the screen level ($\mathrm{kg\,kg^{-1}}$)
$q_{\mathrm{sat,sfc}}$	saturation specific humidity at the surface ($\mathrm{kg\,kg^{-1}}$)
R	thermal resistance of debris ($\mathrm{m^2\,^\circ C\,W^{-1}}$)
R^2	coefficient of determination
R_a	aerodynamic resistance of the canopy ($\mathrm{s\,m^{-1}}$)
R_c	thermal resistance for critical debris thickness ($\mathrm{m^2\,^\circ C\,W^{-1}}$)
$R_{\mathrm{eff}}(Q)$	Model efficiency according to Nash and Sutcliffe (1970) (−)
$R_{\mathrm{eff}}(\log Q)$	Model efficiency according to Nash and Sutcliffe (1970) using logarithmic runoff values (−)
R_{off}	total runoff ($\mathrm{kg\,m^{-2}}$)
RH	relative humidity (dimensionless)
RH_f	relative humidity in the forest canopy
$R_{Z/R}$	Rainfall intensities, used in Z/R-relation for weather radar data adjustment ($\mathrm{mm\,h^{-1}}$)
r	Radius of the infiltrometer (L, m)
r_S	Soil moisture ratio; S is a fraction of C_{fc} (1)
S	fraction of the pore space occupied by liquid water (−)

$S_{\max}$	maximum snow interception (mm)
S_w	fraction of water remaining unfrozen at subfreezing temperatures or unfrozen water content (−)
$SW\downarrow$	short-wave downward radiative flux (W m^{-2})
$SW\uparrow$	short-wave upward radiative flux (W m^{-2})
$\widehat{S}$	Soil water storage; re-scaled soil water storage $\widehat{S}'$ is carried over from time step t to $t+1$ (mm)
$\widehat{S}_N$	Storage of snow water equivalent in the snowpack (mm)
s	local slope
s_e	Effective saturation (−, −)
T	temperature (°C)
T_0	initial temperature (°C)
T_0	reference temperature (°C)
T_0'	reference temperature corresponding to ρ_0 (°C)
T_{air}	air temperature (K)
$T_{\text{air},f}$	air temperature in the forest canopy (K)
$T_{\text{air},sl}$	air temperature at screen level (K)
T_{d}	dew point temperature (K)
$T_{f,C}$	temperature at the freezing point (°C)
T_{fK}	freezing temperature (K)
T_{g}	ground surface temperature (K)
T_{g}	soil temperature
T_{his}	historical temperature over 24 h (K)
T_k	temperature at the kth times (°C)
$T_{\max}$	maximum air temperature (K)
T_{mean}	mean daily air temperature (K)
$T_{\min}$	minimum air temperature (K)
T_n	temperature on the nth day (°C)
T_{s}	snow surface temperature (K)
T_{sfc}	surface temperature (K)
$\widehat{T}$	Mean daily air temperature (°C)
$\widehat{T}_{\text{crit}}$	Critical mean air temperature: threshold between frost or thaw situations and rain or snow events (°C)
$\widehat{T}_{\text{pos}}$	Daily mean air temperature. If $\widehat{T}_{\text{pos}}$ is below $\widehat{T}_{\text{crit}}$, then $\widehat{T}_{\text{pos}}$ is set to $\widehat{T}_{\text{crit}}$ (°C)
t	time (s)
$\widehat{t}_{\text{c}}$	Catchment response time of the total runoff process (days)
$\widehat{t}_{\text{c-bf}}$	Catchment response time of the baseflow component (days)
$\widehat{t}_{\text{c-in}}$	Catchment response time of the interflow component (days)
u	wind speed (m s^{-1})
u^*	dimensionless composite variable of space and time (−)
u_f	wind speed inside the forest canopy (m s^{-1})
$\overline{u}$	mean wind speed (m s^{-2})
V	volume of seasonal snow melt runoff
V	constant with the dimensions of the velocity (m s^{-1})
V_{a}	anemometer-level wind magnitude (m s^{-1})
v	velocity of the electromagnetic wave in a medium (m s^{-1})
W	total soil moisture (liquid and frozen) (kg m^{-2})
W_{F}	frozen soil moisture content (kg m^{-3})
W_{L}	liquid soil moisture content (kg m^{-3})
X	dimensionless hydraulic diffusivity (−)
x_o	Organic matter (MM^{-1}, −)
Y	degree-day sum (°C d)
Z	altitude (m)
Z_{radar}	Radar reflectivities observed with a weather radar, used in Z/R-relation

z	height above ground (m)
z	vertical space coordinate (positive downward) (m)
z_0	roughness length (m)
$z_{0,\mathrm{sfc}}$	surface roughness height (m)
$z_{0,\mathrm{snow}}$	snow roughness height (m)
z_e	roughness element height (m)
z_m	measurement height above ground (m)

Greek

α	surface albedo (dimensionless)
α	Sorptive number (L, m^{-1})
$\alpha_{\mathrm{nir,sfc}}$	near-infrared surface albedo (dimensionless)
$\alpha_{\mathrm{nir,snow}}$	near-infrared snow albedo (dimensionless)
α_{nm}	variable (either one or zero)
α_{snow}	albedo of the snow surface (dimensionless)
$\alpha_{\mathrm{s,sfc}}$	albedo of the visible spectrum at the surface (dimensionless)
$\alpha_{\mathrm{s,snow}}$	snow visible albedo (dimensionless)
α_T	temperature coefficient of resistivity ($^\circ\mathrm{C}^{-1}$)
$\alpha_{Z/R}$	empirical parameter of the Z/R-relation for weather radar data adjustment (−)
$\beta_{Z/R}$	empirical parameter of the Z/R-relation for weather radar data adjustment (−)
β_{BR}	Bowen ratio
β_{e}	evaporation factor
γ_w	Water unitary weight ($\mathrm{ML}^{-2}\mathrm{T}^{-2}$, $9806\,\mathrm{N\,m}^{-3}$)
ΔQ_{m}	latent heat storage change ($\mathrm{W\,m}^{-2}$)
ΔQ_{s}	energy storage within the snowpack ($\mathrm{W\,m}^{-2}$)
Δz	snow depth (m)
$\Delta^l(\alpha)$	Interval between $a^l(\alpha)$ and a^c at any $\alpha \in [0, 1]$; same for $\Delta^r(\alpha)$
δ_{snow}	snow fraction at the surface (fraction)
ε	emissivity (dimensionless)
ε_f	emissivity of the forest (dimensionless)
ε_r	relative dielectric permittivity (−)
ε_{s}	surface emissivity (dimensionless)
ϑ	normalized soil volumetric water content (−)
ϑ_i	vertical soil volumetric water content profile at the time origin (−)
ϑ_0	volumetric water content at the upper boundary (−)
θ	soil volumetric water content (%)
θ_l	local horizon angle (radians)
θ_M	maximum value of the soil volumetric water content (%)
θ_m	minimum value of the soil volumetric water content (%)
θ_{res}	Residual volumetric water content ($\mathrm{L}^3\ \mathrm{L}^{-3}$, −)
θ_s	soil volumetric water content at the saturation (%)
θ_{sat}	Saturated volumetric water content ($\mathrm{L}^3\ \mathrm{L}^{-3}$, −)
$\widehat{\theta}_{\mathrm{fc}}$	Field capacity (1)
$\widehat{\theta}_{\mathrm{pwp}}$	Permanent wilting point (1)
κ	Karman constant
λ	wavelength of radiation (μm) λ
λ	Pore-size distribution index (−, −)
λ_f	frontal area index (dimensionless)
λ_{snow}	heat conductivity of snow ($\mathrm{W\,m}^{-1}\,\mathrm{J}^{-1}$)
μ	Level of presumption
μ_r	relative magnetic permeability (−)
Φ	porosity (−)

Φ_h	horizontal component of the volumetric water content flux ($\mathrm{m\,s^{-1}}$)
Φ_z	vertical component of the volumetric water content flux ($\mathrm{m\,s^{-1}}$)
$\widehat{\phi}$	Soil porosity (1)
φ	azimuth (radians)
ρ	electrical resistivity (Ωm)
ρ_0	reference electrical resistivity corresponding to T_0 (Ωm)
ρ_a	density of air ($\mathrm{kg\,m^{-3}}$)
ρ_f	electrical resistivity of a partially frozen material (Ωm)
ρ_i	electrical resistivity of the same material in unfrozen state (Ωm)
ρ_p	electrical resistivity of the water in the pore space (Ωm)
ρ_snow	snow density ($\mathrm{kg\,m^{-3}}$)
ρ_w	density of water ($\mathrm{kg\,m^{-3}}$)
σ	Stefan-Boltzmann constant ($\mathrm{W\,m^{-2}\,K^{-4}}$)
Ψ	Matric potential ($\mathrm{ML^{-1}T^{-1}}$, kPa)
Ψ_b	Bubbling pressure ($\mathrm{ML^{-1}T^{-1}}$, kPa)
ψ	matric potential (m)
$\psi(\theta)$, $\psi(s)$	Water retention relationship (L, m)
ψ_b	Bubbling pressure (L, m)
ψ_s	air entry potential (m)
ω	diurnal frequency ($\mathrm{s^{-1}}$)
ω_p	precipitable water (cm)

Special

$(+)$	Symbol of fuzzy addition; all fuzzy arithmetic operations are symbolized with brackets, e.g.: $(+)$, (Σ), $(-)$, $(\bullet)$, $(\div)$, $(=)$, $(>)$, $(\leq)$ and $(\neq)$
$\overline{[\ ]}$	Long term mean annual value
$\overline{\langle\ \rangle}$	Long term mean monthly value
[ ]	Annual value
$\langle\ \rangle$	Monthly value
no brackets	Daily value

Abbreviations

PDD	positive degree-day sum
JSPS	Japan Society for the Promotion of Science
SD	standard deviation
DEM	digital elevation model
EFFS	European Flood Forecasting System
ISBA-CROCUS	energy balance-snow model
SVAT	soil-vegetation-atmosphere transfer model
GCM	Global Circulation Model
NWP	Numerical Weather Prediction
LAI	leaf area index
DTM	Digital terrain model
SCA	snow covered area
SRM	Snowmelt Runoff Model
NVE	Norwegian Water Resources and Energy Administration
CDD	cumulative degree-days
PACE	Permafrost and Climate in Europe
DC	direct current
MAAT	mean annual air temperature
SVAT	soil-vegetation-atmosphere transfer
NWP	numerical weather prediction
SOP	Special Observing Period
LUT	Look-Up Tables
MD	mean differences
CM	Chiew and McMahon
NS	Nash and Sutcliffe
ET	evaporation and transpiration
SHAW	Simultaneous Heat and Water
WRCCRF	Wind River Canopy Crane Research Facility
LAI	leaf area index
WRRS	Wind River Ranger Station
EC	eddy-covariance
ROI	Region Of Influence
TCEV	Two Component Extreme Value
LSS	land surface scheme
CLASS	Canadian Land Surface Scheme
GUH	geomorphological instantaneous unit hydrograph
GIS	geographic information system
MGS	Mackenzie GEWEX Study
CAGES	Canadian GEWEX Enhanced Study
RMS	root mean square
TAC	tracer aided catchment
ET	evapotranspiration
DEM	digital elevation models
ERU	Evaporation Response Units
HRU	Hydrological Response Units
RCM	Regional Climate Model
GCM	Global Circulation Models
SEBM	surface energy balance model
DOY	Days of Year
F	fractional vegetation cover
LAI	leaf area index
NDVI	normalized difference vegetation index
SFRM	Subsurface Flow Routing Model
LSHM	Land Surface Hydrology Model
LSFRM	Lateral Subsurface Flow Routing Model
DEM	Digital Elevation Model
USGS	United States Geological Survey
ECMWF	European Center for Medium Range Forecast
LAI	leaf area index
NDVI	Normalized Difference Vegetation Index
AVHRR	Advanced Very High Resolution Radiometer

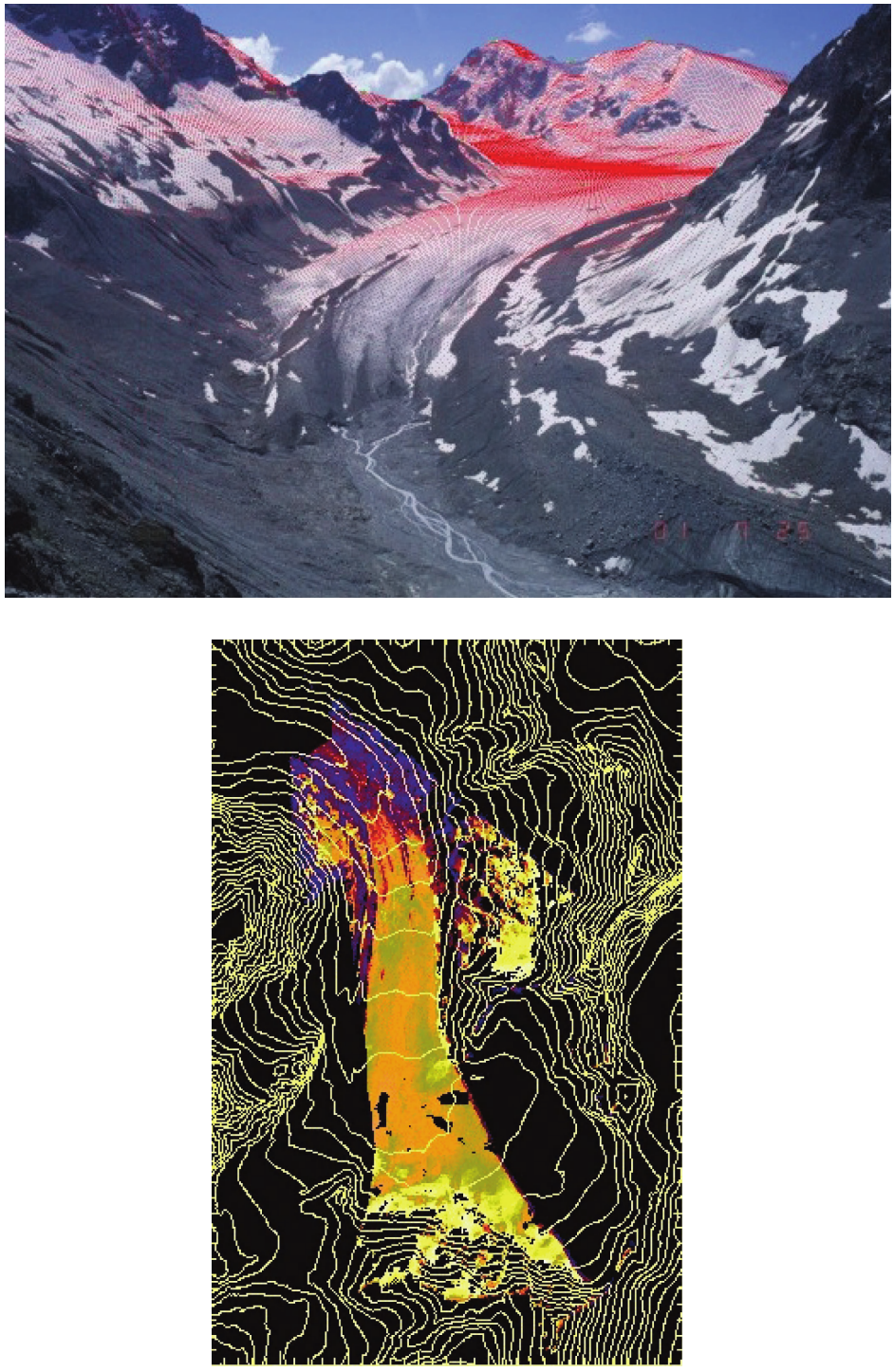


Plate 1 (Figure 3.4) Example of the technique used to estimate the ratio of snow cover and the spatial distribution of albedo, in this case applied to an Alpine glacier, Haut Glacier d'Arolla. Top photograph, the perspective projection of the DEM appears as grey dots, and from these, the georeferenced map of reflectance values on the bottom image is produced

Climate and Hydrology in Mountain Areas. Edited by C. de Jong, D. Collins and R. Ranzi
© 2005 John Wiley & Sons, Ltd. ISBN: 0-470-85814-1

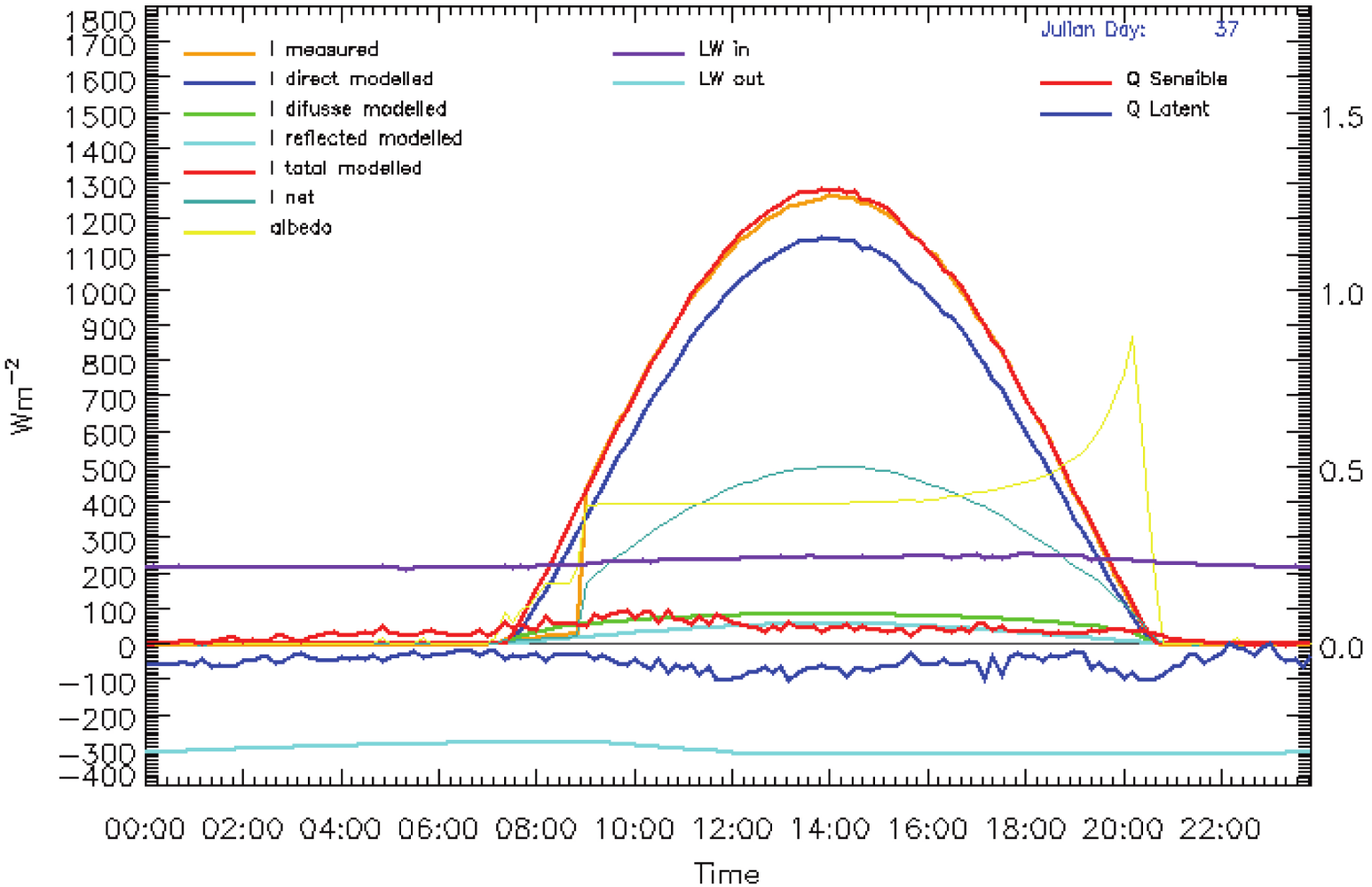


Plate 2 (Figure 3.5) Energy fluxes on a clear day on Loma Larga glacier, 4667 m a.s.l. DOY 37, 6th of February. Note the increasing albedo in the afternoon, an explanatory hypothesis is given in the text

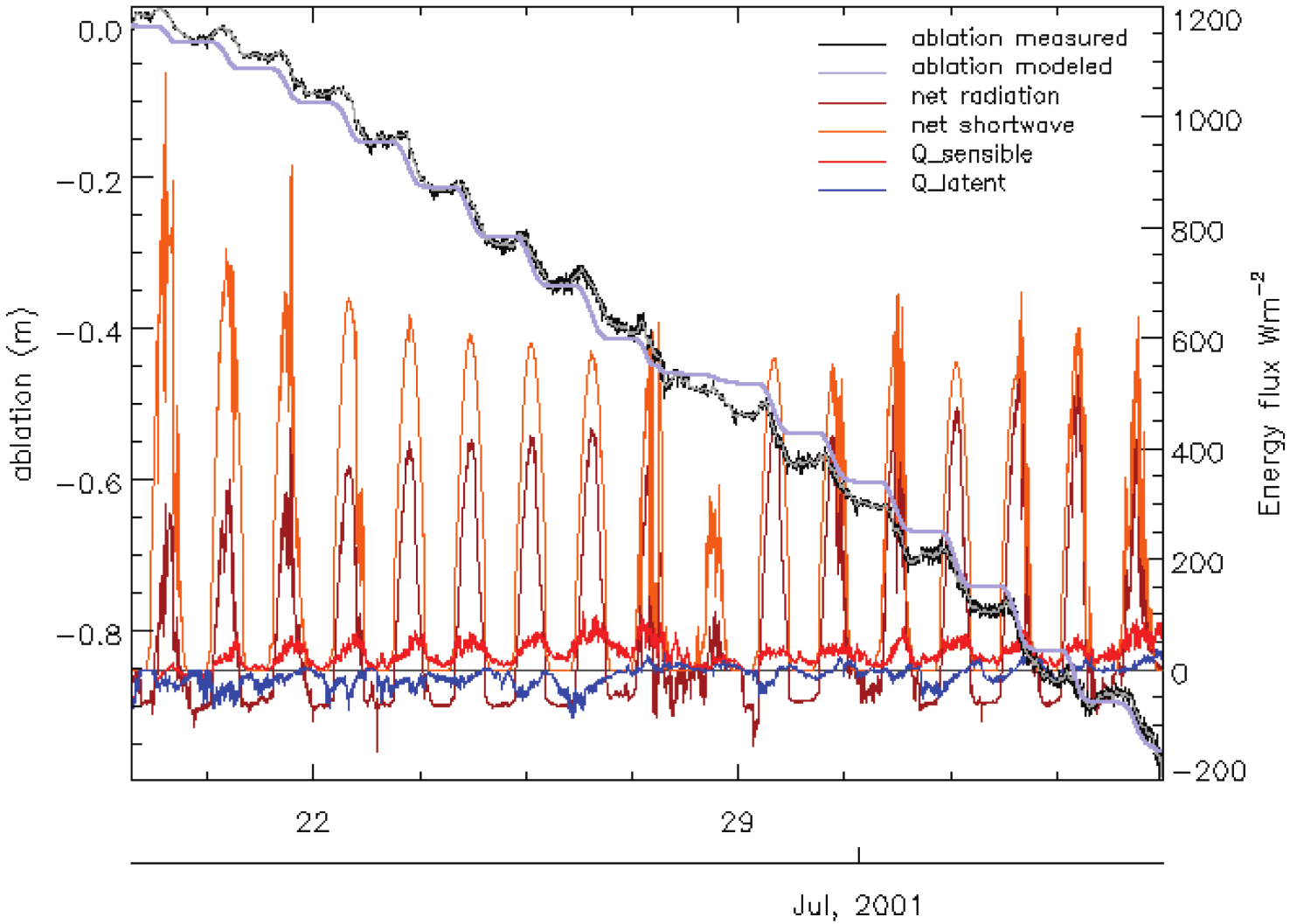


Plate 3 (Figure 3.6) Recorded solar radiation, estimated turbulent fluxes, and recorded and estimated snow ablation on the Haut Glacier d'Arolla from 19 June to 5 July 2001

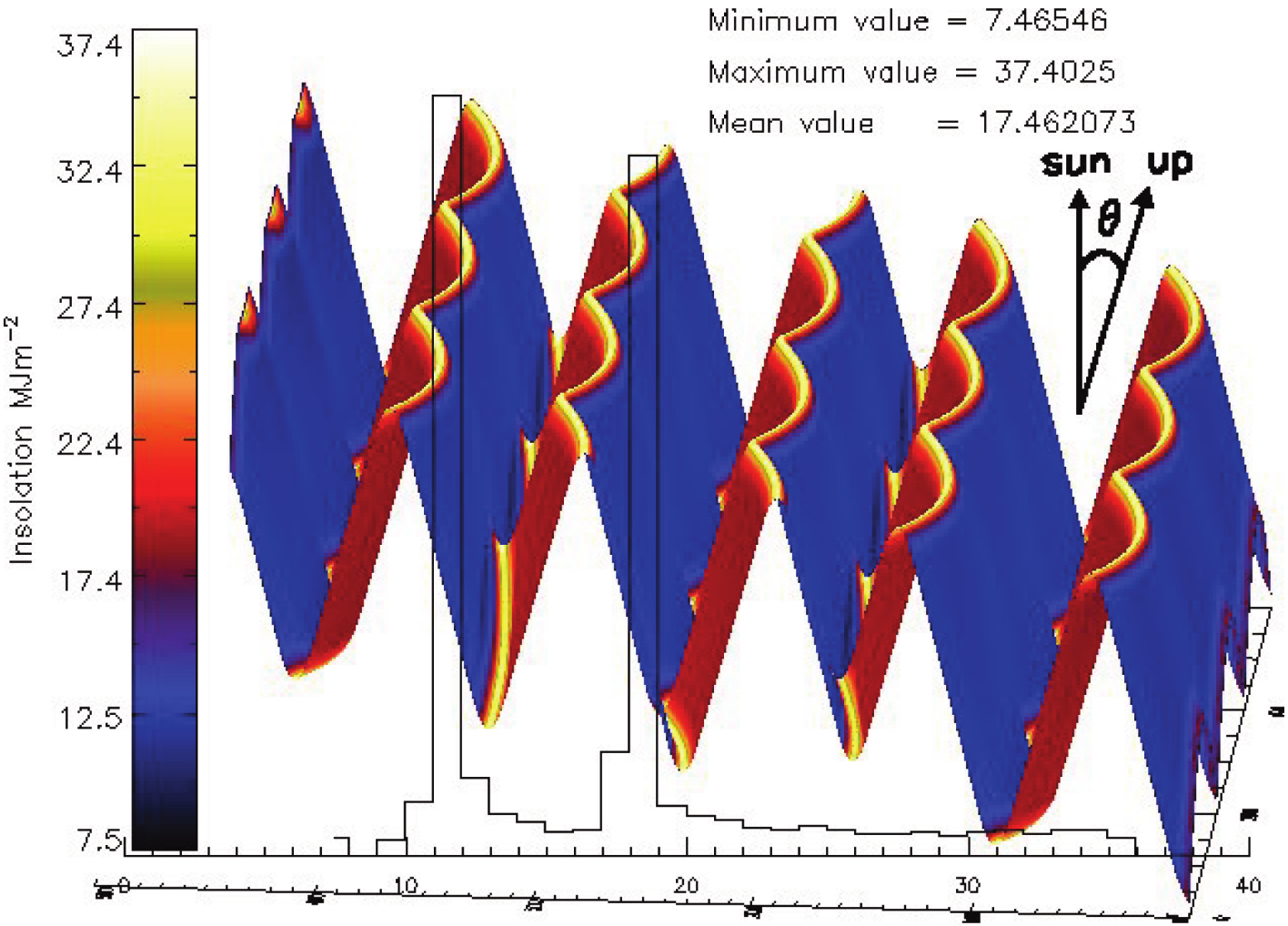


Plate 4 (Figure 3.7) Insolation on penitentes for the 37th day of the year, corresponding to values in Figure 3.5. Superimposed is the histogram of cell values, clearly showing a bimodal distribution of insolation values corresponding to the north-facing and south-facing slopes. The reference system is rotated at an angle θ so that the vertical is the direction of the sun at midday on the summer solstice

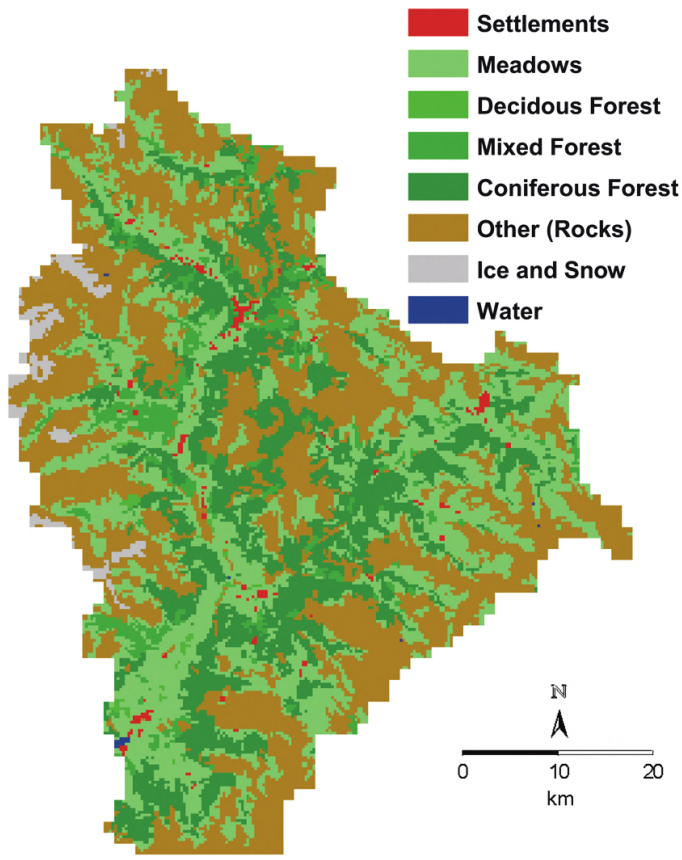
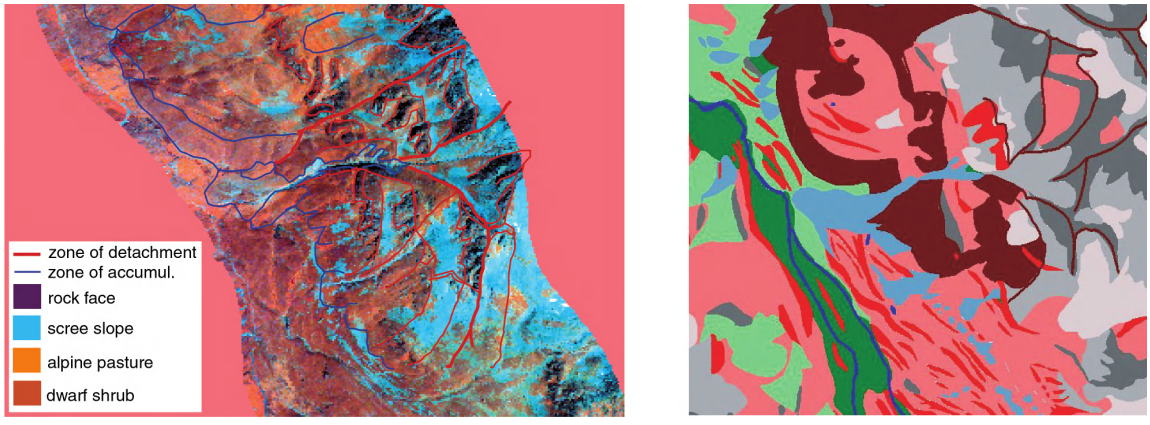


Plate 5 (Figure 4.4) Classified satellite image as provided by the CORINE land cover database



(a) (b)

Plate 6 (Figure 17.3a and b) (a) Remotely sensed CASI (Canadian Airborne System) image of the Duerrboden mass movement in Upper Dischma with a resolution of 5 m in the infrared canal and (b) enlargement of geomorphological map of corresponding area

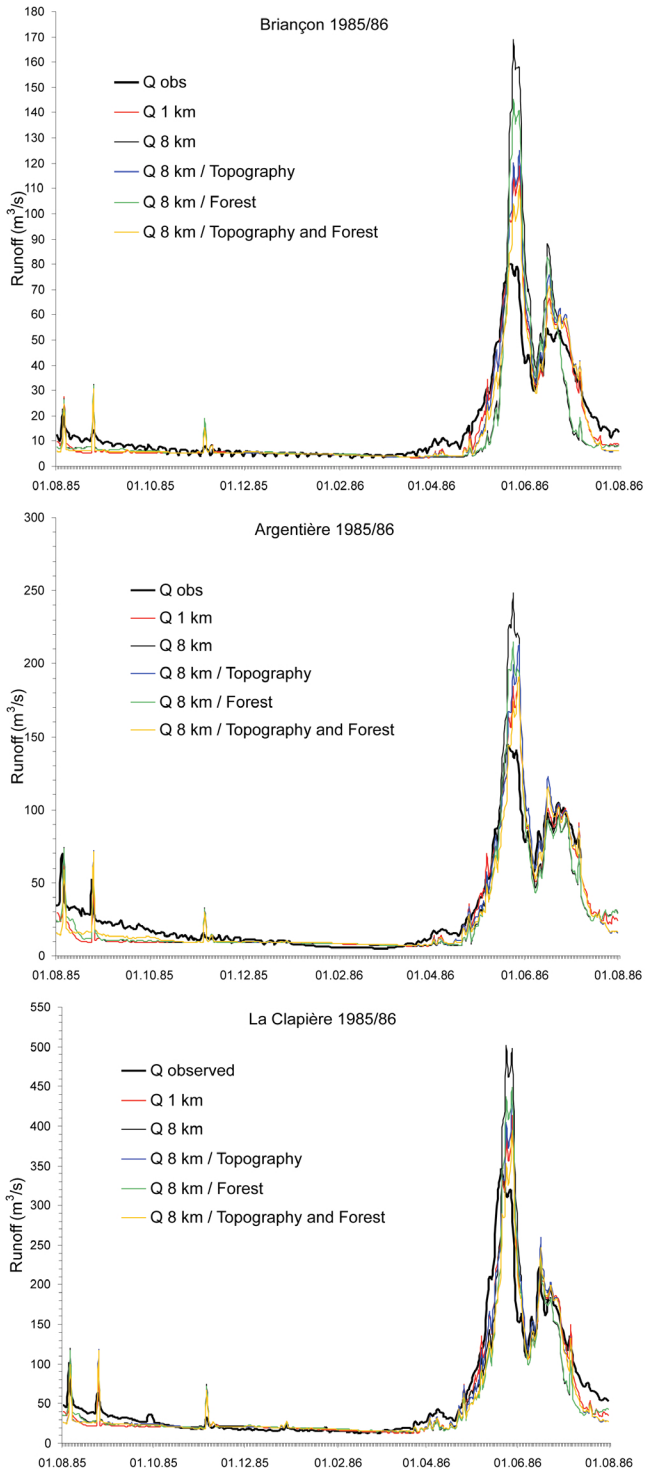


Plate 7 (Figure 4.5) Daily discharges in the upper Durance catchment, observed at the three gauging stations Briançon, L'Argentière and La Clapière for 1985/86 and modelled with different resolutions and subgrid parameterisations

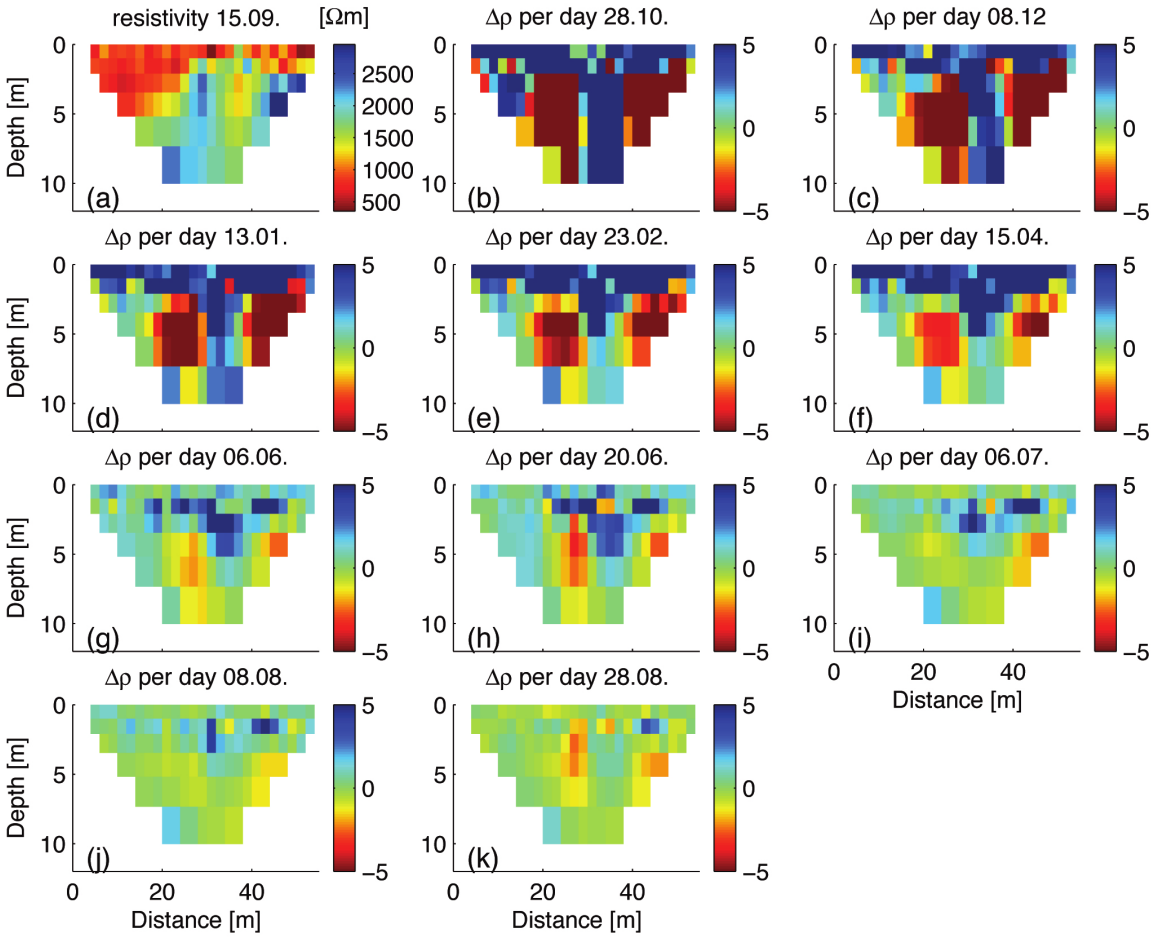


Plate 8 (Figure 6.7) (a) Resistivity model for the measurement on 15.9.1999 as determined by the inversion. (b)–(k) Resistivity difference per day based on the September measurement (a). Blue and red shading denote resistivity increase and decrease, respectively. From Hauck, C. & Vonder Mühll, D. 2003b. Permafrost monitoring using time-lapse resistivity tomography. In: Phillips, M., Springman, S.M. & Arenson, L.U. (eds): *Permafrost. Proc. 8th International Conference on Permafrost*, 21–25 July, Zurich, Switzerland, Vol. 1, 361–366, published by Balkema, Lisse. Reproduced with permission of Taylor and Francis

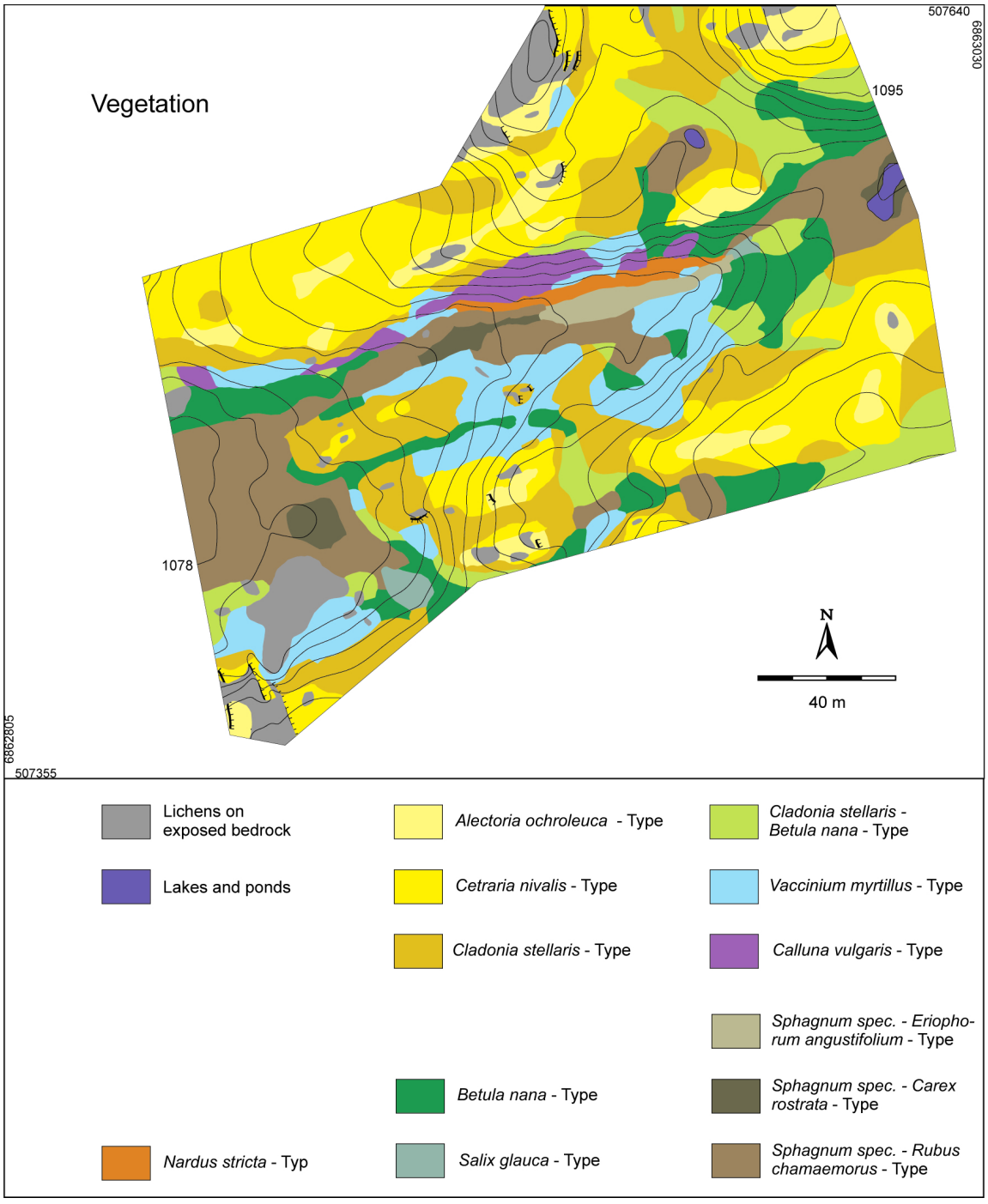


Plate 9 (Figure 13.15) Spatial differentiation of vegetation types in the lower alpine catchment (Löffler 1998)

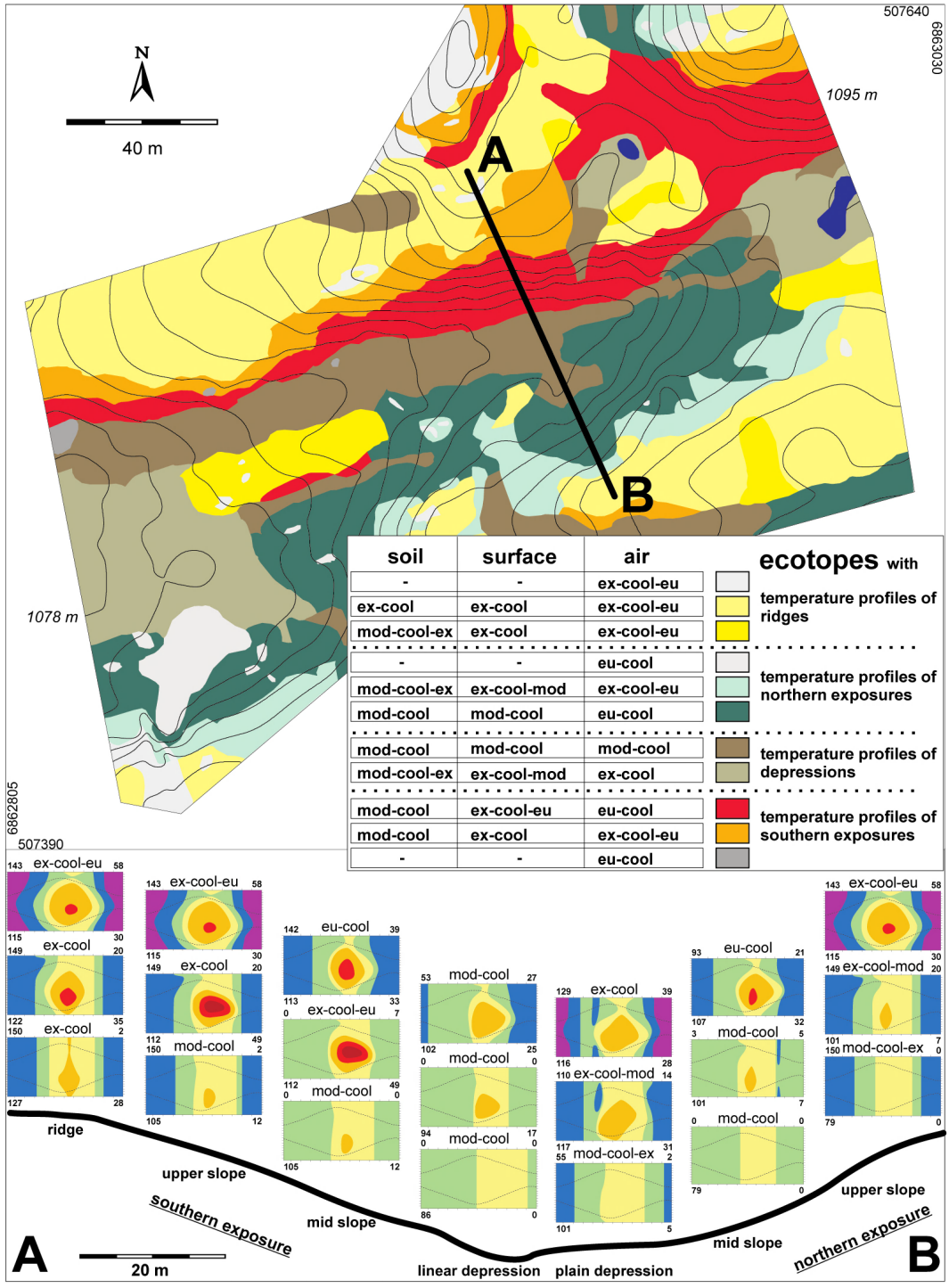


Plate 10 (Figure 13.17) Spatial differentiation of temperature dynamics in the lower alpine belt (Löffler & Wundram 2001). A schematic profile along a characteristic relief gradient is illustrated by thermoisopleth diagrams. Legend is given in Figure 13.19 and Table 13.3

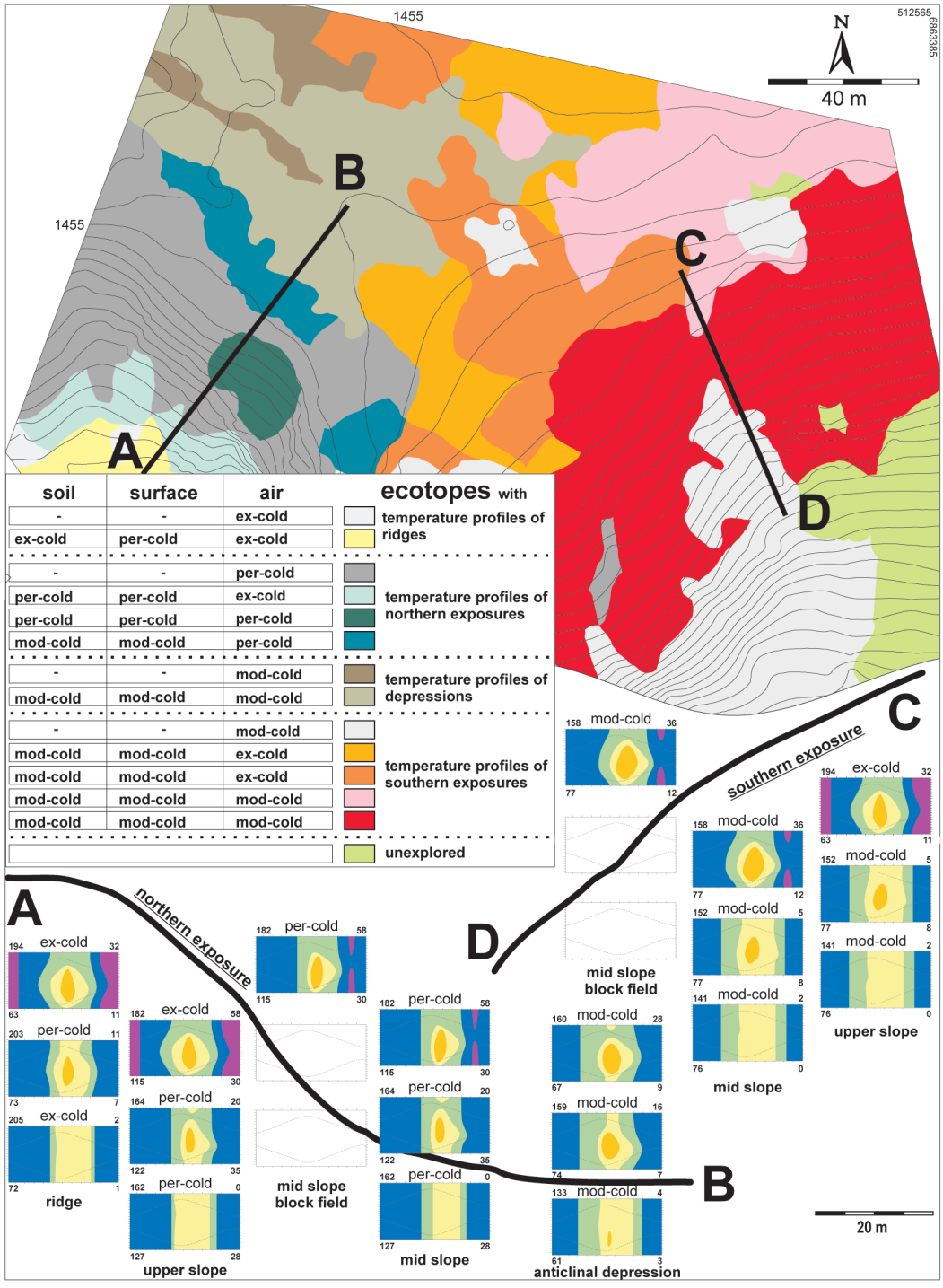


Plate 11 (Figure 13.18) Spatial differentiation of temperature dynamics in the middle-alpine belt (Löffler 2002a). A schematic profile along a characteristic relief gradient is illustrated by thermoisopleth diagrams. Legend is given in Figure 13.19 and Table 13.3

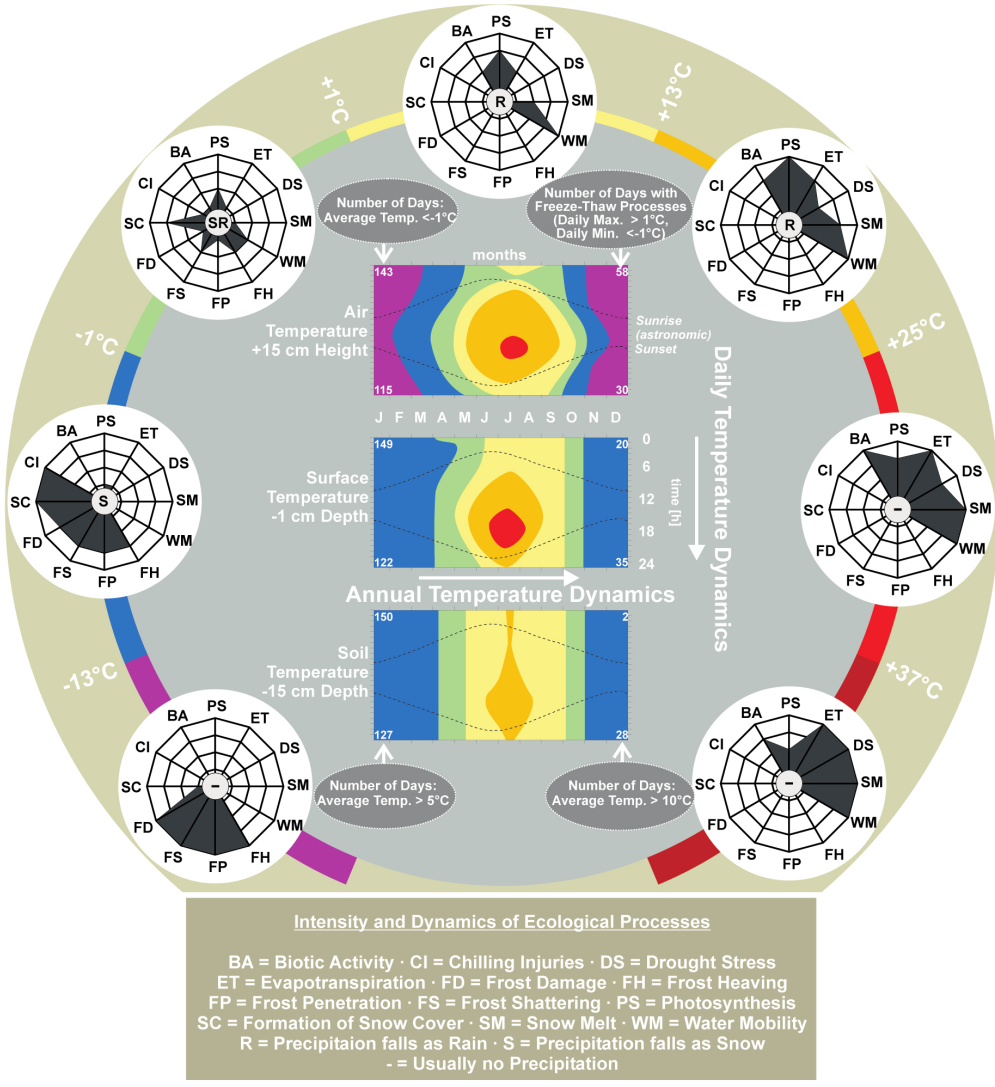


Plate 12 (Figure 13.19) Legend for landscape ecological maps and profiles in Figure 13.17 and Figure 13.18. The figure shows a complex scheme, systematically scaling temperatures according to their landscape ecological influence on ecosystem functioning. The three air, surface, and soil thermoisopleth diagrams show daily and annual changes of seven different ranges of temperatures with similar ecological values for a particular site. Those temperature ranges subdividing the outer circle into seven circular segments are grouped according to data from the literature, own investigations and theoretical considerations on 13 landscape ecological process attributes. Processes like photosynthesis, evapotranspiration, drought stress, and so on are in turn scaled on the individual axes within the small rose diagrams according to their ecological influence under those temperature conditions (from the inside to the outside: no, little, moderate, high and extreme influence). For example, temperatures under –13˚C are defined as no photosynthesis is done by any species, evapotranspiration is extremely reduced, processes like drought stress, snow melt, water mobility, and so on, are absent, but there is the danger of severe frost damage to plants, frost weathering of minerals and bedrock, frost penetration is extreme, frost heaving takes place and there is usually no precipitation under those conditions. As shown by the example of the thermoisopleth triple (lower alpine ridge site), those conditions are only found within the air temperature in +15-cm height during the whole daytime in December and January and during the nights in November and February. The scheme for the classification of temperature dynamics is given in Table 13.2. (Löffler & Wundram 2001). Reproduced by permission of Dr Christof Ellger

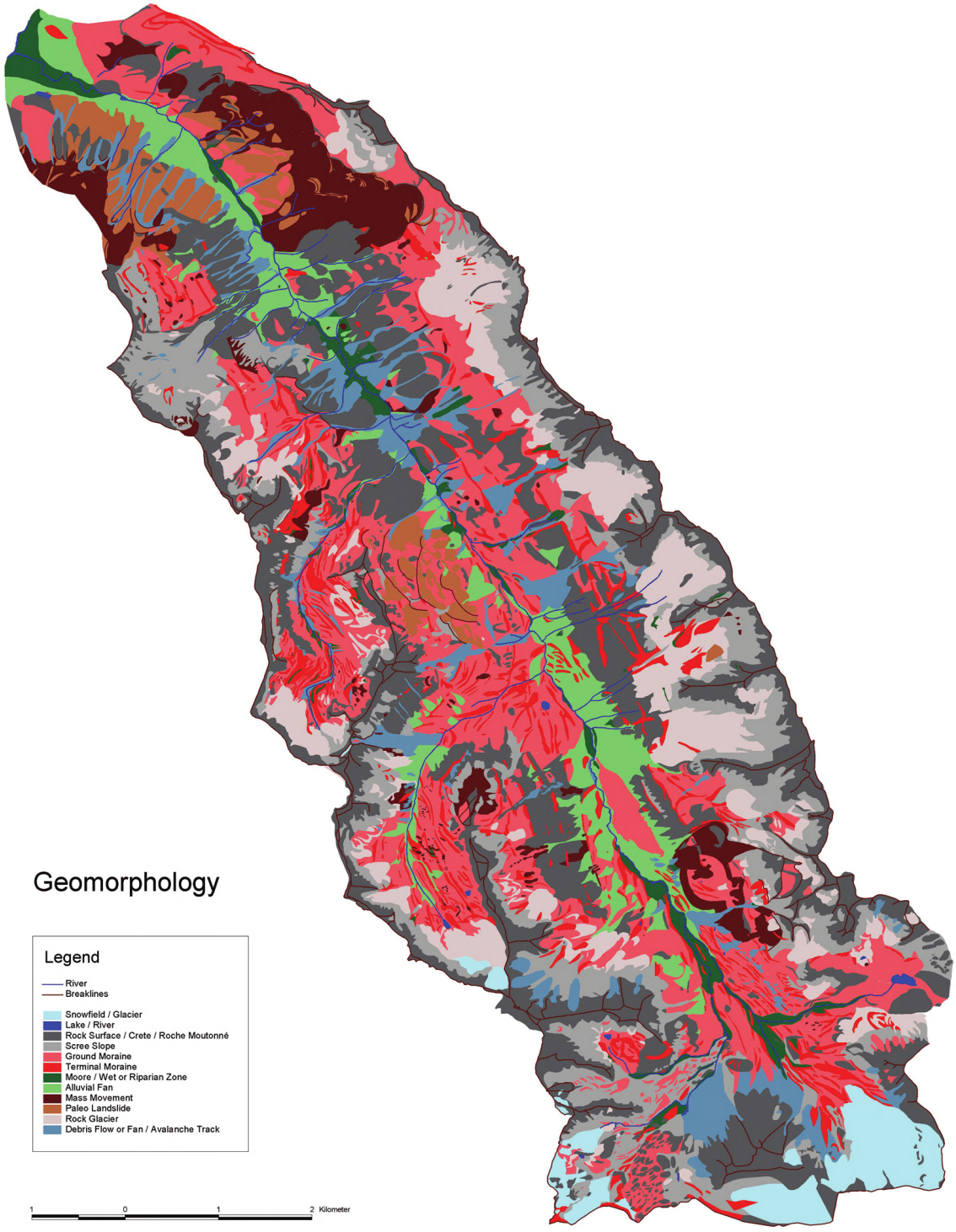


Plate 13 (Figure 17.2) Detailed geomorphological map of the Dischma divided into 14 different zones. The valley is dominated by moraines, scree slopes, rock faces, alluvial fans, glacier and snow fields

Introduction: Climate and Hydrology in Mountain Areas

Undoubtedly, the mountain regions of our world are the main hydrological and climatological triggers or pertubators of the water cycle as well as of complex meteorological patterns including phenomena such as the production or inhibition of rainfall. In terms of their role as water towers, mountain regions form an important supply of snow and/or rain-fed water to the lowlands. In terms of climate, mountain systems develop a considerably complex system of their own, influenced by the often characteristically narrow, deeply incised valleys. It is rare though, to find comprehensive work that combines both the hydrological and climatological aspects of mountain catchments. The purpose of this book is therefore to bring together a very diverse group of scientists from all over the world to present their multidisciplinary research in contrasting mountain environments. This effort was developed by Carmen de Jong in cooperation with Roberto Ranzi and David Collins during the International Year of the Mountains 2002 and is based on cross-disciplinary mountain sessions at EGS/EGU meetings, a diverse team of supportive meeting participants and invited scientists. The ultimate goal was, firstly, to provide a platform for discussion amongst highly motivated and trendsetting mountain groups from different origins and secondly, to combine two hitherto separately treated subject matters – that of hydrology and climatology in mountain areas. Although hydrology and climatology appertain to two separate disciplines, it is important to acknowledge the fact that in nature they are inseparable and that enough crosscutting areas exist that cannot ignore their mutuality. It is not always easy to bring together the different disciplines, but as long as scientists are cooperating strongly in the way observed in this group of authors, such endeavours are possible.

This book covers a wide range of mountain chains including the Alps, Black Forest, Himalayas, Tien Shan, Giant mountains, Norwegian mountains, Laurentian highlands, Appalachian mountains, Rockies, Andes, and Cascade mountains (see Figure 1). From the distribution of study areas covered, it is obvious that several African mountain ranges and other mountains of the southern hemisphere are missing in this volume. It is hoped to incorporate these in future editions.

The graph below (Figure 2) illustrates the correlation between study-area size and elevation. There is a clear lack of studies carried out in the higher altitudes and only six study sites have an average catchment elevation above 4000 m. Amongst these, all except one have catchment areas below 100 km^2. In future, it may be favourable to concentrate research on larger catchments at higher altitudes.

The book is divided essentially into five parts: (1) snow and ice melt, (2) soil water and permafrost, (3) evapotranspiration and water balance, (4) coupling meteorology and hydrology, and (5) climate change impact and mountain hydrology.

Roger Barry introduces the book with a review on alpine climate change and cryospheric responses. In the first section, Rijan Kayastha and his co-authors deal with methods for calculating snow and ice melt in the Himalayas and Pratap Singh and Lars Bengtsson assess methods for interpolation and extrapolation of snow-covered areas using air temperatures in the same region. In contrast, Javier Corripio and Ross Purves introduce a particularly intriguing study on snow and ice penitentes in the central Andes. Uli Strasser then shows how sub-grid parameterization and a forest canopy model can serve to improve snowmelt runoff modelling in the humid, French Alps.

In the second section, Christain Hauck and his co-authors present a coupled geophysical and meteorological approach for monitoring permafrost in the Swiss Alps, while Daniel Bayard and Manfred Stähli monitor the effects of frozen soil on groundwater recharge in the same mountain ranges. A study on the water balance in surface soil is presented by Marilena Menziani and her

Climate and Hydrology in Mountain Areas. Edited by C. de Jong, D. Collins and R. Ranzi
© 2005 John Wiley & Sons, Ltd. ISBN: 0-470-85814-1

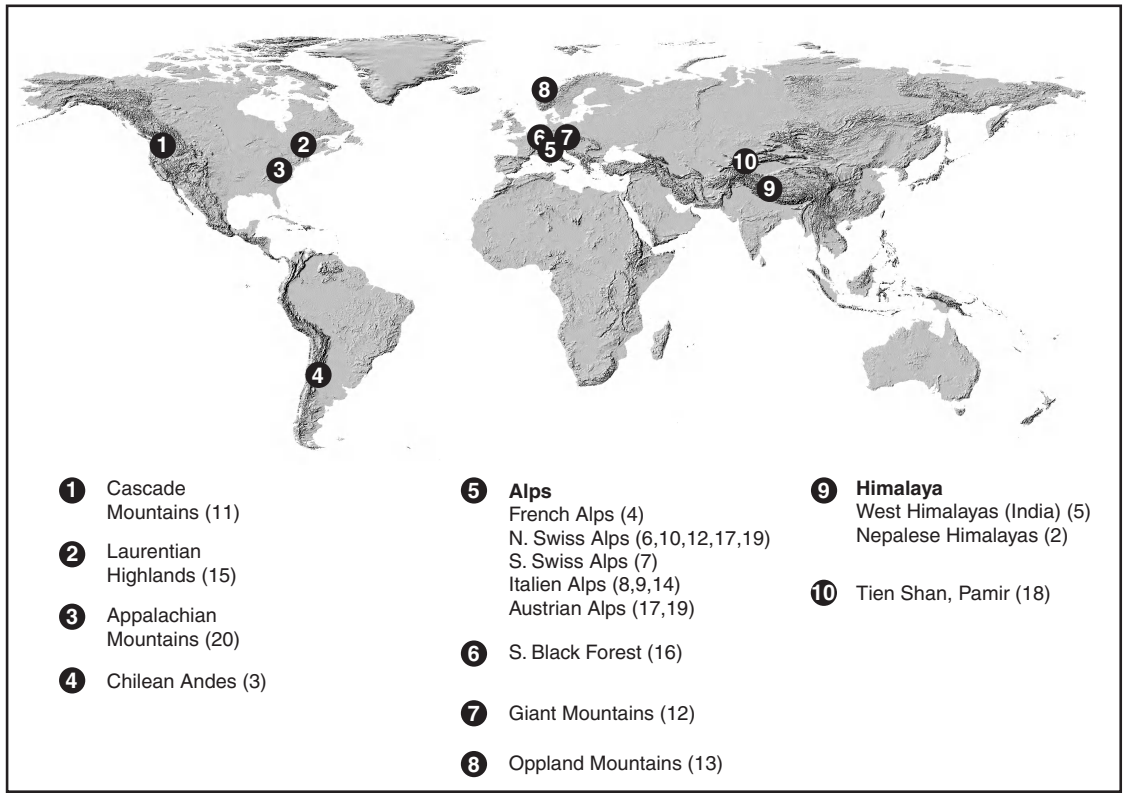


Figure 1 Location of catchments and experimental sites presented in this book. Chapter numbers associated with mountain ranges are indicated in brackets

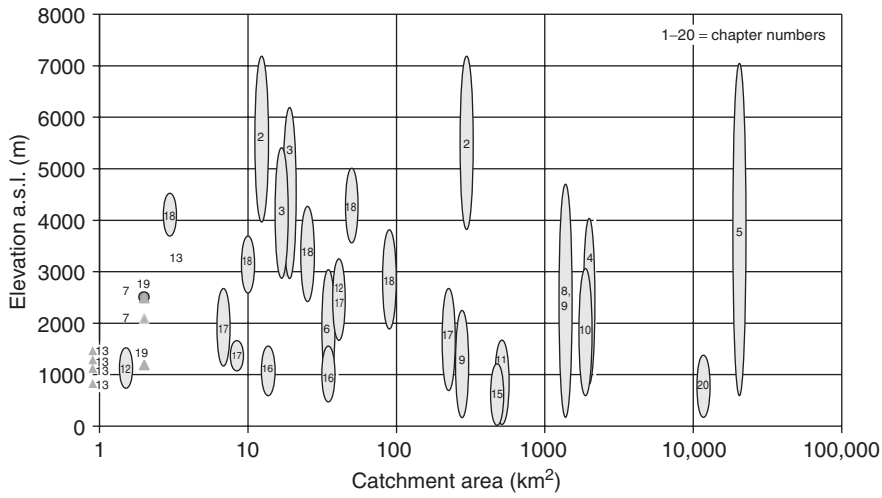


Figure 2 Relation between catchment size and mean catchment altitude for the study sites presented in this volume

co-authors with a combined analytical and measurement approach for an alpine valley in Italy, whereas Stefano Barontini and his co-authors describe saturated hydraulic conductivity and water retention relationships for mountain soils in the same mountain chain.

Gerald Eder introduces the third section with a relatively new approach of water balance modelling using fuzzy parameterization in the Austrian Alps. There is a jump then to Cascade mountains in Washington, USA, where Timothy Link and his co-authors monitor the water relations in an intensively instrumentized old growth douglas fir stand. This is followed by another field-based study by Carmen de Jong and her co-authors, where measurements of condensation and evapotranspiration are compared for the Giant Mountains in Poland and the Swiss Alps. Jörg Löffler and Ole Rößler describe an integrated approach for measuring and modelling the hydrology and ecology of mountain basins in Central Norway.

The fourth section is introduced by an overview from Baldassare Bacchi and Vigilio Villi on runoff and floods in the Alps, emphasizing precipitation and runoff formation in addition to flood frequency analysis. In this section, Charles Lin and his co-authors use an interesting coupled meteorological and hydrological modelling approach based on geomorphological principals for flood simulation in the mountainous Sageunay basin in eastern Canada. Stefan Uhlenbrook and Doerthe Tetzlaff assess convective precipitation using operational weather radar as a tool for flood modelling in the Black Forest, Germany. Geomorphological zoning as a tool for improving the coupling of hydrology and meteorology is proposed by Carmen de Jong and her co-authors for the Austrian and Swiss Alps.

In the final section, Wilfried Hagg and Ludwig Braun analyse the influence of glacier retreat on water yield in the high mountain basins of the Alps and Tien Shan. Staying in the Swiss Alps, Franziska Keller and Stephane Goyette model snowmelt under different climate change scenarios. Finally, Osman Yildiz and Ana Barros model water and energy budgets in the Appalachian mountains under climate variability and hydrological extremes.

In summary, it can be said that the studies integrate an interesting combination of field-based and modelling approaches, with several studies concentrating on the coupling of hydrology and meteorology. The large variety of approaches necessary for well-to-low-instrumented catchments are highlighted and with this comes a general appeal for more long-term monitoring programmes and field-based studies to validate model results. Since mountain regions are remote and difficult environments, a good field-based approach cannot be taken for granted. Thus, the sophistication of field and remote-sensing techniques should keep in pace with the development of modelling concepts, in particular for mountain ranges in developing countries and in arid environments.

Although this comprehensive book has seen a long way from its conception to its production, it is important to state that all chapters were sent to two international reviewers that, with few exceptions, were not authors of the book. We are very grateful to the many hours invested by these voluntary reviewers. It can be imagined that this was not always easy since the subject area is not that widespread.

Our particular thanks go to Martina Knop and Heike Kemmerling of the Geography Department of the University of Bonn for their invaluable administrative support as well as to Martin Gref for his cartographic help and to the family of Carmen de Jong for supporting the long extra hours involved with the reviewing and editing this book. Stefan Taschner of the Department of Civil Engineering at the University of Brescia and Keily Larkins from Wiley are acknowledged for their help in the editorial process.

Carmen de Jong
Roberto Ranzi
David Collins

1

Alpine Climate Change and Cryospheric Responses: An Introduction

ROGER G. BARRY
NSIDC/CIRES, University of Colorado, Boulder, CO. 80309-0449, USA

1.1 INTRODUCTION

As an introduction to the following chapters dealing with changes in snow and ice conditions in high mountain regions, and their hydrological consequences, a brief overview of recent changes in alpine climates and associated cryospheric responses is presented.

Direct observations and proxy records indicate that historical and recent changes in climate in many mountain regions of the world are at least comparable with, and locally may be greater than, those observed in the adjacent lowlands, Pfister (1985). Actual and potential responses in cryospheric variable include a rise in the snowline, a shorter duration of snow cover, glacier recession, break out of ice-dammed lakes, warming of perennially frozen ground, and thawing of ground ice.

The changes – including the loss of ice core records of climate history as tropical glaciers and ice caps warm and melt water destroys the ice stratigraphy – are of scientific importance. There are also critical socioeconomic implications. These include direct effects of the changes on water resources and hydropower generation, on slope stability, and on hazards relating to avalanches and glacier lakes. Indirect effects include economic and social costs for winter tourism based on skiing and associated sports; and impacts on agricultural, industrial, and consumptive use of water that is strongly influenced by the annual cycle associated with snow and ice melt runoff.

1.2 EVIDENCE FOR CHANGES IN CLIMATE IN MOUNTAIN REGIONS

Global mean annual temperature has risen by just over 0.6°C over the last century, with accelerated warming in the last 10 to 15 years. The evidence for changes in climate in mountain areas is both direct and indirect. Observational records are available from the late nineteenth century at a number of mountain observatories, mostly in Europe (Barry 1992). They indicate that mean temperatures have risen by amounts generally comparable with those observed in the lowlands during the twentieth century; however, there are some differences in the pattern of seasonal and diurnal changes. In a survey of available high-elevation data, Diaz and Bradley (1997) present changes in zonally averaged temperatures for 1951–1989 between 30° and 70°N, versus elevation. Mean maximum temperatures increased slightly between 500 and 1500 m, with minor changes at higher elevations, while minimum temperatures rose by about 0.2°C/decade at elevations from 500 m to above 2500 m. In the Rocky mountains, Pepin (2000) documents altitudinal differences in the changes in the Colorado Front Range since 1952, with overall cooling at 3750 m but warming between 2500 and 3100 m. This results in complex changes in lapse rate. In the tropical Andes, mean annual temperature trends have been determined for 268 stations between 1°N and 23°S, for 1939–1998 (Vuille and Bradley 2000). They find an overall warming of about 0.1°C/decade, but the rate tripled to +0.32–0.34°C/decade over the last

Climate and Hydrology in Mountain Areas. Edited by C. de Jong, D. Collins and R. Ranzi
© 2005 John Wiley & Sons, Ltd. ISBN: 0-470-85814-1

25 years. The warming varies with altitude, but there is generally reduced warming with elevation. This is especially apparent on the western (Pacific) slopes of the Andes.

Brown *et al*. (1992) demonstrated that lapse rates between the high plains (1200–1500 m) and three stations at 3200 m in the Colorado Rocky mountains had weakened in the daytime, but strengthened at night. Globally, the decrease in diurnal temperature range is attributed to increased cloud cover, locally augmented by changes in precipitation and soil moisture (Dai *et al*. 1999). An analysis of lapse rates in the Pennines of northern England indicates that atmospheric temperature and moisture level, cloudiness/solar radiation, and wind speed determine lapse rates (Pepin *et al*. 1999). Thus, changes in lapse rate are complex and may result solely or partly from changes in the frequency of cyclonic/anticyclonic circulation regimes. A shallower/steeper lapse rate may be expected under warmer, moister atmospheric conditions/increased solar radiation. The amplitude of diurnal change in lapse rate intensifies under anticyclonic conditions and slack pressure gradients.

In some mountain regions, monitoring of ground temperatures has begun recently. In the northern Tien Shan, permafrost ground temperatures have risen by 0.2–0.3°C over the last 25 years (Gorbunov *et al*. 2000). The depth of seasonal freezing has not changed significantly in the low mountains, but there has been a decrease in the depth between 1400 and 2700 m, while above 3000 m the depth of seasonal freezing is increasing. In the Swiss Alps, Haeberli (1994) estimated permafrost warming by about 1°C between 1880 and 1950, then stabilizing, before accelerated warming in the late 1980s to at least 1992. However, a 10-year borehole record (Vonder Mühll *et al*. 1998) indicates that warming until 1994 was largely compensated by rapid cooling between 1994 and 1996.

Proxy evidence of climatic change is available from changes in glacier size dated by lichenometry and carbon-14, from tree-ring series, and from ice cores, *inter alia.* Numerous accounts from various mountain regions exemplify these results (Luckman 1997; Luckman and Villalba 2001; Solomina 1999; Kaser 1999). These sources become even more important in mountain regions that lack direct records, or where these are of short duration, as in the Andes and other tropical regions (Barry and Seimon 2000). Diaz and Graham (1996) reported a rise of 100–150 m in the altitude of the freezing level in the atmosphere over the inner tropics (10°N–10°S) between 1970 and 1986; this is correlated with a warming in the sea surface over the eastern tropical Pacific. The characteristics of glacier energy balances in the central Andean region is addressed by Corripio and Purves (Chapter 3).

1.3 CRYOSPHERIC RESPONSES

The effects of global warming on the cryosphere in mountain areas are most visibly manifested in the shrinkage of mountain glaciers and in reduced snow cover duration. However, the responses are by no means linear. For example, warmer winters imply higher atmospheric moisture content and more snowfall is associated with an overall increase in precipitation. Records of glacier length and mass balance during the second half of the twentieth century show reductions in continental climatic regimes, but increases in maritime regimes, such as Norway, southern Alaska and coastal areas of the Pacific Northwest in Canada, and the United States. In the Tropics, the rise in freezing level noted above, as well as changes in atmospheric humidity and perhaps cloudiness, in some cases, has given rise to progressive reduction in mountain glaciers and ice caps over the last century. Particularly, dramatic changes are evident in East Africa where there has been a 75% reduction in ice area on Mount Kilimanjaro since 1912 (Hastenrath and Greischar 1997). The ice cover on East African summits will be lost within 20 years or so, unless there is a dramatic shift in climatic conditions.

In an example of subtle changes in snow cover, Böhm (1986) reported a reduction in May–September snow cover at Sonnblick (3106 m), Austria, from 82 days during 1910–1925 to 53 days in 1955–1970. The mean summer temperature was about 0.5°C higher in the second interval. However, the associated change in snow cover duration estimated from average gradients of snow cover duration and temperature lapse rate would only be about 10–11 days (Barry 1990). Such nonlinear responses may arise through local albedo-temperature feedback effects, but this still requires thorough investigation. Keller and Goyette (Chapter 19) provide scenarios of snowmelt in the Swiss Alps under climatic changes.

Large responses are expected in the annual hydrologic regime of rivers where a significant proportion of the runoff is from melt of snow cover and from wastage of ice in heavily glacierized basins. Runoff models under global warming scenarios project a higher and earlier peak of spring runoff from snowmelt and reduced flow in summer (Rango and Martinec 1998). For the upper Rhône, for example, Collins (1987) found discharge correlated with mean summer temperature; a 1°C cooling between 1941–1950 and 1968–1977 led to a 26% decrease in mean summer discharge. Warming trends will

have the opposite effect, but a dominant component of runoff change in heavily glacierized basins is attributable to the reduction in ice area. Chen and Ohmura (1990) calculated an 11% decrease in runoff from a basin of the upper Rhône drainage with 66% ice cover between 1922–1929 and 1968–1972, compared with only 6% decrease in one with about 17% ice cover between 1910–1919 and 1968–1972. In the latter case, the Rhône at Porte du Scex, runoff changes responded also to changes in climate but a decrease in basin precipitation was offset by the effect of warmer summers increasing the ice melt. The introductory chapter and Chapter 18 address this topic using more recent and extensive data.

1.4 SOCIOECONOMIC CONSEQUENCES

Socioeconomic effects of changes in mountain snow and ice characteristics will be both direct and indirect. Direct effects associated with a shorter snow season and shallower snow cover will include the reduction or loss of winter sports facilities, or the necessity for enhanced reliance on snowmaking capabilities, with attendant losses of income and adaptation costs. For the Austrian Alps, losses will be exacerbated at lower elevations. Secondary effects resulting from this change may include the loss of related service activities and income at mountain resorts. Summer tourism may also be affected as scenic mountain glaciers shrink and waste away. Maintaining tourist access to the terminus of the Upper Grindelwald glacier, in retreat since the mid-1980s, for example, has necessitated the construction of a wooden stairway.

The changes in snowmelt runoff and its timing will have direct impacts on hydropower generation and impose requirements for alternative power sources. Power outages and loss of revenue by utility companies may be expected, depending upon the relative contribution of hydropower to total electricity generation. In adjacent lowland areas where spring runoff is a major source of water for irrigation and for stocking reservoirs, there may be even greater economic consequences. Changes in snow pack will also affect soil moisture levels in spring and summer, with implications for soil biota, fire risk, and the productivity of mountain pastures and forests (Price and Barry 1997).

REFERENCES

Barry, R.G. 1990. Changes in mountain climate and glacio-hydrological responses. *Mt. Res. Dev.* **10**: 161–70.

Barry, R.G. 1992. Mountain climatology and past and potential future climatic changes in mountain regions: A review. *Mt. Res. Dev.* **12**: 71–86.

Barry, R.G. and Seimon, A. 2000. Research for mountain area development: Climate fluctuations in the mountains of the Americas and their significance. *Ambio* **29**: 364–70, Corrigendum. Ambio 30, 69.

Böhm, R. 1986. *Der Sonnblick. Die 100-Jährige Geschichte des Observatoriuns und Seiner Forschungstätigkeit*, Oesterreichischer Bunderverlag, Vienna, p. 224.

Brown, T.J., Barry, R.G. and Doesken, N.J. 1992. An exploratory study of temperature trends for paired mountain – plains stations in Colorado, *Sixth Conference on Mountain Meteorology*, American Meteorological Society, Boston, MA, pp. 181–84.

Chen, J.-Y. and Ohmura, A. 1990. On the influence of Alpine glaciers on runoff. In H. Lang and A. Musy, eds., *Hydrology in Mountain Regions I. Hydrological Measurements, The Water Cycle*, *IAHS Publication No. 193*, IAHS Press, Wallingford, CT, pp. 117–25.

Collins, D.N. 1987. Climatic fluctuations and runoff from glacierized alpine basins. In S.L. Solomon, M. Beran and W. Hogg, eds., *The influence of climatic change and climatic variability on the hydrological regime and water resources*. International Association of Hydrology Publication 168, IAHS Press, Wallingford, UK, pp. 77–89.

Dai, A., Trenberth, K.E. and Karl, T.R. 1999. Effects of clouds, soil moisture, precipitation and water vapor on diurnal temperature range. *J. Clim.* **12**: 2451–73.

Diaz, H.F. and Bradley, R.S. 1997. Temperature variations during the last century at high elevation sites. *Clim. Change* **36**: 253–80.

Diaz, H.F. and Graham, N.E. 1996. Recent changes of tropical freezing heights and the role of sea surface temperature. *Nature* **383**: 152–55.

Gorbunov, A.P., Marchenko, S.S. and Seversky, E.V. 2000. Permafrost and seasonally frozen ground response to climate changes in the northern Tien Shan. *Krisfera Zemli* **4**: 11–17.

Haeberli, W. 1994. Accelerated glacier and permafrost changes in the Alps. In M. Beniston, ed., *Mountain Environments in Changing Climates*, Routledge, London, pp. 91–107.

Hastenrath, S. and Greischar, L. 1997. Glacier recession on Kilimanjaro, East Africa, 1912–89. *J. Glaciol.* **43**(145): 4655–59.

Kaser, G. 1999. A review of the fluctuations of modern tropical glaciers. *Global Planet. Change* **23**: 93–103.

Luckman, B.H. 1997. Developing a proxy climate record for the last 300 years in the Canadian Rockies – some problems and opportunities. *Clim. Change* **36**: 455–76.

Luckman, B.H. and Villalba, R. 2001. Assessing the synchroneity of glacier fluctuations in the western cordillera of the Americas during the last millennium. In V. Markgraf, ed., *Interhemispheric Climate Linkages*, Academic Press, San Diego, CA, pp. 119–40.

Pepin, N. 2000. Twentieth century change in the Front Range climate record. *Arct. Antarct. Alp. Res.* **32**: 135–46.

Pepin, N., Benham, D. and Taylor, K. 1999. Modeling lapse rates in the maritime uplands of northern England: Implications for climate change. *Arct. Antarct. Alp. Res.* **31**: 151–64.

Pfister, C. 1985. Snow cover, snowlines and glaciers in central Europe since the sixteenth century. In M.J. Tooley and G.M. Sheail, eds., *The Climate Scene*, George Allen and Unwin, London, pp. 155–74.

Price, M.F. and Barry, R.G. 1997. Climate change. In B. Messerli and J.D. Ives, eds., *Mountains of the World. A Global Priority*, Parthenon Publishing, New York, pp. 409–45.

Rango, A.S. and Martinec, J. 1998. Effects of global warming on runoff in mountain basins representing different climatic zones. In H. Weater and C. Kirby, eds., *Hydrology in a Changing Environment*, Vol. 1, John Wiley, Chichester, pp. 133–39.

Solomina, O. 1999. *Gornoe Oledenenie Severnoi Evrazi v Golotsene (Mountain Glaciation in Northern Eurasia During the Holocene)*, Nauchny Mir, Moscow, p. 263.

Vonder Mühll, D.S., Stucki, T. and Haeberli, W. 1998. Borehole temperatures in alpine permafrost: A ten-year series. In A.G. Lewcowitz and M. Allard, eds., *Proceedings, The 7th International Permafrost Conference*, University of Laval, Quebec, pp. 1089–95.

Vuille, M. and Bradley, R.S. 2000. Mean annual temperature trends and their vertical structure in the tropical Andes. *Geophys. Res. Lett.* **27**: 3885–88.

PART I: SNOW AND ICE MELT

Climate and Hydrology in Mountain Areas. Edited by C. de Jong, D. Collins and R. Ranzi
© 2005 John Wiley & Sons, Ltd. ISBN: 0-470-85814-1

2

Use of Positive Degree-Day Methods for Calculating Snow and Ice Melting and Discharge in Glacierized Basins in the Langtang Valley, Central Nepal

RIJAN B. KAYASTHA, YUTAKA AGETA AND KOJI FUJITA
Dept. of Hydrospheric-Atmospheric Science, Graduate School of Environmental Studies, Nagoya University, Nagoya 464-8601, Japan

2.1 INTRODUCTION

Prediction of melting of snow and ice in a glacierized basin is very important to estimate basin discharge. It is more important in the Himalayas where direct field observations are very difficult to carry out because of rugged and remote mountain terrain. The most important energy source for glacier ablation in the Himalayas is radiation. Many studies have shown that net radiation is the dominant energy source for ablation. The net radiation contributes more than 80% of the total energy supply for ablation in the Nepalese Himalayas (Ohata and Higuchi 1980; Kayastha *et al*. 1999; Kayastha 2001).

Several models and empirical relations have been proposed to calculate glacier ablation in the Nepalese Himalayas, for example, empirical relations to calculate glacier ablation by Ageta and Higuchi (1984), a simplified model for estimating glacier ablation under debris layer by Nakawo and Takahashi (1982) and Rana *et al*. (1996), and energy balance modeling for glacier mass balance on Glacier AX010 by Kayastha *et al*. (1999).

The ablation areas of many glaciers in the Himalayas are covered with debris. Debris has a strong influence on the surface energy balance and melting of the underlying ice. The thermal conductivity (or thermal resistance) and albedo are the main physical characteristics of a debris layer that control heat conduction to the ice–debris interface. Kayastha *et al*. (2000b) studied the practical prediction of ice melting beneath various thicknesses of debris cover on Khumbu Glacier, Nepal, using a positive degree-day factor. Positive degree-day factors for ablation under various debris thicknesses were found and a practical relationship between debris properties and degree-day factor was established for estimating ablation under a debris layer.

A conceptual runoff model called HYCYMODEL is used in Langtang Khola Basin (Khola means a small river in Nepali) by Fukushima *et al*. (1991) to estimate streamflow change by global warming. They used Ageta and Higuchi (1984)'s empirical relation to calculate snow and ice melt. Their study did not take into account the effect of debris on glacier surface, which may accelerate or retard melting of underlying ice depending upon its thickness. Braun *et al*. (1993) applied the conceptual precipitation-runoff model in the same basin for better understanding of hydrological processes and efficient planning and operation of water resources. Similarly, Rana *et al*. (1996) used the same

Climate and Hydrology in Mountain Areas. Edited by C. de Jong, D. Collins and R. Ranzi
© 2005 John Wiley & Sons, Ltd. ISBN: 0-470-85814-1

HYCYMODEL and empirical relation for melting of snow and ice for modeling runoff from the basin with inclusion of effect of debris on melting of underlying ice. All these three runoff models need daily data of air temperature, precipitation, and other parameters.

Regarding a method to predict snow and ice melt in the Himalayas, the method should be simple with a minimum field data requirement. Therefore, the positive degree-day method is applied to estimate snow and ice melt from debris-free areas as well as ice melt under debris layers. The degree-day method is based on the assumption that the melting of snow or ice during any particular period is proportional to the sum of daily mean temperatures above the melting point during that period, and the sum is called the *positive degree-day sum* (PDD). The factor linking ablation to this temperature sum is the positive degree-day factor. The degree-day factor involves a simplification of complex processes that are properly described by the energy balance of the glacier surface and overlaying atmospheric boundary layer (Braithwaite and Olesen 1989). This is because the factors that determine the melt process are correlated with temperature or, in other words, the air temperature contains information on the major energy sources. For example, in the net radiation, the incoming longwave radiation is the dominant component of incoming heat source for melt at surface, which transfers information of air temperature to surface (Ohmura 2001). It is found that under clear sky about 60% of the atmospheric emission is derived from within the first 100 m and 90% from the first 1 km of the atmosphere. When the sky is overcast with the cloud bottom within the first 1 km, more than 90% originates within this layer between the surface and the bottom of the cloud.

Because of its simplicity and reasonably good results, the degree-day concept has been used by many authors. Braithwaite and Olesen (1989) and Reeh (1991) used the degree-day method to calculate melting over the Greenland ice sheet. Laumann and Reeh (1993) and Johannesson *et al*. (1995) used the degree-day method for estimating melt rates on different glaciers in Iceland, Norway, and Greenland. Hock (1999) found that the classical degree-day method yields a good simulation of the seasonal pattern of discharge from a small glacier in Sweden. Braithwaite and Zhang (2000) used the degree-day model to study sensitivity of mass balance of five Swiss glaciers to temperature changes.

In this study, the so-called classical degree-day method is used to estimate snow and ice melt, but the PDDs are calculated from monthly mean air temperatures using the concept of Normal distribution (Braithwaite 1985). The main purpose of this paper is to estimate annual discharge from Langtang and Lirung Khola Basins by the degree-day method using monthly mean air temperature and monthly total precipitation. The method is tested with measured discharge from July 1985 to June 1986 in Langtang Khola Basin and May to September 1996 in Lirung Khola Basin. The interannual variation of discharge from 1985 to 1999 is then analyzed. This paper is organized with six sections. The study area is introduced in Section 2.2, data in Section 2.3, and the methodology in Section 2.4. Results and discussion are described in Section 2.5 and conclusions are in the last section.

2.2 STUDIED BASINS

The investigated basins are located in the Langtang valley, approximately 60 km north of Kathmandu, Nepal. Figure 2.1 shows the location and drainage basins of Langtang Khola and Lirung Khola with hydrological observation sites (S1 and S2) and a meteorological observation site (BH) at an altitude of 3920 m a.s.l. The main physical characteristics of the investigated basins are shown in Table 2.1. The altitudinal distribution of Lirung Khola Basin in every 200 m as shown in Rana *et al*. (1996) is used in this study. In the case of Langtang Khola Basin, snow and ice melt are calculated in every 250 m altitude bands by dividing the drainage basin of 500 m altitude bands as shown in Fukushima *et al*. (1987) into two equal parts.

2.3 DATA USED

Hydrological data used in this study for verifying the calculated discharge are the discharges measured during the hydrological and meteorological observations carried out in Langtang Khola Basin for a full year from July 1985 to June 1986 and from May to September 1996 in Lirung Khola Basin by a joint research team of Japanese and Nepalese scientists. The mean air temperature and total precipitation from July 1985 to June 1986 was 2.7°C and 1225 mm, respectively, at BH. The observed discharge showed that it was mostly concentrated in the period from June to September, coinciding with the summer monsoon period in Nepal. The total observed specific discharge during the above period at S1 was 1358 mm (Fukushima *et al*. 1987). The monthly mean air temperature and monthly total precipitation from 1988 to 1999 are used to estimate the interannual variation of discharge in this study. These were observed at Kyangjing (3920 m a.s.l.), Langtang hydrometeorological observation station (same area of BH) of Department of Hydrology and Meteorology, His Majesty's Government of Nepal.

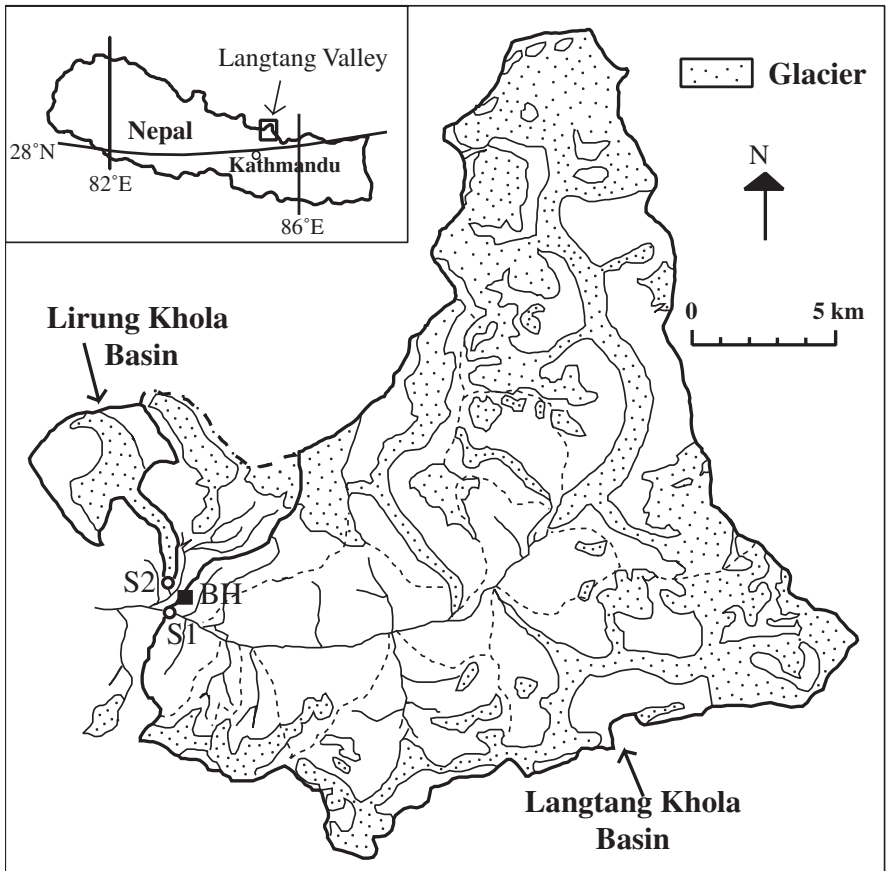


Figure 2.1 A topographical map of the Langtang valley. The thick solid lines indicate the boundaries of Langtang and Lirung Khola Basins. S1, S2 and BH represent hydrological observation sites in Langtang Khola Basin, Lirung Khola Basin and Base House for meteorological observations, respectively

Table 2.1 Main physical characteristics of the investigated basins

Name of the basin	Langtang Khola	Lirung Khola
Name of the area	Langtang valley	Langtang valley
Mountain range	Himalayas	Himalayas
Elevation range of the basin (m a.s.l.)	3840–7200	4000–7200
Elevation range of experimental sites (m a.s.l.)	3840–7200	4000–7200
Latitude	28°08′–28°23′N	28°13′–28°16′N
Longitude	85°35′–85°48′E	85°32′–85°35′E
Area (km^2)	333	13.8
Geology	–	–
Glaciers and permanent snow (%)	38	67
Dominant vegetation type	No vegetation	No vegetation
Forest (%)	0	0
Mean runoff at the catchment outlet (mm)	–	–
Mean precipitation (mm)	618	618

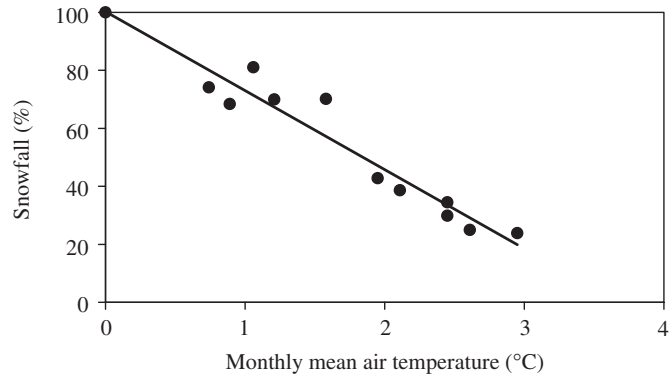


Figure 2.2 Calculated monthly snowfall amount in precipitation versus monthly mean air temperature on Glacier AX010 from June to August in 1978

The tendency of precipitation to increase with altitude is seen in glacier areas in the Nepalese Himalayas (Higuchi *et al*. 1982). In the Langtang valley, the precipitation at 5000 m altitude was 1.3 times larger than at 4000 m in rainy season (Seko 1987). From this observed result, the precipitation was assumed as a function of altitude as follows, since we have precipitation data only at BH.

$$\begin{aligned} P_Z &= P_{\mathrm{BH}} && Z < 4000\,\mathrm{m} \\ &= P_{\mathrm{BH}}\{1 + 0.0003(Z - 4000)\} \\ & && 4000\,\mathrm{m} \le Z \le 5000\,\mathrm{m} \\ &= 1.3\,P_{\mathrm{BH}} && Z > 5000\,\mathrm{m} \end{aligned} \tag{2.1}$$

Estimation of snowfall amount during precipitation event is carried out using the relation obtained on Glacier AX010, east Nepal (Figure 2.2). The relation was obtained by plotting calculated monthly snowfall amount in precipitation versus monthly mean air temperature (Kayastha *et al*. 1999). The mean temperature lapse rate with altitude at Lirung Glacier/BH and Yala Glacier/BH (5.3°C km^{-1} in Fujita *et al*. 1997) is used to derive the temperature at higher altitudes in both basins.

2.4 DEGREE-DAY METHOD

2.4.1 Calculation of positive degree-day sum

The degree-day sum for a period of N days is given by

$$Y = \frac{1}{M} \sum_{m=1}^{m=M} \sum_{n=1}^{n=N} \alpha_{nm} T_{nm} \tag{2.2}$$

where α_{nm} has either a value of unity or zero according to

$$\begin{aligned} \alpha_{nm} &= 1.0 \quad \text{if } T_{nm} \ge 0^{\circ}\mathrm{C} \\ &= 0.0 \quad \text{if } T_{nm} < 0^{\circ}\mathrm{C} \end{aligned} \tag{2.3}$$

If the temperature is assumed to constitute a stationary random series, the time summation in Equation (2.2) can be replaced by an ensemble-summation as follows.

$$Y = N \sum_{k=0}^{k=K} f(T_k) T_k \tag{2.4}$$

where

$$T_k = T_0 + k\Delta T \tag{2.5}$$

and $f(T_k)$ is the probability that the temperature lies in an interval of width ΔT centered on T_k and K is the value of k such that $f(T_k)$ becomes zero. T_0 is zero for the computation of positive degree-days. For the practical application of the Equation (2.4), the probability function $f(T_k)$ must be specified and is assumed that it is given by Normal distribution, which is characterized by two parameters, the mean value and the standard deviation. Under this assumption, monthly degree-days can be calculated as a function of monthly mean temperatures and their standard deviations. The assumption of a Normal distribution of daily mean temperatures is well justified in the ablation season (Braithwaite 1985).

Results of the solution of equation (2.4) are shown in Table 2.2. The results are expressed in the form of degree-days per day, that is, as Y/N, because months have differing lengths of 28, 29, 30, or 31 days. The monthly total degree-days are obtained by multiplying the

Table 2.2 Monthly positive degree-days per day (Y/N) as a function of monthly mean temperature from July 1985 to June 1986 (at 4125 m a.s.l.) and monthly standard deviation (SD). Units are °C

Date	Monthly temp.	SD	Y/N
Jul 1985	7.74	0.77	7.76
Aug	8.31	0.83	8.34
Sep	6.58	1.08	6.61
Oct	2.19	1.95	2.34
Nov	−1.39	1.88	0.26
Dec	−2.07	2.46	0.28
Jan 1986	−5.18	2.99	0.05
Feb	−5.62	2.68	0.02
Mar	−1.93	2.22	0.24
Apr	0.75	2.13	1.29
May	2.91	1.79	2.97
Jun	7.28	1.46	7.31

Y/N by the corresponding length of days in the month. The monthly standard deviations are mean of standard deviations calculated from July 1985 to December 1999 with a few missing months.

2.4.2 Snow and ice melt from glacier and rocky areas

Monthly snow and ice melt from glacier and rocky areas are calculated by multiplying the monthly PDD by the positive degree-day factor for snow or ice ablation. If snow is present on the ice surface of glacier, the available degree-day sum is used first to melt snow and the remaining is used to melt ice. The degree-day factors for snow and ice ablations used in this study are 7.0 and 8.0 mm d^{-1} $°C^{-1}$, respectively, at the altitude up to 5000 m a.s.l., and above 5000 m the factors are 10.5 and 9.5 mm d^{-1} $°C^{-1}$, respectively. These degree-day factors are decided from summer values obtained on Glacier AX010, east Nepal and Yala Glacier in the Langtang valley (Kayastha *et al*. 2000a, 2003). The larger degree-day factors for snow and ice ablation in the Nepalese glaciers than in most of the alpine glaciers in Europe (Table 4 in Braithwaite and Zhang 2000) are mainly due to ablation attributed to absorbed global radiation at the high altitude where the PDD is low because of low summer air temperature. For example, considerable amount of net shortwave radiation, the main energy source for ablation in the Himalayas, was found even at and around 0°C air temperature on Glacier AX010 (Kayastha *et al*. 2000a).

2.4.3 Ice melt under a debris layer

Ice melt under a debris layer is calculated using the degree-day method as explained in Kayastha *et al*. (2000b). The method needs positive degree-day factor for ice ablation and a relation between degree-day factor and debris properties, namely, relation between ratio of degree-day factor for given debris thickness k_d to the factor for ice ablation k_b and ratio of thermal resistance of debris R to thermal resistance for critical debris thickness R_c (Figure 6 in Kayastha *et al*. 2000b). A critical debris thickness is the thickness at which the ablation rate for debris-covered glacier ice is the same as for debris-free ice. In this study, the relation between degree-day factor and debris properties is used that was obtained from field observation carried out on debris-covered part of Lirung Glacier for a short period in June 1995 (Rana *et al*. 1996). Figure 2.3 shows the relation between degree-day factor and debris properties obtained from the observed data at debris thickness from 5 to 13 cm on Lirung Glacier. The critical debris thickness was 9.0 cm and mean thermal conductivity for the debris thickness from 5 to 13 cm was 1.4 W m^{-1} $°C^{-1}$. Since the observations were only on up to 13-cm thick debris layers, which is not representative to whole debris-covered area because there are much thicker parts too and the exact thickness of the debris layer is not known, the thermal resistance was extrapolated up to 50 cm debris layer and its mean value 0.19 m^2 °C W^{-1} is used to get k_d/k_b from the relation in Figure 2.3.

The calculated value of k_d/k_b is 0.54. Since the thickness of debris is thicker on the lower part of glacier than on the higher part, two values of k_d/k_b are used for lower and higher parts, namely, 0.50 for the lower two altitude bands 4125 m and 4375 m a.s.l. in Langtang Khola Basin and 4100 m and 4300 m a.s.l. in Lirung Khola Basins, and 0.58 for the rest of the higher altitude

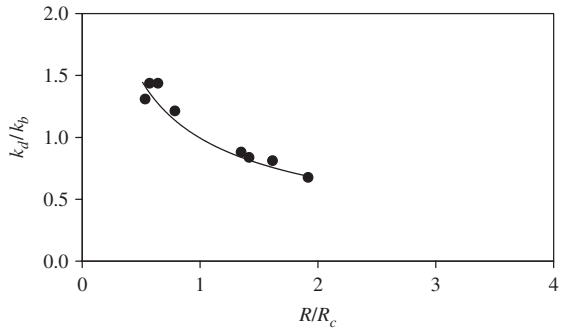


Figure 2.3 Ratio of k_d to k_b versus ratio of R to R_c on Lirung Glacier in June 1995

bands on both basins. Monthly ice melt under a debris layer is calculated by multiplying the monthly PDD by the k_d/k_b and degree-day factor for ice ablation. If snow is present on the debris, the available degree-day sum is used first to melt snow and the remaining is used to melt ice under the debris layer.

Rana *et al*. (1997) mentioned that the average thermal resistance derived from satellite data for the debris-covered part of the Lirung Glacier was 0.14 $m^2\,°C\,W^{-1}$, which is lower than the value derived from field observation. This could be due to the effect of low thermal resistance of supraglacial ponds and exposed ice cliffs on them. However, reasonable value of k_d/k_b can be obtained by changing the value of thermal conductivity. In the case of Lirung Glacier, the thermal conductivity should be 1.35 times larger than the observed thermal conductivity. In this way, if a relation between debris properties and degree-day factors is established for the debris-covered part of a glacier, ice melt under the debris layer can be estimated from the thermal resistance of debris layer derived from satellite data, provided the degree-day factor is known.

2.5 RESULTS AND DISCUSSION

Monthly specific snow and ice melt and rainfall are calculated at the mean altitude of each altitude bands in both basins. The area-averaged snow and ice melt and rainfall is calculated on each altitude bands, and their sum gives the discharge from the whole basin. The total discharge from the basin consists of melting from bare ice, ice melt under debris, snow melt above debris, melting of snow on rock and rainfall.

Variation in observed and calculated monthly discharges in Langtang and Lirung Khola Basins is shown in Figures 2.4 and 2.5, respectively. Figure 2.4

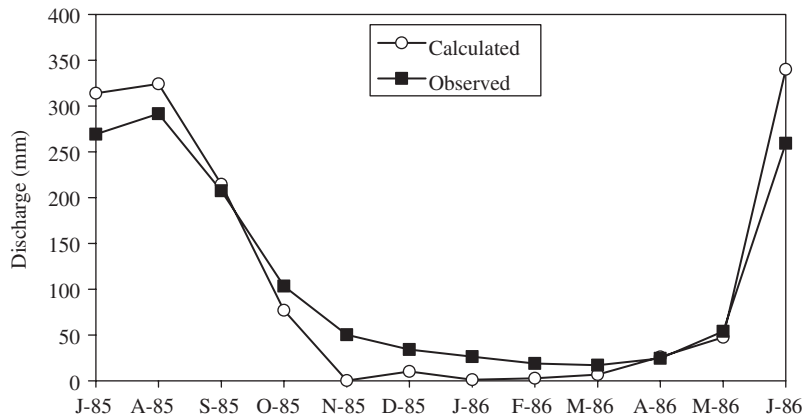


Figure 2.4 Observed and calculated monthly discharges in Langtang Khola Basin from June 1985 to July 1986

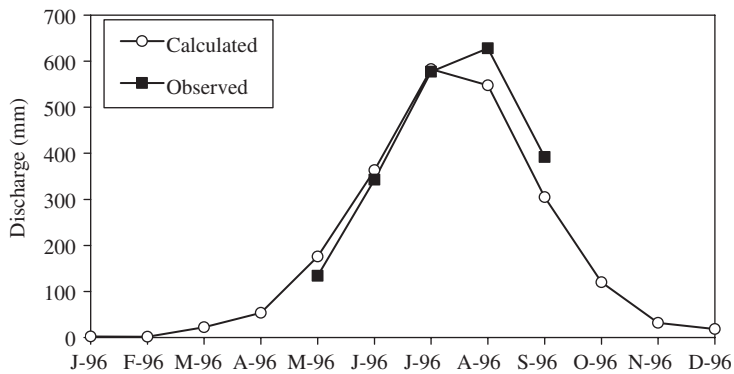


Figure 2.5 Observed and calculated monthly discharges in Lirung Khola Basin in 1996

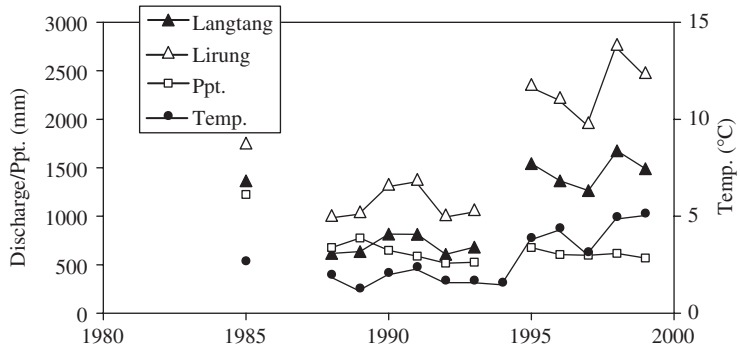


Figure 2.6 Variation in observed annual mean air temperature, total precipitation, and calculated discharges in Langtang and Lirung Khola Basins from July 1985 to June 1986 and from 1988 to 1999. The values plotted in 1985 represent from July 1985 to June 1986

shows the observed and calculated monthly discharges in Langtang Khola Basin from July 1985 to June 1986. Similarly, Figure 2.5 shows the observed and calculated monthly discharges in Lirung Khola Basin in 1996. Data were not available for a few days from May to July (May – 8 days, June – 2 days and July – 5 days) in the observed discharge. Figures 2.4 and 2.5 show that the calculated monthly discharges are quite reasonable compared to observed discharge. The total observed discharge in Langtang Khola Basin was 1357 mm from June 1985 to July 1986, whereas the calculated discharge is 1365 mm. Therefore, the degree-day method using monthly mean air temperature and total precipitation can be a useful tool to estimate discharge from glacierized Himalayan basins where daily hydrometeorological parameters are not available.

Variation in observed annual mean air temperature, total precipitation, and calculated discharges from July 1985 to June 1986 and from 1988 to 1999 in Langtang and Lirung Khola Basins are shown in Figure 2.6. The values from July 1985 to June 1986 are plotted in 1985. The remaining snowfall amount in certain altitude band and year is added to the snowfall amount in January in the next year. Since precipitation data for a few months in 1994 are not available, discharge and precipitation data are not plotted in Figure 2.6. In general, the discharge from both basins is increasing, as temperature increases although the precipitation amount did not change much. It implies that the mass of snow and ice in both basins is depleting. The large discharge from Lirung Khola Basin nearly two times that of Langtang Khola Basin is mainly due to snow and ice melt from comparatively larger glacier-covered area in the basin (67%) than in Langtang Khola Basin (38%).

2.6 CONCLUDING REMARKS

Degree-day method is used to estimate snow and ice melt and discharge using monthly mean air temperature and total precipitation in two glacierized basins viz., Langtang and Lirung Khola Basins in the Langtang valley, Nepal. Lower parts of glaciers in both basins are covered with debris and hence a relation between degree-day factor and debris properties obtained on Lirung Glacier of Lirung Khola Basin is used to estimate ice melt under debris layers. Compared to the simplicity of the method, results are very encouraging. The annual total observed and calculated discharges from Langtang Khola Basin are similar, namely, 1357 mm and 1365 mm, respectively, and for the Lirung Khola Basin as well. Therefore, the current degree-day method can be taken as a useful tool for estimating discharge from glacierized basin in the Himalayas where hydropower and other socioeconomic activities are speeding up but glaciohydrological data are still very scarce. This study shows that the mass of snow and ice in Langtang and Lirung Khola Basins is depleting and hence such changes should be taken into account while formulating any water project in such region. It would be better to have representative degree-day factors for snow and ice ablation and the relation between degree-day factor and debris properties in other glacierized basins so that the method can be used to estimate discharge from the glacierized basins.

2.7 ACKNOWLEDGMENTS

This study was carried out under the Postdoctoral Fellowship Program for Foreign Researchers by the Japan Society for the Promotion of Science (JSPS). We are thankful to Dr. Roberto Ranzi for his constructive review of our paper. We wish to thank

Dr. A. B. Shrestha of Department of Hydrology and Meteorology, Ministry of Science and Technology, His Majesty's Government of Nepal for providing meteorological data of Langtang hydrometeorological Station in the Langtang valley, Nepal.

REFERENCES

Ageta, Y. and Higuchi, K. (1984) Estimation of mass balance components of a summer-accumulation type in the Nepal Himalaya. *Geogr. Ann.* **66**(3): 249–255.

Braithwaite, R. J. (1985) Calculation of degree-days for glacier-climate research. *Z. Gletscherkd. Glazialgeol.* **20**(1984): 1–8.

Braithwaite, R. J. and Olesen, O. B. (1989) Calculation of glacier ablation from air temperature, West Greenland. In: Oerlemans, J. (ed) *Glacier Fluctuations and Climatic Change*. Kluwer Academic Publishers, Dordrecht, pp. 219–233.

Braithwaite, R. J. and Zhang, Y. (2000) Sensitivity of mass balance of five Swiss glaciers to temperature changes assessed by tuning a degree-day model. *J. Glaciol* **46**(152): 7–14.

Braun, L. N., Grabs, W. and Rana, B. (1993) Application of a conceptual precipitation-runoff model in the Langtang Khola Basin, Nepal Himalaya. In: Young, G. J. (ed) *Snow and Glacier Hydrology*. IAHS 218, pp. 221–237.

Fujita, K., Sakai, A. and Chhetri, T. B. (1997) Meteorological observation in Langtang Valley, Nepal Himalayas, 1996. *Bull. Glacier Res.* **15**: 71–78.

Fukushima, Y., Kawashima, K., Suzuki, M., Ohta, T., Motoyama, H., Kubota, H., Yamada, T. and Bajracharya, O. R. (1987) Runoff characteristics in three glacier-covered watersheds of Langtang Valley, Nepal Himalayas. *Bull. Glacier Res.* **5**: 11–18.

Fukushima, Y., Watanabe, O. and Higuchi, K. (1991) Estimation of streamflow change by global warming in a glacier-covered high mountain area of the Nepal Himalaya. In: Bergmann, H., Lang, H., Frey, W., Issler, D. and Salm, B. (eds) *Snow, Hydrology and Forests in High Alpine Areas*. IAHS 205, pp. 181–188.

Higuchi, K., Ageta, Y., Yasunari, T. and Inoue, J. (1982) Characteristics of precipitation during the monsoon season in high-mountain areas of the Nepal Himalaya. In: Glen, J. W. (ed) *Hydrological Aspects of Alpine and High-Mountain Areas*. IAHS 138, pp. 21–30.

Hock, R. (1999) A distributed temperature-index ice- and snowmelt model including potential direct solar radiation. *J. Glaciol.* **45**: 101–111.

Johannesson, T., Sigursson, O., Laumann, T. and Kennett, M. (1995) Degree-day glacier mass-balance modelling with applications to glaciers in Iceland, Norway and Greenland. *J. Glaciol.* **41**(138): 345–358.

Kayastha, R. B. (2001) Study of glacier ablation in the Nepalese Himalayas by the energy balance model and positive degree-day method. D. Sc. thesis, Nagoya University.

Kayastha, R. B., Ohata, T. and Ageta, Y. (1999) Application of a glacier mass-balance model to a Himalayan glacier. *J. Glaciol.* **45**(151): 559–567.

Kayastha, R. B., Ageta, Y. and Nakawo, M. (2000a) Positive degree-day factors for ablation on glaciers in the Nepalese Himalayas: case study on Glacier AX010 in Shorong Himal, Nepal. *Bull. Glaciological Res.* **17**: 1–10.

Kayastha, R. B., Takeuchi, Y., Nakawo, M. and Ageta, Y. (2000b) Practical prediction of ice melting beneath various thickness of debris cover on Khumbu Glacier, Nepal, using a positive degree-day factor. In: Nakawo, M., Raymond, C. F. and Fountain, A. (eds) *Debris-Covered Glaciers*. IAHS 264, pp. 71–81.

Kayastha, R. B., Ageta, Y., Nakawo, M., Fujita, K., Sakai, A. and Matsuda, Y. (2003) Positive degree-day factors for ice ablation on four glaciers in the Nepalese Himalayas and Qinghai-Tibetan Plateau. *Bull. Glaciological Res.* **20**: 7–14.

Laumann, T. and Reeh, L. (1993) Sensitivity to climate change of the mass balance of glaciers in southern Norway. *J. Glaciol.* **39**(133): 656–665.

Nakawo, M. and Takahashi, S. (1982) A simplified model for estimating glacier ablation under a debris layer. In: Glen, J. W. (ed) *Hydrological Aspects of Alpine and High-Mountain Areas*. IAHS 138, pp. 137–145.

Ohata, T. and Higuchi, K. (1980) Heat balance study on the glacier AX010 in Shorong Himal, East Nepal. *Seppyo* Special Issue **41**: 42–47.

Ohmura, A. (2001) Physical basis for the temperature-based melt-index method. *J. Appl. Meteorol.* **40**: 753–761.

Rana, B., Fukushima, Y., Ageta, Y. and Nakawo, M. (1996) Runoff modeling of a river basin with a debris-covered glaciers in Langtang Valley, Nepal Himalaya. *Bull. Glacier Res.* **14**: 1–6.

Rana, B., Nakawo, M., Fukushima, Y. and Ageta, Y. (1997) Application of a conceptual precipitation-runoff model (HYCYMODEL) in a debris-covered glacierized basin in the Langtang Valley, Nepal Himalaya. *Ann. Glaciol.* **25**: 226–231.

Reeh, N. (1991) Parameterization of melt rate and surface temperature on the Greenland ice sheet. *Polarforschung* **59**(3): 113–128.

Seko, K. (1987) Seasonal variation of altitudinal dependence of precipitation in Langtang Valley, Nepal Himalayas. *Bull. Glacier Res.* **5**: 41–47.

3

Surface Energy Balance of High Altitude Glaciers in the Central Andes: the Effect of Snow Penitentes

JAVIER G. CORRIPIO[1] AND ROSS S. PURVES[2]
[1]*Institute of Hydromechanics and Water Resources Management, ETH – Zürich,*
[2]*Department of Geography, University of Zürich, Switzerland*

3.1 INTRODUCTION

The Dry Central Andes stretching from latitude 31°S to 35°S are climatic deserts, yet they support rich agriculture and large urban centres thanks to melt water from glaciers and snow-covered mountains. Most of the agriculture of the Chilean Central Valley is irrigated (Schwerdtfeger 1976), and all drinking water for Santiago de Chile, with over five million inhabitants (one-third of the population of Chile), comes from water reservoirs fed by snow and ice melt during the summer. On the Argentinian side of the Andes, with barely 180 mm of annual precipitation, the provinces of Mendoza (population over 1.5 million) and San Juan are the country's main wine producers, and the region has rich agricultural farms. This production is only possible thanks to a well-developed irrigation system that makes efficient use of the summer melt water from the Cordillera. The contrast between the desert natural vegetation and the lush green of the cultivated farms is evident over the whole province, stressing the vital role of the mountains as ''water towers of the world for the 21st Century''. (Liniger *et al*. 1998)

In this paper, we present results from a field campaign and associated modelling, comparing the components of energy balance in this area with that of Alpine basins and presenting low-cost remote sensing techniques suitable for use in a region where access is difficult and expensive. Particular attention is given to penitentes: surface ablation forms that are common on most glaciers of the Central Andes at high altitude and have an important effect on the energy and mass balance of the snow cover. The relative importance on snow ablation and therefore on water resources will be addressed.

3.2 SITE OF STUDY

The areas of study are two glaciers near the latitude of Santiago de Chile (see map in Figure 3.1): the Juncal Norte glacier near the border with Argentina and south of the Portillo pass, and the Loma Larga glacier on the headwaters of the Maipo river. The characteristics of the upper basins that contain the glaciers are summarised in Table 3.1. An automatic weather station (AWS) was installed on the snow surface and it collected data from 30 November to 11 December 2000 on Juncal and from 22 January to 24 February 2001 on Loma Larga. The instruments were carried with the help of local arrieros and mules from the nearest road to the base camp near the glacier snout and then by the researchers to the glacier location.

Climate and Hydrology in Mountain Areas. Edited by C. de Jong, D. Collins and R. Ranzi
© 2005 John Wiley & Sons, Ltd. ISBN: 0-470-85814-1

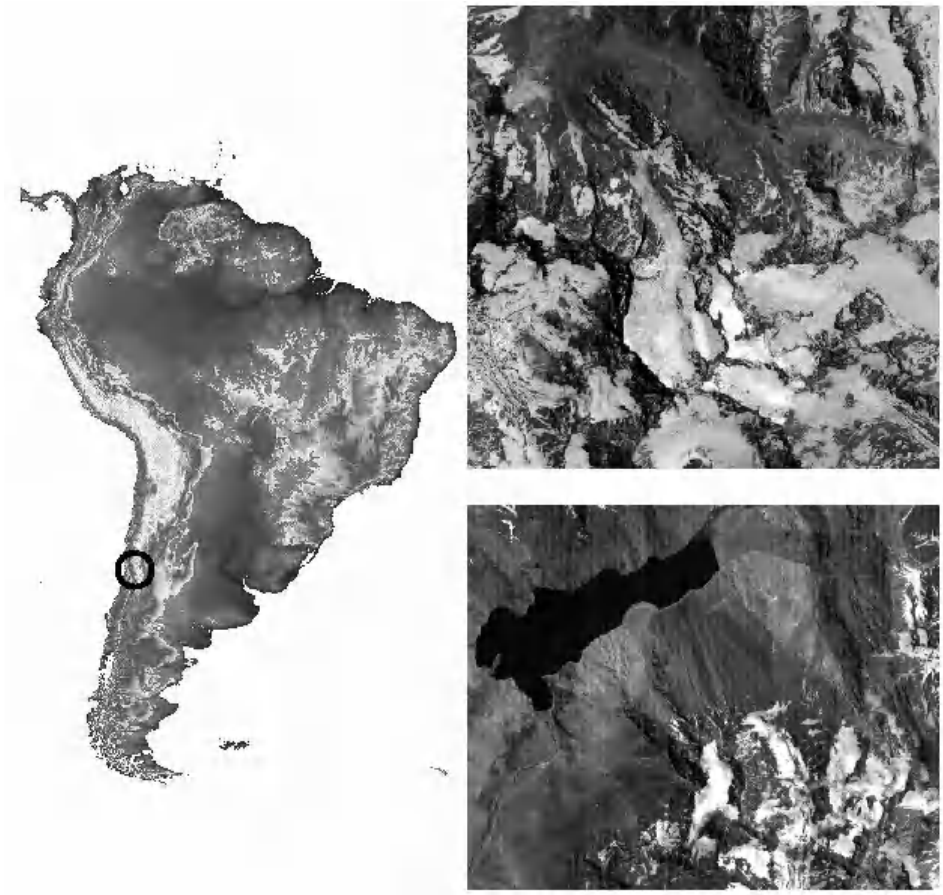


Figure 3.1 The area of study in the Chilean Andes, about 33°S 70°W. In the right upper photograph, Juncal Norte is the main glacier at the lower centre of the image, flowing north. Loma Larga is on the lower right corner of the lower image, in the opposite corner is the Yeso dam, the main water reservoir for Santiago de Chile. Map source: GLOBE project, NOAA, NGDC. Images from Aster: asterweb.jpl.nasa.gov. Courtesy NOAA

Table 3.1 Main characteristics of the upper catchment of the glaciers under study

	Catchment 1	Catchment 2
Name of the basin	Juncal Norte	Loma Larga
Mountain range	Andes	Andes
Elevation range of upper catchment	2900–6100	2900–5404
Elevation range of individual sites	3335	4667
Latitude and longitude	32.98°S, 69.95°W	33.69°S, 70.00°W
Area in km^2	21	18
% glacierised	39	66
Geology	Andesites, trachytes and basalts	Andesites, trachytes and basalts
Vegetation type (dominant)	Alpine xerophytic, desert	Alpine xerophytic, desert
Mean Q at catchment outlet	Unknown	Unknown
Mean h_{sun}	3060 h	3220 h

3.2.1 Climatic setting

Along the 33°S parallel, annual average precipitation ranges from 459 mm in Valparaiso (33.02°S, 71.63°W, 41 m a.s.l.) on the Pacific coast to 356 mm in Santiago (33.45°S, 70.70°W, 520 m a.s.l.) and 180 mm in Mendoza (32.89°S, 68.83°W, 769 m a.s.l.), on the Argentinian side of the Cordillera (Schwerdtfeger 1976). In this region, climatic seasonality is well defined, with dry summers and most of the precipitation occurring during the winter months. The south-western Pacific perturbations reach the mountains only during the winter, producing variable precipitation, which is always in the form of snow at altitude (Lliboutry 1965). During the summer, the weather is extremely dry and stable, characterised by the constant presence of the Pacific anticyclone over the region. In fact, less than 1% of the annual total precipitation is recorded during the December–February period. Frontal activity is infrequent, and precipitation, both on the mountain range and in the lee of the mountains, is mainly due to convective activity (Schwerdtfeger 1976).

The synoptic situation during fieldwork is summarised in Figure 3.2, which shows the surface sea level pressure over South America. As indicated by Lliboutry (1998), a belt of stationary high pressure extends across the Pacific Ocean west of South America, preventing intrusion of moisture-laden air masses to the continent. This stationary anticyclone is also responsible for a minimum in relative humidity over central Chile during the summer months. The same reanalysis data show a mean relative humidity of 35% on the western coast of Chile, at about 33° latitude south, the minimum for the southern hemisphere outside Antarctica. The solar radiation is very intense, with a daily average of over 400 W m^{-2} for the

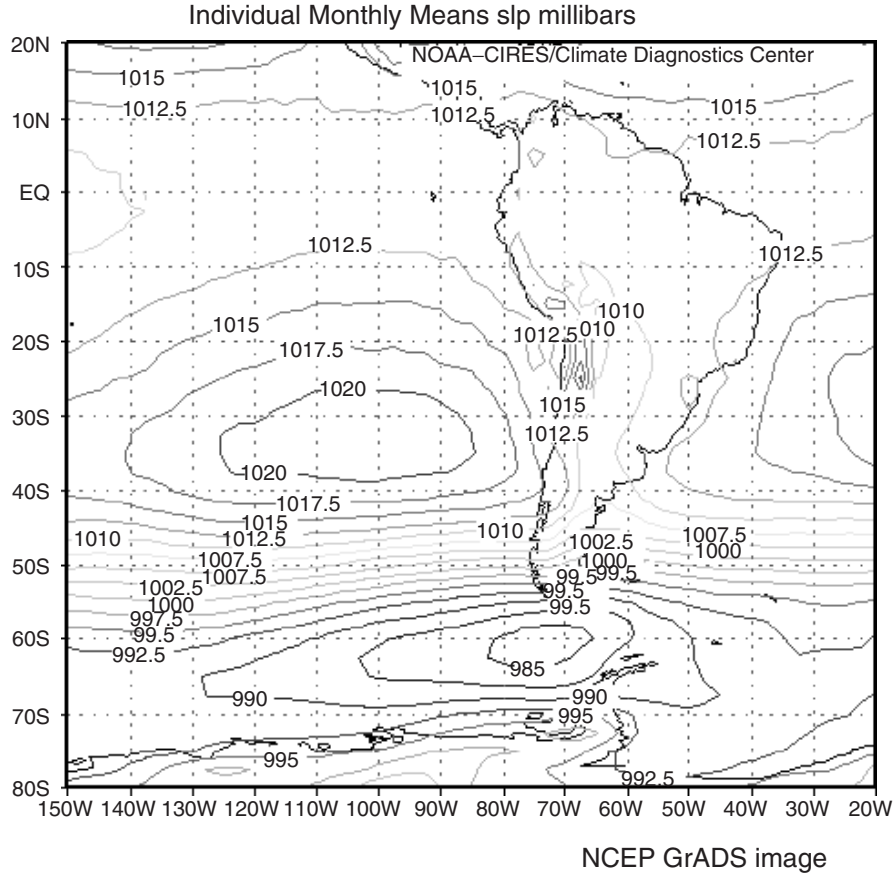


Figure 3.2 Surface sea level pressure averaged from December 2000 to February 2001. The image is a visualisation of NCEP/NCAR reanalysis data provided by the NOAA-CIRES Climate Diagnostics Center, Boulder, Colorado, from their web site at http://www.cdc.noaa.gov/. Courtesy NOAA

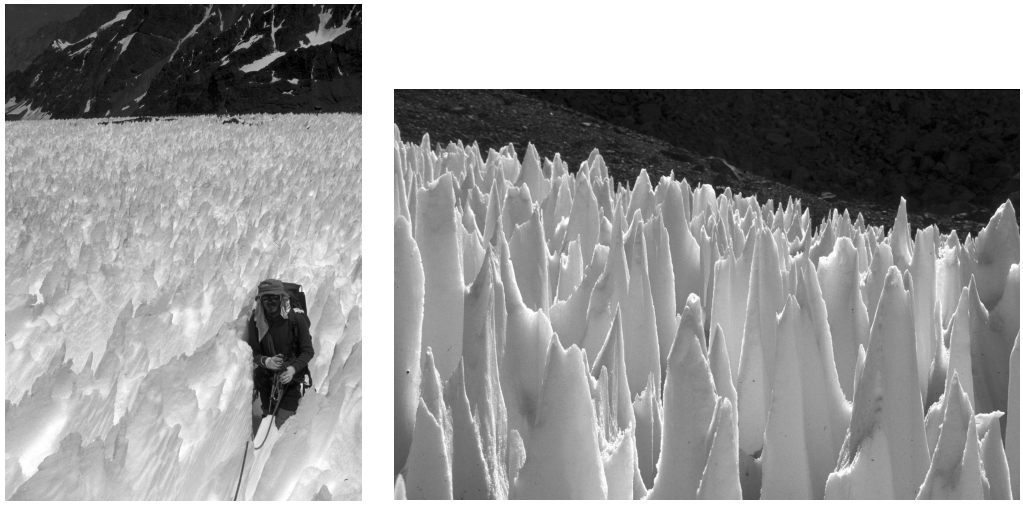


Figure 3.3 Penitentes field on the middle section of the Loma Larga glacier, at about 4500 m a.s.l. The whole glacier above 4000 m is covered in these snow pinnacles, which make difficult the movement of mountaineers and researchers and alters the surface energy balance of the glacier. On the right photograph is a detail of penitentes about 2 m in height

same period, the maximum for both hemispheres during the summer months excluding the South Pole.

The climatic regime of the Dry Central Andes is clearly different from that of subtropical Andes of Bolivia and Peru, further north, characterised by convective intrusions of moist air masses from the Amazon basin during the summer (Vuille *et al*. 1998). Here the ablation session is well defined and characterised by long periods of clear and stable weather. This climatic setting is responsible for the formation of a very peculiar ablation morphology, the snow penitentes, common to all the central Andes and to other dry high mountains such as the Pamirs (Lliboutry 1965, Kotlyakov and Lebedeva 1974).

3.2.2 Snow and ice penitentes

Penitentes were first described in the literature by Darwin (1839). On March 22, 1835, he had to squeeze his way through snowfields covered in penitentes near the Piuquenes Pass, on the way from Santiago de Chile to the Argentinian city of Mendoza, and reported the local belief (that is still held) that they were formed by the strong winds of the Andes. These pinnacles of snow or ice (Figure 3.3) grow over all glaciated and snow-covered areas in the Dry Andes above 4000 m (Lliboutry 1954a, Lliboutry 1954b, Lliboutry 1965). They range in size from a few cm to over five metres. (Lliboutry 1965, Naruse and Leiva 1997).

Lliboutry (1954a, 1954b, 1965) noted that the key climatic condition for the differential ablation that leads to the formation of penitentes is that dew point is always below zero. Thus, snow will sublimate, which requires higher energy input than melting. Once the process of differential ablation starts, the surface geometry of the evolving penitente produces a positive feedback mechanism, and radiation is trapped by multiple reflections between the walls. The hollows become almost a black body for radiation (Lliboutry 1954a), while decreased wind leads to air saturation, increasing dew point temperature and the onset of melting. In this way, peaks, where mass loss is only due to sublimation, will remain, as well as the steep walls, which intercept only a minimum of solar radiation. In the troughs ablation is enhanced, leading to a downward growth of penitentes. A mathematical model of the process has been developed by Betterton (2001), although the physical processes at the initial stage of penitente growth, from granular snow to micropenitentes, still remain unclear.

3.3 METHODOLOGY

Meteorological data collected at two sites in the Andes by an automatic weather station was used to model the energy balance and the relative importance of its components. A summary of the instrumentation is given in Table 3.2. The model is a distributed model of solar radiation that takes into account the spatial variation both

Table 3.2 Instruments used for measuring air temperature, relative humidity, snow temperature, incoming and outgoing short-wave radiation, wind speed and wind direction

Sensor	$T_{\mathrm{air},sl}$	RH	T_s	SW↓	SW↑	$\overline{u}$	u_{xy}
	Vaisala 50Y		107 Thermistor	Kipp & Zonen CM3		RM Young 05103	
Range	−40 to 60°C	0 to 100%	−40 to 60°C	305–2800 nm		0–60 m s^{-1}	360°
Accuracy	±0.5°C	2%	±0.5°C	10%		±0.3 m s^{-1}	3%

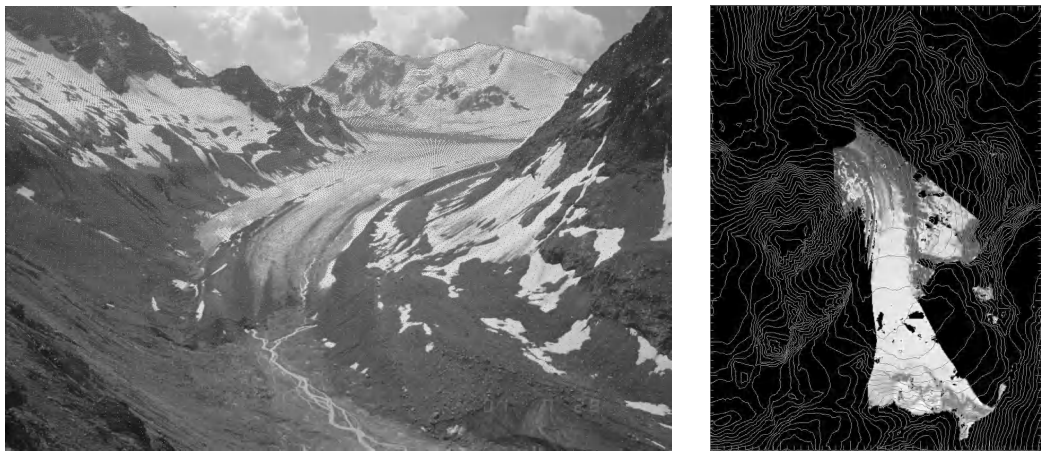


Figure 3.4 (Plate 1) Example of the technique used to estimate the ratio of snow cover and the spatial distribution of albedo, in this case applied to an Alpine glacier, Haut Glacier d'Arolla. On the left photograph, the perspective projection of the DEM appears as grey dots, and from these, the georeferenced map of reflectance values on the right image is produced

in atmospheric transmittance and in diffuse reflected radiation due to surrounding topography. In this case, we focus on the microscale, to assess the effect of ablation morphology on the whole energy balance.

For a correct estimation of the influence of surrounding land cover on reflected diffuse radiation, whether snow free or snow covered, a novel technique using terrestrial photography was developed (Corripio 2003a, Corripio 2004). This consists of georeferencing oblique photographs to a digital elevation modelDEM) and defining a mapping function between the information contained in a given pixel of the image and the corresponding cell of the DEM. This allows a simple estimation of the spatial variation in albedo and thus the influence of the surrounding land cover to be taken into account. This technique depends on the availability of digital elevation models and relies on the identification of accurate ground control points (GCPs). The procedure was not fully developed until after the field campaign, but in order to illustrate its application to mountain terrain, an example for an Alpine glacier is given in Figure 3.4.

3.4 ENERGY BALANCE MODEL

The energy fluxes at the surface of the glacier can be expressed as

$$Q = SW\downarrow(1-\alpha) + L\downarrow - L\uparrow + Q_H + EL_e, \quad (3.1)$$

where $SW\downarrow$ is incoming short-wave radiation, α is snow albedo, L is long-wave radiation, arrows indicating incoming or outgoing, Q_H and EL_e are sensible and latent turbulent fluxes with the atmosphere. Note that neither convective nor advective heat transfer within the snow pack was considered. However, the temperature at 1 m below the snow surface was measured on the lower AWS with a thermistor and found very stable, with a mean value of −0.13°C and a standard deviation of 0.0023, suggesting that most variation in temperature within the snowpack is the result of diffusion from the surface, with little or no heat fluxes from internal layers in accordance with other studies of temperate glaciers during the ablation season (Arnold *et al.* 1996, Obleitner 2000).

3.4.1 Short-wave radiation

The global short-wave radiation was modelled in the following way.

$$SW \downarrow = r^2 I_{sc} \tau_i (F_t + F_{sk} + F_{ms} + F_{sn}), \qquad (3.2)$$

where I_{sc} is the solar constant or 1367 Wm^2; r^2 is the reciprocal of the square of the radius vector of the earth, or correction for the eccentricity of the earth's orbit, which is calculated using Fourier series derived by Spencer (1971); and τ_i represents atmospheric transmittance functions, both for diffuse and direct radiation, which take into account Rayleigh scattering, transmittance by ozone, by uniformly mixed gases, by water vapour and by aerosols, and are computed following a parametric model by Iqbal (1983). The τ – functions incorporate the relative optical path length and pressure corrected air mass, depending on solar zenith angle and altitude. Further updates to Iqbal's model are introduced for the calculation of precipitable water, following Prata (1996) and for ozone layer thickness, which is taken from the NASA Total Ozone Mapping Spectrometer dataset (TOMS–EP 2001). The F – factors are corrections for direct radiation with respect to its angle of incidence (F_t), for diffuse radiation (F_{sk}), multiple scattering (F_{ms}) and reflected radiation by both snow-covered and snow-free surrounding terrain (F_{sn}). The F-terms take into account the horizon obstruction or sky view factor (f_v, Equation 3.6). They are computed in a slightly modified way from Greuell *et al*. (1997) as explained by Corripio (2004), with terrain and solar parameters such as vector normal to the surface, shading, horizon configuration and solar vector calculated after Corripio (2003b).

The results of the model, compared with measured radiation on a clear day, are shown in Figure 3.5, where the differences between modelled and measured data were smaller than the nominal pyranometer accuracy (10%). In this case, the valley is uniformly covered in snow and runs east to west, for different configurations there is a small error introduced by the necessary simplification and symmetry assumption of the terrain configuration parameters.

The albedo at the upper station was fairly constant, with an average value of 0.44 and a standard deviation of 0.07. Its decrease was only 4% over a month. An unusual pattern was observed at the upper AWS in the last hours of the afternoon, when the albedo value rose sharply to almost 1.0. This could be an artifact due to differential shading. Another possible explanation for this behaviour is an increase in reflected diffuse radiation as the sun hit the penitentes' wall from the west at a very low angle. The fact that the increase in albedo happens after 18:00 h, when the solar azimuth enters the south-western

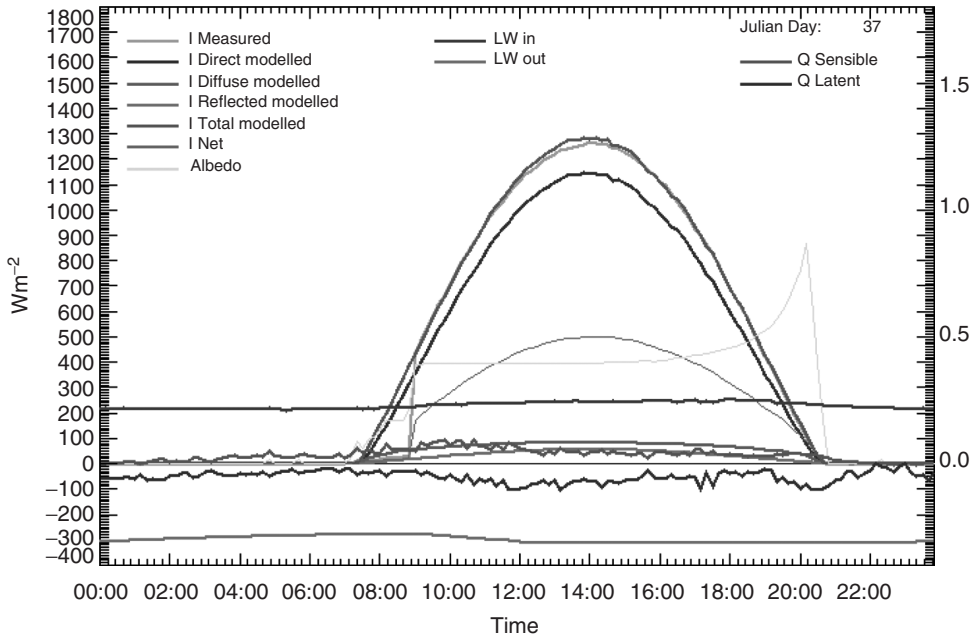


Figure 3.5 (Plate 2) Energy fluxes on a clear day on Loma Larga glacier, 4667 m a.s.l. DOY 37, 6th of February. Note the increasing albedo in the afternoon, an explanatory hypothesis is given in the text

quadrant, adds support to this hypothesis, although the causes are not clear yet.

3.4.2 Long-wave radiation

The incoming long-wave radiation depends on the temperature and composition of the overlying atmosphere, and in mountainous terrain the surrounding relief and snow cover will have an important effect on the total radiative budget (Olyphant 1986). The atmospheric component was calculated following Prata (1996), a formulation that gives the best results according to a survey by Dilley and O'Brien (1998), especially for dry atmospheres as is the case in the Andes.

$$L \downarrow = (1 - (1 + \omega_p)\mathrm{e}^{-(1.2+3\omega_p)^{0.5}})\sigma T_{\mathrm{air},sl}^4, \tag{3.3}$$

where $T_{\mathrm{air},sl}$ is air temperature (K) at screen level, σ is the Stephan–Boltzman constant and precipitable water (ω_p) is calculated as $\omega_p = 46.5\, e_0 / T_{\mathrm{air},sl}$, an empirical equation given by Prata (1996) that is the best fit to extensive data from radiosonde stations around the world, with e_0 the actual vapour pressure, calculated from measured relative humidity and from the saturation vapour pressure, calculated using Lowe 1977 polynomials.

The outgoing long-wave radiation is

$$L \uparrow = \varepsilon \sigma T_s^4, \tag{3.4}$$

where ϵ is snow emissivity, taken as 0.99, and T_s is snow surface temperature.

The value of $L \downarrow$ is further modified according to the horizon configuration or sky view factor (f_v, Equation 3.6) and the snow cover ratio of surrounding ground as

$$L' \downarrow = L \downarrow f_v + L \uparrow (1 - f_v). \tag{3.5}$$

3.4.3 Turbulent fluxes

For the calculation of the turbulent fluxes, the Monin–Obukhov similarity theory was followed, as formulated by Brutsaert (1982). This method calculates heat and vapour transfer from their gradients between surface and measurement heights, taking into consideration wind speed, air density, stability correction, and so on, and accounts for the surface roughness by introducing an aerodynamic roughness length, z_0.

A standard approach for the computation of the roughness length for momentum is to extrapolate the profiles of wind speed under neutral conditions to the level at which wind speed equals zero (Stull 1988, Munro 1989, Greuell and Smeets 2001). However, this procedure requires measurements at atleast two levels and is very sensitive to instrument errors. Therefore, the roughness for the lower site was selected from published mean values for melting snow (Marks and Dozier 1992, Morris 1989, Greuell and Smeets 2001), and it was calculated from microtopographical measurements for the upper site. This upper site is covered in large penitentes, sometimes over 1.5 m in height (Figure 3.3), which results in a very long roughness length. It was calculated as $z_0/z_e = 0.5\lambda_f$, where z_e is the roughness element height and λ_f is the frontal area index or vertical silhouette area per unit ground area (Lettau 1969). Data from wind tunnel experiments and atmospheric observations shows that z_0/h increases linearly with λ_f for $\lambda_f < \lambda_{f,\max}$ (Raupach 1992). The precise form of this function and the value of $\lambda_{f,\max}$ depends on the geometry of the roughness elements, but the above linear relationship was found satisfactory for very rough snow surfaces on Vatnajökull, Iceland, by Smeets, Duynkerke and Vugts (1999). For the present study, with an average penitente height of 1.35 m, separated about 0.8 m, the mean value of z_0 was found to be 20 cm. The frontal area index will change depending on wind direction, and so will the surface roughness length, sometimes to a very large scale (Jackson and Carroll 1977), however, wind direction was observed to be fairly constant, either upvalley or downvalley, which justifies the selected profile. Values for turbulent fluxes plotted on Figure 3.5 correspond to this z_0 value. The transfer mechanisms of momentum and of other scalar admixtures are different at the surface, and consequently the roughness lengths have different values for momentum, water vapour and heat, which were calculated following Andreas (1987).

3.5 MODELLING THE SURFACE MICROTOPOGRAPHY

To assess the effect of the surface ablation morphology on the interception of solar radiation and on the long-wave radiative budget, a high-resolution digital elevation model of the surface with 1 cm grid cell spacing was created, and the solar radiative and long-wave models applied to it. The turbulent heat transfer was considered at the overall scale, but it is expected that sublimation and cooling are more intense on the peaks and on the wind side. Although some effort has been made in determining drag partition on rough surfaces (Raupach 1992), it was only for momentum transfer, and it would be desirable to get more detailed observations on real snow surfaces before extrapolating any modelling results.

The DEM was created according to measured penitente distribution and size, with an average height of 1.35 m and

wavelength of 0.80 m. To add more realism, the base of the troughs was made flat, as there is frequent melting and even small water ponds in these areas. A smoothing filter was passed over the whole surface to avoid unrealistically sharp angles but it resulted in excessive flattening of the peaks. The ''virtual'' penitentes are concave and tilted 11° to the north, the sun direction in the southern hemisphere (note the arrows in Figure 3.7). As real penitentes have overhanging surfaces, these cannot be represented by a mathematical function, which requires a single z-value for every (x, y) pair. By rotating the reference system by an equivalent angle, we can build the DEM with no overhanging surfaces and then rotate the world according to this new reference system. For the calculation of solar irradiation on the penitentes surface (Figure 3.7), we only need to rotate the sun vector through the original reference system an opposite angle by applying the appropriate rotational matrices.

The sky view factor was computed for every grid cell as the finite sum:

$$f_v = \sum_{\varphi=0}^{2\pi} \pi \cos^2 \theta_l \frac{\Delta\varphi}{2\pi} \tag{3.6}$$

where θ_l is the local horizon angle, including the slope of the cell itself, for a given azimuth, φ. This represents the ratio of the area of a projected circle, corresponding to the visible part of the hemisphere to the area of a circle of unit radius corresponding to the whole hemisphere. For a more detailed explanation, see, for example: Nuñez (1980), Dozier *et al*. (1981), Dozier and Frew (1990), or Corripio (2003b, 2003a)

The model calculated angle of incidence of the direct beam, shadows, diffuse reflected radiation and diffuse radiation from the sky. For a detailed discussion, see Greuell *et al*. (1997, appendix) and Corripio (2003b). Reflected radiation was computed for five multiple reflections, which accounts for more than 97% of the energy from this source. Only even reflections were computed, as odd reflections are ''reflected-out'' (Peterson *et al*. 1985). The modified incoming long-wave radiation is a function of the skyview factor, its value outside the penitentes layer and the long-wave emission of surrounding walls.

3.6 RESULTS AND DISCUSSION

The recorded meteorological variables are summarised in Tables 3.3 and 3.4. The most remarkable aspect is the very low relative humidity. High values were normally associated with the presence of clouds, sometimes enveloping the AWS. Relative humidity follows a diurnal cycle, with maxima due to nocturnal cooling and minima normally related to katabatic winds. Winds were light to moderate and fairly constant. Incoming solar radiation was very intense, with average values close to those of perfectly clear days and peaks exceeding 1700 W m^{-2} at the upper AWS. These peaks were higher than the exoatmospheric radiation and were probably caused by enhanced downward flux because of forward scattering of light by large cumulonimbus. Albedo was fairly constant during the whole measurement period, and typically 8% lower on the upper station, where the site was completely

Table 3.3 Recorded meteorological variables and calculated dew point on both glaciers at different times of the day. Noon is about two hours around the daily peak of maximum short-wave radiation, sunrise and sunset are extended two hours after and before the respective events, and night correspond to the period where there is no incoming short-wave radiation. Note that although dew point is a function of temperature and humidity, the recorded variables, its calculated value is given to stress the meteorological conditions necessary for the formation of penitentes as pointed out by Lliboutry (1954b)

Time	Juncal Norte Glacier (3335 m a.s.l.)											
	Noon				Sunrise-set				Night			
	Min	Mean	Max	σ	Min	Mean	Max	σ	Min	Mean	Max	σ
T°C	5.2	11.2	17.3	2.4	1.3	7.2	14.3	2.5	1.2	5.7	10.3	2.1
RH%	10.6	21.8	51.4	6.5	10.4	37.1	75.4	13.7	14.7	44.6	80.3	14.4
u m s^{-1}	0.4	13.6	5.0	2.0	0.1	3.9	11.3	1.9	0.1	3.2	6.5	1.2
Dew Point °C	−18.8	−10.4	−0.6	3.5	−19.3	−7.3	1.1	4.3	−16.5	−6.0	1.6	4.0
	Loma Larga Glacier (4667 m a.s.l.)											
T°C	5.2	11.2	17.3	2.4	1.3	7.2	14.3	2.5	1.2	5.7	10.3	2.1
RH%	10.6	21.8	51.4	6.5	10.4	37.1	75.4	13.7	14.7	44.6	80.3	14.4
u m s^{-1}	0.4	13.6	5.0	2.0	0.1	3.9	11.3	1.9	0.1	3.2	6.5	1.2
Dew Point °C	−18.8	−10.4	−0.6	3.5	−19.3	−7.3	1.1	4.3	−16.5	−6.0	1.6	4.0

Table 3.4 Short-wave radiation and derived albedo at Juncal Norte Glacier (3335 m) and Loma Larga Glacier (4667 m)

	Juncal Norte Glacier			Loma Larga Glacier		
	SW↓ $W\,m^{-2}$	SW↑ $W\,m^{-2}$	Albedo %	SW↓ $W\,m^{-2}$	SW↑ $W\,m^{-2}$	Albedo %
Min	–	–	–	–	–	–
Mean	353	184	0.52	383	163	0.44
Max	1564	810	0.70	1727	737	0.65

covered in penitentes. The calculated dew point was well below zero, with very rare exceptions.

It should be pointed out that there were no reliable measurements of ablation in the area of study. This is not a simple task, as the volumetric change of the penitentes should be measured, besides their growth and lowering. However, to gain some confidence in the modelled data, the energy balance model was applied to the meteorological data recorded on the ablation area at the Haut Glacier d'Arolla, during the ETH summer campaign 2001. The modelled ablation was then compared to ablation measured by a sonic gauge. The results show good agreement, as illustrated in Figure 3.6.

It is interesting to point out the differences in the turbulent fluxes between the Alpine and the Andean glaciers. In the Alps, net turbulent flux was always positive: 16 $W\,m^{-2}$ mean value in the period corresponding to the plotted data, from 19 June to 5 July, with a standard deviation of 29.5. In general, large negative fluxes were associated to precipitation events, where sensible flux was also negative, while in the Andes large negative fluxes were associated with intense evaporation.

The energy balance model applied to the microtopography DEM was run for several clear days with ten-minute time steps to assess the effect of penitentes on the interception of solar radiation. The results for day 37 are shown in Figure 3.7. The maximum total daily value is 490 $W\,m^{-2}$, while the mean value is only 207 $W\,m^{-2}$. The histogram of values shows a bimodal distribution with two peaks (248 and 156 $W\,m^{-2}$) corresponding to the north- and south-facing walls. The same day on a flat surface the modelled (and measured) radiation was 435 $W\,m^{-2}$ (418). The mean values for the summer solstice (21 December) were 230 and 486 $W\,m^{-2}$ for the penitentes and a flat surface, respectively. Although not shown, an inspection of the results for diffuse and reflected radiation reveals that the latter

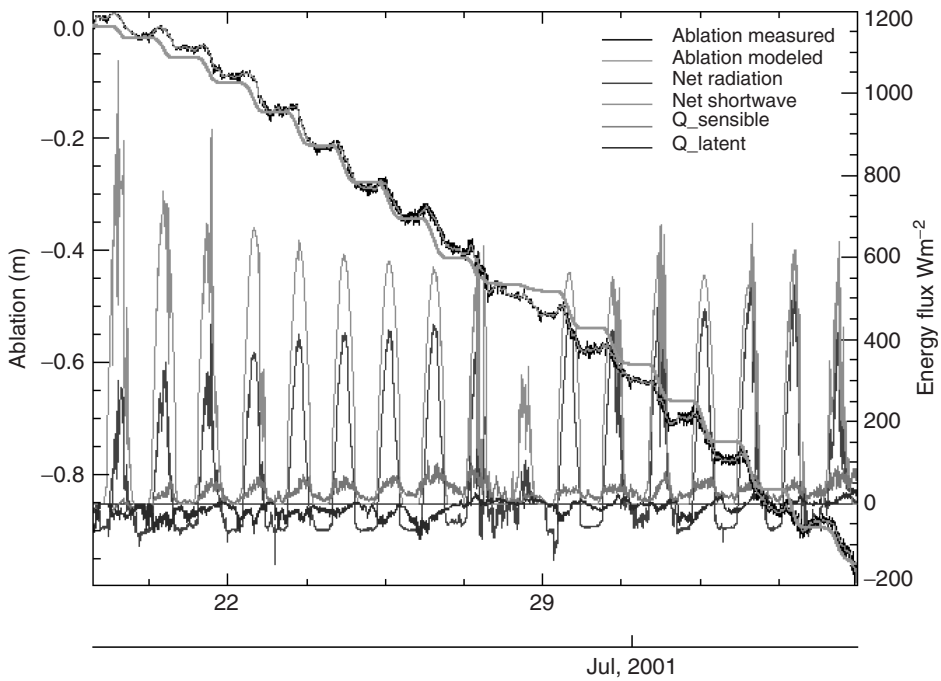


Figure 3.6 (Plate 3) Recorded solar radiation, estimated turbulent fluxes, and recorded and estimated snow ablation on the Haut Glacier d'Arolla from 19 June to 5 July 2001

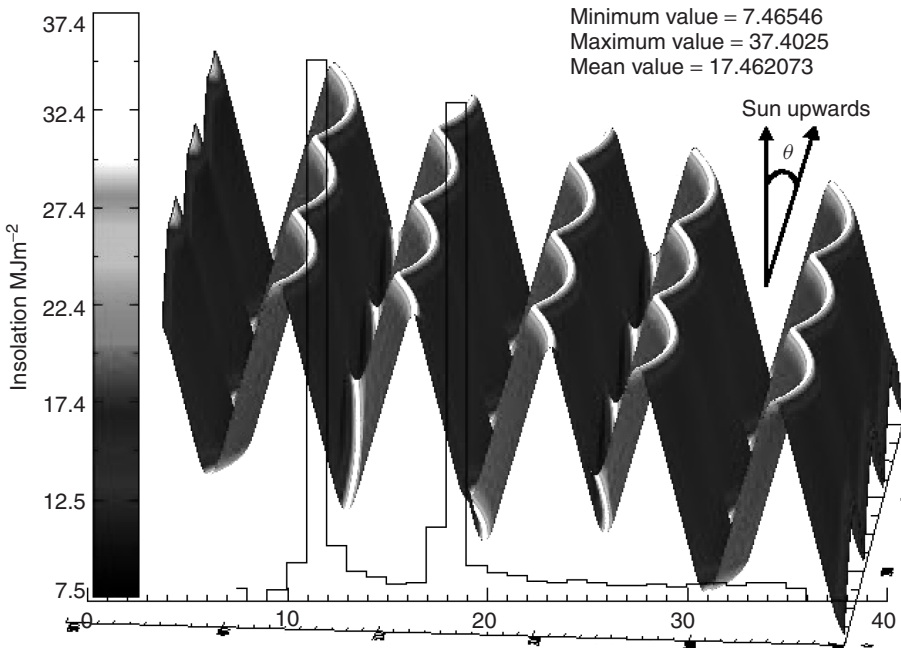


Figure 3.7 (Plate 4) Insolation on penitentes for the 37th day of the year, corresponding to values in Figure 3.5. Superimposed is the histogram of cell values, clearly showing a bimodal distribution of insolation values corresponding to the north-facing and south-facing slopes. The reference system is rotated at an angle θ so that the vertical is the direction of the sun at midday on the summer solstice

Table 3.5 Energy balance partition for flat snow and penitentes ($W\,m^{-2}$)

	SW↓	SWnet	LWnet	Net turbulent flux	Total
Flat snow	435	209	−77	−17	115
Penitentes (mean)	238	133	−38	−28	67

increases downwards and the former increases upwards, with a maximum at the peaks.

Net long-wave radiation increased its mean value from $-77\,W\,m^{-2}$ on a flat surface to $-38\,W\,m^{-2}$ on the penitentes, due to emitted radiation from the surrounding snow walls. Turbulent fluxes decreased their net value from -17 to $-28\,W\,m^{-2}$ on average (Table 3.5). These values are averages for all grid cells, however, surface area is different according to the slope of the cell, and total area is increased on a rough surface, in this case by a factor of 2.8. On the larger scale, we have to assume the conservation of radiative fluxes, and therefore the main change in the overall energy balance is brought about by the increased turbulent fluxes due to increased roughness. This change represents about 2.85 mm of water equivalent melt (mmwe) decrease per day or 342 mmwe for the four principal months of the ablation season. The partition of the energy balance components on the altered snow surface is also important. Thus, the penitentes' walls receive about half of the incoming solar radiation with respect to a flat surface. This compensates for the increase in long-wave radiation and keeps the penitentes' walls generally frozen and dry, while melting occurs only at the bottom of the troughs. The localized melting favours percolation of water, with almost no supraglacial drainage, which in turn reduces loss of water by further evaporation. This corresponds well with the observed situation, although small streams may form lower down and later in the ablation season, as seen on the Horcones glacier on Aconcagua in a different year. Nonetheless, these streams are much smaller than supraglacial rivers observed in the Alps.

3.6.1 Sensitivity of energy balance and implications

This work has addressed the formation of penitentes through an experimental and modelling campaign in the

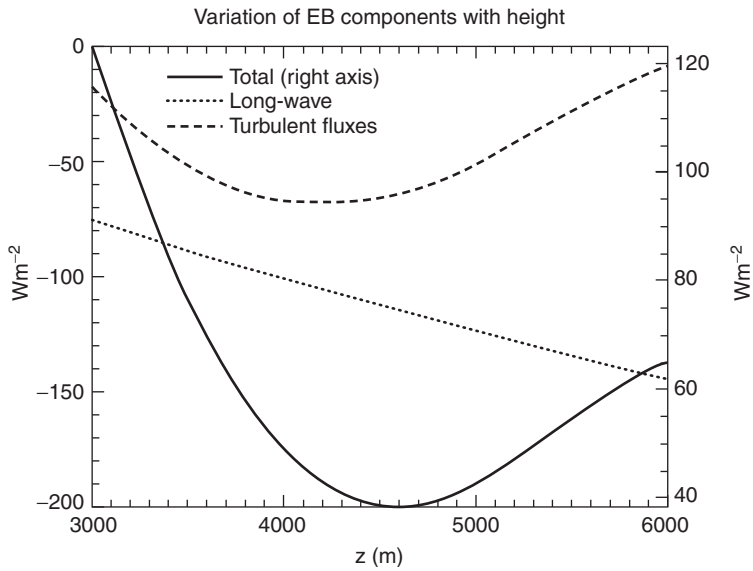


Figure 3.8 Variation of the energy balance components with height for mean recorded values at the lower AWS (3335 m a.s.l.) applying a standard lapse rate ($-0.0065\,\mathrm{Km}^{-1}$). Short-wave global radiation is modified primarily by albedo, which in this case was simplified to a constant value

Andes. Penitentes are a unique and complex form that result from a relatively narrow band of meteorological conditions. Thus, any change in climate is likely to have implications for the formation of penitentes, and thus in turn the mass balance of glaciers as their buffering effect on snow melt, as discussed in the previous section, is reduced.

A simple study of the sensitivity of the energy balance to different parameters and its variation with height was carried out. This is represented in Figure 3.8. We can observe a minimum of the net energy balance at about 4600 m a.s.l., which corresponds well with the maximum extension of penitentes. The shape of the curve is relatively sensitive to initial temperature and relative humidity and very sensitive to wind speed. Wind speed was fairly constant and moderate to light at the upper AWS, with values that are very similar to recorded values in a previous campaign in the Argentinian Andes at similar latitude and height. Increased wind speed decreases dramatically the net energy balance and would prevent the formation of penitentes, as the turbulent fluxes are proportional to roughness. This was observed on the upper section of the Juncal glacier, where wind is higher on unsheltered slopes and snow is less metamorphosed and relatively smooth. However, penitentes were found not far below the summit of Nevado Juncal (6100 m) in a very sheltered location. A similar situation was observed on Cerro Aconcagua, where the snow ablated into penitentes up to an altitude of 5800 m except on the very wind-exposed eastern section (Polish glacier), where flatter snow or bare ice existed. Running the model with a dry adiabatic lapse rate, as may be expected under a katabatic wind regime, results in a shift of the minimum in energy balance to a lower altitude. The same situation could be expected earlier in the season, when air temperature is lower. Observations on Juncal glacier confirmed this, the lower line of penitentes formation migrated upwards from about 3700 m in early December to about 4000 m later in the season. Small penitentes formed at lower elevations gradually became wet, rounded and disappeared over a period of a few weeks.

Through this set of experimental and modelled data, we can make a number of observations about the impact of changes in meteorological variables as follows.

- Increased humidity will hinder the formation of penitentes, both by decreasing the latent heat flux and increasing the net long-wave radiation.
- Increased temperature will shift upwards the lower limit of penitentes formation.
- Stronger circulation with increased wind speeds will decrease or suppress penitentes formation.

This initial sensitivity study does not allow us to comment on the likely implications of climate change on penitentes and subsequent influences on glacier energy

and mass balance. Rather, it demonstrates that penitentes are sensitive to changes in meteorological parameters and that the model developed allows us to form some initial hypotheses about the likely impacts. Further work, including the extensive collection of field data in stable and unstable atmospheric conditions, should shed further light on these processes.

As we have seen, the formation of penitentes occurs within a narrow band of climatic conditions, and their presence provides information on seasonal trends, a point already stressed by Kotlyakov and Lebedeva (1974), thus, one direct application of the relationship between snow surface morphology and climate is the potential use of remote sensing for assessing seasonal climatic conditions. The increased roughness of penitentes is potentially detectable using SAR polarimetry, while changes in albedo may identify the differences between flat snow and penitentes areas through the use of optical remote sensing. To exploit the full potential of this relationship, a better knowledge of the initial stages in the formation of micropenitentes is needed, and that was beyond the scope of this work. Far more detailed micrometeorological measurements in the field or the replication of the process in a cold laboratory under controlled circumstances would be necessary to gain full insight into this process of snow ablation.

3.7 CONCLUSIONS

The climatic characteristics of the Dry Central Andes – low humidity and high solar radiation inputs in stable summers coupled with high evaporation rates and strong radiative cooling – result in a unique snow ablation morphology: penitentes. Modelling and field data suggest that any changes in the meteorological conditions during the initial stages of growth of penitentes early in the ablation season, for example, increased humidity, long-wave radiation or stronger winds, may suppress or hinder their formation. Since the growth of penitentes is self supported in part by a positive feedback mechanism, the consequences of a small change in meteorological conditions may result in a disproportionate change in overall ablation. Modelling work suggests that penitentes enhance conservation of snow cover, and the consequences of their loss might be increased ablation over the whole season, decreased glacier mass balance and faster depletion of water resources. Given the critical nature of snow and ice melt in relation to water resources for human consumption and agricultural resources in the Central Andes, any potential change is worthy of further research.

3.8 ACKNOWLEDGEMENTS

Field work was possible thanks to the support of Professor David Sugden and a research grant from the Carnegie Trust while J. G. Corripio was enjoying a Carnegie Scholarship at the University of Edinburgh. We are grateful for the help given by the Laboratorio de Glaciología, University of Chile, and especially to Andrés Rivera and Jorge Quinteros. Fieldwork was easier and more enjoyable thanks to dedicated field assistants Cameron Thomson and Carlitos Gómez. We would like to thank the Chilean Dirección General de Aguas and acknowledge the support of the ETH, Zürich, especially the Arolla group: Uli Strasser, Francesca Pellicciotti, Paolo Burlando, Martin Funk and Ben Brock. The final version of this paper was improved thanks to the helpful comments and suggestions of the anonymous reviewers.

REFERENCES

Andreas, E. L.: 1987, A theory for the scalar roughness and the scalar transfer coefficients over snow and sea ice, *Boundary Layer Meteorology* **38**, 159–184.

Arnold, N. S., Willis, I. C., Sharp, M. J., Richards, K. S. and Lawson, M. J.: 1996, A distributed surface energy–balance model for a small valley glacier, *Journal of Glaciology* **42**(140), 77–89.

Betterton, M. D.: 2001, Theory of structure formation in snowfields motivated by penitentes, suncups, and dirt cones, *Physical Review E* **63**(056129), 12. http://prola.aps.org/

Brutsaert, W.: 1982, *Evaporation into the Atmosphere: Theory, History, and Applications*, 1984 edn, Reidel, Dordrecht.

Corripio, J. G.: 2003a, *Modelling the energy balance of high altitude glacierised basins in the Central Andes*, PhD thesis, University of Edinburgh. Unpublished.

Corripio, J. G.: 2003b, Vectorial algebra algorithms for calculating terrain parameters from DEMs and the position of the sun for solar radiation modelling in mountainous terrain, *International Journal of Geographical Information Science* **17**(1), 1–23.

Corripio, J. G.: 2004, Snow surface albedo estimation using terrestrial photography, *International Journal of Remote Sensing*, Vol. 25, No. 24, 5705–5729.

Darwin, C.: 1839, *Journal of Researches into the Geology and Natural History of the Various Countries Visited by H. M. S. Beagle, Under the Command of Captain Fitz Roy, R.N., 1832 to 1836*, Henry Colburn, London.

Dilley, A. C. and O'Brien, M. O.: 1998, Estimating downward clear sky long–wave irradiance at the surface from screen temperature and precipitable water, *Quarterly Journal of the Royal Meteorological Society* **124**(549), 1391–1401.

Dozier, J., Bruno, J. and Downey, P.: 1981, A faster solution to the horizon problem, *Computers & Geosciences* **7**, 145–151.

Dozier, J. and Frew, J.: 1990, Rapid calculation of terrain parameters for radiation modelling from digital elevation

data, *IEEE Transactions on Geoscience and Remote Sensing* **28**(5), 963–969.

Greuell, W., Knap, W. H. and Smeets, P. C.: 1997, Elevational changes in meteorological variables along a midlatitude glacier during summer, *Journal of Geophysical Research* **102**(D22), 25941–25954.

Greuell, W. and Smeets, P.: 2001, Variations with elevation in the surface energy balance on the Pasterze, Austria, *Journal of Geophysical Research* **106**(D23), 31717–31727.

Iqbal, M.: 1983, *An Introduction to Solar Radiation*, Academic Press, Toronto.

Jackson, B. and Carroll, J.: 1977, Aerodynamic roughness as a function of wind direction over asymmetric surface elements, *Boundary Layer Meteorology* **14**, 323–330.

Kotlyakov, V. M. and Lebedeva, I. M.: 1974, Nieve and ice penitentes, their way of formation and indicative significance, *Zeitschrift für Gletscherkunde und Glazialgeologie* **Bd X**, 111–127.

Lettau, H.: 1969, Note on aerodynamic roughness-parameter estimation on the basis of roughness-element description, *Journal of Applied Meteorology* **8**, 828–832.

Liniger, H., Weingartner, R. and Grosjean, M. (eds): 1998, *Mountains of the World – Water Towers for the 21st Century*, Mountain Agenda for the Commission on Sustainable Development (CSD), University of Bern.

Lliboutry, L.: 1954a, Le Massif du Nevado Juncal ses penitentes et ses glaciers, *Revue de Géographie Alpine* **42**, 465–495.

Lliboutry, L.: 1954b, The origin of penitentes, *Journal of Glaciology* **2**(15), 331–338.

Lliboutry, L.: 1965, *Traité de Glaciologie, Vol. I & II*, Masson, Paris.

Lliboutry, L.: 1998, Glaciers of the Dry Andes, *in* R. S. J. Williams and J. G. Ferrigno (eds), *Satellite Image Atlas of Glaciers of the World South America*, United States Geological Survey Professional Paper 1386–I. http://pubs.usgs.gov/prof/p1386i/index.html

Lowe, P. R.: 1977, An approximating polynomial for the computation of saturation vapor pressure, *Journal of Applied Meteorology* **16**, 100–103.

Marks, D. and Dozier, J.: 1992, Climate and energy exchange at the snow surface in the alpine region of the Sierra Nevada. 2. Snow cover energy balance, *Water Resources Research* **28**(11), 3043–3054.

Morris, E. M.: 1989, Turbulent transfer over snow and ice, *Journal of Hydrology* **105**, 205–223.

Munro, D. S.: 1989, Surface roughness and bulk heat transfer on a glacier: comparison with eddy correlation, *Journal of Glaciology* **35**(121), 343–348.

Naruse, R. and Leiva, J. C.: 1997, Preliminary study on the shape of snow penitents at Piloto Glacier, the Central Andes, *Bulletin of Glacier Research* **15**, 99–104.

Nuñez, M.: 1980, The calculation of solar and net radiation in mountainous terrain (Risdon, Tasmania), *Journal of Biogeography* **7**(2), 173–186.

Obleitner, F.: 2000, The energy budget of snow and ice at Breidamerkurjökull, Vatnajökull, Iceland, *Boundary Layer Meteorology* **97**, 385–410.

Olyphant, G. A.: 1986, Longwave radiation in mountainous areas and its influence on the energy balance of alpine snowfields, *Water Resources Research* **22**(1), 62–66.

Peterson, W. A., Dirmhirn, I. and Hurst, R. L.: 1985, A theoretical model to determine solar and diffuse irradiance in valleys, *Solar Energy* **35**(6), 503–510.

Prata, A. J.: 1996, A new long–wave formula for estimating downward clear–sky radiation at the surface, *Quarterly Journal of the Royal Meteorological Society* **122**, 1127–1151.

Raupach, M. R.: 1992, Drag and drag partition on rough surfaces, *Boundary Layer Meteorology* **60**, 375–395.

Schwerdtfeger, W.: 1976, *World Survey of Climatology. Climates of Central and South America*, Elsevier, Amsterdam.

Smeets, C., Duynkerke, P. and Vugts, H.: 1999, Observed wind profiles and turbulence over an ice surface with changing surface roughness, *Boundary Layer Meteorology* **92**, 101–123.

Spencer, J. W.: 1971, Fourier series representation of the position of the sun, *Search* **2**, 172.

Stull, R.: 1988, *An Introduction to Boundary Layer Meteorology*, Kluwer Academic Publishers, Dordrecht.

TOMS–EP: 2001, Total Ozone Mapping Spectrometer–Earth Probe data sets. http://toms.gsfc.nasa.gov/eptoms/ep.html

Vuille, M., Hardy, D. R., Braun, C., Keimig, F. and R Bradley, R.: 1998, Atmospheric circulation anomalies associated with 1996/1997 summer precipitation events on Sajama Ice Cap, Bolivia, *Journal of Geophysical Research* **103**(D10), 11191–11204.

4

Using Subgrid Parameterisation and a Forest Canopy Climate Model for Improving Forecasts of Snowmelt Runoff

ULRICH STRASSER[1] AND PIERRE ETCHEVERS[2]

[1]Department of Earth and Environmental Sciences, Section Geography, University of Munich, Munich, Germany, [2]Centre National de Recherches Météorologiques, Centre d'Études de la Neige, METEO-France, Saint Martin d'Hères, France

4.1 INTRODUCTION

Mountainous catchments are the origin of many large rivers and a major source of water availability. They not only are a local resource for freshwater supply and hydropower generation but also considerably influence the runoff regime of the downstream rivers. The increasing needs for a sustainable management of river water resources and the demand for effective flood protection force to compromise between water exploitation and conservation and require a comprehensive knowledge of the dynamics of mountainous river basins. The latter is particularly important for such basins, which are dominated by perennial snow cover and glacierised areas, where spring floods induced by snowmelt usually evolve very quickly and can have disastrous effects, both for the environment and population of the downstream regions. For the quantification and prognosis of such snowmelt induced floods, forecast systems can be set up, consisting of meteorological prognoses coupled with a set of hydrological models to describe the relevant processes that govern the runoff production with proper forecasting accuracy and horizon (e.g., the European Flood Forecasting System (EFFS): http://effs.wldelft.nl).

A number of approaches exist for the spatial discretisation of a catchment to quantify the snowmelt runoff component, the largest surface water input controlling runoff during the melting season: for example, the various versions of the Snowmelt Runoff Model employ a segmentation of the catchment into elevation bands in combination with the areal depletion curve concept (Rango and Martinec 1995). Bell and Moore (1999) provide a detailed discussion of an elevation-based snowmelt model and discuss the number of bands that would be most efficient. Besides the elevation class–based approaches, a variety of subgrid parameterisations have been developed recently to deal with the issue in a more continuous manner (Liston 1999, Luce *et al*. 1999). All those studies show the importance of the orography for snowmelt modelling, with the vertical domain being most significant for the spatial discretisation in mountainous catchments (Braun *et al*. 1994).

A practical way to investigate the resolution impact on snowmelt simulation quality and to detect scale effects consists in using the same model at different resolutions and comparing the results with observations and/or with the highest resolution simulation, considered as the most accurate. Habets *et al*. (1999) compared two simulations

Climate and Hydrology in Mountain Areas. Edited by C. de Jong, D. Collins and R. Ranzi
© 2005 John Wiley & Sons, Ltd. ISBN: 0-470-85814-1

of a large basin with different resolutions ($8 \cdot 8\,km^2$ and $128 \cdot 128\,km^2$). The study shows that results are similar for both resolutions in flat valley areas, but they are very different for the alpine section of the basin. In particular, the simulation of the snowpack evolution is not realistic for spatial elements with a size of 128 km. This result was confirmed by Etchevers *et al*. (2001a), who simulated the waterflows in the Durance catchment with three different resolutions. For the coarsest resolution ($46 \cdot 46\,km^2$), the annual surface water fluxes are well calculated, but the monthly partitioning is not correct. Again, the main cause is the poor simulation of the melting snowpack. With an improved resolution ($8 \cdot 8\,km^2$), the snowmelt and river discharge is better simulated; only the flood peak in spring is still overestimated. For the finest resolution ($1 \cdot 1\,km^2$), this systematical bias is corrected: as the variable altitude of the snow line is modeled more realistic, the melting water reaches the river more gradually and the simulated flood intensity is lower. However, computational requirements are increased by a factor of 64.

Besides elevation, aspect might also be a determinant factor to explain the snowpack evolution in alpine watersheds, but only at a small scale where its effects do not statistically compensate. The same accounts for snowdrift as a source of snowcover variability. For coarse resolution, the most promising strategy to improve the prediction of the snowmelt process dynamics is the consideration of the snow–vegetation interaction.

The goal of this study is to investigate whether a suitable compromise between accuracy and computation time requirements exists for snowmelt simulations and predictions on a regional scale. We apply the ISBA-CROCUS modelling scheme to the upper Durance catchment (Rhône-Alpes/France) at two spatial resolutions (1 km and 8 km) and investigate methods of subgrid parameterisation that can be applied at the coarse 8-km resolution and that lead to improvements in simulations. The following subgrid parameterisation methods are explored: the first is a technique that utilises the high-resolution (1 km) elevation data to derive subgrid information for topography in the 8-km model cells. In principle, this approach is based on the probability distributed principle (Moore 1985): three subareas that are not necessarily coherent are derived for each grid cell by statistically adapting the specific topographical variability. The altitudes of the subareas are used for interpolation of the meteorological variables. The second subgrid parameterisation is a forest climate model to include the effect of a forest canopy on the meteorological conditions that affect the snowpack. Both these subgrid parameterisations do not affect computation time since they are applied to the meteorological variables that are provided offline by the meteorological model. Thirdly, the parameterisation of subgrid topography is combined with the forest climate model.

In all cases, we investigate the effects on daily discharge hydrographs and the mean annual water balance in the basin. The proposed methods are transferable and can be used for improving operational snowmelt flood simulations and forecasts.

4.2 THE MODELS ISBA AND CROCUS

4.2.1 The SVAT model ISBA

The ISBA soil-vegetation atmosphere transfer (SVAT) scheme was developed for the **G**lobal **C**irculation **M**odel (GCM) and **N**umerical **W**eather **P**rediction (NWP) model of the French Weather Service Météo-France (Noilhan and Planton 1989, Noilhan and Mahfouf 1996). ISBA calculates the energy balance of the surface (bare soil, vegetation and snow) on the basis of the force-restore method and has six prognostic variables: the soil water contents of the surface, root zone, deep soil and interception reservoirs, and the surface and deep soil temperatures. The deeper soil layers can feed the root zone by capillary rise, and only the water of the root zone is directly available for transpiration. Two parameterisations are particularly adapted for hydrological purposes: a subgrid surface runoff parameterisation permits the model to take into account the fraction of the cell where the soil surface is saturated, and a minimum base flow parameterisation for dry soil conditions is considered, which permits the model to simulate very small discharges. Both these parameterisations are treated uniformly for the whole watershed (Habets *et al*. 1999). The parameters in ISBA were calibrated by Etchevers *et al*. (2001b) and left unchanged for all model runs.

ISBA calculates surface runoff every 5 min. In this study, the simulated runoff is aggregated to daily values for direct comparison with measured discharge. This direct comparison (without any routing) is sufficient because owing to the large relief and the relatively small size of the catchment the time of concentration is much smaller than one day (Etchevers *et al*. 2001a).

4.2.2 The snow model CROCUS

CROCUS is a one-dimensional snow model initially developed for avalanche risk forecasting; it simulates the evolution of the snow cover characteristics as a function of the meteorological conditions (Brun *et al*. 1989, 1992). The model considers the internal state

of up to 50 layers of the snow pack (parallel to the surface slope) by calculating their temperature, liquid water content, density and snow type using time steps of 15 min. CROCUS takes the following phenomena into account: energy exchanges between the layers of the snow pack and at its interfaces with the soil and the atmosphere, absorption of solar radiation with depth, phase changes, water transmission through the snow pack, mass exchanges due to precipitation and liquid water runoff, compaction and metamorphism of the snow.

The melt rates simulated with CROCUS are routed to ISBA and treated as precipitation falling on that part of the model cell that is not covered with snow. The temperature gradient at the snow–soil interface drives the conduction flux. No direct interaction between snow and vegetation is modeled.

4.3 THE UPPER DURANCE CATCHMENT AND UTILISED DATA

The upper Durance catchment is situated in the southern French Alps (Figure 4.1). Some of its characteristics can be depicted from Table 4.1. Because of the volcanic origin of the subsurface, the water tables are shallow and storage capacity that contributes to summer river discharge is very limited. The climate of the region is mostly dominated by a Mediterranean influence: precipitation occurs mostly in autumn (generally as snow) and due to severe storm events during spring. The relatively small total amount of precipitation and the high average altitude of the catchment are the reason for the comparably small forest coverage of only one-quarter; about half of the catchment is covered by grassland and the remaining quarter is in the high mountain environment with rocks and snow. Besides the Guil, the main tributary of the Durance, there is no other significant river in the watershed. Downstream of La Clapière is the Serre-Ponçon dam, the largest reservoir in France, which is managed with a multi-purpose objective: hydropower generation, water supply for irrigation and recreation.

Table 4.1 Basin characteristics of the upper Durance catchment

Name of the basin	Durance at La Clapière
Mountain range	Rhône-Alpes/France
Elevation range (m)	787–4102
Latitude/Longitude	45°N, 6.5°E
Area (km^2)	2170
Glacierised area (km^2)	2
Forested area (km^2)	26
Dominant vegetation type	Alpine pasture, larch forest
Geology	Limestone and crystalline
Mean discharge at outlet (mm)	713
Mean precipitation (mm)	1064
Mean evapotranspiration (mm)	348

4.3.1 Soil and vegetation data

The soil and vegetation maps of the catchment have been derived using the INRA (**I**nstitut **N**ational de **R**echerches **A**gronomiques) soil database (King *et al*. 1995), a two-year satellite archive of a vegetation index, the AVHRR/NDVI (Champeaux and Legléau 1995) and the CORINE land cover database (Cornaert *et al*. 1996). From the soil types, the sand and clay fractions in each model cell are determined. The vegetation input data consist of the areal fraction, the leaf area index (LAI) and the minimum stomatal resistance. For each vegetation type, a monthly evolution of the vegetation parameters based on the monthly values of the NDVI between prescribed minimum and maximum values is derived. Therefore, only the extremes of the vegetation parameters have to be imposed for each vegetation type. For the 8-km resolution, these data are aggregated according to the method proposed by Noilhan and Lacarrère (1995).

4.3.2 Meteorological data

For the hourly interpolation of the meteorologic input variables, liquid and solid precipitation, incoming radiation fluxes, mean wind speed, air temperature and humidity, the SAFRAN analysis system (Durand *et al*. 1993) is used. Among the principal data sources are the standard meteorological observations (SYNOP), upper-air messages from radiosondes, the ancillary network of visual and automatic surface observations during the winter ski period (NIVO-METEO) and the altitudinal distribution of temperature, wind and humidity as given by the French mesoscale forecast model PERIDOT (grid size of 35 km). For offline applications as the one presented here, the guess field of the European Centre for Medium Range Weather Forecast (ECMWF) analyses are used.

To describe the optimal analysis method applied is beyond the scope of this investigation. It may be of interest, however, to point out that orographic effects were taken into account for a first guess of precipitation on the basis of the 5-km grid analysis as described by Bénichou and Breton (1987).

The meteorological measurements for the Durance watershed consist of one synoptic six-hourly observation

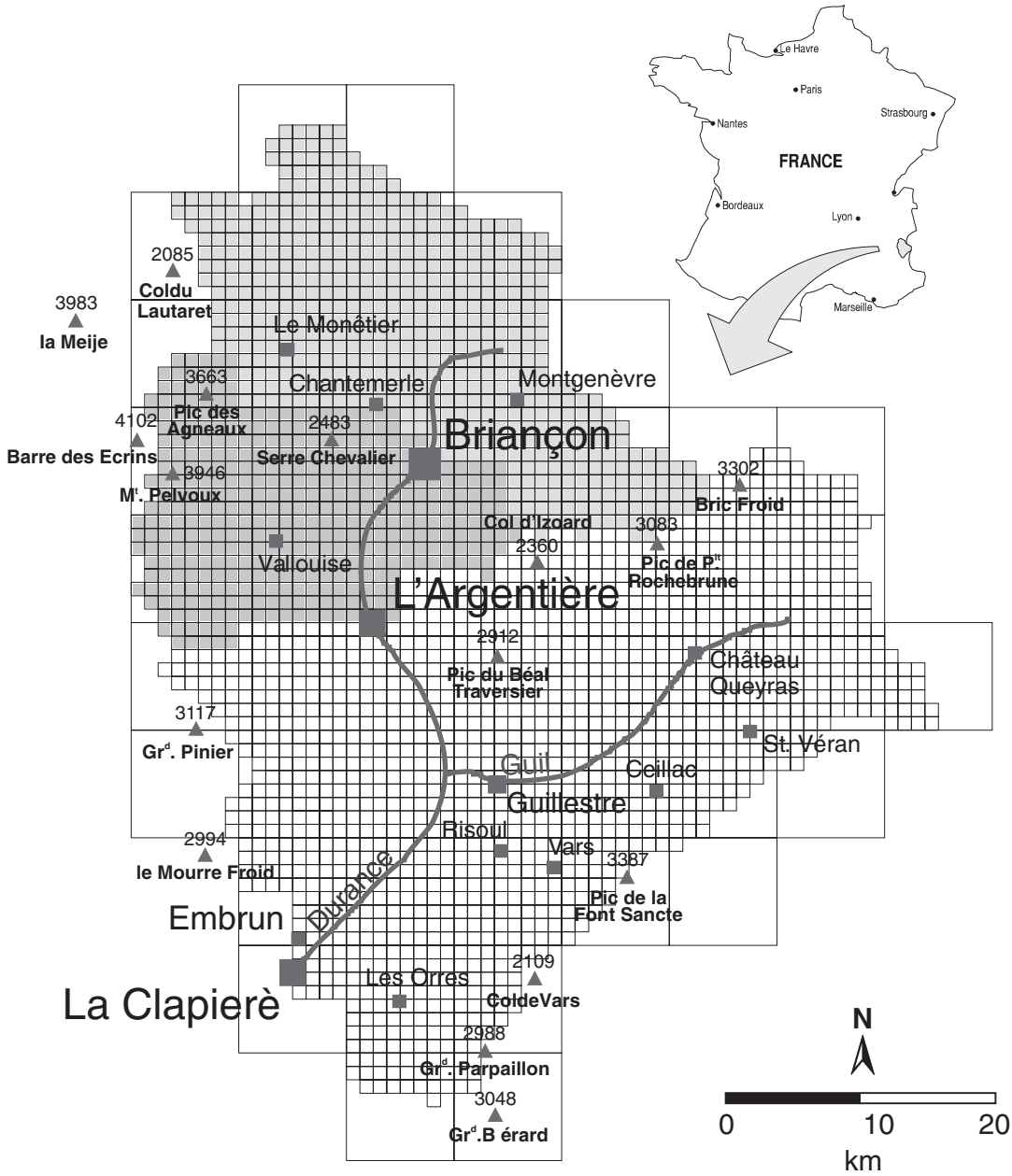


Figure 4.1 The catchment of the upper Durance in the southern French Alps. The grids correspond with the resolutions of 1 km and 8 km. The three subcatchments are separated by the gauging stations Briançon, L'Argentière and La Clapière

of the main meteorological variables in Embrun and daily precipitation observations from 16 stations of the French climatologic network. The incoming radiation fluxes are computed using the radiative transfer scheme of Ritter and Geleyn (1992).

4.3.3 Digital terrain model

The base digital terrain model (DTM) consists of 1-km resolution altitudes for the catchment. The 8-km resolution DTM was generated by averaging the 64 (or

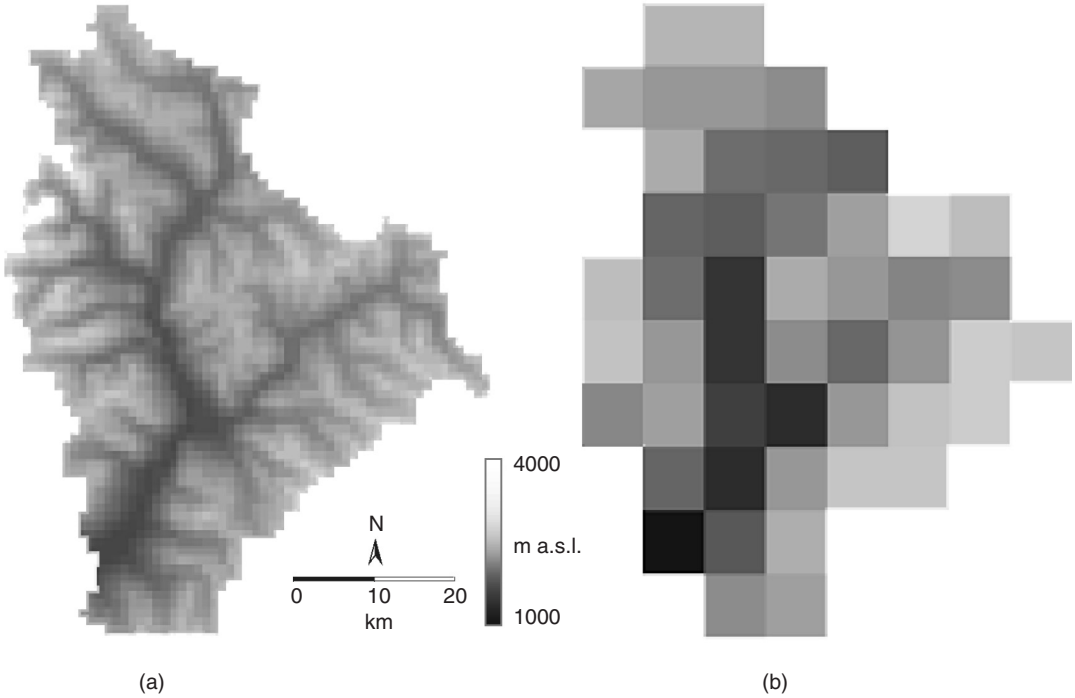


Figure 4.2 Digital terrain model (DTM) for the upper Durance catchment in 1-km resolution (a) as derived with the topographic parameterisation software TOPAZ, (b) the aggregated DTM with 8-km resolution

fewer at the catchment border) 1-km pixels within each 8-km cell (Figure 4.2). DTM correction, the catchment and subcatchment segmentation and the channel network analysis for the identification of the gauging station locations (Briançon, L'Argentière and La Clapière) were performed using the digital landscape analysis tool TOPAZ (Garbrecht and Martz 1997).

4.3.4 Subgrid parameterisation schemes

Subgrid parameterisation I: topography

For the subgrid parameterisation of topography, each 8-km DTM cell is segmented into three subareas of equal size: the 64 pixels inside each cell are sorted, then the lowest pixels are assigned to a ''low'' subarea; the same number of highest pixels are assigned to a ''high'' subarea, and, consequently, the remaining pixels are assigned to a ''mean'' subarea. Then the mean altitude for the three subareas is calculated by simply averaging the pixel altitudes inside each of the three subareas. These are determined separately for each model cell and not necessarily coherent, in contrast to the elevation bands as derived by a conventional segmentation of an entire catchment. The resulting subarea altitudes are then used for the interpolation of the meteorological variables with SAFRAN.

Figure 4.3 shows the resulting mean subarea altitudes for the fifty 8-km cells in ascending order with altitude. It can be seen that the vertical extent between the subarea altitudes within one 8-km cell can reach more than 1000 m because of the steep relief. For cells with only few 1-km pixels inside (close to the watershed divide), the vertical extent is less. The geographical distribution of the standard deviation (sigma) of the pixel altitudes in the 8-km cells shows that the highest values can be found in the valleys of the rivers Durance and Guil and the summit region of the Écrins massif, both being very steep. The smallest standard deviations are again found close to the watershed divide in cells that contain only few 1-km pixels, and in the comparably flat Queyras summit region (in the eastern part of the catchment).

Subgrid parameterisation II: forest climate

The meteorological conditions that affect the snow pack inside a forest canopy vary distinctly from those in

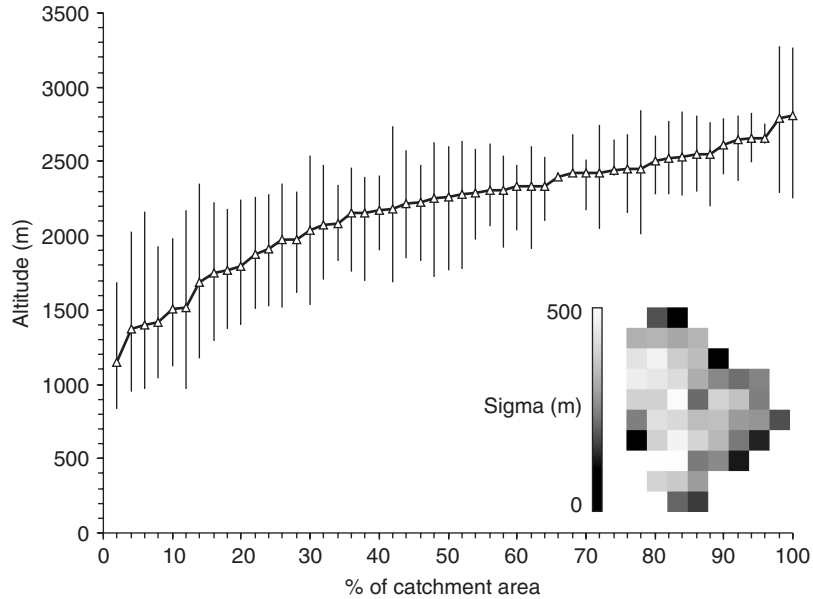


Figure 4.3 Hypsographic curve, altitudes of the three subareas (represented by the bar ends and the triangles) in the 50 model cells of 8-km resolution and geographical distribution of the standard deviation of the 1-km pixel altitudes in each 8-km cell

the open. One of the goals of this study is to quantify the effects of the presence of a forest on the temporal evolution of snowmelt. These processes are considered in the model by modifying the meteorological variables as provided with SAFRAN and a variable albedo parameterisation in CROCUS taking into account the faster decrease of albedo inside the canopy. The main phenomena that affect the climatic conditions inside a forest are the following: shadowing effect of the trees for solar radiation (visible direct and diffuse as well as longwave), longwave radiation of the trees, increase of humidity, reduction of wind speed, reduction of temperature fluctuation amplitudes and interception of precipitation (including sublimation, melt and snow sliding from the branches). To characterise a forest, a certain number of parameters can be used: its density, the type and shape of the trees, their size or the LAI. However, for spatial applications at the scale as the one presented here it is necessary to define mean forest characteristics for the area to be modeled and not look at features of single trees. Here, the mean density of the forest, the mean tree height and the LAI are used.

The forest climate model used in this study was developed and validated by Durot (1999) at the Col de Porte station in the Chartreuse Massive in the French Alps. Since it has not been applied on a regional scale in combination with a distributed hydrological model before, it is described in detail in the following section. The model calculates the modified meteorological variables in a forest canopy, which are then used as input for CROCUS: direct, diffuse and longwave radiation, temperature, humidity, precipitation and wind speed. Thus, two snow covers are modeled separately in each grid cell: one for forest and one for open land conditions. The fraction of each cell that is covered by forest is derived from a landuse map.

The forest climate model

Generally, the reduction of the turbulent exchanges inside the canopy diminishes the sensible and latent heat fluxes, thus making the net radiation fluxes the principal energy sources for snowmelt. The radiative characteristics of a forest have a significant effect on the evolution of the snow cover. The albedo of the forest itself, usually between 0.1 and 0.3, changes considerably with the presence of snow under the trees. On the ground, the incoming radiative fluxes are diminished because of the vegetation cover. To describe this interception process, a wide range of models with different complexity has been developed. The model by Li and Strahler (1986, 1992) is the most detailed one but requires a large number of input parameters that can only be reliably provided for the plot scale. Monteith and Unsworth (1990) use

the exponential decrease of the Beer–Bouguier law to describe the extinction effect, considering the LAI and a coefficient depending on the geometry of the trees as well as the incidence angle of the sun. A detailed historical overview of the different approaches is given by L'Homme (1991).

In this study, a simple formula assuming a linear dependence of the extinction with the forest density (Bowles *et al*. 1994) for both direct and diffuse radiation is applied:

$$Q_{\mathrm{dir},f} = Q_{\mathrm{dir}} \cdot (1 - D_f) \tag{4.1}$$

$$Q_{\mathrm{diff},f} = Q_{\mathrm{diff}} \cdot (1 - D_f) \tag{4.2}$$

Despite the attenuation of the incoming solar radiation, the canopy is also a source of longwave radiation by emitting part of the visible radiation absorbed like a black body in all directions. Thus, for the snow on the ground a new net balance of infrared radiation is calculated, taking into account the extinction of atmospheric radiation and emission of the vegetation:

$$Q_{l,f} = Q_l \cdot (1 - D_f) + D_f \cdot \varepsilon_f \cdot \sigma \cdot T_{\mathrm{air},f}^4 \tag{4.3}$$

The emissivity of the forest depends on the tree type and can be represented by values close to a black body (Berris and Harr 1987). Here, it is assumed to be 0.97. For the radiation temperature of the trees, it is assumed that it is approximately equal to the measured temperature between the leaves (Davis and Hardy 1997), here represented by the estimated air temperature for the canopy. The latter has a vertical gradient that plays an important role for the heat exchange. Mostly during the day, the temperature in the canopy is higher than above, but it decreases rapidly downwards to the ground. During the night, the temperature can be very low outside the canopy, but inside it remains higher. As an effect, the forest temperature and particularly its daily amplitude is less pronounced than in the open. In the annual mean, the forest temperature is lower, but during winter it can be higher. Since it is usually measured directly, only few formulae exist to derive forest canopy temperature from standard observations. Here it is estimated using the model proposed by Obled (1971), which uses the mean daily temperature and a constant scaling parameter $R_c = 0.8$:

$$T_{\mathrm{air},f} = R_c \cdot (T_{\mathrm{air}} - T_{\mathrm{mean}}) + T_{\mathrm{mean}} - \Delta T \tag{4.4}$$

where $T_{\mathrm{mean}} = (T_{\mathrm{max}} + T_{\mathrm{min}}) \cdot 0.5$ and $\Delta T = (T_{\mathrm{mean}} - 273.16)/3$, with ΔT limited to the range $-2^{\circ}\mathrm{C} < \Delta T < +2^{\circ}\mathrm{C}$. With T_{mean} and ΔT, respectively, the daily and seasonal effects on the temperature amplitudes are considered.

Generally, the humidity in the forest is increased because of the evapotranspiration from the trees (during summer). Durot (1999) conducted a series of measurements to evaluate the effect of the vegetation activity. In the mean, the humidity is approximately 10% higher inside the forest canopy ($RH_f = 1.1 \cdot RH$), but this increase is larger if the snow that is intercepted by the trees melts and falls down. In this case, it is estimated to be 20% ($RH_f = 1.2 \cdot RH$), which often leads to conditions close to saturation.

Wind speed is considerably reduced by a forest canopy, little in the corona layer and almost to zero close to the ground. The vertical wind profile depends on the forest type and its density (Jeffrey 1968). Bonan (1991) developed a model describing the wind speed inside the forest canopy depending on the height:

$$u_f(z) = u \cdot \mathrm{e}^{(-a \cdot (1 - z/z_m))} \tag{4.5}$$

The parameter a was found to be equal to 3 for a wide range of conditions (Bonan 1991).

Solid precipitation is always partially intercepted if a vegetation cover is present, and then undergoes a more or less pronounced evaporation. Thus, a forest canopy can have a significant effect on the water resources of a basin. Numerous studies exist, investigating such consequences for the water balance of certain regions. Harding and Pomeroy (1996) found a loss of intercepted snow by evaporation of almost 30% in their study region in the United States. Schmidt (1991) investigated the sublimation of intercepted snow with an artificial tree. On the other hand, Jeffrey (1968) showed that the sublimation losses by interception in the canopy can often be neglected.

Those studies show that the interception phenomenon depends on the region and its climate. Extrapolation of interception rates into other geographical regions often leads to wrong results (Lundberg and Halldin 1994). Satterlund and Haupt (1967) concluded their study that no universal formula exists for the storage of snow and the interception loss because of the complexity of the processes involved after the deposition of snow on the trees.

In the model presented here, the precipitation as provided by SAFRAN is modified for the consideration of the interception processes according to

$$P_f = P - I + P_c + M_t \tag{4.6}$$

In the following, the derivation of I, P_c and M_t will be explained: the total interception is composed by the

interception of solid precipitation (snow) and liquid precipitation (rain). Thereby, the snow interception is calculated considering the maximum snow interception, a cumulative precipitation of the snowfall event and a threshold precipitation:

$$I_s = \frac{S_{\max}}{1 + e^{-k\cdot(P_{\text{snow}} - P_0)}} \tag{4.7}$$

Effectively, the values of $S_{\max}$ and k depend on the density of the snow, being a function of the meteorological conditions and particularly the temperature and wind. For different conditions with low wind speeds and snow densities and for three different types of conifers, Schmidt and Gluns (1991) found $S_{\max} = 5$, $P_0 = 4$ and $k = 0.75\,\text{mm}^{-1}$. They show that the difference of accumulation between various species of trees is less important than the one between different snowfall event types. Therefore, it is the meteorological conditions that mostly affect the process of interception. For low snowfall events (<2 mm), the formula gives unrealistic results; then it is replaced by the simple linear parameterisation (Keller and Strobel 1979):

$$I_s = 0.5 \cdot P_{\text{snow}} \tag{4.8}$$

The amount of intercepted snow on the trees is reduced and, finally, removed from the storage by evaporation, melting, gliding or falling down to the ground, and redistribution by wind. Because of the comparably small height of the intercepted snow (app. 15 cm max.), it can be assumed that in the model the intercepted snow can be represented with a homogeneous snow cover (Durot 1999).

The evaporation of the snow is calculated as latent heat flux from the canopy allowing to introduce a parameter characterising the aerodynamic resistance of the canopy, after Monteith (1965):

$$R_a = \frac{\ln\left(\frac{z_m - d}{z_0}\right)^2}{\kappa^2 \cdot u_f(z_m)} \tag{4.9}$$

d is assumed to be 75%, and z_0 10% of the tree height. Thus, the latent heat flux can be written as

$$Q_e = \frac{L_e \cdot \rho_a}{M_a \cdot P_a} \cdot \frac{0.622 \cdot e_s \cdot T_{\text{air},f} \cdot (RH_f - 1)}{R_a} \tag{4.10}$$

Finally, the evaporation rate for the time step is given by

$$E_v = \frac{Q_e}{L_e \cdot \rho_w} \tag{4.11}$$

The interception of rain is distinctly different from that of snow. Again, a number of empirical or statistical formulas exist to quantify the evaporation losses of water intercepted by trees (e.g., Calder 1986, 1990). According to the bibliographic synthesis of Msika (1993), the rain interception is in the range of 30–45% for pine, spruce and fir. For other species, it is less than 30%. Storage capacity is assumed to be 2.5 mm (Hutchings *et al*. 1988). During a rainfall episode, the interception reservoir is filled with a certain percentage b of the precipitation at every time step. If the storage is filled, the tree cannot intercept more water and the processes of drainage from the tree and evaporation start to reduce the intercepted amount of water:

$$I_p = I_p + b \cdot P_h \text{ with } I_p < I_{\max} \tag{4.12}$$

Evaporation from the interception reservoir is estimated using the classical formula by Penman (1956).

The large amount of needles or leaves and particles falling down from the trees has an important effect on the albedo and its decrease with the densification and metamorphosis of the snow cover surface. Thereby, the reduction of the albedo under trees is faster than for open conditions and decreases to values of 0.45 at melting conditions (Barry *et al*. 1990). To take this effect into account, the ageing parameter for the albedo simulation in CROCUS is multiplied by two, and the minimum albedo is set from 0.7 (open land) to 0.45 for the radiation band 0.3 to 0.8 μm. However, the modified albedo has only little influence on the energy balance of the snow inside the canopy because of the comparably small amount of solar radiation reaching the ground.

The simulated snow cover inside a forest canopy close to Col de Porte, calculated using the meteorological variables achieved with all these modifications, was compared with stake and pit measurements for several seasons; the results showed good agreement (Durot 1999).

The forest density was calibrated for the Col de Porte area and is taken here as spatially constant for the Durance catchment. Future investigations will concern a more physically based interpretation, for example, the derivation of vegetation parameters such as LAI or the normalised difference vegetation index (NDVI) from satellite images and the formulation of a mathematical relationship between the vegetation parameters and the forest density.

The landuse distribution in the upper Durance catchment

For the application of the forest climate model, the spatial fraction of forest in each cell or altitude subarea of a cell,

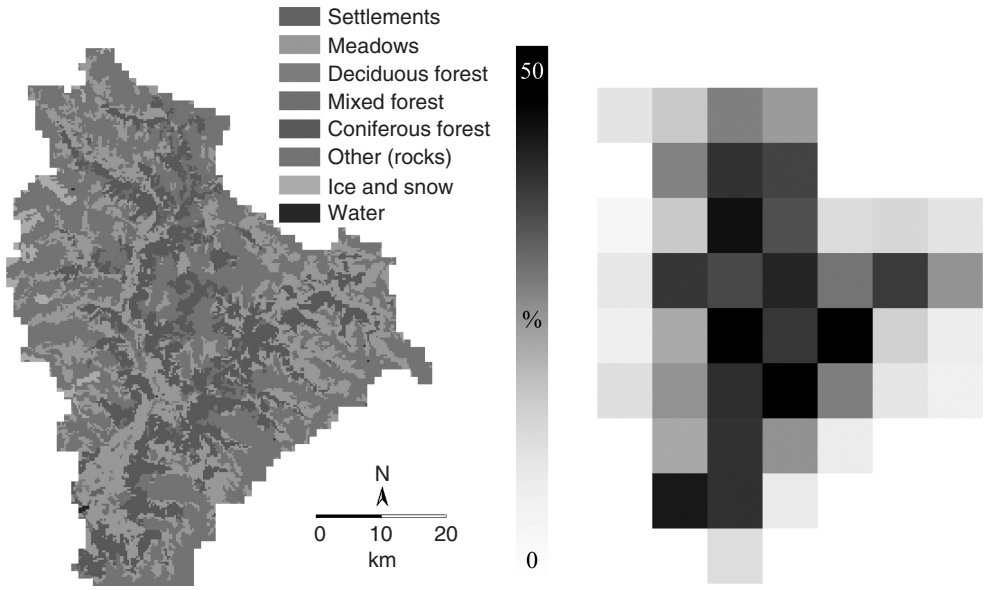


Figure 4.4 (Plate 5) Classified satellite image as provided by the CORINE land cover database (a) and derived forest fraction per 8-km cell for the upper Durance catchment (b)

respectively, has to be determined. Therefore, a two-step analysis is performed: in a first step, the forest fraction per 8-km model cell is calculated for the experiment with the original 8-km resolution. Then the forest fractions for the three subareas inside each of the 8-km model cells are determined for the third experiment, which combines the altitude subareas with the forest climate model.

For all analyses, the landuse map derived from satellite images (NOAA/AVHRR and Landsat) and provided by the CORINE land cover database (Cornaert *et al*. 1996) with an original resolution of 250 m was used. The processing steps applied to the vegetation map include classification, geometrical rectification (rotation and compensation of distortion) and statistical aggregation. The result is illustrated in Figure 4.4. The ''forest'' fraction of the resulting 8-km resolution map (a) takes the ''coniferous forest'' class and half of the ''mixed forest'' class of the original map (b) into account, considering that only conifers, keeping their needles during winter, affect the meteorological variables as simulated by the model.

According to Figure 4.4, the higher fractions of forest cover can be found in the valley bottoms of the Durance and Guil. For the entire catchment, the forest cover is 26% (see Table 4.1).

4.4 RESULTS

The improvement of the modelling results as achieved with the transition from 8 km to 1 km resolution has already been quantified by Etchevers *et al*. (2001a). Here these 1-km resolution results represent the accuracy reference for the subgrid parameterisations as performed in this study.

4.4.1 Comparison of simulated discharges

All three experiments are for the period Aug 1, 1981 to July 31, 1994 without intermediate reinitialization of the state variables. For the first initialisation, a spin-up method is applied: the first year is modeled twice, and then the state variables achieved with the first model run are used to initialise the second for the same year. This procedure enables us to start the simulation with a realistic distribution of soil temperature and moisture. The meteorological variables used are derived from three different interpolations with SAFRAN: one for the 1-km resolution altitudes, one for the 8-km cell altitudes and the third for the three subarea altitudes in each cell.

Because of its typical snowmelt regime, the discharge in the upper Durance catchment is generally very low in autumn and winter, and the main flood peaks occur during spring. The observed maximum of the simulation period (June 8, 1983) is 94 $m^3 s^{-1}$ in Briançon and 374 $m^3 s^{-1}$ in

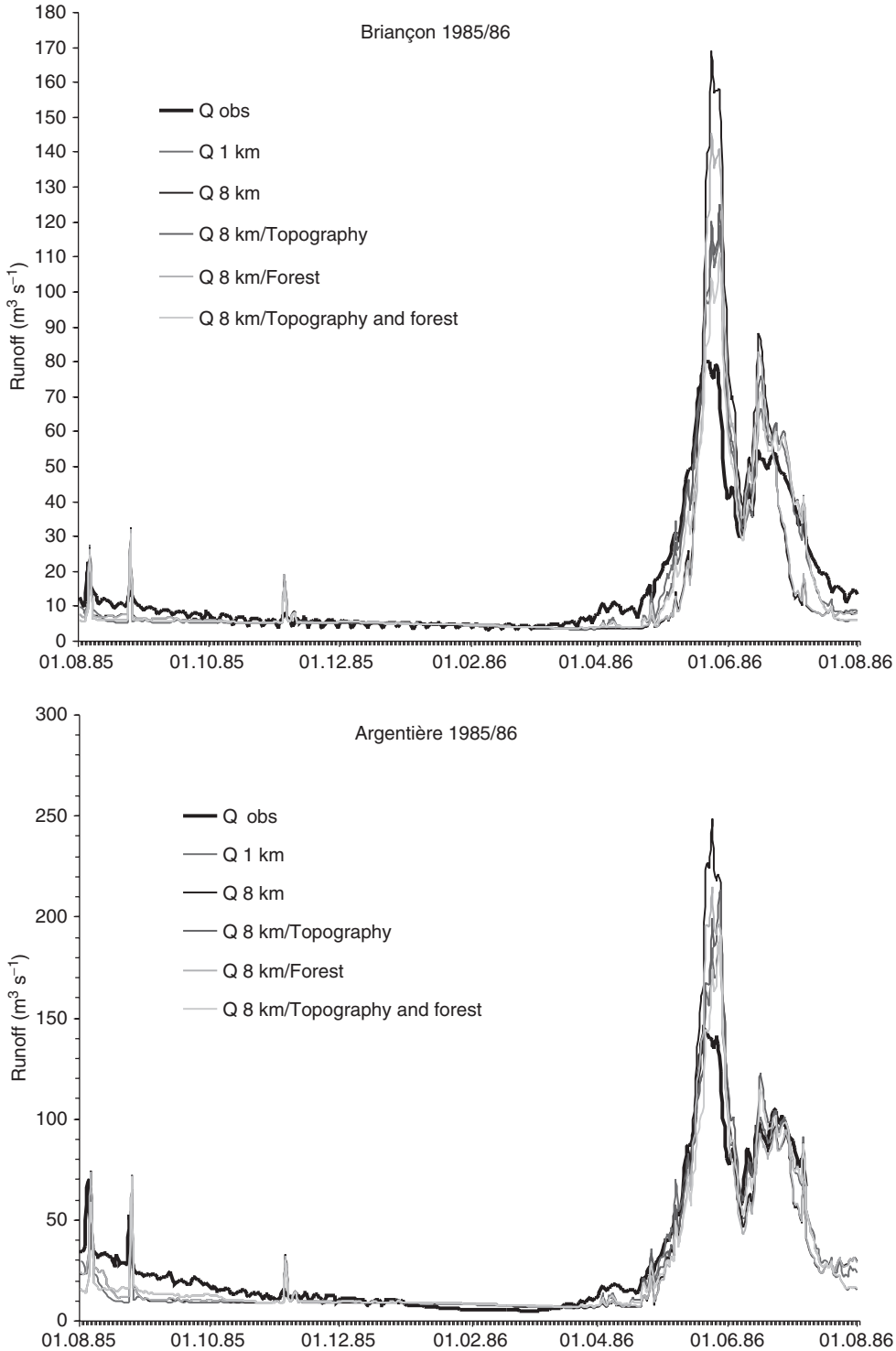


Figure 4.5 (Plate 7) Daily discharges in the upper Durance catchment, observed at the three gauging stations Briançon, L'Argentière and La Clapière for 1985/86 and modelled with different resolutions and subgrid parameterisations

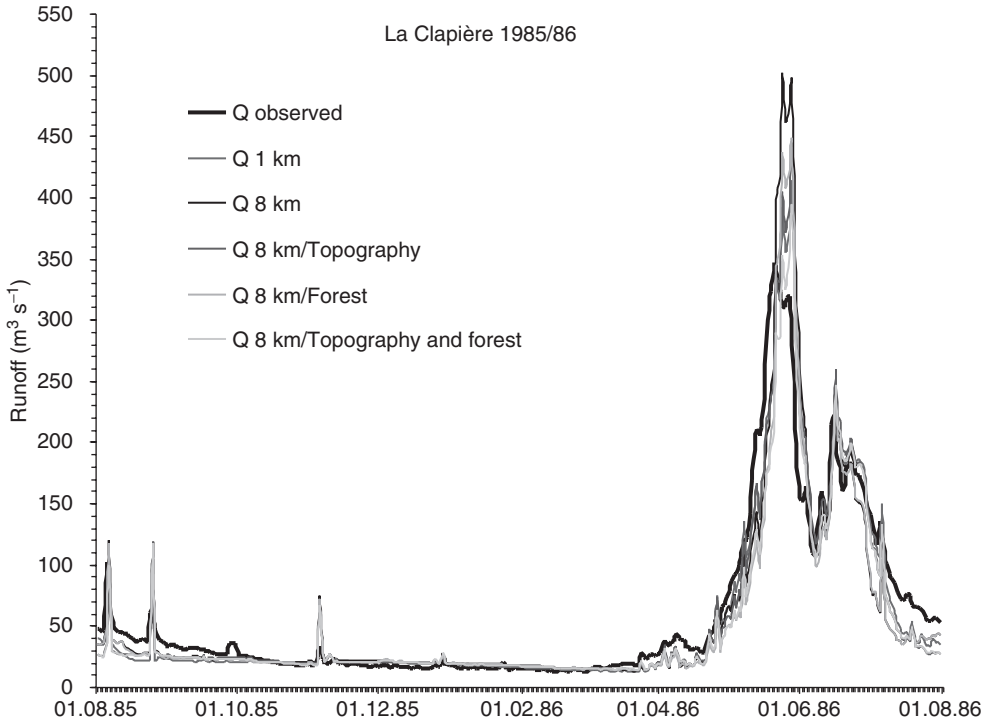


Figure 4.5 (Plate 7) (*continued*)

La Clapière (for L'Argentière, observations are missing for this date). In summer, runoff remains low except when a severe storm affects the watershed.

As an example, Figure 4.5 shows the daily discharges for the three gauging stations located in the catchment for a typical year (1985/86). The small oscillations in discharge that are particularly noticeable at Briançon are due to a small dam upstream (Val Cerveyrette). The indices in the figure legend correspond with the experiments conducted in our study (Table 4.2).

Comparing the measured and simulated discharge for the three different experiments, the results for this particular year can be summarised as follows.

- The large snowmelt runoff peaks in spring are overestimated by all versions of the model; the rates of increase and decrease of simulated streamflow are too rapid.
- This overestimation is largest for Briançon and decreases with increasing catchment size (downstream).
- The overestimation is largest for the original 8-km simulation; the 1-km simulation is always better and thus the reference for the improvements achieved with the three subgrid parameterisation experiments concerning topography, forest climate and their combination.
- The overall error is remarkably reduced in all seasons for the subgrid topography experiment; notably the timing of the onset of snowmelt is better and the rising and recession limbs of the hydrographs are thus closer to the reference.

Table 4.2 Indices that characterise the different datasets and experiments

Index	Dataset/Experiment
obs	Observed at the gauging station
1 km	Reference simulation/1-km resolution
8 km	Reference simulation/8-km resolution
8 km/Topography	Simulation with three separate altitude subareas inside each 8-km cell
8 km/Forest	Simulation with 8-km resolution and application of the forest climate model
8 km/Topography and Forest	Simulation with three altitude subareas inside each 8-km cell as well as application of the forest climate model in each altitude subarea

- The overall error is slightly reduced in all seasons for the forest climate experiment; the rates of increase and decrease of the simulated streamflow are still too rapid.
- The best results compared to the reference simulation are achieved with the combination of the subgrid topography and forest climate parameterisation schemes.

It is apparent that at the 8-km resolution the temporal dynamics of the elevation dependent melting pattern of the snow cover within a model cell cannot be correctly reproduced. With the consideration of the subgrid altitude parameterisation, a significant improvement concerning the snowmelt process is obtained. A smaller improvement is achieved with the forest climate model, but their combination leads to the best representation of the simulated snowmelt peak both in terms of its rising/recession and maximum value. The overestimation of the observed peak discharge, 45.3% with the 8-km resolution experiment for La Clapière, is reduced to 27.5% (subgrid altitude), 29.2% (forest climate) and 14.1% (combination of the two). For Argentière, the overestimation of 71.4% is reduced to 46.2, 48.2 and 31.3%, and for Briançon the overestimation of 110.2% is reduced to 55.5, 81.3 and 38.3%, respectively. The reference overestimations of the peak discharge, simulated with the 1-km resolution experiments, are 19.5, 30.5 and 47.9%, respectively. Similar results were obtained for all 14 years. In some of the years, the results of the combination experiment are even comparable with the 1-km resolution reference (e.g., La Clapière 1985/86).

4.4.2 Statistical criteria

For the quantitative validation of the simulation results, the Nash–Sutcliffe efficiency (Nash and Sutcliffe 1970) and the total runoff amount difference between measurement and simulation is calculated. The Nash–Sutcliffe criterion for the daily discharges is given in Table 4.3 for the three subcatchments modeled.

The table shows that the 8-km results (Nash–Sutcliffe efficiency = 0.73 for La Clapiére) are clearly improved by consideration of the subgrid topography (Nash–Sutcliffe efficiency = 0.77 for La Clapiére) and also slightly improved by application of the forest climate model (Nash–Sutcliffe efficiency = 0.75 for La Clapiére). The combination of both parameterisations leads to results comparable with the 1-km resolution reference, for Briançon the Nash–Sutcliffe criterion is even higher (Nash–Sutcliffe efficiency = 0.63) than the reference (0.61).

Table 4.3 Nash–Sutcliffe efficiency for 14 years of daily discharge (1981/82 to 1994/95) for the gauging stations Briançon, L'Argentière and La Clapière

	Briançon	L'Argentière	La Clapière
1 km	0.61	0.73	0.79
8 km	0.13	0.60	0.73
8 km/Topography	0.59	0.66	0.77
8 km/Forest	0.29	0.66	0.75
8 km/Topography and Forest	0.63	0.69	0.78

Table 4.4 Total runoff amount difference in percentage (modeled – observed) for 14 years of daily discharge (1981/82 to 1994/95) for the gauging stations Briançon, L'Argentière and La Clapière

	Briançon	L'Argentière	La Clapière
1 km	0.01	−3.58	−4.56
8 km	−1.79	−3.39	−5.60
8 km/Topography	−2.48	−3.65	−6.22
8 km/Forest	−5.88	−7.41	−9.68
8 km/Topography and forest	−6.78	−7.87	−10.56

The total runoff amount difference is an indicator if the simulated partitioning of precipitation into runoff and evaporation is correctly represented by the model. As can be seen in Table 4.4, the mean total runoff amount difference is negative for all stations (except for Briançon and the 1-km reference experiment) and increases with growing catchment size (i.e., for the subgrid parameterisation of topography for Briançon −2.5%, for Argentière −3.7% and for La Clapière −6.2%); it also increases with the forest experiment (−5.9, −7.4 and −9.7%) and is largest for the combined experiment (−6.8, −7.9 and −10.6%). This reduction in total runoff is due to the interception losses as parameterised with the forest climate model. However, part of the reduction in modeled runoff with the subgrid parameterisation of topography is due to the reduction in modeled precipitation inputs evident in Table 4.5, attributable to the interpolation of meteorological variables.

If one looks at the interannual comparison of the statistical criteria (Figure 4.6), the following can be observed.

- The differences between the Nash–Sutcliffe efficiencies for the three experiments decrease with growing catchment size because of increasing temporal duration and spatial variation of snowmelt.

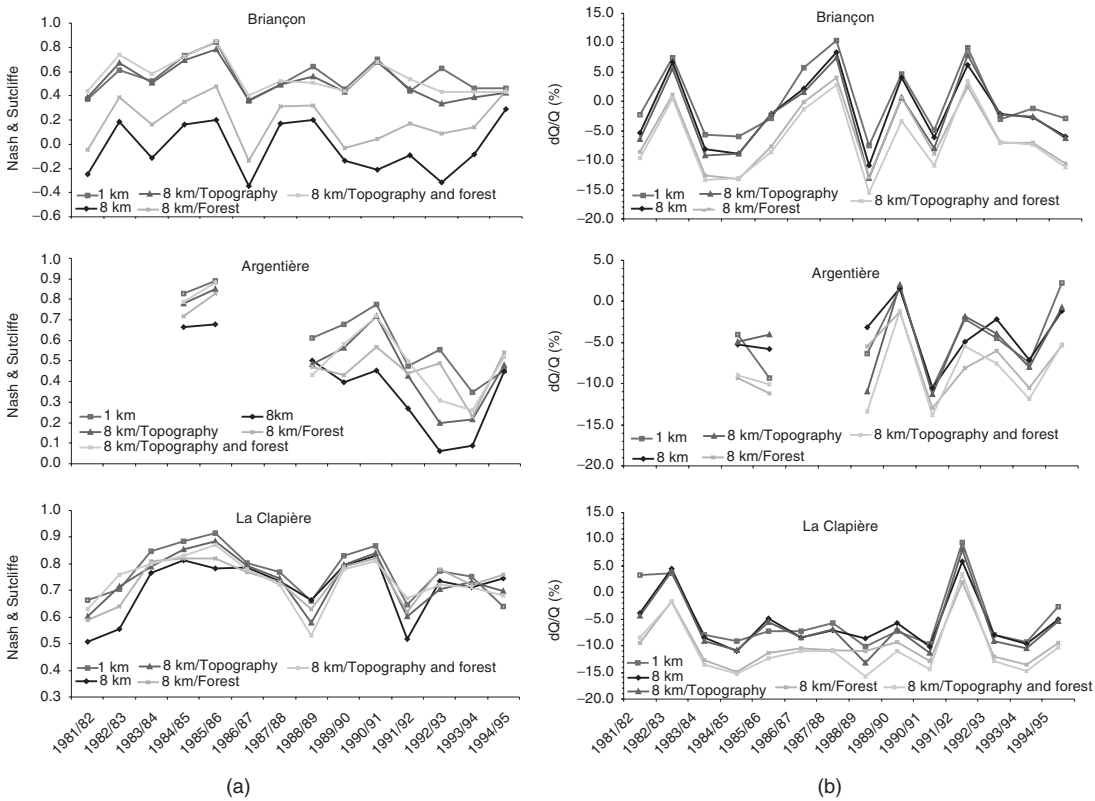


Figure 4.6 Annual evolution of the Nash–Sutcliffe efficiency (a) and total runoff amount differences (b) for the modeled discharge in the upper Durance catchment 1981/82 to 1994/95. For Argentière, observations are not available for the two periods 1981/82 to 1983/84 and 1986/87 to 1987/88

Table 4.5 Mean annual water balance components: basin precipitation, evapotranspiration, runoff and winter forest interception for the upper Durance catchment 1981/82 to 1994/95

	Basin precipitation	Evapotranspiration	Runoff	Winter forest interception
1 km	1064	348	713	–
8 km	1062	357	704	–
8 km/Topography	1057	357	699	–
8 km/Forest	1029	387	673	31
8 km/Topography and forest	1022	394	666	38

- Again, the forest climate model improves the original 8-km reference results slightly, the subgrid topography improves them remarkably and the combination of both shows the best improvement: for the latter, the Nash–Sutcliffe efficiency is almost as good as the one for the 1-km reference, in some seasons even better (e.g., 1982/83, 1991/92 and 1994/95 for La Clapière).
- For single years, the total runoff amount has positive as well as negative differences for all three gauging stations; these differences are in the range of approximately +10 to −15%.

4.4.3 Mean annual water balance

The following section focuses on the evolution of the mean annual water balance components precipitation, actual evapotranspiration, runoff and winter forest interception for the upper Durance catchment 1981/82 to 1994/95 (Table 4.5). Generally, the mean annual amount of precipitation (about half of it as snow) divides into approximately one-third of aET (modeled actual evapotranspiration) and two-thirds of runoff. The range of the precipitation is between 800 mm in the valleys and 1600 mm in the highest regions where the aET

ranges from 600 mm to only 100 mm, respectively. The mean annual snow cover duration for the catchment is 120 days but can be more than 150 days at the higher elevations.

For basin precipitation, the interpolation procedure considering a correction parameter (Bénichou and Breton 1987) results in differences from 2 to 7 mm between the 1-km, the 8-km and the 8-km/Topography experiments. For the two forest experiments, the differences (35 and 42 mm) are caused by the interception loss of precipitation in the forest canopy: some of it evaporates or sublimates and only part of it reaches the ground and thus contributes to runoff.

The mean annual amount of the winter forest interception as simulated with the forest climate model is higher for the combined experiment (38 mm) than for the forest experiment (31 mm) because more forest is situated in the lower or middle altitude subarea of the model cells where the temperatures and thus evaporation are higher than in the upper regions.

4.5 CONCLUSION AND OUTLOOK

The results of the previous studies have shown that the water balance components as simulated with ISBA and CROCUS are not significantly dependent on the model resolution at annual timescales. Even monthly discharges are close to observations. For these temporal scales, the locally established representations of the physical processes used in the SVAT model remain valid.

However, if one compares the daily results with the discharge observations of the three gauging stations located in the watershed, the representation of the snowmelt flood period during spring is poor, particularly for the 8-km resolution. With a transition from 8-km resolution (1 calculation per cell) to 1 km (64 calculations per cell), the model performance can be significantly improved. In this study, two subgrid parameterisations are applied: a division of each 8-km model cell into three altitude subareas for a better representation of the meteorological variability (three calculations per cell), a climate model for the snow cover inside a forest canopy (two calculations per cell) and the combination of the two (six calculations per cell). The goal is to find a proper representation of the phenomena that drive the snowmelt process without exorbitant data requirements and demands on computing resources.

A remarkable improvement of the original 8-km results is achieved with the partition of each model cell in three altitude subareas, mainly for the simulated peak discharges. The improvement due to the application of the forest climate model is smaller; it results in a certain amount of precipitation being retained by interception. The best approximation is achieved with the combination of the two subgrid parameterisations. With both experiments, a better representation of the spatial variability of the snowmelt process has been found. However, the improvements of the simulated discharge peak are accompanied with an underestimation of the total annual discharge amount. It cannot be determined whether this underestimation is induced by incorrect precipitation correction parameters or errors in the partitioning of the water balance components as simulated by the model.

For future investigations, a variety of questions as well as possible improvements remain. Snow cover patterns could be derived by analysing satellite image series that cover the catchment area with appropriate spatial and temporal resolution for the validation of the simulations, though the detection of snow in forest is a difficult task. Remote sensing could also be used to find a better parameterisation of the forest density, which should be a spatially distributed parameter rather than a constant, and related to standard vegetation indices. Furthermore, a sensitivity analysis for the total amount of precipitation using new measurements, for example, rainfall radar, and various correction schemes could be applied to deliver new insights about the statistical evaluation of the different experiments according to the system input.

Nevertheless, the results indicate that the presented subgrid parameterisation schemes are valuable methods to find a compromise between accuracy and the computational requirements for proper consideration of the processes driving snowmelt floods. Such subgrid parameterisations can be recommended for large-scale and operational applications of hydrological models such as regional flood forecasting systems.

4.6 ACKNOWLEDGEMENTS

This study was performed during the first author's one-year stay as visiting scientist at the Centre d'Études de la Neige (METEO-France/CNRM) in St. Martin d'Hères. Katja Durot (LTHE/Grenoble) developed the forest climate model at Col de Porte station and generously shared her experience for its application. The authors profited greatly from discussions with Eric Martin (CEN/Grenoble), Yves Lejeune (CEN/Grenoble), Charles Obled (LTHE/Grenoble) and Peter Molnár (ETH/Zurich), who also read the manuscript and corrected the English. We would also like to thank Ludwig Braun (BADW/Munich) and three anonymous reviewers for providing helpful suggestions

for improvement. Paolo Burlando (ETH/Zurich) and Wolfram Mauser (LMU/Munich) provided hardware and software to produce the final version of the manuscript. Vera Falck and Christian Michelbach (both LMU/Munich) helped design the figures.

REFERENCES

Barry, R., Prevost, M., Stein, J. and Plamondon, A.P. (1990) Application of snow cover energy and mass balance model in a balsam fir forest. *Water Resour. Res.*, Vol. 26, No. 5, 1079–1092.

Bénichou, P. and Breton, O. (1987) Prise en compte de la topographie pour la cartographie des champs pluviométriques statistiques. *Météorologie*, Vol. 7, No. 19, 23–24.

Bell V.A. and Moore, R.J. (1999) An elevation-dependent snowmelt model for upland Britain. *Hydrol. Process.*, Vol. 13, 1887–1903.

Berris, S.N. and Harr, R.D. (1987) Comparative snow accumulation and melt during rainfall in forested and clear-cut plots in the Western Cascades of Oregon. *Water Resour. Res.*, Vol. 23, No. 1, 135–142.

Bonan, G.B. (1991) A biophysical surface energy budget analysis of soil temperature in the boreal forest of interior Alaska. *Water Resour. Res.*, Vol. 27, No. 5, 767–782.

Bowles, D.S., Bingham, G.E., Lall, U., Tarboton, D.G., Rajagopalan, B., Chowdhury, T.G. and Kluzek, E. (1994) Development of mountain climate generator and snowpack model for erosion prediction in the Western United States using WEPP. *Research Completion Report for Phase V submitted to Forestry Service Laboratory*. Intermountain Research Station, U.S. Department of Agriculture, Moscow.

Braun, L.N., Brun, E., Durand, Y., Martin, E. and Tourasse, P. (1994) Simulation of discharge using different methods of meteorological data distribution, basin discretization and snow modelling. *Nord. Hydrol.*, Vol. 25, No. 1–2, 129–144.

Brun, E., David, P., Sudul, M. and Brunot, G. (1992) A numerical model to simulate snow-cover stratigraphy for operational avalanche forecasting. *J. Glaciol.*, Vol. 38, No. 128, 13–22.

Brun, E., Martin, E., Simon, V., Gendre, C. and Coléou, C. (1989) An energy and mass model of snow cover suitable for operational avalanche forecasting. *J. Glaciol.*, Vol. 35, No. 121, 333–342.

Calder, I.R. (1986) What are the limits of forest evaporation? Comment. *J. Hydrol.*, Vol. 124, 119–130.

Calder, I.R. (1990) *Evaporation in the Uplands*. John Wiley & Sons, UK, p. 176.

Champeaux, J.L. and Legléau, H. (1995) Vegetation mapping over Europe using NOAA/AVHRR. *The 1995 Meteorological Satellite Data Users Conference*, Winchester, UK, EUMETSAT, 139–143.

Cornaert, E., De Villele, O. and Ubel, R. (1996) Le programme Européen CORINE: une réponse à une attente des utilisateurs. *CORINE Land Cover*. Institut Français de l'Environnement, France, pp. 8–9.

Davis, R.E. and Hardy, J.P. (1997) Variation of snow cover ablation in the boreal forest: a sensitivity study on the effects of conifer canopy. *J. Geophys. Res.*, Vol. 102, No. D24, 29.

Durand, Y., Brun, E., Mérindol, L., Guyomarc'h, G., Lesaffre, B. and Martin, E. (1993) A meteorogical estimation of relevant parameters for snow models. *Ann. Glaciol.*, Vol. 18, 65–71.

Durot, K. (1999) Modélisation hydrologique distribuée du bassin versant nivo-pluvial de Sarennes. Validation des données d'entrée et développement d'un module de fonte nivale sous forêt. PhD thesis, LTHE, Grenoble.

Etchevers, P., Durand, Y., Habets, F., Martin, E. and Noilhan, J. (2001a) Impact of spatial resolution on the hydrological simulation of the Durance high alpine catchment. *Ann. Glaciol.*, Vol. 32, 87–92.

Etchevers, P., Habets, F. and Golaz, C. (2001b) Simulation of the water budget and the river flows of the Rhône basin from 1981 to 1994. *J. Hydrol.*, Vol. 224, 60–85.

Garbrecht, J. and Martz, L.W. (1997) *TOPAZ: An Automated Digital Landscape Analysis Tool for Topographic Evaluation, Drainage Identification, Watershed Segmentation and Subcatchment Parameterisation; TOPAZ Overview*. U.S. Department of Agriculture, Agricultural Research Service, Grazinglands Research Laboratory, El Reno, Oklahoma (USA), ARS Publication No. GRL 97-2, p. 21.

Habets, F., Etchevers, P., Golaz, C., Leblois, E., Ledoux, E., Martin, E., Noilhan, J. and Ottlé, C. (1999) Simulation of the water budget and the river flows of the Rhône basin. *J. Geophys. Res.*, Vol. 104, No. D24, 31145–31172.

Harding, R.J. and Pomeroy, J.W. (1996) The energy balance of the winter boreal landscape. *J. Clim.*, Vol. 9, 2778–2787.

Hutchings, N.J., Milne, R. and Crowther, J.M. (1988) Canopy storage capacity and its vertical distribution in a Sitka spruce canopy. *J. Hydrol.*, Vol. 104, 161–171.

Jeffrey, W. (1968) Snow hydrology in the forest environment. *Snow Hydrology, Proceedings of Workshop Seminar*. Canadian National Committee for IHD, Ottawa, pp. 1–19.

Keller, H.M. and Strobel, T. (1979) *Predicting Snow Accumulation in Subalpine Forest Stands*. Swiss Forest Research Institute.

King, D., Lebas, C., Jamagne, M., Hardy, R. and Draoussin, J. (1995) Base de données géographiques des sols de France à l'échelle 1/1000000. Technical Report, INRA, France.

L'Homme, J.P. (1991) The concept of canopy resistance: historical survey and comparison of different approaches. *Agric. Forest Meteorol.*, Vol. 54, 227–240.

Liston, G.E. (1999) Interrelationships among snow distribution, snowmelt, and snow cover depletion: implications for atmospheric, hydrologic, and ecologic modeling. *J. Appl. Met.*, Vol. 38, 1474–1487.

Li, X. and Strahler, A.H. (1986) Geometric optical bi-directional reflectance modelling of a conifer forest canopy. *IEEE Trans. Geosci. Remote Sens.*, Vol. GE-24, 906–919.

Li, X. and Strahler, A.H. (1992) Geometric optical bi-directional reflectance modelling of mutual shadowing effects of crowns in a forest canopy. *IEEE Trans. Geosci. Remote Sens.*, Vol. GE-30, 276–292.

Luce, C.H., Tarboton, D.G. and Cooley, K.R. (1999) Subgrid parameterisation of snow distribution for an energy and mass balance snow cover model. *Hydrol. Process.*, Vol. 13, 1921–1933.

Lundberg, A. and Halldin, S. (1994) Evaporation of intercepted snow: analysis of governing factors. *Water Resour. Res.*, Vol. 30, No. 9, 2587–2598.

Monteith, J.L. (1965) Evaporation and the environment. *Symp. Soc. Expl. Biol.*, Vol. 19, 205–234.

Monteith, J.L. and Unsworth, M. (1990) *Principles of Environmental Physics*. Collection Arnold, p. 291

Moore, R.J. (1985) The probability-distributed principle and runoff production at point and basin scales. *Hydrol. Sci. J.*, Vol. 30, No. 30, 273–297.

Msika, B. (1993) Modélisation des relations herbes-arbres sous peuplements de querues pubercens wild et pinus austriaca höss dans les préalpes du sud. Thèse de doctorat, Université de Aix – Marseille III.

Nash, J.E. and Sutcliffe, J.V. (1970) River flow forecasting through conceptual models (1); a discussion of principles. *J. Hydrol.*, Vol. 10, No. 3, 282–290.

Noilhan, J. and Lacarrère, P. (1995) GCM gridscale evaporation from mesoscale modelling. *J. Clim.*, Vol. 8, No. 2, 206–223.

Noilhan, J. and Mahfouf, J.-F. (1996) The ISBA land-surface parametrisation scheme. *Glob. Planet. Change*, Vol. 13, 145–159.

Noilhan, J. and Planton, S. (1989) A simple parametrisation of land surface processes for meteorogical models. *Mon. Weather Rev.*, Vol. 117, 536–549.

Obled, C. (1971) Modèle mathématique de la fusion nivale. Thèse de Doctorat, Institut de Mécanique de Grenoble, p. 170.

Penman, H.L. (1956) Estimating evaporation. *Trans. Am. Geophys. Union*, Vol. 37, 43–46.

Rango, A. and Martinec, J. (1995) Revisiting the degree-day method for snowmelt computations. *Water Res. Bull.*, Vol. 31, 657–669.

Ritter, B. and Geleyn, J.F. (1992) A comprehensive radiation scheme for numerical weather prediction models with potential applications in climate simulations. *Mon. Weather Rev.*, Vol. 120, No. 2, 303–323.

Satterlund, R.D. and Haupt, H.F. (1967) Snow catch by conifers crowns. *Water Resour. Res.*, Vol. 3, No. 4, 1035.

Schmidt, R.A. (1991) Sublimation of snow intercepted by an artificial conifer. *Agric. Forest Meteorol.*, Vol. 543, 1–27.

Schmidt, R. and Gluns, R. (1991) Snowfall interception on branches of three conifer species. *Can. J. Forest Res.*, Vol. 21, No. 8, 1262–1269.

5

Assessment of Snow-covered Areas Using Air Temperatures During Melt in a Mountainous Basin

PRATAP SINGH[1] AND LARS BENGTSSON[2]
[1]National Institute of Hydrology, Roorkee 247 667 (India), [2]Department of Water Resources Engineering, Lund University, S-221 00, Sweden

5.1 INTRODUCTION

Snow is a very important component of the hydrological cycle and it plays a vital role in the water resources in many parts of the world. In a region or basin, snow cover is developed from a series of winter storms and is depleted during spring and summer period because of warmer climate. Depending upon the location of the basin and climatic conditions there, snow cover developed during preceding winter can deplete totally or partially. Snow cover is a major component of water storage on seasonal timescale, and changes in its extent, depth, and its water equivalent have a major impact on alpine and continental water resources. The amount and rate of runoff induced by melt processes in a basin can be related to variation in snow covered area (SCA). There are various hydrological applications of SCA on the basin scale. Modeling of snow melt runoff carried out using SCA data is very important for various practical applications in the field of runoff predictions, reservoir management, electric power production, irrigation practices, flood control, and so on. There are some hydrological models, for example, snow melt runoff model (SRM), that use SCA as an input variable on the daily basis for snow melt computation (Martinec *et al*. 1983). At the same time, variation in SCA plays a crucial role in modeling and simulating alterations of global change effects on water resources, the ecological conditions, the albedo, and ultimately on the radiation budget.

Application of SCA for snow melt modeling studies becomes inevitable for the large and inaccessible Himalayan basins, which experience high snowfall but do not have sufficient meteorological network to quantify it. Early use of remote sensing focused on empirical relationships between SCA and monthly or accumulated runoff (Rango *et al*. 1977; Ramamoorthi 1987). These simple relationships worked well for some applications and particularly in data-sparse regions of the world. Estimation of daily snow melt runoff in the Himalayan river basins using satellite-derived SCA is being increasingly recognized as an immensely useful procedure in water resources research and management (Rango *et al*. 1977; Ramamoorthi and Subba Rao 1981; Gupta *et al*. 1982; Dey *et al*. 1983, 1989; Dey and Goswami 1984; Jain 2001). The prediction of snow melt induced runoff in the Himalayan rivers has a great potential for application in irrigation, hydropower generation, and domestic and industrial water supply.

The SCA has also been used as an indicator of snow reserve or water equivalent in a basin (Meier 1973; Ødegaard and Østrem 1977; Rango *et al*. 1977). Schjødt-Osmo and Engeset (1997) reported that the Norwegian Water Resources and Energy Administration (NVE) uses

Climate and Hydrology in Mountain Areas. Edited by C. de Jong, D. Collins and R. Ranzi
© 2005 John Wiley & Sons, Ltd. ISBN: 0-470-85814-1

information on the changing distribution of snow during the periods of accumulation and, in particular, ablation (Østrem 1974; Andersen 1983). The areal extent of snow is one of the principal variables and is directly related to the summer runoff potential. The snow water equivalent of a snowpack cannot be derived from only the current remote sensing data. However, the derivable snow cover fraction is still a very important parameter to monitor for operational flood forecasting (Schjødt-Osmo and Engeset 1997). Singh *et al*. (1997) and Singh and Jain (2002) used SCA in estimating snow and glacier contributions in the annual flows of Himalayan rivers using the water balance approach. Singh and Singh (2001) have discussed various applications of regional snow cover on the climate system.

Usually, information on the extent of SCA is derived from satellite data because snow can readily be identified and mapped within the visible bands of satellite imagery because of its high reflectance in comparison to nonsnow areas. Therefore, remote sensing is a valuable tool for obtaining snow data for predicting snowmelt runoff as well as climate studies. Use of satellite data for snow mapping has become operational in several regions of the world. Currently, NOAA develops snow cover maps for about 3000 river basins in North America, of which approximately 300 are mapped according to elevation for use in streamflow forecasting (Carroll 1990). NOAA also produces regional and global maps of mean monthly snow cover (Dewey and Heim 1981). Rango (1993) presented a review of the status of remote sensing in snow hydrology. Snow cover mapping with satellite data in the Swiss Alps is reviewed by Seidel *et al*. (1989, 1995). Haefner *et al*. (1997) suggested for setting up snow cover information systems for individual basins or other hydrological units, planning regions or even entire mountain ranges on a long-term perspective. On the practical side, these applications are related to the monitoring of seasonal and yearly alterations of the snow cover under presently existing climatic conditions to simulate and forecast runoff, to map the regional distribution of the water equivalent, and to document the recession processes of the snow cover during the melting period.

In order to get information on SCA, systematic and continuous mapping of snow cover becomes essential for snow hydrological applications. However, in general, there are discontinuities in the SCA data required for the studies. It is difficult to develop SCA database on the daily time scale because of the cost involved in acquiring satellite data, time consumed in the analysis of data, and inaccurate data due to presence of cloud cover. However, in some cases, depending upon the size of the study area, cost factor may not be important, but other factors dominate. In the melt season, the cloud cover represents a major obstacle when deriving information from optical imagery (Schjødt-Osmo and Engeset 1997). The issue related with filtering of cloud cover in the mountainous basins has been discussed in detail by Ranzi *et al*. (1999). They used NOAA-AVHRR data for monitoring areal snowpack in the Southern Alps. Haefner *et al*. (1997) reported that even the acquisition of 5–10 (or more) satellite scenes for a single melting season is rather costly. Even if one can afford the resources, a lot of time is consumed in the analysis. Such problems become more important for the Himalayan basins, which are larger in size and have longer ablation period with higher probability of cloud cover during premonsoon and monsoon period. A higher number of images is needed for such basins for snow melt modeling studies, which need lot of investment and also require much time for analysis.

For modeling of snow melt runoff and river discharge, the spatially distributed energy balance approach is considered as preferred method. This approach allows for computation of spatially distributed melt from the basin. Moreover, such methods also allow for prediction of the spatial distribution of SCA (Melloh *et al*. 1997; Blöschl *et al*. 1991; Blöschl and Kirnbauer 1992; Mittaz *et al*. 2002). For computing the melt from the basin using temperature index method, usually, satellite data are obtained for a few dates in the melt season and linearly interpolated for the period of unavailability of data. This study deals with developing a methodology to interpolate, extrapolate, or fill the missing SCA data during ablation period using temperature data, which is easily available. Following this approach, one can reduce the number of images for the melt period to obtaining SCA. Air temperature can then be used to generate SCA data for the basin.

5.2 METHODOLOGY

The SCA at a particular time after first melt can be considered a function of the initial value of SCA before start of the melting and patterns of the temperature during the melt period. The use of degree-day or temperature index approach is a well-established method for snow melt estimation. At present, there are a number of snow melt models that use this approach for computing snow melt runoff from the basin (Singh and Singh 2001). Melt starts first in the warmer lower parts of a basin, where usually the snow cover is thinnest. Consequently, the snow disappears first from the lower part of the basin. As summer season progresses, the melt continues in the

upper part of the basin. The SCA reduces with time and at each point of time melt can be related to air temperatures. Therefore, cumulative degree-days (CDD) over the melt period should represent the depletion of SCA. CDD is obtained simply by adding the daily mean temperature at the selected station. A seasonal snow cover will disappear at a faster rate during warmer climatic conditions, while it will follow slow depletion under a colder temperature regime. Rango and Martinec (1994) correlated SCA and cumulative depth of melt to infer the changes in SCA under warmer climatic scenarios, which indirectly supports the dependency of SCA on temperature because cumulative melt is mainly governed by the temperature. In this paper, to keep the methodology simple and directly applicable, temperature data of the stations located in or near the SCA are used. For the Himalayan basins melt season sets in about March, therefore March 1 has been considered as reference date for CDD computation and accordingly SCA data is used. However, the choice of reference date for initializing CDD may vary from region to region and accordingly the shape of the graph may vary. Broadly, the reference date should represent the time of when melting starts in the basin, that is, there is no further increase in SCA.

5.3 STUDY BASIN

This study has been carried out for the Satluj river basin up to Bhakra dam (Indian part) located in the western Himalayas. The Satluj river is a highly snowfed river having about 60% contribution of snow and ice melt runoff in its annual flows (Singh and Jain 2002). The Satluj river rises in the lakes of Mansarovar and Rakastal in the Tibetan plateau at an elevation of about 4600 m and forms one of the main tributaries of the Indus river. The physiographical features of the study basin are given in Table 5.1, and location of the basin is shown in Figure 5.1. The altitude of the basin varies from about 500 m to 7000 m, although only a very small area exists above 6000 m. Mean elevation of the basin is about 3600 m. The shape and location of this basin is such that the major part of the basin area lies in the greater Himalayas where heavy snowfall is experienced during winters. A major part of the basin is covered by snow during winter. Owing to large differences in seasonal temperatures and great range of elevation in the

Table 5.1 Main physical characteristics of the investigated basin

Basin	Name
Name of study area	Satluj Basin
Mountain range	Western Himalayas
Elevation range (m.a.s.l.)	500–7000
Latitude	30°95′–33°15′N
Longitude	76°10′–79°10′E
Area (km^2)	22,305
Glaciers and permanent snow (%)	~10
Mean annual rainfall (mm)	~375

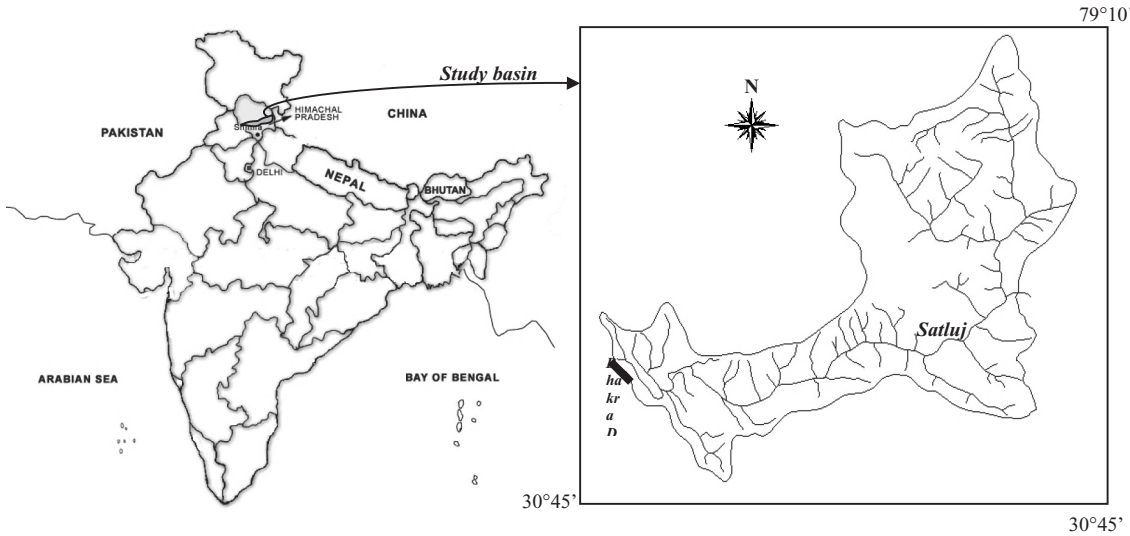


Figure 5.1 Location map of the Satluj River basin (Indian part)

catchment, the snowline is highly variable, descending to an elevation of about 2000 m during winter and retreating to above 4000 m after summer season. The topographical setting and availability of abundant water provide a huge hydropower generation potential in this river, and hence several hydropower schemes already exist, are planned, or are coming up on this river.

5.4 STUDY PERIOD AND DATA USED

The study has been carried out for the melt season (March–August) using five years SCA and temperature data. In general, SCA was available once a month, while daily mean temperatures were available for the whole study period. The daily mean temperatures of two high altitude stations, namely, Kalpa (2436 m) and Kaza (3639 m), were used in this study. March 1 was considered as reference starting point to compute the cumulative degree-days. The information on SCA was determined from the satellite images/digital data. In this study, the satellite data was processed using ERDAS IMAGINE image processing software. First, snow cover area maps were prepared for the study basin and then SCA was determined. Landsat (MSS) (80 m resolution) data have been used for 1987, whereas IRS (LISS-I) (72.5 m resolution) data were used for 1988–91.

5.5 RESULTS AND DISCUSSIONS

The depletion of SCA in Satluj basin with time during summer period and trends of CDD at Kalpa for three ablation seasons (1987, 1988, and 1989) are shown in Figure 5.2. Figure 5.3 shows the relationship between SCA with CDD for Kalpa for different years. It can be noticed from Figure 5.3 that SCA reduces exponentially with CDD for the summer season. Similar trends for all the years confirm such relationship. This relationship can be expressed as

$$\mathrm{SCA} = a^* \exp(-b^* \mathrm{CDD}) \tag{5.1}$$

The derived values of coefficients a and b and coefficient of determination (R^2) for different years are given in the Table 5.2. Changes in the values of coefficients are possible because of changes in initial value of SCA and temperature conditions.

The high value of R^2 for all years shows that the SCA and CDD in the form of Equation (5.1) are highly correlated. Results show that SCA and CDD are

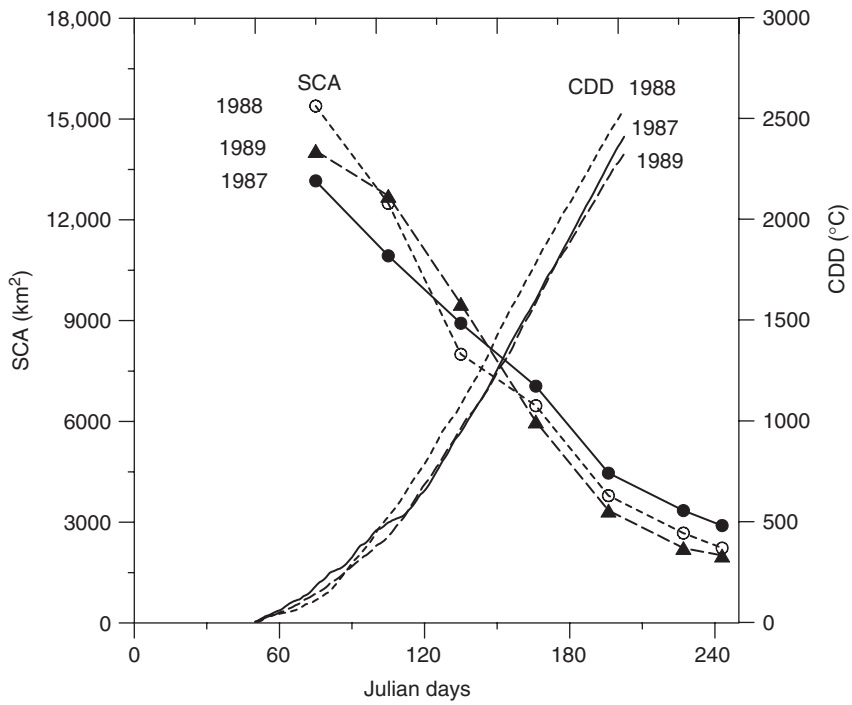


Figure 5.2 Depletion of snow covered area (SCA) with time in the Satluj basin along with trend of daily cumulative degree-days (CDD) observed at Kalpa (2536 m) for different years. CDD was computed March 1 onward

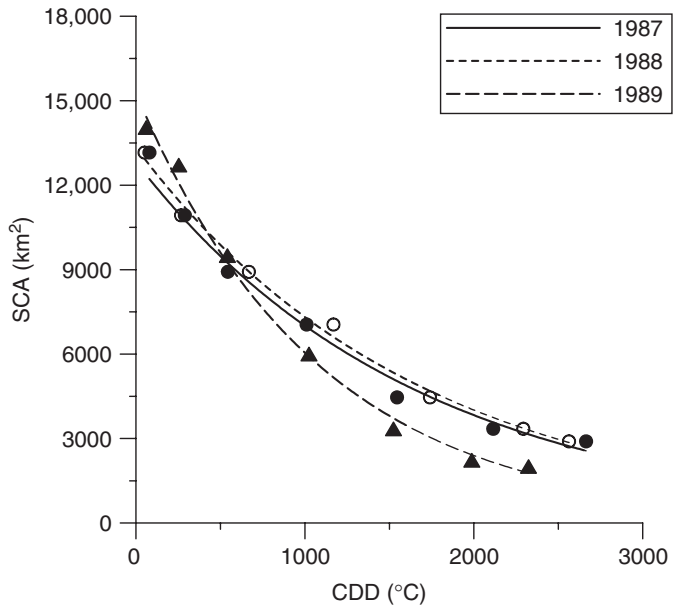


Figure 5.3 Relationship between snow cover depletion and cumulative degree-days (CDD) at Kalpa (2436 m) station

Table 5.2 Values of coefficients a and b used in Equation (5.1) and R^2 for different ablation seasons using Kalpa station (2436 m) data

Melt season	Values of coeff. a as in Equation (5.1)	Values of coeff. b as in Equation (5.1)	Coeff. of determination R^2
1987	12821.6	0.00060	0.98
1988	13337.9	0.00060	0.99
1989	15263.9	0.00092	0.99

not linearly related but rather are related nonlinearly. Exponential relationship implies that initial increment in temperature leads to higher changes in the snow cover area than later increments in temperature of the same magnitude. Such trends can be explained on the basis of distribution of snow in the basin. Consequently, snowpack developed in the basin during winter season is thin at lower altitudes and thick at higher altitudes. During summer, the snow line retreats from the lower altitude to higher altitude and consequently SCA in the basin is reduced. The retreat rate is reduced in the later part of the melt season because of higher depth of snow at high altitudes. Kattlemann (1997) reported rapid melting of snow at low elevations in Sierra Nevada, California, USA. Therefore, accumulation and depletion of snow and temperature conditions attribute to exponential trend of depletion of SCA with CDD. Using SCA and computed snow melt runoff for four years data, Gupta *et al*. (1982) reported a logarithmic relationship between SCA in the end of melt season and the volume of seasonal snow melt runoff for four Himalayan basins. Assuming that snow melt is linearly related with temperature, one can conclude that SCA and CDD should have exponential relationship.

On the basis of the conclusion that a logarithmic relationship exists between SCA in the end of melt season and the volume of seasonal snow melt runoff, as reported by Gupta *et al*. (1982), it can be expressed mathematically as

$$\ln(\text{SCA}) \sim V \tag{5.2}$$

or

$$\text{SCA} \sim \exp(V) \tag{5.3}$$

Assuming that snow melt is linearly related with temperature, one can conclude that SCA and CDD should have exponential relationship. Further, the preceding statement can be expressed mathematically as

$$(\mathrm{d}V/\mathrm{d}t) \sim (T - T_0) \tag{5.4}$$

where T_0 is the reference temperature (0°C). Integrating both sides leads to

$$V \sim \int (T - T_0)\,\mathrm{d}t \tag{5.5}$$

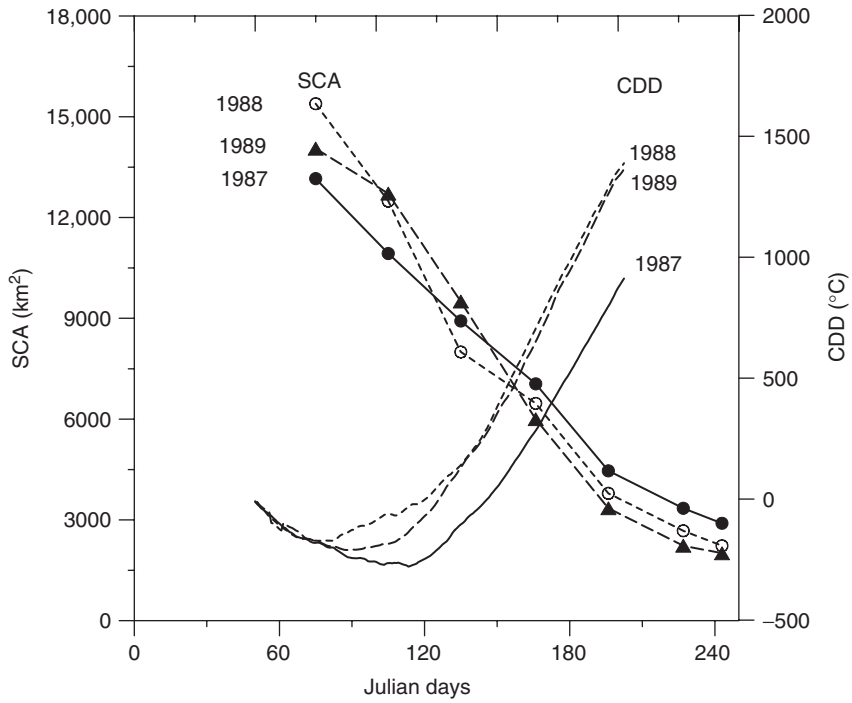


Figure 5.4 Depletion of snow covered area (SCA) with time in the Satluj basin along with trend of daily cumulative degree-days (CDD) observed at Kaza (3639 m) for different years. CDD was computed March 1 onward

The right side of the equation is a possible definition of CDD, so

$$V \sim \text{CDD} \tag{5.6}$$

When combined with the relationship of SCA to V leads to

$$\text{SCA} \sim \exp(\text{CDD}) \tag{5.7}$$

Depletion of SCA for the study basin was also correlated with CDD of another station (Kaza, 3639 m), which is located higher up in the basin (Figure 5.4 and 5.5). The relationship between SCA and CDD was also exponential for this station, but it was disturbed because of negative temperatures in the month of March at this station. As shown in Figure 5.5, in the beginning of melt season cumulative temperatures were negative at this station for all the three years. Cumulative negative temperature disturbed the exponential relationship for this initial period of melt season (Figure 5.5). Therefore, the stations that experience negative temperature during the melt season cannot be used for such applications. However, they can be used for a period after which they experience positive temperature and cumulative temperature is positive. For further application of this study, only Kalpa station was used. Additional snowfall during ablation season will change the relationship between SCA and CDD. Hall and Martinec (1985) have discussed this issue. This aspect has not been dealt in this study. However, there is need to involve these aspects in future.

5.6 APPLICATIONS

There are three major applications of this approach, which are described below.

(a) Interpolation of SCA. Once the relationship between SCA and CDD is established using daily values of CDD and few values of SCA, this equation can be used to interpolate data during the melt period. Using CDD data in the derived equation, one can get daily values of SCA in the basin. The missing data can be generated using known relationship between SCA and CDD.

(b) Simulation of SCA. Because SCA and CDD are exponentially correlated, once the trend of depletion of SCA snow is established in the basin, it can be extended for the later part of the melt season using only CDD.

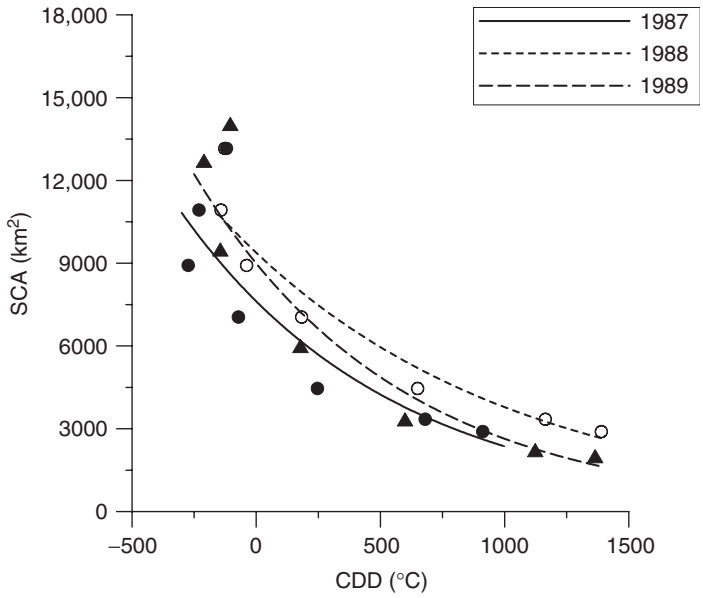


Figure 5.5 Relationship between snow cover depletion and cumulative degree-days (CDD) at Kaza (3639 m) station

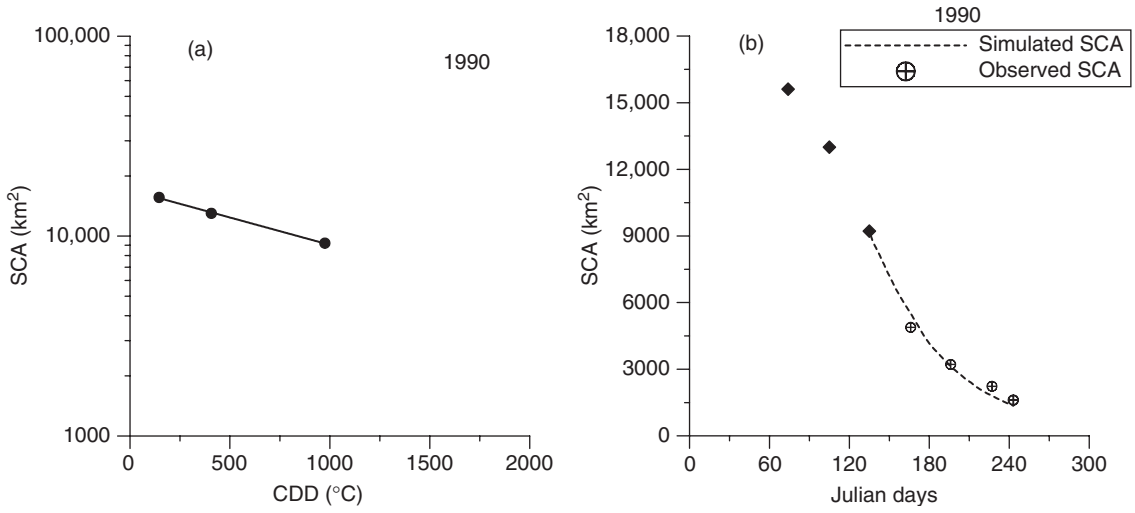


Figure 5.6 (a) Establishment of snow cover depletion trend for 1990 using cumulative degree-days (CDD) of Kalpa for the initial part of the summer. (b) Simulation of depletion of snow covered area (SCA) for the rest of summer using CDD data, and its comparison with observed SCA

Such a procedure is illustrated in Figures 5.6 and 5.7. The two unknowns (a and b) can easily be determined by plotting SCA on log scale and CDD on linear scale. This approach was applied for two years, 1990 and 1991, for simulating daily SCA in the study basin. Simulated SCA was compared with observed SCA in the later part of the melt season. As shown in Figure 5.6 and 5.7, for both years daily SCA was well simulated using this approach. The average error between observed and estimated SCA was about 6% and 8% for the year 1990 and 1991, respectively. The expected error can be further reduced if the data points used to parameterize the exponential curve

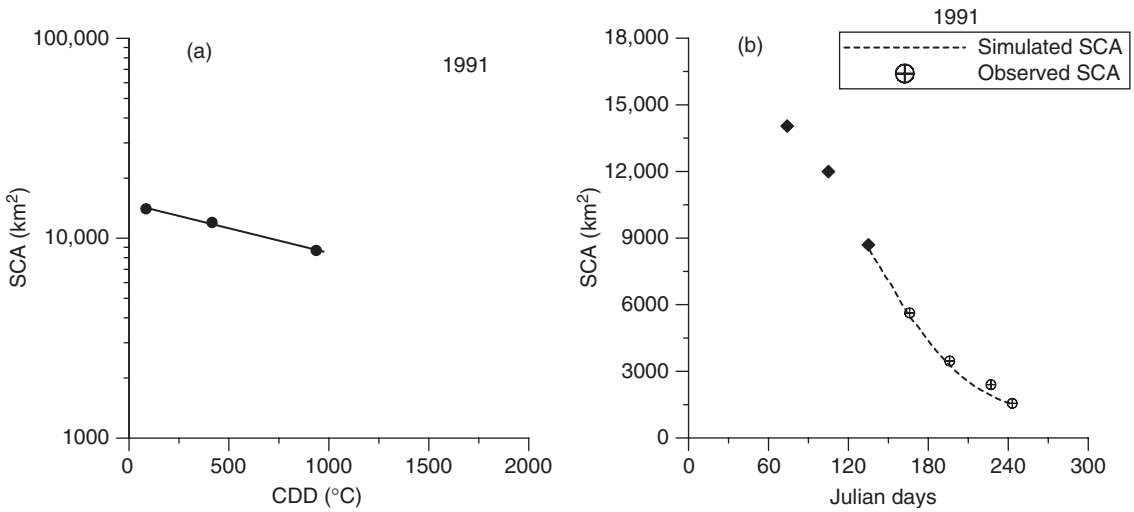


Figure 5.7 (a) Establishment of snow cover depletion trend for 1991 using cumulative degree-days (CDD) of Kalpa for the initial part of the summer. (b) Simulation of depletion of snow covered area (SCA) for the rest of summer using CDD data, and its comparison with observed SCA

are increased. Error in predicting SCA will also depend on the error in predicting the CDD. Thus, following this approach, one can reduce the number of images for the later part of the season. However, for such applications, a setting of depletion trend with CDD is essential.

(c) Impact of climate change on SCA. Important impact of climate change is expected on the hydrological cycle and water management systems (Askew 1991). A temperature increase is expected in the next decades (Schneider 1989). Climate change effects on the hydrological behavior of snowfed rivers has been studied by various researchers (Rango 1992; Singh 1996; Singh and Kumar 1997). Singh and Kumar (1997) carried out detailed study on the effect of different climatic scenarios on different components of runoff for a highly snowfed river in the western Himalayas. Limited studies have been carried out to study the depletion of snow cover under the warmer climatic conditions. Rango and Martinec (1994) examined the influence of changes in temperature and precipitation on snow cover using snow melt runoff model (SRM).

In this study, depletion of SCA has been correlated with temperature, which enables studying the impact of warmer climatic scenarios on SCA. Effect of increase in temperature from 1 to 3°C has been studied on the depletion trend of SCA for the study basin. Depletion of SCA under different climatic scenarios for 1988 ablation period is shown in Figure 5.8. As expected, under warmer climate snow disappears from basin at faster rate, resulting in reduction in extent of SCA after melt season; extent of melting area during summer is increased under warmer climatic conditions. Similar trends were observed for all the years. Figure 5.9 shows that for all the years increase in melting area after the melt season was linearly correlated with increase in temperature. Because the initial SCA in the basin and distribution of temperature over the melt period vary from year to year, the impact of climate change would be different for different years. For the study basin, on average, an increase of temperature by 1, 2, and 3°C increased the melting area by 2.7, 5.1, and 7.2%, respectively. Thus, following the present methodology, one can generate SCA in the basin under new climatic scenarios, which can be used as input to the modeling studies and other applications related to SCAs.

These results are based on the assumption that relationship between SCA and CDD does change under warmer climatic scenario. In fact, initial snow cover conditions and distribution of temperature govern the equation. Because initial snow cover itself will change under climatic conditions, equation between SCA and CDD may also change. Thus, results for the warmer climate may vary as given in this example.

5.7 CONCLUSIONS

Satellite-derived SCA is used for various hydrological and climatological studies. Such information is of practical significance in operational water resources

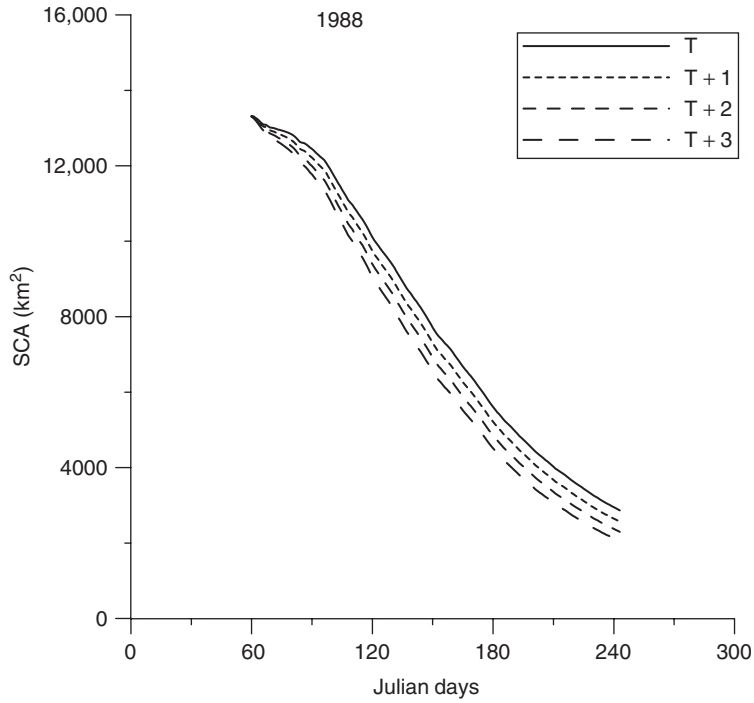


Figure 5.8 Depletion of snow covered area (SCA) in Satluj basin under different climatic scenarios for 1988

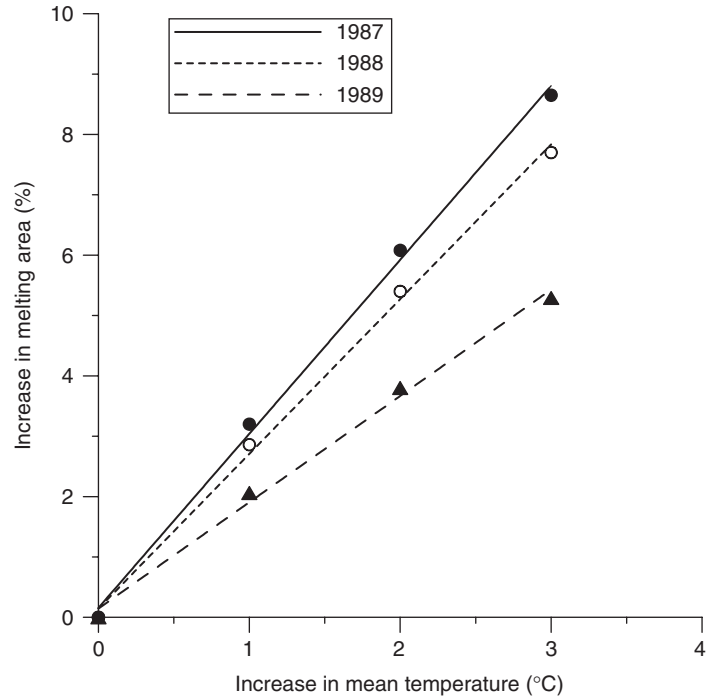


Figure 5.9 Increase in melting area with increase in mean temperature over the melt period in the Satluj basin for different years

practices and is used by water resources managers for various hydrological applications. Primarily, the application of SCA is made for the assessment of snow reserve, modeling of snow melt runoff, flood forecasting, effect of climate change on hydrology, and water balance studies of snowfed rivers. The emphasis of this study is on the snow melt runoff computation from a basin using SCA data on daily time scale. For large and inaccessible basins, like the Himalayan basins, SCA is a very important information for snow melt modeling studies. At the same time, procurement of satellite images on a daily basis becomes very expensive. Higher resolution data for large basins further increases number of images to be used to cover the basin, and data cost also increases proportionally. Analysis of large number of images also takes much time. Under some unavoidable atmospheric conditions like presence of cloud cover, reliable information on SCA is not available. Thus, because of various reasons, satellite data are obtained for a few dates during the melt period and discontinuity in database persists. In this study, a methodology that can be used to interpolate, extrapolate, and/or fill the missing data of SCA is evolved.

A combination of extent of SCA available in the basin just before start of melting and temperature distribution over the ablation season governs the depletion of SCA. Because of changes in these parameters, a different equation is obtained for every season. In this paper, relationship between SCA and CDD has been studied for the Satluj basin (22,305 km^2) located in the Western Himalayan region. It is found that during the ablation season (March–August) SCA depletes exponentially with CDD observed at a station near the SCA. Three years data were used for studying the relationship between SCA and CDD, and similar relationship was observed for all the seasons, confirming that the depletion of SCA is strongly related to CDD. The value of R^2 obtained was above 0.98 for the three years.

The established equations can be used to interpolate/extrapolate SCA data or extending time series of SCA using CDD data. This study also demonstrates, using limited information of SCA in the beginning and middle part of the season, a good application of the established relationship in simulating the SCA for the basin. It is observed that once the depletion trend is established in the basin in the first part of melt season, SCA can be simulated with good accuracy using CDD data for the rest of the melt season. Such applications can reduce the number of required satellite images for obtaining SCA. The variation in extent of SCA with time can also be forecasted using forecasted air temperatures.

On the basis of three years' analysis, an increase in temperature by 1, 2, and 3°C enhanced the melting area of snow over the melt season by 2.7, 5.1, and 7.2%, respectively. For the considered range of temperature increase (1–3°C), it was found that melting area of snow in the basin increased linearly with increase in temperature.

REFERENCES

Andersen, T. (1983) Operational snow mapping by satellites. *Proceedings of the Exeter Symposium*, July 1982, IAHS Publ. No. 138.

Askew, A. J. (1991) Climate and water – a call for international action, *Hydrological Sciences Journal*, Vol. 36, pp. 391–402.

Blöschl, G. and Kirnbauer, R. (1992) An analysis of snow cover patterns in a small alpine catchment, *Hydrological Processes*, Vol. 6, pp. 99–109.

Blöschl, G., Kirnbauer, R., and Gutknecht, D. (1991) Distributed snowmelt simulations in an alpine catchment 1. Model evaluation on the basis of snow cover patterns, *Water Resources Research*, Vol. 27, pp. 3171–3179.

Carroll, T. R. (1990) Operational remote sensing of snow cover in the U.S. and Canada. *Proceedings of National Conference on Hydraulic Engineering*, American Society of Civil Engineers, San Diego, CA.

Dewey, K. F. and Heim, R. Jr. (1981) Satellite observations of variations in northern hemisphere seasonal snow cover, NOAA Technical Report NESS 87, NOAA, Washington, DC, pp. 83.

Dey, B. and Goswami, D. C. (1984) Evaluating a model of snow cover area versus runoff against a concurrent flow correlation model in the Western Himalayas, *Nordic Hydrology*, Vol. 15, pp. 103–110.

Dey, B., Goswami, D. C., and Rango, A. (1983) Utilization of satellite snow cover observations for seasonal streamflow estimates in the Western Himalayas, *Nordic Hydrology*, Vol. 14, pp. 257–266.

Dey, B., Sharma, V. K., and Rango, A. (1989) A test of snow melt runoff model for a major river basin in Western Himalayas, *Nordic Hydrology*, Vol. 20, pp. 167–178.

Gupta, R. P., Duggal, A. J., Rao, S. N., and Sankar, G. (1982) Snow cover area vs. snow melt runoff relation and its dependence on geomorphology – a study from Beas catchment (Himalayas, India), *Journal of Hydrology*, Vol. 58, pp. 325–339.

Haefner, H., Seidel, K., and Ehrler, H. (1997) Applications of snow cover mapping in high mountain regions, *Physics and Chemistry of Earth*, Vol. 22 (3/4), pp. 275–278.

Hall, D. K. and Martinec, J. (1985) *Remote Sensing of Ice and Snow*, Chapman & Hall, London – New York, p. 189.

Jain, S. K. (2001) Modelling of streamflow and sediment studies in the Satluj basin using remote sensing and GIS, PhD Thesis, Department of Earth Sciences, Indian Institute of Technology, Roorkee, India.

Kattlemann, K. (1997) Rapid changes in snow cover at low elevations in the Sierra Nevada, California, U.S.A., *Annals of Glaciology*, Vol. 25, pp. 367–370.

Martinec, J., Rango, A., and Major, E. (1983) *The Snowmelt Runoff Model (SRM) User's Manual*, NASA Reference Publication 1100, NASA/Goddard Space Flight Centre, Greenbelt, Maryland.

Meier, M. F. (1973) Evaluation of ERTS imagery for mapping of changes of snow cover on land and on glaciers. *Symposium on Significant Results Obtained from the Earth Resources Technology Satellite 1*, NASA, New Carrollton, Maryland, Vol. 1, pp. 863–875.

Melloh, R. A., Daly, S., Davis, R. E., Jordan, R. E., and Kenig, G. (1997) An operational snow dynamics model for the Sava River, Bosnia, Proceedings of the Eastern Snow Conference, Banff, Canada, pp. 20–28.

Mittaz, C., Imhof, M., Hoelzle, M., and Haeberli, W. (2002) Snowmelt evolution mapping using an energy balance approach over an alpine terrain, *Arctic, Antarctic, and Alpine Research*, Vol. 34, pp. 274–281.

Ødegaard, H. A. and Østrem, G. (1977) Application of Landsat imagery for snow mapping in Norway, Final Report, Landst-2 Contract 29020, Norwegian Water Resources and Electricity Board, p. 20.

Østrem, G. (1974) The use of ERTS data to monitor glacier behaviour and snow cover- Practical implications for water power production, Proc. 3rd ERTS Symp., Washington, DC, December 1973, pp. 10–14.

Ramamoorthi, A. S. (1987) Snow cover area (SCA) is the main factor in forecasting snowmelt runoff from major river basins. *Large Scale Effects of Seasonal Snow Cover, Proceedings of the Vancouver Symposium*, IAHS, Publ. No. 166, pp. 187–198.

Ramamoorthi, A. S. and Subba Rao, P. (1981) Application of satellite technology for forecasting snow melt runoff of perennial rivers of India, Proceedings Of Second Asian Conference on Remote Sensing, Beijing, China.

Rango, A. (1992) Worldwide testing of the snow melt runoff model with applications for the predicting the effects of climate change, *Nordic Hydrology*, Vol. 23, pp. 155–172.

Rango, A. (1993) Snow hydrology processes and remote sensing, *Hydrological Processes*, Vol. 7, pp. 121–138.

Rango, A. and Martinec, J. (1994) Areal extent of seasonal snow cover in a changed climate, *Nordic Hydrology*, Vol. 25, pp. 233–246.

Rango, A., Salomonson, V. V., and Foster, J. L. (1977) Seasonal streamflow estimation in the Himalayan region employing meteorological satellite snow cover observations, *Water Resources Research.*, Vol. 13, pp. 109–112.

Ranzi, R., Grossi, G., and Bacchi, B. (1999) Ten years of monitoring areal snowpack in Southern Alps using NOAA-AVHRR imagery, ground measurements and hydrological data, *Hydrological Processes*, Vol. 13, pp. 2079–2095.

Schjødt-Osmo, O. and Engeset, R. (1997) Remote sensing and snow monitoring: Application to flood forecasting. In: *Operational Water Management*, Refsgaard, J. C. and Karalis, E. A. (eds), Balkema, Rotterdam; Proceedings of the European Water Resources Association Conference, 3–6 September 1997, Copenhagen, Denmark.

Schneider, S. A. (1989) *Global Warming – are we Entering The Greenhouse Century?* Sierra Club Books, San Francisco, CA, p. 317.

Seidel, K., Bruesch, W., Steinmeier Ch., and Martinec, J. (1995) Real time runoff forecasts for two hydrological stations based on satellite snow cover monitoring, *Proceedings of EARSeL Symposium*, Basel, Switzerland, pp. 253–261.

Seidel, K., Burkhart, U., Baumann, R., Martinec, J., Haefner, H., and Itten, K. I. (1989) Satellite data for evaluation of snow reserves and runoff forecasts, *Proceedings Hydrology and Water Resources Symposium*, Christchurch, NZ, pp. 28–30.

Singh, P. (1996) Effect of global warming on streamflow of a high altitude Spiti river, International Conference on Ecohydrology of Mountain Areas, 23–28 March 1996, Kathmandu, Nepal.

Singh, P. and Jain, S. K. (2002) Snow and glacier melt in the Satluj river at Bhakra Dam in the Western Himalayan region, *Hydrological Sciences Journal*, Vol. 47, pp. 93–106.

Singh, P., Jain, S. K., and Kumar, N. (1997) Snow and glacier melt runoff contribution in the Chenab river at Akhnoor, *Mountain Research Development*, Vol. 17, pp. 49–56.

Singh, P. and Kumar, N. (1997) Impact of climate change on the hydrological response of a snow and glacier melt runoff dominated Himalayan River, *Journal of Hydrology*, Vol. 193, pp. 316–350.

Singh, P. and Singh, V. P. (2001) *Snow and Glacier Hydrology*, Kluwer Academic Publishers, Dordrecht, The Netherlands.

PART II: SOIL WATER AND PERMAFROST

Climate and Hydrology in Mountain Areas. Edited by C. de Jong, D. Collins and R. Ranzi
© 2005 John Wiley & Sons, Ltd. ISBN: 0-470-85814-1

6

Permafrost Monitoring in High Mountain Areas Using a Coupled Geophysical and Meteorological Approach

CHRISTIAN HAUCK[1§], DANIEL VONDER MÜHLL[2§] AND MARTIN HOELZLE[2]

[1]Institute for Meteorology and Climate Research, University of Karlsruhe/ Forschungszentrum Karlsruhe, Germany, [2]Physical Geography Division, Dept. of Geography, University of Zurich, Switzerland, [§]formerly at: Laboratory for Hydraulics, Hydrology and Glaciology (VAW), ETH Zurich, Switzerland

6.1 INTRODUCTION

In the Earth's climate system, the cryosphere plays a special role, because of its sensitivity to even small climate changes. Within the cryosphere, permanently frozen ground (permafrost) in mountainous regions is specifically vulnerable, as temperatures are often close to the melting point of ice (Haeberli & Beniston 1998). Permafrost is a temperature phenomena defined as lithospheric material with a temperature below 0°C continuously for more than one year. Approximately 24% of the Northern Hemisphere land surface is underlain by permafrost (Zhang *et al*. 2003). Of these, a substantial part may be characterised as mountain permafrost, which usually refers to high mountain regions that are predominantly underlain by permafrost, while it is absent in adjacent lowlands, for example, the European Alps. After Keller *et al*. (1998), 5% of the area of Switzerland is underlain by mountain permafrost, whereas only 4% is covered by glaciers.

In view of a warming climate and the recent retreat of most Alpine glaciers, the need for a continuous monitoring of the permafrost evolution in mountainous regions has been identified (Fitzharris *et al*. 1996). This includes long-term temperature monitoring programmes (such as the EU-funded PACE (Permafrost and Climate in Europe) project (Harris *et al*. 2003), as well as improved process understanding and impact assessment of permafrost thawing in the mountains of Europe. Specifically important are thawing permafrost slopes, which may induce natural hazards such as rock falls and debris flows (Harris *et al*. 2001).

In order to understand the processes associated with freezing and thawing of the subsurface, monitoring programs must not be restricted to temperature measurements in deep boreholes, which are costly and often impossible to conduct in remote mountainous terrain. Instead, they should include atmospheric forcing variables as well as subsurface parameters associated with freeze and thaw processes in the ground. Reliable data sets of all components of the energy and water balance can then be used to validate coupled atmosphere–cryosphere models in order to estimate the permafrost response to climatic changes in high mountain regions.

Climate and Hydrology in Mountain Areas. Edited by C. de Jong, D. Collins and R. Ranzi
© 2005 John Wiley & Sons, Ltd. ISBN: 0-470-85814-1

In this study, a 2-dimensional geophysical ground monitoring approach introduced in Hauck (2002) is used in combination with energy balance data to determine the evolution of frozen ground at Schilthorn, Swiss Alps. Changes in subsurface water/ice content were monitored using surface geophysical measurements of the electrical resistivity using a multi-electrode system and a tomographic inversion scheme (Loke & Barker 1996). Resistivity changes are related to changes in the subsurface unfrozen water content, which can be used to determine the amount of freezing and thawing. The 2-dimensional tomographic approach enables the determination of the spatial representativeness of the results and yields information about spatially variable transient processes, like the advance and retreat of freezing fronts. In addition to borehole temperature data, energy balance data are obtained from a meteorological station installed during the PACE project, including measurements of radiation, temperature, humidity, wind speed and direction, as well as snow cover thickness.

In a future step, the obtained geophysical and meteorological data set can be used to validate coupled heat and mass transfer models. The aim of the modelling approach is to predict ground temperatures as well as permafrost degradation rates for different climatic scenarios.

6.2 THEORY

6.2.1 Geophysical measurements (DC resistivity tomography)

The direct current (DC) resistivity technique is based on electrical resistivity differences between different subsurface materials. For typical permafrost material, a marked increase in resistivity at the freezing point was shown in several field and laboratory studies (Hoekstra *et al*. 1975, King *et al*. 1988). Consequently, the application of electric and electromagnetic techniques has a long tradition in the study of permafrost (for a review, see Scott *et al*. 1990, Vonder Mühll *et al*. 2001). With the development of fast, commercially available two-dimensional tomographic inversion schemes, the DC resistivity method has been increasingly applied, especially in mountainous terrain (Hauck & Vonder Mühll 1999, 2003a, Vonder Mühll *et al*. 2000, Kneisel *et al*. 2000, Ishikawa *et al*. 2001, Isaksen *et al*. 2002, Marescot *et al*. 2003, Hauck *et al*. 2003, Ishikawa 2003, Delaloye *et al*. 2003, Reynard *et al*. 2003). As the heterogeneous surface and subsurface characteristics of mountain permafrost terrain often prohibit the application of plane-layer approximations used in standard data processing for 1-dimensional soundings, the 2-dimensional tomographic method greatly improves the quality of data interpretation in resistivity studies on permafrost.

In DC resistivity surveys, electrical current is injected into the ground via two current electrodes. The resistance of the ground is then determined by measuring the electric potential between two other electrodes and dividing by the current. By multiplying the resistance with a geometrical factor depending on the distance between the electrodes and choosing different electrode spacings and locations, the so-called apparent electrical resistivity is determined on a 2-dimensional grid. By using a tomographic inversion scheme (RES2DINV, Loke & Barker 1996), these apparent resistivities can be inverted to yield a 2-dimensional specific resistivity model of the ground. For monitoring purposes, these measurements are repeated at certain time intervals using a permanently installed electrode array, which allows for measurements independent of the snow cover thickness (Figure 6.1). Furthermore, the fixed-electrode array effectively filters resistivity variations because of variable electrode contacts or geological background variations, as mainly temporal resistivity changes are determined (Hauck 2001, 2002).

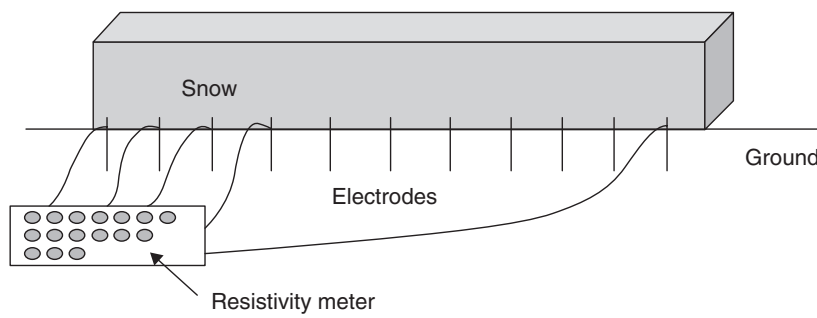


Figure 6.1 Installation setup of the fixed-electrode array at Schilthorn, Switzerland

6.2.2 Resistivity and unfrozen water content

An estimate of the unfrozen water content of the ground through repeated resistivity measurements can be obtained by using a simple approach based on a relation between the resistivity of a material and its pore fluid called Archie's law:

$$\rho = a\rho_p \Phi^{-m} S_w^{-n} \tag{6.1}$$

where ρ is the resistivity of the material, ρ_p is the resistivity of the water in the pore spaces, Φ is the porosity, S_w is the fraction of the pore space occupied by liquid water and a, m and n are empirically determined parameters (Telford *et al*. 1990). In partly frozen material, ionic transport takes place in the liquid phase. Therefore, the resistivity depends not directly on temperature or ice content but on the unfrozen water content S, that is, the fraction of water remaining unfrozen at subfreezing temperatures, which can be substantial even at relatively low temperatures (e.g. Anderson & Morgenstern 1973, Riseborough 2002).

Assuming the pore space of the material was completely filled with water prior to freezing ($S = S_w = 1$ for temperatures above the freezing point) and using Equation (6.1), Daniels *et al*. (1976) showed that the ratio of the resistivity of a partially frozen material ρ_f to that unfrozen ρ_i is related to the unfrozen water content by

$$\rho_f / \rho_i = S^{1-n}. \tag{6.2}$$

King *et al*. (1988) estimated the so-called saturation exponent n between 2 and 3 (for sands) and 5–8 (for clays) using permafrost samples from the North American Arctic.

6.2.3 Dependence on temperature

The dependence of resistivity on temperature differs for temperatures above and below the freezing point. At temperatures above the freezing point, a decrease in temperature changes the resistivity of the material only in so far as the resistivity of the pore water is changed. A decrease in temperature increases the viscosity of water, in turn decreasing the mobility of the ions in the water, which increases the resistivity. A relationship between ρ and temperatures T above the freezing point is given by

$$\rho = \frac{\rho_0}{1 + \alpha_T (T - T_0)}, \tag{6.3}$$

where ρ_0 is the resistivity measured at a reference temperature T_0 and α_T is the temperature coefficient of resistivity, which has a value of about $0.025^\circ C^{-1}$ for most electrolytes (Keller & Frischknecht 1966).

For temperatures below the freezing point, resistivities increase exponentially until most of the pore water is frozen. Using an exponential relationship of the form

$$\rho = \rho_0 e^{-b(T_{f,C} - T)}, \tag{6.4}$$

where ρ_0, b (in $^\circ C^{-1}$) are constants and substituting into Equation (6.2), S can be expressed as

$$S = \exp\left[\frac{b(T_{f,C} - T)}{1 - n}\right], \tag{6.5}$$

where $T_{f,C}$ is the temperature of the freezing point. For a saturation exponent of $n = 2$ (commonly used for rock, Telford *et al*. 1990) and $T_f = 0^\circ C$, Equation (6.5) describes simply an exponential decrease of the unfrozen water content with decreasing temperature (Riseborough 2002). The factor b controls the rate of decrease and can easily be determined from Equation (6.4) if resistivity data for different subzero temperatures are available. By choosing appropriate values for n and b, the temporal evolution of the unfrozen water content can be determined in a qualitative way.

6.3 FIELD SITE AND DATA ACQUISITION

The Schilthorn (2970 m a.s.l., for details see Table 6.1) is located in the Bernese Oberland at the transition between the Prealps in the north and the principle chain of the Bernese Alps in the south (Figure 6.2). It is an east–west

Table 6.1 Characteristics of the Schilthorn field site

	Catchment/study area
Name of the basin/area	Schilthorn
Mountain range	Bernese Alps
Elevation range of entire catchment	790–2970 m
Elevation range of individual sites	2900 m
Latitude and longitude	46°34′N, 7°50′E
Area in km^2	ca 40
Geology	Metamorphic sedimentary rocks, micaceous shales (Glockhaus formation)
% glacierized	0
Vegetation type (dominant)	Small to medium size debris, no vegetation
% forested	0
Mean Q at catchment outlet (mm)	Not determined

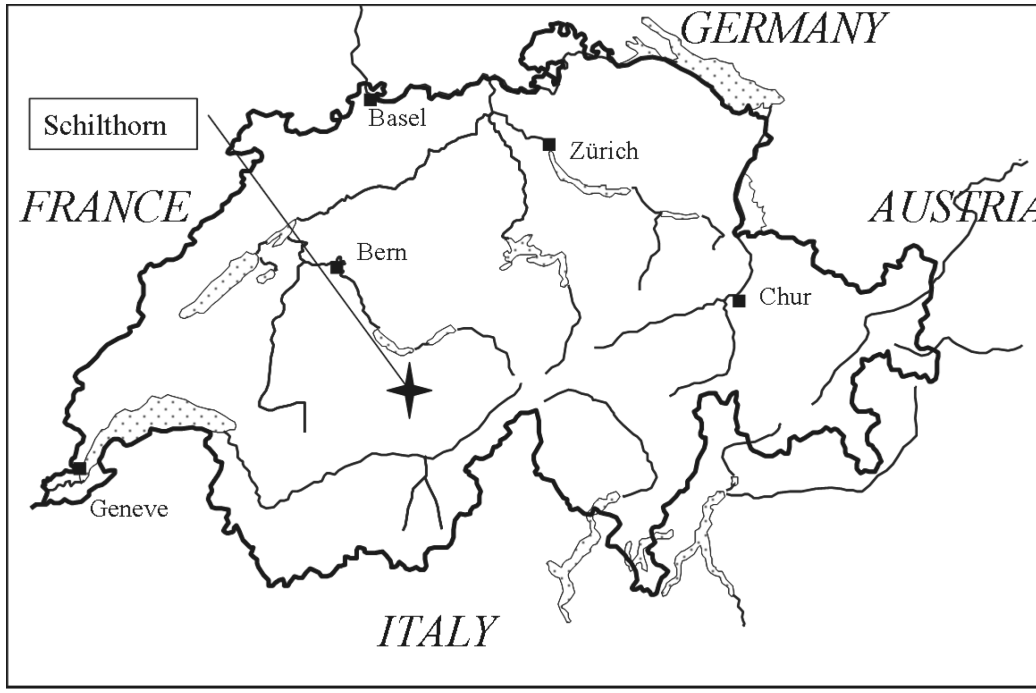


Figure 6.2 Location of the field site Schilthorn in the Bernese Alps, Switzerland

striking crest with north and south facing slopes. The investigation site is located on a small plateau on the north facing slope at 2900 m a.s.l. The mean annual air temperature (MAAT) at the top of Schilthorn is −4°C (estimated from long-term data sets from neighbouring MeteoSwiss stations) and annual precipitation varies from about 1200 mm in the valley bottom (796 m a.s.l.) up to about 2700 mm on the top (Imhof *et al*. 2000). Because of the high amount of precipitation and additional snow input through wind transport, the snow cover persists usually from October to June (Imhof *et al*. 2000, Mittaz *et al*. 2002). Presence of permafrost has been found at the summit when the facilities for the cable car were built. During the construction of the buildings in 1965–67, several ice lenses with a thickness up to 0.5 m were encountered and special construction methods had to be used (Gurtner 1991). However, subsequent investigations showed highly heterogeneous subsurface conditions, both concerning the presumed permafrost distribution (Imhof *et al*. 2000) and geology (inferred from geophysical surveys, Hauck (2001)).

Starting in 1998, three boreholes (14 m in 1998, 100 m and 100 m at an angle of 30° in 2000) were drilled within the PACE project (Vonder Mühll *et al*. 2000, Harris *et al*. 2003). The observed permafrost temperatures are comparatively warm, reaching −0.7°C at 14 m depth (Figure 6.3). Consequently, the ice content is low, and the unfrozen water content is high, leading to low resistivity values compared to typical mountain permafrost occurrences (Hauck & Vonder Mühll 1999, Vonder Mühll *et al*. 2000).

Repeated measurements throughout the year are required in order to correctly relate resistivity variations to changes in temperature and ice content. Monitoring of time-dependent processes (time-lapse) through repeated resistivity measurements has been used in hydrogeological tracer experiments in groundwater studies (e.g. Barker & Moore 1998). These repeated measurements are usually conducted on a timescale of hours or a few days to monitor the propagation of artificially induced tracers or natural rain and/or ground water. For permafrost, timescales of interest are of the order of weeks to months, and the focus is on monitoring the freezing and thawing processes.

A fixed-electrode array allowing repeatable resistivity tomography measurements along a 58 m survey line throughout the year was permanently installed at Schilthorn in September 1999 (cf. Figure 6.1). The 30 stainless steel electrodes were buried 1 m into the ground. Each electrode was connected to a cable via shrinking

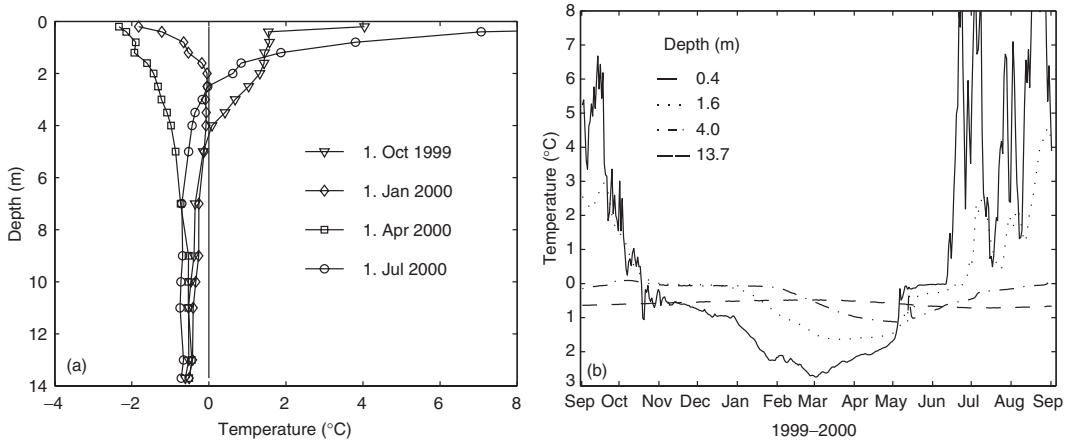


Figure 6.3 (a) Seasonal variation of the vertical temperature profile and (b) temporal evolution of temperature at 4 different depths in the 14 m deep borehole at Schilthorn (Bernese Alps, Switzerland). From Hauck, C. & Vonder Mühll, D. 2003b. Permafrost monitoring using time-lapse resistivity tomography. In: Phillips, M., Springman, S.M. & Arenson, L.U. (eds): *Permafrost. Proc. 8th International Conference on Permafrost*, 21–25 July, Zurich, Switzerland, Vol. 1, 361–366, published by Balkema, Lisse. Reproduced by permission of Taylor and Francis

tubes, which prohibit oxidation of the cable connectors. The cables were connected to a manual switchbox, which is accessible throughout the winter, and were buried for safety reasons in case of avalanches. Resistivity surveys were made by connecting the resistivity meter to the switchbox for each of the selected electrode configurations. This setup allows measurements to be taken throughout the year regardless of the snow cover thickness. An OYO McOhm resistivity meter was used for data acquisition. A whole survey takes approximately 90 minutes.

The measured apparent resistivities were inverted using RES2DINV. Between September 15, 1999, and August 28, 2000, eleven sets of DC resistivity tomography measurements were conducted with the fixed electrode array at Schilthorn. The time span between measurements was roughly one month except for the thawing season 2000, where measurements were conducted every two weeks (June/July). Additionally, an energy balance station including snow height, longwave and shortwave radiation balance, temperature, moisture and wind speed and direction measurements at 1.50 m above the surface was installed in 1999 (Mittaz 2002).

6.4 RESULTS

6.4.1 Laboratory experiments

In order to test the theoretical considerations presented above, laboratory experiments were conducted to determine the resistivity–temperature curves for saturated and dry material from the field site at Schilthorn. For these experiments, a set of miniature electrodes and cables was developed for the use on the laboratory scale (Figure 6.4). This miniature DC resistivity tomography system was originally developed to monitor the migration of contaminants in soils in scaled centrifuge experiments (Depountis *et al*. 1999). The system includes a standard DC resistivity meter and a set of 24 miniature electrodes with 3-cm spacing, which were connected to a switchbox allowing rapid measurements with different electrode combinations. The general setup of the experiments and a more detailed discussion of the results can be found in Hauck (2001). The material sample was contained in an 80 cm × 60 cm × 50 cm plastic box with a water outlet at the bottom and a punctuated tube across the bottom floor for water injection. Temperature was measured using UTL-1 mini-loggers (see e.g. Hoelzle *et al*. 1999). The box containing the sample was placed in a cold room, and measurements were recorded from the outside.

Figure 6.5 shows the resistivity-temperature curves for the saturated and dry Schilthorn material. Thereby, the terminus ''dry'' is used in a qualitative way, as the material was not completely dried to ensure electrical coupling with the electrodes. Two-dimensional tomographic interpretation of the measured resistivity values showed a heterogeneous distribution of the initial water content prior to freezing (not shown here). In Figure 6.5, mean resistivity values along the miniature electrode array were plotted versus the temperature. For temperatures above the freezing point, the small increase of resistivity with decreasing temperatures (Equation (6.3)) is clearly seen.



Figure 6.4 Measurement setup of the laboratory experiments with the miniature DC resistivity system

For temperatures below the freezing point, the resistivity increases exponentially with decreasing temperature. From these curves, the factor b in Equation (6.4) can be estimated for both cases. The exponential increase is larger in the saturated experiment than for the unsaturated material ($b = 0.735^{\circ}\mathrm{C}^{-1}$ vs $b = 0.273^{\circ}\mathrm{C}^{-1}$). This is in good agreement with previous studies, where the largest resistivity increase was found for samples with comparatively high water content (Olhoeft 1978, Seguin 1978).

Calculating the unfrozen water content S using Equation (6.5) and plotting resistivity ρ, unfrozen water content S and temperature T against time for the saturated Schilthorn experiment, the processes described qualitatively above are visualised (Figure 6.6). Thereby, the direction of the ρ-axis is reversed to facilitate the interpretation. As the temperature is approaching the freezing point, the resistivity is increasing slightly, due to a diminished mobility of the ions in the pore water. At the freezing point, the temperature curve flattens, as ice begins to form in the pore spaces. At the same time, the unfrozen water content starts to decrease. Because of the migration of the ions from the freezing phase to the still unfrozen parts of the sample, the freezing point is lowered and the temperature is still decreasing slightly. The resistivity is increasing only slowly, because the

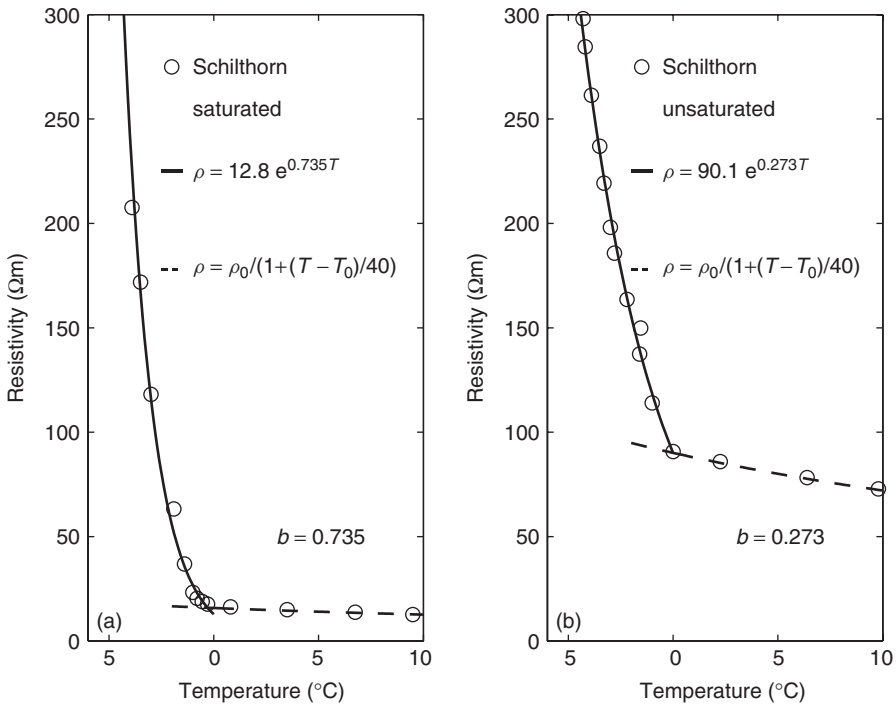


Figure 6.5 Resistivity–temperature relationship determined in the laboratory for two different samples: (a) Schilthorn material saturated with water and (b) Schilthorn material in its initial ''dry'' state

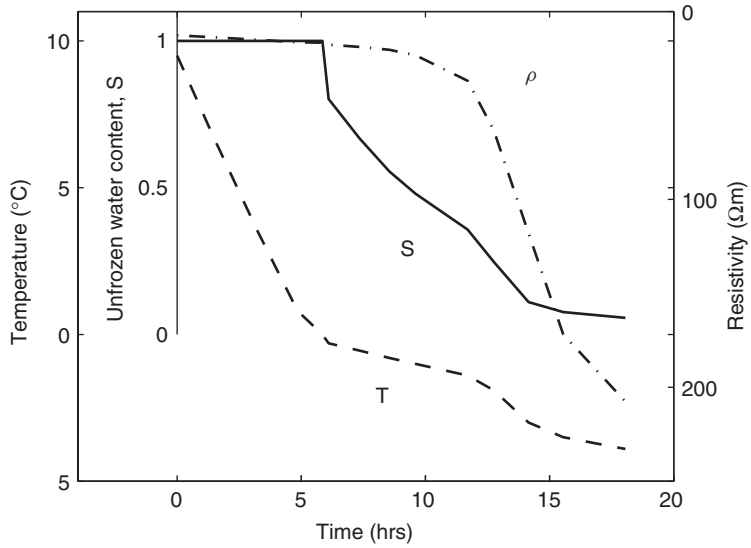


Figure 6.6 Resistivity ρ (broken line), temperature T (dashed) and unfrozen water content S (solid) as a function of time for the laboratory experiment with the saturated Schilthorn material. Note that the ρ-axis is reversed

migration of the ions decreases the resistivity of the unfrozen water, which nearly cancels out the effect of the decrease of *S*. After more than half of the water is frozen, the temperature curve decreases faster (after ca 12 hours) accompanied by a fast increase in resistivity, as less and less unfrozen water is available for electric conduction. Finally, the temperature curve flattens again accompanied by a sharp bend in the curve for the unfrozen water content. As the resistivity is very sensitive to further reductions of the unfrozen pore water, it is still increasing at this point.

6.4.2 Geoelectrical monitoring

Instead of analysing the eleven individual resistivity tomograms between September 1999 and August 2000 in terms of absolute values, the cumulative resistivity differences per day based on the first September measurement are shown in Figure 6.7.

Largest resistivity increases (white shading) were observed in October, when the snow cover was not yet established and cold temperatures could penetrate into the subsurface (Figure 6.7b). Freezing extends along the whole survey line and reaches a depth of 2 m. From October 1999 to April 2000, resistivities increased only slowly because of the insulating snow cover, which arrived in October and effectively decoupled the subsurface thermal regime from the atmosphere. The thereby trapped cold October temperatures propagate downward by heat conduction, subsequently freezing deeper layers. This gradual downshift of the freezing front can

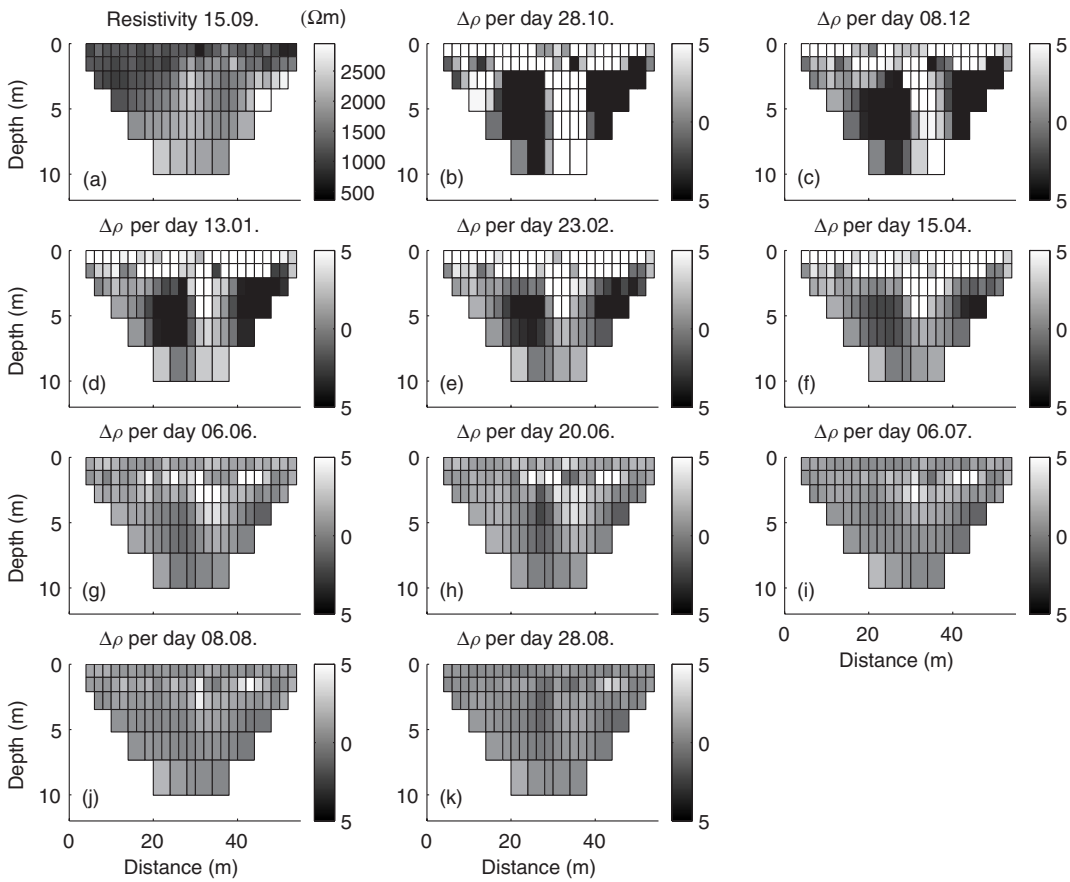


Figure 6.7 (Plate 8) (a) Resistivity model for the measurement on 15.9.1999 as determined by the inversion. (b)–(k) Resistivity difference per day based on the September measurement (a). White and dark shading denote resistivity increase and decrease, respectively. From Hauck, C. & Vonder Mühll, D. 2003b. Permafrost monitoring using time-lapse resistivity tomography. In: Phillips, M., Springman, S.M. & Arenson, L.U. (eds): *Permafrost. Proc. 8th International Conference on Permafrost*, 21–25 July, Zurich, Switzerland, Vol. 1, 361–366, published by Balkema, Lisse. Reproduced by permission of Taylor and Francis

be visualised by plotting ratios of successive resistivity measurements instead of cumulative differences (Hauck 2002, not shown here). During the phase transition, the temperatures remain close to 0°C (the so-called zero-curtain effect), while the resistivities increase, as the unfrozen water content is diminished. From the borehole temperature data shown in Figure 6.3b, it is seen that the zero-curtain effect started at the end of October and lasted until end of December at 1 m depth and until beginning of February at 4 m depth (right hand panel).

In the beginning of May, the temperatures near the surface approached 0°C, and melting of the uppermost layer started. Again, temperatures remained almost constant at 0°C during the phase transition. At the time of the first ''summer'' resistivity measurement (June 2000), most of the frozen water in the uppermost 2–3 m had already melted, which led, together with additional water input by rain, to a wet soaked surface layer, decreasing the resistivity strongly near the surface (grey shading in Figure 6.7g). Between June and July 2000, temperatures increased at all depths down to 10 m with a corresponding resistivity decrease throughout the major part of the survey area. This decrease continued until end of August 2000, thereby almost totally equalising the resistivity increase of the winter months. This can be seen by the predominantly grey shading in Figure 6.7(k) indicating only small resistivity differences between the measurement at the end of August 2000 and the reference measurement of September 15th 1999.

6.5 DISCUSSION

The results shown in the previous section indicate that geophysical methods are not only applicable for the detection and mapping of permafrost occurrences in mountainous areas but can also be used for monitoring purposes of freeze and thaw processes in the shallow subsurface. By conducting 2-dimensional tomographic surveys, the spatial variability of time-dependent processes can be detected. This is in contrast to the commonly used (and much more expensive!) point measurements in boreholes, which may not be representative for the whole study area. The horizontal variability of the temporal resistivity changes shown in Figure 6.7 indicate that freezing and thawing do not occur homogeneously along the 60 m survey length in the presented field case.

Comparing the obtained resistivity data with the temperature data from the borehole and incorporating the theoretical considerations and laboratory results, the vertical and temporal variability of the unfrozen water content (and therefore the relative ice content) can be assessed. In addition, monitoring results from the energy balance station for the same time span are used to relate the resistivity and temperature evolution to the dominant forcing variables, for example, the radiation and the snow cover duration.

6.5.1 Resistivity–temperature relationship

Figure 6.8 shows a scatter plot of all resistivity data points versus each corresponding temperature value from the borehole. As seen in the laboratory results (Figure 6.5), the resistivities increase slowly for decreasing but still positive temperatures. Below the freezing point, which may be estimated from Figure 6.8 to be about −0.2°C, the resistivities increase exponentially with cooling. However, as the data originate from different depths, the rate of increase is not uniform for all data points. Three branches can be identified and corresponding exponential functions can be fitted to the data (shown by the solid lines in Figure 6.8). The uppermost branch includes the two deepest model depths (below 6 m), the central branch consists of the data at 1.6 and 4.3 m depth and the lowermost branch includes the model depths at 0.5 and 2.8 m. The factor b was estimated as $2.422^{\circ}C^{-1}$ (upper), $0.617^{\circ}C^{-1}$ (central) and $0.244^{\circ}C^{-1}$ (lower), respectively. Two other curves were added for comparison (dotted and dashed-dotted lines): the line fitting the laboratory results for the saturated ($b = 0.735^{\circ}C^{-1}$) and the unsaturated Schilthorn sample ($b = 0.273^{\circ}C^{-1}$) are shown in Figure 6.5. The similarity between the two laboratory curves and the results from the two lower branches, corresponding to the active layer, suggest that differences in the amount of water saturation may be the reason for the existence of the two lower branches in Figure 6.8. The data points of the uppermost branch most probably correspond to firm bedrock below the active layer (5–6 m) and cannot be related to the laboratory experiments.

6.5.2 Comparison between energy balance, ground temperature and resistivity evolution

Figure 6.9 shows a comparison between the temperature change in the borehole, the radiation balance and the total resistivity variation at the borehole location. Thereby, the dominant role of the snow cover evolution becomes visible. A permanent snow cover was established at the end of October (Figure 6.9c) and persisted until mid-June. During that time, the temperature within the uppermost 10 m of the borehole remained almost constant (Figure 6.9a), as the ground temperature regime was effectively decoupled from the atmosphere and temperatures stayed at the freezing temperature of the ground. The

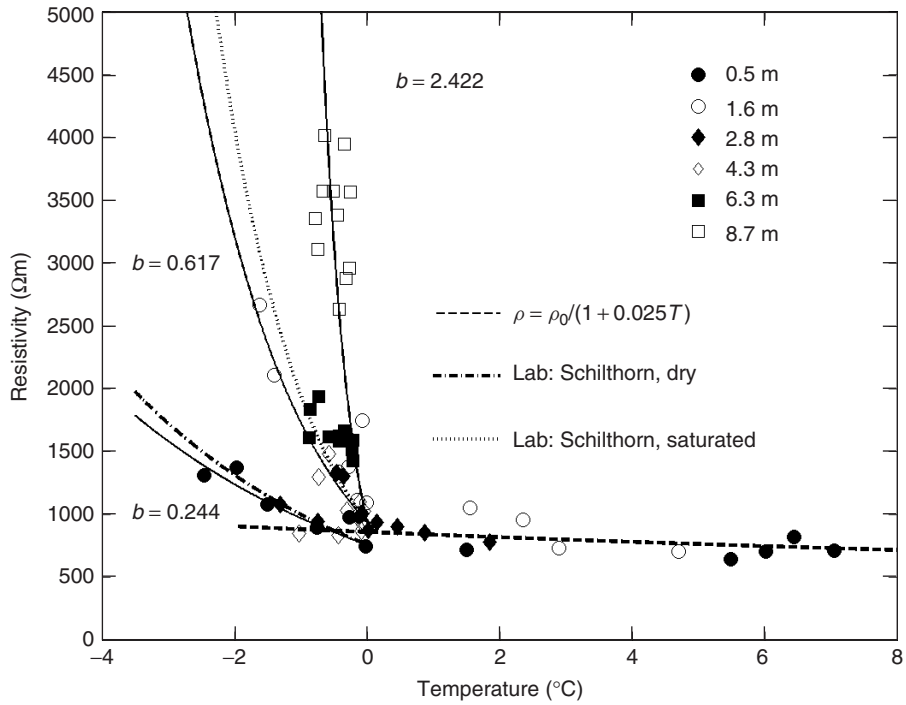


Figure 6.8 Resistivity–temperature relationship for the monitoring data from Schilthorn. The data are in good agreement with Equation (6.3) (dashed line) for temperatures above the freezing point, and split into three branches for temperatures below the freezing point. Each branch shows an exponential increase of resistivity with decreasing temperature, but at different rates (factor b in Equation (6.4), solid lines). The exponential increase rates of the laboratory measurements with the sample material from Schilthorn (saturated and dry state) are shown for comparison (dotted and dashed-dotted lines). Reproduced by permission of American Geophysical Union

net radiation (being the dominant energy flux, see Mittaz *et al*. (2000)) during that time is negative, meaning that cooling takes place at the snow surface (Figure 6.9b). But as the energy flux through the snow cover is negligible during winter (less than 1 W/m^2, Figure 6.9e), the freezing processes in the subsurface can only be induced by the cold October temperatures, which penetrated into the ground before the snow cover arrived and propagated to larger depths through heat conduction. After the melting of the snow cover in June, temperature variability in the borehole is high, coinciding well with the observed variability of the radiation balance (Figure 6.9b). This agreement confirms again the dominant role of the radiation balance for ground temperatures in mountain permafrost terrain.

Figure 6.9(d) shows the evolution of the unfrozen water content, which was calculated using Equation (6.5). The parameter b was chosen from the respective resistivity–temperature relation shown in Figure 6.8. The results for four different depths are shown. In the uppermost layer (0.5 m), the unfrozen water content starts to decrease at the end of October, corresponding to the onset of the negative radiation balance seen in Figure 6.9(b). The minimum is reached in February and subsequently later at greater depth (beginning of June at 8.7 m depth). At larger depths, the evolution of S is nearly sinusoidal, corresponding to the seasonal variation of ground temperature. The minimal value of S is smallest at larger depths (0.2–0.3 below 6 m for $n = 2$) and largest at intermediate depths (0.6–0.8 at 2–4 m for $n = 2$), but depends on the choice of parameters b and n. The larger the n, the smaller the variations of S. King *et al*. (1988) examined a large number of permafrost samples from the North American Arctic. At -2°C, they found unfrozen water contents as high as 0.9 (clay) and as low as 0.2 (sands) depending on the material type.

Finally, Figure 6.9(f) shows the total resistivity variation at the borehole location, calculated as weighted vertical mean. Total resistivities increase steadily until a maximum is reached for the April measurement. From

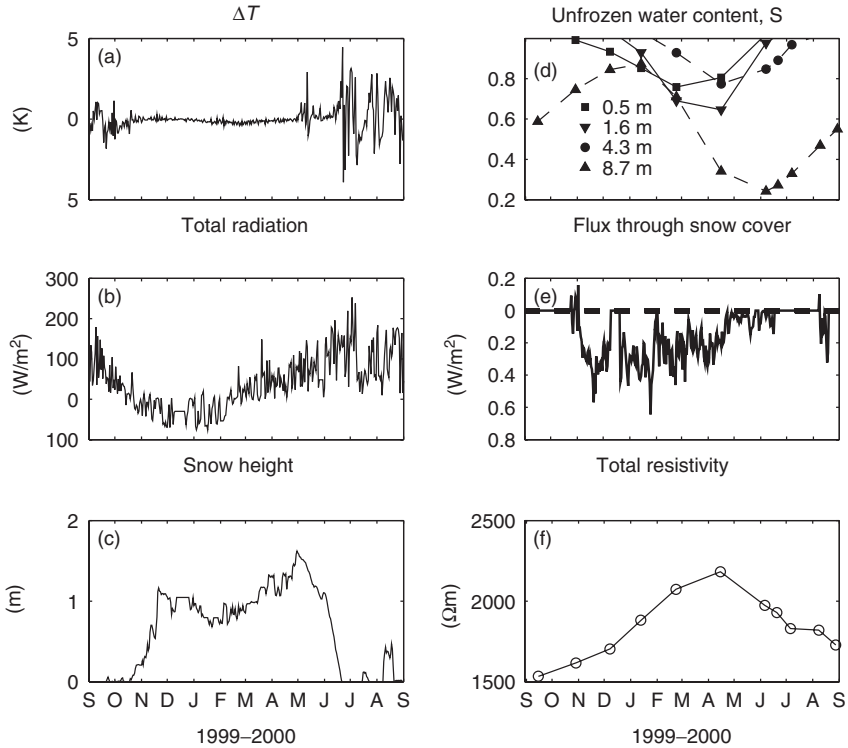


Figure 6.9 Comparison between borehole temperatures, energy balance parameters and resistivity. (a) Total temperature difference per day in the uppermost 10 m in the borehole, (b) net radiation at the energy balance station, (c) snow height, (d) calculated unfrozen water content (Equation (6.5)), (e) energy flux through the snow cover and (f) total resistivity variation at the borehole location (weighted vertical mean). From Hauck, C. & Vonder Mühll, D. 2003b. Permafrost monitoring using time-lapse resistivity tomography. In: Phillips, M., Springman, S.M. & Arenson, L.U. (eds): *Permafrost. Proc. 8th International Conference on Permafrost*, 21–25 July, Zurich, Switzerland, Vol. 1, 361–366, published by Balkema, Lisse. Reproduced by permission of Taylor and Francis

there, resistivities decrease again until September 2000, where a slightly larger value than the initial value in September 1999 is reached. Note that the strong resistivity increase during winter coincides with an almost zero total temperature change in the borehole (Figure 6.9a).

6.6 CONCLUSIONS

A multi-method approach using time-lapse resistivity tomography measurements at a mountain permafrost site in combination with laboratory measurements, borehole temperature and energy balance data has been presented as an example for state-of-the-art monitoring systems in mountain permafrost research. A set of 11 DC resistivity tomography measurements was obtained between September 1999 and September 2000 using a fixed electrode array at Schilthorn, Switzerland. The resulting resistivity changes were analysed in terms of subsurface freeze and thaw processes. Key results from this multi-parameter data set include the following:

- Temporal resistivity changes for permafrost monitoring in high Alpine environments can be accurately determined using a fixed electrode array, which is accessible throughout winter.
- Laboratory experiments using a miniature DC resistivity system can be used to determine material specific resistivity–temperature curves to validate the field data.
- Maximum resistivity changes on Schilthorn were observed in autumn (September–October), before a permanent snow cover has been established, and in late spring (May–June), when the thawing snow cover and additional water from precipitation greatly decreased the resistivity values in the active layer.
- During winter, the snow cover effectively decouples the ground from atmospheric influences. The heat

flux through the snow cover was less than 1 W/m^2, estimated from energy balance measurements. Consequently, a small but steady resistivity increase was obtained during winter, which was due to the trapped, cold October temperatures. From December to May, the freezing front moved gradually downward by thermal conduction, reaching 6 m in mid-April. After the start of the melting season, the resistivities decreased again until the previous September values are reached again at the end of August 2000.

- Resistivity–temperature relationships between the resistivity values at the borehole location and borehole temperatures show good agreement with theory. The increase of resistivity with decreasing temperature is small and linear for temperatures above the freezing point and exponential for temperatures below.
- The calculated temporal evolution of the unfrozen water content shows a strong decrease during the winter months in the active layer and a quasi-sinusoidal behaviour below.
- A comparison between borehole temperatures, resistivity and energy balance data emphasises the dominant role of the snow cover evolution in winter and net radiation in summer. In addition, resistivity monitoring may be used to determine the amount of freezing and thawing in the subsurface in future long-term monitoring programmes.

6.7 ACKNOWLEDGEMENTS

The authors would like to thank the Schilthornbahn AG for logistic support and C. Mittaz for supplying the energy balance data. This study was financed by the PACE project (Contract Nr ENV4-CT97-0492 and BBW Nr 97.0054-1). C. Hauck acknowledges a grant by the German Science Foundation (DFG) within the Graduiertenkolleg Natural Disasters, University of Karlsruhe.

REFERENCES

Anderson, D.M. & Morgenstern, N.R. 1973. Physics, chemistry and mechanics of frozen ground: a review. In: *Proceedings 2nd International Conference on Permafrost*, Yakutsk, Russia, 257–288.

Barker, R.D. & Moore, J. 1998. The application of time-lapse electrical tomography in groundwater studies. *The Leading Edge* **17**: 1454–1458.

Daniels, J.J., Keller, G.V. & Jacobson, J.J. 1976. Computer-assisted interpretation of electromagnetic soundings over a permafrost section. *Geophysics* **41**: 752–765.

Delaloye, R., Reynard, E., Lambiel, C., Marescot L. & Monnet, R. 2003. Thermal anomaly in a cold scree slope (Creux du Van, Switzerland). In: *Proceedings of the 8th International Conference on Permafrost*, Zurich, Switzerland, 175–180.

Depountis, N., Harris, C. & Davies, M.C.R. 1999. The application of miniaturised electrical imaging in scaled centrifuge modelling of pollution plume migration. In: Yong, R.N. & Thomas, H.R. (eds): *Geoenvironmental Engineering*, Thomas Telford, 264–271.

Fitzharris, B.B., Allison, I., Braithwaite, R.J., Brown, J., Foehn, P.M.B., Haeberli, W., Higuchi, K., Kotlyakov, V.M., Prowse, T.D., Rinaldi, C.A., Wadhams, P., Woo, M.-K., Xie Youyou, Anisimov, O., Aristarain, A., Assel, R.A., Barry, R.G., Brown, R.D., Dramis, F., Hastenrath, S., Lewkowicz, A.G., Malagnino, E.C., Neale, S., Nelson, F.E., Robinson, D.A., Skvarca, P., Taylor, A.E. & Weidick, A. 1996. The cryosphere: changes and their impacts. *Climate Change 1995. Contribution of Working Group II to the 2nd Assessment Report of the IPCC*, Cambridge University Press, Cambridge: 241–265.

Gurtner, V. 1991. *Schilthorn Umsteigen. Geschichte und Technik der Schilthornbahn*, 2nd edition, Orell Füssli, Zürich, Switzerland.

Haeberli, W. & Beniston, M. 1998. Climate change and its impact on glaciers and permafrost in the Alps. *Ambio* **27**(4): 258–265.

Harris, C., Davies, M.C.R. & Etzelmüller, B. 2001. The assessment of potential geotechnical hazards associated with mountain permafrost in a warming global climate. *Permafrost and Periglacial Processes* **12**(1): 145–156.

Harris, C., Vonder Mühll, D., Isaksen, K., Haeberli, W., Sollid, J.L., King, L., Holmlund, P., Dramis, F., Guglielmin, M. & Palacios, D. 2003. Warming permafrost in European mountains. *Global and Planetary Change* **39**: 215–225.

Hauck, C. 2001. Geophysical methods for detecting permafrost in high mountains. PhD-thesis, *Mitteilungen der Versuchsanstalt fur Wasserbau, Hydrologie und Glaziologie*, Zürich, Switzerland, p. 171.

Hauck, C. 2002. Frozen ground monitoring using DC resistivity tomography. *Geophysical Research Letters* **29**(21): 2016.

Hauck, C. & Vonder Mühll, D. 1999. Using DC resistivity tomography to detect and characterise mountain permafrost. In: *Proceedings of the 61st European Association of Geoscientists and Engineers (EAGE) conference*, 7–11, June 1999, Helsinki, Finland, Abstract 2–15.

Hauck, C. & Vonder Mühll, D. 2003a. Inversion and interpretation of 2-dimensional geoelectrical measurements for detecting permafrost in mountainous regions. *Permafrost and Periglacial Processes* **14**(4): 305–318.

Hauck, C. & Vonder Mühll, D. 2003b. Permafrost monitoring using time-lapse resistivity tomography. In: Phillips, M., Springman, S.M. & Arenson, L.U. (eds): *Permafrost. Proc. 8th International Conference on Permafrost*, 21–25 July, Zurich, Switzerland, Vol. 1, Balkema, Lisse, 361–366.

Hauck, C., Vonder Mühll, D. & Maurer, H. 2003. Using DC resistivity tomography to detect and characterise mountain permafrost. *Geophysical Prospecting* **51**: 273–284.

Hoekstra, P., Sellmann, P.V. & Delaney, A. 1975. Ground and airborne resistivity surveys of permafrost near Fairbanks, Alaska. *Geophysics* **40**: 641–656.

Hoelzle, M., Wegmann, W. & Krummenacher, B. 1999. Miniature temperature dataloggers for mapping and monitoring of permafrost in high mountain areas: first experience from the Swiss Alps. *Permafrost and Periglacial Processes* **10**: 113–124.

Imhof, M., Pierrehumbert, G., Haeberli, W. & Kienholz, H. 2000. Permafrost investigation in the Schilthorn Massif, Bernese Alps, Switzerland. *Permafrost and Periglacial Processes* **11**(3): 189–206.

Isaksen, K., Hauck, C., Gudevang, E., Oedegaard, R.S. & Sollid, J.L. 2002. Mountain permafrost distribution in Dovrefjell and Jotunheimen, southern Norway, based on BTS measurements and 2D tomography data. *Norsk Geografisk Tidsskrift* **56**: 122–136.

Ishikawa, M., Watanabe, T. & Nakamura, N. 2001. Genetic difference of rock glaciers and the discontinuous mountain permafrost zone in Kanchanjunga Himal, Eastern Nepal. *Permafrost and Periglacial Processes* **12**(3): 243–253.

Ishikawa, M. 2003. Spatial mountain permafrost modelling in the Daisetsu mountains, northern Japan. In: *Proceedings of the 8th International Conference on Permafrost*, Zurich, Switzerland, 473–478.

Keller, F., Frauenfelder, R., Gardaz, J.-M., Hoelzle, M., Kneisel, C., Lugon, R., Phillips, M., Reynard, E. & Wenker, L. 1998. Permafrost map of Switzerland. In: *Proceedings of the 7th International Conference on Permafrost*, Yellowknife, Canada, 557–562.

Keller, G.V. & Frischknecht, F.C. 1966. *Electrical Methods in Geophysical Prospecting*, Pergamon Press.

King, M.S., Zimmerman, R.W. & Corwin, R.F. 1988. Seismic and electrical properties of unconsolidated permafrost. *Geophysical Prospecting* **36**: 349–364.

Kneisel, C., Hauck, C. & Vonder Mühll, D. 2000. Permafrost below the timberline confirmed and characterized by geoelectric resistivity measurements, Bever Valley, Eastern Swiss Alps. *Permafrost and Periglacial Processes* **11**: 295–304.

Loke, M.H. & Barker, R.D. 1996. Rapid least-squares inversion of apparent resistivity pseudosections using a quasi-Newton method. *Geophysical Prospecting* **44**: 131–152.

Marescot, L., Loke, M.H., Chapellier, D., Delaloye, R., Lambiel, C. & Reynard, E. 2003. Assessing reliability of 2D resistivity imaging in permafrost and rock glacier studies using the depth of investigation index method. *Near Surface Geophysics* **1**(2): 57–67.

Mittaz, C. 2002. Energy balance over alpine permafrost. *PhD-thesis*, University of Zurich, Zurich, Switzerland.

Mittaz, C., Hoelzle, M. & Haeberli, W. 2000. First results and interpretation of energy-flux measurements over Alpine permafrost. *Annals of Glaciology* **31**: 275–280.

Mittaz, C., Imhof, M., Hoelzle, M. & Haeberli, W. 2002. Snowmelt evolution mapping using an energy balance approach over an Alpine terrain. *Arctic, Antarctic and Alpine Research* **34**(3): 274–281.

Olhoeft, G.R. 1978. Electrical properties of permafrost. In: *Proceedings 3rd International Conference on Permafrost*, Edmonton, Canada, Vol. 1, 127–131.

Reynard, E., Lambiel, C., Delaloye, R., Devaud, G., Baron, L., Chapellier, D., Marescot, L. & Monnet, R. 2003. Glacier/permafrost relationships in forefields of small glaciers (Swiss Alps). In: *Proceedings of the 8th International Conference on Permafrost*, Zurich, Switzerland, 947–952.

Riseborough, D. 2002. The mean annual temperature at the top of permafrost, the TTOP model and the effect of unfrozen water. *Permafrost and Periglacial Processes* **13**: 137–143.

Scott, W., Sellmann, P. & Hunter, J. 1990. Geophysics in the study of permafrost. In: Ward, S. (ed.): *Geotechnical and Environmental Geophysics*, Society of Exploration Geophysicists, Tulsa, OK, 355–384.

Seguin, M.K. 1978. Temperature-electrical resistivity relationship in continuous permafrost at Purtuniq, Ungava Peninsula. In: *Proceedings 3rd International Conference on Permafrost*, Edmonton, Canada, Vol. 1, 137–144.

Telford, W.M., Geldart, L.P. & Sheriff, R.E. 1990. *Applied geophysics*, 2nd edition, Cambridge University Press.

Vonder Mühll, D., Hauck, C. & Lehmann, F. 2000. Verification of geophysical models in Alpine permafrost using borehole information. *Annals of Glaciology* **31**: 300–306.

Vonder Mühll, D., Hauck, C., Gubler, H., McDonald, R. & Russill, N. 2001. New geophysical methods of investigating the nature and distribution of mountain permafrost with special reference to radiometry techniques. *Permafrost and Periglacial Processes* **12**(1): 27–38.

Zhang, T., Barry, R.G., Knowles, K., Ling, F. & Armstrong, R.L. 2003. Distribution of seasonally and perennially frozen ground in the Northern Hemisphere. In: *Proceedings 8th International Conference on Permafrost*, Zurich, Switzerland, 1289–1294.

7

Effects of Frozen Soil on the Groundwater Recharge in Alpine Areas

DANIEL BAYARD[1] AND MANFRED STÄHLI[2]
[1]EPF Lausanne, GEOLEP, ENAC, 1015 Lausanne, Switzerland, [2]Swiss Federal Research Institute WSL, Zürcherstrasse 111, 8903 Birmensdorf, Switzerland

7.1 INTRODUCTION

Frozen ground is one of the most special features of alpine regions. At lower altitudes, soil frost forms seasonally, depending on weather, topography, snow cover and other surface properties, whereas at higher altitudes (and latitudes) a frost layer may persist year-round (permafrost). Soil frost not only makes great demands on buildings, construction and roads but it also strongly influences the water cycle.

During the last decades, numerous research studies have been carried out demonstrating that *at the local scale* soil frost may drastically reduce or in the worst case impede soil water flow. Laboratory studies using hydraulic (Burt and Williams 1976) or air permeameters (Seyfried and Murdock 1997) were used to estimate the reduction in hydraulic conductivity due to soil freezing, which could be several orders of magnitude. Obviously, the ice content (or air-filled porosity) of the soil plays a decisive role for the hydraulic conductivity, with lower values for ice-rich soil material. However, it is important to stress that frozen soil is not *a priori* impermeable. Laboratory studies (e.g. Stadler *et al*. 2000) and field measurements on small delimited plots (e.g. Johnsson and Lundin 1991; Stähli *et al*. 1999) clearly demonstrated that water infiltration into frozen soils takes place if at the beginning of the snowmelt the soil contains air-filled pores. Whereas the soil frost effect on the water flow is quite well investigated *at the local scale*, we know much less about the importance of frozen soil on the hydrology of larger areas. In studies in which for several years the snowmelt runoff from small catchments was compared with soil frost indicators (Shanley and Chalmers 1998), there was no clear evidence for faster and larger runoff in winters with deep soil frost. One major reason is that deep soil frost usually coincides with a shallow snow cover. With regard to the groundwater recharge during snowmelt, very few studies have been published that illuminate the role of the frozen ground. Thorne *et al*. (1998) presented data from the Canadian Shield showing the groundwater recharge with respect to soil frost conditions for two winters.

Whereas the hydrology of seasonally frozen soils for the most part has been studied experimentally, there are only few examples of numerical simulation models that describe in detail the water infiltration into frozen soils. Most existing soil water transfer models do not include frost effects. One of the first models coupling heat and water fluxes of a layered soil profile was suggested by Harlan (1973). More recently, the models SOIL (Jansson and Halldin 1979), which in the meantime has been renamed and further developed to COUP (Jansson and Karlberg 2001), and SHAW (Flerchinger and Saxton 1989) extended Harlan's concept to detailed soil-vegetation-atmosphere transfer (SVAT) schemes including a process description of soil freezing and thawing, as well as formation and ablation of the snow cover.

Climate and Hydrology in Mountain Areas. Edited by C. de Jong, D. Collins and R. Ranzi
© 2005 John Wiley & Sons, Ltd. ISBN: 0-470-85814-1

Since these models treat only one-dimensional water flow, they have been predominantly tested ''at the plot scale''. However, some applications of these models were run in a quasi 2-d mode, representing hillslope runoff with a sequence of coupled profiles (Stähli *et al*. 2001). Larger-scale groundwater models that include soil frost processes are mostly conceptual (Cherkauer and Lettenmaier 1999; Koren *et al*. 1995; De Gaetano *et al*. 1996). Ippisch (2001) implemented a soil frost routine in a three-dimensional water and heat flow model, but the coupling between the soil and the snow cover was not integrated.

In alpine ski-resorts, tourism, artificial snow production and hydropower supply generate an increasing demand for water, especially during the winter–spring season. Therefore, it is important to thoroughly study the recharge of the aquifer during the snowmelt and to illuminate the effect of a frozen soil surface on the timing and the amount of ground water recharge. This was the starting point for setting up an extensive field experiment in the southern Swiss Alps that will be presented in the following chapter. Our objectives were

- to explore the local effect of seasonally frozen ground on the snowmelt discharge from alpine slopes
- to examine the impact of the spatial and altitudinal variability on frost and snowmelt, so as to regionalize obtained results
- to investigate the key processes that influence groundwater recharge during snowmelt periods
- to determine the large-scale effect of soil frost on aquifer recharge
- to identify soil frost situations that might entail hydrological risks.

7.2 THE HANNIGALP/GD ST BERNARD EXPERIMENT

7.2.1 Concept and idea

The applied methodology is shown in Figure 7.1. Initially, we studied water infiltration at the plot scale by measuring the different discharge components of surface runoff, subsurface flow and deep percolation for two winters (2000/01, 2001/02) at two locations in the southern Swiss Alps (Hannigalp, Gd St Bernard) Figure 7.2. The main purpose was to quantify the local effect of soil frost on the snowmelt infiltration. In addition to the water balance measurements, we ran dye tracer

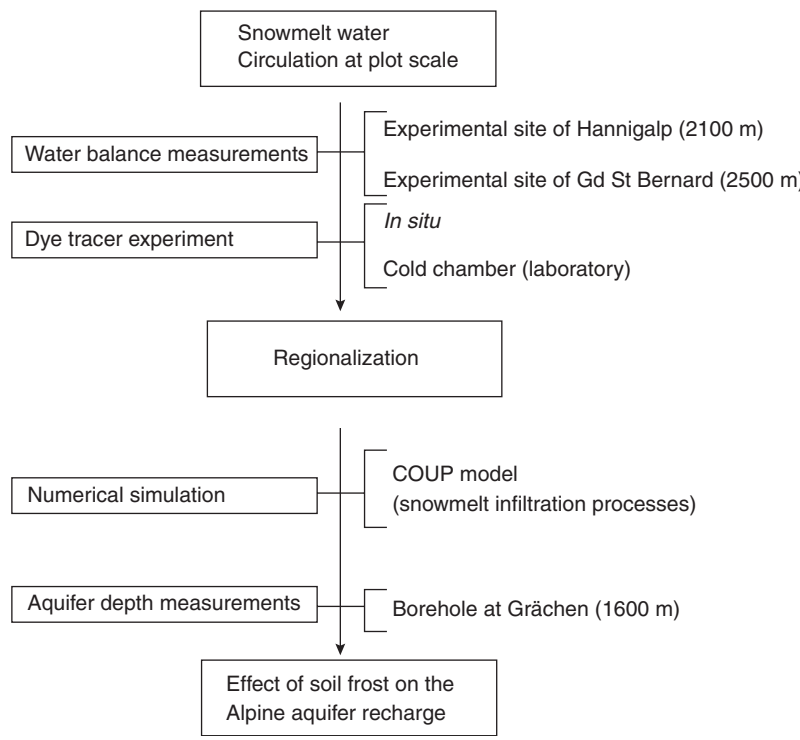


Figure 7.1 Methodology of the project

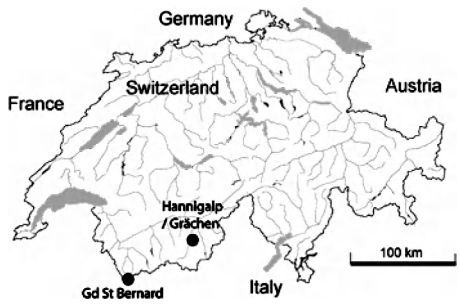


Figure 7.2 Location of the two experimental sites (Basic map provided by BFS GEOSTAT/Bundesamt für Landestopographie). Courtesy BFS GEOSTAT

Table 7.1 Table of site characteristics

	Site 1	Site 2
Name of the site	Hannigalp (Grächen)	Gd St Bernard
Mountain range	Alps	Alps
Elevation	2090 m	2500 m
Latitude and longitude	46°12′; 7°52′	45°52′; 7°10′
Slope and aspect	23%, east	65%, south
Geology	Old till above gneiss (Mischabel-Kristallin)	Gneiss underground
Soil type	Ferric podzol	Ranker/rhegosol
Vegetation type (dominant)	Rhododendron and grass	Grass

experiments *in situ*, as well as in the laboratory to obtain visual and quantitative information on the snowmelt infiltration pathways. By conducting these studies at two locations, which differed in their altitude, exposure and climate, we gained a better insight into the geographical and topographical induced variation of the snow and frost distribution.

Second, a one-dimensional SVAT-model was run to reproduce the detailed water and heat dynamics in the snow and the uppermost 3 m of the soil for the two experimental winters. For that purpose, we selected the model package COUP (Jansson and Karlberg 2001), which is one of the few SVAT-models that describe in detail freezing and thawing of the soil with all its influence on the water transport. The model was extensively calibrated to fit measured snow depth, frost depth and soil water content. By comparing the simulated fluxes with the runoff measurements, we aimed to indicate how well the model described the partitioning between surface runoff, lateral subsurface flow and deep percolation.

Third, long-term simulations were run with the calibrated model to extend our period of observations to earlier winters with known meteorological conditions. We simulated snow depth, snow water equivalent, frost depth and groundwater discharge for the recharge area beneath Hannigalp at a 250 m-resolution, adjusting the meteorological inputs to the altitude. Finally, we compared these results with water-table elevation measurements, so as to evaluate a possible effect of soil frost on the aquifer recharge.

7.2.2 Site description

Although both locations are at a distance of only 80 km from each other, they are characterized by very different microclimates. Hannigalp is one of the driest regions in Switzerland with only 599 m of annual precipitation, whereas Gd St Bernard receives almost four times more precipitation (2100 mm).

The Hannigalp site is surrounded by a coniferous forest, some 100 m below the tree limit. It is part of a slope ranging from 2600 m down to 1600 m, having an average gradient of 30%. The soil is a sandy loam (50–70 cm thick) with a thin hydrophobic organic top soil layer.

At Gd St Bernard (2500 m), the site is located on a wind-exposed pass well above tree-line. The shallow soil is a sandy loam and contains large slate stones at all depths.

The characteristics of the two sites are listed in Table 7.1.

At the foot of the Hannigalp slope close to the village of Grächen (1600 m), the groundwater table has been measured in a piezometer for 10 years. The village is built on ground left by interglacial subsidence. The soil consists of low permeability till material and very permeable rubble. The region above the borehole mainly consists of slope debris deposit and till deposit (Quaternary). Because of the high infiltration capacity of the soil surface, most of the precipitation infiltrates into the soil and little surface runoff occurs.

7.2.3 Local scale measurements

At both sites, we set up a similar experiment. On a delimited soil plot (6 m^2), the different components of the water balance were measured, that is, precipitation, snow water equivalent, surface runoff, subsurface runoff and deep percolation.

At the lower edge of the plot, surface and subsurface runoff were collected from the depth intervals 0 to 3 cm and 3 to 28 cm, respectively (Figure 7.3). The collecting gutters were filled with gravel and sand so

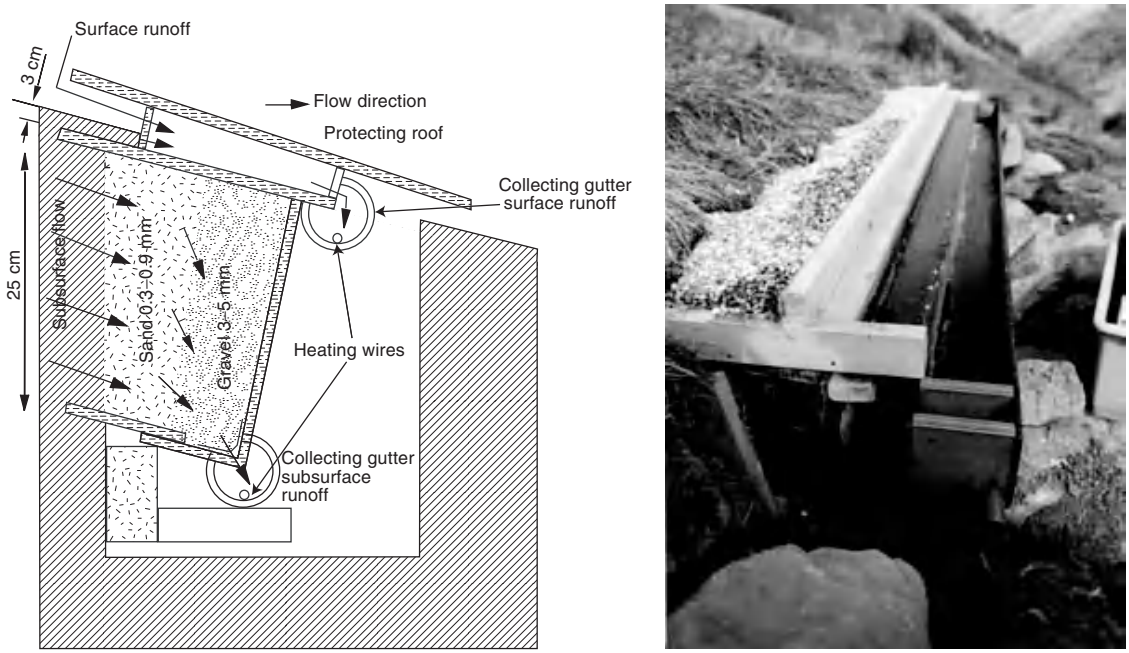


Figure 7.3 Schematic instrumental setup for collecting surface and subsurface lateral runoff. On the right, a picture of a collecting gutter for surface runoff

as to diminish the capillary barrier between the soil and the collecting device, and to allow water to drain to the two collecting gutters under unsaturated conditions. The gutters were equipped with heating wires to prevent water from freezing inside the apparatus. The discharge was measured manually the first winter (once per day), and automatically with a tipping bucket the second winter. Lateral inflow from the terrain above was prevented by a 50-cm-deep open ditch. However, lateral inflow through the snowpack was not inhibited.

On an adjacent plot, the deep percolation was collected at a depth of 40 cm using an open lysimeter with a surface area of 0.52 m^2 (see Figure 7.4). To maintain a hydraulic connection between the lysimeter and the undisturbed soil, the excavated gap was filled with sand and gravel.

Additionally, we measured the liquid soil water content with Time Domain Reflectometry, the soil temperature at depths of 5, 10, 20 and 30 cm using thermocouples, as well as the short wave solar radiation with a pyranometer. Complementary meteorological data (air temperature, precipitation, sky cover, wind speed, relative humidity) were received from the MeteoSwiss station in Grächen.

In both winters, a dye tracer experiment was set up to observe the development of the water flow paths from the surface down to the bedrock (60–80 cm depth) along the route of the snowmelt. In autumn, we selected suitable plots with a length of approximately 5 m and a width of 1 to 1.5 m. At the beginning of the winter, a dye tracer was applied on the selected plots. We used the food dye Brilliant Blue FCF, which has been used in numerous soil physical field studies (e.g. Forrer *et al*. 2000). Brilliant Blue FDF is non-toxic, well visible in normal field soils and, depending on the pH, either neutral or anionic with a rather high mobility. During the spring snowmelt, we returned to the sites and excavated vertical profiles on the tracer plots, starting at the onset of the snowmelt and finishing shortly after the complete melt of the snow. For each date, we excavated two to four profiles. Each profile was then photographed using a digital camera (Nikon Coolpix 990) at a pixel resolution of less than 1.5 mm.

The digital images (Figure 7.5) were processed with the following method (details in Stähli *et al*. 2004). The average level of the color channels was standardized to a reference common for all profiles. Then, we applied a supervised classification procedure to separate the pixels stained with Brilliant Blue tracer from the unstained profile pixels. Next, the image analysis operations *erosion* and *dilation* eliminated erroneously classified single pixels and filled up small gaps in connected stained

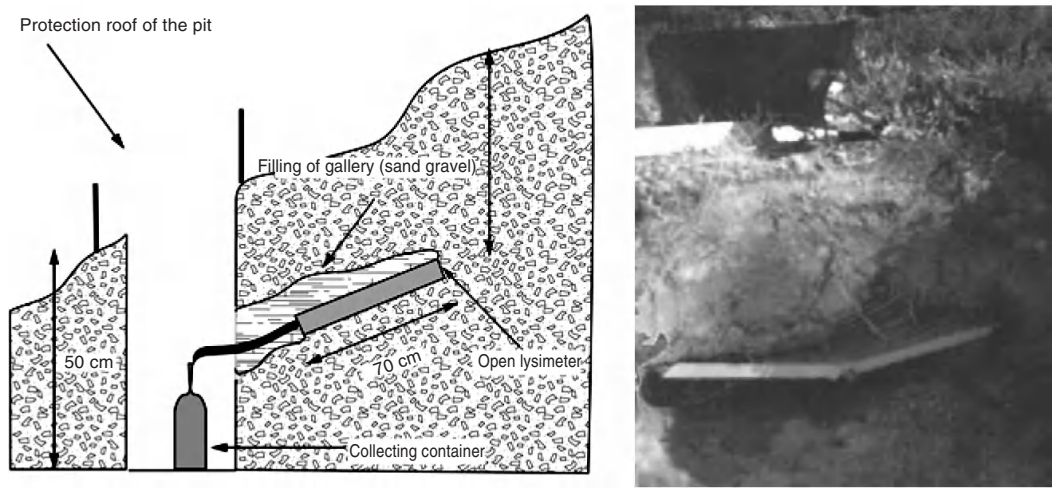
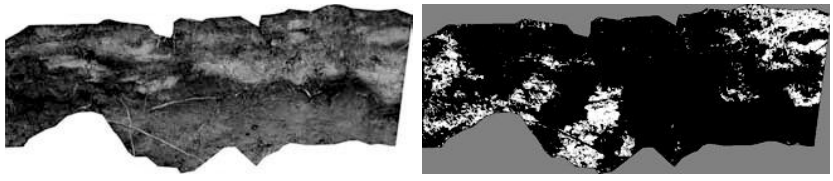


Figure 7.4 Schematic instrumental setup and picture of an open lysimeter



(a) (b)

Figure 7.5 Original RGB-image (a) and map of classified stained areas (b) for a soil profile excavated on 30 April, 2001, at Hannigalp. In (b), the light pixels denote the stained areas

areas. Finally, the depth distribution of the fraction of stained areas was plotted.

7.2.4 Numerical modeling of soil frost and groundwater recharge: the COUP-model

Conceptually, the COUP-model consists of a soil profile with a number of layers of (measured or estimated) physical properties. Water and heat flow between the layers is calculated with the well-known Richards equation and Fourier's law assuming homogeneous, nonpreferential fluxes. Hourly or daily values of standard meteorological variables are the driving forces for the model, and parameterized hydrological properties characterize the soil profile. With regard to winter conditions, COUP simulates a snow cover assuming uniform properties, such as thermal conductivity, liquid water retention or density. Melting of the snowpack is based on a complete surface energy balance calculation. At freezing, both soil water and heat fluxes are coupled. If the soil temperature decreases below 0°C, a user-defined freezing characteristic curve defines the partitioning of heat loss into a latent part (transformation of water to ice) and a sensible part (temperature decrease). During melt periods, the infiltration capacity of the frozen soil depends to a large extent on the available air-filled porosity. Surface runoff, lateral subsurface runoff (from saturated soil layers), as well as deep percolation are examples of resulting outputs from the simulation. The model package is freely available at http://www.lwr.kth.se/english/OurSoftWare/.

The model was applied in the area of Grächen to five different elevation zones ranging from 1600 m to 2600 m. In a first step, we used the field experiment at Hannigalp (2100 m) to calibrate and validate the soil/snow thermal and hydraulic parameters in COUP. The second step consisted of extrapolating the meteorological data, assuming a mean air temperature gradient of -0.88°C/100 m (average winter gradient between Grächen and Hannigalp), an altitudinal variation in the radiation of 1.1 Wm^{-2}/100 m (Marty 2001), and, from adjacent meteorological stations, a precipitation

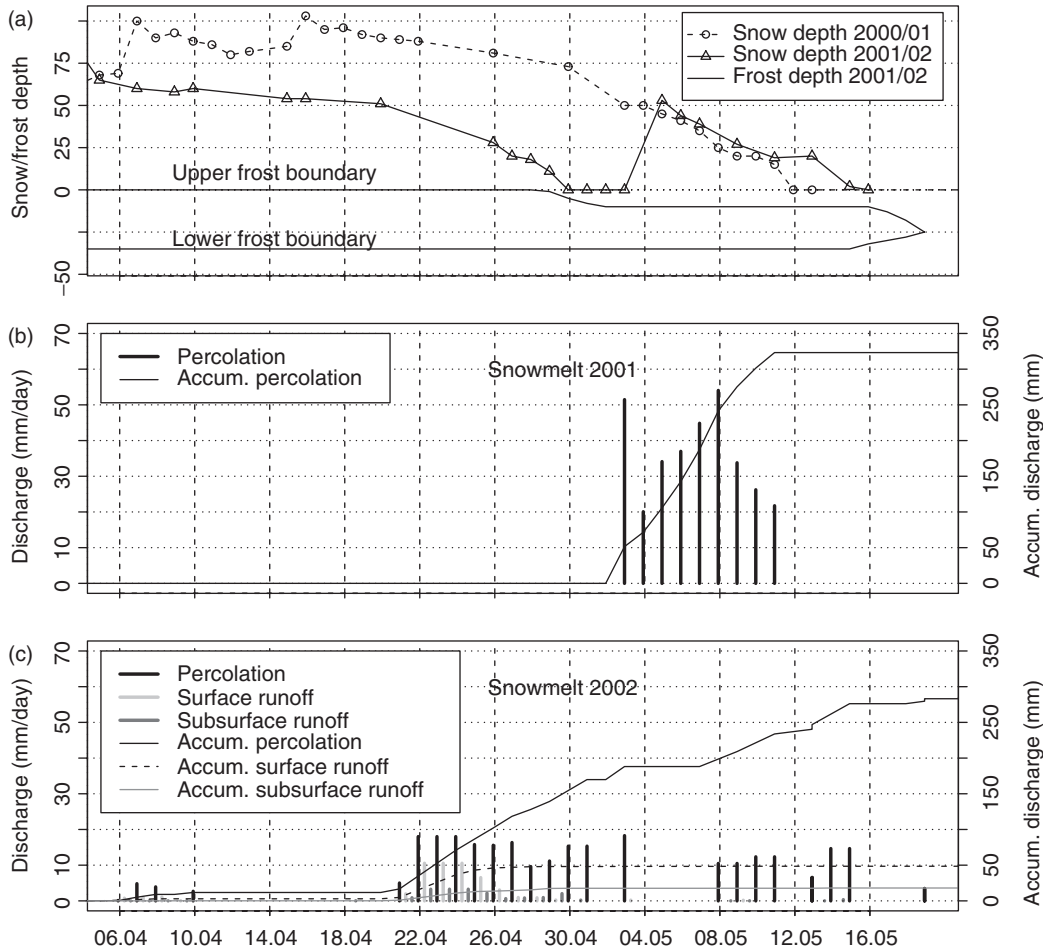


Figure 7.6 Snow and frost depth (a), measured deep percolation, surface runoff and subsurface runoff (daily discharge and total accumulation) for spring 2001 (b) and 2002 (c) at Hannigalp

increase of 2%/100 m. Finally, the simulated snow and frost depths were compared with the water-table rise in spring measured at Grächen.

7.3 SELECTED RESULTS FROM THE TWO-YEAR FIELD EXPERIMENT

7.3.1 Discharge measurements at Hannigalp

The two studied winters had very different weather conditions. Winter 2000/01 was characterized by early snow (60 cm were measured at Hannigalp on 1st November) and a thick snowpack. As a result, the soil remained unfrozen until the end of the snowmelt period. The next winter, a deep and persistent soil frost built up. In late autumn 2001, cold air temperatures (average of −13°C in December) were recorded. As the snow cover was shallow (5 cm in November and December), the soil froze to a depth of 50 cm (Figure 7.6). At the end of the snowmelt, the frozen layer thawed only slowly so that the ground was still frozen to a depth of 45 cm on 15 May.

Discharge was influenced by the physical state of the soil. Under unfrozen conditions, the soil infiltration capacity was high, and the meltwater infiltrated entirely into the ground. As a result, no lateral flow[1] was recorded in spring 2001 (Figure 7.6). Under frozen conditions, a significant amount of meltwater was collected as surface and subsurface runoff. The soil infiltration capacity was

[1] In this text, the term *lateral flow* refers to both surface and subsurface runoff

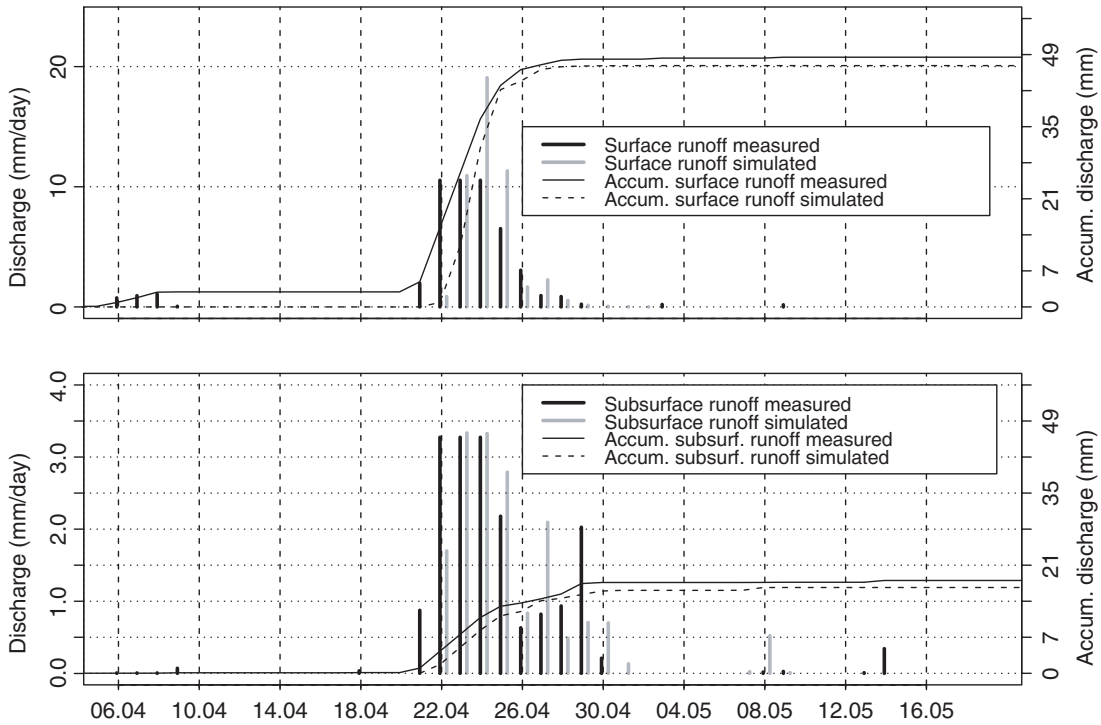


Figure 7.7 Simulated and measured subsurface runoff and surface runoff (daily fluxes and total accumulation) for spring 2002 at Hannigalp

reduced by the pore ice and the presence of a basal ice sheet. This ice sheet built up in March 2002 when a first snowmelt event wetted the whole snowpack. During the main snowmelt, at the end of April 2002, approximately 30% of the total meltwater ran off as lateral flow. When no basal ice sheet was present, the snowmelt discharge was only marginally influenced by the soil frost. This was observed after the massive snowfall (54 cm) in May 2002, which recovered an already bare soil (i.e. no basal ice), the meltwater infiltrated entirely into the ground, despite the fact that the soil was still frozen below a depth of 10 cm.

At Gd St Bernard, the discharge patterns showed a similar behavior in both years. However, because of the steeper slope and to the more intense snowmelt (southerly exposure), a larger portion of meltwater ran off as surface flow. In total, 10% of the meltwater ran off as lateral flow during the first unfrozen winter, whereas this proportion increased to 40% vol. during the frozen winter 2001–02. Similarly to Hannigalp, the presence of a basal ice sheet was the main reason for the increase in the surface runoff.

The COUP-model accurately reproduced the timing and intensity of the surface and subsurface discharge during the main snowmelt event in spring 2002 (Figure 7.7). However, no discharge from the snowpack was simulated during the first snowmelt event in early April 2002, resulting in a slight shift (one day) in the lateral flow during the final snowmelt. At the onset of the final melt period, the simulated soil was still too dry compared to the measurements, and therefore all meltwater was able to infiltrate into the ground. Consequently, in a second run the soil infiltration capacity was reduced to account for the presence of basal ice, which steadily increased the surface runoff.

7.3.2 Dye tracer experiment

In this section, the observations from the dye tracer experiment at Hannigalp are summarized. The stained water flow paths observed in most of the excavated profiles showed a pronounced heterogeneous pattern. Distinct preferential flow fingers formed at the soil surface and led down to the somewhat coarser soil layer at 40–80 cm, just above the bedrock, where the water was able to spread. According to our observations, the hydrophobic soil surface, small ant channels and plant

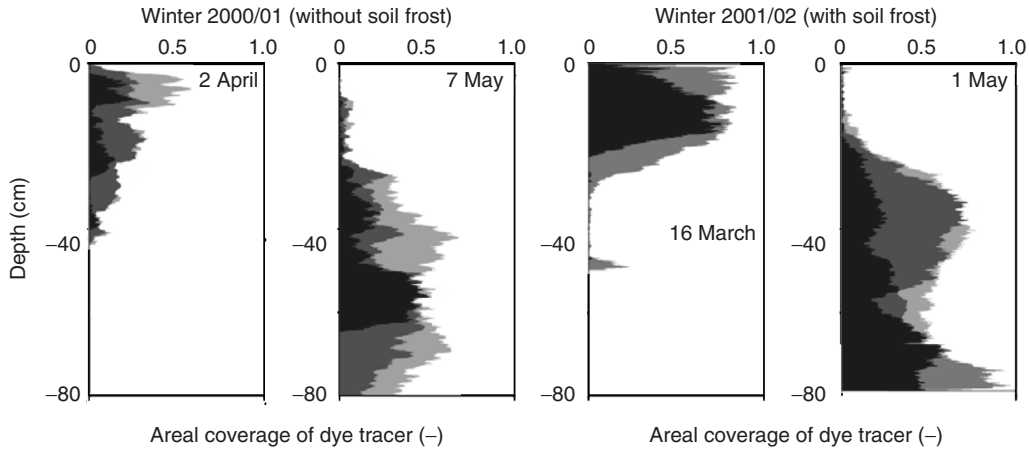


Figure 7.8 Depth profiles of areal coverage of pixels stained with dye tracer for all profiles excavated on two dates of spring 2001 and 2002 at Hannigalp: one date shortly after the start, and the other during the final phase of the snowmelt. Consecutive profiles from the same date superimposed on each other

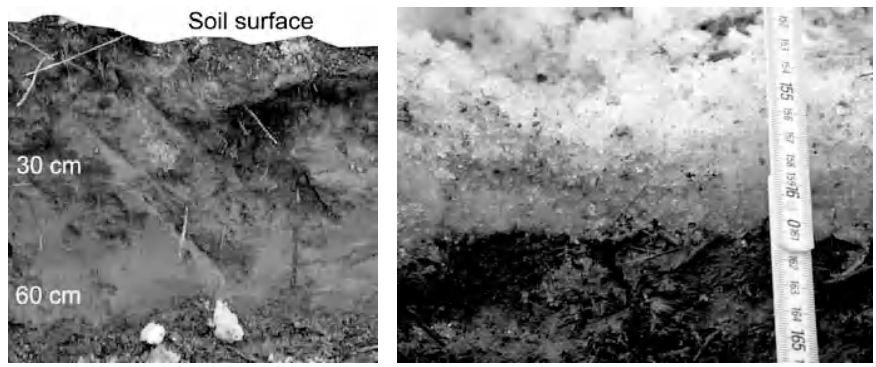


Figure 7.9 (a) Image of a soil profile excavated on March 16, 2002, showing the infiltrated meltwater concentrated in the uppermost 25 cm above frozen soil. (b) During spring 2002, a thin ice layer formed on the soil surface because of melting and refreezing

roots were main generators of the preferential water flow. Not more than 50% of the uppermost soil layers were pervaded in the winter 2000/01 (Figure 7.8). During that first winter (without soil frost), we did not notice indications for impeded water flow at any depth. Toward the end of the snowmelt, the stained infiltration front penetrated further down in the profile.

In the second winter (with massive soil frost down to a depth of 50 cm), the first snowmelt produced a slightly different infiltration pattern: the stained water concentrated in the top 25 cm, impeded by the underlying frozen soil layer (Figure 7.9). However, in the course of the spring, the stained water percolated downward although the soil frost persisted to the end of the snowmelt. In a similar fashion to the previous year, preferential flow paths formed in the upper part of the profile and spread in the coarser subsoil material. Although the stained profiles clearly showed considerable infiltration and percolation through the frozen soil, we also discovered considerable amounts of stained water 10 to 20 m downslope of the experimental site originating from lateral surface runoff. A closer examination confirmed that the thin ice layer on the soil surface (cf. previous section) had triggered that surface runoff. With our tracer experiment, we were able to confirm this layer in spite of its relatively thin (<5 cm) extent (Figure 7.9).

To sum up, an impeding effect of the frozen soil was observed only during the first phase of the snowmelt. For the specific soil at Hannigalp, nevertheless, most of the meltwater was able to infiltrate into the frozen soil. More impeding than the frozen soil itself was the basal ice layer that built up on the surface.

7.4 LARGER-SCALE EFFECT OF SEASONAL SOIL FROST ON THE AQUIFER RECHARGE AT SNOWMELT

With the calibrated COUP-model, we simulated a period of 30 years for each elevation zone. The simulated snow depth at 1600 m was compared to the measured one at Grächen (Figure 7.10). The snow depth was mostly satisfactorily reproduced by the model (coefficient of determination $R^2 = 0.84$). In particular, onset and end of the snow period were well timed. The main differences were observed in January and February, when the snow depth was mostly underestimated by the model. Reasons for this error are twofold. On the one hand, the applied daily resolution in the meteorological inputs underestimates the snowmelt, because of the smoothing of the temperature gradient between the atmosphere and the snow during the daytime. On the other, the solar radiation at Grächen, which was not directly measured but estimated from the cloud cover, may have been underestimated in winter, because of the complex mountain topography, and the relatively low position of the sun in the sky at that latitude.

On the basis of these model simulations, we classified each winter as ''frozen'' (considerable soil frost during the snowmelt in >80% of the area), ''partially frozen'' or ''unfrozen'' (no soil frost during the snowmelt in >80% of the area). Since the beginning of the water table elevation measurements in 1992, three winters were ''frozen'' (1996 = winter 1995/96, 1998 and 2002), five winters ''unfrozen'' (1993, 1995, 1997, 2000, 2001), and two winters ''partially frozen'' (1994, 1999).

For each winter, we compared the water-table rise during the snowmelt with the accumulated winter precipitation (expressed as the areal average snow water equivalent at the start of the snowmelt) (Figure 7.11). The large water-table rise of 8 to 12 m normally starting in April and finishing by the end of June may be regarded as an indicator of aquifer recharge, neglecting any effect induced by the geology or the topography on the recharge.

The rise was lowest for the three ''frozen'' winters (less than 8 m). These winters were characterized by a shallow snowpack during the whole winter, resulting in a deep soil frost at each altitudinal zone. For the ''unfrozen'' winters, the rise was considerable (>10 m), even when comparatively little winter precipitation was recorded, as in winter 1996/97. Especially interesting is the comparison between the two ''extreme'' winters 1997 and 2002. They were characterized by contrasting precipitation distribution, explaining the differences in the thermal soil state at snowmelt. In 1997, an early and thick snowpack prevented the soil from freezing in November and December, whereas the precipitation between January and May remained far below average.

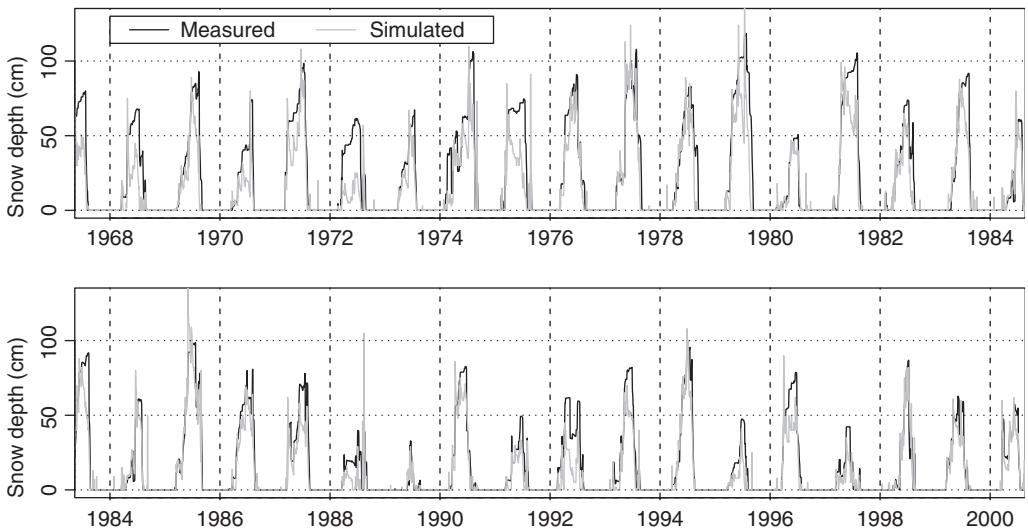


Figure 7.10 Measured and simulated snow depth at Grächen (1600 m) for the period 1968 to 2000

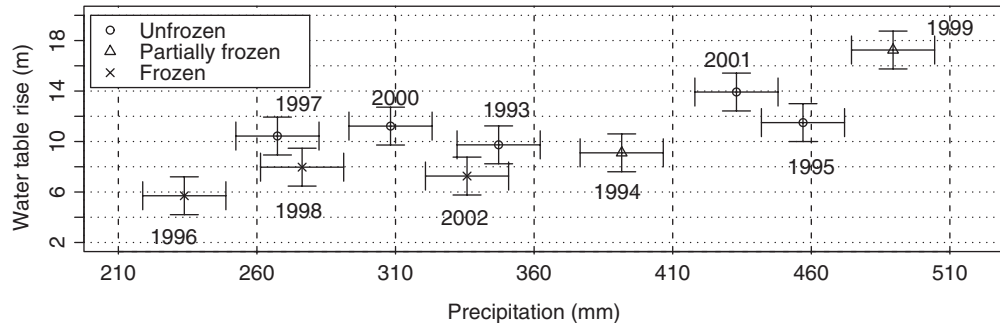


Figure 7.11 Water-table rise during the snowmelt at Grächen versus winter precipitation (i.e areal average snow water equivalent at the start of the snowmelt) shown for each spring from 1993 to 2002

On the other hand, the relatively high amount of winter precipitation in 2002 was mainly caused by a large snowfall in May 2002, when more than 130 mm of precipitation fell within four days. Despite significant differences in the winter precipitation, the water-table rise was 31% lower during the frozen winter 2002 than during the unfrozen winter 1997. Such a result may indicate that a partly frozen soil influences the snowmelt discharge over large areas. However, this interpretation should be viewed with caution because, on the one hand, little is known about the hydraulic behavior of the catchment, and, on the other, the error in the winter precipitation is large, because of the strong local variability in the precipitation.

The two ''partially frozen'' winters 1994 and 1999 illustrate the difficulty in accurately modeling the frost depth aerial extension when, at the onset of the winter, large variation in the snow depth exists. Indeed, despite a similar frost extension (the two lowest zones, between 1600 and 2000 m, were simulated as frozen, and the higher areas as unfrozen) both winters were characterized by contrasting effects on the water-table rise. In spring 1994, the rise was less than 10 m despite considerable snowfall, in contrast to spring 1999, when it was greatest (17.25 m).

7.5 DISCUSSION AND CONCLUSIONS

The results from Hannigalp and Gd St Bernard corroborate the very sensitive relation between snow cover and soil frost. A shallow snowpack enables the ground to freeze deeply, whereas a thick snowpack may insulate the ground preventing soil frost – even at such high altitudes. From the simulation results, we noted that the occurrence of frost on the two experimental fields was sporadic and depended on the late autumnal and early winter weather conditions. So it is not surprising that during the last 10 years, a deep soil frost was encountered during three winters only at Hannigalp.

A frozen soil may influence the snowmelt discharge pattern considerably, as shown by the dye tracer experiment and the plot discharge measurements. Under frozen soil conditions, the penetration of the infiltrating wetting front was delayed, compared to unfrozen conditions. With regard to the lateral runoff, an increase from nil (unfrozen winters) to approximately 35% (frozen winters) of the total meltwater was observed. This drastic change was mainly caused by the presence of a sheet of ice at the base of the snowpack. When this basal ice layer had disappeared, most meltwater infiltrated into the ground, as shown by the late snowmelt event in May 2002 at Hannigalp. We believe that the formation of the basal ice sheet is favored by the rather cold mean soil temperature, the long snow cover period and the early snowmelt events, as the snow cover period is long enough to allow a substantial latent heat transfer between the wet basal snowpack and the upper frozen soil boundary. However, further investigations on the formation of basal ice-layers are needed. In sub-alpine areas, where the snow cover periods are shorter and snowmelt more intense, the presence of a basal ice sheet seems to be rare. In such areas, the soil ice content, as well as refreezing of snowmelt in the soil pores are the major factors that influence the amount of lateral runoff (Stadler *et al*. 1996).

During the main snowmelt period, we observed that a part of the recorded surface water infiltrated the soil some 100 m below the experimental plot where the soil was already free of snow and unfrozen. Such a result demonstrates the importance of the soil texture, structure and steepness, as well as the underlying geological structure on the amount of surface runoff. Although the soil texture was similar at both experimental sites, considerably more lateral runoff was measured at Gd St

Bernard, as the experimental plot was located on a much steeper slope than at Hannigalp.

Finally, in Grächen we noted the water-table rise at snowmelt was reduced by 10–30% during frozen winters. This decrease is less marked than the groundwater recharge at Hannigalp, where, from simulation results, the deep seepage diminished between 20 and 50% of the total meltwater during frozen winters. The very permeable soil allowed most meltwater to re-infiltrate the soil in lower areas where frost was absent. These results support other studies showing that the effect of seasonal frost on the water circulation diminishes with increasing areal extension of the studied field (Thorne *et al*. 1998; Cherkauer and Lettenmaier 1999).

The following statements sum up our experiments and simulations.

- For the development or absence of soil frost both thickness and timing of the snow cover are decisive.
- Surface runoff depends largely on the presence of an ice layer at the base of the snowpack and the amount of soil moisture at the onset of the winter.
- A frozen soil considerably influences the discharge during snowmelt periods at the local scale.
- At larger scales, however, a considerable portion of meltwater is able to infiltrate the unfrozen ground somewhere downslope, due to spatial variability of the soil frost, of the hydraulic soil properties and of the steepness of the slope.
- In very permeable soil, soil frost reduces the water-table rise in spring only marginally.

Generalizing these results, we conclude that despite a massive snow cover, deep soil frost forms during specific winters at these altitudes, influencing the degree of groundwater recharge. A change in the discharge patterns due to seasonal frost may have relevant implications for the general water circulation, particularly with respect to flooding. During rain on snow events, the soil infiltration capacity is further reduced by the presence of frost. It results in an acceleration of the outflow from the snowpack, which in turn increases the amount of surface runoff, hence potentially increasing the risk for flooding.

REFERENCES

Burt TP, Williams PJ (1976) Hydraulic conductivity in frozen soils. *Earth Surf Proc* **1**: 349–360.

Cherkauer KA, Lettenmaier DP (1999) Hydrologic effects of frozen soils in the upper Mississippi River basin. *J Geophys Res* **104**(D16): 19,599–19,610.

De Gaetano AT, Wilks, SS, McKay M (1996) A physically based model of soil freezing in humid climates using air temperatures and snow cover data. *J Appl Meteorol*, **35**: 1009–1027.

Flerchinger GN, Saxton KE (1989) Simultaneous heat and water model of a freezing snow-residue-soil system I. Theory and development. *Trans ASAE* **32**(2): 565–571.

Forrer I, Papritz A, Kasteel R, Flühler H, Luca D (2000) Quantifying dye tracers in soil profiles by image processing. *Eur J Soil Sci* **51**(2): 313–322.

Harlan, RL (1973) Analysis of coupled heat-fluid transport in partially frozen soil. *Water Resour Res* **9**: 1314–1323.

Ippisch O (2001) Coupled transport in natural porous media. Dissertation, University of Heidelberg, Germany, p. 145.

Jansson P-E, Halldin S (1979) Model for the annual water and heat flow in a layered soil. In: Halldin S (ed) *Comparison of Forest and Energy Exchange Models*. International Society for Ecological Modelling, Copenhagen, pp. 145–163.

Jansson P-E, Karlberg L (2001) Coupled heat and mass transfer model for soil-plant-atmosphere systems. TRITA-AMI Report 30 87, ISSN 1400-1306, KTH Stockholm, Sweden.

Johnsson H, Lundin L-C (1991) Surface runoff and soil water percolation as affected by snow and soil frost. *J Hydrol* **122**: 141–159.

Koren VI, Duan QI, Schaake JC (1995) Modeling of the effect of frozen ground on snowmelt/rainfall processes. International GEWEX workshop on cold season/region hydrometeorology. Banff, Alberta, pp. 78–82.

Marty C (2001) Surface radiation, cloud forcing and greenhouse effect in the Alps. Dissertation, ETHZ Institute for Climate Research, p. 122.

Seyfried MS, Murdock MD (1997) Use of air permeability to estimate infiltrability of frozen soil. *J Hydrol* **202**: 95–107.

Shanley JB, Chalmers A (1998) The effect of frozen soil on snowmelt runoff at sleepers river, *Vermont Hydrol Process* **13**: 1843–1857.

Stadler D, Bründl M, Wunderli H, Auckenthaler A, Flühler H (1996) Field measurements of water transport in frozen soils. *Hydrol Process* **10**(10): 1293–1304.

Stadler D, Stähli M, Aeby P, Flühler H (2000) Dye tracing and image analysis for quantifying water infiltration into frozen soils. *Soil Sci Soc Am J* **64**: 505–516.

Stähli M, Bayard D, Wydler H, Flühler H (2004) Snowmelt infiltration into alpine soils visualized by dye tracer technique. *Arct Antarct Alp Res* **36**(1): 128–135.

Stähli M, Jansson P-E, Lundin L-C (1999) Soil moisture redistribution and infiltration in frozen sandy soils. *Water Resour Res* **35**: 95–103.

Stähli M, Nyberg L, Mellander P-E, Jansson P-E, Bishop KH (2001) Soil frost effects on soil water and runoff dynamics along a boreal transect: 2. Simulations. *Hydrol Process* **15**: 927–941.

Thorne GA, Laporte J, Clarke D (1998) The effect of frozen soils on groundwater recharge and discharge in Granitic rock terrane of the Canadian shield. *Nord Hydrol* **29**: 371–384.

8

Water Balance in Surface Soil: Analytical Solutions of Flow Equations and Measurements in the Alpine Toce Valley

MARILENA MENZIANI[1], SERGIO PUGNAGHI[1], SERGIO VINCENZI[2] AND RENATO SANTANGELO[1]

[1]Dipartimento di Ingegneria dei Materiali e dell'Ambiente – Osservatorio Geofisico, Università di Modena e Reggio Emilia, Via Vignolese 905, 41100 Modena, Italy, [2]ISMAR, Grandi Masse, CNR, S. Polo 1364, 30125 Venezia, Italy

8.1 INTRODUCTION

Hydrological models are based on the efficient and robust description of the different aspects of the hydrological cycle achieved by the parameterisation of the major pathways in this cycle: precipitation and evaporation (Brutsaert 1991). While rainfall data are, almost everywhere, easily available, evaporation measurements are still rare. However, on a global basis, evaporation is a component of the hydrological cycle almost as important as precipitation. In fact, continental precipitation is of the order of 0.80 m/y, and evaporation amounts to, roughly, 0.50 m/y (Brutsaert 1991). The surface soil moisture and the exchange of heat and moisture between the land surface and the atmosphere are of great importance in different fields like hydrology, meteorology and agriculture. The knowledge of the state of saturation of a soil and its spatial and temporal trends is a key factor to improve hydrological models (flood forecast) and meteorological numerical weather prediction (NWP) models. In fact, the atmosphere and the underlying land surfaces represent a heavily coupled system (Eagleson 1978; Brubaker and Entekhabi 1995; Brubaker and Entekhabi 1996). The evaporation process consists of two main consecutive stages. In the first stage, when the soil is wet and conductive enough to supply water at a rate commensurate with the evaporative demand, the evaporation rate is limited by external meteorological conditions (atmosphere limited stage). During the second stage of evaporation, the evaporation rate is limited by the rate at which the soil can deliver moisture towards the evaporation zone (soil limited stage; Hillel 1980b). Furthermore, the soil water content and other soil properties determine the runoff production in response to atmospheric precipitation. Nowadays, the capacity of meteorological models to provide accurate quantitative rainfall forecasts at the scale of flood-prone basins remains rather limited, especially for small mountain catchments in the Mediterranean regions. The lead times necessary to save property, and sometimes lives, imply that forecasters cannot rely only on observed rainfall. Obled and Djerboua (2000) suggest that to foresee much beyond the response time of the catchment (few hours), accurate models, knowledge of soil characteristics and hydrological observations are requested.

These aspects were the main scientific objectives concerning the hydrological tasks of the MAP programme. The MAP-hydrology research activities also

Climate and Hydrology in Mountain Areas. Edited by C. de Jong, D. Collins and R. Ranzi
© 2005 John Wiley & Sons, Ltd. ISBN: 0-470-85814-1

aimed to improve the understanding of orographically influenced precipitation events and related flooding episodes and to improve the numerical prediction of moist processes in regions with complex topography, including interactions with land-surface processes (Binder 1996). The Lago Maggiore and, in particular, the Ticino–Toce watershed (CH-I) was one of the test sites of the MAP Special Observing Period (SOP; Binder and Schar 1996). The climatology of the southern slope of the Alps clearly shows distinct local precipitation maxima (Bougeault *et al*. 1998), and one of these, both for precipitation amounts and for frequency of heavy precipitation, occurs in the Lago Maggiore area (Canton Ticino – Northern part of the Piedmont region). The MAP-SOP (7 September–15 November 1999) was a very large experimental effort over the Alps mountain range, during which several Italian teams (Hydrology Working Group and Planetary Boundary Layer Working Group) operated jointly in the Lago Maggiore target area.

In the first part of this chapter, a user-friendly algorithm is presented to evaluate the water mass balance at the soil surface. The mass balance is obtained by means of soil moisture measurements at different depths. The soil moisture is measured by means of time domain reflectometry (TDR), which is a relatively new technique based on measuring the apparent dielectric constant of the soil. The apparent dielectric constant is related to the propagation velocity of an electromagnetic pulse travelling in the soil. The relationship between the dielectric constant and the soil volumetric water content is described by Topp *et al*. (1980) and Ledieu *et al*. (1986), among others, in an empirical fashion using both polynomial and linear forms. The algorithm to estimate the water mass balance at the surface was applied to the soil moisture data collected at a hydrological station installed in a wide meadow located between the mountain slope and the Toce River. A short drought period (in July) and the major precipitation event (IOP-02, in September) may be seen in the soil moisture data set measured in this Alpine Valley.

In the second part of the chapter, the Richards equation is taken into account. Numerical solutions of partial differential equations can be obtained using different finite-difference and finite-element approximations. Nevertheless, analytical solutions are of great interest because they allow insight into the physics of the processes. Here, two different approaches to obtain exact solutions of the Richards equation are presented. One is used to solve the non-linear equation in which the gravity term is neglected (diffusion equation); the other allows to derive solutions to the linearized Richards equation. The solution of the non-linear one-dimensional equation is based on the method suggested by Philip (1960). This method allows obtaining the soil water content evolution if the hydraulic diffusivity is known; vice versa it will give the diffusivity if the soil water content is known. This procedure can be used to create a table of hydraulic diffusivity functions on the basis of the experimental data features. During drying periods, the soil moisture vertical profile may present an inflection point; however, this kind of solution cannot be obtained if the hydraulic diffusivity is a monotonic increasing function of the soil volumetric water content. Another characteristic of all the solutions obtained using this method is that the cumulative evaporation is always proportional to the square root of the time. The second method is based on the linearised Richards equation. With this approximation, arbitrary initial and boundary conditions can be assumed obtaining valid solutions that represent the experimental data both during infiltration and evaporation periods. The solutions of the linearised Richards equation may be derived also using input fluxes at the surface (Warrick 1975; Basha 1999; Chen *et al*. 2001).

8.2 STUDY SITE

The research field site was located in a wide meadow in front of the hydropower plant of Pallanzeno (Long. 8.260°E, Lat. 46.047°N), in the Toce River valley, which is a classical glacial basin located in the North Piedmont (Italy), see Table 8.1 (Ranzi *et al*. 2003) and Figure 8.1. This test site is at 250 m (a.s.l.) and is located between the

Table 8.1 Basin characteristics

Basin	Toce at Candoglia
Name of the area	Val d'Ossola
Mountain range	Northern Italian Alps
Elevation range of the basin (m a.s.l.)	196–4633
Elevation range of experimental sites (m a.s.l.)	199–1770
Latitude	45°54′–46°28′N
Longitude	7°52′–8°29′E
Area (km^2)	1532
Geology	Metamorphic
Glaciers and permanent snow (%)	2
Dominant vegetation type	Deciduous and coniferous forests
Forests (%)	70
Mean runoff at catchment outlet (mm)	1382
Mean precipitation (mm)	1557

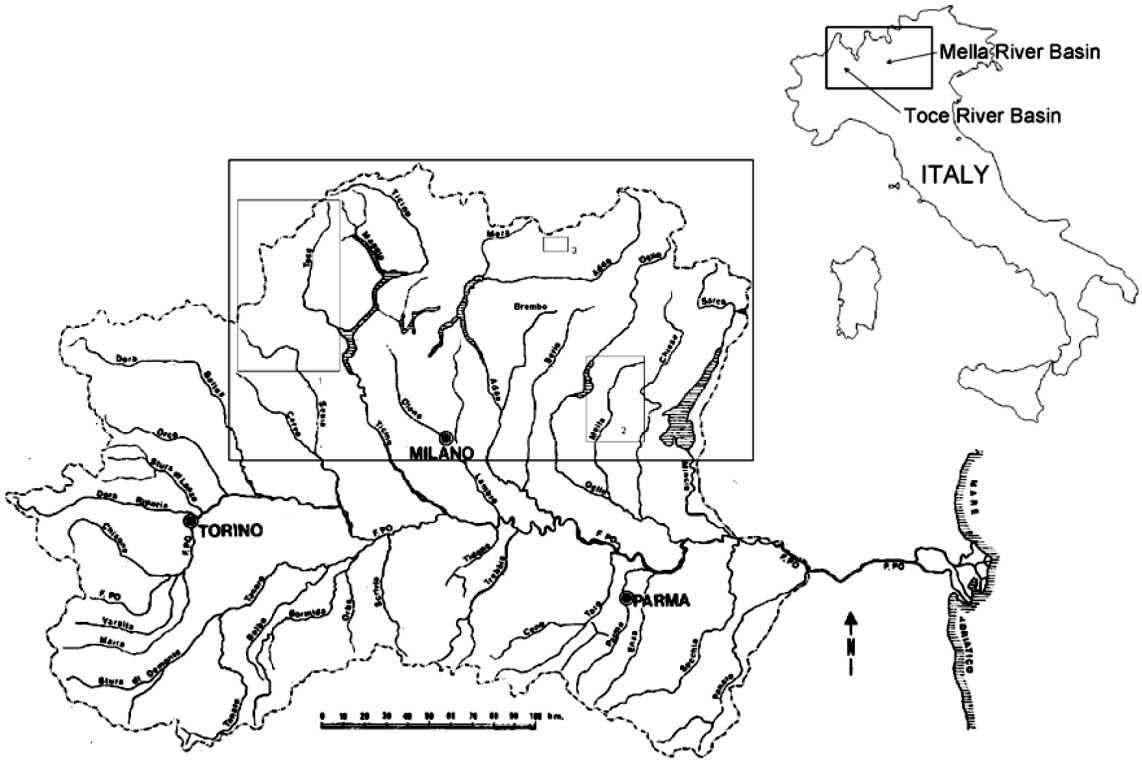


Figure 8.1 General map of Italy and detailed map of the Po basin. The study area (Toce River Basin) is located in the small rectangular frame on the left

mountain slope and the Toce River (about 300 m away). The grass of the meadow was regularly cut so the grass height varied from 10 to 30 cm.

An automatic station was set up installing 15 buriable probes connected to a TDR system (Soilmoisture Equipment Corporation 2000) by a multiplexer. Twelve probes were installed horizontally at the following depths [cm]: 5, 7.5, 10, 12.5, 15, 20, 25, 30, 35, 40, 47 and 50. Three probes were installed vertically to measure the mean soil moisture of three successive soil layers: 0–20, 25–45 and 50–70 cm. The measurements were collected automatically (at a time step of 4 h) starting at the end of March and ending on November 15, 1999 (end of the MAP-SOP). Air temperature and precipitation data were available from the station at the hydropower plant.

According to the USDA soil texture classification, the first 40 cm of soil of the study site (Pallanzeno) is a silty loam poor in organic matter. Three soil samples were collected at three different depths. The upper depth (0–10 cm) had a higher percentage of clay compared to the two lower depths while the soil organic matter content decreases as usual from the surface to the deep layers (see Table 8.2). In Table 8.3, two different values (*in situ* and in laboratory) of the hydraulic conductivity at the saturation (K_s) are reported; the superficial layer (0–14 cm) was measured in laboratory while the value for the deeper layer was obtained by means of an *in situ* infiltration test. The real value of K_s is expected to be between the two measured values reported in Table 8.3. Because of the difficulties related to the *in situ* test, the value of the saturated hydraulic conductivity (K_s) is, most likely, closer to the laboratory value (Falappi *et al*. 2000). The soil water content at saturation (θ_s) has been assumed to be equal to 92.5% of porosity (Van Genuchten *et al*.

Table 8.2 USDA textural classification

Depth [cm]	Sand [%]	Silt [%]	Clay [%]	Organic matter [g kg^{-1}]
0–10	31.0	56.9	12.1	34
10–20	35.0	62.6	2.4	29
20–40	40.1	57.6	2.3	24

Table 8.3 Soil hydraulic characteristics

Parameter	Value
K_s (laboratory)	2.26 10^{-7} [m s^{-1}]
K_s (*in situ*)	1.89 10^{-4} [m s^{-1}]
Φ (porosity)	0.61
$\theta_s = 0.925\Phi$	0.562
θ_{max} (measured)	56 [%]

1991); this value equals the maximum soil water content measured at Pallanzeno during the IOP-02. The porosity and the soil water content at saturation values are also reported in Table 8.3. The soil analyses and the water retention curves have been carried out by the research unit of the University of Brescia and Istituto Agrario di San Michele all'Adige (Falappi *et al*. 2000; Eccel *et al*. 2000).

The soil moisture characteristic curve and the unsaturated hydraulic conductivity can be described respectively by the following power functions (Campbell 1985).

$$\psi = \psi_s \left(\frac{\theta}{\theta_s}\right)^{-b} \qquad K = K_s \left(\frac{\theta}{\theta_s}\right)^{2b+3}, \tag{8.1}$$

where θ is the soil water content; ψ_s is the air entry potential; K_s is the saturated hydraulic conductivity of the soil. ψ_s and b are the offset and the slope of the log–log water retention curve. From the soil samples collected at Pallanzeno, three water retention curves were obtained for the three different layers described in Table 8.2 (see Figure 8.2). The values of ψ_s and b for the three soil layers are reported in Table 8.4.

In Figure 8.3, the mean daily values of the soil volumetric water content measured at 5, 15, 25, 40 cm depth during the experiment are reported. The daily precipitation amounts are shown in the same plot. The month of April 1999 was characterised by only one heavy precipitation event (59.2 mm on April 15–16). During the first 14 days of the month, the soil showed a drying trend. The heavy precipitation event produced a fast rise of the soil moisture at all the measured depths. Because of an instrumental failure, no readings were available in May. From June to the end of July, the soil moisture maintained a general decreasing trend (neglecting the days after the precipitation events). On July 27, the most superficial layer (horizontal probe at 5 cm) reached the minimum measured soil

Table 8.4 Parameters obtained from the water retention curves

Depth [cm]	Air entry potential ψ_s [m]	b [−]
0–10	−0.33	4.2
10–20	−0.14	4.3
20–40	−0.07	4.6

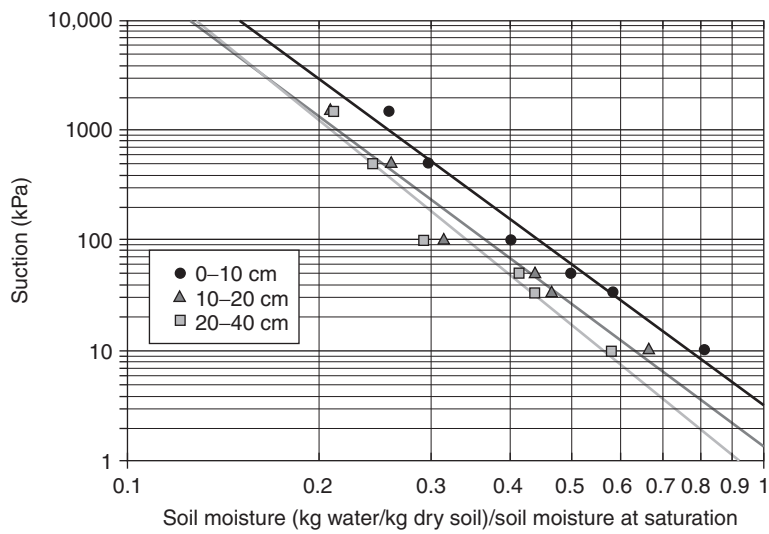


Figure 8.2 Water retention curves for the three different layers 0–10, 10–20, 20–40 cm of soil sampled at Pallanzeno. The offset and the slope give the air entry potential ψ_s and the exponent b of power functions (8.1) respectively

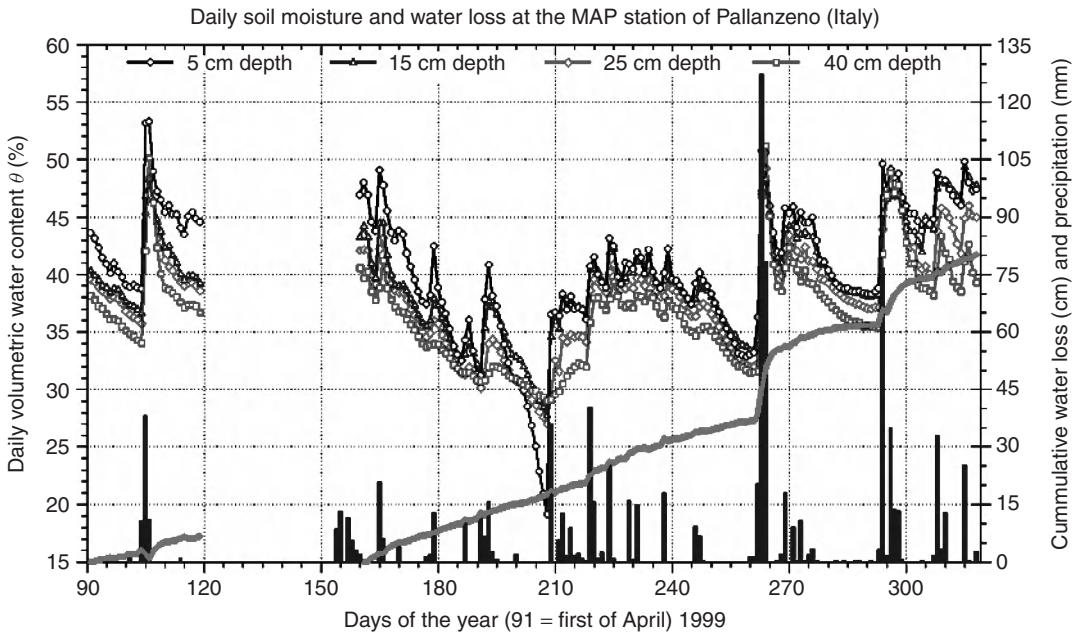


Figure 8.3 The trend of the daily mean of the soil water content θ of the whole period of measurement is shown. The data of the probes at 5 cm (circle), 15 cm (triangle), 25 cm (diamond) and 40 cm (square) are reported. The vertical bars are the daily cumulative precipitation values. The thick solid line represents the cumulative evaporation

volumetric water content value: 17.7% (not evident in Figure 8.3 because of the average effect). August was quite rainy, and the soil moisture remained almost constant; a new minimum was reached on September 17. On 19–21 of September (MAP-IOP-02), a total precipitation of 225.4 mm produced the maximum soil moisture value measured: 56.0% (probe at 5 cm; not evident in Figure 8.3 because of the average effect); this value represents the saturation of the soil investigated. October showed a new decreasing trend in the soil water content until a new precipitation event (76.4 mm) on October 21 (MAP-IOP-08). Afterwards, the soil moisture maintained high values at all depths until the end of the measurement period.

A diurnal cycle is present in the TDR soil moisture experimental data at all depths (Menziani *et al*. 2000). This cycle does not represent a cycle in the soil water content, but it results from the daily cycle of temperature. Temperature affects the TDR data in two different ways: dielectric constant of the soil (Roth *et al*. 1990; Pepin *et al*. 1995) and the behaviour of the electronics of the instrument. Nevertheless, the amplitude of this daily cycle is lower than the instrumental accuracy (±2%) and therefore does not affect our ability to use the data.

8.3 TDR TECHNIQUE

The soil water content measurements performed at Pallanzeno utilised the TDR technique. TDR was originally developed by the telecommunications industry to localise breaks, short circuits and the presence of water in buried coaxial cable. With TDR, for example, a break is located by applying a fast-rise electrical pulse at the free end of the cable and then measuring the time it takes for a signal to travel to and reflect back from the point of disruption. Topp *et al*. (1980) altered this technique by applying the electrical pulse to probes inserted into the earth. The pulse shape and the transit time along the probes depend on the properties of the soil, on the probe length and on the type of termination where the pulse is reflected. The reflection depends on the equivalent load impedance of the circuit; in TDR measurements, the lines are usually open and this produces a reflected pulse in phase with the incoming pulse. The velocity of the pulse, propagating down the probe, reflected at the end and running back to its source is:

$$v = \frac{c}{\sqrt{\varepsilon_r \cdot \mu_r}} \tag{8.2}$$

where v is the velocity of the electromagnetic wave in the transmission lines embedded in the medium; c is the

velocity of the electromagnetic wave in the void; ε_r and μ_r are the relative dielectric permittivity and the relative magnetic permeability, respectively.

Because of the large difference between the dielectric constant of water and the other constituents of the soil (e.g. air, mineral particles), the speed of a voltage pulse in parallel transmission buried lines is essentially dependent on the volumetric water content of the soil (Topp *et al*. 1980). Because virtually all soils lack ferromagnetic materials, μ_r can be assumed equal to the unit. Therefore, inserting in the soil a probe of known length, the *apparent dielectric constant* K_a is:

$$K_a = \left(\frac{c \cdot \Delta t}{L}\right)^2 \tag{8.3}$$

where Δt is the time required to the signal to reach the end of the wave-guide (travel time) and L is the wave-guide length.

K_a is so termed because the imaginary part of the complex permittivity is negligible with respect to the real part at the usual frequencies 10 MHz–1 GHz (Dirksen and Dasberg 1993) used for TDR soil moisture measurements; thus, K_a essentially represents the real part. The value of the apparent dielectric constant, given by Equation (8.3) measuring the travel time (Δt) along the wave-guide of length L, is a sort of mean value in the volume around the probe. The travel time can be calculated by analysing the TDR trace. The TDR trace depends on both the type of the wave-guide and on the dielectric (soil) under investigation. In the TDR trace, the start time, at the beginning of the wave-guide, and the reflection time, at the end of the wave-guide, have to be exactly identified. Usually, the start time corresponds to the maximum of the derivative of the incoming pulse TDR trace. The *Soilmoisture* buriable probes present a V dip feature at the beginning of the trace; the bottom of the V corresponds to the start time of the pulse in the wave-guide. The reflection time can be estimated analysing the TDR trace using the method of the tangent lines (see an example in Figure 8.4). This method permits finding the point of reflection of the electromagnetic pulse travelling down the wave-guide (Menziani *et al*. 1996). Soil water content is then calculated from the apparent dielectric constant by means of empirical relationships (Topp *et al*. 1980; Ledieu *et al*. 1986; Roth *et al*. 1990; D'Urso 1992; Heimovaara 1993; Heimovaara and de Water 1993) or experimentally determined Look-Up Tables (LUTs, *Soilmoisture* TRASE system I technical manual 2000). They give similar results but LUTs have a wider volumetric water content range of application. The greatest differences between the *Topp equation* in percentage (8.4) and the *Soilmoisture* LUT are found for values of $\theta > 40\%$ (Menziani *et al*. 2000).

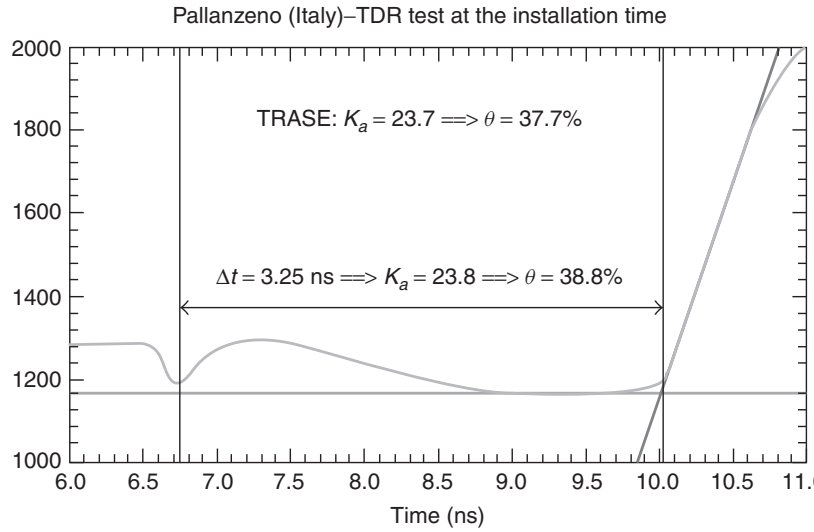


Figure 8.4 Analysis of a TDR trace obtained by a buriable probe installed at the hydrological station of Pallanzeno. The pulse travel time Δt is the difference between the reflection time at the end of the probe and the start time at the beginning of the wave-guide. The reflection time is identified by means of the tangent lines method; the start time is identified by the V dip. K_a is obtained by Equation (8.3) and θ is obtained by the Topp Equation (8.4). The results of the TRASE system (using LUT data) are also reported in the figure

$$\theta = (-530 + 292 \cdot K_a - 5.5 \cdot K_a^2 + 0.043 \cdot K_a^3)/10^2 \tag{8.4}$$

In this work, the *Soilmoisture* LUT for the *buriable* probe was used.

8.4 THE WATER MASS BALANCE

The water vapour flux at the soil–air interface is usually estimated, on the basis of meteorological data, using the surface energy balance method (Bowen ratio) or measuring the turbulent transport (eddy correlation method). Here, the water mass balance at the soil surface is obtained, under simple assumptions, by means of soil moisture measurements at different depths. A simple formula to compute the amount of water added or withdrawn in a given volume of soil, during a certain period, is presented.

The soil water content θ and its flux are related by the conservation equation (Hillel 1980a). Considering a volume element inside a soil column of unitary cross section and depth H_c,

$$\frac{\partial \theta}{\partial t} + \frac{\partial \Phi_z}{\partial z} + (\mathrm{div}_h \Phi_h) = 0 \tag{8.5}$$

where Φ_z is the flux of θ along the vertical direction z (pointing downward), and the last term is the horizontal divergence of the horizontal flux component.

Integrating the above Equation (8.5) with respect to z and t, the following expression is obtained.

$$\begin{aligned} &- L_H(t) + \int_0^t \Phi_z(H_c, t') \cdot \mathrm{d}t' + \int_0^t \int_0^{H_c} \mathrm{div}_h \Phi_h \, \mathrm{d}z' \, \mathrm{d}t' \\ &\quad = \int_0^t [P_i(t') - E_i(t')] \cdot \mathrm{d}t' = P_{\mathrm{cum}}(t) - E_{\mathrm{cum}}(t) \end{aligned} \tag{8.6}$$

$L_H(t)$ is defined as

$$L_H(t) = \int_0^{H_c} [\theta(z', 0) - \theta(z', t)] \cdot \mathrm{d}z' \tag{8.7}$$

Considering only the evaporation (or *evapotranspiration*) process, $L_H(t)$ is the soil–water loss from $t = 0$ up to t; $E_i(t)$ and $P_i(t)$ are the instantaneous evaporation and precipitation, respectively; $E_{\mathrm{cum}}(t)$ and $P_{\mathrm{cum}}(t)$ are the related cumulative functions.

Assuming negligible the horizontal flux and $\Phi_z(H_c, t) = 0$, Equation (8.6) becomes

$$E_{\mathrm{cum}}(t) = L_H(t) + P_{\mathrm{cum}}(t) \tag{8.8}$$

$E_{\mathrm{cum}}(t)$ is expected to be a continuous and increasing monotonic function. Departures from this behaviour denote that some other intervening phenomena have not been considered, or have been underestimated.

Using the daily mean of the soil moisture experimental data, $E_{\mathrm{cum}}(t)$ is obtained by means of Equation (8.8) and shown in Figure 8.3. All the data of the horizontal probes installed at Pallanzeno were taken into account to estimate $E_{\mathrm{cum}}(t)$, therefore the studied soil column is $H_c = 50$ cm height. Because of the lack of data in May, $E_{\mathrm{cum}}(t)$ is represented by two pieces of curve; the first one is for April, and the second is for the data from June to November. The behaviour is essentially monotonic and continuous except for the decrease in April and the steep increases coinciding with the two heavy precipitation events at the end of September and October. The dip in $E_{\mathrm{cum}}(t)$ during the precipitation event in April indicates that the neglected fluxes are significant. The two step-like shape of the $E_{\mathrm{cum}}(t)$ curve in September and October suggest that the total water precipitated is much greater than the increase in the water content of the first 50 cm of soil. The unaccounted loss has to do with bottom drainage and/or surface runoff. During the summer period, the mean daily evaporation is about 4 mm per day, while a lower value (about 2.5 mm per day) has been found in April. The cumulative function $E_{\mathrm{cum}}(t)$ also indicates that the evaporation is mainly atmosphere limited, but periods of soil limited evaporation (Hillel 1980b; Brutsaert and Chen 1995) can be detected (e.g. end of July and before the heavy precipitation of September 20 and October 21).

8.5 ANALYTICAL SOLUTIONS

Unsaturated flow processes have to take into account changes of soil water state and content, during flow. The relationships among the soil water content, matric potential and hydraulic conductivity determine such changes. The solution of these flow problems is often obtained by means of numerical methods or analytically, as shown here, based on approximations. Analytical solutions are of great interest because they allow gaining insight into the physical processes. Two different methods to obtain exact solutions of the flow equation are discussed: one is used to solve the non-linear equation by neglecting gravity term (diffusion equation); the other allows deriving solutions to the linearised moisture flow equation.

Considering one-dimensional flow in the vertical direction z (pointing downward), the Darcy law extended to the unsaturated flow is:

$$\Phi_z = -K(\theta) \cdot \frac{\mathrm{d}H}{\mathrm{d}z} \tag{8.9}$$

where H is the hydraulic head equal to the sum of the matric potential and the gravitational head.

To obtain the general flow equation and account for transient and steady flow processes, the conservation Equation (8.5) in the vertical is introduced to obtain the Richards equation:

$$\frac{\partial\theta}{\partial t} = \frac{\partial}{\partial z}\left[K(\theta)\cdot\left(\frac{\partial\psi}{\partial z}-1\right)\right] = \frac{\partial}{\partial z}\left[D(\theta)\cdot\frac{\partial\theta}{\partial z}\right]-\frac{\partial K(\theta)}{\partial\theta}\cdot\frac{\partial\theta}{\partial z} \tag{8.10}$$

$D(\theta) = K(\theta)\cdot(\partial\psi/\partial\theta)$ is the hydraulic diffusivity, which is usually an increasing function of soil wetness (Hillel 1980a).

8.5.1 Solution of the diffusion equation

Processes may also occur in which the gradient of the gravitational head is negligible compared to the strong matric potential gradient. One of these processes is evaporation. In such cases, the non-linear Equation (8.10) becomes the diffusion equation:

$$\frac{\partial\theta}{\partial t} = \frac{\partial}{\partial z}\left[D(\theta)\cdot\frac{\partial\theta}{\partial z}\right] \tag{8.11}$$

Let us assume:

$$\vartheta = \frac{\theta-\theta_m}{\theta_M-\theta_m} \tag{8.12}$$

where θ_m and θ_M are the minimum and maximum values of the soil volumetric water content during the considered process; during the evaporation process θ_M and θ_m are the initial an final values, respectively. The normalised water content (8.12) ranges between 0 and 1.

It is useful to write $D(\vartheta) = D_0\cdot X(\vartheta)$; where D_0 is a constant with the dimensions of a diffusivity [$m^2\ s^{-1}$] and $X(\vartheta)$ is a dimensionless diffusivity.

If the boundary conditions characterising the problem are

$$\vartheta = 1, z \geq 0, t = 0; \quad \vartheta = 0, z = 0, t > 0 \tag{8.13}$$

Equation (8.11) can be solved analytically introducing a variable $u(z,t)$ and knowing *a priori* one of the two relationships: $X = X(u)$ or $\vartheta = \vartheta(u)$ (Philip 1960). The method described in the following permits obtaining the unknown function ϑ or D setting $u = z/\sqrt{4\cdot D_0\cdot t}$ (Boltzmann transformation; Brutsaert 1982) so that Equation (8.11) reduces to an ordinary differential equation for $\vartheta(u)$:

$$\frac{d}{du}\left[X(u)\cdot\frac{d\vartheta}{du}\right]+2\cdot u\cdot\frac{d\vartheta}{du}=0 \tag{8.14}$$

with the boundary conditions for the variable u: $\vartheta = 0, u = 0; \vartheta = 1, u \to \infty$.

Since the limit of the vertical flux $[-D\cdot(\partial\vartheta/\partial z)]$ is zero as z approaches infinity, the previous Equation (8.14) yields:

$$-X(u)\cdot\frac{d\vartheta}{du}+\int_u^\infty 2\cdot u'\cdot\frac{d\vartheta}{du'}\cdot du' = 0 \tag{8.15}$$

From Equation (8.15), the vertical water flux is:

$$\Phi_z(t) = -\frac{2\cdot D_0}{\sqrt{4\cdot D_0\cdot t}}\cdot\int_u^\infty u'\cdot\frac{d\vartheta}{du'}\cdot du' \tag{8.16}$$

and, at the surface ($z = 0$), becomes:

$$\Phi_0(t) = -\frac{2\cdot D_0}{\sqrt{4\cdot D_0\cdot t}}\cdot\int_0^\infty u'\cdot\frac{d\vartheta}{du'}\cdot du' \tag{8.17}$$

The time integral of the flux at the surface (8.17) yields the cumulative evaporation:

$$E_{cum}(t) = -\sqrt{4\cdot D_0\cdot t}\cdot\int_0^\infty u'\cdot\frac{d\vartheta}{du'}\cdot du' \tag{8.18}$$

The boundary conditions (8.13), which allow the application of the Boltzmann transformation, imply that the vertical flux at the surface is always proportional to $t^{-1/2}$ and, of course, the cumulative evaporation $E_{cum}(t)$ is proportional to the square root of time.

Assuming a known function for the water content $\vartheta(u)$ *a priori*, Equation (8.15) gives the dimensionless diffusivity as a function of the variable u:

$$X(u) = \frac{2\cdot\int_u^\infty u'\cdot\frac{d\vartheta}{du'}\cdot du'}{\frac{d\vartheta}{du}} \tag{8.19}$$

Note that the function $X(u)$ is always positive and that it does not change substituting the function $[1-\vartheta(u)]$ in $\vartheta(u)$; that is, it is capable of treating infiltration instead of evaporation.

Vice versa, assuming the function $X(u)$ *a priori*, the soil water content $\vartheta(u)$ is obtained from Equation (8.14), which can be rewritten as:

$$\frac{d}{du}\left[X(u)\cdot\frac{d\vartheta}{du}\right]+\frac{2\cdot u}{X(u)}\cdot\left[X(u)\cdot\frac{d\vartheta}{du}\right]=0 \tag{8.20}$$

This is a first-order differential linear equation for $\left[X(u)\cdot\frac{d\vartheta}{du}\right]$, which, integrated between 0 and u, gives:

$$X(u)\cdot\frac{d\vartheta(u)}{du} = \left[X(u)\cdot\frac{d\vartheta(u)}{du}\right]_{u=0}\cdot e^{-\int_0^u\frac{2\cdot u'}{X(u')}\cdot du'} = A\cdot e^{-\int_0^u\frac{2\cdot u'}{X(u')}\cdot du'} \tag{8.21}$$

It can be highlighted that the lhs of (8.21) and the constant A are the flux Φ_z and the flux at the surface Φ_0, respectively, both divided by $(-D_0/\sqrt{4 \cdot D_0 \cdot t})$. That is:

$$\Phi_z(u) = \Phi_0 \cdot \mathrm{e}^{-\int_0^u \frac{2 \cdot u'}{X(u')} \cdot \mathrm{d}u'} \tag{8.22}$$

From the previous Equation (8.21), integrating from u to ∞:

$$\vartheta(u) = \vartheta(u \to \infty) - A \cdot \int_u^\infty \frac{\mathrm{e}^{-\int_0^{u''} \frac{2 \cdot u'}{X(u')} \cdot \mathrm{d}u'}}{X(u'')} \cdot \mathrm{d}u'' \tag{8.23}$$

according to the assumed boundary condition: $\vartheta(u \to \infty) = 1$.

This methodology can be used to create a table of functions $D(\vartheta)$ on the basis of the experimental water content data, or vice versa to have a catalogue of possible solutions $\vartheta(z, t)$ on the basis of known hydraulic diffusivity functions.

Example: the function $X(u)$ is known

In this example, a particular dimensionless diffusivity is considered:

$$X(u) = u^\kappa \tag{8.24}$$

This function gives different analytical solutions depending on the value of the real constant κ, from (8.23).

From Equation (8.21),

$$\frac{\mathrm{d}\vartheta(u)}{\mathrm{d}u} = A \cdot u^{-\kappa} \cdot \mathrm{e}^{-\frac{2}{2-\kappa} \cdot u^{2-\kappa}} \tag{8.25}$$

It should be noted that only if $(\kappa < 2)$ the flux is null for $u \to \infty$ (i.e., $z \to \infty$, $t > 0$). Finally,

$$\vartheta(u) = 1 - \frac{\Gamma\left(\frac{1-\kappa}{2-\kappa}, u^{2-\kappa}\right)}{\Gamma\left(\frac{1-\kappa}{2-\kappa}\right)} \tag{8.26}$$

In (8.26), the denominator of the fraction is the gamma function and the numerator is the complementary gamma function as defined by Tricomi (1954). From this expression, another constraint for κ is obtained. In fact, if $\kappa \geq 1$, the solution diverges for $u \to 0$. That is, Equation (8.26) is finite everywhere only if $(0 < \kappa < 1)$.

In Figure 8.5, the behaviour of the dimensionless diffusivity $X(\vartheta)$, according to Equations (8.24) and (8.26), is presented for three different values of the parameter κ. It is easy to verify that, in the aforementioned range for the parameter $\kappa\,(0 < \kappa < 1)$, the dimensionless

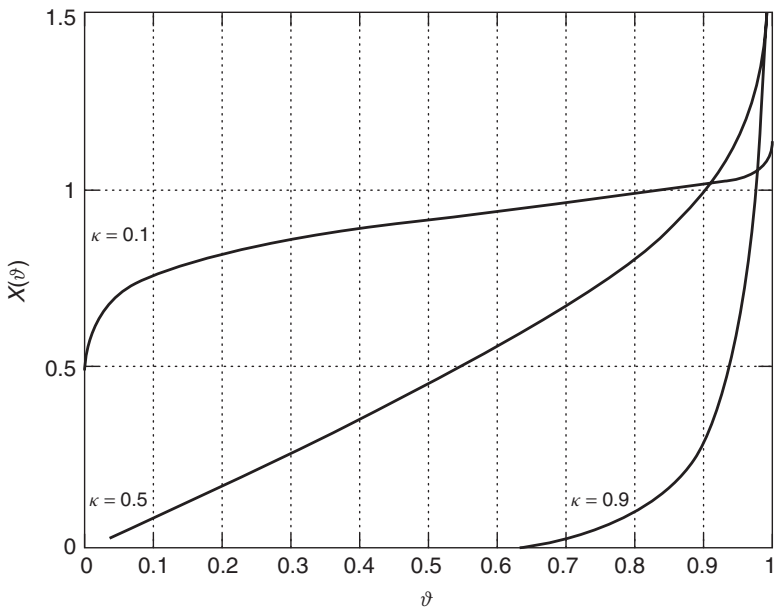


Figure 8.5 Behaviour of the dimensionless diffusivity $X(\vartheta)$, according to Equations (8.24) and (8.26), for three different values of the parameter κ. It is easy to verify that all the three curves have to be monotonic increasing function since $0 < \kappa < 1$. Moreover, only the functions with $0 < \kappa < 1/2$ have an inflection point (curve with $\kappa = 0.1$ in the figure)

diffusivity $X(\vartheta)$ increases from zero to infinity. Moreover, if $0 < \kappa < 1/2$, $X(\vartheta)$ has an inflection point for $X = \left(\frac{1}{2} - \kappa\right)^{\kappa/(2-\cdot\kappa)}$ corresponding to $\vartheta = 1 - \Gamma\left(\left(\frac{1-\kappa}{2-\kappa}\right), \left(\frac{1}{2} - \kappa\right)\right) \Big/ \Gamma\left(\frac{1-\kappa}{2-\kappa}\right)$. This can be seen in Figure 8.5 where only the curve ($\kappa = 0.1$) has the inflection point.

Example: the function $\vartheta(u)$ is known

Experimental vertical profiles of the soil water content, which are initially convex in their upper part, during evaporation process, may sometimes become concave (Hillel 1980b; Menziani *et al*. 1999). This is more probable during strong drying processes. The inflection point appearing in the soil moisture profile allows discerning the development of a drying front, which moves downward.

Directly from Equation (8.11),

$$\frac{\partial^2 \vartheta}{\partial z^2} = \frac{\frac{\partial \vartheta}{\partial t} - \frac{\mathrm{d}D(\vartheta)}{\mathrm{d}\vartheta} \cdot \left(\frac{\partial \vartheta}{\partial z}\right)^2}{D(\vartheta)} \tag{8.27}$$

Since $(\partial\vartheta/\partial t)$ is negative during the drying process, from Equation (8.27) it is clear that an inflection point can be present along the soil moisture profile only if $D(\vartheta)$ has a minimum. This behaviour of the diffusivity function may be related to vapour diffusivity, which increases as the soil dries (Hillel 1980b).

In this example, a soil water content function is assumed, which may or may not present the inflection point depending on the parameter α:

$$\vartheta(u) = 1 - \mathrm{e}^{-u^\alpha} \tag{8.28}$$

The second derivative of (8.28) with respect to z shows that $\vartheta(z)$ profile does not present the inflection point if $\alpha \leq 1$. If $\alpha > 1$, the profile has an inflection point moving downward: $z_f = ((\alpha - 1)/\alpha)^{1/\alpha} \cdot \sqrt{4 \cdot D_0 \cdot t}$. Replacing (8.28) in Equation (8.19), we obtain:

$$X(u) = \frac{2}{\alpha} \cdot \left[u^{2-\alpha} + \frac{1}{\alpha} \cdot \frac{\mathrm{e}^{u^\alpha} \cdot \Gamma\left(\frac{1}{\alpha}, u^\alpha\right)}{u^{\alpha-1}} \right] \tag{8.29}$$

If $\alpha \leq 1$, $X(u)$ is an increasing function of u; $X(u)$ has a minimum if $1 < \alpha < 2$. $X(u)$ is a decreasing function of u if $\alpha \geq 2$.

Introducing the transformation $u = [-\log(1 - \vartheta)]^{(1/\alpha)}$ in (8.29), obtained from (8.28), the dimensionless diffusivity function $X(\vartheta)$ is:

$$X(\vartheta) = \frac{2}{\alpha} \cdot \left\{ \begin{array}{l} [-\log(1-\vartheta)]^{\left(\frac{2}{\alpha}-1\right)} \\ \\ + \dfrac{1}{\alpha} \cdot \dfrac{\Gamma\left[\frac{1}{\alpha}, -\log(1-\vartheta)\right]}{(1-\vartheta) \cdot [-\log(1-\vartheta)]^{\left(1-\frac{1}{\alpha}\right)}} \end{array} \right\} \tag{8.30}$$

The behaviour of the dimensionless diffusivity $X(\vartheta)$, according to Equation (8.30), for three different values of the parameter α (0.9, 1.0, 1.1) is presented in Figure 8.6. Since $\frac{\mathrm{d}X}{\mathrm{d}\vartheta} = \frac{\mathrm{d}X}{\mathrm{d}u} \Big/ \frac{\mathrm{d}\vartheta}{\mathrm{d}u}$, taking into account (8.28) and (8.29), it is obvious that $X(\vartheta)$ is everywhere increasing if $\alpha \leq 1$ while it has a minimum if $1 < \alpha < 2$.

8.5.2 Solution of the linearised moisture flow equation

A general method to solve analytically the one-dimensional linearized Richards Equation (8.31) is discussed next.

$$\frac{\partial \vartheta}{\partial t} = D \cdot \frac{\partial^2 \vartheta}{\partial z^2} - V \cdot \frac{\partial \vartheta}{\partial z} \tag{8.31}$$

where ϑ is the normalised soil water content (8.12); D is the hydraulic diffusivity and V is the derivative of the hydraulic conductivity with respect to water content. Here, D and V are taken as constants. The gravity term is taken into account. In some cases, the constant V may assume a different meaning. For example, Equation (8.31) may describe the diffusion from a fixed source in a moving homogeneous medium with velocity V.

The limited utility of the linearized Richards equation is well known, but it may be justified by its simplicity or it may be reasonable in some specific situations (Warrick 1975; Basha 1999; Chen *et al*. 2001). In the following, the solution of (8.31) is obtained as the sum of two classes of solutions derived for complementary boundary conditions. Therefore, any initial condition and boundary condition can be used to solve Equation (8.31).

The first class of solutions results from choosing the following boundary and initial conditions.

$$\vartheta = \vartheta_i(z), z \geq 0, t = 0; \quad \vartheta = 0, z = 0, t > 0 \tag{8.32}$$

ϑ_i is the vertical profile of the soil water content at the origin of the time integration.

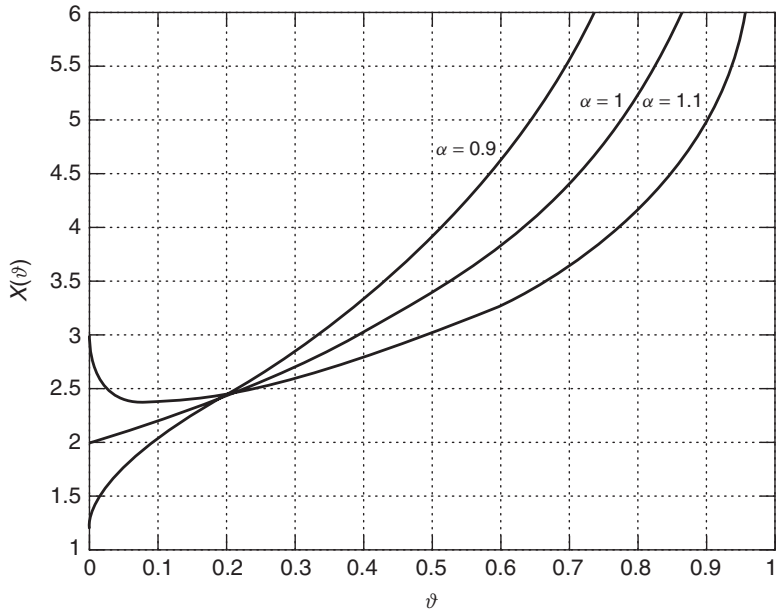


Figure 8.6 Behaviour of the dimensionless diffusivity $X(\vartheta)$, according to Equation (8.30), for three different values of the parameter α (0.9, 1.0, 1.1). $X(\vartheta)$ is everywhere increasing if $\alpha \leq 1$ while it has a minimum if $1 < \alpha < 2$

In order to solve the linearized Richards Equation (8.31) with the (8.32) conditions, the method of separation of variables is used. Following the known procedure to solve the heat diffusion equation (similar to Equation (8.31) with $V = 0$; see, for example, Carslaw and Jaeger (1986)), the first class of solutions is obtained:

$$\vartheta_1(z,t) = \frac{e^{\left(\frac{V\cdot z}{2\cdot D} - \frac{V^2\cdot t}{4\cdot D}\right)}}{\sqrt{\pi}\cdot\sqrt{4\cdot D\cdot t}} \cdot \int_0^\infty \vartheta_i(z') \cdot e^{-\frac{V\cdot z'}{2\cdot D}} \cdot \left[e^{-\left(\frac{z-z'}{\sqrt{4\cdot D\cdot t}}\right)^2} - e^{-\left(\frac{z+z'}{\sqrt{4\cdot D\cdot t}}\right)^2} \right] \cdot dz' \tag{8.33}$$

The second class of solutions is obtained from Equation (8.31) subject to the following boundary and initial conditions:

$$\vartheta = 0, z \geq 0, t = 0; \quad \vartheta = \vartheta_0(t), z = 0, t > 0 \tag{8.34}$$

where ϑ_0 is the surface boundary condition and

$$\vartheta_2(z,t) = \frac{2}{\sqrt{\pi}} \cdot \int_0^t \vartheta_0(t') \cdot e^{-\frac{[V\cdot(t-t')-z]^2}{4\cdot D\cdot(t-t')}} \cdot \frac{z\cdot 4\cdot D}{2\cdot[4\cdot D\cdot(t-t')]^{3/2}} \cdot dt' \tag{8.35}$$

Therefore, for a generalized situation specified by

$$\vartheta = \vartheta_i(z), t = 0, z > 0; \quad \vartheta = \vartheta_0(t), z = 0, t > 0 \tag{8.36}$$

the solution of Equation (8.31) can be expressed as

$$\vartheta(z,t) = \vartheta_1(z,t) + \vartheta_2(z,t) \tag{8.37}$$

Moreover it is important to add that since $\vartheta(z,t)$ and the conductive flux $(-D\cdot(\partial\vartheta/\partial z))$ both satisfy the Equation (8.31), then the total flux $(-D\cdot(\partial\vartheta/\partial z) + V\cdot\vartheta)$ also satisfies (8.31). This is important because the flux at the surface is often the known boundary condition.

Example

The soil water content vertical profiles obtained from this example have an inflection point or not depending on the time and on the value of a parameter β defined below. Furthermore, the soil moisture at the surface increases gradually with time.

The following boundary conditions are assumed.

$$\vartheta = 0, t = 0, z > 0; \quad \vartheta = \vartheta_0(t) = 1 - e^{-\beta\cdot t}, \quad z = 0, t > 0 \tag{8.38}$$

where β, which is suitable to write as $4\cdot a^2\cdot D$, is a positive constant with the dimension of one over time.

With the boundary conditions described in (8.38), (8.37) reduces to (8.35) and yields:

$$\begin{aligned}\vartheta(z,t) &= 1-\frac{1}{2}\cdot\left[\operatorname{erfc}\left(\frac{V\cdot t-z}{\sqrt{4\cdot D\cdot t}}\right)\right.\\ &\left.-\mathrm{e}^{\frac{V\cdot z}{D}}\cdot\operatorname{erfc}\left(\frac{V\cdot t+z}{\sqrt{4\cdot D\cdot t}}\right)\right]-\frac{1}{2}\cdot\mathrm{e}^{\frac{V\cdot z}{2\cdot D}-4\cdot a^2\cdot D\cdot t}\\ &\cdot\left\{\mathrm{e}^{2\cdot z\cdot\sqrt{\left(\frac{V}{4\cdot D}\right)^2-a^2}}\right.\\ &\cdot\operatorname{erfc}\left[\frac{z}{\sqrt{4\cdot D\cdot t}}+\sqrt{\left[\left(\frac{V}{4\cdot D}\right)^2-a^2\right]\cdot 4\cdot D\cdot t}\right]\\ &+\mathrm{e}^{-2\cdot z\cdot\sqrt{\left(\frac{V}{4\cdot D}\right)^2-a^2}}\\ &\left.\cdot\operatorname{erfc}\left[\frac{z}{\sqrt{4\cdot D\cdot t}}-\sqrt{\left[\left(\frac{V}{4\cdot D}\right)^2-a^2\right]\cdot 4\cdot D\cdot t}\right]\right\}\end{aligned}\tag{8.39}$$

Solution (8.39) holds for $\beta \le (V^2/(4\cdot D))$. For $\beta > (V^2/(4\cdot D))$, the solution (here not reported) can be expressed by the error function of complex variable. For $\beta = (V^2/(4\cdot D))$, Equation (8.39) reduces to:

$$\begin{aligned}\vartheta(z,t) = 1-\frac{1}{2}\cdot&\left[\operatorname{erfc}\left(\frac{V\cdot t-z}{\sqrt{4\cdot D\cdot t}}\right)-\mathrm{e}^{\frac{V\cdot z}{D}}\right.\\ &\left.\cdot\operatorname{erfc}\left(\frac{V\cdot t+z}{\sqrt{4\cdot D\cdot t}}\right)\right]-\mathrm{e}^{\frac{V\cdot z}{2\cdot D}-\frac{V^2\cdot t}{4\cdot D}}\\ &\cdot\operatorname{erfc}\left(\frac{z}{\sqrt{4\cdot D\cdot t}}\right)\end{aligned}\tag{8.40}$$

which permits to compute the time t_0 after which the inflection point appears. From the second derivative of (8.40), $t_0 = 2.25\cdot(D/V^2)$ is obtained. Figure 8.7, obtained using $V = 4\cdot 10^{-7}\,\mathrm{m\cdot s^{-1}}$ and $D = 10^{-8}\,\mathrm{m^2\cdot s^{-1}}$, shows the behaviour of three soil moisture profiles obtained by Equation (8.39) for three different values of the time (1, 3, 5 days) and for two values of the parameter β. The dashed profiles are obtained for $\beta = 4\cdot 10^{-6}\,\mathrm{s^{-1}}$ (i.e. $\beta = (V^2/(4\cdot D))$), which means $t_0 \approx 1.6$ days. The curve for $t = 1$ day ($t < t_0$) does

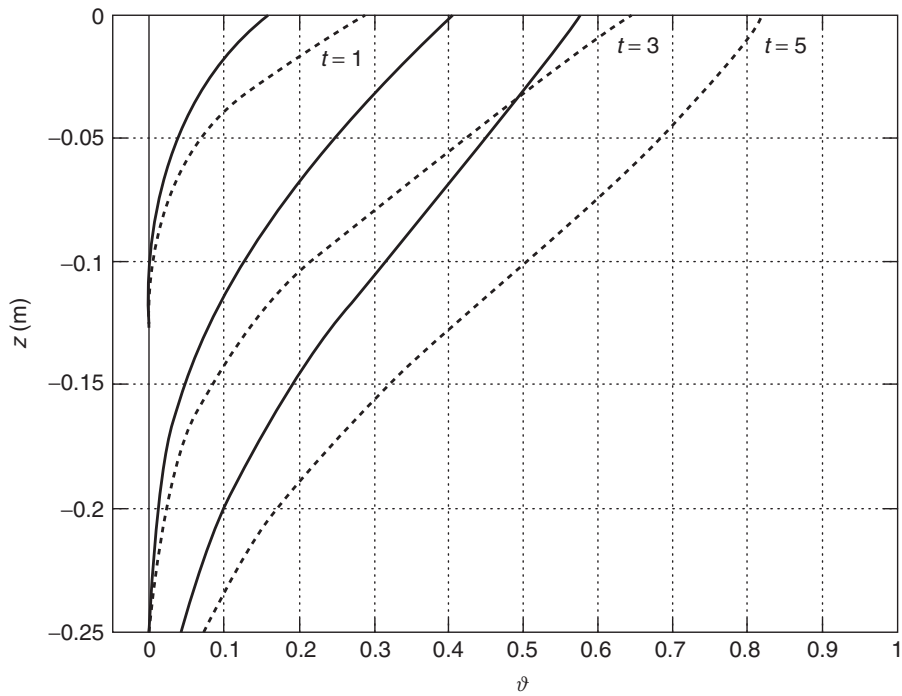


Figure 8.7 Behaviour of the theoretical soil moisture profile obtained by Equation (8.39) for three different values of the time (1, 3, 5 days) and for two values of the parameter β. The dashed curves are for $\beta = 4\cdot 10^{-6}\,\mathrm{s^{-1}}$ and the solid lines are for $\beta = 2\cdot 10^{-6}\,\mathrm{s^{-1}}$

not have the inflection point, which is present in the other two curves, corresponding to $t = 3$ and $t = 5$ days, that is, $t > t_0$. The solid line profiles are obtained for $\beta = 2 \cdot 10^{-6}\,\mathrm{s}^{-1}$; the inflection point ($t = 3$ and $t = 5$ days) is located closer to the surface with respect to the previous case.

Experimental data

During the period of measurements at the Pallanzeno station, two were the main hydrological events. The first happened during the summer period (dry event) before the MAP-SOP and the second during the second Intensive Observing Period (IOP-02, wet event).

Dry event

The trend of the experimental data collected during the dry event (21–25 July 1999) suggests a time dependence of the soil moisture at the surface. This experimental case may be modelled in a way similar to the example of Section 8.5.2. Using the following boundary conditions:

$$\vartheta = 1, t = 0, z > 0; \quad \vartheta = \vartheta_0(t) = \mathrm{e}^{-\beta \cdot t}, \quad z = 0, t > 0 \tag{8.41}$$

the theoretical soil moisture simply results:

$$\begin{aligned}\vartheta(z,t) &= \frac{1}{2} \cdot \left[\operatorname{erfc}\left(\frac{V \cdot t - z}{\sqrt{4 \cdot D \cdot t}} \right) - \mathrm{e}^{\frac{V \cdot z}{D}} \cdot \operatorname{erfc}\left(\frac{V \cdot t + z}{\sqrt{4 \cdot D \cdot t}} \right) \right] + \frac{1}{2} \cdot \mathrm{e}^{\frac{V \cdot z}{2 \cdot D} - 4 \cdot a^2 \cdot D \cdot t} \\ &\cdot \left\{ \mathrm{e}^{2 \cdot z \cdot \sqrt{\left(\frac{V}{4 \cdot D}\right)^2 - a^2}} \right. \\ &\cdot \operatorname{erfc}\left[\frac{z}{\sqrt{4 \cdot D \cdot t}} + \sqrt{\left[\left(\frac{V}{4 \cdot D} \right)^2 - a^2 \right] \cdot 4 \cdot D \cdot t} \right] \\ &+ \mathrm{e}^{-2 \cdot z \cdot \sqrt{\left(\frac{V}{4 \cdot D}\right)^2 - a^2}} \\ &\left. \cdot \operatorname{erfc}\left[\frac{z}{\sqrt{4 \cdot D \cdot t}} - \sqrt{\left[\left(\frac{V}{4 \cdot D} \right)^2 - a^2 \right] \cdot 4 \cdot D \cdot t} \right] \right\}\end{aligned} \tag{8.42}$$

In fact, treating a dry case, the theoretical soil moisture changes from 1 to 0 and the solution (8.42) is one minus solution (8.39).

Figure 8.8 shows the evolution of the soil moisture in the upper 40 cm of soil. The experimental data (symbols) are the mean daily profiles observed at Pallanzeno from July 21 to July 25. The solid lines are the corresponding theoretical trends obtained from the analytical solution (8.42) and from (8.12) assuming $\theta_m = 5\%$, $\theta_M = 30\%$, $D = 5 \cdot 10^{-9}\,\mathrm{m}^2\,\mathrm{s}^{-1}$, $V = 4 \cdot 10^{-7}\,\mathrm{m\,s}^{-1}$ and $\beta = 1.6 \cdot 10^{-6}\,\mathrm{s}^{-1}$. The value of β was chosen on the basis of the experimental soil water content values measured at 5 cm below the surface. The condition $\beta \leq (V^2/(4 \cdot D))$ is verified by the values of parameters V and D. The mean hydraulic diffusivity introduced in the linearized flow equation was computed by the relationship suggested by Crank (1956) for the drying processes. The values of θ_m, θ_M and V were derived from the experimental data. The matching of linear solution and experimental data is mainly affected by the non-uniform initial condition (21 July 1999) and by the inhomogeneity of the soil layer (see also the section below). Furthermore, a not-short period (five days) is modelled.

Wet event

During IOP-02 (19–21 September 1999), the heaviest precipitation event of the MAP-SOP, a cumulative precipitation of 225.4 mm was recorded at Pallanzeno. The observations describing the behaviour of the soil moisture in the 0–40 cm layer, during the initial part of the event (from September 19 at 16:00 h to September 20 at 08:00 h), are compared with a solution derived from the previously described methodology (Section 8.5.2).

Assuming the boundary condition (8.38) as β approaches infinity, the solution of Equation (8.31) is:

$$\vartheta(z,t) = 1 - \frac{1}{2} \cdot \left[\operatorname{erfc}\left(\frac{V \cdot t - z}{\sqrt{4 \cdot D \cdot t}} \right) - \mathrm{e}^{\frac{V \cdot z}{D}} \cdot \operatorname{erfc}\left(\frac{V \cdot t + z}{\sqrt{4 \cdot D \cdot t}} \right) \right] \tag{8.43}$$

The mean hydraulic diffusivity introduced in the linearised flow equation was computed by the relationship suggested by Crank (1956) for the infiltration process. The experimental data suggest the presence of a wetting front moving downward. Similarly, Equation (8.43) has an inflection point that moves downwards with a velocity related to the constant V. The velocity of the inflection point approaches V as the time increases. Identifying the inflection point with the experimental wetting front, an estimation of V is obtained. The evolution of the soil moisture in the upper 40 cm of soil is presented in Figure 8.9. The data begin on September 19 at 16:00 h

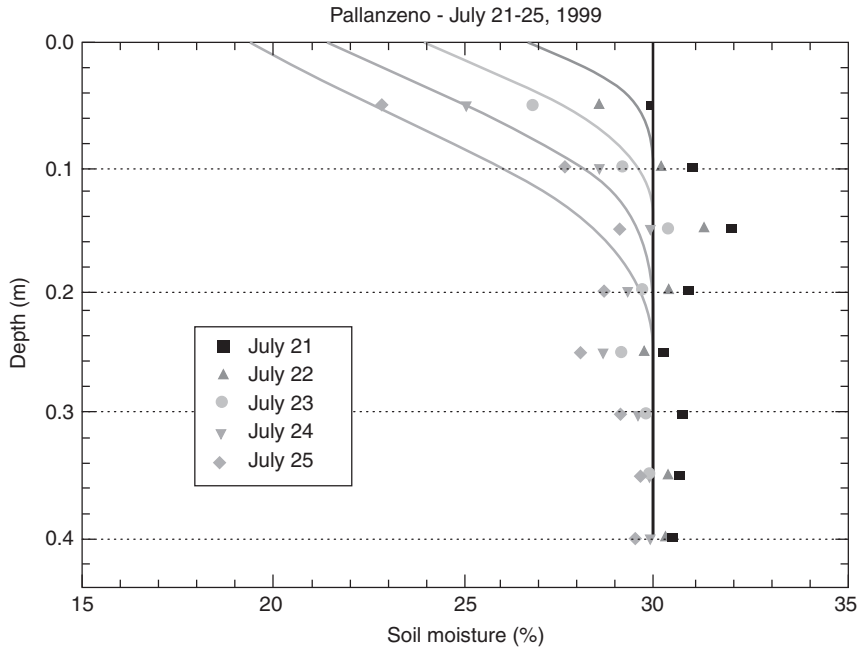


Figure 8.8 Dry event. Evolution of the daily mean soil moisture at Pallanzeno in the 0–40 cm soil layer from July 21 to July 25. The experimental profiles (symbols) are compared with the theoretical trends (solid lines) obtained from Equation (8.42)

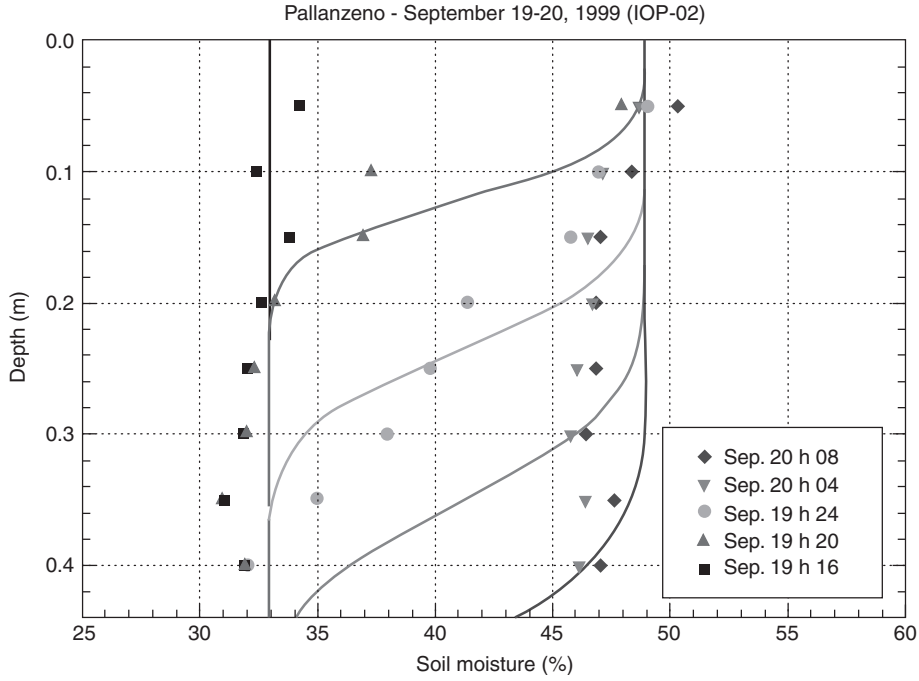


Figure 8.9 Wet event. Evolution of the soil moisture at Pallanzeno in the 0–40 cm soil layer from September 19 at 16:00 h to September 20 at 08:00 h. The experimental profiles (symbols) are compared with the theoretical trends (solid lines) obtained from Equation (8.43)

and end on September 20 at 08:00 h, with a time step of four hours. The experimental profiles (symbols) are compared with the theoretical trends (solid lines) obtained from the analytical solution (8.43) and from (8.12) assuming $\theta_m = 33\%$, $\theta_M = 49\%$, $D = 5 \cdot 10^{-8}\,\mathrm{m^2\,s^{-1}}$, $V = 8 \cdot 10^{-6}\,\mathrm{m\,s^{-1}}$. The modelled behaviour matches the experimental data mainly at the first two time steps, that is, after four and eight hours from the beginning of precipitation, when essentially the upper part of the soil is involved in the infiltration process. Falappi *et al*. (2000) reported different values of the saturated hydraulic conductivity (obtained both in laboratory and *in situ*) depending on the depth of the soil involved in the measurement. These data suggest that the hydraulic conductivity at saturation increases with the depth of the soil layer. The main differences between the experimental data and the theoretical solution, obtained for a homogeneous soil, should therefore be related to the not perfect homogeneity of the considered soil. For example, the shape of the soil moisture profile on September 19 at 24:00 h (circles) can be better fitted by the linear solution using a slightly greater value of the hydraulic diffusivity. A similar effect is obtained modifying the parameter V.

8.6 CONCLUSIONS

The experimental soil moisture measurements carried out during an international fieldwork have been presented. The solutions of the flow equation for the unsaturated zone (both for drying cases and infiltration cases) highlight different soil moisture profile according to the soil characteristics, which can be recognised in the experimental data.

The observations describing the behaviour of the moisture in the 0–40 cm soil layer during a drought period and during the heaviest precipitation event, IOP-02 of the MAP-SOP, are compared with two different solutions derived from the methodology described in Section 8.5.2.

A water balance algorithm to estimate the cumulative evaporation from the soil water content experimental measurements was presented. From the computed cumulative evaporation, the first and the second stages of evaporation can also be distinguished in this rainy Alpine Valley.

Meteorological and hydrological working groups of the MAP experiment collaborate strongly because NWP models and runoff and/or flood events prediction models need meteorological data as well as soil hydraulic characteristics and soil water content data. Meteorological stations are widely spread over the territory; this is not the case of experimental hydrological stations. The data collected at the Pallanzeno station are still being studied, and the results must be compared with the ones obtained by the other hydrological and meteorological research units.

An interesting evolution of this work will be related to the solution of the linearised flow equation using the precipitation as boundary condition. If the intensity of precipitation is lower than the infiltration capacity of the soil, it can be assumed as the prescribed vertical flux at the air–soil interface. The main advantages of this evolution are that precipitation measurements are much more common than soil moisture measurements and that precipitation events may be approximated by means of functions, which permit to obtain closed-form solutions.

8.7 ACKNOWLEDGEMENTS

We wish to thank the Italian Electrical Energy Company ENEL for the permission to install our instrumentation on their properties and for the help given during the whole period of measure. We also thank them for their rain gauge data.

The Italian Council of Research (CNR) and the Italian Ministry of the University and of the Scientific and Technological Research (MURST), in part, funded this work.

Finally, we wish to thank the two reviewers of this work for their helpful suggestions and their help in making this paper clearer and more complete.

REFERENCES

Basha H A (1999) Multidimensional linearized nonsteady infiltration with prescribed boundary conditions at the soil surface. *Water Resources Research* **35**(1): 75–83.

Binder P (1996) MAP and surface hydrology. *MAP Newsletter* **5**: 11–12.

Binder P and Schar C (eds) (1996) *MAP Design Proposal*. Schweizerische Meteorologische Anstalt, Krähbühlstrasse 58, CH-8044 Zürich.

Bougeault P, Binder P and Kuettner J (ed) (1998) MAP Science Plan. Available at MAP Data Centre http://www.map.ethz.ch/splan/spindex.htm

Brubaker K L and Entekhabi D (1995) An analytic approach to modeling land-atmosphere interaction, 1, construct and equilibrium behavior. *Water Resources Research* **31**(3): 619–632.

Brubaker K L and Entekhabi D (1996) Analysis of feedback mechanisms in land-atmosphere interaction. *Water Resources Research* **32**(5): 1343–1357.

Brutsaert W (1982) Some exact solutions for non linear desorptive diffusion. *Journal of Applied Mathematics and Physics (ZAMP)* **33**: 540–546.

Brutsaert W (1991) The formulation of evaporation from land surfaces. In: Bowles D S and O'Connell P E (eds) *Recent*

Advances in the Modeling of Hydrologic Systems. Kluwer Academic Publishers, pp. 67–84.

Brutsaert W and Chen D (1995) Desorption and the two stages of drying of natural tallgrass prairie. *Water Resource Research* **31**: 1305–1313.

Campbell G S (1985) *Soil Physics with BASIC*. Elsevier, Amsterdam.

Carslaw H S and Jaeger J C (1986) *Conduction of Heat in Solids*. Clarendon Press, Oxford.

Chen J M, Tan Y C, Chen C H and Parlange J Y (2001) Analytical solutions for linearized Richards equation with arbitrary time-dependent surface fluxes. *Water Resources Research* **37**(4): 1091–1093.

Crank J (1956) *The Mathematics of Diffusion*. Oxford University Press, London and New York.

Dirksen C and Dasberg S (1993) Improved calibration of time domain reflectometry for soil water content measurements. *Soil Science Society of America Journal* **57**(3): 660–667.

D'Urso G (1992) Impiego della riflettometria in dominio temporale (TDR) per la misura del contenuto d'acqua dei suoli in presenza di profili di umidità non uniformi. *Rivista di Ingegneria Agraria* **1**: 35–44.

Eagleson P S (1978) Climate, soil, and vegetation. 1. Introduction to water balance dynamics. *Water Resources Research* **14**(5): 705–712.

Eccel E, Toller G and Sicher L (2000) Field and laboratory soil measurements in the Toce Valley (Italy), during the MAP-SOP 1999 TOCEX experiment: the contribution of ISMA. Technical Report 10 VI, Università di Brescia – Dip. di Ingegneria Civile, http://civserv.ing.unibs.it/utenti/ranzi/MAP/SOP/tr06ismaa.PDF.

Falappi L, Barontini S, Clerici A, Grossi G, Savoldi E and Ranzi R (2000) Field and laboratory soil measurements in the Toce Valley (Italy), during the MAP-SOP 1999 TOCEX experiment. Technical Report 10 III, Università di Brescia – Dip. di Ingegneria Civile, http://civserv.ing.unibs.it/utenti/ranzi/MAP/SOP/tr03dicbs.PDF.

Heimovaara T J (1993) Time domain reflectometry in soil science: theoretical background, measurements, and models. Ph.D thesis, University of Amsterdam, Amsterdam.

Heimovaara T J and de Water E (1993) A computer controlled TDR system for measuring water content and bulk electrical conductivity of soils. Report No. 41, Laboratory of Physical Geography and Soil Science, University of Amsterdam, Amsterdam.

Hillel D (1980a) *Fundamentals of Soil Physics*. Academic Press, New York.

Hillel D (1980b) *Applications of Soil Physics*. Academic Press, New York.

Ledieu J, De Ridder P, De Clerck P and Dautrebande S (1986) A method of measuring soil moisture by time-domain Reflectometry. *Journal of Hydrology* **88**: 319–328.

Menziani M, Pugnaghi S, Pilan L, Santangelo R and Vincenzi S (1999) Field experiments to study evaporation from a saturated bare soil. *Physics Chemistry Earth (B)* **24**(7): 813–818.

Menziani M, Pugnagli S, Vincenzi S and Pilan L (2000) Mesoscale Alpine Programme (MAP) soil moisture TDR measurements at pallanzeno – lago maggiore target area. Technical Report 10 V, Università di Brescia – Dip. di Ingegneria Civile, http://civserv.ing.unibs.it/utenti/ranzi/MAP/SOP/tr05unimo.PDF.

Menziani M, Rivasi M R, Pugnaghi S, Santangelo R and Vincenzi S (1996) Soil volumetric water content measurements using TDR technique. *Annali di Geofisica* **39**: 91–96.

Obled Ch and Djerboua A (2000) Quantitative Precipitation Forecasts: a real-time exercise during the MAP experiment. Technical Report 10 VII, Università di Brescia – Dip. di Ingegneria Civile, http://civserv.ing.unibs.it/utenti/ranzi/MAP/SOP/tr07lthe.PDF.

Pepin S, Livingstone N J and Hook W R (1995) Temperature-dependent measurement errors in time domain reflectometry determinations of soil water. *Soil Science Society of America Journal* **59**: 38–43.

Philip J R (1960) General method of exact solution of the concentration-dependent diffusion equation. *Australian Journal of Physics* **13**: 1–12.

Ranzi R, Bacchi B and Grossi G (2003) Runoff measurements and hydrological modelling for the estimation of rainfall volumes in an Alpine basin. *Quarterly Journal of the Royal Meteorological Society* **129**: 653–672.

Roth K, Schulin R, Fluhler H and Attinger W (1990) Calibration of time domain reflectometry for water content measurement using a composite dielectric approach. *Water Resources Research* **26**(10): 2267–2273.

Soilmoisture Equipment Corporation (2000) *6050X1 Operating Instructions*. Soilmoisture Equipment Corporation, Goleta, CA (http://www.soilmoisture.com).

Topp G C, Davis J L and Annan A P (1980) Electromagnetic determination of soil water content: measurements in coaxial transmission lines. *Water Resources Research* **16**(3): 574–582.

Tricomi F (1954) *Funzioni Ipergeometriche Confluenti*. Cremonese, Roma.

Van Genuchten M Th, Leij F J and Yates S R (1991) The RETC code for quantifying the hydraulic functions of unsaturated soils, Version 1.0. Report 600/2-91/065 Ada, Oklahoma, OK.

Warrick A W (1975) Analytical solutions to the one-dimensional linearized moisture flow equation for arbitrary input. *Soil Science* **120**: 79–84.

9

Saturated Hydraulic Conductivity and Water Retention Relationships for Alpine Mountain Soils

STEFANO BARONTINI, ALBERTO CLERICI, ROBERTO RANZI AND BALDASSARE BACCHI

Department of Civil Engineering, University of Brescia, Brescia, Via Branze 38, I-25123, Italy

9.1 INTRODUCTION

In mountain areas, the surface runoff can represent a large portion of the total runoff. This can be observed by analysing flood hydrographs of mountain watersheds: the rising and falling limb of the stormflow hydrograph are very steep, and the baseflow recession is rapid, compared to that of basins with large floodplain areas. In a short time, generally a few hours depending on the size of the basin, a discharge close to the antecedent baseflow is reached, indicating that the flood volume is mainly contributed from surface or near-surface paths. Then, with the aim of a better understanding of the complex phenomenon of runoff formation in mountain watersheds, to have an appropriate description of the partitioning between surface and sub-surface runoff becomes of great hydrological importance both by a physical and a conceptual point of view. As stated in a century of research activity, the keys of this partition are the infiltration capacity of the upper soil layers and the soil hydraulic properties. With flood-producing rainfall intensities of the order of 10 mm/h or more, which are typical of mountain areas in extratropical climates, soils with low saturated hydraulic conductivity, less than 10^{-6} m/s, can lead to a typical Hortonian-overland flow, while other hillslope soils characterised by values about $10^{-4} \div 10^{-5}$ m/s, can contribute to the flood event mainly by sub-surface flow and return flow (Dunne 1978, Kirkby 1985). Percolation through very permeable soils or rock formations recharges the groundwater, and its discharge contributes to the interstorm hydrographs. Particularly in humid and high permeable vegetated slopes, often found in mountain areas, the infiltration phenomenon can sometimes be regarded as the joint effect of a diffusive phenomenon mainly governed by the capillary effects acting in the soil micropores, and a gravity transport wave taking place in the macropores already existing in the soils or originated by roots, animals and desiccation cracks (Beven 1982, Smith and Hebbert 1983, German and Beven 1985). Therefore, the knowledge of the soil hydraulic properties, such as the soil vertical conductivity K and water retention relationship between the matric potential Ψ and volumetric soil moisture content θ, has great importance both locally and over the whole basin. As it has been stated by several authors (see e.g. Salter and Williams 1965 and following, Campbell 1974, Haverkamp and Parlange 1986, Pachepsky and Rawls 1999), the physical characteristics of the soil, as, for example, the grain size distribution curve and the organic matter content, affect its hydraulic behaviour. This dependence is, however, impossible, or at least very difficult, to estimate for real soils with different pedogenesis and land use.

Climate and Hydrology in Mountain Areas. Edited by C. de Jong, D. Collins and R. Ranzi
© 2005 John Wiley & Sons, Ltd. ISBN: 0-470-85814-1

Uncertainties are moreover relevant in mountain soils, characterised by high variability not only because of their physical characteristics but also by the activity of erosion, transport and sedimentation processes.

From a practical point of view, in order to represent the dynamics of water in the soil, several theoretical or empirical formulas of the two soil functions $K(\theta)$ and $\Psi(\theta)$, have been proposed in the literature (e.g. Burdine 1952, Gardner 1958, Brooks and Corey 1964, Mualem 1976, Clapp and Hornberger 1978, Van Genuchten 1980). But as the water retention relationship $\Psi(\theta)$ can be estimated after widely accepted laboratory measurements, for instance, with the Richards' extractors (Richards 1949) or with pressure chambers (Klute 1986), the measurement of the soil saturated conductivity K_s is still affected by a higher uncertainty. So various field and laboratory methods have been proposed by several authors to estimate it (e.g. Klute and Dirksen 1986, Sisson and Van Genuchten 1991, Reynolds and Elrick 1990 and 1991, Santini *et al*. 1995, Benson *et al*. 1997) and empirical approaches have been suggested as well (e.g. Hazen 1911, Kozeny 1927, Boadu 2000).

The aim of the experimental investigations presented here was the estimation of the stormflow response during floods in mountain basins of the Italian Alps. The specific objective is the estimation at the point and basin scale of the soil saturated conductivity K_s and of the water retention relationships $\Psi(\theta)$ in mountain not completely developed soils. In fact, capillarity mainly governs the imbibition at the beginning of the storm, while saturated conductivity is representative of the infiltration rate and of the resulting runoff at the end of the storm. A proposal of average values has been attempted for classes of soils and land use of the whole basin, in view of a ''physically based'' application of hydrological models for flood forecasting in the respective areas. Moreover, the soil functions are useful also to understand surface moisture and heat fluxes. Thus, climatological studies can benefit from the results summarised in this work.

In the next section, the theory of the infiltration of water in an unsaturated porous media is briefly recalled. Then, in the third section, the experimental equipment and the test areas are presented. The single ring infiltrometer method was chosen as a good compromise between easiness to perform the infiltration tests, logistics and reliability of the retrieved information. Because of its easy and inexpensive building and the easiness of performing the measurements, it is still widely used during field campaigns or experimental basins (Wu *et al*. 1999, Braud *et al*. 2001), especially in mountain areas where transportation and logistics are difficult (Orlandini *et al*. 1999). As experimental equipment in order to investigate the water retention curves of soil samples from the same sites, the Richards' extractors were used during the laboratory analysis. The two investigated areas, the Toce River basin and the Mella River basin, were selected as target areas of wide investigations concerned on the study of the runoff production and flood forecasts in Alpine areas. These areas are representative of basins characterised, respectively, by metamorphic and sedimentary rocks in the Southern Alps.

As a result of the wide and extensive field and laboratory investigations, the hydraulic properties of the upper soil layers in two mountain basins of the Italian Alps are presented and discussed in the following fourth section. A comparison of different methods to estimate the vertical saturated conductivity from field data is presented. Then a classification of K_s is attempted on the basis of the grain size texture and on the basis of pedogenesis and land use was attempted. Some consideration of the sensitivity of the water retention relationship to organic matter content, soil texture and land use is also presented.

Therefore, a methodology based on the use of the single ring infiltrometer and the classification of the upper soil on the basis of a mixed pedogenetic and land-use basis is proposed and compared with laboratory analysis to determine the vertical soil saturated conductivity at the basin scale. More difficult seems instead to be the estimation of the water retention relationship for soils for which the organic matter content, texture and land use are not known *a priori*.

9.2 THEORETICAL ASPECTS

9.2.1 Richards' equation and constitutive laws

The infiltration process is a particular case of the dynamic of a darcian flux in an unsaturated porous media. On the basis of a continuum meso-scale analysis, under the hypothesis of an isothermal process of an incompressible fluid in a non-deformable isotropic medium, the infiltration can be physically described by the known Fokker–Planck's or Richards' equation (Richards 1931):

$$\nabla \cdot [D(\theta)\nabla\theta + K(\theta)\mathbf{k}'] = \frac{\partial\theta}{\partial t}, \tag{9.1}$$

where $\theta[-]$ is the volumetric soil moisture, $\mathbf{k}'$ is the z-axis unitary vector, positive upward, and $D(\theta)$ $[L^2T^{-1}]$ is the hydraulic diffusivity in the porous medium. $D(\theta)$ is related to the unsaturated hydraulic conductivity $K(\theta)$ $[LT^{-1}]$ and to the water retention relationship $\psi(\theta)$ [L] by

$$D(\theta) = K(\theta)\frac{d\psi(\theta)}{d\theta}. \tag{9.2}$$

It is important to remember that $\psi(\theta) = \Psi(\theta)/\gamma_w$, where Ψ is the matric potential in terms of pressure, or energy per unitary volume, and γ_w is the water unitary weight. Therefore, ψ is the energy/unit weight needed to transfer, against the capillary forces, a quantity of water from a reference state to the situation of interest: it has a negative value. Moreover, the hysteretic behaviour of the matric potential (see e.g. Eagleson 1970, Bear 1972, Cavazza 1981) is often neglected and a simplification consists in considering infiltration as an imbibition process.

Two kinds of constitutive laws are introduced (Gardner 1958, Brooks and Corey 1964) that will be used in the following because of their simplicity in regard to the number of experimental points used.

Gardner (1958) proposed an exponential mono-parametric form for the water retention relationship and a linear form to express the dependence of the soil unsaturated conductivity from the volumetric water content. Let s_e be the effective degree of saturation, given by the relation below:

$$s_e = \frac{\theta - \theta_{\text{res}}}{\theta_{\text{sat}} - \theta_{\text{res}}} \tag{9.3}$$

where θ_{res} and θ_{sat} represent the residual and the saturated water content, respectively. Then the water retention relationship and the soil unsaturated conductivity are written as

$$s_e = \mathrm{e}^{\alpha\psi}; \quad K(s_e) = K_s s_e \tag{9.4}$$

where the parameter α [L^{-1}], called *sorptive number*, generally varies between 5 and 0.2 m^{-1} (Philip 1968). The sorptive number is an index of the importance of the gravitational effects versus the capillary effects: it becomes greater as the soil gets coarser and the gravitational effects increase in importance. Warrick (1974) observed that the water retention relationship proposed by Gardner is useful to interpret the behaviour of the soil for moisture values not far from saturation. Therefore, it can be effective to simulate the infiltration process in humid climates and during the flood season, when soil moisture is generally not very low. Such conditions are of key interest for our study, focused on the flood formation in mountain basins.

Brooks and Corey (1964) represented the water retention relationship as a two-parametric power law in the form

$$s_e = \begin{cases} \left(\dfrac{\psi}{\psi_b}\right)^{-\lambda} & |\psi| \geq |\psi_b| \\ 1 & |\psi| < |\psi_b| \end{cases} \tag{9.5}$$

where ψ_b [L] is the bubbling pressure, that is, the minimum value of the matric potential at which the gas phase is continuous, and λ[−], named *pore-size distribution index*, is a dimensionless number representing the medium structure. The soil unsaturated conductivity a be then expressed as a power law of s_e in the form $K(s_e) = K_s s_e^a$, where the value of a varies on the basis of the theoretical model adopted (see e.g. Burdine 1952, Mualem 1976).

It can be seen that the shape of the water retention relationship plays an important role in the estimation of the soil unsaturated conductivity, so the set of necessary parameters in order to completely define the problem is limited to the soil saturated conductivity, K_s the characteristic moistures, θ_{res} and θ_{sat}, and the parameters of the water retention relationship.

9.2.2 Soil saturated conductivity after field data

Several different methods, both mono-dimensional (eventually with the introduction of scale effects, for example, Wu *et al*. 1999, Braud *et al*. 2001) and bi-dimensional with axial symmetry, have been presented and compared in the literature to interpret the infiltration process from a single ring infiltrometer. Here, two mono-dimensional quasi-steady methods and a two-dimensional axial-symmetric method are presented.

The first method we used to estimate the soil vertical saturated conductivity K_s after *in situ* experiences is the traditional method derived by the application of Darcy's law (1856) to a quasi-steady, uniform, mono-dimensional flow in a saturated porous media with finite volume (further it will be referred to as the *Darcy's method*). Under the above hypothesis, the momentum equation can be therefore discretised obtaining the following Equation (9.6):

$$\mathbf{q} = -K_s \frac{\Delta H}{\Delta z}\mathbf{k}' \tag{9.6}$$

being $\mathbf{q} = q\mathbf{k}'$ [LT^{-1}] the apparent velocity of the fluid in the porous medium, Δz the soil length inside the infiltrometer, say, $L_{\text{inf}} = 0.1$ m (Figure 9.1), and H [L] the total water head. For a saturated soil $H = H_{\text{geo}} + p/\gamma_w$ [L], where H_{geo} is the geodetic head and p/γ_w the piezometric head, where γ_w is the unitary weight of the water. As the ground is assumed as reference level, the geodetic head H_{geo} is equal to the height z above ground.

By taking the soil core and the volume of fluid inside the infiltrometer as a control volume and $\mathbf{n}'$ being the surface unitary vector positive outward, the conservation of mass is given by the Equation (9.7):

$$\mathbf{q} \cdot \mathbf{n}' = -\frac{\mathrm{d}h}{\mathrm{d}t} \tag{9.7}$$

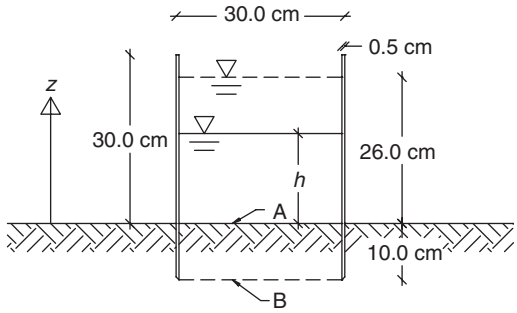


Figure 9.1 Descriptive sketch of the single ring infiltrometer method

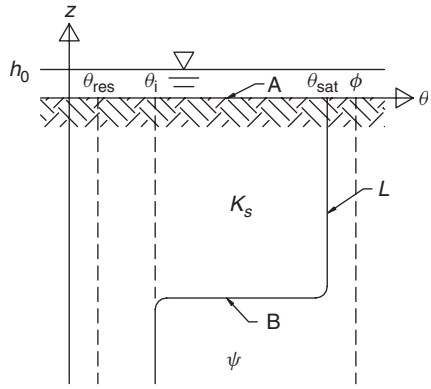


Figure 9.2 Descriptive sketch of the Green and Ampt (1911) infiltration conceptual model

in which h is the water level inside the infiltrometer and it is equal to the hydraulic head at point A in Figure 9.1. At the bottom of the control volume (B in the sketch), $\mathbf{n}'$ is equal to $-\mathbf{k}'$, so by the substitution of Equation (9.6), Equation (9.7) can be integrated between A and B yielding to the cumulative drawdown versus time curve. The soil saturated conductivity K_s can be therefore estimated as it is the only unknown parameter in the cumulative infiltration curve.

The second mono-dimensional method adopted to estimate the soil saturated conductivity from field data is an application of the Green and Ampt (1911) conceptual infiltration model and will be referred to as the *GA method*. A sharp wetting front (named B, Figure 9.2) is supposed to penetrate to a depth L into the soil. The model applies to the process until it is strictly mono-dimensional. In order to respect this condition, the saturated soil depth $L(t) = I(t)/(\theta_{sat} - \theta_0)$, where $I(t)$ is the cumulated drawdown of the water table and θ_0 the initial volumetric soil moisture, shall be less than the length D of the infiltrometer in the soil. Let ψ be the matric potential below the interface between the wet front and the soil at initial dry moisture conditions (Chow *et al*. 1988), then the Green and Ampt's infiltration model can be modified restoring the dependency of the infiltration by a variable head ponding on the soil surface:

$$\frac{\mathrm{d}I(t)}{\mathrm{d}t} = K_s \frac{h(t) + L(t) - \psi}{L(t)}. \tag{9.8}$$

In the previous equation, h_0 is the initial depth of the water inside the infiltrometer, and $h(t) = h_0 - I(t)$ is the current water depth, that is, equal to the hydraulic head on the upper surface of the saturated soil control volume (A in the sketch). Even if such an application of the GA model takes into account the matric potential below the wetting front, the given description of the phenomenon can be seen as dominated by a transport behaviour. Anyway, since the infiltration process is characterised also by the diffusion of the soil moisture, the wetting front (B in the sketch) is often strongly smoothed. So we took into account such a behaviour by estimating the matric potential ψ as the average matric potential over the interval (θ_{sat}; θ_0). Knowing the initial soil moisture θ_0 and the parameters of the water retention relationships derived after laboratory tests – in this case the Brooks and Corey's form was used – , ψ was estimated with the equation below:

$$\psi \approx \frac{\int_{s_{e,o}}^{s_e=1} \psi(s)\,\mathrm{d}s}{1 - s_{e,o}}. \tag{9.9}$$

A value of K_s can be therefore derived by Equation (9.8), for instance, by a linear regression.

Finally, a two-dimensional axially symmetric method is presented. The seminal solution for the steady infiltration from a shallow circular pond of negligible depth, with an axial symmetry, was originally proposed by Wooding (1968) who ''heroically'' (Philip 1984) integrated the Richards equation linearised by using the Gardner's constitutive law. Afterwards, the Wooding solution was widely used in its original form, or it was adapted to different field and test conditions (e.g. Raats 1971, Reynolds *et al*. 1985, Weir 1987, Perroux and White 1988, Reynolds and Elrick 1990 and 1991, Quadri *et al*. 1994, Evett *et al*. 1999, Bagarello *et al*. 2000, Schwartz and Evett 2002).

To take account of the effects of the ponding depth, soil capillarity and scale effects due to the ratio between the ring diameter and the depth of ring insertion into the

soil, we used the formulation proposed by Reynolds and Elrick (1991). Further, it will be referred to this method as the *RE method*.

In the RE approach, K_s is given by the following relation.

$$\frac{\mathrm{d}I(t)}{\mathrm{d}t} = K_s\left[1 + \left(h^* + \frac{1 - s_{e,o}}{\alpha}\right)\frac{1}{\pi r G_e}\right] \qquad (9.10)$$

where h^* is the steady ponding depth inside the infiltrometer ($h^* > 0.05$ m), α is the Gardner's sorptive number, r is the radius of the infiltrometer. Finally, in the above relation the shape parameter G_e is expressed by:

$$G_e = 0.316\frac{L_{\mathrm{inf}}}{r} + 0.184 \qquad (9.11)$$

where L_{inf} is the depth of ring insertion into the soil (between 0.03 m and 0.05 m in Reynolds and Elrick 1991) and r is the radius of the infiltrometer (between 0.05 and 0.10).

9.3 EXPERIMENTAL METHODS

9.3.1 The experimental equipment

The method of the single ring infiltrometer, with a falling head measurement of the infiltration rate was used during the field campaign.

According to the ASTM standard, in order to apply this method, iron cylinders with a height of 0.4 m were driven into the soil (see Figure 9.1) for a length of about 0.1 m and filled with water up to a few centimetres below their upper border (a standard head of 0.26 m was adopted). Then the infiltration rate and the cumulated infiltration curve were measured. During these campaigns, a 0.3-m and a 0.36-m diameter infiltrometer were used. This choice seemed to be a good compromise between the aim of determining an average behaviour over the local inhomogeneities of the soils and the logistic difficulties of a field campaign in a mountain area. Moreover, flat or sub-horizontal areas were chosen to perform the infiltration tests so that the soils selected were homogeneous on the horizontal dimension, and the axial symmetry of the infiltration process was a realistic hypothesis.

As a comparison with *in situ* data, by the observation that the soil saturated conductivity was generally expected to be less than 10^{-4} m/s, a falling head permeameter (Klute and Dirksen 1986, Rossi Pisa 1997) was considered useful to estimate in laboratory the soil saturated conductivity over almost undisturbed soil cores (diameter 0.10 m and height 0.14 m) with a volume of about 0.001 m^3.

The water retention relationship of the soils was estimated using a 5 bar and 15 bar Richards' extractor (Richards 1949) with up to six pressure heads. Even if it could be more reliable to maintain the original composition and structure of the samples, the non-negligible skeletal fraction, due to the non-complete development of the upper soil layers, suggested to previously sieve the samples at the sieve ASTM No. 10 (2 millimetres width). Some experiences were also done on bulk and crumbled soils to verify the influence of the soil sieving measurement of the water retention relationship. Results are presented in the fourth section.

The organic matter of the soil was determined by burning the oven-dried samples in a muffle furnace at a temperature of 440°C. Finally, the grain size distribution was performed by wet sieving and sedimentation and the soil was classified. The ASTM standards were followed during the laboratory experiences.

9.3.2 Target areas

Two Alpine basins were investigated during our campaigns: the Toce River basin, located in the Northern Italian Alps, and the Mella River basin, in the Central Italian Alps (see Figure 9.3 and Table 9.1).

The first basin was investigated during an international research project (Bacchi and Ranzi 2000), in an area close to Lago Maggiore, selected as a main scientific target in the Mesoscale Alpine Programme. In 1999, several experiments took place there, aimed at understanding the influence of orography on meteorological (Bougeault *et al*. 2001) and hydrological processes (Ranzi *et al*. 2003). Because the area investigated experiences some of the most severe floods in Europe, with a mean specific peak annual flow of 1 $\mathrm{m}^3/\mathrm{s}/\mathrm{km}^2$ for basins of about 1000 km^2, a key issue was the understanding of flood production in that environment (Bacchi *et al*. 2002, Kouwen and Benoit 2002, Jasper *et al*. 2002, Montaldo *et al*. 2002), where the control of upper soils in partitioning water into surface and sub-surface runoff is fundamental.

The Toce River basin can be considered representative of mountain basins with mainly metamorphic rocks, steep slopes and high runoff production. The tectonic of the Toce River basin is characterised by three main units: from the North to the South the Pennidic system, the Austro-Alpine system and the Southern Alps system can be distinguished (Clerici and Cantoni 2000). From a geomorphologic point of view, the basin is characterised by layers of morainic overburden slope debris in a clayey matrix and bare rock on the steeper slopes. Glaciers covered the entire area until about 16,000 years BP. The massive ice- and snow-melt since then, the heavy rainfall of the area (some of the highest in Europe), and

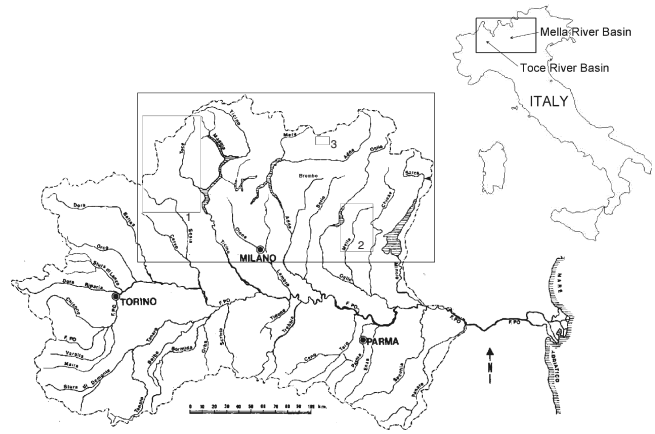


Figure 9.3 Location of the investigated basins, referring to the Po River Basin: (1) Toce; (2) Mella; (3) Bracciasco, investigated by Orlandini *et al*. (1999)

Table 9.1 Main physical characteristics of the investigated basins

Basin	Toce at Candoglia	Mella at Stocchetta
Name of the area	Val d'Ossola	Valtrompia
Mountain range	Northern Italian Alps	Central Italian Alps
Elevation range of the basin (m a.s.l.)	196–4633	181–2215
Elevation range of experimental sites (m a.s.l.)	199–1770	196–2063
Latitude	45°54′–46°28′N	46°35′–45°52′N
Longitude	7°52′–8°29′E	10°07′–10°25′E
Area (km^2)	1532	312
Geology	Metamorphic	Limestones and carbonatic rocks
Glaciers and permanent snow (%)	2	–
Dominant vegetation type	Deciduous and coniferous forests	Deciduous and coniferous forests
Forests (%)	70	56
Mean runoff at catchment outlet (mm)	1382	670
Mean precipitation (mm)	1557	1260

Source: Ranzi *et al*. (2002), Ranzi *et al*. (2003).

the slope steepness and length provide high energy to shape the landscape. As a consequence of the intense erosional, transport and eluviation process soils are not completely developed. A deep alluvial layer, with mainly sand and silt, can be observed along the medium and lower course of the river. Here, 146 soil experimental sites were selected to estimate the soil saturated conductivity in the upper (0–0.3 m) soil layer. In order to retrieve more detailed information, 80 sites were located in the Anza River Valley (a right-side tributary of the main Toce Valley, 40 sites) and in the Melezzo Occidentale River Valley (a left-side tributary, 40 sites). A subset of 83 samples was used to measure the water retention relationship of the soils. Also some samples from rock sites were investigated in order to predict the soil saturated conductivity of the outcropping rocks and to complete the surface saturated conductivity maps of the basins, but this does not relate to the topics of this paper, and results will not be discussed here.

The other basin, the Mella River basin (Ranzi *et al*. 2002), was investigated within the CNR-VAPI RIVERS project, aimed at the characterisation of the hillslope response in representative basins in Italy. It reaches an altitude of 2215 m and was selected as representative

Table 9.2 Infiltration tests and areal frequency of the experimental sites in the Toce River basin and in the Mella River basin

Basin	Area [km^2]	N° of experimental sites	N° of infiltration tests	Areal density [km^{-2}]
Toce River basin (total)	1800	146	404	0.081
Anzasca Valley	254	40	130	0.157
Vigezzo Valley	57	40	140	0.702
Mella River basin	311	80	223	0.257

of the prealpine ridges of the Central Italian Alps, characterised by dominant limestones, dolostones and carbonatic rocks, with some metamorphic and volcanic rocks in the Northern part. The basin belongs to the system of the Southern Alps, also called Southern Calcareous Alps. Its tectonic is mainly divided in two zones: the upper- and medium- Valtrompia Valley, with several faults and folds, and the lower valley, less rough, characterised by several smooth folds. At the higher altitudes, there are morainic bodies due to the last glaciations. The principal alluvial deposits formed by the sedimentary action of the Mella River is characterised by gravel and, in the lower course, sand. Slope debris are present close to tectonic contacts and the most fragile rocks. Here 80 sites of the surface soils were identified on the basis of a 2-km regular grid. In each site, the soil saturated conductivity of the upper soil layer was measured and compared after *in situ* and laboratory analysis. The water retention relationship was also measured in laboratory over soil samples coming from each experimental site.

In Table 9.2, the number of experimental sites and its areal density is represented together with the number of the performed infiltration tests.

9.3.3 Preliminary analysis and selection of the experimental sites

Before locating the experimental sites and in order to retrieve from them the best representativeness of the different geological and soil conditions, for both basins three preliminary maps were compiled on the basis of both the *in situ* investigations and the existing literature and maps.

At first, a lithologic map was compiled where soils were distinguished on the basis of the genesis of the sediment, that is, alluvial, glacial (moraine) and from the action of gravity, such as slope debris, for example. Surface rocks, instead, were distinguished on the basis of the different genesis of the infiltration paths, that is, fractures, schistosity, preferential paths derived from Karst action in carbonate rocks. Seven different classes were identified in the Toce River basin, while ten different classes were identified in the Mella River basin.

Then a land-use map was produced by choosing, for both the basins, six different land-use classes: non-covered soils and rocks, meadows and grass-covered soils, forests, glaciers, cultivated areas, discontinuous urban fabrics.

By a cross comparison of these two preliminary maps, a final map of proneness of surface soil layers to infiltration was compiled obtaining seven and seventeen different soil classes, respectively, for the Toce River basin and for the Mella River basin. In the Mella River basin, in particular, a higher number of classes was identified to keep in evidence the different expected saturated permeability for soils covering different underlying lithology. These resulting maps were used to select the experimental sites with regard to the areal representativeness of the single classes. Finally, the soil saturated conductivity of each class was estimated by arithmetic- and geometric-averaging the values obtained. Some exceptions were applied for the cases where single values were too different from the average of their class and seemed to be representative only of their particular site. In the Toce River basin, the saturated conductivity of the soil classes was sometimes found systematically different when coming from different areas of the basin: in these cases, two different averages were estimated.

9.3.4 Performance of the infiltration and laboratory tests

Four field infiltration tests were tried at each experimental site. The adopted experimental layout is described below.

The first test was generally done on the soil surface under natural moisture conditions; then the soil was (almost) saturated with about 0.1 m^3 of water slightly poured out over a circular area of about 1 m^2 around the infiltrometer. In order to help the process of saturation of the upper soil layers during the water pouring, and to prevent the runoff of the water over the surface, two holes (diameter 0.01 m, depth 0.15 m) were made along eight equally spaced directions. Then the second surface test, that is, the surface test under modified ''saturated'' soil moisture, was performed. The degree of saturation was afterwards verified in laboratory over a core sampled after the modified-moisture infiltration test. Finally, two other infiltration tests were performed at the same sites, but at lower soil depths, about 0.1 and 0.2 m deep.

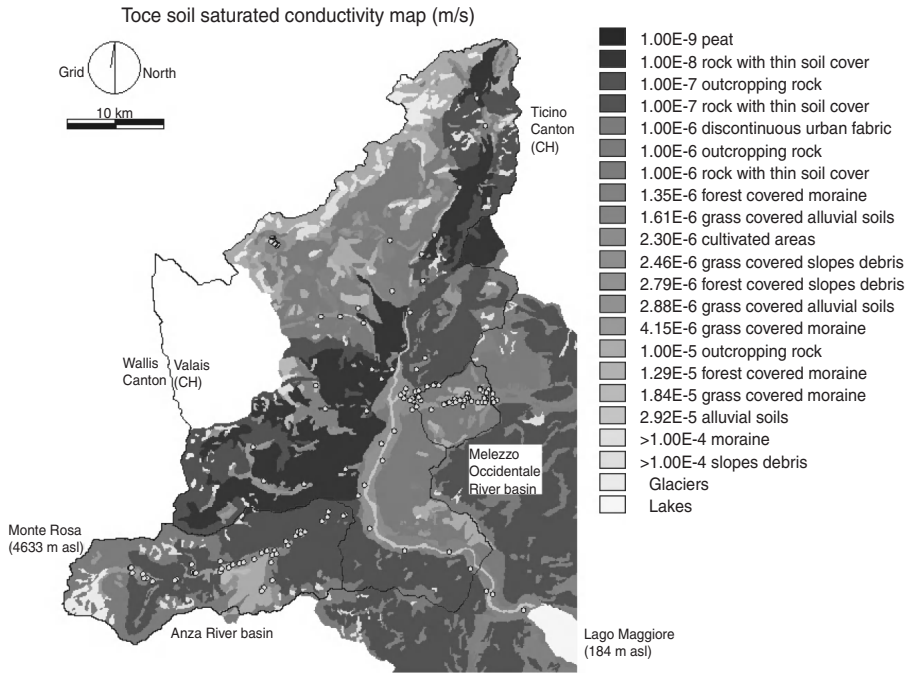


Figure 9.4 Surface soil saturated conductivity map for the Italian Toce River basin (after Clerici and Cantoni 2000). For the values in legend, the Reynolds and Elrick method (see the text for details) is adopted

For each site, surface samples of the soil were collected to perform soil moisture measurements, soil saturated conductivity and water retention tests in laboratory. Two more soil cores were taken, when the soil was deep enough, to measure the soil saturated conductivity after laboratory analysis also for the lower layers and to verify possible discontinuities in the profile of the grain size distribution.

In laboratory, the core samples were weighed and saturated for at least 16 h before performing the falling head permeability test. The sample was weighed another time to verify any change in the soil moisture and finally oven dried at 105°C for 24 h. Then the soil sample was divided into two parts: one being used to determine the grain size distribution curve, and the other to determine the water retention relationship. To perform this experience, the soil was previously sieved at the 2-mm sieve, then three samples (height about 1 cm, diameter 8 cm) of sieved soil were laid on a Richards' porous plate that was previously saturated. Then the samples were saturated by imbibition from the porous plate and a pressure of (10, 33, 50, 100, 500, 1500 kPa) was imposed in the Richards' apparatus. After drainage, the moisture of the samples was measured by oven drying.

9.3.5 Experimental results

As a result of the experimental campaigns, the surface saturated conductivity maps of the soils of the Toce River and of the Mella River basins were compiled at the scale of 1:100,000 and 1:25,000, respectively. In Figure 9.4, the soil saturated conductivity map derived with the Reynolds and Elricks method of the Italian Toce basin is represented joint with the catchment boundary. The legend proposed for the surface soil vertical saturated conductivity, with the specification of the number of the experimental values, the geometric average and the maximum and minimum value, is also reported in Table 9.3. Here, the results obtained by applying the Darcy method and the RE method are compared. In order to apply the Darcy method (see Section 9.2.2), the final limb of the modified moisture infiltration curve was used. A mono-dimensional flow could be hypothesised, and the soil around the infiltrometer could be considered saturated with a water head coincident to the soil surface level. The RE method was instead applied using the final limb of the natural moisture infiltration curve (see for details Section 9.4.1). The proposed legend for the surface soil vertical saturated conductivity in the Mella River basin is reported in Table 9.4. Also in this case the legend was derived applying both the Darcy and the

Table 9.3 Surface soil saturated conductivity of the Toce River basin derived using the Darcy and the Reynolds and Elrick (1991) method. In brackets, the number of the measurements used for the estimation of the saturated conductivity is reported († = arithmetic average, ‡ = geometric average)

Class	K_s [m/s] (Darcy †)	K_s [m/s] (Darcy ‡)	$K_{s,\max}$ [m/s] (Darcy)	$K_{s,\min}$ [m/s] (Darcy)	K_s [m/s] (RE †)	K_s [m/s] (RE ‡)	$K_{s,\max}$ [m/s] (RE)	$K_{s,\min}$ [m/s] (RE)
Forest-covered slope debris	3.59E-05 (6)	3.10E-05	5.84E-05	1.13E-05	3.23E-06 (2)	2.79E-06	4.87E-06	1.60E-06
Grass covered alluvial soils	3.89E-05 (40)	1.30E-05	2.09E-04	9.23E-07	2.50E-06 (12)	1.61E-06	6.60E-06	9.30E-08
Forest-covered moraine	2.83E-05 (5)	1.33E-05	6.12E-05	4.79E-07	1.88E-06 (5)	1.35E-06	3.27E-06	1.95E-07
Grass-covered alluvial soils	5.45E-05 (23)	2.80E-05	2.20E-04	1.98E-06	4.10E-06 (10)	2.88E-06	1.10E-05	6.54E-07
Grass-covered moraine	5.08E-05 (28)	2.09E-05	2.23E-04	1.62E-07	7.20E-06 (11)	4.15E-06	2.01E-05	5.35E-07
Grass-covered slope debris	1.45E-04 (7)	1.15E-04	2.25E-04	1.63E-05	2.74E-06 (3)	2.46E-06	4.40E-06	1.40E-06
Grass-covered moraine	1.85E-04 (15)	1.21E-04	8.22E-04	9.90E-06	1.18E-04 (5)	1.84E-05	5.38E-04	2.95E-06
Forest-covered moraine	2.31E-04 (4)	2.23E-04	3.44E-04	1.79E-04	1.44E-05 (2)	1.29E-05	2.08E-05	7.97E-06
Alluvial soils	2.23E-04 (1)	2.23E-04	2.23E-04	2.23E-04	2.92E-05 (1)	2.92E-05	2.92E-05	2.92E-05
Cultivated areas	9.98E-05 (9)	7.03E-05	2.09E-04	1.30E-05	2.47E-06 (3)	2.30E-06	3.16E-06	1.31E-06

RE method. The arithmetic and geometric averages, the number of the experimental values, and the maximum and minimum value are reported in this table.

9.4 DATA ANALYSIS

9.4.1 Soil saturated conductivity

Even if a strictly mono-dimensional solution, with no account for downstream and lateral capillary effects nor scale effects, is roughly representative of the field physical phenomenon, we attempted to use the Darcy's method especially for the experimental sites (Melezzo Occidentale River basin and Anza River basin) whose water retention relationships were unknown.

In the investigated cases by observing that, after the long imbibition, the soil around the infiltrometer could be considered almost saturated, a piezometric head $p/\gamma_\omega = D$ (see Figure 9.1 and Section 9.2.2) was assumed downstream the infiltrometer. The hypothesis was tested during the laboratory analysis verifying that the 98% of the soils reached saturation at the end of the modified-moisture infiltration tests, and the other soils were close to the saturation. The regression to determine K_s was therefore applied to the data of the final stage of the modified-moisture cumulative infiltration curve.

This method was then applied to the upper soils of the Toce River and of the Mella River basin and compared with the GA (Toce River basin) method and with the RE method (Toce and Mella River basin). In Figure 9.5, the scatter of the soil saturated conductivity of the Toce River basin is represented: it can be seen that the Darcy's method provides an estimate of K_s on average about 1 order of magnitude higher than the RE method, on average. The same behaviour, with a regression coefficient $R^2 = 0.4705$, was observed for the saturated conductivity of the Mella River basin soils. On the other hand, by taking into account the matric potential (GA method) at the wetting front, a better estimate of K_s is provided even using a mono-dimensional representation. In particular, the GA method was applied to the first set of data (about 15 minutes' recording) of the natural-moisture cumulative infiltration curve, until it could be hypothesised that the process was mainly mono-dimensional (see also Section 9.2.2 for details). The RE method, on the other hand, was applied to the final limb of the natural-moisture cumulative infiltration curve in order so that the hypothesis of having an almost constant internal pond was more realistic than at the beginning of the test. Because a soil sample was taken before the beginning of the tests, a reliable estimation of the initial saturation s_e was available. There is a slight difference between the experimental geometry and that proposed by the authors.

A quite good agreement on average, even with a high dispersion, was found (Figure 9.6) between the estimate of the soil saturated conductivity after laboratory experiments and field data (GA method and RE method). The soil volume, and the surface area as well, investigated by the infiltrometer is greater than that of the soil cores for the laboratory measurements. As a consequence, it is more likely that macropores are included in the infiltrometer soil. However, a systematic bias between the laboratory and the RE estimates is not evident. The high dispersion of the data and the limited number of samples for each soil type discourages the attempt to estimate a scale factor (see e.g. Focardi *et al*. 1997, Merz *et al*. 2002) characterising the whole experimental set. In Figure 9.7, the geometric average for each soil class (Toce River basin) is represented, and the RE field method, the Darcy's method and the laboratory estimates are compared.

Table 9.4 Surface soil saturated conductivity for the Mella River basin derived using the Darcy and the Reynolds and Elrick (1991) method. In brackets, the number of the measurements used for the estimation of the saturated conductivity is reported († = arithmetic average, ‡ = geometric average)

Class	K_s [m/s] (Darcy †)	K_s [m/s] (Darcy ‡)	$K_{s,\max}$ [m/s] (Darcy)	$K_{s,\min}$ [m/s] (Darcy)	K_s [m/s] (RE †)	K_s [m/s] (RE ‡)	$K_{s,\max}$ [m/s] (RE)	$K_{s,\min}$ [m/s] (RE)
Discontinuous urban fabric	3.68E-04 (6)	2.67E-04	6.33E-04	2.84E-05	6.20E-06 (6)	4.11E-06	1.55E-05	7.04E-07
Cultivated and wooden agricultural areas	9.78E-04 (3)	2.39E-04	2.76E-03	3.52E-05	5.14E-06 (2)	3.54E-06	8.87E-06	1.42E-06
Grass cov. debris and slope deb.	7.03E-04 (6)	3.45E-04	2.27E-03	1.85E-05	8.83E-05 (6)	1.54E-05	4.57E-04	1.26E-06
Forest cov. debris and slope deb.	1.24E-03 (11)	7.46E-04	2.58E-03	1.67E-05	1.59E-05 (5)	1.31E-05	2.83E-05	4.94E-06
Grass-covered recent alluvia	8.47E-04 (7)	6.73E-04	1.58E-03	1.72E-04	2.81E-05 (6)	1.25E-05	5.41E-05	2.59E-07
Forest-covered recent alluvia	6.71E-04 (7)	1.51E-04	2.99E-03	3.49E-06	8.51E-06 (5)	3.08E-06	3.22E-05	2.50E-07
Grass-covered eluvial-colluvial dregs	5.96E-04 (13)	2.78E-04	3.27E-03	2.23E-05	2.32E-05 (10)	8.32E-06	1.36E-04	8.01E-07
Forest-covered eluvial-colluvial dregs	9.80E-04 (3)	5.73E-04	2.35E-03	2.19E-04	9.51E-06 (1)	9.51E-06	9.51E-06	9.51E-06
Grass-covered glacials	2.57E-04 (3)	1.84E-04	4.07E-04	4.88E-05	4.54E-06 (2)	4.04E-06	6.62E-06	2.47E-06
Grass-covered alluvial fans	1.26E-03 (2)	9.44E-04	2.10E-03	4.25E-04	1.49E-04 (1)	1.49E-04	1.49E-04	1.49E-04
Forest-covered alluvial fans	5.61E-04 (2)	5.51E-04	6.67E-04	4.56E-04	3.67E-05 (1)	3.67E-05	3.67E-05	3.67E-05
Grass-covered conglomerates	1.25E-06 (1)	1.25E-06	1.25E-06	1.25E-06	1.29E-07 (1)	1.29E-07	1.29E-07	1.29E-07
Forest-covered conglomerates	8.37E-04 (2)	6.90E-04	1.31E-03	3.63E-04	2.43E-05 (2)	2.18E-05	3.51E-05	1.36E-05
Grass-covered sand-stones	1.18E-03 (3)	1.05E-03	2.04E-03	7.14E-04	2.34E-05 (2)	2.34E-05	2.35E-05	2.33E-05
Grass cov. limest., dolom. limest., dolost.	4.06E-04 (3)	3.96E-04	5.37E-04	3.20E-04	6.95E-06 (3)	6.54E-06	1.05E-05	5.08E-06
Forest cov. limest., dolom. limest., dolost.	2.34E-03 (5)	1.87E-03	5.12E-03	5.74E-04	5.52E-05 (3)	5.37E-05	7.44E-05	4.36E-05
Grass-covered gneiss	1.21E-03 (3)	1.69E-04	3.33E-03	4.78E-06	3.18E-06 (2)	2.81E-06	4.68E-06	1.69E-06

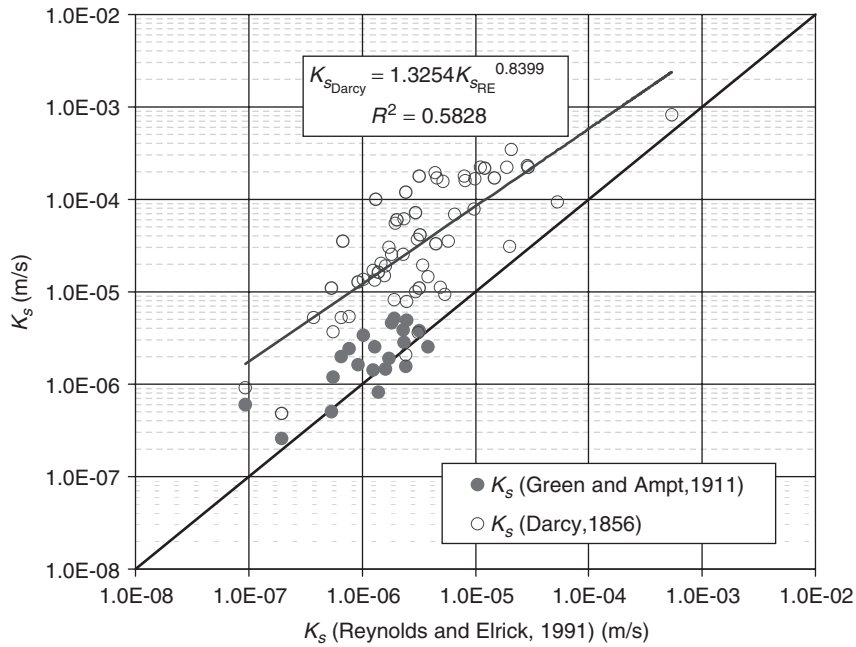


Figure 9.5 Comparison of different estimates of the saturated conductivity after field data for some soils of the Toce River basin

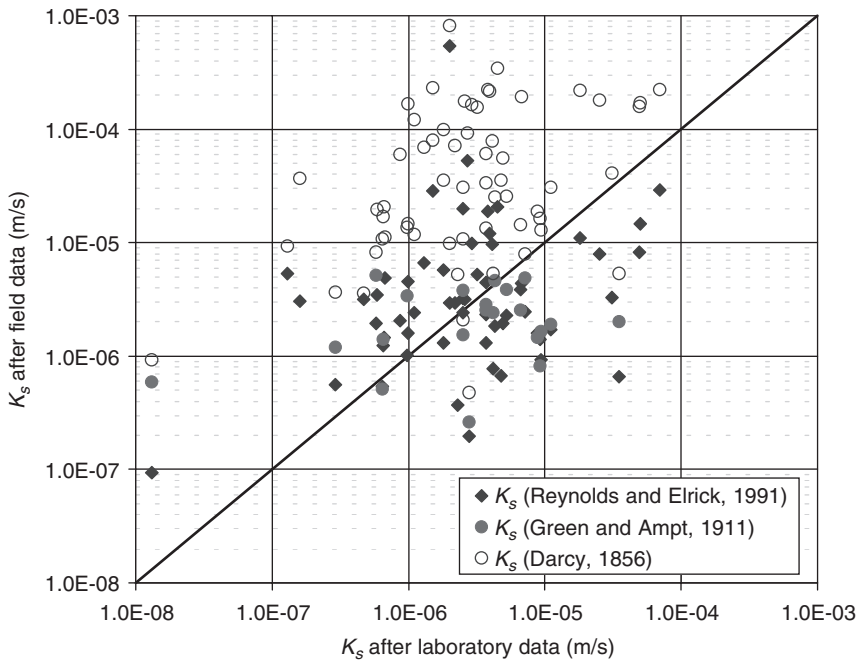


Figure 9.6 Comparison of different estimates of the saturated conductivity after field and laboratory data for some soils of the Toce River basin

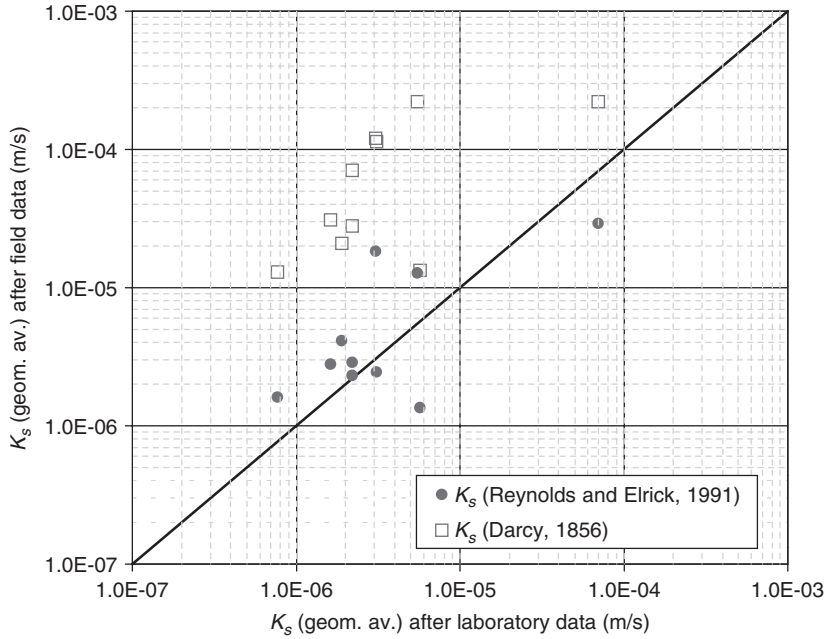


Figure 9.7 Comparison between different estimates of the soil saturated conductivity for the pedogenetic and land-use classes of the Toce River basin map

In order to characterise the behaviour of water in the upper soil layers, in particular, after a long imbibition process as happens during heavy rainfall events when the soil on the surface can be considered almost saturated, the saturated conductivity of the first layers of the soil was investigated. The soil saturated conductivity is generally expected to decrease with the depth of the upper soil layers. The trend is due to the presence of an impervious layer of non-completely decayed organic matter and eluvial particles, altered by the physical and chemical processes on the soil surface, and to the finer texture of the soil particles. Such results, which are often assumed by hillslope hydrological models (Beven and Kirkby 1979), were also found during these field campaigns by comparing the estimate of the upper layer with the lower layers saturated conductivity. In Figure 9.8, the lower layers K_s (Darcy method), normalised using the surface saturated conductivity, are presented for the soils of the Melezzo Occidentale River basin and of the Anza River basin. So it can be expected that once the soil surface is saturated, such as at the end of heavy rainfall events, the response of the soil to the rainfall is mainly governed by the lower layers with lower soil saturated conductivity.

As often assumed in modelling the hillslope runoff response (Beven and Kirkby 1979, Kirkby 1985), an exponential decay of the saturated conductivity with depth can be used to fit the observations:

$$\frac{K_s(z)}{K_s(0)} = \mathrm{e}^{fz}, \tag{9.12}$$

where z is positive upward as previously assumed, and $K_s(0)$ is the surface soil saturated conductivity. From our data over vertical saturated conductivity, a value of the exponential decay constant $1/f = 0.19\,\mathrm{m}$ was found. This value is consistent with the range of the decay constant of the saturated lateral conductivity (between 0.2 and 0.4 m) estimated by Beven (1983) over a 27 soils set. However, the high dispersion of data keeps in evidence the importance of the depth of the single horizons due to the different local pedogenetic processes and the degree of development of the soil. Moreover, these inhomogeneities point out the difficulty, for applications involving the investigated areas, to extend a theoretical framework of the hillslope runoff process to the whole basin.

Finally, because of the competition between erosional, transport and sedimentation processes, soils are expected to be coarser as the altitude increases, and so also the soil saturated conductivity, mainly due to the macropores between the soil particles, is expected to increase. The

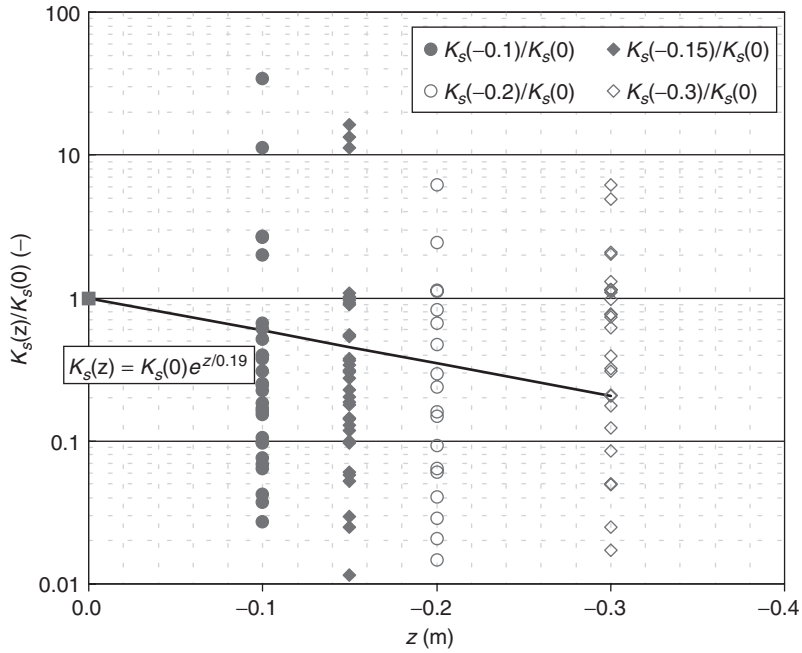


Figure 9.8 Comparison between the saturated conductivity in the upper soil layers (field data of the soils of the Anza River basin and of the Melezzo Occidentale River basin)

saturated conductivity of the soils of the Toce River basin, estimated after laboratory analysis, is plotted versus the altitude of the experimental site. In a qualitative agreement with results reported for another mountain basin of the central Italian Alps (Orlandini *et al*. 1999), an increase in soil saturated conductivity of about 1 order of magnitude over a 2000-m altitude increase can be observed in Figure 9.9. The slope and the correlation of the regression line of the logarithms of K_s versus altitude is different from zero with a 0.05 significance, although the spread of the data is very high.

9.4.2 Water retention relationships

Some samples from the Toce River basin and from the Mella River basin were investigated to attempt a classification of the water retention parameters. The experimental water retention relationships are interpolated using the Gardner and the Brooks and Corey theoretical relationship. In Figure 9.10, the Brooks and Corey relationships of two different soils of the Toce River basin are plotted together with the experimental points. The variation of the pore-size distribution index λ is also superimposed. As it can be seen, the pore-size distribution index λ decreases with finer soil texture, such that, at the same saturation degree, more energy is needed to extract a unitary weight of water.

The standard practice to estimate the water retention parameters for hydrological and climatological models (PILPS 1994) on the basis of the texture classification seems not to be completely reliable, at least for these mountain soils. In Figure 9.11, in fact, average values for the Brooks and Corey's parameters, with the standard deviation as error bar, are represented versus the ASTM grain size classification: a clear trend of the parameters does not seem to be recognisable with increasing characteristic soil grain size. Some sandy soil samples from the Toce River basin (Eccel *et al*. 2001) and the samples from the Mella River basin were investigated to observe the sensitivity of the water retention parameters to the organic matter x_o.

In Figure 9.12, the Brooks and Corey's parameters of the water retention relationship, the pore-size distribution index and the bubbling pressure are plotted against the organic matter for three soils characterised by dominant sand. The pore-size distribution index λ seems to be more sensitive than the bubbling pressure Ψ_b to the organic matter x_o: in particular, at increasing values of x_o a decrease of λ can be observed. So, applying Equation (9.5), the same effective saturation s_e needs a great energy to be extracted as the organic matter

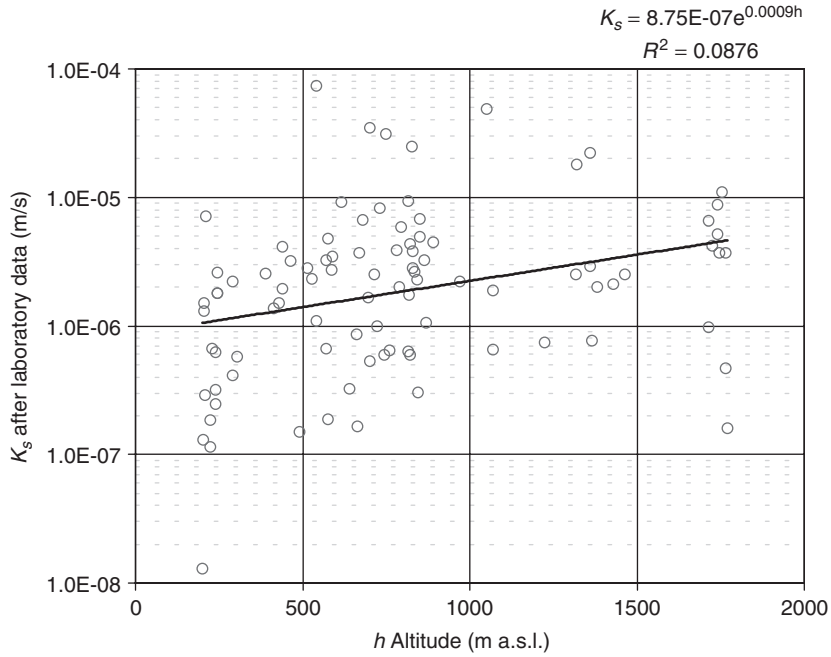


Figure 9.9 Dependency on the altitude of the saturated conductivity of the soils of the Toce River basin (laboratory analysis)

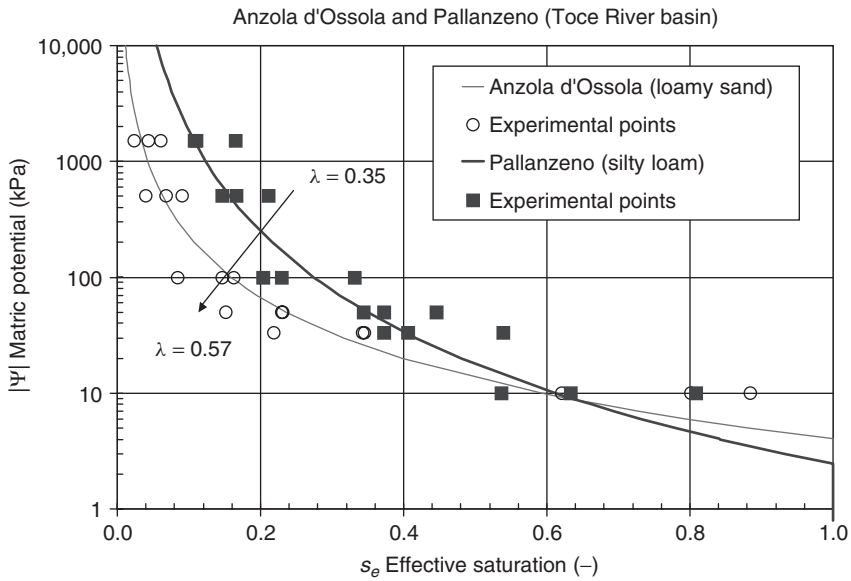


Figure 9.10 Soil water retention relationships of a loamy sand and of a sandy loam sample from the Toce River basin: experimental data and Brooks and Corey theoretical relationship

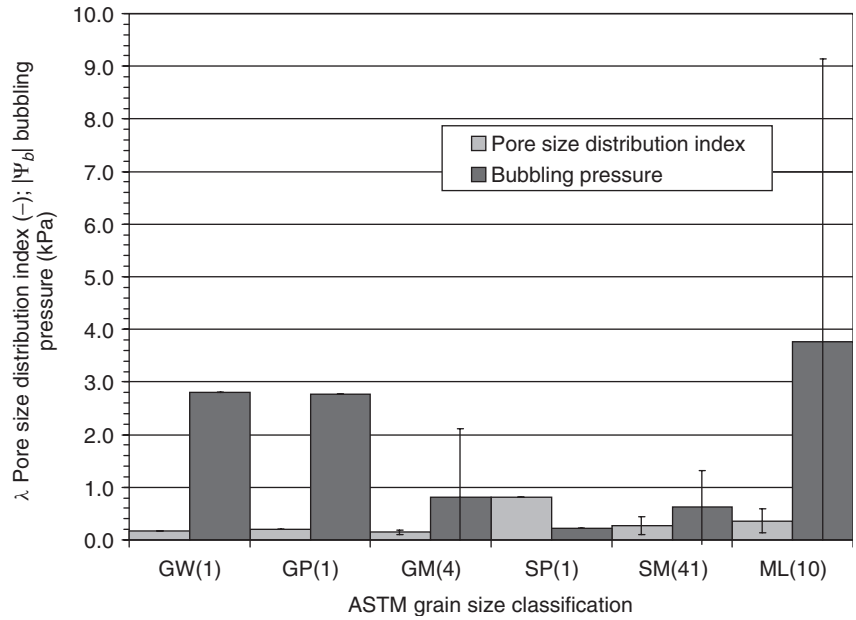


Figure 9.11 Average values of the Brooks and Corey's parameters of some soils of the Toce River basin plotted versus the ASTM grain size classification. The standard deviation is represented as error bar. In brackets, the number of the experienced soils is represented

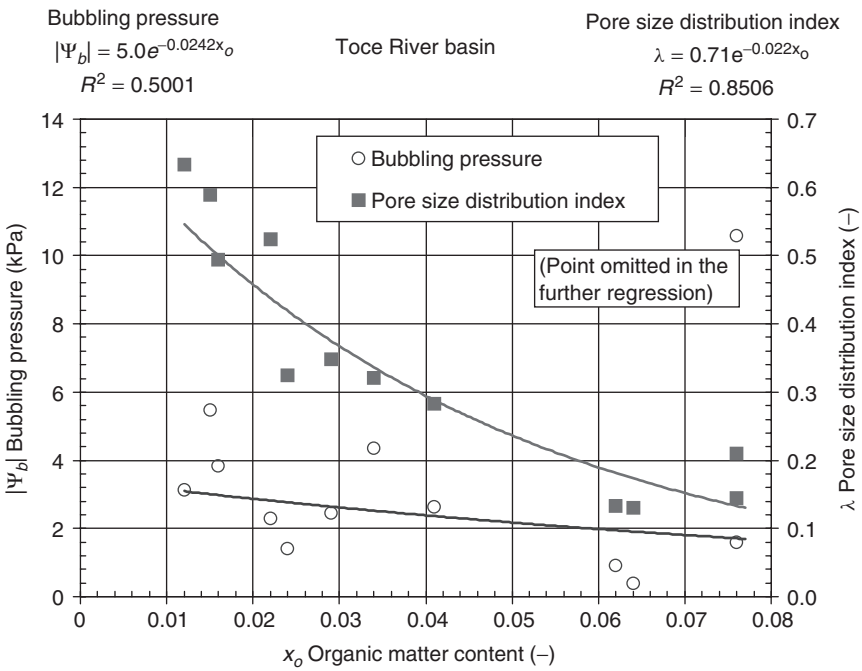


Figure 9.12 Brooks and Corey's parameters plotted against the organic matter content (x_o) for some sandy soils of the Toce River basin

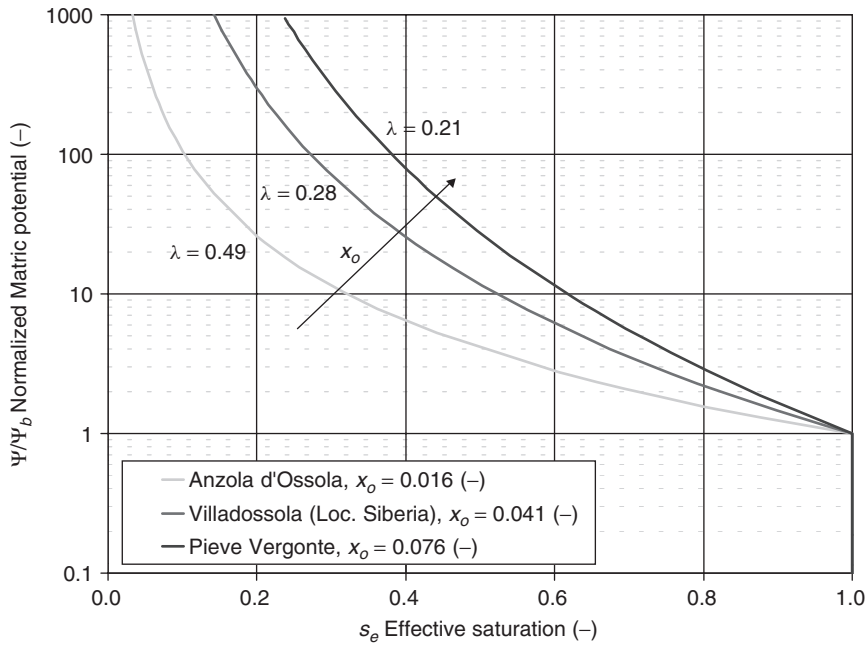


Figure 9.13 Water retention relationships of three sandy soils of the Toce River basin characterised by different organic matter content (x_o)

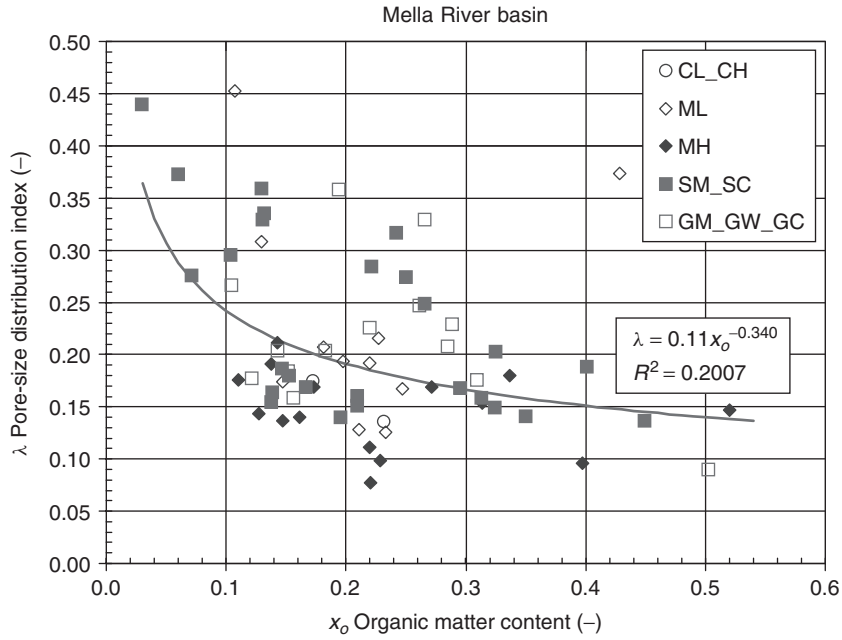


Figure 9.14 Sensitivity of the pore-size distribution index of some soils of the Mella River basin to the organic matter content and to grain size distribution

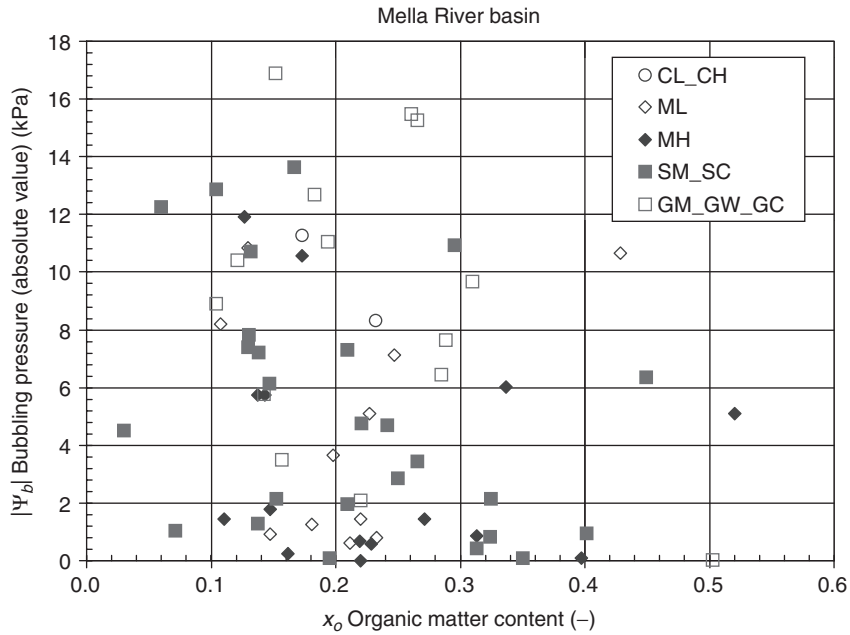


Figure 9.15 Sensitivity of the bubbling pressure of some soils of the Mella River basin to the organic matter content and to the grain size distribution

increases, and the effect is more evident at lower soil moisture contents. This fact is kept in evidence in Figure 9.13, which represents three water retention relationships of the same soils, normalised in regard to the bubbling pressure.

Also for the samples from the Mella River basin, a similar behaviour for different soil classes was observed, both on the basis of a texture classification (Figures 9.14 and 9.15) and on the soil saturated conductivity classes (not presented in the figures). The pore-size distribution index of different soils of the same class seems to be quite sensitive to the organic matter, while a trend is hard to recognise for the bubbling pressure. Considering particularly Figure 9.14, the organic matter seems to significantly affect the variation of the pore-size distribution index particularly for sand- and gravel-soils, with a decreasing λ with increasing x_o. Observing the high spread of the data of the same textural class, the organic matter content seems to have almost the same importance in the determination of the pore-size distribution index as the grain size distribution.

As previously mentioned, the water retention relationships of some soils were measured also over bulk and crumbled samples to verify the sensitivity of this technique to the sieving. Therefore, the moisture values, corrected with the skeletal fraction to homogenise them with the values measured over sieved samples, were compared with the corresponding water retention values of the same soils sieved at 2 mm. A good agreement (Figure 9.16) can be observed, so that the water retention relationships derived over sieved samples could be considered quite representative of the soil conserving its original structure. The agreement is better as the soil moisture decreases, that is, for higher values of the suction, as it has been pointed out in Salter and Williams (1965), but also at higher moisture values, the difference between moisture in disturbed and non-disturbed samples is low. The practice of sieving the samples if the skeletal fraction is high, as in the investigated soils, can be therefore considered quite reliable in determining the water retention relationships.

9.5 CONCLUSIONS

In the context of a long-term research programme, 146 and 80 sites of two mountain basins in the Italian Alps were investigated in order to produce realistic maps of the hydrological properties of surface soils. The two basins are dominated by metamorphic and sedimentary rocks, respectively, and soils have a small thickness so that the runoff and flood formation is heavily controlled by the upper soil layers. For their

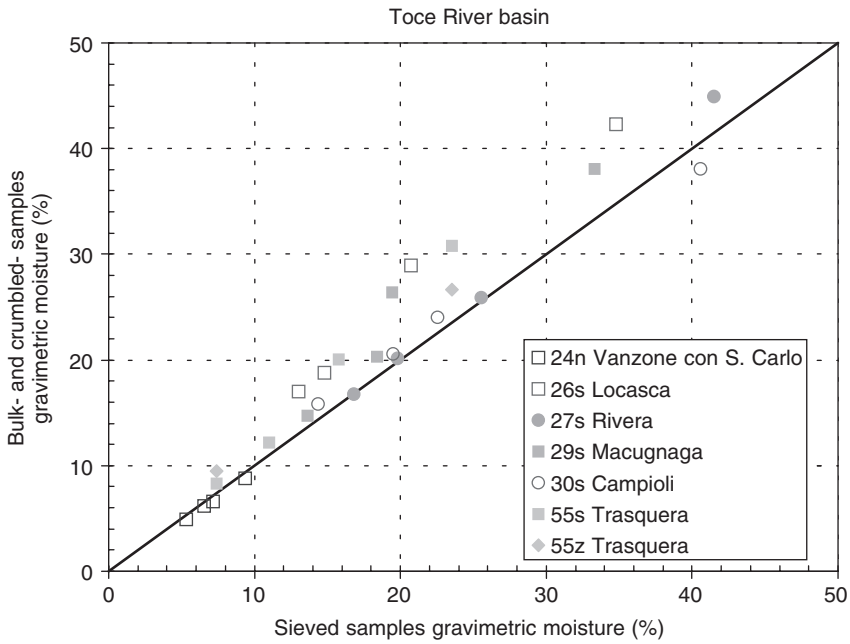


Figure 9.16 Comparison between the moisture of sieved- and bulk- or crumbled- samples for some soils of the Toce River basin

characteristics, the investigated areas are representative of the typical geopedological conditions of the mountain basins in the Italian Alps. This research seems then to be of some interest because, at the date, there is only little experimental information about the hydraulic behaviour of the upper soil layers of experimental basis in this side of the Alps. On the other hand, a comparison can be done with the values of the upper layer saturated conductivity of the adjacent Ticino watershed (Eidg. Forschungsanstalt für Landwirtschaftlichen Pflanzenbau 1980). The soil saturated conductivity expected for soils in the Ticino River basin is on average 1 order of magnitude higher than that expected for soils in the Toce River basin. From a hydrological point of view, the two basins seem to be characterised by a completely different mechanism of stormflow formation.

The single ring infiltrometer was used, as a standard reference method, to conduct field campaigns. The traditional way of interpreting the field infiltrometer data, based on an application of the Darcy's law, lead to values of the vertical soil saturated conductivity higher than those observed after laboratory analysis. Therefore, other methods, namely, Green and Ampt, modified with respect to the ponding depth in the infiltrometer; and Reynolds and Elrick (1991), to better take into account the ponding depth and the infiltrometer geometry, were applied to give a more realistic representation of the process. The application of these two methods resulted in soil saturated conductivities closer to those obtained in laboratory with a falling head permeameter without any evident bias that would be *a priori* expected because of the different size of soil volume. Moreover, a bias of about 1 order of magnitude with quite a good agreement was observed between the Darcy method and the Reynolds and Elrick method. Saturated conductivity ranging from 2.92×10^{-5} to 1.35×10^{-6} m/s was observed for soils with different pedogenesis and land use in the Toce basin, while for the Mella river the vertical saturated conductivity ranges between 1.49×10^{-4} and 1.29×10^{-7} m/s.

Also the first layers of the soil were investigated and for several sites a less permeable layer was found just a few centimetres below the surface. In particular, for the soils of the Toce riverbasin, the exponential decay constant was estimated about 0.19 m. Therefore, considering the water path across the first soil layers, the infiltration should be governed by the lower layers of the soil and the runoff production as well, at least in a ''hortonian-infiltration excess'' theoretical framework.

The saturated conductivity of the soils of the Toce River basin was plotted versus altitude and a weak, but statistically significant, positive trend of the surface soil saturated conductivity can been observed as the altitude increases. Such a behaviour is probably due to

the eluvium of the smaller particles in the higher soils and to the differential sedimentation as the slope gradient decreases downstream.

The water retention relationships of sieved and bulk or crumbled samples were measured finding that the traditional method of sieving the soil to prepare the samples does not seem to affect the results. The organic matter was found to have almost the same influence on the soil textural class in determining the pore-size distribution index and the behaviour of the water retention relationships especially at low degrees of saturation. In particular, a decreasing of the pore-size distribution index was found at the increasing of the organic matter content in the soil. The exponential law $\lambda = 0.71 \exp(-0.022 x_o)$, and the power law $\lambda = 0.11 x_o^{-0.340}$ were proposed respectively for the soils of the Toce River basin and of the Mella River basin.

This means that for hydrological and climatological applications, further research efforts are needed to provide methods to estimate first the spatial variability of organic matter, more than soil texture at the basin scale or land use. The wide spread of the data within each soil and land-use class, depending on the site location, poses serious limitations on the accuracy of the derived maps at the basin scale, even when derived after extensive investigations. Uncertainties up to 1 order of magnitude or even higher in the estimation of saturated conductivities of unknown soils can still remain after extensive measurements. How these uncertainties affect the reproduction of flood events in mountain basins will be the subject of future analyses.

9.6 ACKNOWLEDGEMENTS

This research was conducted in the context of the projects RAPHAEL (Contract ENV4-CT97-0552), CNR – GNDCI ''VAPI RIVERS'' and CNR- ''MAP''. The students who helped us for several months in the field and laboratory to collect most of the data we analysed are gratefully thanked.

Two anonymous reviewers are acknowledged for their suggestions and criticism to the first version of the manuscript.

REFERENCES

Bacchi B, Grossi G, Ranzi R, Buzzi A (2002) On the use of coupled mesoscale meteorological and hydrological models for flood forecasting in midsize mountain catchments: operational experience and verification. In: Wu B, Wang Z-Y, Wang G, Huang GGH, Fang H, Huang J (eds) *Proceedings of the 2nd International Symposium on Flood Defence*. Beijing, 10–13 September 2002, ed. by Wu *et al*., Science Press, New York, ISBN 1-880732-54-0, Vol. II: 965–972. Science Press, New York.

Bacchi B, Ranzi R (eds) (2000) Runoff and atmospheric processes for flood hazard forecasting and control. Contract ENV4-CT97-0552 Final Report, Brescia.

Bagarello V, Iovino M, Tusa G (2000) Factors affecting measurement of the near-saturated soil hydraulic conductivity. *Soil Science Society of America Journal* **64**: 1203–1210.

Bear J (1972) *Dynamics of Fluids in Porous Media*. Dover, New York.

Benson CH, Gunter JA, Boutwell GP, Trautwein SJ, Berzanskis PH (1997) Comparison of four methods to assess hydraulic conductivity. *Journal of Geotechnical and Geoenvironmental Engineering* **123**: 929–937.

Beven KJ (1982) On subsurface stormflow: predictions with simple kinematic theory for saturated and unsaturated flows. *Water Resources Research* **18**: 1627–1633.

Beven KJ (1983) *Introducing Spatial Variability into TOPMODEL: Theory and Preliminary Results*. Report of the Department of Environmental Sciences, University of Virginia.

Beven KJ, Kirkby MJ (1979) A physically-based variable contributing area model of basin hydrology. *Hydrological Science Bulletin* **24**: 43–69.

Boadu FK (2000) Hydraulic conductivity of soils from grain-size distribution: new models. *Journal of Geotechnical and Geoenvironmental Engineering* **126**: 739–746.

Bougeault P, Binder P, Buzzi A, Dirks R, Houze R, Kuettner J, Smith RB, Steinacker R, Volkert H (2001) The MAP special observing period. *Bulletin of the American Mathematical Society* **82**: 433–462.

Braud I, Varado N, Galle S, Haverkamp R, Lebel T, Reggiani P (2001) Modélisation hydrologique du bassin versant de l'Ouémé à l'aide du modèle POWER. *Proceedings of the Atelier de Modélisation de l'Atmpsphère*, Toulouse, Décembre 3–4, 2001, **107**: 110.

Brooks RH, Corey AT (1964) *Hydraulic Properties of Porous Media*, Hydrology paper No. 3. Colorado State University, Fort Collins, CO.

Burdine NT (1952) Relative permeability calculation from pore-size distribution data. *Petroleum Transactions of the American Institute of Minning, Metallurgical and Petroleum Engineers* **198**: 71–77.

Campbell GS (1974) A simple method for determining unsaturated conductivity from moisture retention data. *Soil Science* **117**: 311–314.

Cavazza L (1981) *Fisica del Terreno Agrario*. UTET, Torino.

Chow VT, Maidment DR, Mays LW (1988) *Applied Hydrology*. McGraw-Hill, London.

Clapp RB, Hornberger GM (1978) Empirical equations for some soil hydraulic properties. *Water Resources Research* **14**: 601–604.

Clerici A, Cantoni A (2000) Misure in Sito ed in Laboratorio della Velocità di Infiltrazione e della Permeabilità dei Terreni Superficiali nel Bacino del Fiume Toce (Piemonte, Italia). Technical Report of the Dept of Civil Eng No. XIII/2000, Università di Brescia, Brescia.

Darcy H (1856) *Le Fontaine Publiques de la Ville de Dijon*. Dalmont, Paris.

Dunne T (1978) Field study of hillslope flow processes. In: Kirkby MJ (ed) *Hillslope Hydrology*. Wiley Interscience, New York 227–293.

Eagleson PS (1970) *Dynamic Hydrology*. McGraw-Hill, New York.

Eccel E, Sicher L, Toller G (2001) The field and laboratory measurements of soil hydraulic properties in the MAP – SOP 1999 TOCEX Experiment. Technical Report 10.VI, edited by R. Ranzi e B. Bacchi, Dipartimento di Ingegneria Civile dell'Università di Brescia, Brescia.

Eidg. Forschungsanstalt für Landwirtschaftlichen Pflanzenbau (1980) *Bodeneignungskarte der Schweiz*. Eidg. Drucksachen- und Materialienzentrale, Bern.

Evett SR, Peters FH, Jones OR, Unger PW (1999) Soil hydraulic conductivity and retention curves from tension infiltrometer and laboratory data. In: Van Genuchten MTh, Leij FJ, Wu L (eds) *Proceedings of the International Workshop Characterization and Measurement of the Hydraulic Properties of Unsaturated Porous Media*. University of California, Riverside 541–551.

Focardi P, Gabbani G, Gargini A, Pressi E (1997) Confronto di Risultati di Prove Sperimentali di Permeabilità Eseguite con Metodi Diversi su un Limo con Sabbia Argilloso. Pubblicazione n°1586 CNR – GNDCI. *Geologia Tecnica e Ambientale* **4/97**: 29–38.

Gardner WR (1958) Some steady-state solutions of the unsaturated moisture flow equation with application to evaporation from water table. *Soil Science* **85**: 228–232.

German PF, Beven K (1985) Kinematic wave approximation to infiltration into soils with sorbing macropores. *Water Resources Research* **21**: 990–996.

Green WH, Ampt GA (1911) Studies on soil physics. I flow of air and water through soils. *Journal Agric Science* **4**: 1–24.

Haverkamp R, Parlange JY (1986) Predicting the water-retention curve from particle size distribution: 1. Sandy soils without organic matter. *Soil Science* **142**: 325–339.

Hazen A (1911) Discussion of ''Dams on sand foundations'' by AC Koenig. *Transactions of the American Society of Civil Engineers* **151**: 153–163.

Jasper JH, Gurtz J, Lang H (2002) Advanced flood forecasting in Alpine watersheds by coupling meteorological observations and forecasts with a distributed hydrological model. *Journal of Hydrology* **267**: 40–52.

Kirkby MJ (1985) Hillslope Hydrology. In: Anderson MG, Burt TP (eds) *Hydrological Forecasting*. John Wiley & Sons.

Klute A (1986) Water retention: laboratory methods. In: Klute A (ed) *Methods of Soil Analysis, Part I, Physical and Mineralogical Methods*. Soil Science Society of America, Madison.

Klute A, Dirksen C (1986) Hydraulic conductivity and diffusivity: laboratory methods. In: Klute A (ed) *Methods of Soil Analysis, Part I, Physical and Mineralogical Methods*. Soil Science Society of America, Madison.

Kouwen N, Benoit R (2002) Regional forecasting of river flows using a high resolution numerical weather model coupled to a hydrological model. Proceedings of the International Conference on Flood Estimation. Bern March 6–8, 2002. In print.

Kozeny J (1927) Uber Kapillare Leitung des Wassers in Boden. *Sitzungsber Akad Wiss Wien Math Naturwiss Kl Abt 2a* **136**: 271–306.

Merz B, Bárdossy A, Schiffer GR (2002) Different methods for modelling the areal infiltration of grass field under heavy precipitation. *Hydrological Processes* **16**: 1383–1402.

Montaldo N, Toninelli V, Mancini M, Rosso R (2002) Coupling limited area models with distributed hydrologic models for flood forecasting: the Toce Basin case study. *International Association of Hydrological Sciences* **274**: 229–236.

Mualem Y (1976) A new model for predicting the hydraulic conductivity of unsaturated porous media. *Water Resources Research* **12**: 513–322.

Orlandini S, Perotti A, Sfondrini G, Bianchi A (1999) On the storm flow response of upland Alpine cathments. *Hydrological Processes* **13**: 549–562.

Pachepsky YaA, Rawls WJ (1999) Accuracy and reliability of pedotransfer functions as affected by grouping soils. *Soil Science Society of America Journal* **63**: 1748–1757.

Perroux KM, White I (1988) Designs for disc permeameters. *Soil Science Society of America Journal* **52**: 1205–1215.

Philip JR (1968) Steady infiltration from buried point sources and spherical cavities. *Water Resources Research* **4**: 1039–1047.

Philip JR (1984) Steady infiltration from circular cylindrical cavities. *Soil Science Society of America Journal* **48**: 270–278.

PILPS (1994) *Soil Moisture Simulation. A report of the RICE and PILPS Workshop*. International Gewex Project Office, Publication Series No. 14, p. 179.

Quadri MB, Clothier BE, Angulo-Jaramillo R, Vauclin M, Green SR (1994) Axysimmetric transport of eater and solute underneath a disk permeameter: experiments and numerical model. *Soil Science Society of America Journal* **58**: 696–703.

Raats PAC (1971) Steady infiltration from point sources, cavities and basins. *Soil Science Society of America Proceedings* **35**: 689–694.

Ranzi R, Bacchi B, Grossi G (2003) Runoff measurements and hydrological modelling for the estimation of rainfall volumes in an Alpine basin. *Quarterly Journal of the Royal Meteorological Society* **129**: 653–672.

Ranzi R, Bochicchio M, Bacchi B (2002) Effects on floods of recent afforestation and urbanisation in the Mella River (Italian Alps). *Hydrology and Earth System Sciences* **6**(2): 239–253.

Reynolds WD, Elrick DE (1990) Ponded infiltration from a single ring: I analysis of steady state flow. *Soil Science Society of America Journal* **54**: 1233–1241.

Reynolds WD, Elrick DE (1991) Determination of hydraulic conductivity using a tension infiltrometer. *Soil Science Society of America Journal* **55**: 633–639.

Reynolds WD, Elrick DE, Clothier BE (1985) The constant head well permeameter: effect of unsaturated flow. *Soil Science* **139**: 172–180.

Richards LA (1931) Capillary conduction of liquids through porous medium. *Physics* **1**: 318–333.

Richards LA (1949) Methods of measuring soil moisture tension. *Soil Science* **68**: 95–112.

Rossi Pisa P (1997) Conducibilità idraulica del suolo saturo. In: Pagliai M (ed) *Metodi di Analisi Fisica del Suolo*. *Ministero per le Politiche Agrarie – Istituto Sperimentale per la Nutrizione delle Piante, Franco Angeli Edizioni*, Milano.

Salter PJ, Williams JB (1965) The influence of texture on the moisture characteristics of soils. I. A critical comparison of techniques for determining the available-water capacity and moisture characteristic curve of a soil. *Journal of Soil Science* **16**: 1–15.

Santini A, Romano N, Ciollaro G, Comegna V (1995) Evaluation of a laboratory inverse method for determining unsaturated hydraulic properties of a soil under different tillage practices. *Soil Science* **160**: 340–351.

Schwartz RC, Evett SR (2002) Estimating hydraulic properties of a fine-textured soil using a disc infiltrometer. *Soil Science Society of America Journal* **66**: 1409–1423.

Sisson JB, Van Genuchten MTh (1991) An improved analysis of gravity drainage experiments for estimating the unsaturated soil hydraulic functions. *Water Resources Research* **27**: 569–575.

Smith RE, Hebbert RHB (1983) Mathematical simulation of interdependent surface and subsurface hydrologic processes. *Water Resources Research* **19**: 987–1001.

Van Genuchten MTh (1980) A closed-form equation for predicting the hydraulic conductivity of unsaturated soils. *Soil Science Society of America Journal* **44**: 892–898.

Warrick AW (1974) Time-dependent linearised infiltration. I. Point sources. *Soil Science Society of America Journal* **38**: 383–386.

Weir GJ (1987) Steady infiltration from small shallow circular ponds. *Water Resources Research* **23**: 733–736.

Wooding RA (1968) Steady infiltration from a shallow circular pond. *Water Resources Research* **4**: 1259–1273.

Wu L, Pan L, Mitchell J, Sanden B (1999) Measuring saturated hydraulic conductivity using a generalized solution for single-ring infiltrometers. *Soil Science Society of America Journal* **63**: 788–792.

PART III: EVAPOTRANSPIRATION AND WATER BALANCE

Climate and Hydrology in Mountain Areas. Edited by C. de Jong, D. Collins and R. Ranzi
© 2005 John Wiley & Sons, Ltd. ISBN: 0-470-85814-1

10

Water Balance Modeling with Fuzzy Parameterizations: Application to an Alpine Catchment

GERALD EDER[1], HANS-PETER NACHTNEBEL[1] AND MURUGESU SIVAPALAN[2]

[1]Institute of Water Management, Hydrology and Hydraulic Engineering, University of Natural Resources and Applied Life, Muthgasse 18, A-1190 Vienna, Austria, [2]Centre for Water Research, University of Western Australia, 35 Stirling Highway, Crawley W.A. 6009, Australia

10.1 INTRODUCTION

Hydrologists often find themselves in situations in which they have to determine parameter and input values for hydrological models on the basis of uncertain information. In many cases of catchment modeling there is no or inadequate information available to estimate the parameter and input values with the kind of precision required of deterministic models. If only data from point observations and measurements are available, the modeler faces great difficulty interpreting and using this data for the modeling effort at the catchment scale. The problem of lack of data is especially critical in ungaged catchments since there is no prospect of estimating the parameter values by calibration. Thus, methods that permit the incorporation of all sources of information, especially uncertain and heuristic information, would be very valuable toward the development of hydrological predictive models. In recent years, calls to include the ability to estimate measures of predictive uncertainty as part of the development of hydrological models have increased, especially in the light of our realization of ''equifinality'' of model structures and parameterizations (Beven 2001; Freer *et al*. 1995). Equifinality is the term given to the phenomenon whereby many or infinite combinations of parameter values (and even model structures) can give rise to the same levels of fit to observed data, making the identification and estimation of parameter values a nontrivial task, especially when models are overly complex. Hydrologists have in the past tended to aim for higher and higher levels of precision in model formulations, parameterizations and computations while ignoring the quality of information that serves as the basis for their inference. It has been suggested that this problem can be addressed more easily with fuzzy logic than with some other methods (Dubois and Prade 1986, 1988; Franks and Beven 1999; Franks *et al*. 1997).

There are two alternative approaches for the incorporation and prediction of uncertainty in hydrological models: (i) the traditional stochastic approach based on the treatment of all parameters and variables as random variables, with specified or derived probability distributions; and (ii) methods based on fuzzy logic, a radically different approach not based on the treatment of the variables as random variables but as fuzzy numbers, and offering a number of advantages compared to the stochastic approaches. Methods based on the stochastic approach

Climate and Hydrology in Mountain Areas. Edited by C. de Jong, D. Collins and R. Ranzi
© 2005 John Wiley & Sons, Ltd. ISBN: 0-470-85814-1

are already widely established in hydrology (Garen and Burges 1981; Gelhar 1986), and interpretation of their results for decision-making is fairly straightforward and well established. However, catchment hydrological systems are extremely complex, comprising nonlinear interactions of many interdependent processes. Consequently, stochastic approaches have the disadvantage that the mapping of uncertainties between inputs and parameters to the outputs cannot be done analytically, and can only be done through Monte Carlo procedures, which are highly computationally intensive, except for the simplest of models. Stochastic methods have the additional disadvantage that with the information currently available, it is not possible, or at the very least not easy, to completely prescribe the probability density functions of all of the inputs and parameter values.

As opposed to the difficulty in estimating precise values of catchment properties, model parameters or their probability distributions, hydrologists, with experience, should be in a better position to specify the intervals within which the catchment properties, and hence the model parameters, may lie. In the fuzzy water balance model presented in this paper, fuzzy membership functions are used to characterize catchment physiographic properties, and consequently parameter values, and model predictions of hydrologic state variables and fluxes are also presented in terms of fuzzy membership functions.

Despite the paucity of actual measured databases from which probability distributions can be estimated for various catchment characteristics and climatic inputs, much heuristic information is available and can be supplied by ''experts'' who have worked in the respective regions. The fuzzy approach has the advantage that it can deal with any available quantitative information, and can also incorporate qualitative and heuristic information (Türksen 1991; Civanlar and Trussel 1986; Hisdal 1994). Computations within the fuzzy framework, using the rules of fuzzy arithmetic, are easy and straightforward. The fuzzy approach has the additional advantage that the model outputs are characterized by grades of fuzzy membership, expressing the reliability of the model predictions, thus leading to a realistic estimation of predictive uncertainty. The theory of fuzzy systems on which this method is based (Zimmermann 1995) can therefore bring us one step closer to resolving a hydrological dilemma, namely about how to develop models of a complexity commensurate with the quality of, and uncertainty in, meteorological input data and the catchment's physiographic properties.

On the other hand, fuzzy approaches have the disadvantage that the interpretation of the results coming from analyses and simulations based on fuzzy logic are not widely known or understood in natural sciences and in engineering practice. Because of the inability to convert fuzzy predictions into probability distribution functions of model outputs, engineers tend to show a preference for traditional stochastic methods in spite of their inherent disadvantages discussed before.

10.1.1 Scientific objectives

In this paper, we present an application of the fuzzy modeling approach to the Upper Enns catchment in central Austria. On the basis of fuzzy temperature and precipitation time series, and fuzzy parameter values relating to catchment physical properties, and fuzzy climatic inputs, we estimate the runoff components including surface flow, interflow and baseflow, as well as snow cover, evapotranspiration and soil water storage, at timescales ranging from a day to the whole year. The key scientific objectives of the study are, briefly, as follows.

- To present a formulation of a lumped water balance model based on fuzzy logic, and explore its suitability for continuous precipitation-runoff modeling;
- To demonstrate the ability of the fuzzy model to quantify the relative importance of various parameters and input values;
- To demonstrate the interconnections between model complexity, predictive uncertainty and accuracy of predictions.

In this respect, this paper represents merely an initial application of the fuzzy logic methodology to the Upper Enns catchment. The extension of the model to address the more general problem of prediction of ungaged catchments is left for future work, this paper representing the first few steps of this enormously challenging task.

10.1.2 Outline of this paper

This paper begins with a discussion of the sources of uncertainty and imprecision in hydrological modeling, followed by a brief, basic introduction to the theory of fuzzy logic. We next give an introduction to the Upper Enns case study catchment and present the description of the water balance model, at the daily time step, that has been developed previously for this catchment (Eder *et al*. 2003). The model is based on a small set of physically meaningful catchment parameters that serve as surrogate indicators of emergent properties of the catchment's hydrology with changing timescales, most

of the parameters being estimated *a priori* from available spatial information, such as soils maps.

A state-space approach (Özelkan and Duckstein 2001) is adopted for the presentation of the model equations, and the model is then expressed in a fuzzy framework. Because of fuzzy parameters and climatic inputs, all model state variables or outputs will also be fuzzy, and the state transition and output functions can be constructed through rules of fuzzy arithmetic. On the basis of analysis of all available information, we then describe the formulation of the parameters and input variables of this model for this catchment, within the new fuzzy framework, in terms of fuzzy membership functions. Following this section, we present applications of the fuzzy water balance model to this catchment and utilize the model, through systematic and step-by-step sensitivity analysis, to investigate the relative importance of model parameters, climatic inputs and model structure (complexity) on the resulting uncertainty of model predictions.

10.2 UNCERTAINTY AND IMPRECISION

Sources of uncertainty in hydrological modeling can be separated into two groups: (1) structural uncertainty, and (2) parameter uncertainty. Structural uncertainty refers to uncertain knowledge of the overall functioning of the catchment and the uncertainty in the model structures used to capture this. Parameter uncertainty refers to the uncertainty of the inputs to, and the parameters of, an assumed model structure.

10.2.1 Structural uncertainty

We still do not have a perfect understanding of the climate, soil, vegetation and topographic controls on water balance, therefore leading to inadequate representations of catchment water balance in hydrological models. Attempts at applying physically based models at the catchment scale have not been entirely successful owing to lack of data or to model overparameterization. The theories on which these models are based are dependent on small-scale physics, whereas the model applications are often at the catchment scale. A large number of conceptual models have been built, and their performances evaluated. Alley (1984), Franchini and Pacciani (1991) and Chiew *et al*. (1993) compared a number of frequently applied water balance models of different levels of complexity. Their conclusions are clear and consistent. For example, Alley (1984) stated that simulated values of a state variable, such as soil moisture storage, differ strongly among models with optimized parameters, sometimes indicating an entirely different type of basin response to precipitation. Therefore, the physical appropriateness of many model structures and parameters, as well as that of the assumed state variables, has been unclear. Often, many different models are shown to produce similar fits to observed data, thus leading to structural uncertainty.

Model development requires the support of data analysis, interpretation, hypothesis testing and the reconciliation of model concepts with field observation (Beck 1994). The distillation of hypothesis is essential to model formulation and may help eliminate unsound preconceptions more swiftly than might otherwise be the case (Wheater and Beck 1995; Eder *et al*. 2003). Yet mostly this is not the way model structures are chosen or adopted. Instead, they are often chosen arbitrarily, the choices made *a priori* on the basis of previous system knowledge, or on model structures adopted by others.

In previous work (Eder *et al*. 2003), an alternative, data driven, ''downward'' approach to model conceptualization (Sivapalan *et al*. 2003), based on emergent properties with changing time scales, was presented. This approach was followed to build models, through hypothesis testing, based on the use of signatures of runoff variability, progressively at the annual, then monthly and finally daily timescales. Hydrological processes seen as essential at a smaller scale may not be dominant on a different, larger scale. The resulting, insightful definition of the model structures also includes the selection of the minimum but appropriate set of model parameters, thus reducing modeling uncertainties due to overparameterization. The concept of emergent properties (Eder *et al*. 2003) had helped in the formulation of sound and parsimonious models with parameters mostly estimated *a priori* and giving good predictions. This study therefore does not focus on the uncertainties inherent in the model conceptualization, rather it builds on the results of Eder *et al*. (2003). A parsimonious model construct, taken from the previous study, using daily input data and physically meaningful model parameters that can in principle be estimated *a priori*, is applied to compute the long-term annual and monthly water balances within a fuzzy logic framework.

10.2.2 Parameter uncertainty

Considerable uncertainty can be expected in the estimation of climatic input variables (i.e. precipitation, temperature), of the observations with which we evaluate the model predictions (i.e. discharge), and of the model parameter values (i.e. soil moisture capacity). A new approach to dealing with these uncertainties in the

computation of regional water balance is the objective of this work. As in all natural sciences, it is difficult to exactly determine the physical, hydrological and meteorological variables with crisp measures. There are likely to be serious uncertainties in determining these properties even at the point or plot scale. The spatial extrapolation, or scaling up, of information from the point or small plot scale to the catchment scale is an additional difficulty, and the resulting uncertainty tends to get worse the more diverse the monitoring (point or plot) and modeling (catchment) scales are. In this regard, we can talk of random and systematic errors inherent in the observations, and errors associated with the scaling up of information from the point or plot (observation) scale to the catchment (or modeling) scale.

Random errors

The random error in the act of observation may occur because of unnoticed alteration of the standardized measurement condition. For example, when measuring precipitation, deviations may be caused, for instance, by the blocking of the drainage mechanism of the rain gauge, accidentally incorrect reading, and confusion during the date registration procedure. Sometimes, these data errors are filtered out. Data uncertainties arising from random errors are not included in the estimation of fuzzy model inputs and parameter values used in this study, but can be easily included in subsequent extensions of this study.

Systematic errors

Systematic errors can be caused by specific measurement and computational techniques. Such errors arise when applying a rating curve prepared before a devastating flood event to the river water levels in the post-flood situation, and thus not accounting for changes to the riverbed morphology. Errors in precipitation measurements can occur, especially in high-elevation zones, because of strong winds causing precipitation to be blown past the gage.

Another type of error may occur because of the spatial extrapolation of point observations from a monitoring network with a density and distribution that are not sufficient to fully capture the spatial variability of parameters or variables. Especially in Alpine regions, the density and location of point observations are of great importance in order to represent the very diverse topographic and local meteorological characteristics. In general, micro- to meso-scale variations of climatic features and soil properties increase with increasing topographic complexity of the terrain (Christakos 1992). The placement of observation sites would have to be denser in mountainous regions than in flat areas, in order to attain the same quality in spatial extrapolations of the observations. But the opposite is in fact true, as detailed information, for instance, on soil characteristics, is mainly mapped in intensively used agricultural regions in the lower valley zones but very sparsely in high-elevation zones. The same also applies to the network of climate monitoring stations. The accuracy of various interpolation techniques depends strongly on the positioning of monitoring stations. Using data from monitoring stations at locations that do not account for the spatial characteristics of the study area will introduce uncertainty in the regionalized estimates. The quality of water balance estimates relies heavily on the evaluation period of the meteorological observations. These have to be carried out over many years (to produce sufficiently long time series), according to standardized rules for instruments and observations with largely unchanged local conditions during the reference period, for us to have confidence in predictions of water balance into the future.

Later on in this paper, we will shed more light on the uncertainties involved in the estimation of parameter and input values that are used in our water balance model. These estimations of input data and parameter values, and their associated uncertainty measures, serve as the basis for the specification of fuzzy membership functions.

10.2.3 Experiential information

Measurements or estimates of physical and meteorological variables at the point or plot scale are associated with inherent errors or uncertainties. The up-scaling procedures used to scale up from the point or plot scale to the catchment scale introduce additional uncertainties, governed by the adequacy of the spatial extrapolation procedure used in the model. The interpretation or processing of point observations for obtaining the corresponding estimates at the catchment scale often rely on the experiences and intuitive feel of experts about the general catchment characteristics and climate, about the small-scale variability of catchment properties, and meteorological variables.

But the expert information is not always given in quantitative terms, and instead may be expressed in heuristic terms, such as ‘‘large’’ or ‘‘small’’. For example, referring to a catchment’s soil depth, an expert may express the catchment’s mean soil depth as ‘‘somewhat deeper than 0.5 m’’. How can we map these expressions of human thinking, expressed verbally as above, in a mathematically useful manner without losing

the character of imprecision? It turns out that methods based on fuzzy logic do indeed allow us to do this. They can be used to incorporate both the uncertainties inherent in traditional estimates of catchment properties, as well as the imprecision of heuristic statements and estimations made by experts. These methods are discussed in the next section where the basic principles of fuzzy theory are outlined in the context of the water balance modeling to be presented later on in this paper.

10.3 FUZZY MEMBERSHIP FUNCTIONS

Zadeh (1965) first defined a fuzzy set by generalizing the mathematical concept of an ordinary set. From those early days, applications of this new concept of uncertainty have been successful in a wide range of topics. In this section, we briefly introduce the generalities of the relevant fuzzy theory while the associated basic arithmetic rules are presented in the Appendix. In particular, we discuss the concept and formulation of membership functions, which form the basis for the definition of fuzzy model parameters and variables. However, instead of repeating much of the fuzzy mathematical concepts presented elsewhere (Kaufmann and Gupta 1991; Özelkan and Duckstein 2001), we quickly turn the focus to aspects of its application.

If experts are asked about the mean profile depth of lithosol, the common soil type of the high topographic elevation zones in the headwaters of the Upper Enns catchment, the answer may be given in the following terms: Soils in this regions are ''*shallow, approximately around 20 cm*''. Another expert's opinion could be that the mean soil depth is ''*most likely to be greater than 100 mm but very unlikely to be greater than 300 mm*''. Others may intuitively think of the soils having a depth of a ''*few decimeters*''. Experts base their estimates not only on the interpretation of a few plot scale measurements but also on their heuristic experiences within the region of interest, including extraneous or surrogate information, such as geological maps. The combination of these verbal statements and point measurements and their transcription into a crisp estimate of the mean regional soil depth at the catchment scale is somewhat difficult. If one is forced to cope with limited information for model parameterizations, it may be more practical to treat uncertainty about these estimates, with whatever information is available, and to locate the unknown true value inside some closed interval. The first statement mentioned 20 cm as the soil depth, but it did not mean precisely 20 cm. Other information such as the one included in the second statement is much more conservative, being aware that point measurements of soil depth fluctuate between 100 mm and 300 mm. The specification of the mean soil depth can thus be expressed in intervals of confidence, such that the unknown true value is located inside the closed interval $[d^l, d^r]$ where d^l and d^r stand for the left and right interval boundaries – in fuzzy logic this is defined as the *interval of confidence* [100 mm, 300 mm].

A fuzzy number may be considered as an extension of the concept of the interval of confidence. Instead of defining just one interval of confidence, the latter is considered at several levels, which may be called *levels of presumption* μ. From the lowest ($\mu = 0$) to the highest level of presumption ($\mu = 1$), multiple levels of presumption may be defined. Continuing with the example of soil depth, in general, we can say that the larger we define the interval for the unknown mean soil depth, the smaller is our level of presumption in making that statement. Conversely, with a smaller interval of confidence the level of presumption is higher, the highest level of presumption being attained when the interval of confidence shrinks to a single crisp value, say, 200 mm $[d^l = d^r = d^c = 200\,\text{mm}]$ For example, the mean catchment soil depth may be expressed using a triangular function, relating interval of confidence to level of presumption. The interval of confidence at the lowest levels of presumption ($\mu = 0$) can be defined as [100 mm, 300 mm], this being a very conservative estimate. On the other hand, say, we estimate the mean profile depth as 200 mm at the highest level of presumption ($\mu = 1$). We can thus relate the interval of confidence to multiple levels of presumption that lie in the range [0, 1] – this is called the *fuzzy membership function*. For a continuous transition of the level of presumption μ in the range [0, 1], any finite number of characteristic values, or a continuous function, can be defined. An example of the resulting fuzzy membership function of the mean catchment soil depth is presented in Figure 10.1. Note that the theory of fuzzy sets should not be confused with the theory of probability, and a fuzzy set is *not* a random variable. A fuzzy set is merely an extrapolation of the concept of the interval of confidence to multiple levels of presumption in the range [0, 1].

Defining formally, $\widehat{D}$ is called a fuzzy set of a referential set, for example, R, if the set consists of ordered pairs such that

$$\widehat{D} = \{[d, \mu_D(d)]: \forall d \in R; \mu_D(d) \in [0, 1]\} \qquad (10.1)$$

Again referring to the example cited above d may be the suspected soil depth at multiple levels of presumption within [0, 1], whereas $\widehat{D}$ is the membership function of the estimated mean soil depth. On the basis of the definition of a fuzzy set and the coupled concepts of the

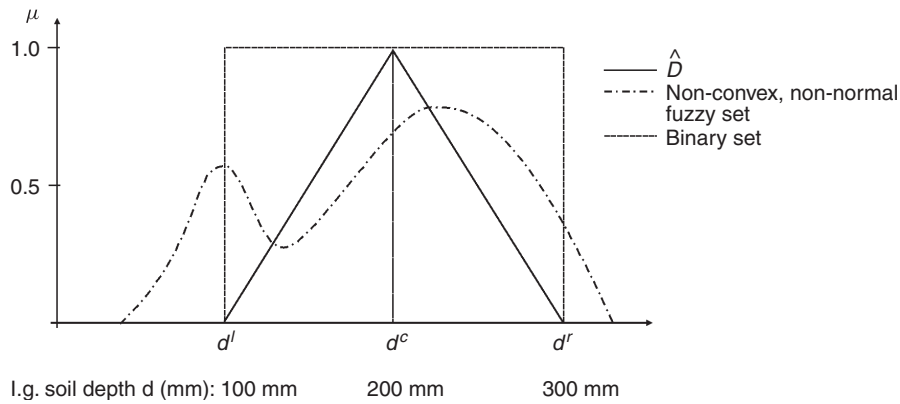


Figure 10.1 A binary set, a non-normal and non-convex fuzzy set, and a triangular fuzzy number

level of presumption and interval of confidence, a fuzzy number is defined as a fuzzy subset.

A fuzzy number $\widehat{D}$ in R is a fuzzy subset in R that is convex and normal (Kaufmann and Gupta 1991) (Figure 10.1). Normality in the context of fuzzy sets means that there exists at least one value of $d \in \widehat{D}$ such that $\mu_D(d) = 1$. A fuzzy set is (quasi) convex if the membership function of $\widehat{D}$, $\mu_D(d) \in [0, 1]$, does not show a local extreme and the membership function of $\widehat{D}$ is always nondecreasing on the left of the single peak, and nonincreasing on the right of the single peak.

A triangular fuzzy number is a special type of a fuzzy number with two linear functions on either sides of the peak. Left–right symmetry is not a necessary condition for a triangular fuzzy number. A simple method of defining a triangular fuzzy number is by assessing the symmetric or semi-symmetric membership function with three points (Dubois and Prade 1980), as generally used in this study: $\widehat{D} = (d^l, d^c, d^r) = (100\,\text{mm},\ 200\,\text{mm},\ 300\,\text{mm})$. Of course, any crisp number can be defined as a triangular fuzzy number with $d^l = d^c = d^r : \widehat{D} = (200\,\text{mm},\ 200\,\text{mm},\ 200\,\text{mm})$.

10.4 CASE STUDY CATCHMENT: LOCATION, CLIMATE AND HYDROLOGY

The study catchment for the application presented in this paper is the Upper Enns catchment with its outlet at Liezen. This catchment is located in the Austrian Central Alpine region north of the main Alpine ridge (see Figure 10.2), and stretches almost linearly from West to East. The Enns river and its tributaries drain parts of the Niedere Tauern, the Dachstein and the Totes Gebirge (Table 10.1). The low elevation zones are mainly extensively used grasslands or arable lands free from wooded areas, whereas the adjacent mountain slopes are typically covered with coniferous forests.

The Upper Enns catchment is characterized by an Alpine climate. The meso-climate within the basin is highly variable because of the shielding effects of the Salzburger Alpen in the north, the Hohen Tauern in the west and the Julischen Alpen (Julijske Alpe in Slovakia) in the south of the main Enns valley, and due to the strong changes in elevation of the valley–ridge system of the mountains. Thus, the Upper Enns catchment belongs to a moderately dry mountain region of the Alps. Regional mean monthly precipitation shows strong seasonal variations, with the first maximum in July (160 mm) due to summer storms with high intensities, a second but small peak in December (100 mm), interrupted by the minima in February (60 mm) and October (70 mm). Estimates of mean monthly evapotranspiration for the Upper Enns catchment vary seasonally, with a maximum of around 60 mm in July and a minimum of almost zero in the winter months of November to March, corresponding to seasonal fluctuations of mean air temperatures of $+12^\circ$C in August to -1.5°C in January.

For part of the year, the precipitation falls in the form of snow, during times when temperatures remain below freezing, leading to the temporary accumulation on the ground as snowpack. Once the temperatures warm up during the spring, the snowpack begins to melt, and contributes to both soil moisture storage and snowmelt runoff. Snow accumulation during winter and melt during spring introduce elements of carry over of storage and time delays to the hydrologic system. They cause a reduction of discharge in winter, which is then mainly fed from groundwater storage that is gradually depleted. In spring, the melting snowpack increases the discharge to its maximum level and also leads to the recharge of

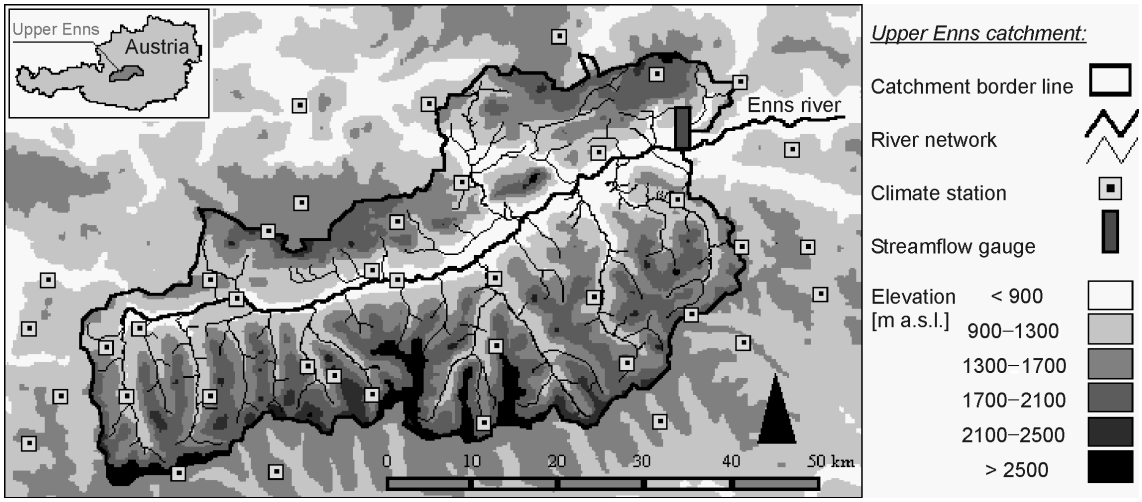


Figure 10.2 The topography of the Upper Enns catchment with river network, catchment boundary, and hydro-meteorological monitoring stations. Reproduced by permission of John Wiley & Sons Ltd.

Table 10.1 Table of basin characteristics

Name of the basin/area	Upper Enns catchment
Mountain Range	Alps
Elevation range of entire catchment [m a.s.l]	700–2995
Latitude and longitude	13.30°–15°E and 47°–48°N
Area in km^2	2116
Geology	Dominantly limestone
% glacierized	0
Vegetation type (dominantly)	Grasslands (700–800 m a.s.l), coniferous forests (800–1800 m a.s.l), alpine pasture (1800–3000 m a.s.l)
Mean (1972–1993) Q at catchment outlet [mm]	940
Mean (1972–1993) P [mm]	1200
Mean (1972–1993) E (if determined) [mm]	270
Mean (1972–1993) T [°C]	4

the groundwater table. Hydrological characteristics of the Upper Enns catchment have been previously described in detail by Nachtnebel *et al*. (1993) and Eder *et al*. (2001, 2003).

10.5 BASIC MODEL CONSTRUCT

The water balance model we use here is a lumped conceptual model, based on a daily time step, developed and tested previously by Eder *et al*. (2003) for the Upper Enns catchment. The model incorporates the processes of runoff generation by the mechanisms of saturation overland flow (whenever soil moisture storage capacity is exceeded), interflow (shallow subsurface flow) whenever soil moisture storage exceeds the limited storage capacity corresponding to the soil's field capacity, and deep groundwater flow (or baseflow). Evapotranspiration is simply assumed to be equal to the potential evapotranspiration estimated by the Thornthwaite method, except during precipitation events when fluxes of evapotranspiration are neglected. Precipitation is partitioned into rainfall or snowfall based on a single threshold air temperature, and snowfall accumulates into a snowpack during the winter months. The model applies a temperature – index algorithm for simulating snow processes. The rate and timing of the snowmelt process are estimated on the basis of the same threshold air temperature, and a fixed snowmelt factor.

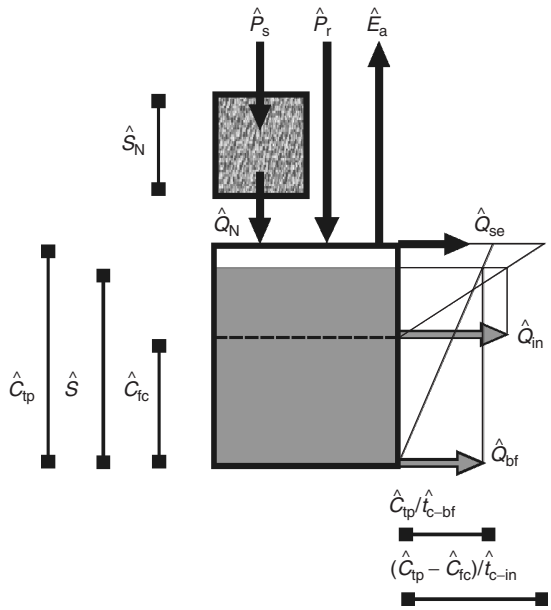


Figure 10.3 Water balance model concept accounting for snowmelt runoff ($\hat{Q}_N$), saturation excess runoff ($\hat{Q}_{se}$), inter flow ($\hat{Q}_{in}$) and base flow ($\hat{Q}_{bf}$)

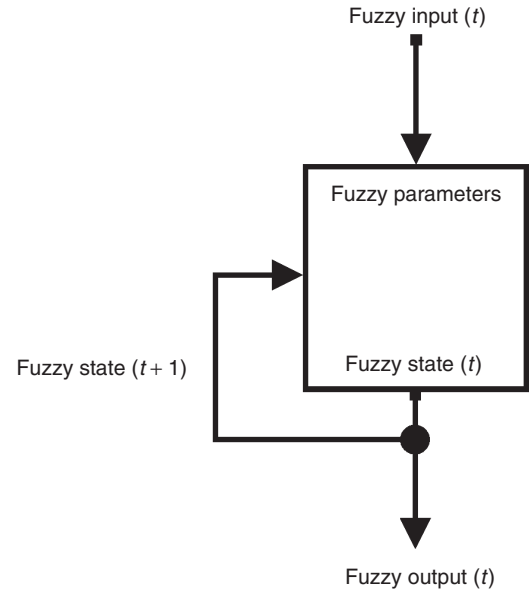


Figure 10.4 The fuzzy water balance model approach: fuzzy input data and fuzzy parameters result in fuzzy outputs. Carry-over of fuzzy system states from time t to $t+1$

The model structure is presented schematically in Figure 10.3. The water balance dynamics of the catchment is characterized by the following two coupled equations, involving two state variables representing soil moisture storage and snow water storage, respectively (refer to the list of symbols and abbreviations and their brief descriptions):

$$S(t+1) = S(t) + \{P_r(t) - E_a(t) - Q_{se}(t) - Q_{in}(t) - Q_{bf}(t) + Q_N(t)\}\Delta t \quad (10.2)$$

$$S_N(t+1) = S_N(t) + P_s(t)\Delta t - Q_N(t)\Delta t \quad (10.3)$$

The structure of the model was arrived at through a systematic, data-driven procedure known as the *downward approach* (Klemes 1983). This version of the model uses eight parameters, all of which were estimated *a priori* for the Upper Enns catchment; the physical meanings of these parameters and the details of their estimation are provided in Eder *et al*. (2003). The input data required for the running of the model are P and E_p. The model uses the parameters C_{fc} {a function of (D_{tp}, θ_{fc}, θ_{pwp})}, C_{tp} {a function of (D_{tp}, ϕ, θ_{pwp})}, T_{crit}, m_f, t_{c-in} and t_{c-bf}.

In this paper, this model is recast from its formerly deterministic form into a new, fuzzyfied form, based on the types of fuzzy membership functions mentioned above and associated rules of fuzzy arithmetic briefly summarized in the Appendix. With the change to fuzzy form, the model now uses fuzzy input data and parameter values (Figure 10.3), and in turn produces various time series of fuzzy model outputs (fluxes) and system states (Figure 10.4). These are: $\hat{P}_r$, $\hat{P}_s$, $\hat{Q}_N$, $\hat{S}_N$, $\hat{E}_a$, $\hat{S}$, $\hat{Q}_{se}$, $\hat{Q}_{in}$ and $\hat{Q}_{bf}$.

The justification for the choice of membership functions for the various fuzzy parameters and input data is described next.

10.6 ESTIMATION OF FUZZY PARAMETERS AND INPUTS

Because of uncertainties in the observation of various point data, and because of insufficient knowledge about the spatial distribution of catchment physiographic properties and climate inputs, the estimation of mean catchment properties and climatic variables is difficult, leading to uncertainty in the specification of model parameters and climatic inputs. In this paper, such uncertainties are expressed by means of fuzzy membership functions for each of the model parameter values and climatic inputs.

We have chosen to use triangular membership functions to describe the fuzziness of all parameters and climate inputs used in the model. Triangular membership functions are the simplest to use, although any other

shapes of membership functions could be used if proved to be more appropriate for any physical reason. Mathematical operations with triangular fuzzy numbers always result in fuzzy numbers, which are not necessarily triangular any more, but still retain a unique maximum at the highest level of presumption. Computational results obtained from the fuzzy water balance model for the highest level of presumption are therefore identical to results of a conventional (deterministic) water balance model of the same structure.

10.6.1 Climatic inputs: precipitation and temperature time series

The meteorological monitoring network of the Austrian Hydrological Survey is relatively dense in the region of the Upper Enns catchment and consists of 40 precipitation and 12 temperature stations. On the basis of the point observations, the external-drift-kriging procedure (Ahmed and de Marsily 1987; Journel 1989) was applied to generate spatial distributions of precipitation and temperature. This kriging procedure for nonstationary random functions uses a surrogate variable, which is linearly correlated with the estimator. In this case, the estimator is either precipitation or temperature, with topographic elevation being used as the surrogate variable since it has an important bearing on both temperature and precipitation. Results of the kriging procedure are summarized in terms of lumped catchment estimates of both temperature and precipitation at the daily timescale.

The accuracy of precipitation measurements has been discussed over many years in some European countries, and significant progress has been achieved to correct precipitation data for systematic errors (Sevruk 1986). In general, however, data users are still provided with uncorrected precipitation measurements. Recommendations on the correction of precipitation data are limited in Austria, especially for the Upper Enns catchment. Thus, the Swiss (Sevruk 1983, 1986) and the German (Richter 1995) experiences are combined, with what little of the Austrian experience is available, to define the membership functions of fuzzy precipitation estimates that will serve as inputs to the water balance model. Estimates of the average correction factors for the hydrological year (October to August) range between a minimum of 10% and a maximum of over 25% in the highest elevations of Switzerland (Sevruk 1986). The seasonal variation of the correction factors, for instance, at the monitoring station at Davos (1580 m a.s.l.), a station close to Austria and with similar meteorological features to those of the Upper Enns catchment, fluctuates almost sinusoidally between about 30% in March and about 8% in July.

Forty (40) climate stations in the region represent a relatively dense network, which helps make the uncertainty introduced by the regionalization of precipitation gage data to be relatively low, compared to uncertainties associated with the point scale measurements themselves. The dependence of precipitation on topographic elevation is well mapped by the 40 stations. Estimated fuzzy numbers for precipitation used here are based on the results of Sevruk (1983, 1986) and Richter (1995).

As a first approximation, the regionalized daily precipitation estimates are defined as triangular fuzzy numbers (Table 10.2) – the center values of the triangular fuzzy numbers are set to the uncorrected precipitation estimates, while the right and left values correspond to correction factors of +20% and −2%, respectively. The highly asymmetric shape of the triangular fuzzy numbers for precipitation data signifies that overestimation of catchment average precipitation is thought to be highly unrealistic; this is because precipitation measurements generally underestimate the true precipitation volumes (Sevruk 1986).

Compared to precipitation measurements, point measurements of temperature are much more accurate, and the spatial coverage with 12 temperature stations in the Upper Enns catchment is relatively dense. Deviations of the mean regional temperature estimates from the true values are considered to be low. Fuzzy numbers of temperature are defined on more realistic uncertainty measures. Neither under- nor overestimation of temperature could be found to be more evident, and hence a symmetrical, triangular fuzzy membership function with left and right values deviating with ±1.5°C from the center value (Table 10.2) was adopted, with the center value taken to be equal to the kriged (area-averaged) value.

Table 10.2 Estimates of triangular fuzzy numbers for model input data and parameters

Fuzzy model	Input variables
$\widehat{T}$ [°C]	$(T + 1.5, T, T - 1.5)$
$\widehat{P}$ [mm]	$(0.98P, P, 1.20P)$
Fuzzy model	**Parameter**
$\widehat{m}_f$ [mm/°C/d]	(0, 1.5, 3)
$\widehat{T}_{\text{crit}}$ [°C]	(0, 1, 2)
$\widehat{C}_{\text{tp}}$ [mm]	(250, 310, 370)
$\widehat{C}_{\text{fc}}$ [mm]	(100, 125, 150)
$\widehat{t}_{\text{c-in}}$ [day]	(7, 13, 19)
$\widehat{t}_{\text{c-bf}}$ [day]	(40, 46, 51)

On the basis of these temperature values, the fuzzy magnitude of the potential evapotranspiration was computed using the classical Thornthwaite equation (Thornthwaite 1948).

10.6.2 Differentiation between rain and snow, snowmelt and accumulation

Standard precipitation measurements do not record the type of precipitation (snow or rain), but only the total amount (snow water equivalent in the case of snowfall). The current model uses a threshold air temperature to determine the form of precipitation (snow or rain), and this temperature is used also to determine the rate of snow accumulation or depletion, in the latter case the air temperature acting as a surrogate for available radiant energy. It is quite likely that the threshold air temperature that has to be exceeded before snowmelt starts is similar in magnitude but perhaps not identical, to the transition air temperatures used to determine the form of precipitation as either snow or rain. However, for the sake of model parsimony both threshold temperatures are collapsed into a single critical temperature $\widehat{T}_{\text{crit}}$. The snowmelt algorithm is based on the use of two parameters: a snowmelt factor $\widehat{m}_f$ and the critical air temperature $\widehat{T}_{\text{crit}}$.

In Eder *et al*. (2003), the snowmelt factor m_f was estimated on the basis of the calculated short and long wave radiation values, and considering the catchment's topographic features, cloud cover, vegetation cover, and estimated emissivity of air. The results were similar to those obtained in previous studies on the Enns catchment by Nachtnebel *et al*. (1993) and Fuchs (1998), to those of Braun (1985) who analyzed snowmelt characteristics of various catchments in Germany, and to those obtained from Lauscher's work (1982) in the Vienna region. The melt factor, $\widehat{m}_f$, and the threshold air temperature, $\widehat{T}_{\text{crit}}$, exhibit temporal variations within the day, as well as through the whole winter season, and also a spatial variability that depends strongly on topographic features. Uncertainties in the estimation of these parameters can never be fully resolved. The estimates of the fuzzy parameter values presented in Table 10.2 are the best possible estimates obtained from their variation between winter seasons of different years and spatial variation throughout the catchment.

10.6.3 Soil properties

Even though numerous field measurements on soil properties such as soil depth and porosity are available on the plot scale within the study region, it is difficult to determine crisp mean values at the catchment scale. The lowest section of the main valley floor of the Enns river passes through a wide valley predominantly covered by Histosols, Gleysols, Fluvisols and Podsols with spatial coverage of approximately 1%, 3%, 3% and 36% of the total catchment area, respectively. As one follows the river course upstream, the soil depth decreases gradually with increasing elevation as well as slope, and the alluvial soils are replaced by Cambisols on about 22% and Rendzinas on roughly 25% of the catchment area. Rankers and Lithosols, bleached soils of small depth above the rock stratum, and skeletal soils, which consist of an imperfectly weathered mass of rock fragments with little fine granular material cover about 5% and 4% of the Enns catchment, respectively. In those elevated zones, the storage capacity of the soils is almost negligible. Approximately 1% of the study area shows bare rock, located in the highest elevations at or around the mountaintops.

Realistic estimates of the mean profile depths, $\widehat{D}_{\text{tp}}$, up to bedrock, or to an impermeable soil layer, and the soil porosity, $\widehat{\phi}$, have been made for all types of soils observed in the catchment area, through detailed field measurements (Österreichische Bodenkartierung 1980, 1981, 1985, 1986, 1992) and published in an Austrian soils map (Österreichische Akademie der Wissenschaften 1979). Permanent wilting point $\widehat{\theta}_{\text{pwp}}$ and field capacity $\widehat{\theta}_{\text{fc}}$ are calculated according to Baumer (1989) for all profile layers of each soil type.

Estimated soil properties of all soil types predominant in the Upper Enns catchment are presented in detail in Eder *et al*. (2003). In this paper, these estimates are treated as fuzzy numbers and redefined in terms of their membership functions. They are also used to estimate the catchment-scale profile soil moisture storage capacity, $\widehat{C}_{\text{tp}}$, and the catchment-scale soil moisture storage capacity up to field capacity, $\widehat{C}_{\text{fc}}$, using the following formulas:

$$\widehat{C}_{\text{tp}}(=)\left(\sum_{i=1}^{I}\right)\widehat{D}_{\text{tp},i}(\bullet)(\widehat{\phi}_i(-)\widehat{\theta}_{\text{pwp},i})(\bullet)(\widehat{p}c_j/100) \tag{10.4a}$$

$$\widehat{C}_{\text{fc}}(=)\left(\sum_{i=1}^{I}\right)\widehat{D}_{\text{tp},i}(\bullet)(\widehat{\theta}_{\text{fc},i}(-)\widehat{\theta}_{\text{pwp},i})(\bullet)(\widehat{p}c_j/100) \tag{10.4b}$$

for I = number of different soil types $\widehat{C}_{\text{tp}}$ and $\widehat{C}_{\text{fc}}$ are parameters of the lumped, water balance model, both in turn being treated as fuzzy numbers, estimates of which are also presented in Table 10.2.

10.6.4 Catchment drainage characteristics

The model incorporates three mechanisms of runoff generation. Quick runoff $\widehat{Q}_{se}$ is assumed to occur when the soil profile storage capacity, $\widehat{C}_{tp}$, is exceeded. The two subsurface runoff components are also conceptualized as functions of soil moisture storage $\widehat{S}$: baseflow $\widehat{Q}_{bf}$ is assumed to be linearly proportional to $\widehat{S}$, and interflow $\widehat{Q}_{in}$ is assumed to switch on only when $\widehat{S}$ exceeds some threshold, taken here to be that corresponding to the soil's field capacity, that is, $\widehat{C}_{fc}$. The rates of baseflow and interflow are governed by two characteristic delay times $\widehat{t}_{c-bf}$ and $\widehat{t}_{c-in}$, respectively, both of which are also parameters of the models. The method of estimation of these drainage parameters, through an inverse procedure from a representative (master) recession curve extracted from available runoff measurements, is described in Wittenberg (1994) and was adopted in our previous work (Eder *et al*. 2003).

The transition between surface runoff, interflow and baseflow in the streamflow record is not sharp but gradual, and therefore it is very difficult to separate these with a view to estimating the residence times $\widehat{t}_{c-bf}$ and $\widehat{t}_{c-in}$ unambiguously. In the case of Alpine catchments, it is known that during the winter season, since temperatures remain below freezing and precipitation does not contribute to runoff, the main contributions to discharge mainly come from drainage of groundwater. Consequently, the lowest part of the master recession curve extracted from winter low flow records is chosen for the determination of the response time for baseflow, $\widehat{t}_{c-bf}$. For the estimation of the delay time for interflow, $\widehat{t}_{c-in}$, the upper part of the master recession curve is used, and the nonlinear, transition part, lying between these upper (interflow) and lower (baseflow) parts of the master recession curve is left out of the analysis. The master recession curve is based on flow records only during major breaks in the precipitation record to avoid contamination by flow contributions from surface runoff.

In Eder *et al*. (2003), these drainage parameters are estimated from master recession curves based on streamflow gaging at Admont, the closest discharge monitoring station to Liezen. The master recession curve is based on flow records only during major breaks in the precipitation record to avoid contamination by flow contributions from surface runoff. In this paper, these previous estimates of catchment response times are redefined as center values of symmetric triangular fuzzy numbers. Left and right values of the triangular fuzzy numbers are defined on the basis of sensitivity analyses of recession curves that considered the uncertainties due to the compilation of the master recession curve using data from different years and to the vague definition of the separation criterion between interflow and baseflow. The transition between surface runoff, interflow and baseflow in the streamflow record is not sharp but gradual, and therefore it is very difficult to separate these with a view to estimating the residence times $\widehat{t}_{c-bf}$ and $\widehat{t}_{c-in}$ unambiguously. Estimates of fuzzy membership functions are presented in Table 10.2.

10.6.5 Discharge

In later sections, the simulated monthly and annual discharges are compared with observed discharge measurements. It is a matter of fact that gaged discharge records can also contain inherent measurement errors (IAHR 1987). The magnitude of error differs for different measuring techniques, is dependent on the discharge volume, might show seasonal variations (i.e. because of vegetation, snow and ice), and the physical positioning of the gauge as well as the maintenance of the instrumentation may have an influence on the quality of measurements. In general, comparison of model predictions and observations should also account for the uncertainty in the discharge measurements. However, as a first step, this is not attempted in this paper. Rather, the observed discharge values are kept to their crisp estimates as this paper focuses on the fuzziness of only the model predictions.

10.7 MATHEMATICAL FORMULATION

The soil moisture store is updated daily using the water balance equation:

$$\begin{aligned}\widehat{S}(t+1)(=)\widehat{S}(t)(+)\widehat{P}_{r}(t)\Delta t(-)\widehat{E}_{a}(t)\Delta t \\ (-)\widehat{Q}_{se}(t)\Delta t(-)\widehat{Q}_{in}(t)\Delta t(-)\widehat{Q}_{bf}(t)\Delta t \\ (-)\widehat{Q}_{N}(t)\Delta t \qquad (10.5)\end{aligned}$$

Similarly, the snow water equivalent in the snowpack is also updated daily using the following balance equation:

$$\widehat{S}_{N}(t+1)(=)\widehat{S}_{N}(t)(+)\widehat{P}_{s}(t)\Delta t(-)\widehat{Q}_{N}(t)\Delta t \quad (10.6)$$

Note that $\widehat{Q}_{N}$ appears in both water balance equations as the melt water is assumed to contribute to the soil water store rather than flowing directly to the river. Equations (10.5) and (10.6) are fuzzified versions of the deterministic Equations (10.2) and (10.3) presented above.

Form of precipitation: The total daily precipitation depth is partitioned into depths of snow and rainfall according to the critical temperature $\hat{T}_{\text{crit}}$ as threshold:

$$\begin{aligned} \hat{P}_{\text{r}}(=)\hat{P} \qquad & \text{if } \hat{T}(>)\hat{T}_{\text{crit}} \\ \hat{P}_{\text{s}}(=)\hat{P} \qquad & \text{if } \hat{T}(\leq)\hat{T}_{\text{crit}} \end{aligned} \tag{10.7}$$

Conversion from potential to actual evapotranspiration:

$$\begin{aligned} \hat{E}_{\text{a}}(=)\,\text{Min}\,\{\hat{E}_{\text{p}};\, \hat{S}/\Delta t\} \qquad & \text{if } \hat{P}(=)\,0 \\ \hat{E}_{\text{a}}(=)\,0 \qquad & \text{if } \hat{P}(\neq)\,0 \end{aligned} \tag{10.8}$$

where $\hat{E}_{\text{p}}$ is the daily potential evapotranspiration rate, estimated by the Thornthwaite method (Thornthwaite 1948).

Snowmelt:

$$\hat{Q}_N(=)\,\text{Min}\,\{\hat{m}_f(\bullet)(\hat{T}(-)\hat{T}_{\text{crit}});\, \hat{S}_N/\Delta t\} \tag{10.9}$$

The snowmelt $\hat{Q}_N$ is computed using a temperature-index approach (World Meteorological Organization 1986), where $\hat{T}$ is taken to be a measure of the energy driving the snowmelt to be used in combination with the melt factor $\hat{m}_f \cdot \hat{T}_{\text{crit}}$ signifies the critical threshold air temperature that has to be exceeded before snowmelt starts and $\hat{T}$ denotes the mean air temperature within the time interval, here, a day. If T is below $\hat{T}_{\text{crit}}$, then $\hat{T}$ is set to $\hat{T}_{\text{crit}}$.

Saturation excess runoff: Saturation excess runoff is produced if and when the net additions to the bucket via precipitation and evaporation are such that the storage of water in the bucket exceeds the capacity of the bucket, denoted by $\hat{C}_{\text{tp}}$. Thus, the rate of runoff generation is given by:

$$\hat{Q}_{\text{se}}(=)\,\text{Max}\,\{0;\, (\hat{S}(-)\hat{C}_{\text{tp}})/\Delta t\} \tag{10.10}$$

Interflow:

$$\hat{Q}_{\text{in}}(=)\,\text{Max}\,\{0;\, (\hat{S}(-)\hat{C}_{\text{fc}})(\div)\hat{t}_{\text{c-in}}\} \tag{10.11}$$

where $\hat{C}_{\text{fc}}$ is the bucket storage capacity until field capacity $\hat{\theta}_{\text{fc}}$.

Baseflow:

$$\hat{Q}_{\text{bf}}(=)\hat{S}(\div)\hat{t}_{\text{c-bf}} \tag{10.12}$$

The fuzzy arithmetic used in the equations that describe the water balance model essentially deal with the mathematical operations of addition, subtraction, multiplication and division, and is summarized briefly in the Appendix. Other mathematical operations, such as the comparison of two fuzzy numbers (i.e. $\hat{T}(>)\hat{T}_{\text{crit}}$), are also discussed in the Appendix.

10.7.1 Carry-over of system states

By the rules of fuzzy arithmetic presented in the Appendix, the magnitudes of the fuzziness of the modeled system state variables (snow water equivalent, $\hat{S}_N$, and soil moisture, $\hat{S}$), computed using Equations (10.5) and (10.6) above, will continue to increase over time. For example, in the case of $\hat{S}_N$, more and more highly uncertain snow accumulation and depletion processes take place as winter progresses and leads to a continuous increase of fuzziness of $\hat{S}_N$. In late spring, with rising temperatures $\hat{S}_N$ reaches zero, hence fuzziness of $\hat{S}_N$ also vanishes.

Similarly, the uncertainty of simulated soil moisture also increases over time as a consequence of uncertain processes such as, for example, infiltration, percolation and lateral flows. Fuzziness of soil moisture can diminish only when the soil moisture bucket empties. This is not a realistic possibility in the Upper Enns catchment or in any other catchment. When the Upper Enns catchment was modeled, the soil moisture storage (state variable) hardly ever reached zero in the 21-year simulation period, since inputs into the soil moisture bucket are distributed throughout the year (driven by lumped values of precipitation and snowmelt). The fact that the fuzziness of the soil moisture state variable continues to grow with time in an unbounded manner is clearly a serious disadvantage for its application to continuous fuzzy water balance modeling. Unlike in the case of snow water equivalent, there is no mechanism for the fuzziness of simulated soil moisture values to be brought back to zero from time to time.

One possible approach that enables restricting the fuzziness of modeled soil moisture is to defuzzify (i.e. transformation of a fuzzy number to a crisp representative (Mayer *et al*. 1993)) the soil moisture storage at each time step before it is carried over into the next time step. Consequently, the fuzziness of the simulated results merely reflects the uncertainty that is introduced into the modeling procedure during only one single time step, not the fuzziness that is carried over from previous time steps. Another possibility, as pointed by one reviewer, is to apply the ''extension principle'' of fuzzy logic. Results of applications of the extension principle may yield a narrower support than when fuzzy arithmetic is used for multiple operations, leading to greater uncertainty. Given a formula $f(x)$ and a fuzzy set $\hat{A}$ defined by $\mu_{\hat{A}}(x)$, how do we compute the membership function of $f(\hat{A})$? How this is done is what

is called the *extension principle* (Zadeh 1978). What the extension principle says is that $f_\alpha(\widehat{A}) = f(\widehat{A}(\alpha))$. The formal definition is: $[f(\widehat{A})](y) = \sup_{x|y=f(x)}\{\mu_{\widehat{A}}(x)\}$. (Extension Principle – Example: Let $f(x) = ax + b; a \in \widehat{A} = [1, 2, 3], b \in \widehat{B} = [2, 3, 5]$, and $x = 6$, then $f(x) = 6\widehat{A} + \widehat{B} = [8, 15, 23]$.

The application of the extension principle is beyond the scope of this rather exploratory paper. However, this fundamental weakness of fuzzy logic needs to be resolved and we leave it for future research.

In this paper, as a partial solution, it was decided to introduce a formulation that partially accounts for the carry over of uncertainty from previous time steps. This is done partially because, as indicated before, unconstrained carry over of fuzziness at each time step would lead to an unbounded increase of the fuzziness of soil moisture storage. In this formulation, we assume that if the crisp measure of soil moisture storage is equal to the maximum storage capacity of the bucket, then all of the fuzziness is carried over from $t - 1$ to t. On the other hand, when the crisp value of soil moisture storage is zero, then fuzziness vanishes and no fuzziness is carried over. Both situations are rather extreme situations and hardly ever occur; consequently full carry over of uncertainty and no carry over of uncertainty are not expected. But the lower the soil moisture storage the less of the fuzziness of the soil moisture at time step $t - 1$ is carried over to time step t. In the transition between empty and full model buckets, the extent of carry over of fuzziness is assumed to be linear.

Fuzziness of $\widehat{S}$ computed at time step $t - 1$ is re-scaled into $\widehat{S}'$ for input at time t; the carry over of fuzziness of soil moisture storage is modeled as a function of the so-called soil moisture ratio, r_S: $\widehat{S}'(t) = f(\widehat{S}(t), r_S)$ (see the Appendix for the mathematical formulation). This formulation of restricting the carry over of uncertainty is clearly not based on a physical explanation at this stage. This is left for future work to clarify and extend. The logic behind this formulation is that when the soil moisture storage is high most likely the absolute measure of fuzziness is also high, and vice versa. Because of increasing predictive uncertainty with increasing absolute values of modeled soil moisture, one can never definitely state if soil moisture capacity is reached. Sure, the fuzzy number for soil moisture is constrained on the upper side by the maximum soil moisture capacity and at the lower side by zero. This means that with general increasing soil moisture the fuzzy number becomes more and more asymmetric. While the aim of this study is to present a more general idea of fuzzy water balance modeling, there exists considerable potential for further advances in the use of fuzzy techniques. This study is restricted to illustrating the application of fuzzy logic to quantify the relative impact of uncertainty estimates of model parameters and climatic inputs, and of model structural complexity, on the fuzziness of model predictions.

10.8 ANNUAL AND MONTHLY WATER BALANCES

10.8.1 Model performance with fuzzy parameters and climatic inputs

The fuzzy water balance model described in the previous section is implemented using fuzzy estimates of daily precipitation, mean daily temperature and physically based model parameters from the Upper Enns catchment over a period of 21 years. The resulting time series of streamflows from the model are processed to generate daily, monthly and annual water balances. In this paper, for the sake of brevity, the focus is on annual and monthly model water balances, whereas only statistical measures of the model performance are presented at the daily time step.

In Figure 10.5(a), monthly time series of fuzzy precipitation and fuzzy potential evapotranspiration (model input), as well as simulated fuzzy estimates of actual evapotranspiration, are presented for the 1975–1979 period. In comparison to time series of crisp values usually presented as a continuous graph, in this case the intervals of confidences of fuzzy values at a certain level of presumption are joined together and are visualized as continuous ''ribbons''. In Figure 10.5(a), and in every following figure, the level of presumption (μ) chosen for presentation is 0.8.

The parameters governing the water holding capacity of the soil, that is, $\widehat{C}_{\text{tp}}$ and $\widehat{C}_{\text{fc}}$, appear in Figure 10.5(b) as constant values over time. The time variation of the fuzzy state variables of soil moisture, $\widehat{S}(t)$, and snow water equivalent, $\widehat{S}_N(t)$, are set in relation to $\widehat{C}_{\text{tp}}$ and $\widehat{C}_{\text{fc}}$. The results from the continuous simulation of the water balance model show, in the case of the seasonal accumulation and depletion of snow, that the higher the snow water equivalent the higher also its fuzziness. The same is true of the soil moisture storage.

In order to gain insights into the generation of calculated fuzzy water balance components presented in Figure 10.5 (at μ of 0.8), the results of one particular day, that is, May 1, 1997, are presented in Figure 10.6. On that day in spring 1997, potential evapotranspiration is low as temperature is still low at that time of the year (Figure 10.6(a)). Precipitation is much higher than potential evapotranspiration on this particular day. The fuzzy numbers of the state variables concerning the soil moisture and the snow storage as well as water holding

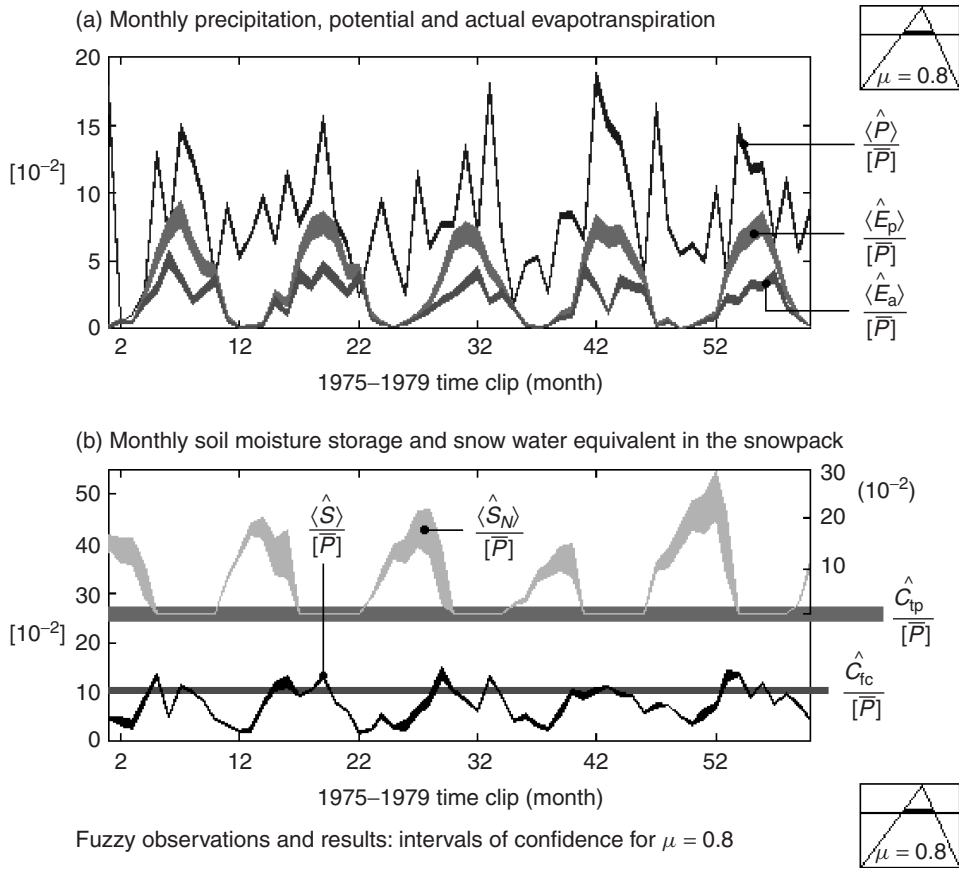


Figure 10.5 (a) Fuzzy climatic input variables precipitation ($\hat{P}$) and potential evapotranspiration ($\hat{E}_p$) serve as input for the basic water balance model that results in simulated actual evapotranspiration ($\hat{E}_a$), (b) fuzzy snow cover (water equivalent) ($\hat{S}_N$), and soil moisture ($\hat{S}$) presented in relation to fuzzy water holding capacity of the total soil profile ($\hat{C}_{tp}$) and until field capacity ($\hat{C}_{fc}$)

capacity of the soil profile are presented for the same date in Figure 10.6(b). In particular, it may be noted that at a high level of presumption, say, 0.8, the soil moisture is clearly higher than field capacity, whereas at low levels of presumption the uncertainty of soil moisture increases such that soil moisture could be larger or smaller than field capacity.

The concept of fuzzy membership functions, which is based on an infinite number of intervals of confidences between the lowest and the highest levels of presumption (0 and 1), does not allow one to judge if it is more likely that soil moisture is higher or smaller than field capacity, say, for the level of presumption of 0.2. This is because the interval of confidence for field capacity is located within the interval of confidence for soil moisture. Another interesting point to note is that the fuzzy numbers for potential evapotranspiration, and storage measures, soil moisture and snow water equivalent, are not triangular fuzzy numbers any more, even though they have been generated on the basis of triangular fuzzy numbers of input and parameter values. Generally, May is a month with high snowmelt, which is difficult to predict precisely, that is, because of fuzzy estimates for temperature and melt factors. Consequently, calculated storage values of the snowpack are also fuzzy.

The use of 0.8 as the level of presumption (Figure 10.6) results in specific magnitudes for the intervals of confidence of different fuzzy numbers on any given day. The absolute magnitudes of the intervals of confidences change over time, and these may also change seasonally.

The performance of the fuzzy water balance model is presented in terms of characteristic signature plots and hydrographs, which are compared to corresponding graphs based on observed streamflows (Figure 10.7). The

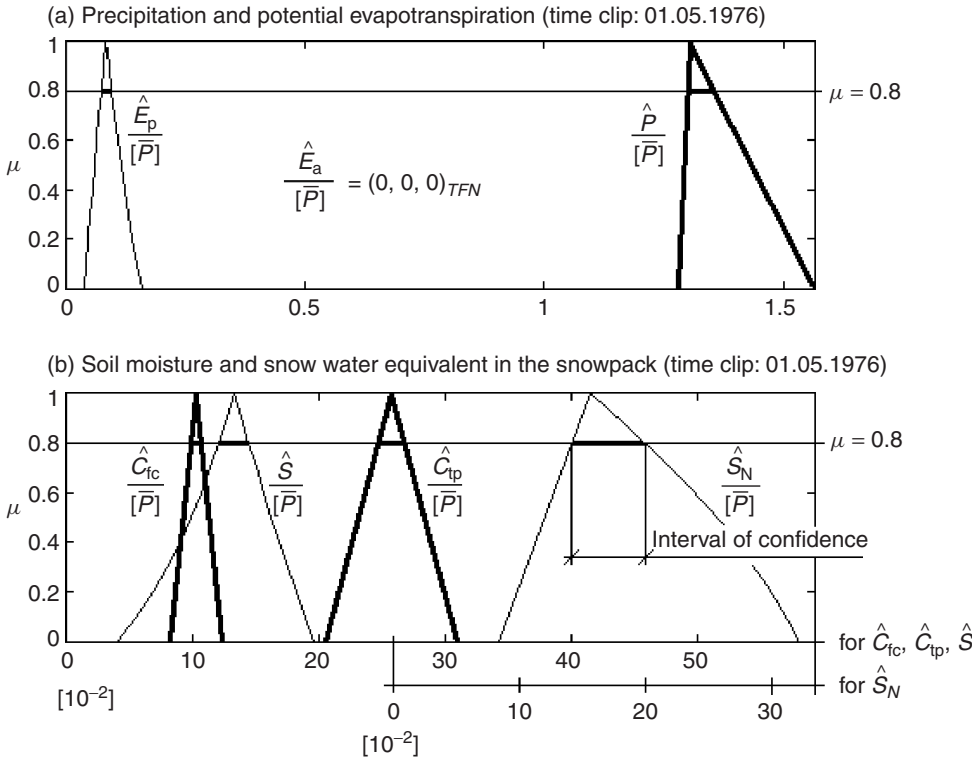


Figure 10.6 Fuzzy membership functions of model input (precipitation $\widehat{P}$ and potential evapotranspiration $\widehat{E}_p$), parameters (profile water holding capacities $\widehat{C}_{tp}$ and $\widehat{C}_{fc}$) and system state variables (soil moisture $\widehat{S}$ and snow water equivalent $\widehat{S}_N$) on the 1st of May 1976

parsimonious model, with just eight parameters, gives good predictions of the signature plots and streamflow hydrographs at the monthly and annual time scales, which was anticipated because of satisfactory results obtained in the previous study (Eder *et al*. 2003). The crisp graph visualizes model results for μ of 1.0, equivalent to the model results from the deterministic water balance model of the previous study (Eder *et al*. 2003) based on crisp input data and parameter values. These predictions could be improved with further calibration of the parameter values, but this is not the purpose of this exercise. Rather, we use the model to understand the contributions of the various parameters and inputs to the resulting fuzziness of the model predictions.

The results show that simulated high flows exhibit high fuzziness, whereas low flows are less fuzzy (Figure 10.7c and 10.7d). Monthly results have been aggregated to annual estimates that were presented in Figure 10.7(a) and 10.7(b) also for a level of presumption of 0.8. At this stage, one has to accept that the fuzzy results are a direct product of the transformation of fuzzy parameters and input data through the water balance model (Table 10.2). Next, the relative sensitivity of parameter estimates and the set of input data on the overall fuzziness of simulated discharges is investigated.

10.8.2 Model accuracy and sensitivity to fuzzy parameters and climatic inputs

The fuzzy climatic input variables introduce much less uncertainty than the eight fuzzy model parameters. This is demonstrated in Figure 10.8(a–d), which presents the simulated fuzzy discharge generated using fuzzy input data (precipitation and temperature) but crisp (defuzzified) estimates of parameter values. This suggests that bigger contribution to uncertainty in the predictions of the water balance model comes from fuzziness of the model parameters than from fuzziness of the meteorological inputs.

We next turn to a possible ranking of the various parameters in terms of their individual contributions to

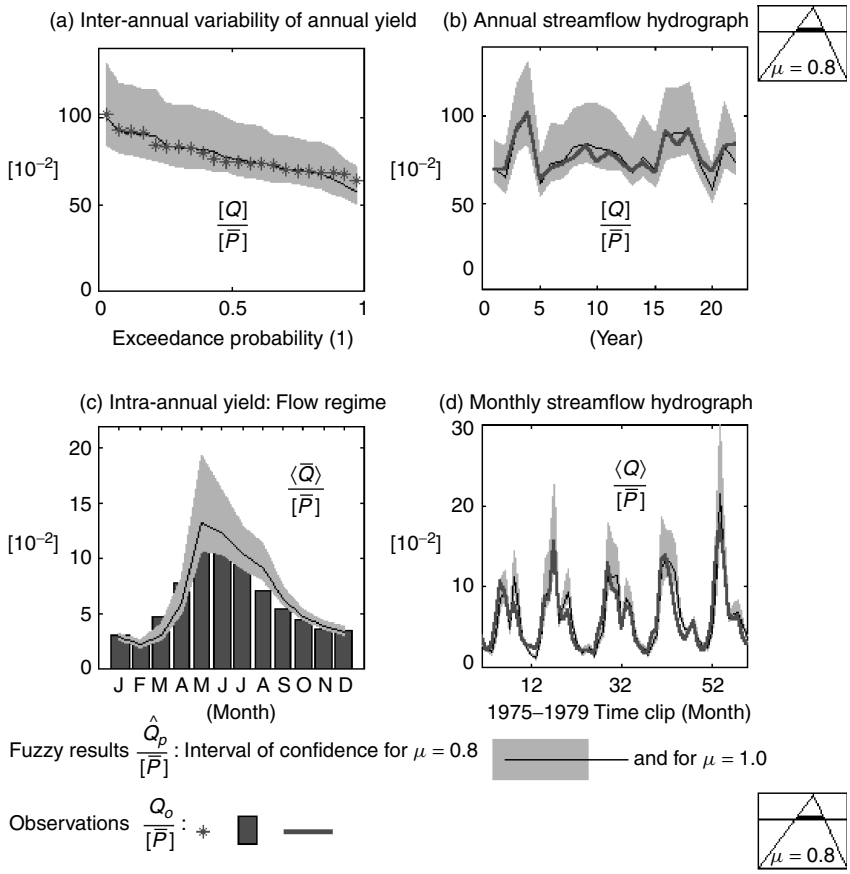


Figure 10.7 Annual and monthly simulated versus observed discharge: Intervals of confidence at the level of presumption of 0.8 generated with the basic water balance model accounting for saturation excess runoff, inter flow and base flow with fuzzy values for climatic input variables and parameters

the overall uncertainty of simulated model results. This was achieved by repeatedly running the model with each parameter held constant (crisp), while letting all other parameters to remain fuzzy and estimating overall, bulk measures of uncertainty. The following ranking of parameters and climatic input variables, ranging from high to low contributions to total uncertainty of the simulated discharge, was consequently arrived at: $\widehat{C}_{\mathrm{fc}}, \widehat{t}_{\mathrm{c-in}}, \widehat{t}_{\mathrm{c-bf}}, \widehat{T}, \widehat{P}, \widehat{T}_{\mathrm{crit}}, \widehat{m}_f, \widehat{C}_{\mathrm{tp}}$.

Table 10.3 lists all parameters and input variables with their potential to overall model uncertainty. Here, the fuzziness of model predictions is evaluated through two criteria, the mean ($\vdash\dashv$), and mean squared ($\vdash\dashv^2$) of the absolute magnitude of the interval of confidence of simulated daily discharge at the level of presumption of 0.8. If a parameter or input variable is set to a crisp value and both evaluation criteria show high

Table 10.3 Mean absolute ($\vdash\dashv$) and mean squared magnitude of the intervals of confidence ($\vdash\dashv^2$) of simulated daily discharge $\frac{\widehat{Q}_p}{[\overline{P}]}$ at a selected level of presumption μ of 0.80 that is dependent on fuzzy input data and parameters for the 1972–1993 period

Estimation of climatic input and parameter values: crisp or fuzzy	$\vdash\dashv$ [1]	$\vdash\dashv^2$ [1]
All fuzzy	0.956	0.076
All fuzzy except P	0.720	0.043
All fuzzy except T	0.716	0.043
All fuzzy except C_{tp}	0.743	0.046
All fuzzy except C_{fc}	0.577	0.028
All fuzzy except $t_{\mathrm{c-in}}$	0.603	0.030
All fuzzy except $t_{\mathrm{c-bf}}$	0.652	0.035
All fuzzy except m_f	0.752	0.047
All fuzzy except T_{crit}	0.737	0.045

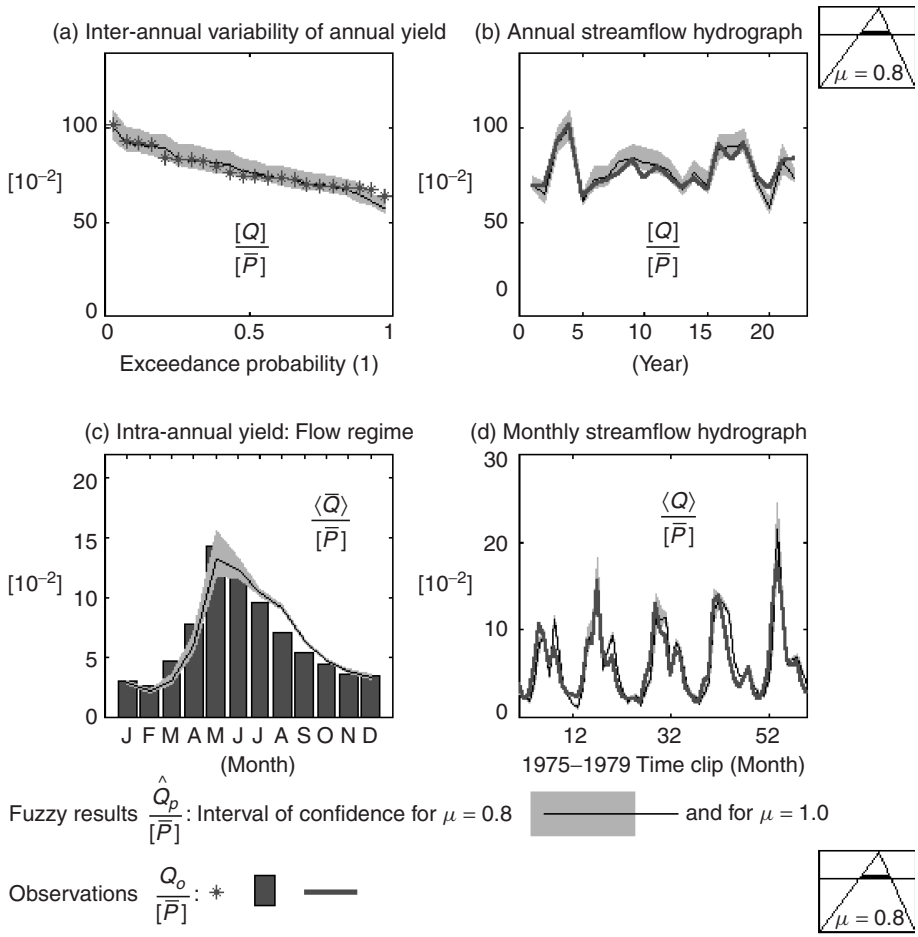


Figure 10.8 Performance of the basic water balance model with fuzzy input data but crisp (defuzzyfied) estimates for model parameters

deviations to the initial case when all input variables and parameters are fuzzy, then the influence on the overall model uncertainty is larger than in other cases. Among all factors, the parameter accounting for field capacity $\widehat{C}_{\mathrm{fc}}$ has the largest contribution to the uncertainty of model predictions. The next two in the list, in terms of their contributions, are the runoff delay times for interflow $\widehat{t}_{\mathrm{c-in}}$, and baseflow $\widehat{t}_{\mathrm{c-bf}}$. These are followed in order by the climatic inputs of $\widehat{T}$, $\widehat{P}$, followed by parameters relating to snowmelt, namely, $\widehat{T}_{\mathrm{crit}}$, $\widehat{m}_f$ and $\widehat{C}_{\mathrm{tp}}$. These results can be potentially useful to improve the estimation of the most influential parameters, or to make modifications to the model structure to avoid the use of parameters that are difficult to estimate, or those that contribute the most to the uncertainty of model predictions. This is investigated next.

10.8.3 Reducing model complexity

The estimation of the soil moisture capacity, $\widehat{C}_{\mathrm{fc}}$, is highly fuzzy because of difficulties in estimating soil depth, soil porosity, field capacity and permanent wilting point. Model simulations also demonstrated that $\widehat{C}_{\mathrm{fc}}$ also contributed the most to the fuzziness of the model predictions. Similarly, the estimation of delay times for subsurface flow paths, $\widehat{t}_{\mathrm{c-bf}}$ and $\widehat{t}_{\mathrm{c-in}}$, are also fuzzy because of the lack of detailed information on subsurface flow properties of the soils. A reduction of the levels of fuzziness of these parameters is not feasible unless significant advances are made in the field estimation of the soil properties. We therefore explore an alternative route in order to reduce the uncertainty in model results – in this case, we investigate if simplification of the model

can lead to more robust models, namely, models with less uncertain predictions.

Collapsing the two subsurface flow components, $\widehat{Q}_{in}$ and $\widehat{Q}_{bf}$, into just one results in a simpler model concept with a single subsurface flow component, $\widehat{Q}_{ss}$, is a possibility to reduce the number of parameters, especially the three most fuzzy and influential, namely, $\widehat{C}_{fc}$, $\widehat{t}_{c-bf}$ and $\widehat{t}_{c-in}$. This alternative model structure thus accounts for just two runoff components, saturation excess runoff $\widehat{Q}_{se}$ and subsurface runoff $\widehat{Q}_{ss}$. The water balance model for the soil moisture storage, Equation (10.5), is accordingly modified, and is reproduced below.

$$\widehat{S}(t+1)(=)\widehat{S}(t)(+)\widehat{P}_r(t)\Delta t(-)\widehat{E}_a(t)\Delta t(-)\widehat{Q}_{se}(t)\Delta t (-)\widehat{Q}_{ss}(t)\Delta t(-)\widehat{Q}_N(t)\Delta t \quad (10.13)$$

The convention for the carry over of fuzzy soil moisture states described in the Appendix applies here, too. The subsurface flow is expressed as:

$$\widehat{Q}_{ss}(=)\widehat{S}(\div)\widehat{t}_c \quad (10.14)$$

In this new simpler model, one soil parameter, $\widehat{C}_{fc}$, is no longer used, and the two drainage parameters, $\widehat{t}_{c-bf}$ and $\widehat{t}_{c-in}$, are replaced by a single parameter, $\widehat{t}_c$, which can be estimated more unambiguously because a separation criterion is no longer necessary. The catchment response time $\widehat{t}_c$ is estimated from the whole of the master recession curve, being representative of the total subsurface flow. The parameter is again estimated as a triangular fuzzy number with a center value of 21 days, being the result from the new recession analyses. The width of the fuzzy number is estimated according to

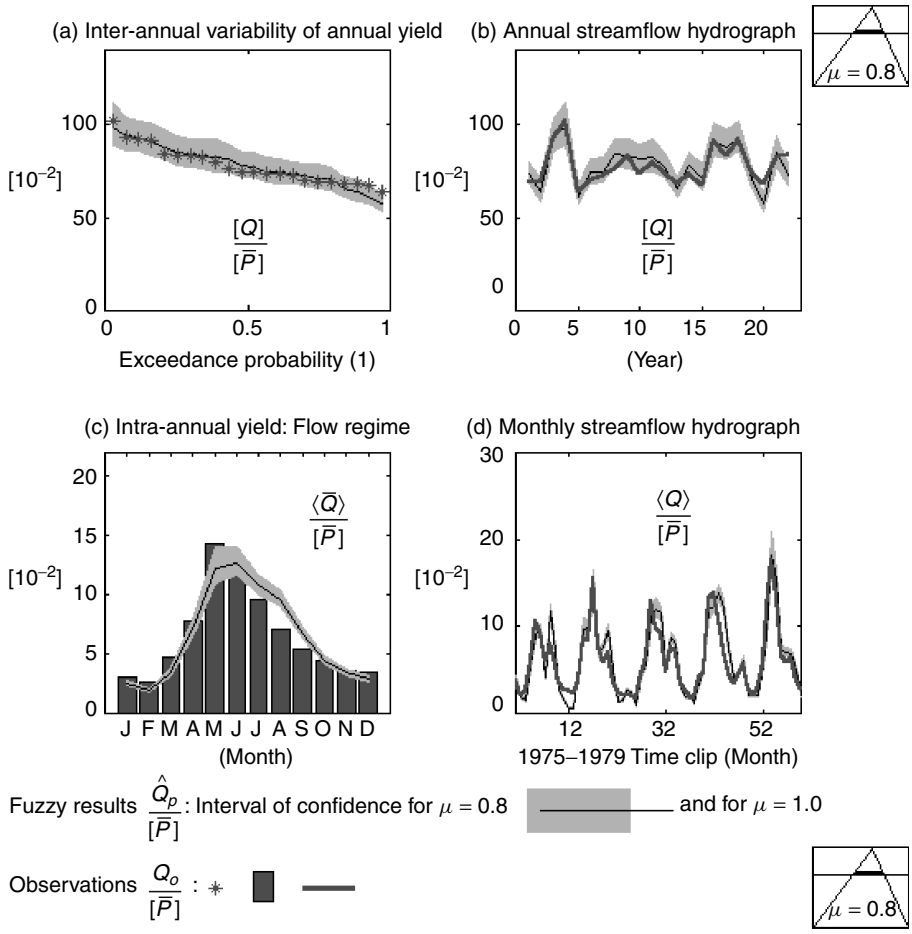


Figure 10.9 Performance of the alternative water balance model accounting for saturation excess runoff and a single subsurface flow component based on fuzzy parameters and fuzzy input data

Table 10.4 Criteria of uncertainty and measures of accuracy for the basic and the alternative water balance model: mean absolute ($\vdash\dashv$) and mean squared ($\vdash\dashv^2$) width of the intervals of confidence of simulated daily and monthly discharge $\frac{\widehat{Q}_p}{[\overline{P}]}$ at $\mu = 0.80$ for the 1972–1993 period; model accuracy criteria based on observed $\frac{\widehat{Q}_o}{[\overline{P}]}$ versus simulated daily and monthly discharge $\frac{\widehat{Q}_p}{[\overline{P}]}$ for $\mu = 0.80$

		$\vdash\dashv$	$\vdash\dashv^2$	MD	r	CM	NS
Basic model	Day	0.956	0.076	0.812	0.853	63.411	58.732
Equations (10.3) to (10.12)	Month	29.096	70.235	18.619	0.919	73.487	73.042
Alternative Model	Day	0.472	0.018	0.868	0.845	55.886	61.521
Equations (10.4) to (10.10), (10.13) and (10.14)	Month	14.360	17.108	20.039	0.907	67.639	71.766

$$\text{NS [\%]} = 100\left(1 - \frac{\sum_{i=1}^{n}\left(\sqrt{Q_{o,i}} - \sqrt{\widehat{Q}_{p,i}}\right)^2}{\sum_{i=1}^{n}\left(\sqrt{Q_{o,i}} - \sqrt{\overline{Q}_{o,i}}\right)^2}\right),\ \text{CM [\%]} = 100\left(1 - \frac{\sum_{i=1}^{n}\left(\sqrt{Q_{o,i}} - \sqrt{\widehat{Q}_{p,i}}\right)^2}{\sum_{i=1}^{n}\left(\sqrt{Q_{o,i}} - \sqrt{\overline{Q}_{o,i}}\right)^2}\right),\ r\text{[1], and MD [1]} = \frac{1}{n}\sum_{i=1}^{n}\left|\frac{Q_{o,i}}{[\overline{P}]} - \frac{\widehat{Q}_{p,i}}{[\overline{P}]}\right|$$

the sensitivity of the catchment response time to the selection of flow records from different seasons and years. The triangular membership function $\widehat{t}_c = (15, 21, 27)$ is estimated on the basis of these analyses.

The simple alternative model (Equations (10.6)–(10.10), (10.13) and (10.14)) is based on just six parameters. Simulations by this alternative model (Figure 10.9) are much less uncertain than the results generated with the original model (Figure 10.7). On the other hand, the results are similar in magnitude to those generated by the original model with crisp parameter estimates but fuzzy climatic inputs (Figure 10.8).

The results of the basic model and the simpler alternative model are now compared through quantitative measures. Table 10.4 displays uncertainty criteria ($\vdash\dashv$, $\vdash\dashv^2$) and certain accuracy criteria for daily as well as monthly discharges. The performances of the models are evaluated in terms of the match of simulated and observed discharges described by the sum of the mean differences (*MD*), coefficient of correlation (r), Chiew–McMahon criterion (Chiew and McMahon 1994) (*CM*) and Nash–Sutcliffe criterion (Nash and Sutcliffe 1970) (*NS*). Crisp measures of observed discharge and the simulated defuzzified model results, defined as the values at the highest level of presumption (Mayer *et al.* 1993), are compared.

As demonstrated by Figure 10.9, the uncertainty criteria show a significant reduction of fuzziness with the application of the simpler model for the daily as well as the monthly simulations. On the other hand, the estimated accuracy criteria show just a small reduction of model performance with the alternative, simple model structure, compared to that of the original model. In the case of the daily predictions, the Nash–Sutcliffe criterion even suggests a slightly improved performance. In other words, the simplification of the model has led to a significant reduction in predictive uncertainty, while experiencing no apparent reduction in the accuracy of model predictions.

10.9 SUMMARY AND CONCLUSIONS

This paper has presented the application of a fuzzy, lumped water balance model to the Upper Enns catchment in central Austria. The paper covered the basic principles of fuzzy logic and the associated arithmetic and showed how these can be used to construct the fuzzy water balance model. The model is then used, with realistic estimates of the uncertainty of catchment characteristics (for model parameters) and climatic inputs, to estimate the uncertainty of runoff predictions at the annual, monthly and daily time scales. The results are routinely presented in terms of ribbons (or strips or bands) of confidence in the model predictions, which in itself can be extremely valuable if they can be properly interpreted for water resources decision-making.

In addition, the model was used to investigate the relative sensitivity of model predictions, in particular, predictions of uncertainty of the catchment water balance, to the uncertainty in the various parameters and climatic inputs. It was found, for example, that the model predictions were much more sensitive to model parameterizations than to climatic inputs. The relative importance of the various parameters as well as

input variables is also investigated, and it is found that the field capacity was the most important parameter, followed by the subsurface routing parameters, the climate inputs of temperature and precipitation, the threshold air temperature, snowmelt factor and lastly the bucket capacity. This gives the clue as to which of these parameters must be estimated with more confidence in the future, and how increased confidence in model parameters and inputs will increase the confidence in the model predictions.

Finally, the model was also used to investigate the effect of decreased model complexity on the accuracy and uncertainty of model predictions. To do this, the shallow subsurface flow and baseflow were combined into a single subsurface runoff component, thus saving two of the most significant parameters, and the accuracy and uncertainty of the resulting simplified model were recalculated and compared to those of the original model. The results showed that while model accuracy worsens just slightly the uncertainty actually decreases significantly, suggesting that if only monthly or annual predictions are required, then the simpler model is not only sufficient (based on accuracy) but is also indeed preferable (because of improved predictive uncertainty).

Through this simple illustration, the utility and serious difficulties of the fuzzy logic approach were demonstrated to be integrated into water balance models. The fuzzy approach can also be used to investigate the relative importance of various parameters, inputs and processes for the development of comprehensive water balance models, and can indeed be used to simplify the models based on systematic sensitivity analyses of the kind presented in this paper. This can lead to parsimonious models in the future, and models that are capable of predicting not just the mean response but also confidence in the predictions. In this paper, we also highlighted the difficulty with the use of rules of fuzzy arithmetic in a continuous fashion, as the fuzziness in the predictions tend to grow cumulatively. We utilized an ad hoc mechanism to control this growth at every time step. However, a more formal and correct approach needs to be found within the framework of fuzzy logic. This is beyond the scope of this exploratory study and is left for further research.

10.10 ACKNOWLEDGEMENTS

The research was supported in part by a travel grant provided to the first author from the Austrian Federal Ministry of Education, Science and Culture to spend a few months at the Centre for Water Research, the University of Western Australia. The work was completed while the third author was at the Delft University of Technology on a Visiting Professorship. The authors are grateful to these three institutions for their generous support.

10.11 APPENDIX

10.11.1 Basic rules of fuzzy arithmetic

Fuzzy arithmetic is easiest to present using the α-level set notation (Figure 10.10). For $\widehat{X}(\alpha) = [x^l(\alpha), x^r(\alpha)]$, the lower and upper bounds of $\widehat{X}(\alpha)$ are indicated by $x^l(\alpha)$ and $x^r(\alpha)$, respectively (Özelkan and Duckstein 2001):

Fuzzy addition:

$$\widehat{X}(\alpha)(+)\widehat{Y}(\alpha) = [x^l(\alpha) + y^l(\alpha), x^r(\alpha) + y^r(\alpha)] \tag{10.15}$$

Fuzzy subtraction:

$$\widehat{X}(\alpha)(-)\widehat{Y}(\alpha) = [x^l(\alpha) - y^r(\alpha), x^r(\alpha) - y^l(\alpha)] \tag{10.16}$$

Fuzzy multiplication:

$$\widehat{X}(\alpha)(\bullet)\widehat{Y}(\alpha) = [x^l(\alpha) \cdot y^l(\alpha), x^r(\alpha) \cdot y^r(\alpha)] \tag{10.17}$$

Fuzzy division:

$$\widehat{X}(\alpha)(\div)\widehat{Y}(\alpha) = [x^l(\alpha) \div y^r(\alpha), x^r(\alpha) \div y^l(\alpha)] \tag{10.18}$$

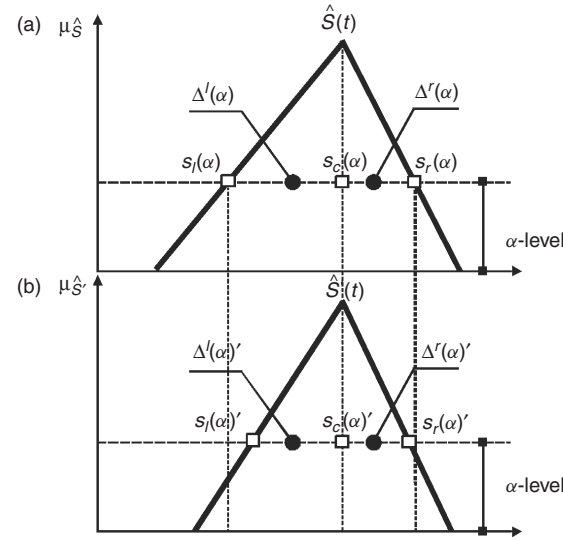


Figure 10.10 Controlled carry over of uncertainty of soil moisture from time t to $t + 1$

10.11.2 Comparison of two fuzzy numbers

In order to ascertain the form of precipitation, that is, rain or snow, we have to decide if $\widehat{T}(>)\widehat{T}_{\text{crit}}$ or $\widehat{T}(\leq)\widehat{T}_{\text{crit}}$. For example, on May 1, 1976 $\widehat{T} = (1^{\circ}\text{C}, 2.5^{\circ}\text{C}, 4^{\circ}\text{C})$, while $\widehat{T}_{\text{crit}} = (0^{\circ}\text{C}, 1^{\circ}\text{C}, 2^{\circ}\text{C})$, which means that the two fuzzy membership functions overlap. Different approaches for the comparison of fuzzy numbers have been tested such as through defuzzification of both fuzzy numbers into crisp values. The crisp representatives of fuzzy numbers were defined by either the centers of gravity or the values at the highest levels of presumption, with very similar results. The presented results are based on the second concept.

10.11.3 Carry-over of system state uncertainty from time t to $t + 1$

In this paper, the carry over of fuzziness between time steps is achieved by rescaling the fuzziness of $\widehat{S}$ computed at time step $t - 1$ into the corresponding value $\widehat{S}'$ at time t through the so-called soil moisture ratio, which is defined as:

$$r_S = 1 - \frac{S(t)}{C_{\text{tp}}} \tag{10.19}$$

where S and C_{tp} are the defuzzified crisp equivalents of the fuzzy estimates $\widehat{S}$ and $\widehat{C}_{\text{tp}}$. Referring to Figure 10.10, the rescaling of the fuzziness of soil moisture storage is described, in the usual manner, by:

$$\widehat{S}'(t) = (s^{l\prime}, s^{c\prime}, s^{r\prime}) = (s^c - \Delta^l(\alpha = 0)', s^c, s^c + \Delta^r(\alpha = 0)') \tag{10.20}$$

where s^l, s^c, and s^r denote the characteristic left (for $\alpha = 0$), center (for $\alpha = 1$) and right values (for $\alpha = 0$) of a triangular fuzzy number, respectively, and $s^{l\prime}$, $s^{c\prime}$, and $s^{r\prime}$ denote the re-scaled values. The restriction on complete carry over is achieved by rescaling the left and right deviations $\Delta^l(\alpha)$ and $\Delta^r(\alpha)$ (of the lower and upper bounds from the center value) by the soil moisture ratio r_S. As indicated in Figure 10.10, for a general value of α this rescaling is represented by:

$$\Delta^l(\alpha)' = \Delta^l(\alpha) - \Delta^l(\alpha) \cdot r_S \tag{10.21}$$

$$\Delta^r(\alpha)' = \Delta^r(\alpha) - \Delta^r(\alpha) \cdot r_S \tag{10.22}$$

Note that when the bucket is empty, $r_S = 1$, whereas when the bucket is full $r_S = 0$. Thus, as per Eqs (10.21) and (10.22), we see that when the bucket is empty, the model loses all memory of the fuzziness in previous time steps, and there is thus absolutely no carry over of fuzziness. On the other hand, when the bucket is full, all of the fuzziness from the previous time step is carried over. The approach presented above is next used to scale the fuzziness from t to $t + 1$, using the newly computed fuzziness, $\widehat{S}'$, and moisture ratio, r_S, at time t; the process continues in this way into the future.

REFERENCES

Ahmed S, de Marsily G (1987). Comparison of geostatistical methods for estimating transmissivity using data on transmissivity and specific capacity. *Water Resour. Res.*, **23**(9): 1717–1737.

Alley W M (1984). On the treatment of evapotranspiration, soil moisture accounting, and acquifer recharge in monthly water balance models. *Water Resour. Res.*, **20**(8): 1137–1149.

Baumer O W (1989). Predicting unsaturated hydraulic parameters. In: *Indirect Methods for Estimating the Hydraulic Properties of Unsaturated Soils*, Eds. van Genuchten M Th, Leij F J, *Proceedings of the International Workshop on Indirect Methods for Estimating Hydraulic Properties of Unsaturated Soils*, University of California, Riverside, CA, October 11 – 13, 1989.

Beck M B (1994). Understanding uncertain environmental systems. In: *Predictability and Nonlinear Modeling in Natural Sciences and Economics*. Eds. Grasman J, van Straten G, pp. 294–311. Kluwer, Dordrecht.

Beven K J (2001). *Rainfall-Runoff Modelling – The Primer*. John Wiley & Sons, Chichester, U. K., 360p.

Braun L N (1985). Simulation of snowmelt-runoff in lowland and lower Alpine regions of Switzerland. *Zürcher Geographische Schriften 21*: Geographisches Institut, Eidgenössische Technische Hochschule, Zürich, Switzerland.

Chiew F H S, McMahon T A (1994). Application of the daily rainfall – runoff model MODHYDROLOG to 28 Australian catchments. *J. Hydrol.*, **153**: 383–416.

Chiew F H S, Stewardson M J, McMahon T A (1993). Comparison of six rainfall-runoff modelling approaches. *J. Hydrol.*, **147**: 1–36.

Christakos G (1992). *Random Field Models in Earth Sciences*. Academic Press. ISBN 0-12-174230-X.

Civanlar M R, Trussel H J (1986). Constructing membership functions using statistical data. *Fuzzy Set. Syst.*, **18**: 1–13.

Dubois D, Prade H (1980). *Fuzzy Sets and Systems: Theory and Applications*. Academic Press, New York.

Dubois D, Prade H (1986). Fuzzy sets and statistical data. *Eur. J. Oper. Res.*, **25**: 345–356.

Dubois D, Prade H (1988). *Possibility Theory: An Approach to Computerized Processing of Uncertainty*. Plenum Press, New York.

Eder G, Nachtnebel H P, Loibl W (2001). *Raumzeitlich Differenzierte Wasserbilanzierung der Flusseinzugsgebiete Gurk und Gail. Projektnr. KA 40/99*. The Austrian Federal Ministry of Education, Science and Culture, Vienna, and the Austrian Provincial Government of Carinthia, Klagenfurt, Austria.

Eder G, Sivapalan M, Nachtnebel H P (2003). Modeling water balances in Alpine catchment through exploitation of emergent properties over changing time scales. *Hydrol. Process.*, **17**, 2125–2149, doi: 10.1002/hyp.1325.

Franchini M, Pacciani M (1991). Comparative analysis of several conceptual rainfall-runoff models. *J. Hydrol.*, **122**: 161–219.

Franks S W, Beven K J (1999). Conditioning a multiple-patch SVAT model using uncertain time-space estimates of latent heat fluxes as inferred from remotely sensed data. *Water Resour. Res.*, **35**: 2751–2761.

Franks S W, Gineste Ph, Beven K J, Merot Ph (1997). On constraining the predictions of a distributed model: the incorporation of fuzzy estimates of saturated areas into the calibration process. *Water Resour. Res.*, **34**: 787–797.

Freer J, Beven K J, Ambroise B (1995). Bayesian estimation of uncertainty in runoff prediction and the values of data: an application of the GLUE approach. *Water Resour. Res.*, **32**: 2161–2173.

Fuchs M (1998). Modeling snowmelt runoff in an Alpine watershed. Thesis 10–98, Department for Water Management, Hydrology and Hydrological Engineering. University for Agricultural Sciences, Vienna, Austria.

Garen D C, Burges S J (1981). Approximate error bounds for simulated hydrographs. *Trans. Am. Soc. Civ. Eng.*, **107**, HY11, 1519–1534.

Gelhar L W (1986). Stochastic subsurface hydrology from theory to applications. *Water Resour. Res.* (special issue), **22**: 135S–45S.

Hisdal E (1994). Interpretative versus perspective fuzzy theory. *IEEE Trans. Fuzzy Syst.* **12**: 22–26.

IAHR (1987). *Discharge and Velocity Measurements: Proceedings of the Short Course on Discharge and Velocity Measurements*. Zurich. 26–28. August. Ed. Müller A, Balkema, Rotterdam, Netherlands, ISBN 90 6191 7824.

Journel A (1989). Fundamentals of geostatistics in five lessons. *Short Course in Geology 8*. Amer. Geophys. Union, Washington, DC.

Kaufmann A, Gupta M M (1991). *Introduction to Fuzzy Arithmetic – Theory and Applications*. Van Nostrand Reinhold, ISBN 0-442-23007-9.

Klemes V (1983). Conceptualization and scale in hydrology. *J. Hydrol.*, **65**: 1–23.

Lauscher F (1982). Die temperaturen der termine mit schneefall und regen. Wetter und leben. *Z. Angew. Meteorol.* **34**(4): 241–245.

Mayer A, Mechler B, Schlindwein A, Wolke R (1993). *Fuzzy Logic – Einführung und Leitfaden zur Praktischen Anwendung*. Addison-Wesley. ISBN 3-89319-443-6.

Nachtnebel H P, Baumung S T, Lettl W (1993). Abflussprognosemodell für das Einzugsgebiet der Enns und der Steyr. IWHW STEWEAG-Enns93 Report, Institute of Water Management, Hydrology and Hydraulic Engineering, University of Agricultural Sciences (IWHW-BOKU), Vienna, Austria.

Nash J E, Sutcliffe J V (1970). River flow forecasting through conceptual models. Part I – a discussion of principles. *J. Hydrol.*, **27**: 282–290.

Österreichische Akademie der Wissenschaften (1979). *Atlas der Republik Oesterreich, Kartentafel IV/4*. Kommission fuer Raumforschung. Bearbeitung: Fink J, Walder R, Rerych W, Vienna, Austria.

Österreichische Bodenkartierung. Radstadt K B 1986. Schladming K B 1980. Gröbming K B 1981. Irdning K B 1985. Rottenmann K B 1992. *Bodenkarte und Erlaeuterungen zur Bodenkarte*. M 1:25.000. Austrian Ministry for Agriculture and Forestry, Vienna.

Özelkan E C, Duckstein L (2001). Fuzzy conceptual rainfall-runoff models. *J. Hydrol.*, **253**, 41–68.

Richter D (1995). *Ergebnisse methodischer Untersuchungen zur Korrektur des systematischen Messfehlers des Hellmann-Niederschlagsmessers. Graph. Darstellung*. Selbstverl. d. Dt. Wetterdienstesb194, Offenbach am Main, ISBN 3-88148-309-8.

Sevruk B (1983). Correction of measured precipitation in the Alps using the water equivalent of new snow. *Nord. Hydrol.*, **14**(2): 49–58, Lyngby.

Sevruk B (1986). Correction of precipitation measurements: Swiss experience. *Zürcher Geogr. Schriften*, **23**: 187–196. Zürich, Switzerland.

Sivapalan M, Blöschl G, Zhang L, Vertessy R (2003). Downward approach to hydrological prediction. *Hydrol. Process.*, **17**, 2101–2111, doi: 10.1002/hyp.1425.

Thornthwaite C W (1948). An approach towards a rational classification of climate. *Geogr. Rev.*, **38**(1): 55–94.

Türksen I B (1991). Measurement of membership functions and their acquisition. *Fuzzy Set. Syst.*, **40**: 34–43.

Wheater H S, Beck M B (1995). Modelling upland stream water quality: Process identification and prediction uncertainty. In: *Solute Modeling in Catchment Systems*. Ed. Trudgill S T, pp. 305–324. John Wiley & Sons, Chichester, U. K.

Wittenberg H (1994). *Nonlinear Analysis of Flow Recession Curves*. pp. 61–67. IAHS Publication no. 221.

World Meteorological Organization (1986). Inter-comparison of models of snowmelt runoff. Operational Hydrology, Report No. 23. Secretariat of the World Meteorological Organisation, Geneva, Switzerland.

Zadeh L A (1965). Fuzzy sets. *Inf. Control*, **8**: 338–353.

Zadeh L (1978). Fuzzy sets as a basis for a theory of possibility. *Fuzzy Sets Syst.*, **1**(1): 3–28.

Zimmermann H J (1995). *Fuzzy Set Theory and Its Applications*. Kluwer, Dordrecht.

11

Water Relations of an Old-growth Douglas Fir Stand

TIMOTHY E. LINK[1], GERALD N. FLERCHINGER[2], MIKE UNSWORTH[3] AND DANNY MARKS[2]

[1]Dept. of Forest Resources, University of Idaho, Moscow, ID 83844-1133, USA, [2]USDA Agricultural Research Service, Northwest Watershed Research Center, 800 Park Blvd., Boise, ID 83712, USA, [3]Oregon State University, College of Oceanic and Atmospheric Sciences, COAS Administration Building 104, Corvallis, OR 97331, USA

11.1 INTRODUCTION

In many areas of the world, growing populations depend on forested upland areas as a source of high-quality water resources. In many regions, competing resource demands for timber production, municipal and irrigation water supplies, and survival of endangered species emphasize the need to understand how forest vegetation affects hydrological fluxes. Many montane forests occur across steep hydroclimatic gradients and may be relatively sensitive to climate change; therefore, an understanding of the water relations of forests is needed to assess the hydrologic effects of changing climates. This is particularly important in Mediterranean climates characterized by cool, wet winters, and warm, dry summers when evaporation and transpiration (ET) exceed precipitation. Hydrological dynamics of forest ecosystems also affect carbon fluxes through their influence on foliar CO_2 exchange, heterotrophic and autotrophic respiration, fine root turnover, and the decay of downed wood (Waring and Running 1998). An understanding of the mechanisms that control hydrological fluxes from forests is also necessary to understand the biogeochemical dynamics of upland areas (Waring and Running 1998).

Hydrological processes in the near surface environment are strongly influenced by the presence of vegetation. Forest canopies may intercept a large portion of the incident precipitation, ranging from approximately 10 to 40% of the annual water balance, depending on canopy and environmental conditions (Dingman 2002). Evaporation of intercepted precipitation reduces the throughfall below forest canopies and the amount of water entering the soil profile. Transpiration is also a major component of the forest water balance, with rates under well-watered conditions typically ranging from 2 to 12 mm day^{-1}, depending on canopy and climate conditions (Jones 1992). On a global basis, ET accounts for approximately 61% of gross precipitation (Maidment 1993). Quantification of these fluxes is especially important in forested areas to assess hydrological changes associated with changing land-use and vegetation patterns.

A large number of investigations have been completed to assess the impact of forest harvest on the annual water yields of catchments (Stednick 1996) and peak flows (e.g. Bowling *et al*. 2000; Jones and Grant 1996; Thomas

Climate and Hydrology in Mountain Areas. Edited by C. de Jong, D. Collins and R. Ranzi
© 2005 John Wiley & Sons, Ltd. ISBN: 0-470-85814-1

and Megahan 1998). Many empirical studies on the effects of forest harvest on catchment hydrology indicate increased water yield and increased low flows in a four- to eight-year period following canopy removal, which is attributed to decreased ET (Harr *et al*. 1982; Hicks *et al*. 1991; Keppeler and Ziemer 1990). In some watersheds that initially exhibited increased water yields following logging, yield was observed to eventually decrease below predicted values relative to control (unharvested) treatments. Decreases were attributed to the regrowth of species in the riparian zone, which increased ET fluxes within these watersheds (Harr and McCorison 1979). Canopy removal in small catchments generally produced an increase in small (i.e. <1 year return interval) peak flows (Wright *et al*. 1990; Ziemer 1981; Harr *et al*. 1975; Jones and Grant 1996; Thomas and Megahan 1998); however, there is considerable debate concerning the magnitude of peak increases in large catchments (e.g. Jones and Grant 1996; Thomas and Megahan 1998; Jones and Grant 2001; Thomas and Megahan 2001). To help assess the impacts of land-cover alteration, an improved understanding of how local-scale canopy and climate conditions affect the forest water balance is needed.

Physically based numerical models are powerful tools that can be used to improve our understanding of the mechanisms controlling hydrological fluxes. These techniques are particularly useful in mountainous, forested areas to provide an estimate of fluxes that would otherwise be very difficult to measure due to complex logistics of working in remote and rugged terrain. There are a number of physically based soil–plant–atmosphere models that simulate mass and energy transfer processes through layered soil–vegetation–atmosphere systems (e.g. Flerchinger *et al*. 1996b; Wigmosta *et al*. 1994; Sellers *et al*. 1996; Williams *et al*. 2001). The Simultaneous Heat and Water (SHAW) model discussed in this chapter integrates the coupled transport of mass and energy through a soil–vegetation–atmosphere system into a simultaneous solution (Flerchinger and Saxton 1989; Flerchinger *et al*. 1996b). Individual components of the model have been validated, including the effect of vegetation on soil temperature and moisture (Flerchinger and Pierson 1997), snowmelt (Flerchinger *et al*. 1994; Flerchinger *et al*. 1996a), soil freezing (Flerchinger and Saxton 1989), ET and surface energy budgets (Flerchinger *et al*. 1996b), and radiometric surface temperature (Flerchinger *et al*. 1998). The model was recently modified for use in forested environments and validated against measurements of evaporation, transpiration, soil water content, and temperature profiles (Link *et al*. 2004a).

Concern regarding the impacts of land-cover alterations on surface mass and energy fluxes emphasize the need to understand the magnitude and seasonal variability of water fluxes from forested areas. Quantification of these fluxes for old-growth canopies provides an end-member reference point for unmanaged, old forests, for comparison to younger age classes that currently comprise large tracts of forestlands. Our primary objective in this study was to estimate the local-scale water fluxes from an old-growth forest for two contrasting years. Our specific objectives were to:

- Parameterize and validate the physically based SHAW model for an old-growth forest canopy.
- Estimate the annual magnitudes of major water-balance components.
- Explore the temporal dynamics of the primary water-balance components.
- Assess how latent and sensible energy fluxes vary during the summer months.

11.2 METHODS

11.2.1 Conceptual framework

Our forest water-balance investigation was composed of complementary measurement and modeling programs. The measurement program was undertaken in an intensively instrumented forest stand to create a data-rich environment for model validation and testing. The measurements were used to parameterize and validate the SHAW model to provide an estimate of forest water fluxes over the 1999 and 2000 water years.

11.2.2 Site description

This study was conducted at the Wind River Canopy Crane Research Facility (WRCCRF), located within the T.T. Munger Research Natural Area of the Gifford Pinchot National Forest, in southwestern Washington, USA (Figure 11.1). The site is located on a gently sloping alluvial fan in the Wind River Valley in the Cascade Mountains. Site characteristics are listed in Table 11.1. A Liebherr 550HC tower crane is located in the center of the 4 ha study area, and was used as a sensor platform for micrometeorological measurements (Figure 11.2). The crane is 85 m high, with a jib range of 87 m that inscribes a 2.3 ha circular area within the plot where hydrological measurements were made. The physical setting, ecological characteristics, and infrastructure of the WRCCRF are described in detail by Shaw *et al*. (2004).

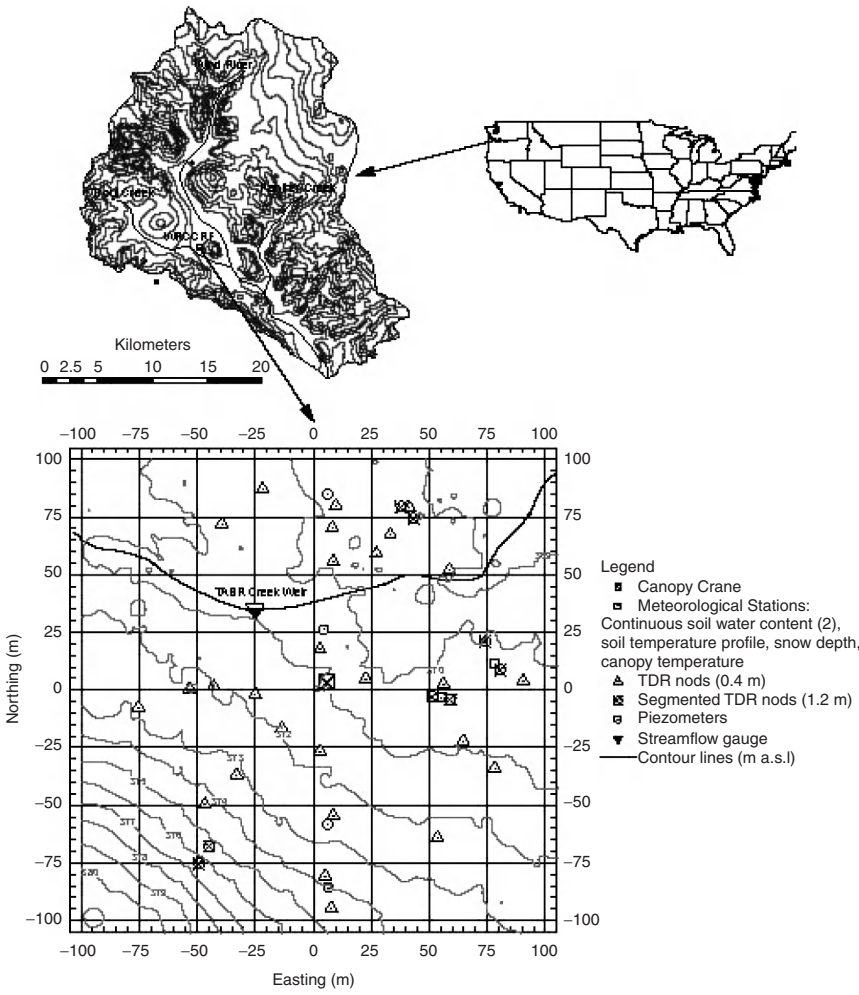


Figure 11.1 Location of the Wind River Basin and the WRCCRF in Washington State, USA

Table 11.1 Basin characteristics

Name of basin	Wind River, Washington
Mountain range	Cascades, USA
Elevation range of entire catchment (m)	60–1600
Elevation range of individual sites (m)	368–381
Latitude and longitude	45° 49′N, 121° 57′W
Area (km^2)	582
Geology	Mainly basalt and alluvium
% glacierized	0
Vegetation type (dominant)	Douglas fir/western hemlock forest
% forested	97%
Mean Q at catchment outlet (mm)	1850

Dominant vegetation species at the site are Douglas fir (*Pseudotsuga menzesii*), western hemlock (*Tsuga heterophylla*), and western red cedar (*Thuja plicata*), with many individual trees exceeding 500 years in age. The canopy height is approximately 60 m, with the tallest trees reaching 65 m (Ishii *et al*. 2000). The canopy exhibits many old-growth characteristics, including a high degree of spatial heterogeneity, a multilayered canopy, and a high degree of biodiversity in the plant community (Franklin and Spies 1991). Understory tree species include pacific yew (*Taxus brevifolia*), Pacific silver fir (*Abies amabilis*), and vine maple (*Acer circinatum*). Dominant species of the lowest layer include salal (*Gaultheria shallon*), Oregon grape (*Berberis nervosa*) and vanilla leaf (*Achlys triphylla*). The average leaf area



Figure 11.2 Wind River Canopy Crane Research Facility (WRCCRF). Photo by Al Levno, USFS PNW/OSU Forest Science Data Bank

index (LAI) of the site was 8.6 ± 1.1, ranging from 9.3 ± 2.1 to 8.2 ± 1.8 measured by the vertical line intercept method over a three-year period (Thomas and Winner 2000).

A thick litter layer composed of coarse and fine woody detritus, needles, leaves, and mosses, ranges from roughly 0.02 to 0.10 m depth across the site. Soils at the site originated as a deep volcanic ash deposit, and are described as shotty loamy sands and sandy loams. Soils are classified as frigid andisols, with low bulk densities ($800-1100\,kg\,m^{-3}$), and high porosities (0.5–0.75) (Dyrness 2003).

Climate at the site is characterized by cool, wet winters and warm, dry summers, with an average annual precipitation of 2470 mm, measured at the Wind River Ranger Station (WRRS) approximately 2.5 km south of the site. Less than 10% of the precipitation occurs between June and September (Shaw *et al*. 2004). Snowfall is most common from November to March and varies widely between years because the site is located near the lower limit of the transient snow zone. Mean annual air temperature is 8.7°C, with the mean monthly maximum of 17.3°C occurring in August and the mean monthly minimum of −0.1°C occurring in January. Soil freezing occurs rarely at the site and is limited to the top several mm of soil.

11.2.3 Measurement program

A series of meteorological stations were installed in a profile on the crane tower, on the forest floor, and within an open field approximately 500 m from the forest edge. Net radiation was measured at 85 m on the top of the tower using a 4-component net radiometer that senses four separate streams of upwelling and downwelling solar and thermal radiation (Kipp and Zonen, CNR-1). Combination air temperature and relative humidity sensors (Vaisala, HMP35C), and ultrasonic anemometers (Handar/Vaisala, WAS425 & Solent Gill, HS) were installed at 68, 57, 40, 23, 12 and 2 m. Precipitation was measured above the canopy on the crane counter jib with a weighing rain gauge (Belfort, 6071) and at the open station using both weighing (Belfort, 5-780) and tipping-bucket (Texas Electronics, TE-525) gauges. Snow depth was recorded at the open site and within the crane circle, beneath a closed canopy and within a large (∼25 m diameter) canopy gap with sonic snow depth sensors (Judd Communications). Data were recorded at 30-minute intervals.

A roving array of rain gauges was installed within the crane circle to measure throughfall during the rainfall season, and to characterize the interception characteristics of the canopy. The gauge array consisted of 44 manually measured collectors and 24 automated tipping buckets (Texas Electronics, TE-525I) equipped with individual event dataloggers (Onset Computer, HOBO Event). Gauges were installed in a stratified random sampling pattern and randomly relocated every 4 to 8 weeks. Throughfall was measured during the snow-free periods from 8 April to 8 November, 1999 and from 30 March to 4 December, 2000.

A distributed array of soil water content sensors was installed throughout the crane circle (Figure 11.1). Volumetric water content was measured at 28 locations in the top 0.40 m of the soil every three to four weeks using time domain reflectometery (TDR, Soil Moisture Equipment, Trase 6050XI). Water content profiles were also measured at 8 locations over depths ranging from 0 to 0.15 m, 0.15 to 0.30 m, 0.30 to 0.60 m, 0.60 to 0.90 m, and 0.90 to 1.20 m with segmented TDR probes (Environmental Sensors, Type A), interrogated with a portable TDR unit (Environmental Sensors, MP-917). Water contents in the top 0.30 m of the soil were monitored continuously at four locations using frequency reflectometers (Campbell Scientific, CS615).

Net ecosystem water vapor flux (ET) was measured with an eddy-covariance (EC) system installed at 73 m on the crane tower (data provided courtesy of K.T. Paw U and M. Falk). The source area contributing to the ET measurement (the footprint) extends typically less than 100 m upwind during unstable daytime conditions, but may extend more than 1 km upwind during stable conditions at night (beyond the range of uniform forest conditions in some directions). Full details of the system, methods, and data corrections are given by Paw U *et al*. (2004). EC data were available for the 1999

period through 31 July, 1999 at the time this analysis was completed.

Overstory transpiration was estimated by scaling sap flux measurements obtained using a heat dissipation method (Granier 1985) (data courtesy of N. Philips and B. Bond). Six dominant Douglas-fir individual trees were instrumented with three to five sensors installed about 4 m above the ground. Measurements from the individual sensors were scaled to the tree level, then to the stand level. The scaling process involves several sources of uncertainty; therefore, these measurements were used to provide only an approximation of seasonal transpiration trends. Details of the sap flux measurements made at this site are described in Phillips *et al*. (2002) and concerns on scaling sap flux measurement to the entire stand are addressed in Unsworth *et al*. (2004).

Groundwater surface elevation was measured weekly at 4 piezometers located along a north–south transect across the site. Streamflow on TABR Creek, a small ephemeral stream that crosses the site was measured at a calibrated 90° v-notch weir.

11.2.4 Modeling program

Water-balance simulations of the WRCCRF were made using the SHAW model. The SHAW model simulates a vertical, one-dimensional system composed of a vegetation canopy, snowcover (if present), litter, and soil profile. A conceptual diagram of the model structure is shown in Figure 11.3. The model integrates the detailed physics of interrelated mass and energy transfer through the multilayer system into one simultaneous solution. Hourly predictions include evaporation, transpiration, snow depth, runoff, and profiles of soil water content and temperature.

Upper boundary conditions are defined by meteorological variables (solar radiation, air temperature, humidity, windspeed, and precipitation) measured above the canopy. Lower boundary conditions are defined by soil temperature and soil water content, potential or flux at a specified depth. A layered system is established though the model domain, with each layer represented by a node. After computing fluxes at the upper boundary, the heat, liquid water, and vapor fluxes between layers are simulated. Vegetation height, biomass, leaf area index, rooting depth, and leaf dimension are specified by the user. Details of the numerical implementation of the SHAW model are presented in Flerchinger (2003) Flerchinger *et al*. (1998, 1996b), and Flerchinger and Saxton (1989).

For this investigation, the SHAW model was modified to simulate saturated flow in soils and to more accurately simulate ET from forest vegetation. Modifications to the model included improved parameterizations for intercepted rainfall storage, canopy conductance to water vapor transport, and transmission of radiation within the canopy. Details of the modifications and implementation of the model for the WRCCRF canopy are provided in Link *et al*. (2004a).

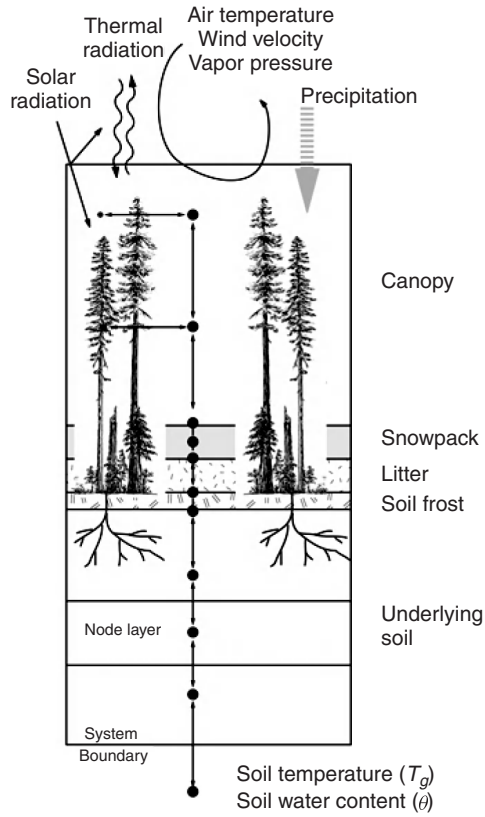


Figure 11.3 Conceptual diagram of the Simultaneous Heat and Water (SHAW) Model. Reproduced with permission from Link *et al*., Simulation of water and energy fluxes in an old growth seasonal temperate rainforest using the Simultaneous Heat and Water (SHAW) model; published by American Meteorological Society, 2003

Simulations were completed for the 1999 and 2000 water years. In summary, the canopy was simulated as a single species with an LAI of 8.6, rooting depth of 1.2 m, and maximum stomatal conductance of 4.2 mm s^{-1}, based on measurements at the site. The soil was simulated as two relatively high hydraulic conductivity layers from 0 to 0.50 and 0.50 to 1.00 m, overlying a low conductivity lower layer from 1.00 to 2.00 m, based on soil properties measured on 18 cores collected at the site. The canopy, litter, and soil layers were represented as 10, 6, and 24 nodes respectively in the model domain.

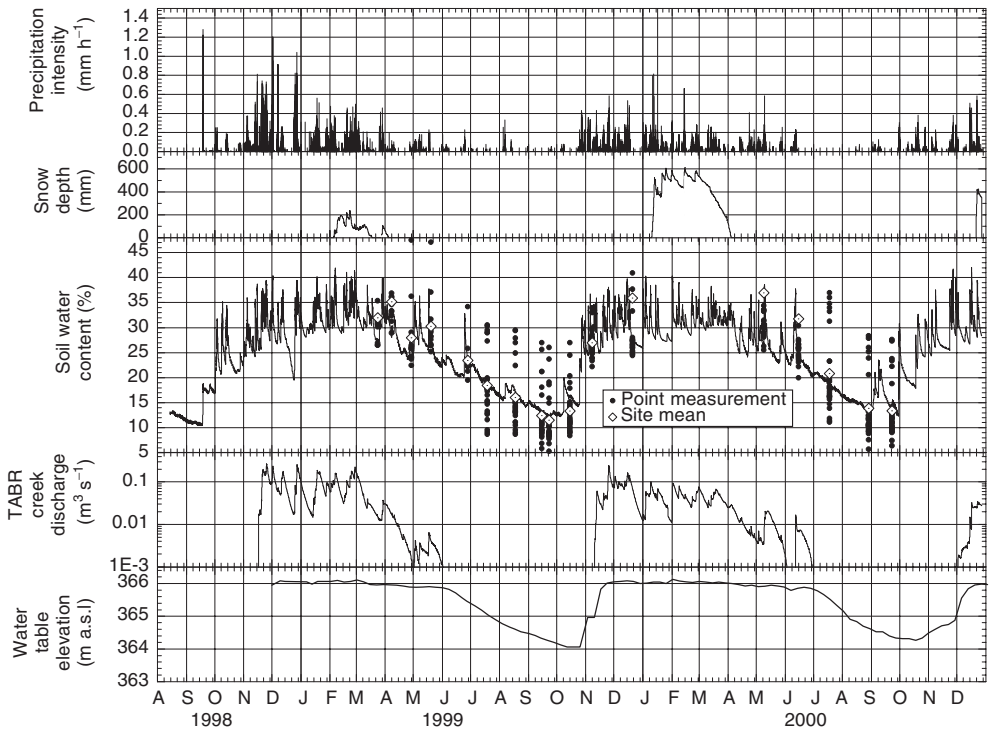


Figure 11.4 Precipitation intensity, snow depth, soil moisture, water table elevation, and streamflow at WRCCRF, hy1999–2000. Snow depth was recorded in a canopy gap and represents a maximum depth at the site. The range and mean of individual soil water content measurements are shown with symbols (•, ◇) and the approximate site average soil water content is shown by the record from a continuously logged proxy sensor

11.3 RESULTS AND DISCUSSION

11.3.1 Climate and rainfall interception measurements

A summary of the hydrological conditions during the 1999 and 2000 water years is shown in Figure 11.4. This figure illustrates important features of the hydroclimatic regime of the Pacific Northwest region of the United States. In this region, there is a progressive decline of soil moisture, streamflow, and groundwater levels through the dry summer months, followed by replenishment of water during wet winters.

Precipitation during the 1999 and 2000 water years was slightly greater (+5 and +0%, respectively) than the long-term (1931–1977) average annual precipitation of 2470 mm measured at the WRRS. Mean monthly temperatures during the winter periods ranged from 0.5 to 3.0°C above average. During warmer than average conditions in 1999, precipitation occurred mainly as rain, and snowcover at the site consisted of isolated snow patches in canopy gaps. Snow conditions were more typical in 2000, when a shallow continuous snowcover developed at the site lasting approximately 10 weeks. The spring seasons in both years were characterized by wetter than average conditions, followed by drier than average summers (Link 2001).

During the 1999 period when throughfall was measured, 451 mm of rainfall occurred and 103 mm (23%) was evaporated from the canopy. The proportion of interception loss was similar during the 2000 measurement period, with 619 mm of rainfall measured and 155 mm (25%) lost to evaporation. The canopy saturation storage capacity derived from the throughfall measurements increased from an average of 3.0 mm in the spring and fall, to 4.1 mm in the summer, probably as a result of seasonal leaf area changes. The storage volume per unit leaf area was about 0.4 mm m^{-2}, much higher than values estimated in plantation forests. The high value for the WRCCRF canopy is apparently due to the additional storage capacity of stems, branches, and the large canopy epiphyte community consisting of lichens and bryophytes, that can absorb from 2 to 12

times their dry weight of water (Nash and Wirth 1988; Proctor 1982). Details of the throughfall measurements and derivation of canopy interception parameters are provided by Link *et al*. (2004b).

11.3.2 Simultaneous heat and water model (SHAW) validation

The SHAW model was modified using the 1999 dataset and validated using the 2000 dataset. The SHAW model is physically based and requires little calibration. Parameter adjustments during the development year were limited to measured and estimated soil properties (specifically, saturated hydraulic conductivity and the pore size distribution index) to more accurately simulate observed drainage trends. The model was validated against detailed measurements of snowcover, throughfall, and soil moisture, and estimates of transpiration and ET to verify that the model reasonably reproduced both the absolute magnitudes and general trends of the primary hydrological fluxes. A detailed discussion of the model validation is presented by Link *et al*. (2004a) and is summarized herein.

In 1999, the model simulated the development and ablation dates of the shallow snowcover in a canopy gap to within four 4 days. In 2000, the development date preceded the measured date by eight days, and the melt out date preceded the measured dates by four days beneath dense canopy and eight days in a large gap. Given the spatial variability of snowcover in this environment, we feel that the simulation of snowpack dynamics was reasonably represented by the model. Accurate simulation of snowcover ablation timing is important due to the strong control that the snowcover exerts on the timing of soil warming and onset of transpiration.

Simulated throughfall during the 1999 and 2000 rainfall seasons was 0.7 and 1.1% greater than the mean measured throughfall, indicating that the model can effectively simulate evaporation during the growing season. Throughfall estimates during the winter periods from November through March could not be validated with the existing instrumentation given the challenges of measuring throughfall in the transient snow zone.

Simulated transpiration and measured sap flux scaled to the plot are shown in Figure 11.5. The model reasonably simulates both the general seasonal decline in transpiration and the short-term variability that results from changing weather conditions. Isolated days where simulated sap fluxes are negligible are associated with infrequent midsummer wet days. The measured sap flux exhibits less variability than the simulated transpiration, possibly due to hydraulic capacitance in the tree stems, which may damp the response of sap flux to changing environmental conditions. For the period that sap flux measurements were available, the total transpiration simulated by the model was 184 mm, compared to 210 mm estimated from the scaled sap flux measurements. Given the uncertainties and potential errors associated with scaling individual sap flux measurements to the entire site, we consider these data to indicate acceptable performance of the model.

The daily simulated ET fluxes and measured fluxes from the 73-m EC system are shown in Figure 11.6. EC flux measurements are affected by the size of the areal flux source as determined by wind speed, direction, and atmospheric stability (Baldocchi 1997; Lee 1998) and are also influenced by the crane tower when wind direction is outside the optimal direction of fetch. The data presented in Figure 11.6 are not filtered for inappropriate fetch direction and do not include advected fluxes and

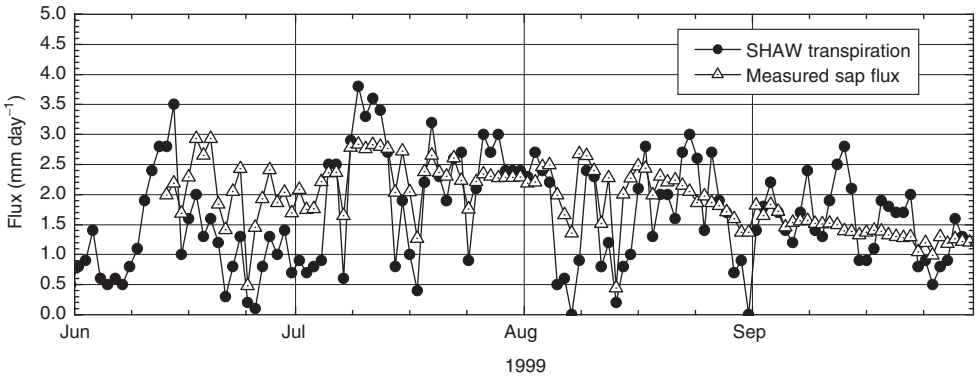


Figure 11.5 Simulated transpiration and measured sap flux scaled to the plot scale from six dominant Douglas-fir trees

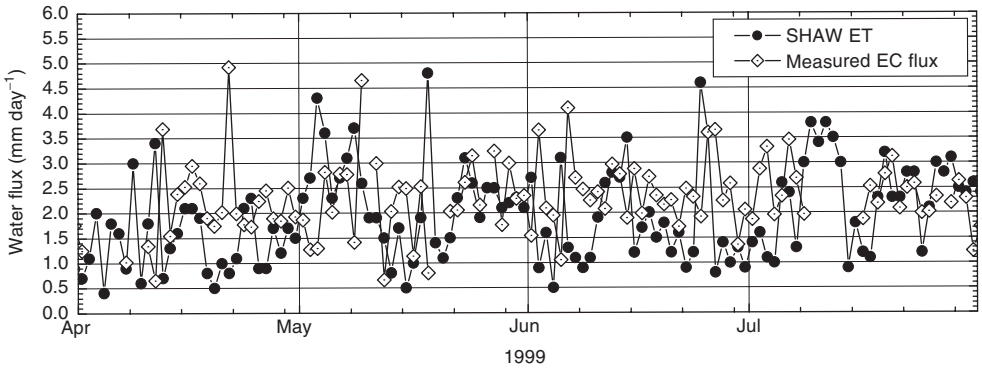


Figure 11.6 Simulated evaporation + transpiration and measured water flux from the eddy-covariance (EC) system at 73 m

therefore are considered as estimates of total ecosystem water flux. Despite uncertainties in the EC flux data, the model reasonably matches the general magnitudes and trends of the EC data during the period for which data are available. Using more rigorous screening for wind direction, modeled ET fluxes were within 10% of EC fluxes during 10–17 day periods analyzed in detail by Unsworth *et al*. (2004), and closely matched diurnal EC flux trends (Link *et al*. 2004a).

Simulated and measured soil water content (θ) in the top 0.30 m of the soil profile for the 1999 and 2000 water years are shown in Figure 11.7. The measured soil water content trend displayed in Figure 11.7 is from a sensor located in a canopy gap that was identified as a proxy for the site average (see Figure 11.4). The proxy sensor in the gap received slightly more precipitation than the site average, due to lower canopy interception, and therefore displayed a greater response to precipitation events than the modeled site average. Despite this discrepancy, the average model efficiency for the two years was 0.90, root mean square difference was 2.1 vol^{-1}, and relative mean bias difference was +2.8%, indicating very good agreement between the measurements and simulated θ. Simulated θ in the 0.30–0.60, 0.60–0.90, and 0.90–1.20 m soil layers also exhibited good agreement with the mean segmented TDR probe measurements taken every 3–6 weeks, indicating that the model effectively simulated the seasonal evolution of the soil water profiles in this system (Link *et al*. 2004a). These data provide the best evidence of the model's ability to simulate ET, since virtually all fluxes from the soil reservoir after drainage ceases in the late spring are due to transpiration (soil evaporation being negligible).

Given the good quantitative agreement between the measured and simulated throughfall, estimated transpiration and soil moisture, the SHAW results can be used to provide reasonable estimates of the components and dynamics of the site water balance.

11.3.3 Simulated seasonal water flux trends

A summary of the simulated annual site water balance is shown in Table 11.2. Drainage accounts for the majority of the incoming precipitation, comprising 84 and 74% of the annual water balance in 1999 and 2000, respectively. ET accounted for a smaller proportion of the water balance, approximately 18 and 23% of incoming precipitation for the respective years. Evaporation of water from the canopy, litter, and shallow soils were slightly less than half (~43%) of the annual ET. Overland flow at the site was negligible since the soils rarely froze and exhibited high infiltration capacities typical of forested systems. Storage changes accounted for a minor portion of the water balance, and were mainly affected by the timing of the seasonal shift from dry to wet conditions.

Simulated water balance trends for the 1999 and 2000 water years are shown in Figures 11.8 and 11.9. All trends

Table 11.2 Simulated water-balance summary

Component	Year	
	1999	2000
Precipitation	2596	2482
Drainage	2184	1833
Evaporation	200	250
Transpiration	278	321
Storage change	−48	88

Note: All units are in mm.

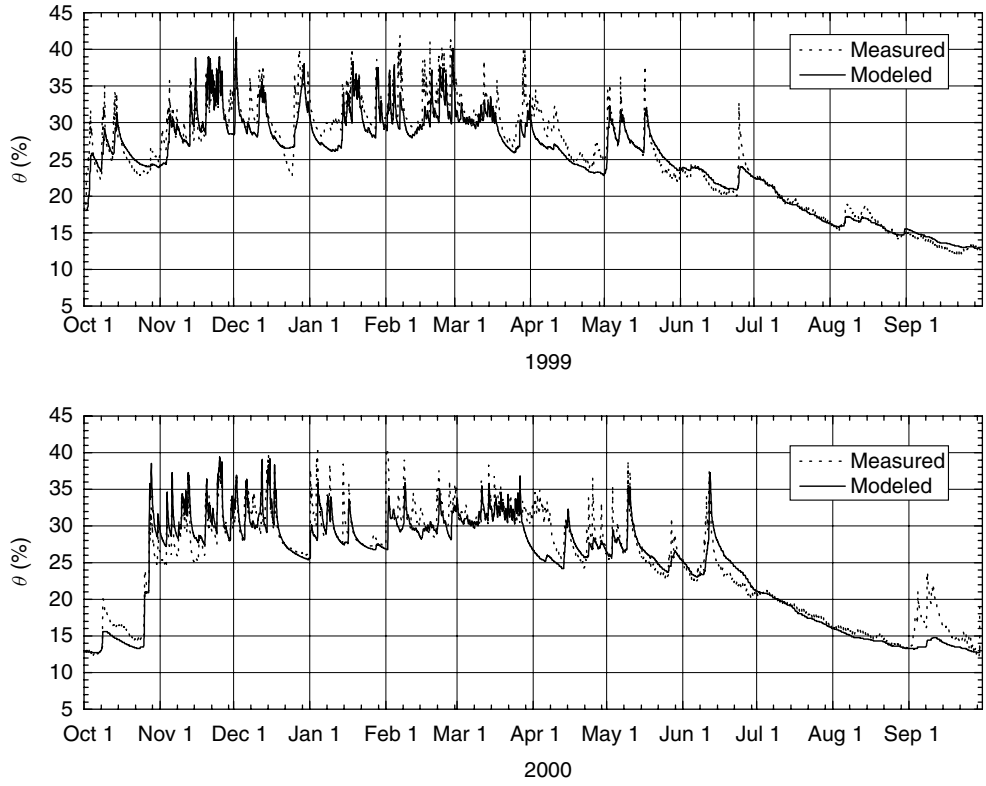


Figure 11.7 Measured and simulated (0–0.30 m) soil water contents. Reproduced with permission from Link *et al*., Simulation of water and energy fluxes in an old growth seasonal temperate rainforest using the Simultaneous Heat and Water (SHAW) model; published by American Meteorological Society, 2003

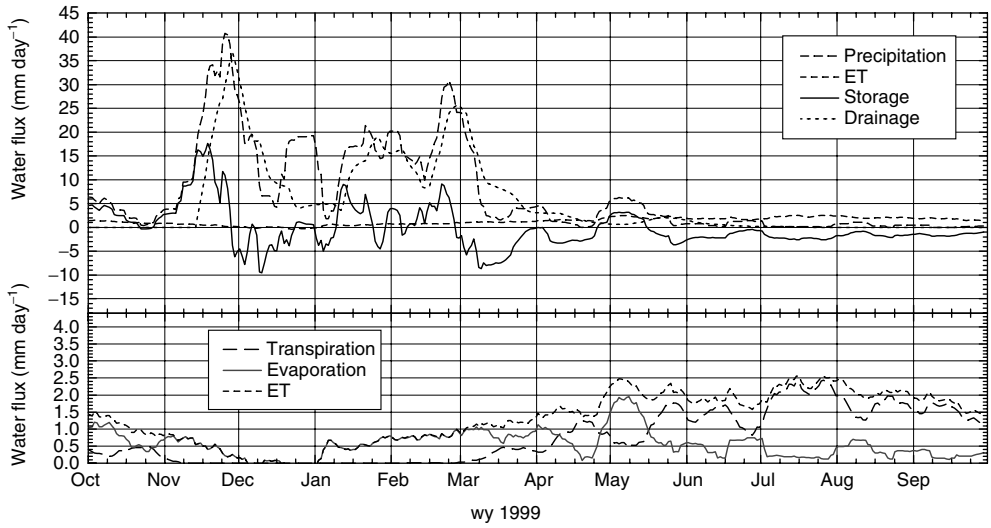


Figure 11.8 Simulated WRCCRF water balance for the 1999 water year

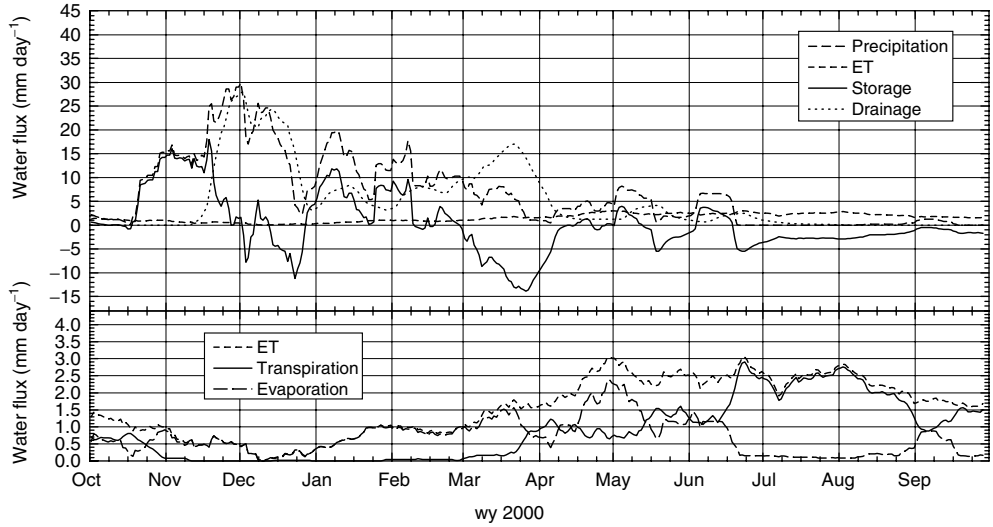


Figure 11.9 Simulated WRCCRF water balance for the 2000 water year

were smoothed with a 15-day moving average to clearly depict seasonal variations in water-balance components. The storage term is the total storage in the system, dominated by the soil and snowpack reservoirs. Positive storage indicates that the system was gaining water. The lower plot in Figures 11.8 and 11.9 shows an expanded view of the evaporation and transpiration components.

The beginning of the water years was characterized by dry conditions, which transitioned to wet conditions in the mid-fall months. Replenishment of the soil reservoir is indicated by several weeks of positive storage, before drainage started to occur. The timing of the simulated drainage closely corresponded to the observed initiation of streamflow in the intermittent channel that drains the site (see Figure 11.4). Drainage during the 1999 winter was closely associated with precipitation input, given the lack of snowfall during this season. Drainage during the 2000 winter was also associated with precipitation but exhibited a distinct snowmelt pulse in March. The transition from a water-surplus to a water-deficit condition where ET exceeded precipitation occurred in mid-May of 1999 and mid-June of 2000. Shortly after this transition, drainage ceased and the soil water reservoir was progressively depleted by transpiration and small rates of litter and soil evaporation.

Simulated ET was very low in the winter, remained relatively high through the late spring and summer, and gradually decreased starting in early August. Simulated evaporation was very low during the winter, and increased throughout spring due to frequent rainfall and warm temperatures. Evaporation decreased rapidly during the summer with the onset dry conditions, but remained slightly above zero due to isolated precipitation events and litter drying. Transpiration began almost immediately after soils warmed following snowpack ablation, peaked in the early summer, and gradually declined through late summer. During the spring and fall, ET patterns tended to mirror each other, when wet-canopy conditions increased evaporation and reduced transpiration.

The simulated ET pattern at WRCCRF contrasted with measured ET trends at a nearby dry ponderosa pine forest stand that experiences a similar Mediterranean climate (Metolius FLUXNET site). Unlike the WRCCRF canopy, the Metolius site exhibited lower ET rates in summer relative to the spring months (Anthoni *et al*. 2002; Anthoni *et al*. 1999). The higher ET rates at WRCCRF were also reflected in the ratios of sensible to latent heat fluxes, or Bowen ratios (β_{BR}) from the ecosystem. During the warm season (day 165 to 235), estimated β_{BR} values at WRCCRF were lower (1.22–1.32) than were observed at the Metolius site (1.51–1.70) (Wilson *et al*. 2002), indicating higher ET rates.

The weekly average turbulent heat flux partitioning during the dry season from July through September is shown in Figure 11.10. The plot format is similar to the one used by Wilson *et al*. (2002) to compare the warm-season β_{BR} between different ecosystems. Dotted lines on the plots are constant values of β_{BR} and solid diagonal lines are constant values of net turbulent fluxes that are within 1% of net radiation during this period when computed on a weekly basis. Numbers on the

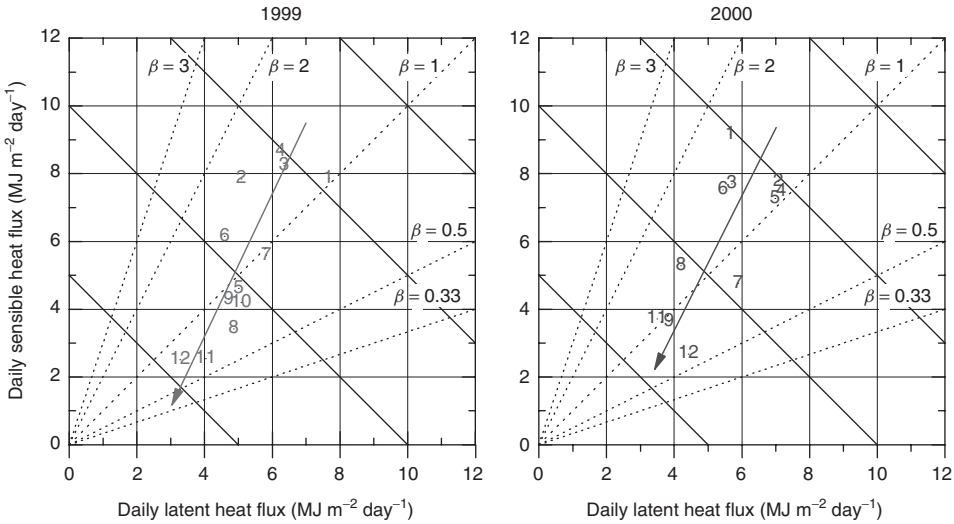


Figure 11.10 Simulated evolution of average weekly turbulent fluxes during the dry season at WRCCRF. Numbered points are the average weekly flux from the first week of July (week 1) through the fourth week of Sept. (week 12). Dotted lines denote constant Bowen ratios (β_{BR}) and solid lines denote constant net turbulent fluxes

plots represent sequential weekly periods where 1 is the first week of July and 12 is the last week of September. The arrows on the plots show the general trend of the turbulent flux partition. The climate at the site becomes more continental throughout the summer as vapor pressure deficits increase and net radiation declines. During this period, latent heat fluxes declined less rapidly than sensible heat fluxes, producing the observed β_{BR} decrease from values >1 in July to values <1 in September. This trend is opposite to the trend observed at the Metolius FLUXNET site in the Pacific Northwest under similar climatic conditions (Anthoni *et al*. 2002). The decreasing β_{BR} trend indicates that this canopy continued to transpire water during late summer dry conditions, whereas the other canopy, located in a drier area, exhibited reduced transpiration rates. This trend may result from higher water availability (a combination of shallow groundwater at the WRCCRF and ash-derived soils with a high plant-available water content) coupled with the presence of an effectively conducting root and stem system for supporting the transpiration flow. Consequently, the canopy can maintain relatively high transpiration fluxes through the dry season.

The simulation results for the WRCCRF canopy raise questions about how ET fluxes vary spatially in mountainous areas. For example, relatively high late-season transpiration fluxes were simulated for the WRCCRF canopy, which consists of old-growth vegetation in a relatively wet, valley-bottom location with deep loamy soils. Other younger forests (with less root development) and forests on steep, rocky slopes, more typical of montane environments may not be able to access as much water late in the dry season. Conversely, mature stands in drier sites may compensate with greater rooting depths to maintain transpiration and productivity. Detailed water and energy-balance measurement sites are not commonly located on slopes due to logistic difficulties of conducting measurements in these locations. We suggest that future forest water flux studies should focus on mountain slope areas, as has been suggested for carbon flux studies (Schimel *et al*. 2002). It is important for studies to include a focus on below-ground components, such as soil and rooting depth, to constrain parameters that are frequently estimated when parameterizing process models.

11.4 CONCLUSIONS

Results from the SHAW simulations exhibited good agreement with measured throughfall and soil moisture profiles and with estimates of transpiration and ET fluxes from the crane plot. We therefore feel that the model can be used to provide good estimates of the water-balance dynamics of the WRCCRF site. Model results indicated that for the two study years, ET on average accounted for approximately 9 and 12% of the annual water balance, respectively. Evaporation of intercepted water during the rainfall season accounted for almost

25% of the water balance, probably due to relatively high canopy saturation storage resulting from the abundant canopy epiphyte populations. Transpiration rates peaked in early summer, followed by a decline resulting from decreasing net radiation and soil moisture depletion. Decreasing Bowen ratios during the summer dry period indicated that the system was able to maintain relatively high transpiration rates relative to drier forests, probably because of a shallow water table, high plant-available water content of the site soils, and the effective root system of the old-growth vegetation.

11.5 ACKNOWLEDGMENTS

Support for this research was provided by the Western Regional Center (WESTGEC) of the National Institute for Global Environmental Change (NIGEC), the U.S. Forest Service, and the Agricultural Research Service, Northwest Watershed Research Center. Sap flux data were provided by Dr. Nathan Phillips (Boston University) and Dr. Barbara Bond (Oregon State University). Eddy-covariance data were provided by Matthias Falk and Dr. Kyaw Thaw Paw U (University of California, Davis). Site photo was provided by the Forest Science Data Bank, a partnership between the Department of Forest Science, Oregon State University, and the U.S. Forest Service Pacific Northwest Research Station, Corvallis, Oregon. Significant funding for the data bank was provided by the National Science Foundation Long-Term Ecological Research program (NSF Grant numbers BSR-90-11663 and DEB-96-32921). The authors also thank two anonymous reviewers whose comments improved this manuscript.

REFERENCES

Anthoni, P., B. E. Law, and M. H. Unsworth. 1999. Carbon and water vapor exchange of an open-canopied ponderosa pine ecosystem. *Agricultural and Forest Meteorology* **95**: 151–168.

Anthoni, P., M. H. Unsworth, B. E. Law, J. Irvine, D. D. Baldocchi, S. V. Tuyl, and D. Moore. 2002. Seasonal differences in carbon and water vapor exchange in young and old-growth ponderosa pine ecosystems. *Agricultural and Forest Meteorology* **111**(3): 203–222.

Baldocchi, D. 1997. Flux footprints within and over forest canopies. *Boundary Layer Meteorology* **85**: 273–292.

Bowling, L. C., P. Storck, and D. Lettenmaier. 2000. Hydrologic effects of logging in western Washington, United States. *Water Resources Research* **36**(11): 3223–3240.

Dingman, S. L. 2002. *Physical Hydrology*. 2nd ed. New York: Macmillan College Publishing.

Dyrness, C. T. 2003. *Soil Descriptions and Data for Soil Profiles in the Andrews Experimental Forest, Selected Reference Stands, RNA's, and National Parks: Long-Term Ecological Research*. Corvallis, OR: Forest Science Data Bank: SP001 [Database] 2001 [cited May 8 2003]. Available from http://www.fsl.orst.edu/lter/data/abstract.cfm?dbcode=SP001.

Flerchinger, G. N. 2003. *The Simultaneous Heat and Water (SHAW) Model: User's Manual* [electronic publication]. Technical Report NWRC 2000-10 2000, Northwest Watershed Research Center, USDA Agricultural Research Service, [cited March 15 2003]. Available from ftp://ftp.nwrc.ars.usda.gov/download/shaw/SHAWUsersManual.pdf.

Flerchinger, G. N., J. M. Baker, and E. J. A. Spaans. 1996a. A test of the radiative energy balance of the SHAW model for snowcover. *Hydrological Processes* **10**: 1359–1367.

Flerchinger, G. N., K. R. Cooley, and Y. Deng. 1994. Impacts of spatially and temporally varying snowmelt on subsurface flow in a mountainous watershed: 1. Snowmelt simulation. *Hydrological Sciences Journal* **39**(5): 507–520.

Flerchinger, G. N., C. L. Hanson, and J. R. Wight. 1996b. Modeling evapotranspiration and surface energy budgets across a watershed. *Water Resources Research* **32**(8): 2539–2548.

Flerchinger, G. N., W. P. Kustas, and M. A. Weltz. 1998. Simulating surface energy fluxes and radiometric surface temperatures for two arid vegetation communities using the SHAW model. *Journal of Applied Meteorology* **37**: 449–460.

Flerchinger, G. N., and F. B. Pierson. 1997. Modelling plant canopy effects on variability of soil temperature and water: Model calibration and validation. *Journal of Arid Environments* **35**: 641–653.

Flerchinger, G. N., and K. E. Saxton. 1989. Simultaneous heat and water model of a freezing snow-residue-soil system I. Theory and development. *Transactions of the American Society of Agricultural Engineers* **32**(2): 565–571.

Franklin, J. F., and T. A. Spies. 1991. Composition, function, and structure of old-growth Douglas-fir forests. In *Wildlife and Vegetation of Unmanaged Douglas-Fir Forests*, edited by L. F. Ruggerio, K. B. Aubry, A. B. Carey, and M. H. Huff. Portland, OR: US Department of Agriculture, Forest Service, 71–80.

Granier, A. 1985. Une nouvelle méthode pour la mesure du flux de sève brute dans le tronc des arbres. *Ann. Sci. For.* **42**(2): 193–200.

Harr, R. D., W. C. Harper, J. T. Krygier, and F. S. Hsieh. 1975. Changes in storm hydrographs after road-building and clear-cutting in the Oregon coast range. *Water Resources Research* **11**(3): 436–444.

Harr, R. D., A. Levno, and R. Mersereau. 1982. Streamflow changes after logging 130-year-old Douglas fir in two small watersheds. *Water Resources Research* **18**: 637–644.

Harr, R. D., and F. M. McCorison. 1979. Initial effects of clearcut logging on size and timing of peak flows in a small watershed in western Oregon. *Water Resources Research* **15**(1): 90–94.

Hicks, B. J., R. L. Beschta, and R. D. Harr. 1991. Long-term changes in streamflow following logging in western Oregon and associated fisheries implications. *Water Resources Bulletin* **27**: 217–226.

Ishii, H., J. H. Reynolds, E. D. Ford, and D. C. Shaw. 2000. Height growth and vertical development of an old-growth *Pseudotsuga-Tsuga* forest in southwestern Washington State, U.S.A. *Canadian Journal of Forest Research* **30**: 17–24.

Jones, H. G. 1992. *Plants and Microclimate*. 2nd ed. New York: Cambridge University Press.

Jones, J. A., and G. E. Grant. 1996. Peak flow responses to clear-cutting and roads in small and large basins, western Cascades, Oregon. *Water Resources Research* **32**(4): 959–974.

Jones, J. A., and G. G. Grant. 2001. Comment on ''Peak flow responses to clear-cutting and roads in small and large basins, western Cascades, Oregon: A second opinion'' by R. B. Thomas and W. F. Megahan. *Water Resources Research* **37**(1): 175–178.

Keppeler, E. T., and R. R. Ziemer. 1990. Logging effects on streamflow: Water yield and summer low flows at Caspar Creek in northwestern California. *Water Resources Research* **26**: 1669–1679.

Lee, X. 1998. On micrometeorological observations of surface-air exchange over tall vegetation. *Agricultural and Forest Meteorology* **91**: 39–49.

Link, T. E. 2001. The water and energy dynamics of an old growth-seasonal temperate rainforest. Ph.D. dissertation, Environmental Sciences Graduate Program, Oregon State University, Corvallis, 169.

Link, T. E., G. N. Flerchinger, M. Unsworth, and D. Marks. 2004a. Simulation of water and energy fluxes in an old growth seasonal temperate rainforest using the Simultaneous Heat and Water (SHAW) model. *Journal of Hydrometeorology* **5**(3): 443–457.

Link, T. E., M. Unsworth, and D. Marks. 2004b. The dynamics of rainfall interception by a seasonal temperate rainforest. *Agricultural and Forest Meteorology* **124**(3–4): 171–191.

Maidment, D. R. 1993. *Handbook of Hydrology*. New York: McGraw Hill.

Nash, T. H. III, and V. Wirth, eds. 1988. *Lichens, Bryophytes and Air Quality*. Stuttgart: Gebr. Borntraeger Verlagsbuch-handlung, Science Publishers.

Paw U, K. T., T. H. Suchanek, S. L. Ustin, J. Chen, W. Winner, S. Thomas, T. Hsiao, R. Shaw, T. King, M. Falk, D. Pyles, and D. Matista. 2004. Carbon dioxide exchange between an old growth forest and the atmosphere. *Ecosystems* **7**(5): 513–524.

Phillips, N., B. J. Bond, N. G. McDowell, and M. G. Ryan. 2002. Canopy and hydraulic conductance in young, mature and old Douglas-fir trees. *Tree Physiology* **22**: 205–211.

Proctor, M. C. F. 1982. Physiological ecology: water relations, light, and temperature responses, carbon balance. In *Bryophyte Ecology*, edited by A. J. E. Smith. London: Chapman & Hall.

Schimel, D., T. G. F. Kittel, S. Running, R. Monson, A. Turnipseed, and D. Anderson. 2002. Carbon sequestration studied in western U. S. mountains. *Eos, Transactions American Geophysical Union* **83**(40):445, 449.

Sellers, P. J., D. A. Randall, G. J. Collatz, J. A. Berry, C. B. Field, D. A. Dazlich, C. Zhang, G. D. Collelo, and L. Bounoua. 1996. A revised land surface parameterization (SiB2) for atmospheric GCMs. Part I: Model formulation. *Journal of Climate* **9**(4): 676–705.

Shaw, D. C., J. F. Franklin, K. Bible, J. Klopatek, E. Freeman, S. Greene, and G. G. Parker. 2004. Ecological setting of the Wind River old-growth forest. *Ecosystems* **7**: 427–439.

Stednick, J. D. 1996. Monitoring the effects of timber harvest on annual water yield. *Journal of Hydrology* **176**: 79–95.

Thomas, R. B., and W. F. Megahan. 1998. Peak flow responses to clear-cutting and roads in small and large basins, western Cascades, Oregon: A second opinion. *Water Resources Research* **34**(12): 3393–3403.

Thomas, B. R., and F. W. Megahan. 2001. Reply. *Water Resources Research* **37**(1): 181–183.

Thomas, S. C., and W. E. Winner. 2000. Leaf area index of an old-growth Douglas-fir forest estimated from direct structural measurements in the canopy. *Canadian Journal of Forest Research* **30**: 1922–1930.

Unsworth, M. H., N. Phillips, T. Link, B. Bond, M. Falk, M. Harmon, T. Hinckley, D. Marks, and K. T. Paw U. 2004. Components and controls of water flux in an old growth Douglas fir/western hemlock ecosystem. *Ecosystems* **7**: 468–481.

Waring, R. H., and S. W. Running. 1998. *Forest Ecosystems: Analysis at Multiple Scales*. 2nd ed. New York: Academic Press.

Wigmosta, M. S., L. W. Vail, and D. P. Lettenmaier. 1994. A distributed hydrology-vegetation model for complex terrain. *Water Resources Research* **30**(6): 1665–1679.

Williams, M., B. J. Bond, and M. G. Ryan. 2001. Evaluation of different soil and plant hydraulic constraints on tree function using a model and sap flow data from ponderosa pine. *Plant Cell and Environment* **24**: 679–690.

Wilson, K. B., D. D. Baldocchi, M. Aubinet, P. Berbigier, C. Bernhofer, H. Dolman, E. Falge, C. Field, A. Goldstein, A. Granier, A. Grelle, T. Halldor, D. Hollinger, G. Katul, B. E. Law, A. Lindroth, T. Meyers, J. Moncrieff, R. Monson, W. Oechel, J. Tenhunen, R. Valentini, S. Verma, T. Vesala, and S. Wofsy. 2002. Energy partitioning between latent and sensible heat flux during the warm season at FLUXNET sites. *Water Resources Research* **38**(12): 30.

Wright, K., K. H. Sendek, R. H. Rice, and R. B. Thomas. 1990. Logging effects on streamflow: Storm runoff at Caspar Creek in northwestern California. *Water Resources Research* **26**: 1657–1667.

Ziemer, R. R. 1981. Storm flow response to road building and partial cutting in small streams of northern California. *Water Resources Research* **17**: 907–917.

12

Comparison of Evapotranspiration and Condensation Measurements between the Giant Mountains and the Alps

CARMEN DE JONG[1], MARCO MUNDELIUS[2] AND KRZYSZTOF MIGAŁA[3]

[1]Geography Department, University of Bonn, Germany, [2]Institut für Gewässerkunde und Binnenfischerei, Berlin, Germany, [3]Institute of Geography, Department of Meteorology and Climatology, University of Wroclaw, Poland

12.1 INTRODUCTION

Several important parameters of the water cycle such as evaporation, transpiration and condensation have been largely neglected in mountain areas even though they form an important interface between ecology, hydrology and meteorology (de Jong in press). An accurate knowledge of these fundamental parameters is essential to further our understanding of possible climate variations as well as the redistribution of pollutants. Up-to-date, estimations and extrapolations of evaporation and transpiration in steep, high-altitude terrain do not adequately accommodate their spatial and temporal heterogeneity, nor are special components such as condensation considered (Gurtz *et al*. 1999). Diurnal and nocturnal dynamics of evaporation, transpiration (LeDrew 1975) and condensation should be measured in the field in order to produce a satisfactory basis for modelling and to contribute to our understanding of regional water fluxes.

Evapotranspiration, the process by which water is lost into the atmosphere by transpiration through the stomata of plants or freed directly from the surface by evaporation, is generally derived from meteorological variables at single Bowen Ratio stations and at meteorological stations. 'Although evapotranspiration data in mountain areas are almost non-existent, it is these losses rather than potential evaporation which are most significant for vegetation growth' (Barry 1992). Few studies have focused on direct and regionally distributed field measurements in the mountains (Calder *et al*. 1984, Cernusca *et al*. 1999, Körner *et al*. 1978, Graber *et al*. 1999, Staudinger and Rott 1981, Wright 1990). Our knowledge of these water fluxes is therefore usually reduced to modelling results, single station observations or derivations from the difference between long-term precipitation and discharge (Gurtz *et al*. 2003, Stewart and Rouse 1976). However, meteorological stations rarely cover spatial and temporal diversity of evapotranspiration since they are neither logistically feasible nor affordable in large enough numbers on steep slopes in mountain catchments. This is due, in particular, to the sensitivity, heavy weight and high costs of the equipment. For Bowen Ratio stations, in particular, it is the intensive maintenance of dew mirrors that is a limiting factor for remote, unstaffed stations. In addition, the Bowen Ratio method depends on the validity of the Monin–Obukhov Similarity Theory, which is not

Climate and Hydrology in Mountain Areas. Edited by C. de Jong, D. Collins and R. Ranzi
© 2005 John Wiley & Sons, Ltd. ISBN: 0-470-85814-1

appropriate for this type of terrain since it is not flat and not horizontally homogeneous. Even so, the Bowen Ratio method has been applied as a common method in high mountain areas (Bernath 1990, Konzelmann *et al*. 1997). For the latter, data from stations placed only on the valley floor and at one higher elevation site are extrapolated linearly in order to regionalize evapotranspiration for a whole valley.

Furthermore, these methods are not developed to account for nocturnal variations of evapotranspiration. Nevertheless, it is essential to refer to continuous, high-resolution field data to be able to validate model results. With the advance of low cost, electronic equipment, the development of alternative measuring systems is becoming increasingly feasible. A clear subdivision into potential evaporation, actual evapotranspiration and condensation is necessary. Studies based on field experiments in the Dischma valley, Switzerland, from 1995 to 1999 (de Jong *et al*. 2002, de Jong in press) show that these components are subject to very small scale temporal fluctuations according to local climatic conditions and regional aspects.

Condensation, a much-neglected component of the water cycle in nearly all environments, is the process by which fog or moist air is horizontally and/or vertically advected and deposited as water droplets or rime ice if the surface is super-cooled. It is not only an important exchange mechanism for water in the surface layer and roughness sublayer but also a potential pollutant source since it can promote the input of chemicals, such as SO_2, from cloud water interception (Acker *et al*. 1999). There is evidence that high-elevation sites in Eastern Europe, such as the Black Triangle at the junction of Poland to the Czech Republic and former East Germany, receive greater amounts of atmospheric pollutants than surrounding low-elevation areas. Since the Giant Mountains (Karkonosze Mountains) form the first orographic barrier in this region, they are particularly prone to the absorption of contaminants through fog deposition. Long-term monitoring stations with passive cloud and fog collectors were installed in Mumlava, Karkonosze Mountains, in an attempt to assess horizontal and vertical fog deposition and pollutants (Migała and Szymanowski 1999, Sobik and Migała 1993). The results give evidence about average amounts and duration of fog for the study area presented in this paper. Investigations in the zone between 800 and 1200 m a.s.l. show that the pollution by fog droplets is 3–4 times greater than that from normal precipitation (Pereyma *et al*. 1997), particularly in winter.

The two main objectives of this presentation are to

- measure and compare evaporation, transpiration and condensation at hourly and weekly intervals in summer in two mountain catchments;
- explain the differences between evaporation, transpiration and condensation for a humid climate (Dischma, Alps, Switzerland) and a foggy climate (Giant Mountains, Poland);

Table 12.1 Comparison of physical, climatological, hydrological, geological and landuse characteristics for the catchment in the Giant Mountains, Poland and Dischma, Switzerland

Catchment	Szrenica, Giant Mountains, Poland	Dischma, Alps, Switzerland
Location	Polish/Czech boundary	Graubünden, E. Alps
Size (km^2)	1.67	43
Length (km)	2.1	14
Altitude (m)	680–1435	1500–3100
Average Grad. (°)	16.5	30
Glaciers (km^2)	None	Scaletta (0.66) Chüalp (0.3)
Geology	Mainly gneiss and slates, granite,	Mainly gneiss, some amphibolite
Soils	Syrosem, regosols, muirs, etc.	Regosols, podsols
Vegetation	Sub-alpine- (shrubs and grass) and alpine	Mainly alpine grass, dwarf shrubs, forest (spruce, larch, and pine)
Annual aver. snow cover[a]	186 days[a]	225 days[b]
Mean rainfall (summer/annual)[a] (mm)[a]	450 (mid-May to July)/1420[a]	500 (mid-June to mid-Sept)/1200[b]
Mean July temp (°C)[a]	10 (at 1110 m)[a]	12 (at 2000 m a.s.l)[b]
Mean discharge (summer/annual)[a] (mm)	–[a]	800/1200[b]
Mean evapotranspiration (mm)[a]	–[a]	300 (at 2000 m a.s.l)[b]

[a](Migała and Szymanowski, 1999).
[b](Wildi and Ewald 1986).

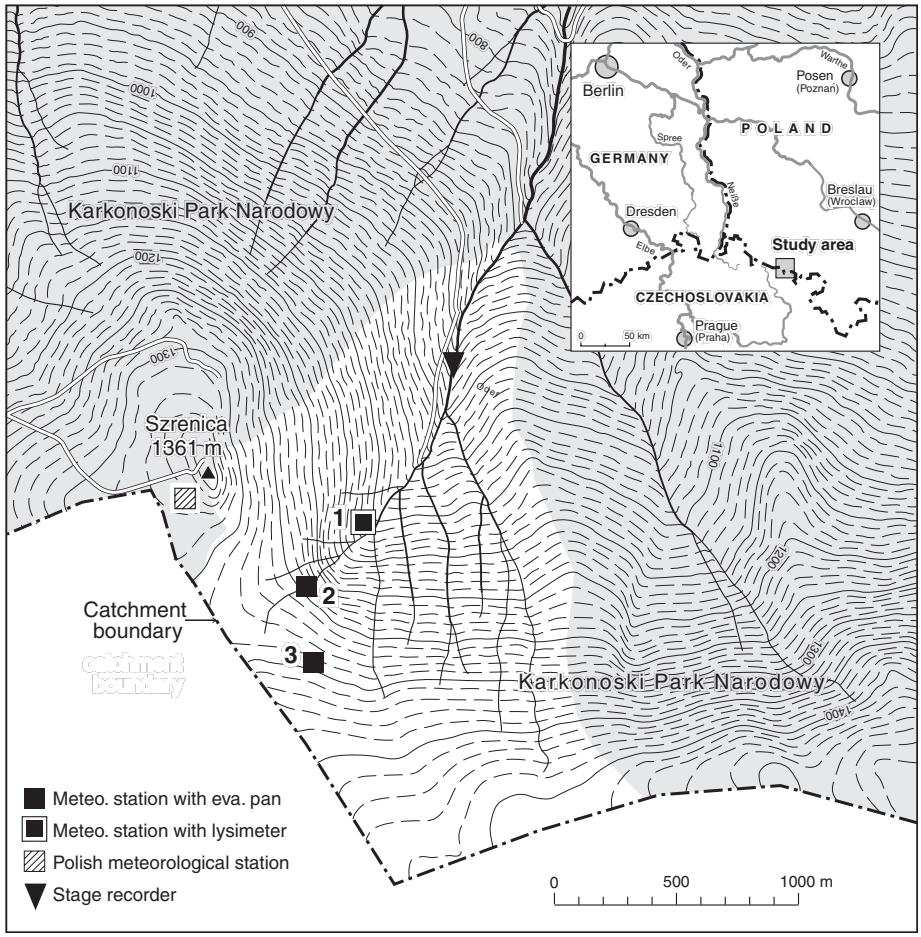


Figure 12.1 Mountain Szrenica catchment with experimental sites, Giant Mountains, Poland

12.2 STUDY AREAS

12.2.1 Szrenica, Giant Mountains (Karkonosze), Poland

The Szrenica study site (Figure 12.1) is a small headwater basin of the River Oder to the west of Mountain Szrenica (called *Reifträger*, in German meaning rime cap). It is part of the Giant Mountains and forms the natural and political boundary between Poland and the Czech Republic (Table 12.1). The Giant Mountains belong to one of the highest mountain chains in Silesia and mark the only region with mountain characteristics between Scandinavia and the Alps. Precipitation occurs on 62% of days during the year. The Giant Mountains experience as much as 240 fog days per year and average relative humidity can frequently surpass 80% as a result of condensing cloud masses (Dore *et al*. 1999). They therefore belong to one of the most fog-dominated regimes of all European mountains. On days with all-day fog, radiation is considerably reduced. It is estimated that fog contributes up to 15% of precipitation (Sobik and Migała 1993). The accumulation of winter rime reaches 83.4 kg/m^2 per annum at Mount Szrenica. This particular climate is influenced by the relatively low altitude of the Giant Mountains, their orographic effect relative to the atmospheric circulation patterns combined with their distance to the sea. The climate is strongly influenced by maritime and to a lesser extent by continental conditions (Migała *et al*. 2002). Winters are very cold and snow-rich, whereas summers are cool to warm (measured since 1961 at the Meteorological Observatory of the University of Wroclaw at Mount Szrenica) with less precipitation.

The catchment extends from the highest point at 1435 m a.s.l. to the confluence of the Plóczka at 680 m

a.s.l. To the west, the catchment is bordered by the Peak of Mount Szrenica and to the east by the steep, rocky boundary of the Szklarska valley. The Mt. Śnieżka (1602 m a.s.l.) forms the highest peak of the Giant Mountains. The rocks are mainly metamorphic (Handtke 1993). Soils are acid and oligotrophic with a rather high content of organic matter. Geomorphologically, the catchment has been glaciated, and there is evidence of periglacial and fluvial activity (Berg 1915). Extensive block fields extend from the peak areas down to 700 m a.s.l. Moraines cover the lower valley floors. There is a marked spring horizon at 1310 m a.s.l. The vegetation is dominated by montane beech, fir and spruce forest between 800 and 1200 m and spruce forest between 1000 and 1200 m interspersed with fern, moss, grass, orchids and shrubs such as blueberries and mossberries. Dwarf pine (Krummholz) is dominant in the subalpine zone between 1200 and 1500 m, as are sedges, moss, grass and sphagnum in the moors. There is a narrow alpine zone in the uppermost zones above the tree line up to 1300 m (Szczepankiewicz-Symayrka and Mielcarek 1997, Soukupová *et al*. 1995).

Several local wind systems affect the catchment. The orographically induced Mumlava wind system (foehn) typically sweeps over the peaks and forms corresponding leeside turbulence. These leeside winds encourage the deposition of precipitation and pollutants. Föhn winds occur during the summer months and are responsible for more than half of the annual evaporation (Drukman *et al*. 1997). As in the Dischma, strong daytime temperature gradients can develop between the ground surface and air on the steep slopes. During the night, thermally induced katabatic winds dominate with downslope air movement as opposed to anabatic effects that cause upslope air movement during the daytime.

12.2.2 Dischma Valley, Grisons, Switzerland

The Dischma catchment is located south of Davos in Graubuenden (Grisons), eastern Switzerland near the Austrian border (Figure 12.2). It is a typical elongated, glaciated high alpine valley (see Table 12.1 for details) with a central NNW–SSE axis and the remains of the Scaletta glacier at its southern boundary (Vögele 1984). The climate in summer is dominated by low-pressure systems moving from the Weissfluhjoch in the north-west up the Dischma valley and occasionally replaced by a stable, alpine föhn wind moving in from the Engadin in the south-east. At the local scale, thermally induced winds control the moisture and rainfall transfer within the valley. Evaporation and transpiration amounts to approx. 300 mm over the summer (June to September) and is highest on the steep, lower valley slopes (1900–2200 m), low on the valley floor and decreases again on the highest slopes (de Jong *et al*. 2002). Water recharge comes from rainfall, snowfall and condensation within the vegetation and on rocky surfaces. Condensation was quantified for the first time in this area in 1998. The Dischmabach (river), characterized by a glacier and rain-fed regime in the summer, drains the moraine-covered valley floor together with several tributaries. As for the Giant Mountains, the catchment has steep slopes consisting mainly of metamorphic rocks (Cadisch 1929). Geomorphologically, the Dischma consists of corries, moraines, rock glaciers, paleo-landslides, glaciated trough slopes, scree cones and some debris flow deposits. Only about one-tenth of the valley is covered by forest, the remaining area consisting mainly of alpine pasture and shrubs as well as scree slopes, rock surfaces, snow and ice fields and small lakes (Fischer 1990, Wildi and Ewald 1986).

The strongly structured terrain and orography has an important influence on the hydrological and micro-meteorological processes in the Dischma. Because of the small scale at which processes occur, extrapolation of meteorological variables is difficult. A mountain-valley wind (valley breeze) develops for certain periods of the day, and slope winds only exist as long as there are strong temperature gradients between the ground surface and air (Hennemuth 1986). On clear sky days with meta-stable air layering, air temperatures increase by as much as 3°C at the same pressure level between the valley outlet and the highest ridges at the valley head, thereby developing a clear upvalley wind (Ulrich 1987).

12.3 EXPERIMENTAL DESIGN

The interpretation of regional evaporation, transpiration and condensation in this paper is based on comparison of the two mountain catchments during the snow-free mid-summer season.

For the Szrenica test area, results are presented for the period between May 15 and July 7, 2001. The three main test stations correspond with the three main vegetation zones of the sub-catchment close to the upper tree line (Table 12.2(a) and Figure 12.1): a lower zone with blueberries and grass, a zone with shrubs and ferns and the highest zone with dwarf pine. Both an evaporation pan and lysimeter are installed at the lowest elevation Station 1. Stations 2 and 3 consist of an evaporation pan and a drop collector. Whereas station 1 lies in a less exposed region at the lower end of a nivation depression, station 2 lies at the transition between the steep walls of a small valley head and the flatter divide. Since it is

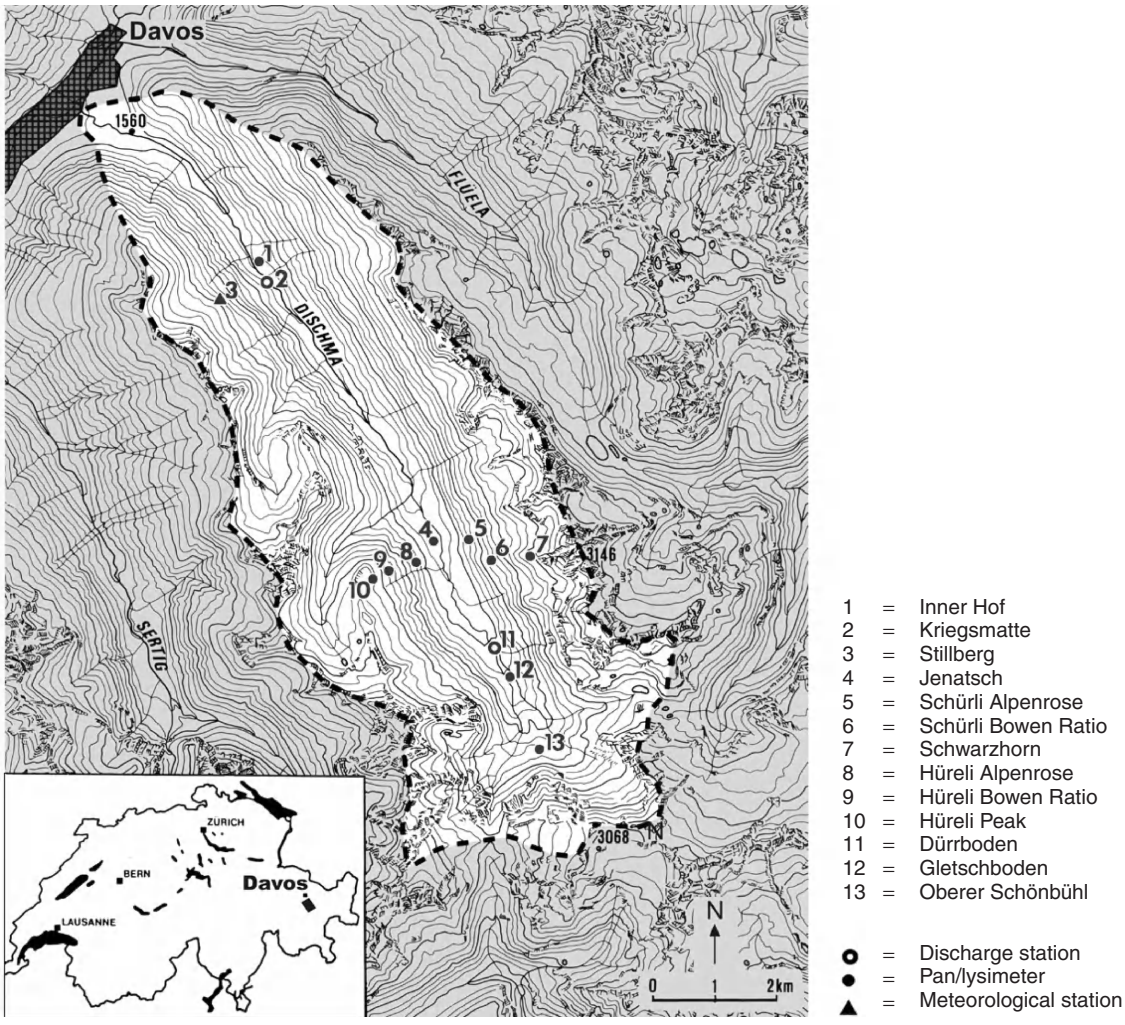


Figure 12.2 Dischma catchment with experimental sites, Grisons, Switzerland

located below a saddle structure, it is very exposed. While windward winds cause a jet effect, leeward winds create a leeside eddie with strong turbulence so that temperature differences are minimized under both conditions. Station 3 lies on the flatter divide and being the highest station it is most exposed.

In the Dischma, field data are presented from measurements made at seven individual sites (Table 12.2(b) and Figure 12.2(b)) in the upper valley from the midsummer season of 1999 as part of a detailed hydrological field experiment (VERDI) carried out between 1995 and 1999. Since the Dischma valley is heavily incised and resulting insolation patterns are very diverse, sites were chosen at representative locations along the east-oriented Hüreli and west-oriented Schürli slopes and along the valley floor. Both rich and poor alpine pasture as well as alpenrose shrubs were instrumented at sites with different aspects ranging from 1960 to 2600 m in altitude. Evaporation pans and lysimeters were placed at three sites on the Schürli slope, including Schürli Alpenrose (5), Schürli Bowen Ratio (6) and Schwarzhorn (7), two sites on the Hüreli slope including Hüreli Alpenrose (8) and Hüreli Bowen Ratio (9) and at three sites on the valley floor, Inner Hof (1), Jenatsch (4) and Gletschboden (12) and one site at the valley head, Oberer Schönbühl (13) (Figure 12.2(b)).

Table 12.2 (a) Giant Mountains. (b) Dischma. Combined evapotranspiration and condensation measuring test sites together with meteorological stations

(a)

	Station 1	Station 2	Station 3
Location	valley bottom	concave slope	plateau-ridge
Elevation (m a.s.l.)	1030	1190	1285
Gradient (°)	14.7	23.5	11.5
Aspect	NNE	NNE	NEE
Exposure	Nearly flat	Concave	Nearly flat
Vegetation type	Blueberry, moss	Grass, fern	Dwarf spruce
Vegetation height	40 cm	100–120 cm (fern)	100 cm
Meteorological Station	Profile station/ Reinhardt	Profile station/ Reinhardt/Drop Collector	Profile station/ Reinhardt/Drop Collector
Wind speed Ht. (m)	2.0	2.0	2.0
Upper arm Ht. (m)	1.50	1.50	1.50
Lower arm Ht. (m)	0.10	0.10	0.10
ET micro-measuring station	Evaporation pan/lysimeter	Evaporation pan	Evaporation pan

(b)

	Inner Hof	Hüreli Alpenrose (HA)	Jenatsch (J)	Schürli Alpenrose (SA)	Gletschboden	Oberer Schönbühl	Schwarzhorn
Location	Valley bottom	Trough slope	Valley bottom	Trough slope	Valley bottom	Upper valley head	Slope ridge below rock face
Elevation (m a.s.l.)	1610	2070	1960	2070	2080	2361	2600
Gradient (°)	15	30	2	30	5	2	30
Aspect	SW	E-NE	None	W	None	N	West
Exposure	Convex	Concave	Flat	Concave	Concave	Flat	Convex
Vegetation type	Rich meadow	Alpenrose	Grass	Alpenrose	Alpenrose	Poor pasture	Poor pasture
Vegetation height (cm)	40	35	20	35	35	8	5
Meteorological Station	Profile station/ Reinhardt	Profile station/ Reinhardt	Bowen Ratio	Profile station/ Reinhardt	Profile station/ Reinhardt	Profile station/ Reinhardt	Profile station/ Reinhardt
Wind speed Ht. (m)	2.15	2.10	3.45	2.10	2.25	2.25	2.10
Upper arm Ht. (m)	1.60	1.85	2.80	1.70	1.75	1.67	1.56
Lower arm Ht. (m)	1.20	0.32	0.87	0.40	0.45	0.20	0.24
ET micro-measuring station	Evapo. pan/ lysimeter	Evapo. pan/ lysimeter	evapo. pan/ lysimeter	Evapo. pan/ lysimeter	Evapo. pan/ lysimeter	Evapo. pan/ lysimeter	Lysimeter

Data will not be presented from site 6 and 9 because of lack of overlap for the analysis period.

12.3.1 Evaporation pan and lysimeter

The evaporation pan is based on an automated micro-measuring system that was developed to determine evaporation losses and condensation gains on the steep mountains slopes of the Dischma valley (de Jong *et al*. 2002). Since then, it has been tested and implemented in Gut Frankenforst (Siebengebirge, Germany). The system consists of small, permanently installed water-filled evaporation pans placed on automatic weighing scales (Figure 12.3(a) and de Jong *et al*. 2002). Evaporation pans are set into the ground, ensuring that the water surface is level with the average surrounding ground surface in order to minimize wind impact and to maximize the dominance of the local microclimate of the surrounding vegetative cover. Since the scales underneath the evaporation pans had to be adapted in size to the steep slope gradients, their capacity is limited to 5 kg. All water losses by evaporation (positive weight difference) and water gain through condensation (negative weight difference), as well as rainfall, are weighed accurately (with a resolution of ± 1 g and an error

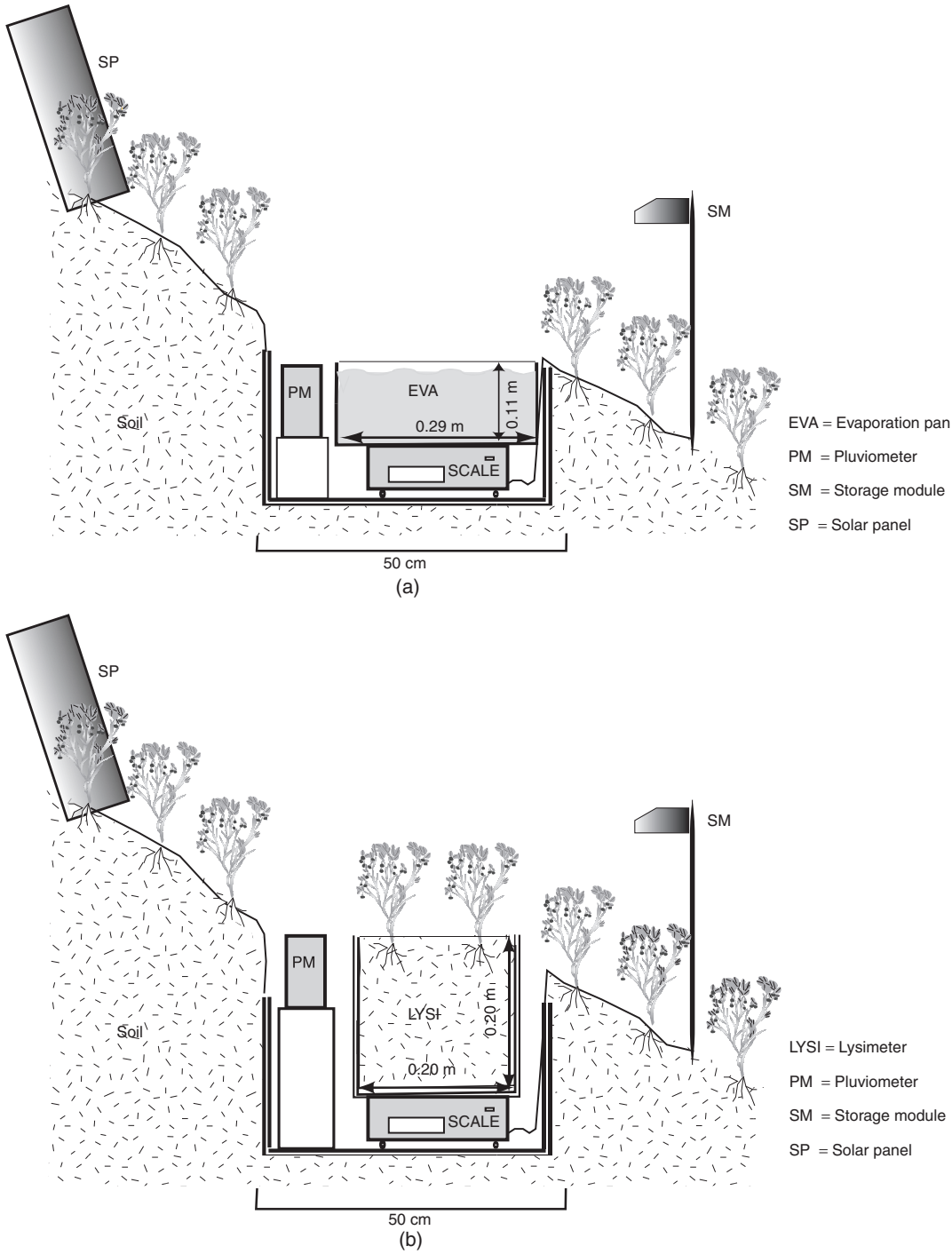


Figure 12.3 Micro-measuring system on steep slopes to determine (a) potential evaporation based on water-filled evaporation pan and (b) evapotranspiration based on soil and vegetation-filled lysimeters

of 0.3% or an equivalent of 0.015 mm). The units used are millimetres. Measurements are taken simultaneously at each site during the mid-summer season. At windy sites, a smoothing function, based on a moving mean value over 40 minutes ($X_1 = (x_{10} + x_{20} + x_{30} + x_{40})/4$, $X_2 = (x_{20} + x_{30} + x_{40} + x_{50})/4 \ldots$) is applied to the time series, where x_{10} is a measurement taken at a 10-minute interval.

The lysimeter measuring system is based on the same automated principle as the evaporation pans (Figure 12.3(b)). A complete plant or several plants are removed with roots and soil, inserted in a container and then reinstalled in the same locality they were taken from. The different plants inserted in the lysimeter were well adapted to their new setting and did not suffer in texture or appearance during the experimental periods (Figure 12.4). This indicates their capability of surviving extreme climatic conditions.

In both environments, evapotranspiration measurements are higher than potential evaporation. The remarkable differences between the results of the lysimeter and evaporation pan demonstrate the sensitiveness of the measuring system. There are several reasons for the differences: firstly, the surface of the blueberry shrubs in the lysimeter is larger than the free water surface. Evaporation from the lysimeters is exclusively controlled by the process of transpiration, such that the stomatal control can greatly augment transpiration in relation to the free water surface. Secondly, the plants protrude approximately 20 cm above the ground while the water level in the pans is even with the surrounding soil surface amongst the shrubs. Since the evaporation pan forms a free surface to the air, it is unlikely to underestimate potential evaporation. Both systems are equally reliable under alpine conditions, but it seems that the dynamics of evaporation are slightly better presented by lysimeters since their reaction is specific to plant type and allows more precise detection of nocturnal variations.



Figure 12.4 Example of optimal integration of lysimeter vegetation with its surroundings in the field (Station 1, Giant Mountains)

The uniqueness of this experimental study lies in the fact that potential evaporation and evapotranspiration can be measured and analyzed at 10-minute intervals, a time resolution that has not been presented for mountain environments before. If these time intervals were to be averaged or augmented, important phases of condensation would be leveled out completely and short, but important impacts such as morning or evening changes in wind direction and their effects on evaporation or condensation would be lost. Since other important dynamics or changeovers such as the onset of clouds, fog, sunrise or the termination of rainfall do not occur steadily over one hour but are a matter of minutes and may produce the largest dynamics of the day or night, it is very important to resolve evaporation and condensation processes at an appropriate resolution, that is, 10 minutes.

12.3.2 Drop collector

The drop collector is a pipe construction that consists of a circular plastic lid mounted on top of a vertical pipe. This construction was developed by the Meteorological Observatory of the University of Wroclaw. Horizontally and vertically accumulated moisture from the lid drains from the rim of the lid along a line into a collector. The diverted water caught in the collector is measured.

12.3.3 Meteorological profile and Bowen Ratio stations

Each experimental site consists of a basic meteorological profile station or a Bowen Ratio Station (Table 12.1) combined with a self-developed evaporation-condensation micro-measuring unit. All measurements were continuously recorded in self-constructed data loggers at 10-minute intervals. At the meteorological stations, air temperature and relative humidity were recorded at two levels above the ground in addition to solar radiation and wind direction (Conrad sensors) and wind speed (Reinhardt) (Table 12.1). The lower level of the Profile stations are located at the upper limit of the canopy. At the Bowen Ratio Stations, the same variables were recorded in addition to soil heat flux and dew point. Since dew point was not measured at all stations, the results will not be presented here. A small rain-o-matic collector with a tipping bucket was installed as an additional source for measuring rainfall at the evaporation and transpiration measuring sites.

12.4 RESULTS AND DISCUSSION

The results for the two study sites are presented at three different scales: hourly, daily and weekly. Measurements are taken at a very high temporal resolution to ensure detailed comparison for single days or weeks. Although the two test days chosen are subject to different local conditions, they have similar weather conditions, that is, no rain, fine weather in the morning and only some clouds in the afternoon and evening. Considering the season from June to mid-September observed at the Stillberg station over the past 30 years (WSL, Birmensdorf, Turner 1988), summers in the Dischma are typically wetter than winters, and sequences with precipitation exceeding 5 mm/day are common. It is for this reason that the weekly period selected has a succession of wet days. At the Szrenica site, summers are typically drier than winters with some evening fog at the higher sites (according to the 100 year Meteorological Observatory, Pereyma *et al*. 1997).

12.4.1 Hourly variations

In order to compare the two catchments, the results of a full test day are presented for May 27 2001 for Szrenica (Figure 12.5) and for August 5 1999 in the Dischma (Figure 12.6) for all selected stations.

Szrenica

The meteorological variables show that May 27 was a mostly fine day with some clouds passing between 11–16:00 and a thin cloud layer settling in after 18:00 (Figure 12.5(a)). Maximum wind speeds fluctuate around 15 m/s between 03 and 04:00, 4 m/s from 10:00 to 14:00, 15 m/s at 17:00 and 13 m/s around 23:00 (Figure 12.5(b)). Wind speeds are lowest during periods of maximum radiation.

Evapotranspiration and condensation are higher for the lysimeter at station 1 than for all other pan stations (Figure 12.5(d)). Evapotranspiration forms a well-developed bimodal distribution with a first phase between 07 and 12:00 and a second phase from 12 to 19:00. Between sunrise and sunset, there are two peaks of transpiration (0.21 mm/10 min. at 09:20 and 0.14 mm/10 min. at 14:30 with a break at noon). In contrast, evaporation starts 30 minutes later and rises slowly until noon with 0.07 mm/10 min. During the afternoon, there are three successive evaporation peaks just above 0.1 mm/10 min., but evaporation stops suddenly shortly after 16:00. In the late afternoon and night, condensation dominates (with approximately 0.1 mm/10 min. for both evaporation pan and lysimeter) alternating at roughly hourly intervals with evapotranspiration. Pronounced differences remain between lysimeter and evaporation pan. Whereas pan evaporation takes hours to gain momentum in the morning at station 1 because of low wind speeds, the pans at station 2 and 3 already reach maximum values of 0.2 mm/10 min. between 09:00 and 10:00. Potential evaporation follows similar patterns at station 2 and 3 (Figure 12.5(f) and (g)). During the afternoon, growing wind speeds and changing properties of incoming air masses (e.g. fog) are responsible for a rapid switch between evaporation and condensation at all evaporation stations. For station 2, evaporation declines much more slowly and only terminates at 20:00. At station 3, it already terminates at 17:00. Low-level condensation is pronounced throughout the day and night and may be explained by the influence of altitude on the formation of clouds and deposition of moist air through fog.

Most of the evapotranspiration dynamics can be explained in terms of radiation, wind speed and temperature gradients (Figure 12.5(a)–(c)). At station 1, the temperature gradient is highest at 11:00, decreasing rapidly thereafter. At station 2, the maximum temperature gradient is not well developed and generally lower than at station 1 (Figure 12.5(c)). It increases between 06 and 08:00 parallel with station 1 but fluctuates at a ratio of 1.1 because of significant exposure to wind. There is only a weak decrease in the temperature gradient after 14:00. The strong increase between 07:00 and 09:00 at station 2 and 07:00 and 11:00 at station 1 coincides with the steep increase in evaporation at the stations. High wind speeds encourage evaporation and evapotranspiration in the afternoon at station 1 and 3 but less so at station 2 where the temperature gradient is already decreasing as a result of strong topographical differences. North-easterly to south-easterly winds set in the afternoon and mobilize warm, upslope air from the valley floor that reinitialize another short phase of evaporation. Neither evapotranspiration from the lysimeter nor from the evaporation pan reacts in parallel to radiation. Evapotranspiration from the lysimeter is initiated with radiation onset but terminates before sunset.

The striking contrast between the patterns of evapotranspiration from the lysimeter and evaporation from the evaporation pan at station 1 cannot be explained by meteorological data alone. The inverse patterns are not exceptional since this contrast is measured for all days (Figure 12.7(d)–(g)). All other evaporation pans have very similar regimes and are comparable to the lysimeter.

In total, there were approximately 5 mm of evapotranspiration, 3 mm of evaporation and 1 mm of condensation during the daytime at station 1. At night, the

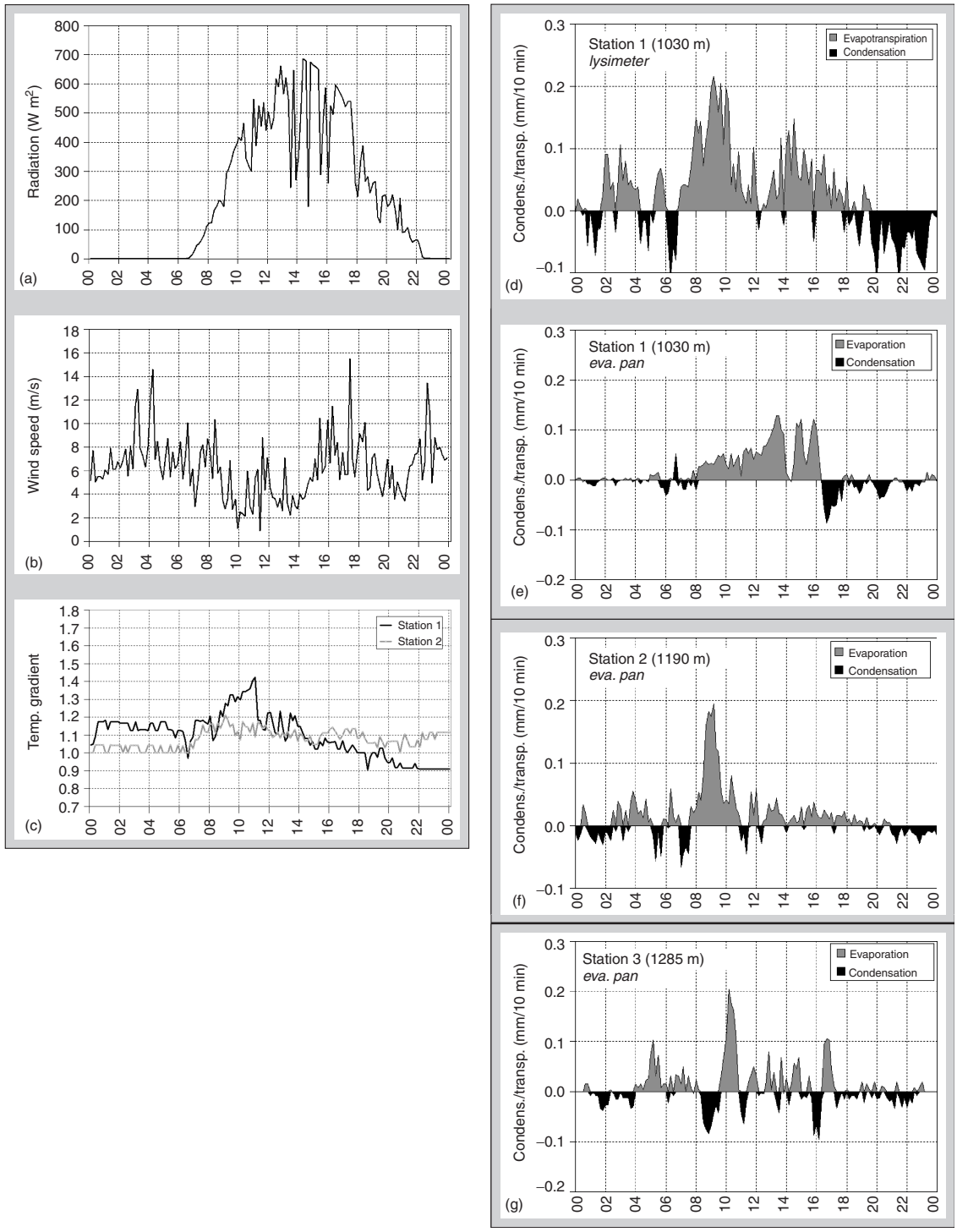


Figure 12.5 Typical daily cycles of (a) incoming radiation (station 1 and station 2), (b) maximum wind speed (station 1), (c) temperature gradient (T_{low}/T_{up}) (station 1), (d) evapotranspiration and (e) potential evaporation for station 1 and (f) potential evaporation at station 2 and (g) at station 3 at 10-minute intervals on May 27, 2001 for Szrenica, Poland

lysimeter measured 1 mm of water loss, whereas the pan gained 1.6 mm of water. In other words, approximately 9 litres of water are mobilized over 1 m^2 of vegetation, whereas little more than 4 litres are mobilized over 1 m^2 of free water surface, a difference close to 50% (Figure 12.8).

In summary, evapotranspiration behaves in accordance with the physical setting of the three sites, especially topography and vegetation. The lowest station (1) is situated in a rather moist location at the lower end of a nivation depression close to a small stream surrounded by blueberries and moss-covered rocks. Station 2 lies on a small hummock next to a steep channel, and is wind-exposed with low vegetation and at the lower cloud boundary. The last station is surrounded at its upper edge by dwarf pines and forms a less wind-exposed stand of dwarf spruce with substantial influence of fog. Under these conditions, maximum evaporation occurs at station 2 in contrast to the wetter lower station 1 and the flatter station 3. A general gradient of evaporation only exists between station 1 and 3 but not with station 2 since it is influenced by wind as a result of its special topographical setting.

Dischma

Figure 12.6(a)–(c) illustrates the influence of dominant meteorological variables on evapotranspiration and evaporation on August 5 in the Dischma. As in the Polish example, the day was not quite cloud-free. The daily average wind speeds experiences a maximum between 14:00 and 18:00, and radiation decreases in this phase with incoming cloud fields. The temperature gradient in the upper valley starts increasing between 04:00 and 08:00 and flattens between 08:00 and 16:00, with an abrupt decrease between 15:00 and 16:00 due to upcoming wind and clouds. It decreases rapidly thereafter until 20:00, increasing rapidly once more between 20:00 and 21:00, then fluctuating at a constant level until midnight. An asymmetry in meteorological variables has developed between morning and evening because of incoming clouds and air masses.

With the exception of Schwarzhorn, all sites experience a short, intensive rainfall event between 22:00 and 23:00, reaching a maximum of 1.7 mm/10 min. At Schwarzhorn, rainfall persists from 19:00 to 24:00. At Inner Hof and Jenatsch, rainfall peaks at 22:00, at Schönbühl toward 23:00, at Gletschboden at 23:00 and at Schürli and Hüreli at 22:00. The rain moves in fast from the north. In the lower valley, it begins and ends earlier, therefore evapotranspiration begins sooner after rainfall. In the higher regions, evapotranspiration can only set on at the end of rainfall, which is after midnight.

Evapotranspiration takes place between 07:00 and 21:00 in the whole valley with the exception of Schwarzhorn, which does not start until 09:00 and already ends at 16:00 (Figure 12.6(d)). On the valley floor at Inner Hof (Figure 12.6(i)) and less so at Jenatsch (Figure 12.6(g)), there is a short spell of condensation around 16:00 followed again by evapotranspiration. At Hüreli Alpenrose, condensation takes place over a short period at 13:00. At Gletschboden (Figure 12.6(m)), there is no condensation and in contrast to Jenatsch and Inner Hof, the lysimeter records the strongest evapotranspiration period immediately after 10:00 in the morning. The Schwarzhorn site (Figure 12.6(d)) does not conform to the other sites. Here, evapotranspiration is uniformly high and is initiated late (after 08:00), experiences an early peak at 14:00 and terminates early (16:00). Rates of evapotranspiration reach 0.12 mm/10 min. for prolonged periods. Some sites experience late peak evapotranspiration, for example, at 15:00 at Schönbühl and Inner Hof (Figure 12.6(e) and (i)) and 17:00 at Jenatsch.

The lowest evaporation rates are measured at Schönbühl (<0.05 mm/10 min) and the highest at Inner Hof (0.06 mm/10 min). This can be explained by the differences in locations: whereas Inner Hof is situated more on a slope, it experiences less air saturation and is surrounded by a very diverse wet meadow, Schönbühl is close to the glacier with stagnating wet areas, higher humidity and very short grass. Evapotranspiration and evaporation rates are very high after the short rainfall event (i.e. 0.13 mm/10 min. maximum at Inner Hof (Figure 12.6(i) and (j))). Overall, it can be stated that with the exception of Schönbühl all sites have the same local pattern of evapotranspiration and evaporation, although the pattern is less evident for smaller fluctuations in the afternoon.

The Schwarzhorn site has a completely different regime. Incoming cold air switches off evapotranspiration far earlier. Inner Hof and Jenatsch, both located in the rich pasture zone, are also locally affected by this phenomenon. The expected decrease of evaporation with increasing elevation, increasing air humidity, decreasing temperature and poorer vegetation only counts for the evaporation pans situated along the longitudinal valley axis at Schönbühl (Figure 12.6(f)), Jenatch (Figure 12.6(h)) and Inner Hof (Figure 12.6(j)). However, the three lysimeters respond quite uniformly, and Schönbühl, in particular, transpires substantially more than Jenatsch. A weak elevational gradient of evapotranspiration exists, but regional differences must be considered in terms of botany, that is, plant type and density.

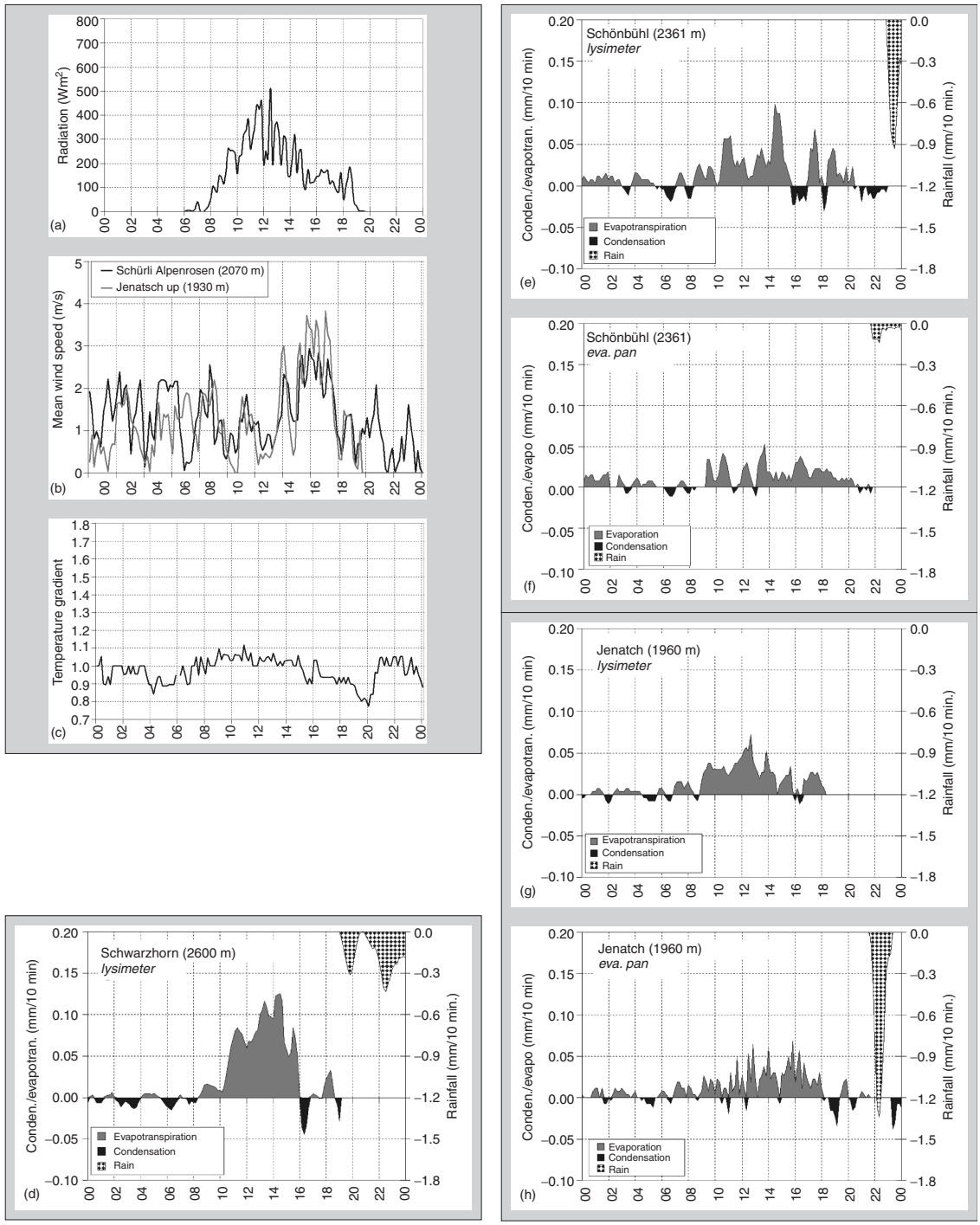
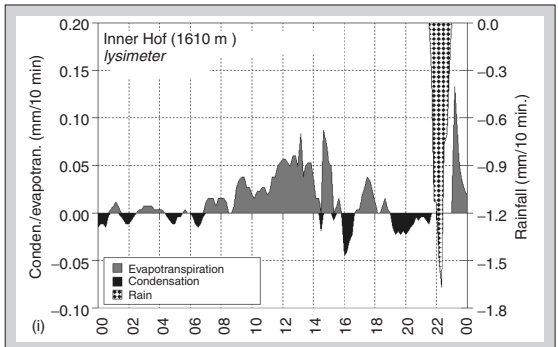
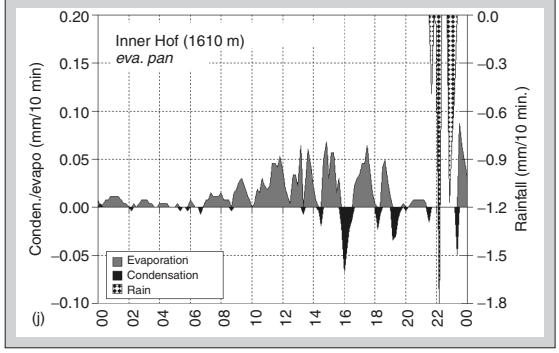
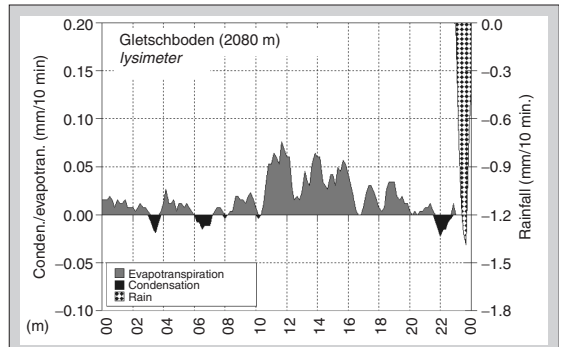
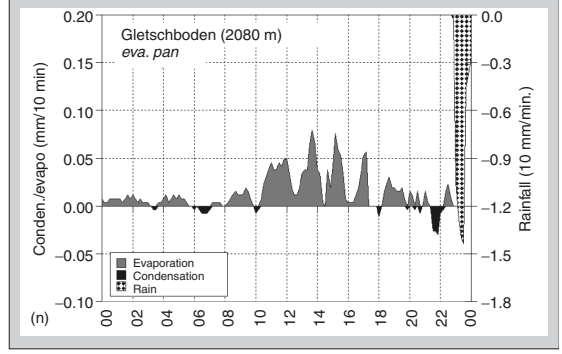


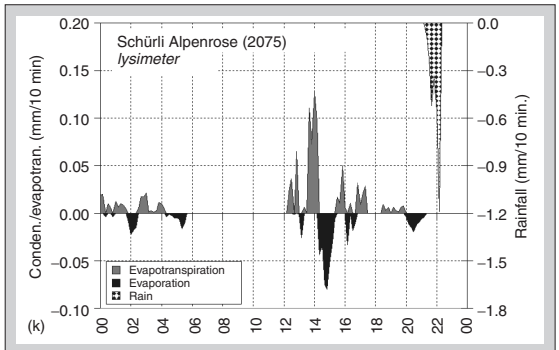
Figure 12.6 Comparison of (a) incoming radiation (Jenatsch), (b) average wind speed (Schüreli Alpenrose and Jenatsch) and (c) temperature gradient (Gletschboden) at 10-minute intervals; evapotranspiration, potential evaporation, condensation and rainfall for (d) Schwarzhorn, (e) and (f) Schönbühl, (g) and (h) Jenatch, (i) and (j) Inner Hof, (k) and (l) Schüreli Alpenrose, (m) and (n) Gletschboden and (o) and (p) Hüreli Alpenrose at 10-minute intervals for August 5, 1999 for Dischma, Switzerland. Periods with no data indicate data loss. Nearly no rainfall was recorded at (f) and (h) since the evaporation pan was already full

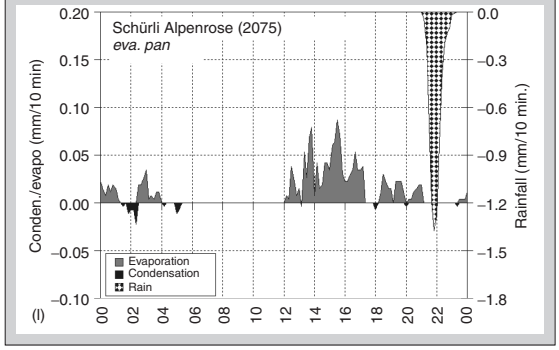

Inner Hof (1610 m)
lysimeter
Conden./evapotran. (mm/10 min)
Rainfall (mm/10 min.)
Evapotranspiration
Condensation
Rain
(i)

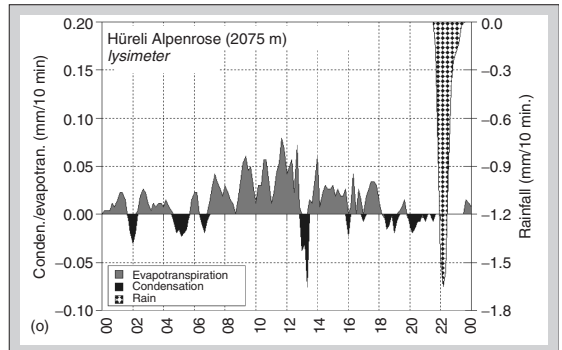

Inner Hof (1610 m)
eva. pan
Conden./evapo (mm/10 min)
Rainfall (mm/10 min.)
Evaporation
Condensation
Rain
(j)

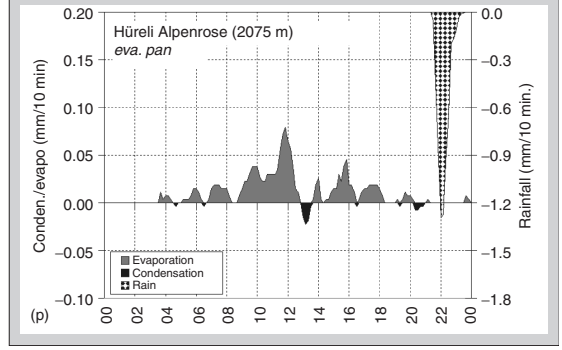

Gletschboden (2080 m)
lysimeter
Conden./evapotran. (mm/10 min)
Rainfall (mm/10 min.)
Evapotranspiration
Condensation
Rain
(m)


Gletschboden (2080 m)
eva. pan
Conden./evapo (mm/10 min)
Rainfall (10 mm/min.)
Evaporation
Condensation
Rain
(n)


Schürli Alpenrose (2075)
lysimeter
Conden./evapotran. (mm/10 min)
Rainfall (mm/10 min.)
Evapotranspiration
Evaporation
Rain
(k)


Schürli Alpenrose (2075)
eva. pan
Conden./evapo (mm/10 min)
Rainfall (mm/10 min.)
Evaporation
Condensation
Rain
(l)


Hüreli Alpenrose (2075 m)
lysimeter
Conden./evapotran. (mm/10 min)
Rainfall (mm/10 min.)
Evapotranspiration
Condensation
Rain
(o)


Hüreli Alpenrose (2075 m)
eva. pan
Conden./evapo (mm/10 min)
Rainfall (mm/10 min.)
Evaporation
Condensation
Rain
(p)

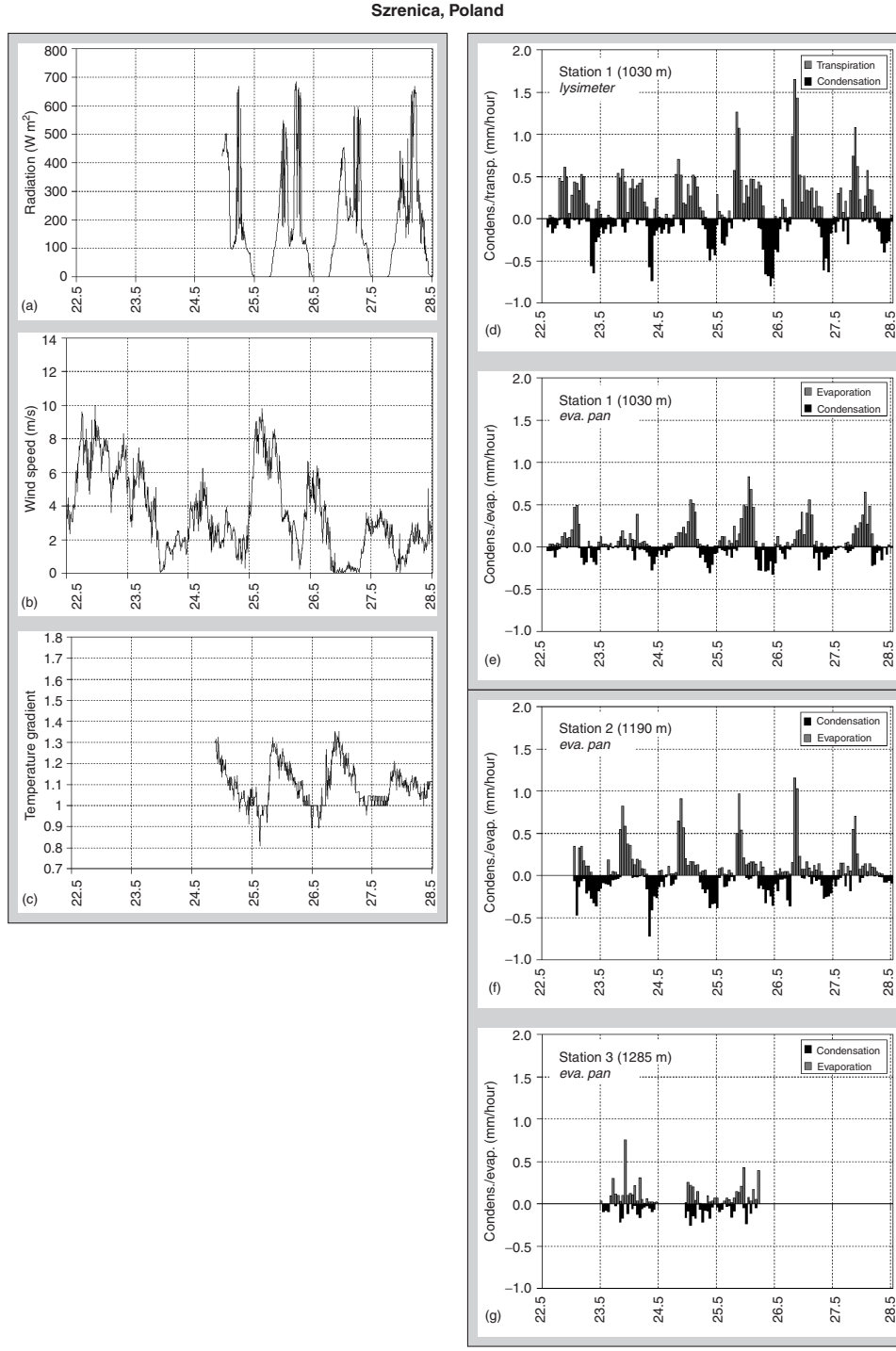


Figure 12.7 Comparison of meteorological variables at Szernica, Poland (22–28.5.01): (a) radiation per 10 min. at station 1, (b) maximum wind speed per 10 min. at station 1 (c) temperature gradient at station 1, (d) evapotranspiration and condensation at station 1, (e) potential evaporation and condensation at station 1, (f) potential evaporation and condensation at station 2, (g) potential evaporation and condensation at station 2

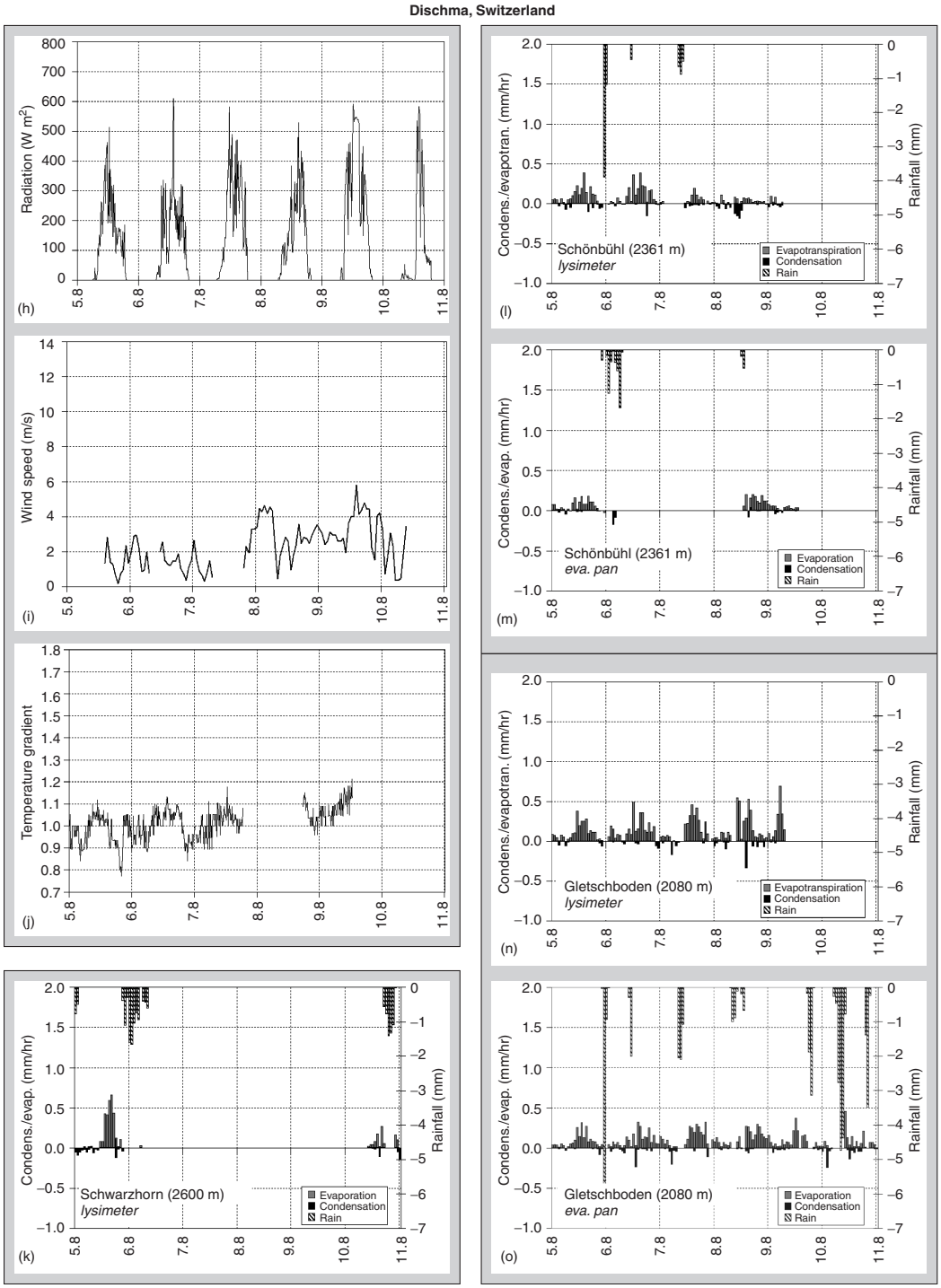


Figure 12.7 ***(continued)*** and at Dischma (5–11.8.1999) (h) radiation per 10 min. at Jenatsch (i) maximum wind speed per 10 min. at Jenatsch (j) temperature gradient at Gletschboden, (k) evapotranspiration and condensation Schwarzhorn (l) evapotranspiration and condensation Schönbühl, (m) potential evaporation and condensation Schönbühl (n) evapotranspiration and condensation at Gletschboden, (o) potential evaporation and condensation Gletschboden. Blank spaces indicate missing data due to battery failure

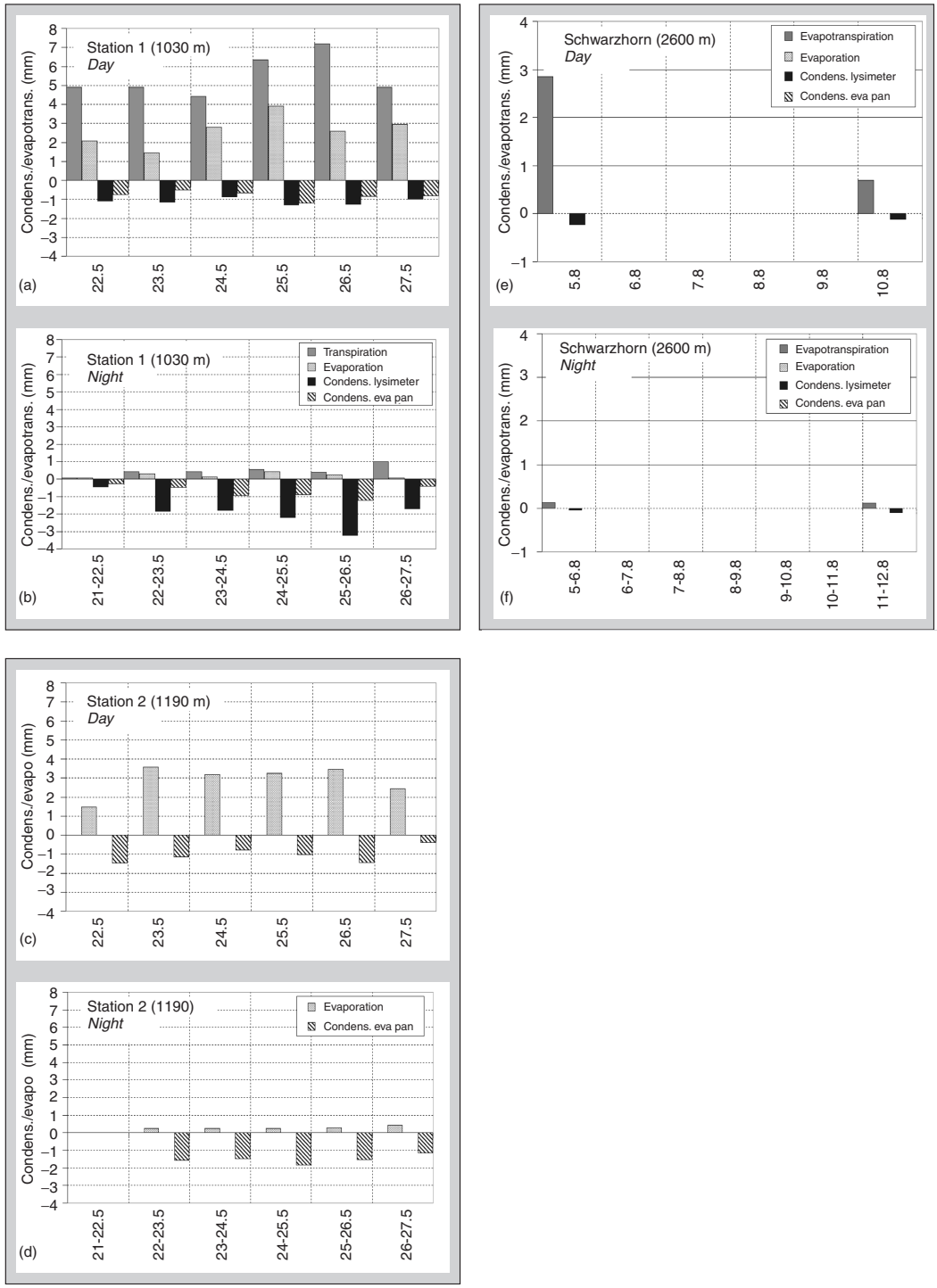
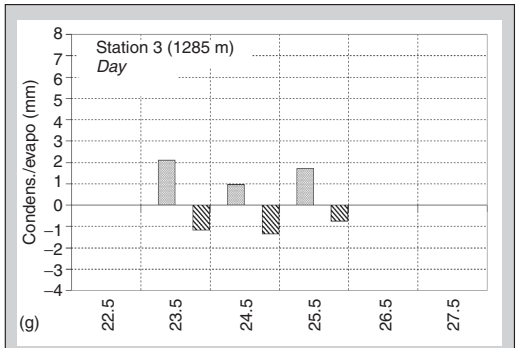
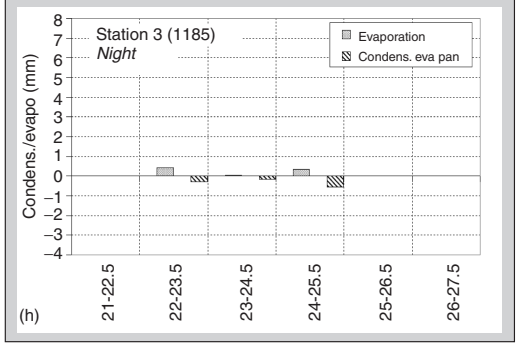
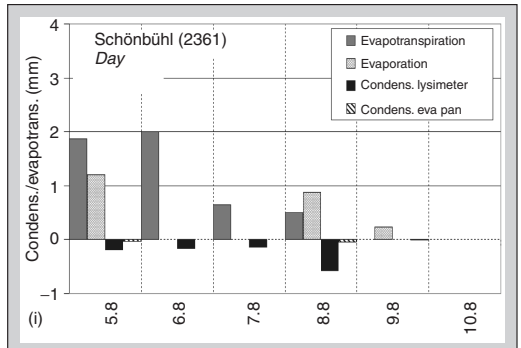
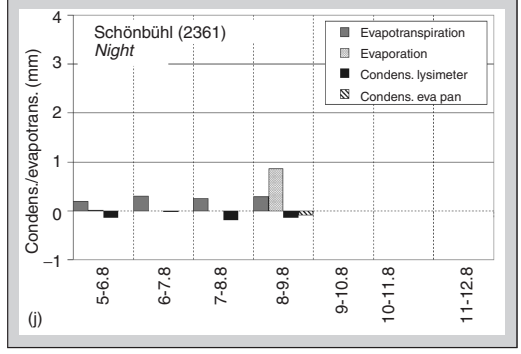


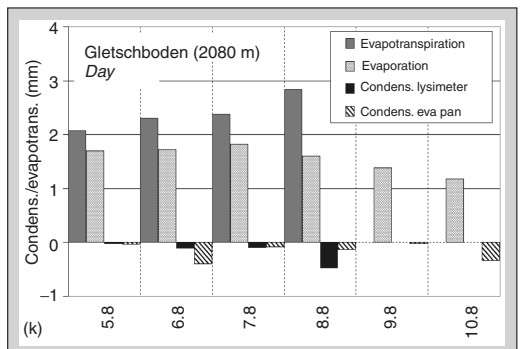
Figure 12.8 Comparison of transpiration, evaporation and condensation in lysimeters and evaporation pans at Szernica, station 1, by (a) day and (b) night, station 2 by (c) day and (d) night and station 3 (e) day and (f) night and in the Dischma, Schwarzhorn by (g) day and (h) night, at Schönbühl by (i) day and (j) night and at Gletschboden by (k) day and (l) night. Zero data indicates data loss through battery failure

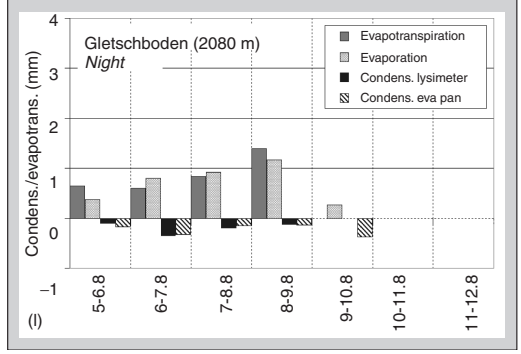

Station 3 (1285 m)
Day
Condens./evapo (mm)
8
7
6
5
4
3
2
1
0
−1
−2
−3
−4
22.5
23.5
24.5
25.5
26.5
27.5
(g)


Station 3 (1185)
Night
Evaporation
Condens. eva pan
Condens./evapo (mm)
8
7
6
5
4
3
2
1
0
−1
−2
−3
−4
21-22.5
22-23.5
23-24.5
24-25.5
25-26.5
26-27.5
(h)


Schönbühl (2361)
Day
Evapotranspiration
Evaporation
Condens. lysimeter
Condens. eva pan
Condens./evapotrans. (mm)
4
3
2
1
0
−1
5.8
6.8
7.8
8.8
9.8
10.8
(i)


Schönbühl (2361)
Night
Evapotranspiration
Evaporation
Condens. lysimeter
Condens. eva pan
Condens./evapotrans. (mm)
4
3
2
1
0
−1
5-6.8
6-7.8
7-8.8
8-9.8
9-10.8
10-11.8
11-12.8
(j)


Gletschboden (2080 m)
Day
Evapotranspiration
Evaporation
Condens. lysimeter
Condens. eva pan
Condens./evapotrans. (mm)
4
3
2
1
0
−1
5.8
6.8
7.8
8.8
9.8
10.8
(k)


Gletschboden (2080 m)
Night
Evapotranspiration
Evaporation
Condens. lysimeter
Condens. eva pan
Condens./evapotrans. (mm)
4
3
2
1
0
−1
5-6.8
6-7.8
7-8.8
8-9.8
9-10.8
10-11.8
11-12.8
(l)

Comparison of the three alpenrose sites (Figure 12.6(k) and (l); (m) and (n); (o) and (p)) shows that evaporation and evapotranspiration dominate at Hüreli and Gletschboden at night with little condensation. Considerable amounts of nocturnal CO_2 release due to alpine plant respiration was also observed by Körner (1999). Evapotranspiration persists longest on the valley floor at Gletschboden, followed by Schürli then Hüreli. Gletschboden and Hüreli reach their maximum at 12:00, but Schürli follows later at 14:00–15:00. Schüreli has both the highest transpiration and condensation rates.

The pattern of daily evapotranspiration and evaporation is complicated, but indicates some coherence over time. However, over space there is no single general rule of thumb (such as one gradient concept) that may apply to the interpretation of evapotranspiration, and the impact of plant distribution on evapotranspiration dynamics is substantial. If water loss and gain are balanced for each other, the highest lysimeter station Schwarzhorn loses the highest amount of water (2.8 l/m^2), Gletschboden loses only 2.5 l/m^2 and Schönbühl loses 1.5 l/m^2 on the same day. Neither evapotranspiration theory nor functions would allow this case to arise under linear assumptions. However, under natural conditions the effects of extremely high local wind speeds on evapotranspiration may outweigh all other factors (Figure 12.8(g) and (h), (i) and (j) and (k) and (l)).

12.4.2 Daily and weekly variations

The daily variations of evapotranspiration and condensation in the Dischma (Figures 12.7 and 12.8) are influenced by a sequence of wet days that frequently caused data loss at the more remote sites Schwarzhorn and Schönbühl. In general, rainfall occurs in the evening with three days of rainfall in the morning and no rain on the first day. In the Dischma, rainfall decreases the dynamics of evapotranspiration only marginally compared to Szrenica. In contrast, for the week in Poland (Figure 12.7), there is an absence of rain with long, fine weather periods but a more dominant influence of fog and some clouds at midday and in early afternoon. As such, the dynamics of condensation are far more pronounced at this site.

Szrenica

In contrast to the Dischma, the weather in the Szrenica catchment was continuously fine (Figure 12.7(a)–(c)). Patterns of radiation were very regular with a strong increase in radiation in the morning, clouds and fog in the afternoon and secondary peaks in radiation due to cloud break up in the late afternoon and early evening. Maximum wind speeds behave inversely to radiation. The higher the radiation, the weaker the wind speed. Similarly, wind speeds are very high at night. The local temperature gradient between the lower and upper arm of the meteorological station increases strongly in the early morning and reaches a maximum toward 10:00, decreasing up to 22:00. Minimum values are obtained by surface cooling during the nighttime.

In this catchment, evapotranspiration and condensation from the lysimeter especially at station 1 is very regular on a day-to-day basis (Figure 12.7(d)). On May 26 evapotranspiration reaches more than 1.5 mm/hour. Parallel with radiation, there is frequent bimodality in the water exchange patterns, with rapidly increasing evapotranspiration between 10:00 and 11:00 and a secondary maximum in the late afternoon. Maximum condensation occurs at 22–23:00. The bimodality in evapotranspiration can be explained by the daily cloud cover. Clouds appear in the early afternoon but in the late afternoon the sun often reappears for a short time. The temperature gradient (Figure 12.7(c)) increases in parallel with the strongest increase in evapotranspiration. As already observed (Figure 12.5(e)), the distribution of evaporation at station 1 (Figure 12.7(e)) is asymmetrical and peaks in the afternoon. Evaporation at the higher station 2 follows a different pattern but at a slightly higher level. Particularly strong exchange processes between condensation and evaporation are developed at the highest station 3. There are large sums of condensation in relation to evaporation.

The sums of the daily and nightly evaporation seem realistic (Figure 12.8(a)–(d), (e) and (f)). At station 2, sums fluctuate between 1.5 and 3.5 mm during the daytime and fall below 0.5 mm during the night. The contrast between the sums of evaporation and evapotranspiration at station 1 are striking. Daily sums of evapotranspiration range between 4.5 and above 7 mm, whereas evaporation ranges between 1.4–3.9 mm/day. During the night, sums of condensation in the lysimeter are impressively high and oscillate between 0.3 and 3.2 mm, whereas condensation in the evaporation pan only ranges between 0.2 and 1.2 mm. At station 2 and 3, amounts of daytime condensation are similar. Evaporation at station 3 fluctuates between 1 and 2 mm. At station 1, evapotranspiration mostly goes parallel with evaporation. Even at this scale, it is remarkable that the lysimeters were far more active (up to double the amount) than the evaporation pans. Concerning average evaporation values, station 2 is most active (3.2 mm/day), followed by station 1 (2.9 mm/day) and station 3 (2.2. mm/day), so that there is no linear altitudinal gradient (Table 12.3(a)). Average condensation is highest at station 2 (2.5 mm/day), followed by station 1

Table 12.3 Average daily sums of evapotranspiration (ET)/evaporation (E) and condensation for the test week at (a) station 1–3 at Szrenica and (b) Schwarzhorn, Schönbühl and Gletschboden stations in the Dischma

(a)

	Station 1 lysi	Station 1 pan	Station 2 pan	Station 3 pan
Station	mm/day	mm/day	mm/day	mm/day
ET or E	5.9	2.7	3.2	2.2
Condensation	3.0	1.9	2.5	1.4
Total water loss	2.9	0.8	0.7	0.8

(b)

	Schwarzhorn lysi	Schönbühl lysi	Schönbühl pan	Gletschboden lysi	Gletschboden pan
Station	mm/day	mm/day	mm/day	mm/day	mm/day
ET or E	2.0	1.6	1.4	4.0	2.3
Condensation	0.5	0.5	0.2	0.5	0.5
Total water loss	1.5	1.1	1.2	3.5	1.8

(2.3 mm/day) and station 3 (1.4 mm/day). Evaporation is highest at station 2 and so is condensation. These results reflect the topographic situation of station 2 (see Section 12.4.1) as well as the foggy and windy nature of the site, which is responsible for the highest amount of water gain and loss.

Dischma

Meteorological variables derived from the reference station Gletschboden (Figure 12.7(h) to (j)) show that radiation was weakened by clouds for all days between August 5 and 11. The worst day with most rain was August 10, whereas the best afternoon was observed on the August 9. During the first phase of the test week, winds were poorly developed. This situation changed after August 8, when wind speed increased from 2 to 4 m/sec. The sequence of precipitation events is remarkable (Figure 12.7(o)). August 5 was the only day with hardly any precipitation. During the test week, it rained frequently at night, during the morning and afternoon. On August 10, there were two precipitation events that caused data loss at various measuring stations. Temperatures were moderate at the beginning of the week, cooling toward the end. The temperatures and rain measured are typical for the summer months in this alpine region.

The daily pattern of evapotranspiration and condensation is very well developed, but there are clear reactions to the rainfall events, especially at Gletschboden (Figure 12.7(n) and (o)). Rainfall on the August 6, 7 and 8 repeatedly causes high amounts of rapid interception evapotranspiration. If precipitation occurs at night, resulting evapotranspiration occurs even during the night. Rapid reactions to rainfall are also recorded from the evaporation pans.

The lysimeters at Schwarzhorn, Schönbühl and Gletschboden do not react uniformly (Table 12.3(b)). Whereas the Schwarzhorn site registers 3 mm/day of evapotranspiration for the warmest day (August 6) and <1 mm day on the coldest day (August 9), Schönbühl registers <2 mm and 0.3 mm/day, respectively, and Gletschboden registers 2 mm/day with no measurement available for the last day. The pan evaporation results are lower: whereas Schönbühl registers 1.2 mm/day and 0.2 mm/day for the warmest and coldest day, Gletschboden registers only 1.6 mm/day and 1.2 mm/day. Evapotranspiration nearly always culminates in the early and late afternoon with a secondary peak after rainfall events. Nocturnal evaporation and evapotranspiration contribute as much as 10% of daily values. Nocturnal condensation can be as high as evapotranspiration at the Schwarzhorn and Schönbühl stations.

The weekly evapotranspiration values in the Dischma reflect first a decreasing gradient along the valley floor, then an increasing gradient from the upper valley floor to the vicinity of the peaks (Figure 12.8), although data for the Schwarzhorn is only available for two days during the test week. Evapotranspiration maxima of up to 3 mm are obtained for Schwarzhorn and Gletschboden, but only 2 mm for Schönbühl. Both nightly evaporation and condensation is highest on the valley floor at Gletschboden, which is situated close to the Dischma river and lowest at Schwarzhorn. The sum of average

day- and nighttime values of evapotranspiration and condensation approximate 2 and 0.5 mm at Schwarzhorn. At Schönbühl, the lysimeter transpires 1.6 mm and condensates 0.5 mm, whereas the evaporation pan evaporates 1.4 mm versus 0.2 mm of condensation: The lowest station at Gletschboden experiences the highest value, that is, 4 mm of transpiration versus 0.5 mm of condensation. Pan evaporation is only 0.3 versus 0.5 mm of condensation.

As in Szrenica, evaporation values are lower than evapotranspiration and there are substantial differences among the valley floor, the middle slopes and the peak areas.

12.5 CONCLUSION

Little is known about the diurnal and nocturnal interactions and variability of condensation, evaporation and transpiration in mountain environments. Intensive field experiments are described using automatically recording lysimeters and evaporation pans during the snow-free period above the tree line. Results are compared between the humid Dischma valley in east Switzerland and the fog-influenced Szrenica catchment in the Giant Mountains in Poland. Water fluxes are directly measured within alpine shrubs, grass, pasture and dwarf spruce and coupled with meteorological information at each site. Differences in condensation between vegetated and nonvegetated surfaces are highest in the early morning and late evening when plant dynamics react to extreme temperature changes. Potential evaporation and evapotranspiration are often similar in pattern but in principle evaporation is always lower than evapotranspiration. The values depend strongly on plant type, valley shape and climatic influences. Daily condensation in Szrenica is between 3 and 10 times higher than in the Dischma because of the fog influence. Evapotranspiration is more comparable even though the Dischma receives large amounts of rain during the selected week.

The observations show that evapotranspiration in mountain catchments not only depends on physical processes but also on the heterogeneity of both the terrain and plant cover with its complex biological regulatory mechanisms. In both catchments, soil moisture is not a limiting factor since precipitation is abundant, soils have a high humus content and the shallow root horizon is capable of storing significant amounts of water. Traditionally, it was thought that the stomatal control of transpiration is regulated only by light, CO_2, relative humidity, water supply to plants and air temperature. However, the results of evapotranspiration measurements show that for warm summer nights alpine shrubs continue to keep their stomata open during the late evening and early morning in both catchments and that interception evaporation and evapotranspiration can occur under near saturated conditions immediately after rainfall events. Although soil temperature and soil moisture were not determined for all measuring periods, evapotranspiration and the switchover to condensation could be explained by the variability in radiation, temperature and wind speed. Since wind plays an important role in the local exchange of moist and dry air masses over mountain micro- and macro topography, it has a strong influence on transpiration. By ventilating the lower surface layer, winds can easily transport away surplus water vapor. The transport efficiency of wind is largely dependent on surface roughness, but this is of decreasing importance during high wind speeds typical for high altitudes. Since winds can be very gusty over mountain topography, wind-induced transpiration can be instantaneous and highly sporadic over time. Therefore, small variations in transpiration and condensation can only be adequately observed and explained using appropriate measuring techniques, and it is essential to adapt the approach and field methodology to mountain conditions.

In general, interpretations of evapotranspiration are valid only for flat terrain or at least for sites with a long enough wind fetch. However, these concepts do not stand for steep mountain topography since, among other factors, advection of energy is neglected. Theories postulated for flat terrain cannot be applied to mountain catchments such as the Dischma. Normally, all atmospheric water exchange processes are explained by only taking into account small eddies, that is, by assuming that eddy size is proportional to the dimensions of the measurement arms (1–2 m) of climate or Bowen Ratio stations. Therefore, countergradient effects are not taken into account and new interpretations and theories have to be tackled. A second problem associated with mountainous terrain is that researchers tend to rely heavily on turbulence theories based on similarity: similarity assumes turbulence of air over flat terrain. Yet, stratification is not planar along the surface layer in typical alpine catchments such as the Dischma or Szrenica and therefore such assumptions cannot be transferred to steep terrain.

Results from different slope and valley profiles in both study areas indicate that there is no general steady or linear decrease of evapotranspiration or

condensation with height as indicated by Baumgartner *et al*. (1983). The total water loss or gain between evaporation/evapotranspiration and condensation at the Polish site indicates an inverse gradient: the lowest values for evaporation are measured at the lowest station and the maximum values at the highest station. The values for middle station lie exactly in between. In the Dischma, the situation is more complex. A preferential zone of evapotranspiration is developed on the sheltered lower valley trough slopes because of higher incoming radiation and lower wind speeds. Evapotranspiration does not decrease steadily with altitude above the trough slope because sheltered zones such as corries or the foot of rock faces are subject to high radiation and evapotranspiration can obtain values similar to those on the lower valley slopes. Similar altitudinal variability has been mentioned by Körner (1999).

Evapotranspiration and condensation is a reflection of plant physiology and is strongly adapted to mountain topography. Several years of investigations in the Dischma show that it only decreases along the valley floor up to an altitude of 2000 m, then increases strongly across the lower valley slopes and levels off over the higher slopes with islands of extremely high evapotranspiration in between depending on exposure to wind and length of insolation. Evaporation and associated condensation run more or less parallel with evapotranspiration up to the given altitude of 2000 m. Above this height, evaporation continues to decline steadily and the gap between evaporation and evapotranspiration grows. This divergence is an important result that should be considered in extrapolations and modelling of evapotranspiration. Although the interpretation of these results is limited to measurements during snow-free summer months (from 1995 to 1999), it can be assumed that the evaporation of snow during the winter and spring is subject to similar spatial characteristics.

In view of future experimental studies, this comparison shows that the results are reproducible and applicable in other mountain regions. Evaporation, evapotranspiration and condensation are extremely sensitive parameters that react very rapidly to fluctuations in basic meteorological and hydrological parameters. Even so, zones with relatively stable evapotranspiration, such as the valley floor or trough slopes, can be differentiated from zones with more variable evapotranspiration such as corries, arêtes and trough surfaces. (See Chapter 17 for more details on spatial descretization and model parameterization). Our determination of evapotranspiration can be improved as long as we consider that the regional variability is larger than normally assumed from distributions derived from two point correlations. Also, it must be kept in mind that by relying only on valley stations, the true patterns of evaporation and evapotranspiration and the real transits in vegetation remain unresolved. The most representative sites are therefore to be found on the opposite-facing lower trough slopes.

For modelling and validation purposes, it is proposed to use results from the low-cost evapotranspiration measuring equipment as introduced in this chapter. This is particularly important for mountain regions in developing countries. Climatic variables that are easy to determine should be used to calculate and/or explain evapotranspiration and condensation patterns. This should include in particular wind speed and temperature gradient measurements where humidity cannot be determined reliably. First, modelling results with a semi-distributed approach using the MMS modelling system (Leavesley *et al*. 2002) for the Dischma show that the Priestley–Taylor approach can be applied as a robust evaporation formula for mountain regions, however, this requires several meteorological stations that can determine dew point. For the Gletschboden, Schürli and Hüreli slope sites, calculations of evaporation for the year 1998 showed a close correlation (0.8) between the evaporation pan measurements and calculated evaporation even for high-resolution intervals. This approach will be developed by incorporating both measured and modelled evapotranspiration and condensation in the highly complex units inherent to mountain catchments.

12.6 ACKNOWLEDGMENTS

These studies were financed by a Habilitation Fellowship of the Deutsche Bundesstiftung Umwelt and a DAAD study award at the University of Wroclaw. We are grateful to the FU Berlin for financing two complementary pilot projects in the Dischma and for the help of numerous staff and students from the Department of Geography, Department of Meteorology, Department of Informatics and Department of Space Sciences of the Free University of Berlin, the WSL Birmensdorf and SLF Davos, the University of Wroclaw, Meteorological Observatory and Giant Mountains National Park. We are also thankful to the cartographers, Brauer-Jux, Martin Gref and Gerd Storbeck of the Department of Geography, University of Bonn, and to Joachim Schulz, Department of Geography, Free University of Berlin, for the study area maps. We are grateful to the critical comments made by Peter Ergenzinger.

REFERENCES

Acker, K., Wieprecht, W., Möller, D., Auel, R., Kalaß, D., Zwozdziak, A., Zwozdziak, G. and Kmiec, G., 1999. Results of cloud water and air chemistry measurements at Mt. Szrenica in Poland, Proceedings of EUROTRAC-2 Symposium '98, Vol. 1, *Transport and Chemical Transformation in the Troposphere*, P.M. Borrell and P. Borrell (Eds.). WITPress Computational Mechanics Publications, Southampton, 448–452.

Barry, R., 1992. *Mountain Weather and Climate*, Routledge Physical Environment Series, University of Cambridge.

Baumgartner, A., Reichel, E. and Weber, G., 1983. *Der Wasserhaushalt der Alpen*. Oldenburg Verlag, München, 343.

Berg, G. 1915. Die Vergletscherung an den Teichen des Riesengebirges. *Zeitschrift für Deutsche Geologische Gesellschaft*, **67**(3): 63–82.

Bernath, A., 1990. Evaporation measurements in the Alpine basin Gletsch during the ALPEX/RHONEX project, *Hydrology in Mountain Regions. I. Hydrological Measurements: The Water Cycle*. International Association of Hydrological Sciences, Publication No. 193, p. 53–60.

Cadisch, J., 1929. *Zur Geologie von Davos*, 110. Jahresversammlung der Schweizerischen Naturforschungs Gesellschaft, Davos, 83–92.

Calder, I.R., Hall, R.L., Harding, R.J. and Wright, I.R., 1984. The use of a wet-surface weighing lysimeter system in rainfall interception studies of heather (Calluna vulgaris). *Journal of Climate and Applied Meteorology*, **23**: 461–474.

Cernusca, A., Newesley, C. and Price, D., 1999. Water relations of ecosystems and hydrology of catchments. In *Land-use changes in European mountain ecosystems. ECOMONT – concepts and results*, A. Cernusca, U. Tappeiner and N.G. Bayfield (Eds.). Blackwell Wissenschaftsverlag, Berlin.

de Jong, C., List, F. and Ergenzinger, P., 2002. Experimental hydrological analyses in the Dischma based on daily and seasonal evaporation. *Nordic Hydrology*, **33**(1): 1–14.

de Jong, C., in press. The contribution of condensation to the water cycle under high mountain conditions, *Hydrological Processes*, C. de Jong, F. Whelan and B. Messerli (Eds.). Special Issue: Mountain Hydrology, Wiley.

Dore, A.J., Sobik, M. and Migała, K., 1999. Patterns of precipitation and pollutant deposition in the western Sudete mountains, Poland. *Atmospheric Environment*, **33**: 3301–3312.

Drukman, I., Migała, K. and Sobik, M., 1997. Selected characteristics of wind speed structure in the West Karkonosze Mountains. Climatological Aspects of Environmental Protection in Mountain Areas. *Acta Universitatis Wratislaviensis*, **1950**: 67–74.

Fischer, H., 1990. *Simulation der räumlichen Verteilung von Pflanzengesellschaften auf der Basis von Standortskarten*. Dargestellt am Beispiel des MAB Testgebiets Davos. Nr. 9202, Heft **122**, PhD thesis, Geobotanisches Institut ETH, Stiftung Rübel.

Graber, W.K., Siegwolf, R.T.W. and Furger, M., 1999. CO_2 and water vapour exchange between the composite test area and the atmosphere over Monte Bondone, *Land-Use Changes in European Mountain Ecosystems: ECOMONT Concepts and Results*, A. Cernusca, U. Tappeiner and N. Bayfield (Eds.). Blackwell Wissenschafts-Verlag, Berlin, Wien etc., 268–271.

Gurtz, J., Baltensweiler, A. and Lang, H., 1999. Spatially distributed hydrotope-based modelling of evapotranspiration and runoff in mountainous basins. *Hydrological Processes*, **13**(17): 2751–2768.

Gurtz, J., Zappa, M., Jasper, K., Lang, H., Verbunt, M., Badoux, A. and Vitvar, T., 2003. A comparative study in modelling runoff and its components in two mountainous catchments. *Hydrological Processes*, **17**(2): 297–311.

Handtke, R., 1993. *Flussgeschichte Mitteleuropas*: Skizzen zu einer Erd-, Vegetations- und Klimageschichte der letzten 40 Millionen Jahre. Enke, Stuttgart.

Hennemuth, B., 1986. Thermal asymmetry and cross-valley circulation in a small alpine valley. *Boundary Layer Meteorology*, **36**: 371–394.

Konzelmann, T., Calanca, P., Müller, G., Menzel, L. and Lang, H., 1997. Energy balance and evapotranspiration in a high mountain area during the summer. *Journal of Applied Meteorology*, **36**: 966–973.

Körner, C., 1999. *Alpine Plant Life*, Functional plant ecology of high mountain ecosystems. Springer, Berlin.

Körner, C., Hoflacher, H. and Wieser, G., 1978. Untersuchungen zum Wasserhaushalt von Almflächen im Gasteiner Tal, *Ökologische Analysen von Almflächen im Gasteiner Tal*, österreichisches MAB Hochgebirgsprogramm Hohe Tauern. Universitätsverlag Wagner, Wien.

Leavesley, G.H., Markstrom, S.L., Restrepo, P.J. and Viger, R.J., 2002. A modular approach to addressing model design, scale, and parameter estimation issues in distributed hydrological modelling. *Hydrological Processes*, **16**: 173–187.

LeDrew, E.F., 1975. The energy balance of a mid-latitude alpine site during the growing season 1973. *Arctic and Alpine Research*, **7**: 301–314.

Migała, K. and Szymanowski, M., 1999. AWS measurements in the extremal climatic conditions of the High Sudetes, *ICEAWS 1999 Proceedings, International Conference on Experience of Automatic Weather Stations*, Vienna.

Migała, K., Liebersbach, J. and Sobik, M., 2002. Rime in the giant mountains (The Sudetes, Poland). *Atmospheric Research*, **64**(1): 63–73 (11), Elsevier Science.

Pereyma, J., Sobik, M., Szczepankiewicz-Symayrka, A. and Migała, K., 1997. Contemporary climatic conditions and topoclimatic differentiation of the Karkonosze mountains, *Climatological Aspects of Environmental Protection in Mountain Areas*. Acta Universitatis Wratislaviensis, Vol. 1950, 75–94.

Sobik, M. and Migała, K., 1993. The role of cloudwater and fog deposits on the water budget in the Karkonosze (giant) mountains. *Alpex Regional Bulletin*, Swiss Meteorological Institute, **21**: 13–15.

Soukupová, L., Kociánová, M., Jenik, J. and Sekyra, J. 1995. Arctic-alpine tundra in the Krkonose, the Sudetes, *Yearbook of Scientific Papers from the Karkonoze National Park*. Opera Corcontica, Krkonosske práce. Vrchlabi.

Staudinger, M. and Rott, H., 1981. Evapotranspiration of two mountain sites during the vegetation period. *Nordic Hydrology*, **12**: 207–216.

Stewart, R.B. and Rouse, W.R., 1976. Simple models for calculating evaporation from dry and wet tundra surfaces. *Arctic and Alpine Research*, **8**(3): 263–274.

Szczepankiewicz-Symayrka, A. and Mielcarek, A., 1997. Bioclimatic conditions in the subalpine zone of the Karkonosze Mts (the environment of Swiss mountain pine), [w:], *Climatological Aspects of Environment Protection in Mountain Areas*, K. Migała and J. Pereyma (Eds.). Acta Universitatis Wratislaviensis, Prace Instytutu Geograficznego, seria C, Meteorologia i Klimatologia, IV, 95–102.

Turner, H., 1988. Das Klima der Versuchsfläche Stillberg. *Schweizerische Zeitschrift für Forstwesen*, **139**: 743–750.

Ulrich, W., 1987. *Simulationen von thermischen induzierten Winden und Überströmungssituationen*. PhD Thesis, **57**, Meteorologiches Insitut, Universität München, München, pp. 180.

Vögele, A.E., 1984. Untersuchungen zur Geomorphologie und jungquartären Talgeschichte des Dischma (Davos, Kt. Graubünden). PhD thesis, Physische Geographie, 14, Geographisches Institut der Universität Zürich.

Wildi, O. and Ewald, K., 1986. Der Naturraum und dessen Nutzung im alpinen Tourismusgebiet von Davos. *Ergebnisse des MAB-Projektes Davos*. 289, Eidgenössische Anstalt für das forstliche Versuchswesen, Birmensdorf.

Wright, I.R., 1990. A lysimeter for the measurement of evaporation from high altitude grass, *Hydrology in Mountainous Regions 1. Hydrological Measurement*. International Association of Hydrological Sciences, Publication No. 194, Lausanne, 79–87.

13

Climatologic and Hydrologic Coupling in the Ecology of Norwegian High Mountain Catchments

JÖRG LÖFFLER AND OLE RÖßLER
University of Oldenburg, Institute of Biology and Environmental Sciences, PO Box 2503, D-26111 Oldenburg, Germany

13.1 INTRODUCTION

Coupled climatologic and hydrologic investigations of high mountain landscapes in Norway are a great challenge, especially where strong meteorological and topographical gradients dominate the boreal altitudinal zones. Human impacts during the past centuries have been important in these types of landscapes, especially involving logging, peat cutting, lichen harvesting for winter fodder and extensive pasturing in the upper birch forest and alpine belts. Besides traditional summer pasture in the mountainous areas, reindeer domestication, especially in northern Norway, has had a broad-scale influence on the mountain environment (Löffler 2000). Its fragility in relation to environmental change and increasing land-use pressure has forced a major focus on high mountains within the discussion of sustainable development (Messerli & Ives 1997). Management of the mountain watersheds has received highest priority with regard to global freshwater resources (Mountain Agenda 1998). Problems and perspectives of Norwegian mountains have been recognised (Bernes 1993, Kaltenborn 1999). Mountains as water towers are important within its highly developed water power industry.

The objectives of the research program reported here are to analyse high mountain ecosystem functioning within different spatial and temporal scales in order to understand the mechanisms that determine the limits of land use. Furthermore, these mechanisms are to be understood within the framework of future global warming. Process-oriented studies have been established to emphasise long-term measurements with the following aims.

- Quantification of vertical and micro-spatial energy and water fluxes
- Process-oriented mapping and spatial modelling
- Analysis of landscape ecological interactions as determined by climate and hydrology
- Synthesising landscape functioning principles that determine the ecology of the high mountain environment.

The most decisive factor in the high mountain landscapes of the Norwegian Scandes is its complex topography determining climatologic and hydrologic gradients, which in turn effect soil development, nutrient fluxes and plant distribution (Köhler *et al*. 1994). These gradients are complex, and their ecological impact on the high mountain environment is not yet fully understood (Körner 1999). Extensive data are available on high mountain ecology, especially on plant life

Climate and Hydrology in Mountain Areas. Edited by C. de Jong, D. Collins and R. Ranzi
© 2005 John Wiley & Sons, Ltd. ISBN: 0-470-85814-1

and vegetation organisation, for over a century (Dahl 1998, Wielgolaski 1998, Moen 1999, Wielgolaski 2001). During the 1970s and 1980s, the Norwegian mountains were part of the International Biological Programme, focused on ecosystem functioning at different sites for a global comparative synthesis (Rosswall & Heal 1975, Wielgolaski 1975, Bliss *et al*. 1981). Local research on spatial dynamics and functioning of alpine ecosystems has been carried out by Mosimann (1985).

Hydrologic investigations with an ecological approach are rare in the Norwegian mountains. On the other hand, many hydro-geological surveys are provided by hydropower development in Norway (Faugli 1994a, 1994b, 1994c, Håland & Faugli 1994 among others). Although early studies dealt with the complexity of mountain environments in Norway (i.e. Dahl 1956), the present scientific challenge is to extend our knowledge on fine-scale temperature and snow cover differentiations as well as gradients between the oceanic and continental regions (Fægri 1972).

In the Scandes, snow is a decisive factor affecting both hydrologic and ecological systems. Snow-ecosystem studies show that feedbacks between snow, vegetation and climate are complex and occur at multiple scales (Walker *et al*. 2001). Although the patterns of snow distribution change little from year to year, its amount varies significantly. The most important factor affecting snow accumulation is wind. Strong winds are usually recorded in winter, and this affects both snow depth and distribution as well as its protective role for plants. Snow blown off ridges and windward-exposed slopes accumulates in lee positions, depressions or narrow valleys, where it may last far into the summer. This uneven snow distribution is commonly known as the *conservative distribution of snow* (Gjærevoll 1956). Moisture and stability of soils are affected by the distribution and thickness of the snow cover (Dahl 1956). Thus, the combined impact of topography, wind and snow cover has important effects on the high mountain vegetation.

This paper focuses on landscape ecological investigations, especially analyses of spatial and temporal snow dynamics, moisture, and temperature gradients in the central Norwegian high mountains. Interrelations between vegetation cover, periglacial patterns, soil types, humus forms, snow cover thickness, snow-melt and resulting water balance features as well as air, surface, and soil temperature regimes are analysed and mapped in detail (Löffler 1998). Primary results show that the local energy budget is the most important factor for physical, chemical and biotic processes (Löffler 1999, Löffler & Wundram 2001, 2003).

13.2 APPROACH

The ''landscape ecological complex analysis'' (Mosimann 1984a, 1984b, 1985), which quantifies landscape processes at the micro scale, is used as a basis for this study. Approaches for ecosystem functioning in different landscapes have been the subject of much discussion (e.g. Leser 1986, Rempfler 1989, Potschin & Wagner 1996, Potschin 1996, 1998, Döbeli 2000).

On the basis of a landscape ecological approach, climatologic and hydrologic coupling is used to explain landscape functioning patterns with a high spatial and temporal resolution. Ecosystem dynamics are analysed over the lower and middle-alpine belts in the continental and oceanic central Norwegian high mountains by means of continuous time series of measurements. Figure 13.1 shows a process-correlation model after Mosimann (1997), integrating the concept of vertical landscape analysis within a seasonal perspective. Water and energy fluxes are regarded as primary interactive processes between different structural compartments of the Norwegian high mountain ecosystem. The most important processes determining input fluxes into the ecosystems are solar radiation and precipitation. The topography with its strong structural elements controls insolation. Resulting heat radiation controls air temperatures, heat flow controls surface and soil temperatures. In combination with wind speed and direction, the relief also controls snow accumulation during the autumn and winter. During spring snow melt, the water equivalent of the snow pack results in a certain amount of surface water. In combination with the infiltration capacity, it affects the entire soil water system, while snow cover isolates against temperatures extremes. Energy and water balance in turn are correlated with different factors of the vegetation, fauna, and soil compartments. The model integrates the cyclicity of seasonal dynamics within the ecosystems.

The process-oriented approach over different spatial scales follows current principles and paradigms in geography (e.g. Haase *et al*. 1991, Billwitz 1997, Leser 1997, Bastian & Schreiber 1999, Bastian & Steinhardt 2002). The econ concept is used as a basis for extrapolating local point measurements into ecotopes of structural quasi-heterogeneity (Löffler 2002b). In a second step, spatial processes are characterised and structural boundaries mapped in ecotope mosaics. Spatio-temporal characterisations enable a higher level of heterogeneity on the basis of ecochores (Löffler 2002c). Ultimately, the investigations should allow regionalisation of the high mountain landscapes of Norway.

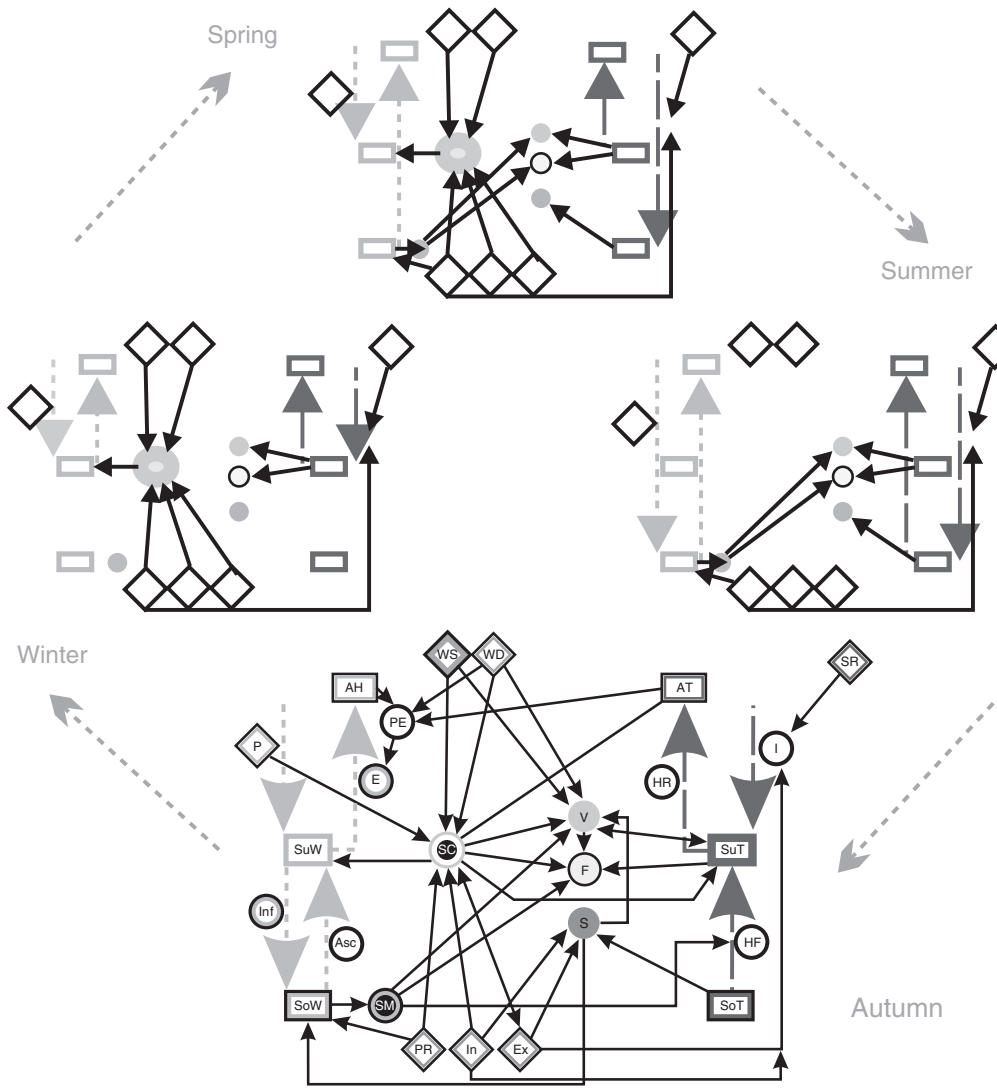


Figure 13.1 Research approach shown as a process-correlation model within a seasonal perspective (Löffler 2002a). The model integrates vertical fluxes of water and energy at a site and uses complex factor constellations determining their intensity and dynamics. Reproduced by permission of Dr Christof Ellger

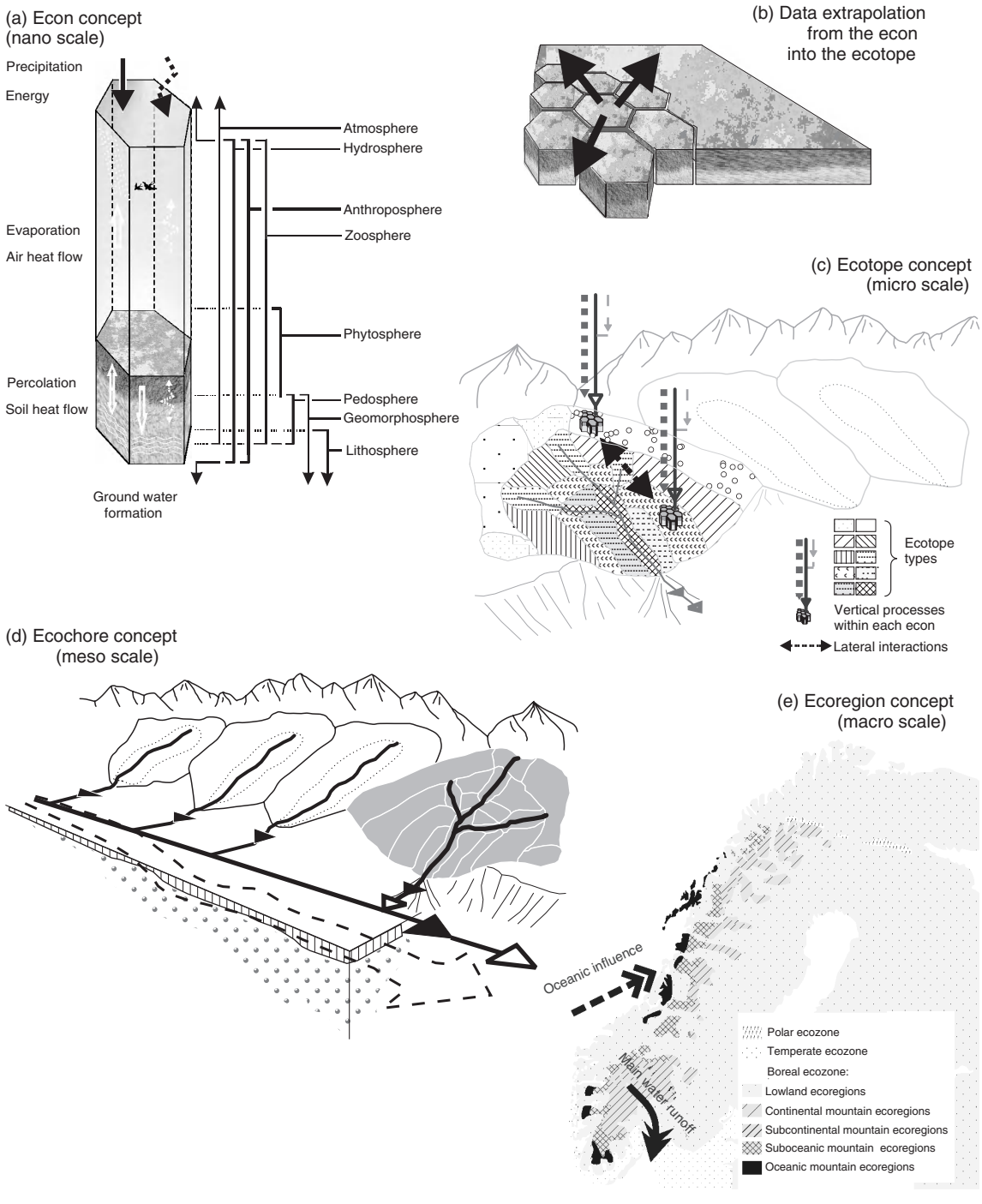

(a) Econ concept
(nano scale)
Precipitation
Energy
Evaporation
Air heat flow
Percolation
Soil heat flow
Ground water formation
Atmosphere
Hydrosphere
Anthroposphere
Zoosphere
Phytosphere
Pedosphere
Geomorphosphere
Lithosphere
(b) Data extrapolation from the econ into the ecotope
(c) Ecotope concept
(micro scale)
Ecotope types
Vertical processes within each econ
Lateral interactions
(d) Ecochore concept
(meso scale)
(e) Ecoregion concept
(macro scale)
Oceanic influence
Main water runoff
Polar ecozone
Temperate ecozone
Boreal ecozone:
Lowland ecoregions
Continental mountain ecoregions
Subcontinental mountain ecoregions
Suboceanic mountain ecoregions
Oceanic mountain ecoregions

Figure 13.2 shows the different spatial scales and concepts applied for this study. Vertical landscape structure is analysed with the nano-scale. Representative sites are established for field investigations on the basis of larger areas comprising of similar econs. Theoretical considerations concerning the econ concept have to be transposed from the vertical dimension into space. For this, the ecotope concept strictly combines landscape reality and derives its methodical advantages from the econ concept, from which vertical structures and processes are adopted. Larger landscape complexes are regarded as ecotope mosaics. This spatial arrangement of ecotopes is analysed as part of larger landscape units within heterogeneous landscape mosaics. On the meso-scale, landscape complexes are aggregated from a mosaic of ecotopes and result in a completely new emerging spatial unit as the ecochore. Ecotopes are delineated into sub-catchments that are analysed according to their chorological arrangement within a valley system. All those ecotope mosaics assembled within several catchments in turn follow the same landscape ecological functioning principle from the micro scale. Processes of larger extent are the object of investigation. Such processes that correspond between the single ecoregions find their origin within the ecochores, transposed through the spatial level of ecochore mosaics and resulting in characteristic attributes of each ecoregion. Figure 13.2 illustrates the different levels of emergence analyses from the catchment to the altitudinal level, and finally, to the oceanic-continental level of a mountain chain. Ecoregions within Scandinavia are demonstrated as a spatial mosaic of different climatic regions and with superimposed spatial processes. Those processes determine the spatial arrangement of the regions as well as the result of interactions between single regional units. Climatic control and hydrological dynamics within those regional ecosystems are apparent at this macro scale of analysis.

13.3 STUDY SITES

The mountain chain of the Norwegian Scandes has a clearly defined oceanic–continental gradient (Figure 13.3). The western mountain regions are influenced by strong oceanic conditions, and more continental climates are found 100 km to the east. In both regions, the alpine zone can be differentiated into a lower alpine belt, dominated by scrub and heather communities, a middle-alpine belt, dominated by grassy vegetation, and a high alpine belt with vegetation patches in a blocky environment (Dahl 1986). Although little is known about the differentiation of the high mountain climate in Norway, the arid and continental mountain region of Norway Vågå/Oppland (ca. 61°53′N; 9°15′E) has an annual precipitation of about 300–400 mm/a. The alpine environment begins at the tree-line at about 1000–1050 m and ends at the highest peak, the Blåhø at 1618 m a. s. l. The transition zone between the lower-alpine and the middle-alpine belts lies around 1350 m a. s. l. The oceanic mountain region Stranda/Møre og Romsdal (62°03′N; 7°15′E) is found in the inner fjords of western Norway and has humid conditions with annual sums of precipitation of about 1500–2000 mm/a. The alpine environment within this western investigation area reaches from the tree-line at about 840–80 m to the highest peak, the Dalsnibba with 1476 m a.s.l. Four representative mountain catchments are chosen for each altitudinal belt (Figure 13.4, Figure 13.5, Table 13.1).

13.4 METHODS

An extensive program of spatial analysis and process measurements was carried out for different landscape ecological parameters within a complex landscape ecological analysis following Mosimann (1984a, 1984b). The methodological concept for high mountain landscape ecological research in Norway was designed for different scales using a hierarchy of models (Figure 13.6).

Figure 13.2 Concept and definition of landscape units at different spatial scales (Löffler 2002a). Figures 13.2(a) modified after Fortescue 1980, (c) and (d) after Leser 1997. Def. *''econ'':* ''*. . . a concrete part of the landscape with vertical structure of landscape components. These components are determining characteristic processes between the compartment spheres of the landscape. Thus, an econ is a small delimitable area that has been chosen out of a larger landscape unit serving as a basis for the analysis of vertical landscape structure and functioning. Similar terms are:* ''tessera'', ''ecotope holon'', ''landschaftsökologischer Standort'' . . .'' (Löffler 2002b). Def. *''ecotope'': ''. . . (gr. ''topos'': locality) a spatial manifestation of different econs of the same structure and functioning spatially connected with each other. Ecotopes represent the landscape sphere and its related systems of landscape complexes (ecosystems) within the topological dimension (spatial micro scale). They are characterised through concrete structural attributes and size mappable. Processes of vertical landscape functioning are analysed within an econ that is defined as the spatial representative of the ecotope . . .*'' (Löffler 2002c). Further theoretical abstraction of chorological dimension (: gr. ''choros'': ''space'') dealing with heterogeneous landscape complexes leads to the aggregation of mosaics of ecotopes to such completely new spatial units that are analysed as *''ecochores''*. Landscape complexes of higher geographical dimension are represented by the theoretical concept of *''ecoregions''* (Löffler 2002c). Reproduced by permission of Dr Christof Ellger

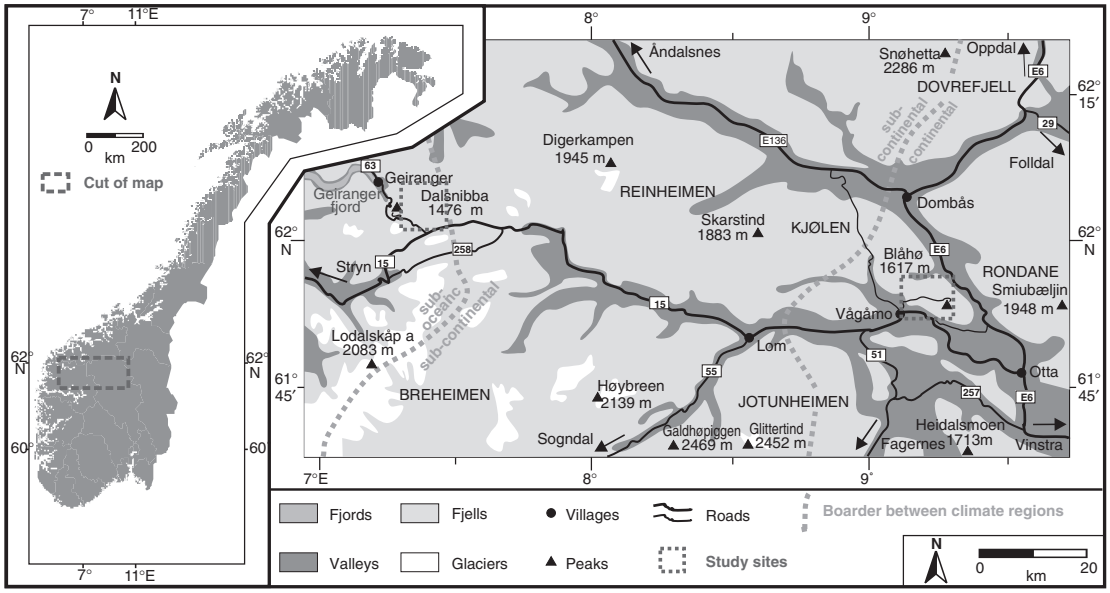


Figure 13.3 Location of the study sites and research design in central Norway (Löffler *et al*. 2001)

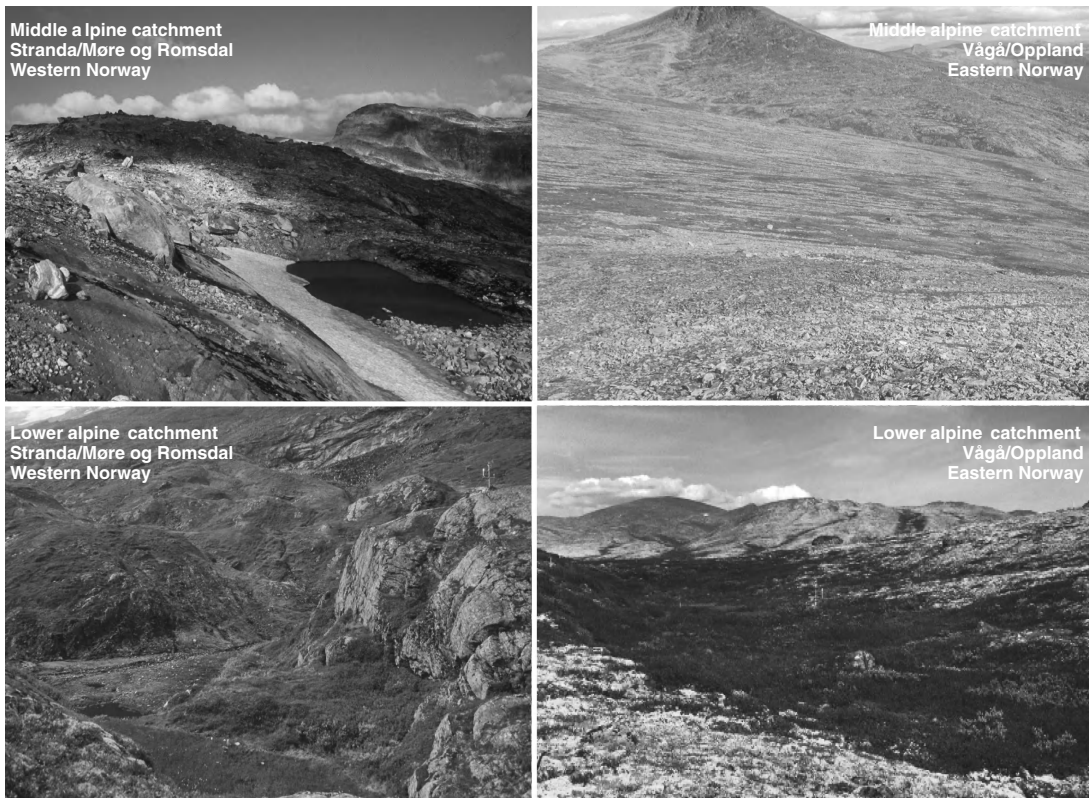


Figure 13.4 Photos of catchments in the lower- and middle-alpine belt of western and eastern Norway (photos from western Norway by R. Pape, from eastern Norway by J. Löffler)

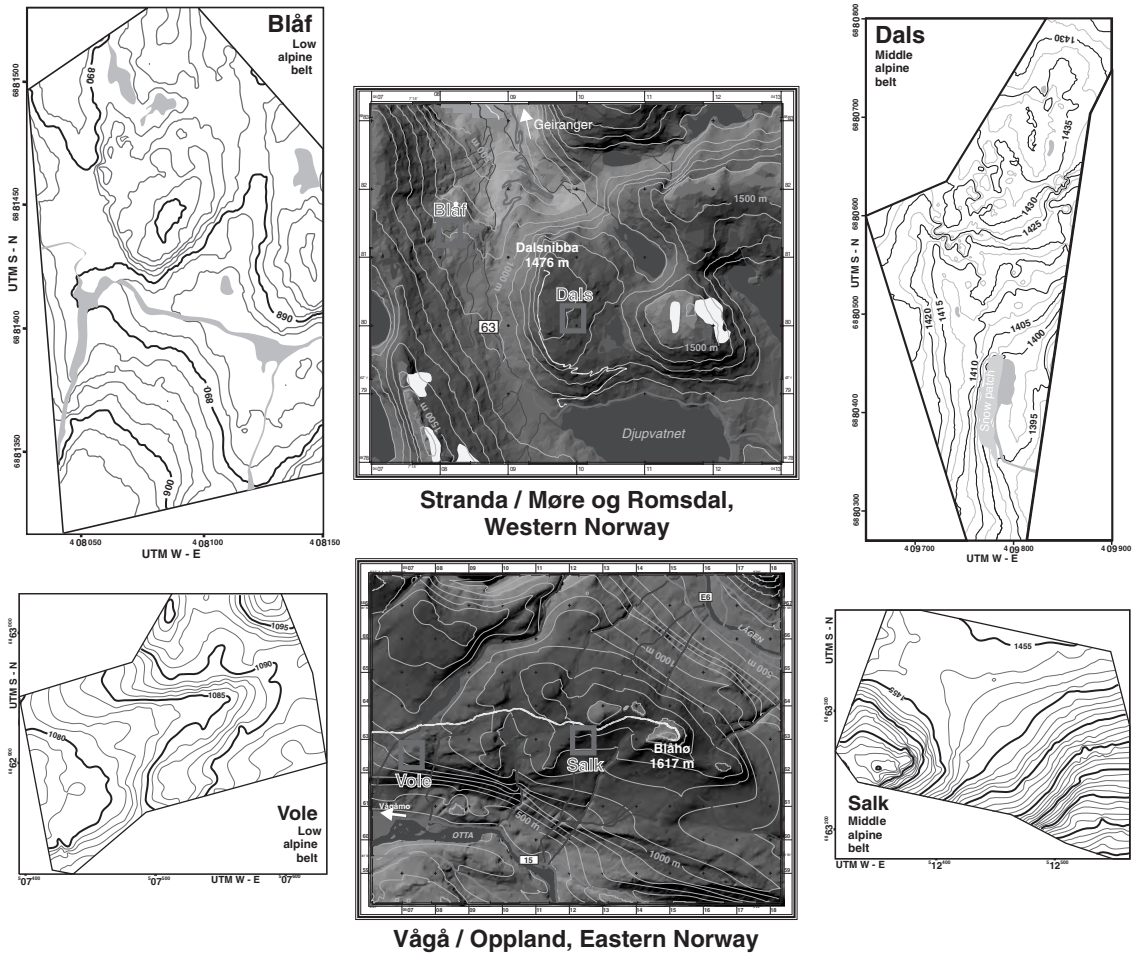


Figure 13.5 Topography of study sites and catchments in the lower and middle-alpine belts (DEM and GIS routines by R. Pape and D. Wundram, field surveys also by O. Rößler and J. Naujok)

Table 13.1 Table of the basin characteristics

	Catchment 1	Catchment 2	Catchment 3	Catchment 4
Name of the basin/area	Vole	Salknappen	Blåfjell	Dalsnibba
Mountain range	Scandes	Scandes	Scandes	Scandes
Elevation range of individual sites	1050–1100 m a.s.l	1400–1470 m a.s.l	850–900 m a.s.l	1350–1430 m a.s.l
Latitude and longitude	UTM 6862900-507400	UTM 6863200-512400	UTM 6881350-408050	UTM 6880300-409700
Area in km^2	0.03	0.038	0.02	0.068
Geology	Mainly phyllit	Mainly phyllit	Mainly gneiss	Mainly gneiss
% glacierized	0	0	0	0
Vegetation type (dominant)	Lower alpine	Middle alpine	Lower alpine	Middle alpine
% forested	0	0	0	0

Source: Reproduced by permission of Dr Andreas Dittmann.

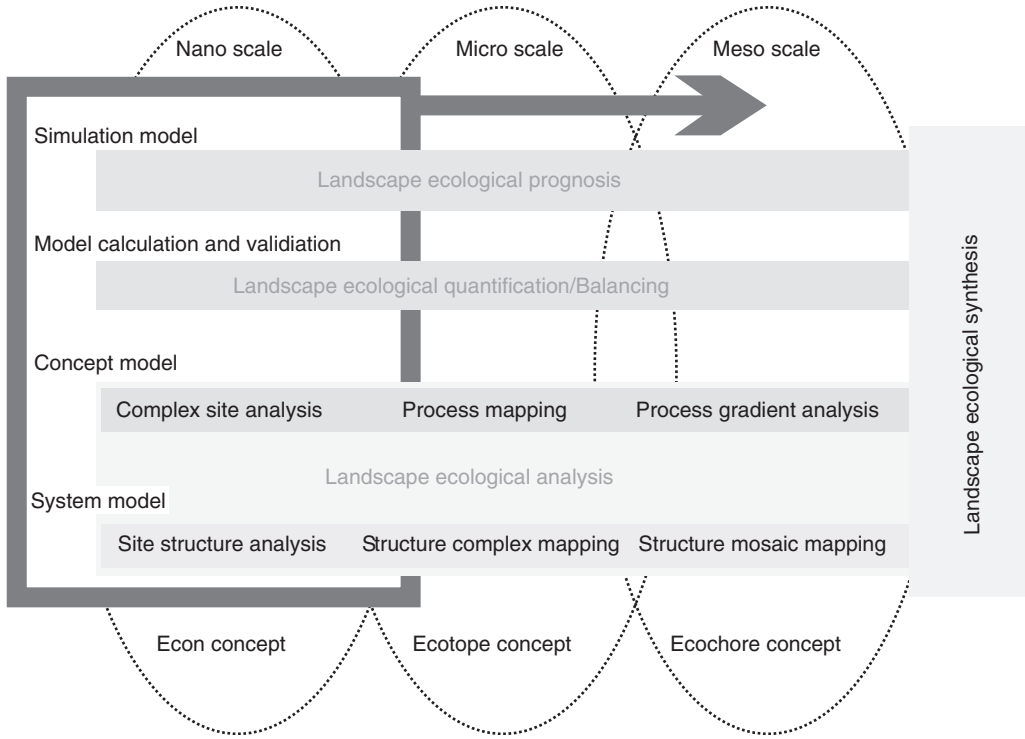
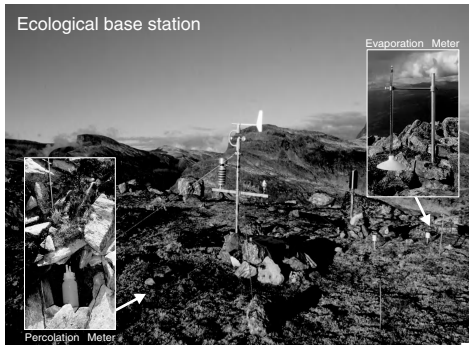


Figure 13.6 Methodological concept of high mountain landscape ecological research on different scales using a hierarchy of models for abstraction (Löffler 2002a). Reproduced by permission of Dr Christof Ellger

Single methodological principles were combined within different geographical dimensions. Landscape structures were derived from the theoretical ecosystem model to determine landscape processes. Furthermore, process measurements formed the basis of quantitative models that were to be validated from secondary results. Finally, simulation of landscape ecological processes should allow forecasting future scenarios.

Each catchment was equipped with one ecological base station, several ecological major and minor stations as well as several water level stations. The spatial organisation of measurements and technical equipment strictly followed a spatio-temporal approach for each station (Figure 13.7). They were arranged with the highest possible spatial resolution, the most quantitative measurements, and most cost-effective instruments available. Seasonal ecosystem dynamics was measured throughout the entire year at hourly intervals from a network of permanent stations. Each ecological base station was installed in ridge position. Each four additional data logger stations were located in southern and northern mid slope position as well as in depressions. Data loggers were used to measure air [+200, +100, +15, +5 cm], surface [−1 cm] and soil [−5, −15, −30 cm] temperatures; precipitation, solar radiation and air humidity [+100 cm]; soil moisture [−5, −15, −30 cm]; as well as wind direction and wind speed [+200 cm]. Additionally, spatial variability of temperature, soil moisture and wind speed were investigated at various locations. Air temperatures [+200, +100, +15, +5 cm], surface and soil temperatures as well as soil moisture [−1, −5, −15 cm] were investigated using hand-held measurements at 36 sites in each catchment during typical climatic situations (high, low and transitional pressure situations, characteristic wind directions, etc.) over the unfrozen seasons between 1991 and 2003. Soil moisture was measured daily. At well-drained sites, free-draining near-surface percolation lysimeters were used for water and matter balancing. Poorly drained sites consisted of a network of water level stations quantifying the spatial dynamics of stagnation processes. During the winter season, snow accumulation was mapped and quantified by means of snow pack surveys as well as snow property measurements for snow water equivalent. Additionally, snow-melt dynamics was observed by means of colour tracers injected at certain sites and traced by means of



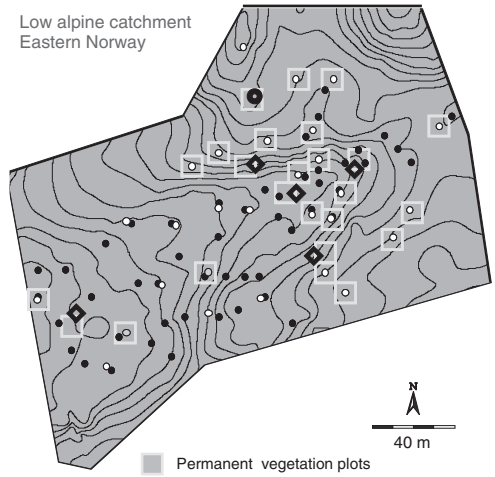
● Ecological base station

- Air Pressure
- Wind direction (2 m)
- Wind speed (2 m,1 m,15 cm)
- Global radiation (1 m)
- Precipitation (1 m,15 cm)
- Air humidity (1 m,15 cm)
- Air temperature (2 m,1 m, 15 cm, 5 cm)
- Evaporation (15 cm)
- Soil temperature (–1 cm, –5 cm, –15 cm, –30 cm)
- Percolation (–5 cm)
- Biotic activity (–5 cm, –15 cm)
- Soil moisture (–5 cm, –15 cm, –30 cm)

◆ Major ecological station

- Wind speed (2 m,1 m, 15 cm)
- Air humidity (15 cm)
- Air temperature (1 m,15 cm, 5 cm)
- Evaporation (15 cm)
- Soil temperature (–1 cm, –5 cm, –15 cm, –30 cm)
- Percolation (–5 cm)
- Biotic activity (–5 cm, –15 cm)
- Soil moisture (–5 cm, –15 cm, –30 cm)





○ Minor ecological station

- Wind speed (2 m,1 m,15 cm)
- Air humidity (15 cm)
- Air temperature (1 m,15 cm,5 cm)
- Soil temperature (–1 cm, –5 cm, –15 cm, –30 cm)
- Soil moisture (–5 cm, –15 cm, –30 cm)

● Water level station





Figure 13.7 Spatial organization of measurements and use of technical equipment at different types of stations including sensor positions (Photos: R. Pape) (after: Löffler 2002a, Wundram 2003). Reproduced by permission of Dr Andreas Dittmann

snow profiles. Spatial data extrapolation was based on a digital elevation model derived from topographic surveys of approx. 1000 points for each catchment.

Spatio-temporal data were fed into a digital database and processed in a GIS. Spatial data layers such as mapped vegetation types, relief, snow cover, and so on, were used to define structural ecotope types. Functional attributes were extrapolated into the ecotope types and spatially correlated with structural information layers (Löffler & Wundram 2001, 2003). Statistically deduced ecological patterns were quantified and generalised for all catchments with respect to scale. Qualitative and quantitative interrelations between the ecosystem compartments were synthesised over high levels of complexity.

13.5 RESULTS OF CLIMATOLOGIC AND HYDROLOGIC COUPLING

13.5.1 Local climatologic and hydrologic dynamics

The meteorological oceanic–continental gradient is sketched by general data (Table 13.2). Annual mean temperatures in the low-alpine west are higher than those of the east, middle-alpine values being similar. Annual maxima are similar in western and eastern low-alpine belts, higher in the eastern middle-alpine belt. Annual minima are lowest in western and eastern low alpine, differences being larger in continental Norway. Summer and autumn minima are similar in the same belts of both regions; the latter slightly lower in eastern middle alpine. Spring maximums are much higher in both altitudinal belts of the west; spring minima are lower in the east, especially in the low-alpine belt. It is shown that temperature dynamics is not strictly explained by principle rules of regional meteorological changes.

Vertical water fluxes are illustrated by four examples from the lower and middle-alpine altitudinal belt in the western and eastern Norwegian high mountain region. Figure 13.8 shows the temporal dynamics of vertical water fluxes.

During the summer months, the eastern Norwegian mountains are characterised by relatively low precipitation. Despite ridge positions are generally the driest localities, a lack of soil moisture during the driest summer period was not measured. Influences of precipitation on soil moisture variability were quite low, since percolation processes were reduced except for intense rainfalls. Moreover, the coarse silty sand with a low field capacity showed volumetric moisture content of 20–30% throughout this dry season. Thus, in the lower alpine belt, upward movement of subsurface water under dense lichen cover even though was extremely retarded, while evaporation rates were high under dry and windy conditions. Evaporation rates were generally high, and sometimes higher than precipitation during rainfall events. Middle-alpine conditions are to be characterised by slightly higher precipitation, lower temperatures and sparse vegetation cover. This constellation led to a more pronounced soil moisture variability, but lower evaporation rates.

Soil moisture was not a limiting factor in the high mountain landscapes during dry summer conditions; for example, competition between plant species resulting in the ecological distribution of phytocoenoses is more dependent on oversupplies of water. Water fluxes on lower alpine ridges were reduced because of the homogenous surface conditions during warm and dry but short summer periods. A dense vegetation layer is important since it isolates high radiation inputs and soil heat fluxes. Summer soil temperatures generally decreased strongly away from the surface at all well-drained sites. Therefore, soil moisture content under vegetation cover was not reduced during dry periods.

Table 13.2 Temperature of western and eastern altitudinal belts (Löffler 2003). Data from western valley and low-alpine stations interpolated by adiabatic coefficient (0.6 K/100 m) for comparison of same altitude of eastern stations; calculated values used given in brackets. Air temperatures (AirT) from western and eastern valley stations (WestValley, EastValley) and from low and middle-alpine stations (WestLA, WestMA, EastLA, WestMA)

	WestValley AirT	WestLA AirT	WestMA AirT	EastValley AirT	EastLA AirT	EastMA AirT
Annual mean	(3.0) 6.8	(0.7) 1.9	−1.4	1.7	−1.2	−1.9
Annual max	(15.7) 19.5	(16.0) 17.2	12.9	18.2	16.7	15.5
Annual min	(−17.3) −13.5	(−24.6) −23.4	−22.9	−26.8	−29.2	−19.9
Spring max	(10.2) 14.0	(9.7) 10.9	8.5	10.8	7.6	4.9
Spring min	(−3.4) 0.4	(−3.6) −2.4	−9.7	−5.0	−11.1	−11.0
Summer min	(5.5) 9.3	(2.4) 3.6	−0.1	4.7	2.3	0.1
Autumn min	(−6.5) −2.7	(−9.1) −7.9	−8.2	−6.9	−10.0	−11.6

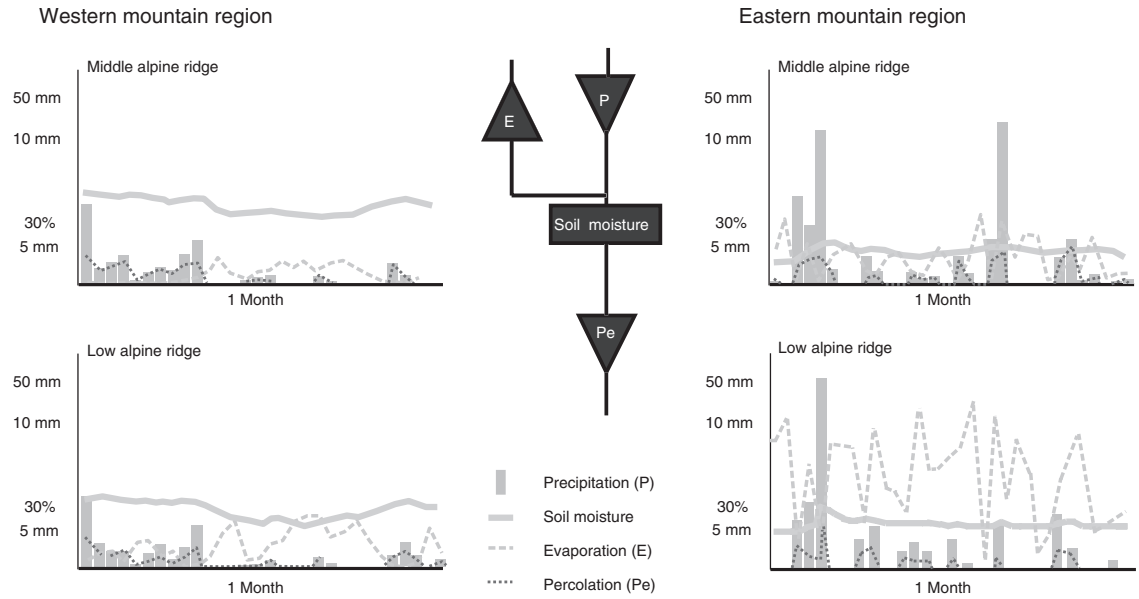


Figure 13.8 Vertical water fluxes in ridge positions of the lower- and middle- alpine altitudinal belt in western and eastern Norway during one representative dry summer month; here: August 2001 (after: Löffler 2002a). Reproduced by permission of Dr Christof Ellger

Water balance on middle-alpine ridges was dominated by higher water inputs and reduced evaporation rates because of lower temperatures. Direct solar radiation did not intensify soil heat fluxes and soil moisture remained high, although soil evaporation was dominant in sparse and patchy vegetation. On the one hand, high evaporation rates were a result from high air temperatures, low relative humidity and strong wind speeds, a common phenomenon during high-pressure weather situations. On the other hand, high evaporation rates occurred during rainy periods as a result of dry air mass exchange in areas with local convective precipitation. This phenomenon was common in the lower altitude of the alpine belts. Cloud formation and increased precipitation mostly occurred at higher altitudes during such periods. Similar results have been found in high mountain ecosystems of the Alps (de Jong & Ergenzinger 2002).

The western mountain region has higher precipitation totals than those found in continental Norway, and thus the ecosystem dynamics is supposed to be much different (Moen 1999, Löffler 2003). Calling from the measurements lower- and middle-alpine ridge positions were characterised by high soil moisture throughout the driest summer periods. Compared with the eastern mountain ridges, soil moisture was roughly 10% higher in the lower alpine ridge and 20% higher in the middle-alpine ridge positions. Constant rainfall and short periods without precipitation caused highly saturated soils under otherwise unaltered conditions. Percolation was reduced to precipitation events, and since intense rainfall rarely occurred in oceanic summer conditions, percolation amounts were relatively low. High air humidity and cloud cover reduced evaporation substantially; especially under colder middle-alpine conditions. During warm and dry periods, evaporation in the lower alpine regions increased, but absolute rates were permanently lower than those found under continental conditions. The ridge positions are covered by dense lichen heath in the lower and middle-alpine belt, despite high soil moisture and high air humidity. Vegetation distribution in the western high mountains therefore cannot be explained by hydrologic patterns alone. Instead, snow cover conditions determine the spatial arrangement of plant associations. Lichen heath on alpine ridge positions thus corresponds with a thin snow cover during winter. The seasonal dynamics of characteristic air, surface and soil temperatures at different sites in the lower- and middle-alpine belt is very important for ecosystem functioning in the continental to oceanic mountain regions. General principles of vertical temperature dynamics during different seasons are characterised by snow cover influence during winter, exposure to solar radiation in summer and topography relative to soil water saturation during the year (Figure 13.9, Figure 13.10 and Figure 13.11).

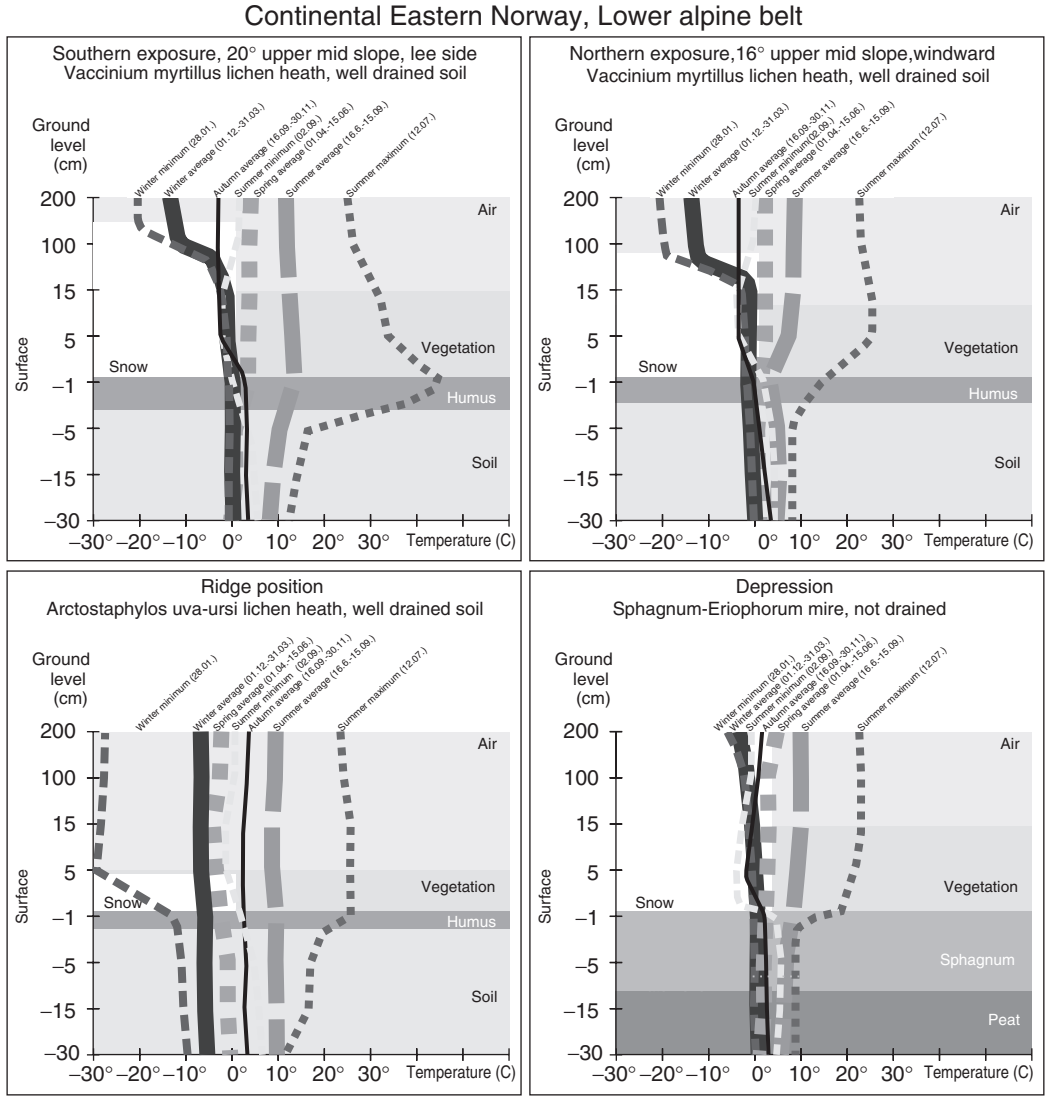


Figure 13.9 Vertical temperature profiles at different sites in the lower alpine belt of the eastern Norwegian high mountains 1999. Data are based on long-term investigations with meteorological stations, temperature data loggers and additional manual measurements; curvatures of different profiles are schematic and based on generalisation interpolation in between sensor positions, respectively (Löffler 2002a). Reproduced by permission of Dr Christof Ellger

Continental and oceanic lower alpine slopes

Continental and oceanic lower alpine slope sites showed gradual differences with regard to lee- and windward snow pack under similar winter temperature conditions. Average winter temperature profiles remained similar around 0°C. The snow cover isolates against frost and hindered deep soil freezing processes. Freeze–thaw action during spring was possible on northern and southern exposed slopes. Intense solar radiation heated up the ground surface to temperatures comparable to those of the summer but did not effect the deeper layers. On northern exposures, maximum summer air temperatures reached around 20°C under oceanic and 25°C under continental conditions. Therefore, soil temperatures during spring snow melt were identical for both aspects under both conditions. The minimum summer temperature profile showed an inversion. In

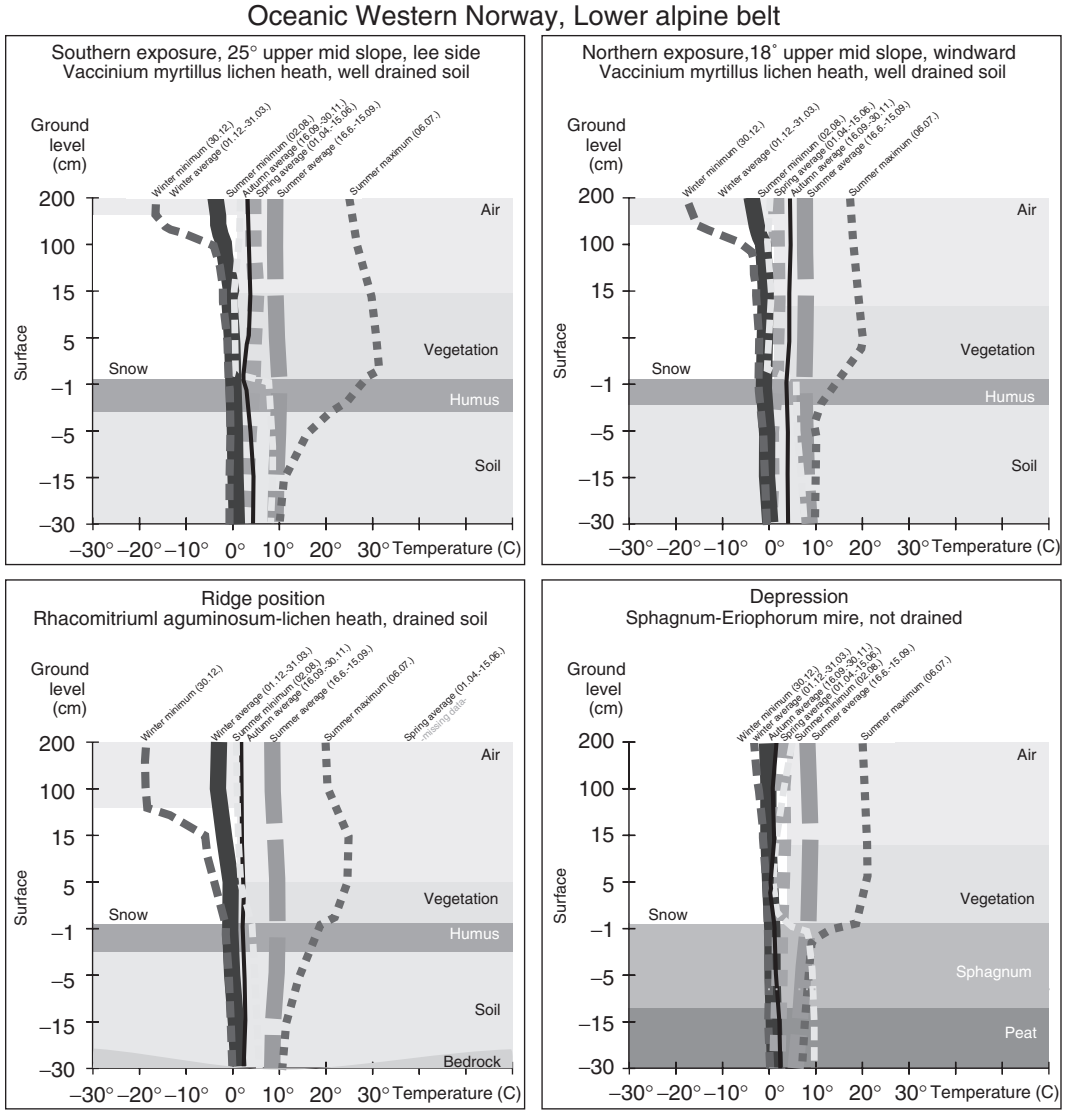


Figure 13.10 Vertical temperature profiles at different sites in the lower alpine belt of the western Norwegian high mountains. Data are based on long-term investigations with meteorological stations, temperature data loggers and additional manual measurements; curvatures of different profiles are schematic and based on generalisation interpolation in between sensor positions, respectively. Data for specific events are given as an example of the year 2001

contrast to the oceanic conditions, air temperatures near the ground dropped sharply below 0°C because of night frosts. During summers, the air near the ground, the surface, and the upper soil layers reached highest temperatures on south-facing slopes, but soil temperatures in deeper ground remained identical in both exposures. Highest temperatures were found on continental southerly exposed surfaces, with maximum values above 45°C, while the oceanic southerly slopes reached around 30°C.

Continental and oceanic lower alpine ridges and depressions

Temperature profiles along ridge positions differ from those of well-drained slope sites, even under extreme

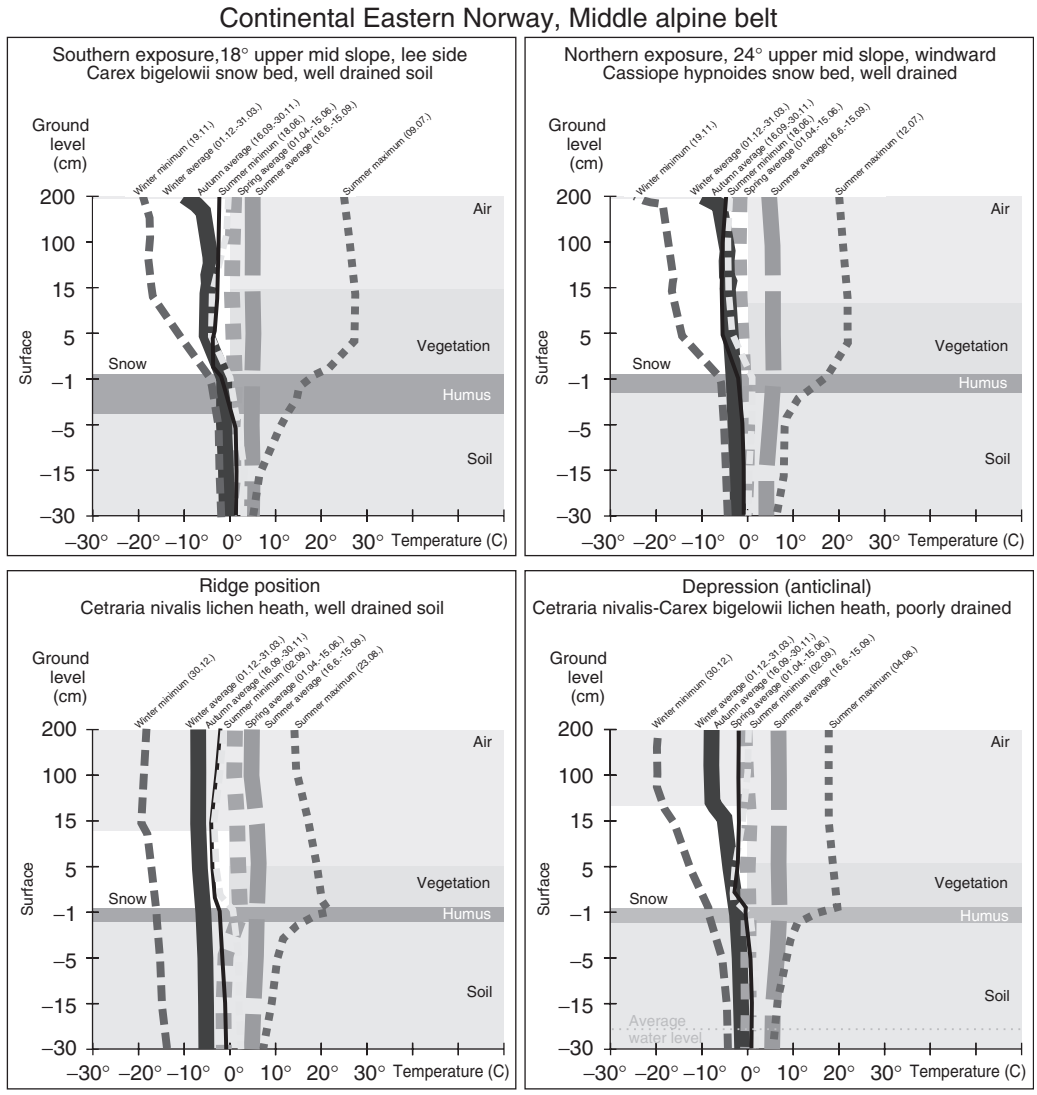


Figure 13.11 Vertical temperature profiles at different sites in the middle-alpine belt of the eastern Norwegian high mountains. Data are based on long-term investigations with meteorological stations, temperature data loggers and additional manual measurements; curvatures of different profiles are schematic and based on generalisation interpolation in between sensor positions, respectively. Data for specific events are given as an example of the year 1999 (Löffler 2002a). Reproduced by permission of Dr Christof Ellger

winter conditions. With deeper snow cover and higher soil moisture, oceanic ridge sites showed little variability of near-ground soil and air temperatures. While extreme annual amplitudes of more than 65 K were experienced under continental conditions, those at oceanic ridge sites reached only around 40 K. Depressions differ from all sites as they remained wet throughout the year and retained a thick snow cover. The examples chosen characterise wet mires with similar vegetation cover in the continental and oceanic mountains and approximately 2 m snow pack during winter. In addition, saturated *Sphagnum* moss and peat material also isolated against summer overheating, causing gentle soil temperature gradients. Air temperature profiles reflected summer warming effects away from the ground. Overlying air masses sheltered by the pronounced relief caused the

stabilisation of warm air layers above cool and wet mire surfaces. Summer minima were lowest during high-pressure temperature inversions. While continental summer minima dropped dramatically below 0°C, oceanic depressions seldom reached the freezing point.

Continental middle-alpine slopes

Middle-alpine slopes were gradually differentiated according to snow melt. North- and south-facing slopes retained equal snow packs and had similar winter temperature profiles. South-facing upper mid-slopes melted out earlier and were thus exposed sooner to summer minimum temperatures while the north-facing slopes remained isolated during this period. Freeze–thaw action during spring occurred on north- and south-facing slopes but did not penetrate far into the ground. Intense solar radiation caused maximum air temperatures in southern as well as northern exposures but did not significantly affect surface and soil temperatures. The uppermost soil temperatures during summer periods remained below 18°C but dropped to 5°C at greater depths. Average summer temperatures are constant at around 5°C.

Continental middle-alpine ridges and depressions

Ridge positions were characterised by highest annual temperature amplitudes near the ground surface. Winter conditions were extreme but negative air temperature was limited near the ground to an average snow layer of 15–20 cm. Summer temperatures were equal to those of the mid-slopes. Depressions in the middle-alpine belt were covered by wet, poorly drained mineral soils. In anticlinal positions, grassy lichen-dominated vegetation types occur where the snow cover was thin during winter. The example had minimum winter temperatures that affected the deeper ground. The deeper mineral soil layer had its average water level at 20-cm depth and was characterised by maximum soil temperatures at 5°C. Summer minima were found in the depressions during temperature inversions, but cold air flows did not last throughout the night as relief gradients allowed air flow down to the lower alpine belt. Nocturnal minima occurred earlier than in the lower alpine depressions and did not show such extreme near-ground air temperatures fluctuations.

13.6 SPATIAL PATTERNS OF CLIMATOLOGIC AND HYDROLOGIC DYNAMICS

Important factors determining hydrologic regimes in different ecotopes include topography, aspect and the winter snow pack. Soil moisture conditions correspond with vegetation cover, humus and top soil layers. Two spatial data sets can be used to illustrate the seasonal dynamics within the water balance: snow cover and soil moisture.

Figure 13.12 gives an impression of snow cover conditions in continental eastern Norway. Lower- and-middle alpine conditions are demonstrated for two catchments. As precipitation increases with height and the snow pack is thicker during winter, it covers the entire catchment in the middle-alpine belt. Here, late snow cover was more persistent in early summer than in the lower alpine belt. The lower alpine catchment in turn was characterised by thick snow accumulations in depressions, but snow-free ridge positions throughout the winter. Lower alpine snow lasted longest in foot-slope positions, but melted out earlier than the middle-alpine snow beds. The snow-free period in summer was short: 13–15 weeks in the lower alpine belt and 11–12 weeks in the middle alpine belt, respectively. Figure 13.13 illustrates the spatio-temporal distribution of snow cover in a lower alpine catchment of the continental mountains. Because of prevailing wind from the north to north-west and high wind speeds during the winter season, the east–west-oriented catchments received lee-side snow accumulation on the southern exposed slopes, where the snow cover melted out in late June. North-facing slopes were characterised by windward snow packs that melted out about three weeks earlier than the latest snow cover in the lower alpine belt. Ridge positions remained more or less snow-free during winter, so that upper slope positions had little snow cover and early snow melt. Depending on surrounding topography, depressions either formed the deepest snow packs or were snow-free because of wind exposure.

Different structural compartments of ecosystems determine the water balance. Besides relief, the mineral fraction of the soil influences the type of water fluxes and soil moisture variability (Figure 13.14). Highly complex vegetation patterns result from the distribution of snow and liquid water. Interactions between landscape structures and hydrologic dynamics were analysed for the lower alpine catchment in the eastern mountain region. Figure 13.14 shows the spatial distribution of substrates. A large proportion of the total catchment area is covered by a dominant glacial till that is up to 100 cm in depth and consists of silty sand and a high coarse fraction. In contrast, ridge positions have a substrate formed by *in situ* weathering of the phyllitic bedrock and consisting of a coarse-rich sandy silt of up to 30 cm thickness. Locally, a few periglacial block fields occur. The depressions are covered by peat, with a maximum thickness of 160 cm.

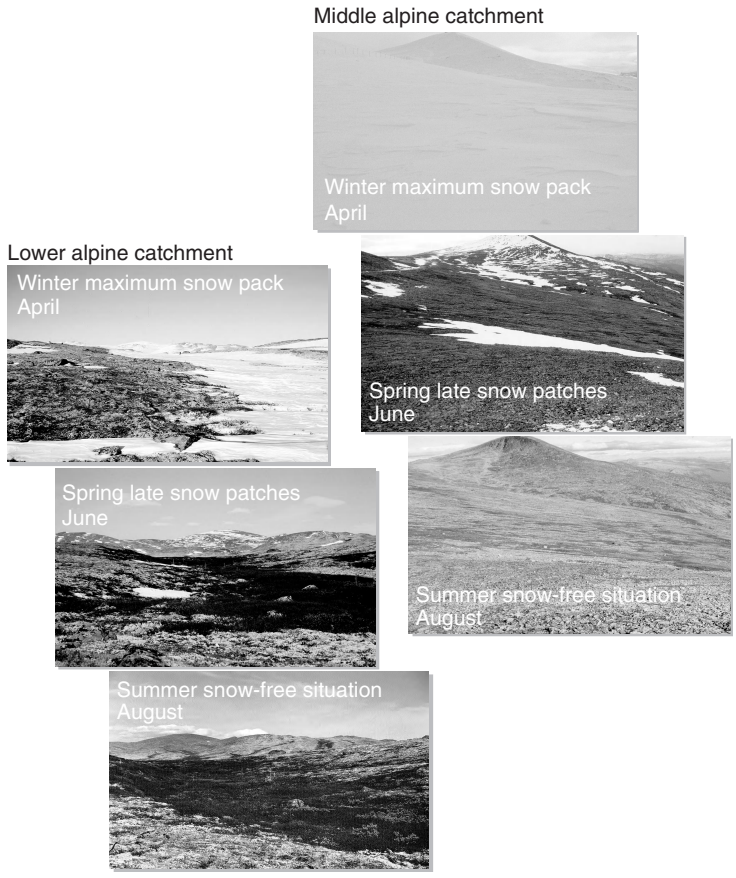


Figure 13.12 Catchment areas of the lower- and middle-alpine belt and their seasonal dynamics of snow cover and vegetation phenology in continental eastern Norway (Photos by J. Löffler) (Löffler 2002a). Reproduced by permission of Dr Christof Ellger

The mineral substrates are permeable, but organic layers often tend to water logging.

Figure 13.15 shows a map of the distribution of vegetation types in the lower alpine catchment of continental Norway. Ridge positions are covered by lichen heaths. Three different types can be differentiated along a snow gradient of 0 and 30 cm thickness. *Alectoria ochroleuca* indicates extreme conditions without snow during winter. *Cetraria nivalis* requires only a thin snow cover of 5–10 cm, while *Cladina stellaris* appears where snow extends from 10–30 cm. Those sites that have a thick snow pack that melts in early summer but provides sheltered against late frosts are characterised by shrubs like *Betula nana, Vaccinium myrtillus*, or *Calluna vulgaris*. Late snow beds with maximum depths of 400 cm in southern foot-slope locations are characterised by *Nardus stricta*, which can survive extreme conditions with a wet, warm and short growing season. Depressions show a mosaic of different mire vegetation types along a moisture gradient. *Sphagnum – Carex* types are found in the wet mires where surface water is to be found throughout the year, while *Sphagnum – Eriophorum* types with a water table about 0 to 5 cm below the surface. The *Sphagnum – Rubus chamaemorus* type is characterised by a water level varying between 0 and 15 cm below the surface. All in all, the very fine-scale spatial differentiation of vegetation is the result of a combination of topography, snow cover and ground-water level.

Figure 13.16 illustrates the spatio-temporal variability of soil moisture conditions, directly corresponding with processes such as frost penetration, snow cover and snow melt for the same region. The distribution of different soil moisture profiles showed fine-scale differentiation according to the complex topography. While ridges and convex slopes endured driest conditions throughout the

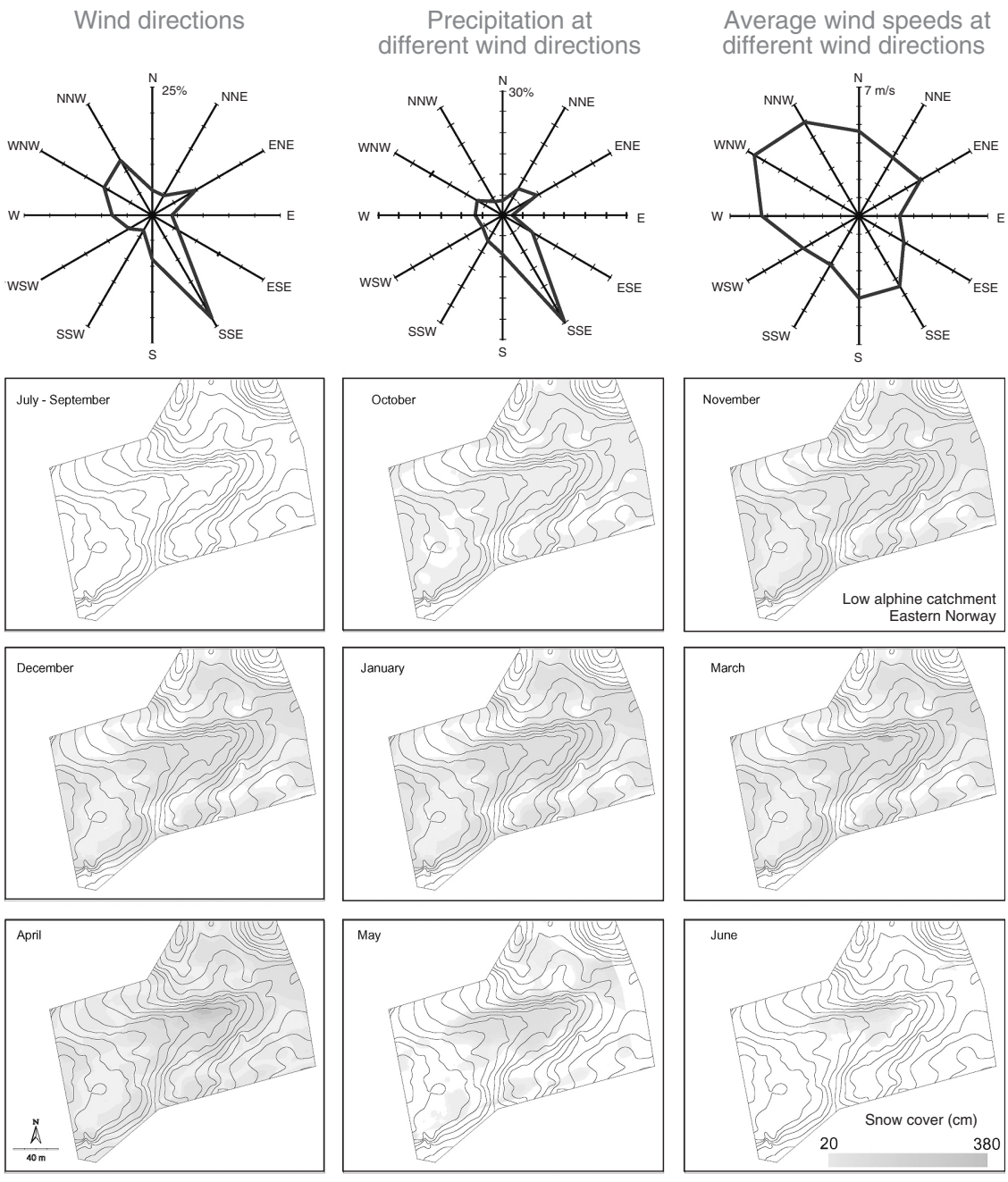


Figure 13.13 Spatial dynamics of snow cover conditions. Formation of snow cover is influenced by prevailing winds, but most important are highest wind speeds during winter. Topographical conditions and snow cover were examined by levelling ~1000 during different seasons. Spatial data modelling was based on measurements as well as a digital elevation model and were extrapolated according to their dominant character for the period of 1991–2003. (Snow surveys and maps by D. Wundram and J. Löffler) (Löffler 2003). Reproduced by permission of Dr Andreas Dittmann

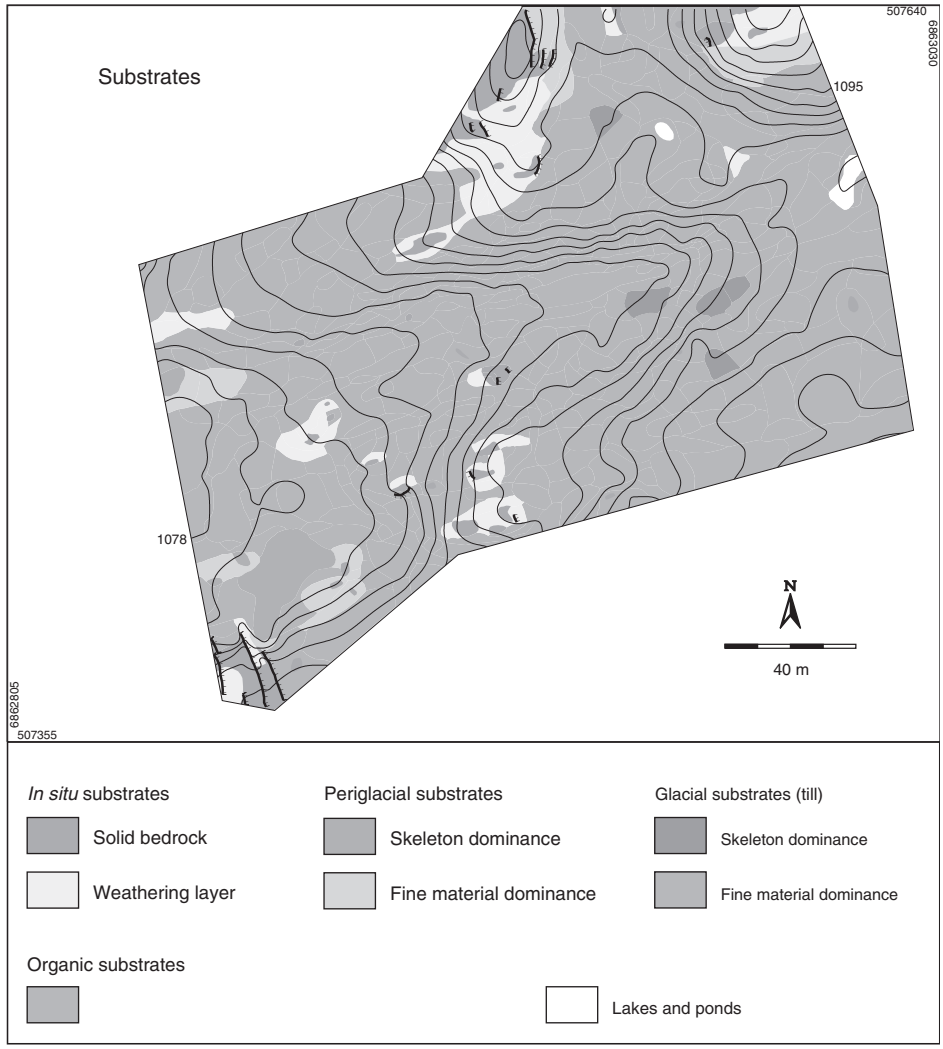


Figure 13.14 Spatial differentiation of types of ground substrate in the lower alpine catchment (Löffler 1998)

year, soil moisture was constantly high. The interactive hydrologic process was characteristic for the lower alpine belt. Concave profiles tended to be wet and functioned as temporary surface runoff and stagnating ecotopes. Wet conditions were dominant during and after snow melt. However, tracer experiments showed that most of the melt water ran directly downhill over frozen surface, and therefore passed through the entire mountain catchment as surface runoff before penetrating the ground. Thus, the snow pack did not supply a higher volume of water to the ecotopes. Late melting of frozen ground correlated with the availability of liquid water in the soils. This specific process constellation was typical for the water balance of the continental high mountain regions of central Norway. Erratic, high rainfall events characteristically resulted from convective precipitation patterns, but their effect lasted for only hours or days and did not explain permanently high water saturation in the depressions of the catchments.

13.6.1 Spatio-temporal landscape ecological synthesis

By synthesising the principles of landscape functioning according to ecosystem reactions, the results from quantifying procedures are used to explain ecosystem

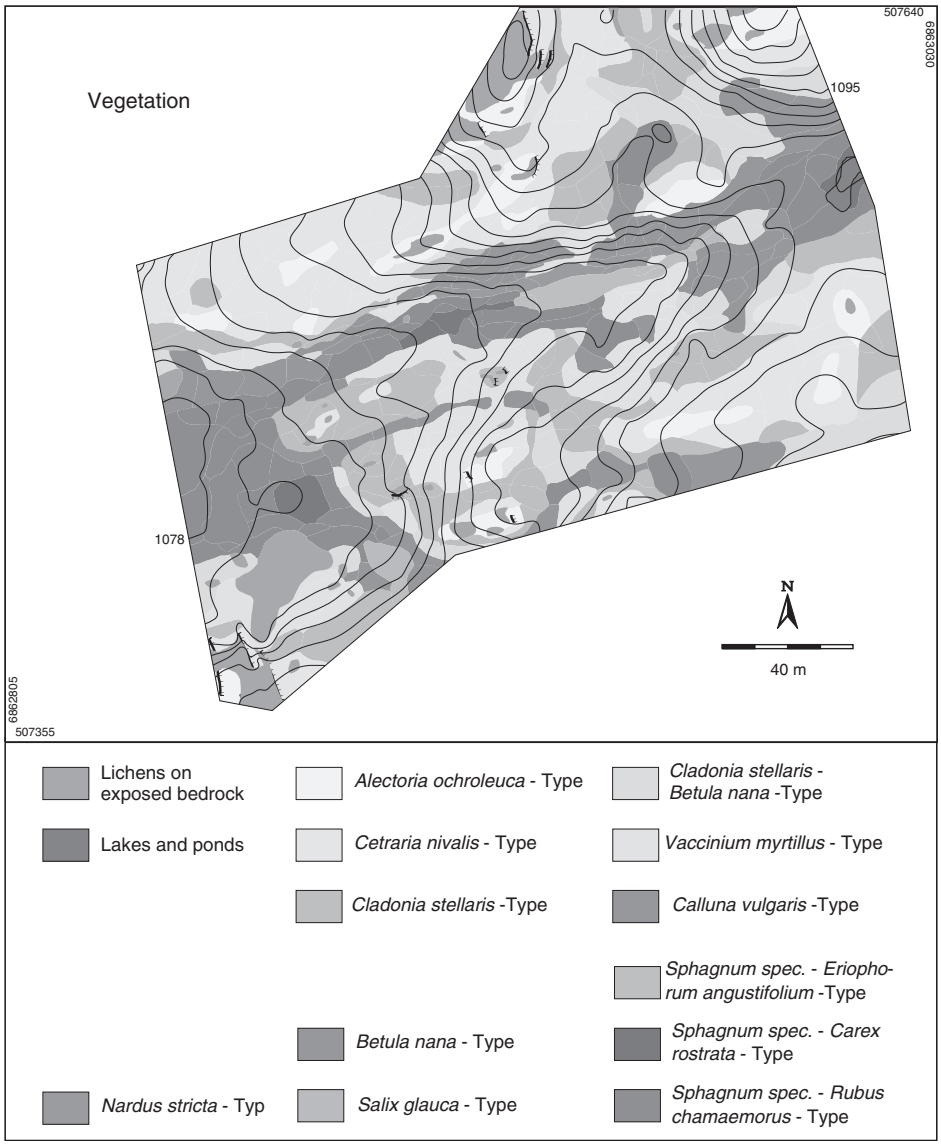


Figure 13.15 (Plate 9) Spatial differentiation of vegetation types in the lower alpine catchment (Löffler 1998)

interrelations. For this purpose, a hierarchy of a process-oriented characterisation of ecotopes is defined according to specific landscape functioning attributes. Daily and seasonal air, surface, and soil temperature variations are used to aggregate dynamics of different functional features for each type of structurally delimited ecotope. Differences along spatial and temporal temperature gradients are illustrated in two maps from small catchments in the lower and middle-alpine belt (Figure 13.17 and Figure 13.18). Within this frame, temperature data are classified into seven temperature intervals for spatial ecological interpretation. A legend for each ecotope describes temperature intervals and ecological significance for 13 different landscape ecological parameters. Moreover, temperature attributes show the duration of daily means, duration of frosts, the annual amplitude and the duration of daily maximum (Figure 13.19).

This scaling procedure can directly be adopted to the raw data set to produce the thermoisopleth diagrams.

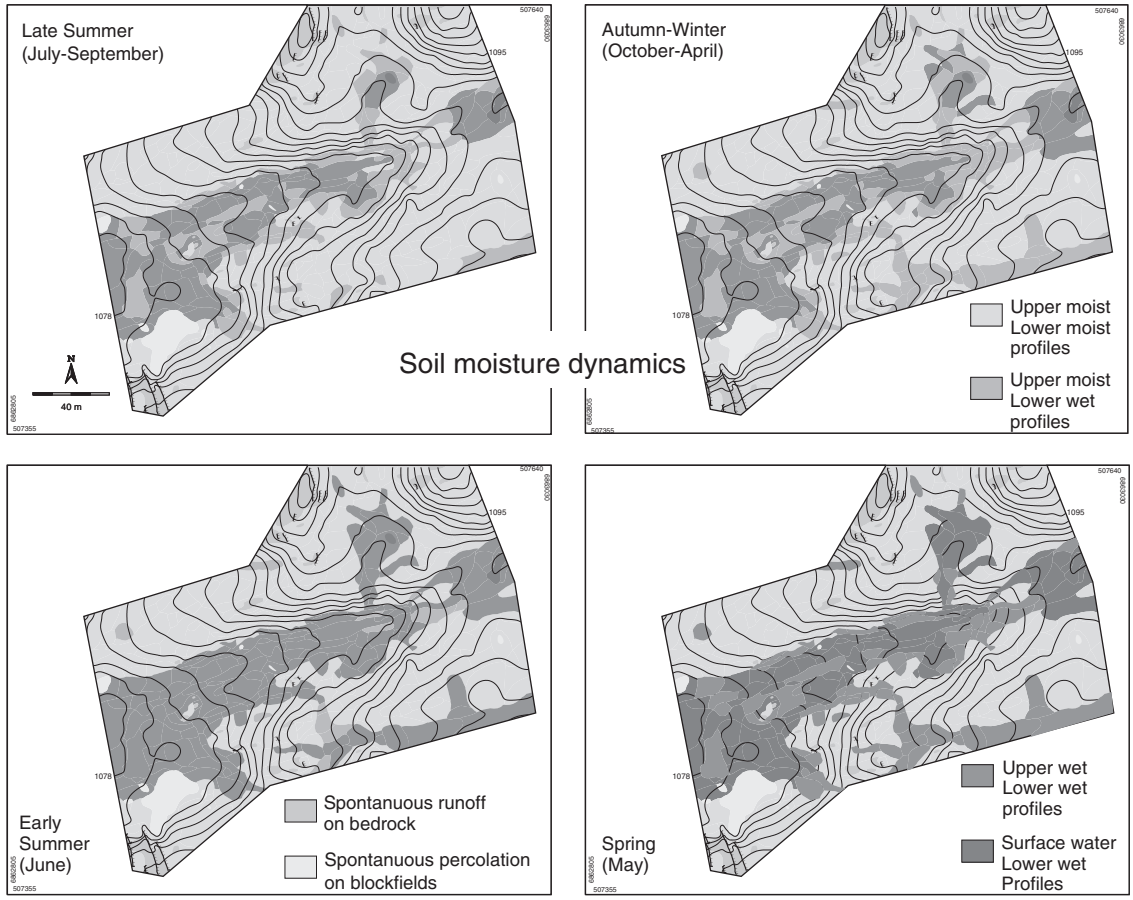


Figure 13.16 Spatial dynamics of soil moisture (Löffler 2005). Maps are based on spatial surface water measurements by water level stations and soil moisture mapped from hand-held TDR-measurements during different seasons (at ∼400 locations). Data are based on long-term field experiments and are generalised according to dominant characteristics for the region since 1991. The classification of soil moisture follows Löffler (1998). Short-term temporal changes in soil moisture conditions are examined by continuous TDR-logger measurements at single sites. Frozen soil conditions are not analysed during winter except on sites with TDR-loggers. The last measurement taken before the winter is representative until springtime. (Measurements modelling and maps by D. Wundram and J. Löffler). Reproduced by permission of Dr Andreas Dittmann

According to the analysis of dominant temperature attributes, the data were also classified for each temperature layer (Table 13.3).

Figure 13.17 and Figure 13.18 show resulting landscape ecological units of temperature dynamics for two examples from the lower- and middle-alpine belt. The primary attribute for the different ecotopes is their topographical position within the catchment. Therefore, a schematic profile along a characteristic relief gradient is illustrated by means of thermoisopleth triples. In conclusion, the figures describe spatio-temporal complexity of high mountain landscape functioning on the ecotope level. They show the pronounced daily air and surface temperature contrasts during the summer period in all ecotope types. Higher soil moisture content leads to less differentiation, while aspect is the most important factor during diurnal variations. High daily summer soil temperature variations are distinct on ridges and southerly exposed slopes but less marked in northern exposure and depressions. Annual variations of the spatial air temperature distribution depend on snow cover thickness and duration of snow cover. Ecotopes with thick snow cover differ from those without snow pack according to the duration of transitional seasons. Spring and autumn air temperature dynamics combined with frost activity and freeze-thaw-processes

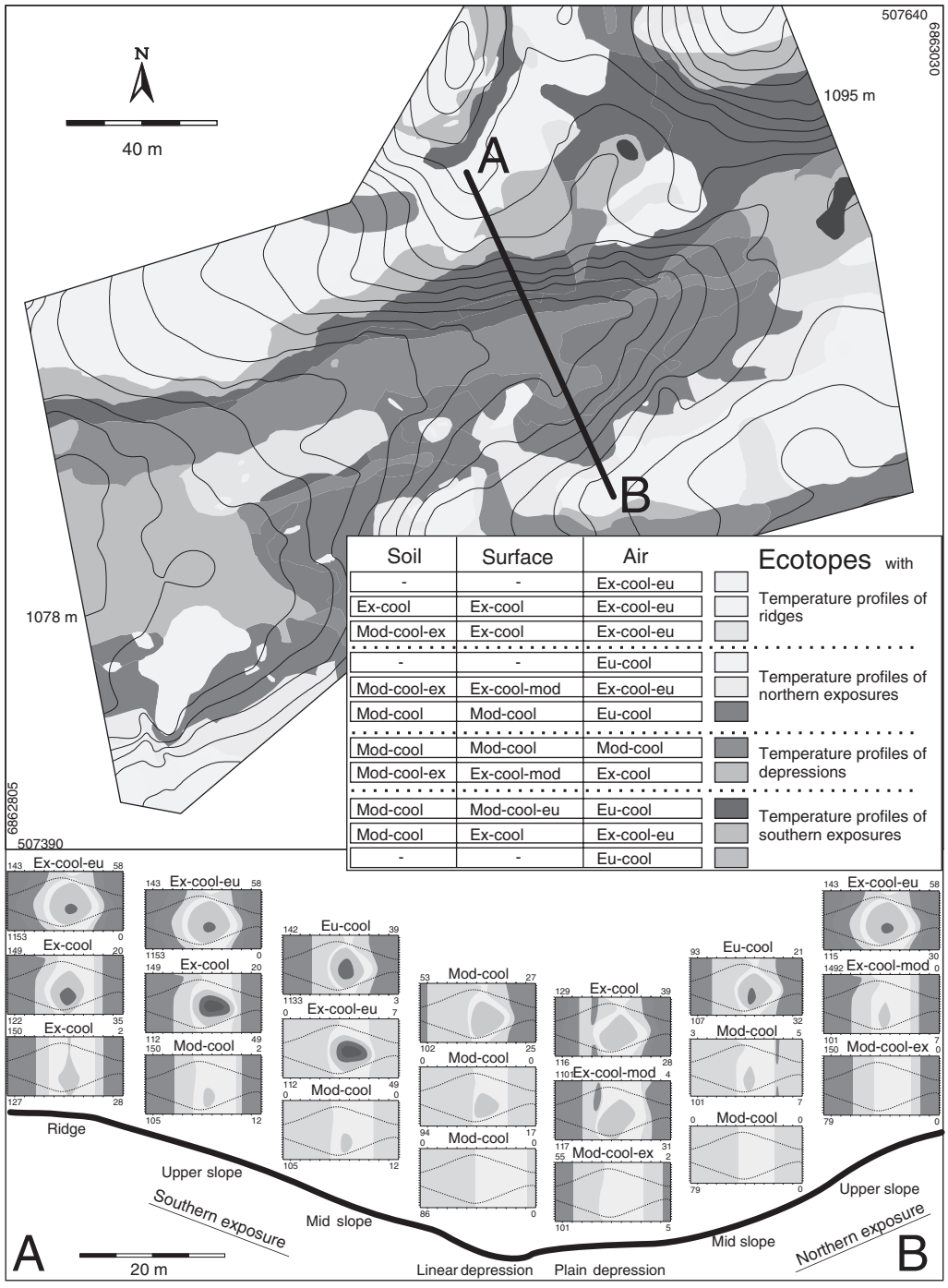


Figure 13.17 (Plate 10) Spatial differentiation of temperature dynamics in the lower alpine belt (Löffler & Wundram 2001). A schematic profile along a characteristic relief gradient is illustrated by thermoisopleth diagrams. Legend is given in Figure 13.19 and Table 13.3

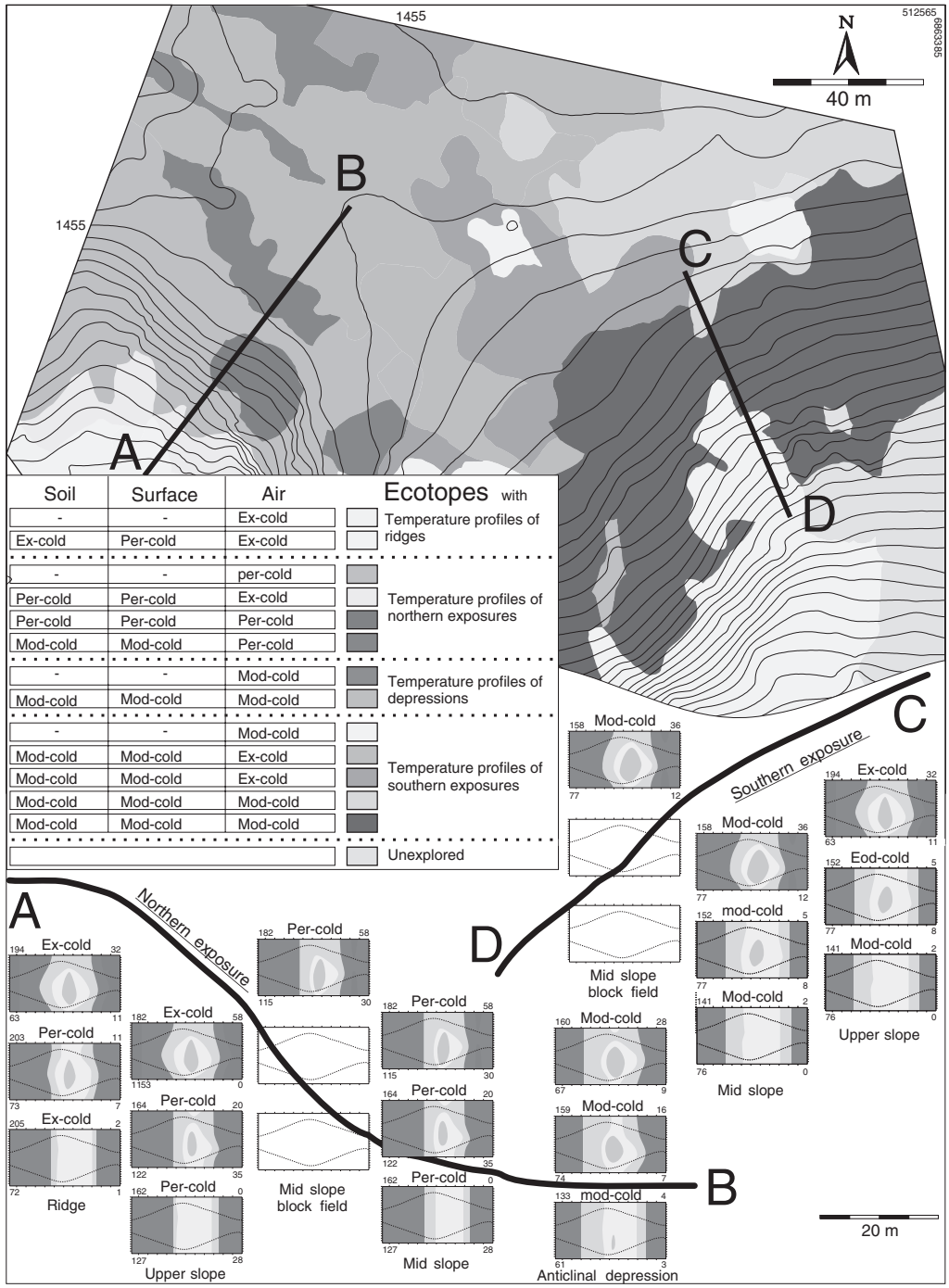


Figure 13.18 (Plate 11) Spatial differentiation of temperature dynamics in the middle-alpine belt (Löffler 2002a). A schematic profile along a characteristic relief gradient is illustrated by thermoisopleth diagrams. Legend is given in Figure 13.19 and Table 13.3

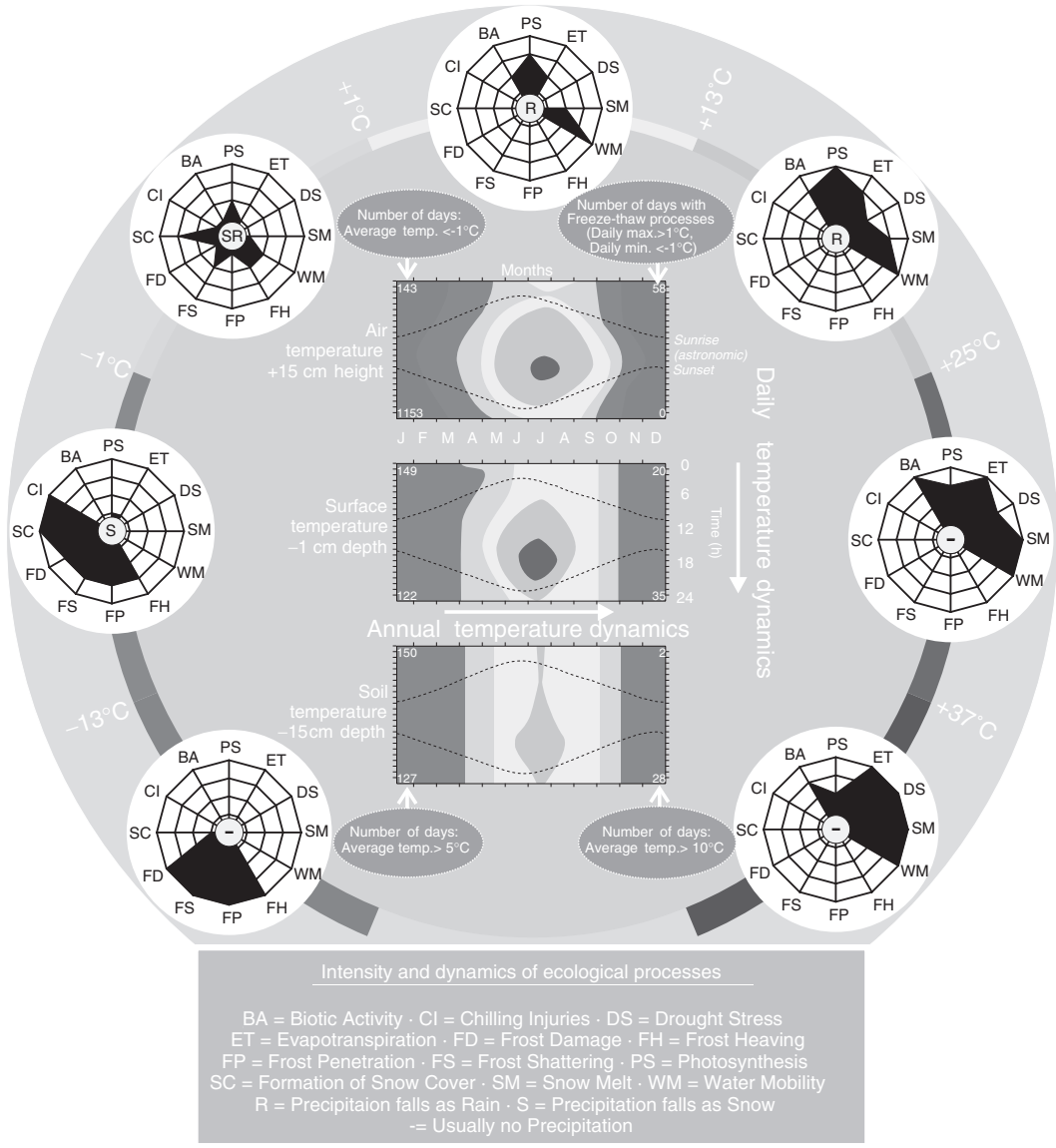


Figure 13.19 (Plate 12) Legend for landscape ecological maps and profiles in Figure 13.17 and Figure 13.18. The figure shows a complex scheme, systematically scaling temperatures according to their landscape ecological influence on ecosystem functioning. The three air, surface, and soil thermoisopleth diagrams show daily and annual changes of seven different ranges of temperatures with similar ecological values for a particular site. Those temperature ranges subdividing the outer circle into seven circular segments are grouped according to data from the literature, own investigations and theoretical considerations on 13 landscape ecological process attributes. Processes like photosynthesis, evapotranspiration, drought stress, and so on are in turn scaled on the individual axes within the small rose diagrams according to their ecological influence under those temperature conditions (from the inside to the outside: no, little, moderate, high and extreme influence). For example, temperatures under −13°C are defined as no photosynthesis is done by any species, evapotranspiration is extremely reduced, processes like drought stress, snow melt, water mobility, and so on, are absent, but there is the danger of severe frost damage to plants, frost weathering of minerals and bedrock, frost penetration is extreme, frost heaving takes place and there is usually no precipitation under those conditions. As shown by the example of the thermoisopleth triple (lower alpine ridge site), those conditions are only found within the air temperature in +15-cm height during the whole daytime in December and January and during the nights in November and February. The scheme for the classification of temperature dynamics is given in Table 13.2. (Löffler & Wundram 2001). Reproduced by permission of Dr Christof Ellger

Table 13.3 Classification of temperature dynamics (Löffler & Wundram 2001). The table shows a hierarchical classification of air, surface, and soil temperatures according to 8 different attributes: (1) duration of daily means >10°C (minimum temperature for tree growth) and (2) >5°C (minimum temperature for grass growth), (3) duration of frost (in 5 dominant classes), (4) annual temperature amplitude (in 9 dominant classes) and duration of daily maxima (5) >25°, (6) >13°, (7) <−1° and (8) <−13°C (in 9 dominant classes)

	Temperature type	code	Duration of daily means [in months]		Duration of frost [in months]	Annual amplitude [K]	Duration of daily maximum [in months]			
			>10°C	>5°C			>25°C	>13°C	<−1°C	<−13°C
Air	Extreme-cold	Ex-cold	Never	<3	>6	>45	Never	<1	>6	<1
	Persistent cold	Per-cold	Never	<3	>6	<40	Never	<1	>6	Never
	Moderate-cold	Mod-cold	Never	<3	<6	<40	Never	>1	<6	Never
	Extreme-cool (eutherm)	Ex-cool-eu	>1	>3	<6	>45	<1	<3	<6	<1
	Extreme-cool	Ex-cool	>1	>3	<6	>45	Never	<3	<6	<1
	Moderate-cool	Mod-cool	>1	>3	Never	<40	Never	<3	<3	Never
	Eutherm-cool	Eu-cool	>1	>3	<6	>40	<1	>3	<6	Never
Surface	Persistent-cold	Per-cold	Never	<3	>6	<30	Never	<1	>6	Never
	Moderate-cold	Mod-cold	Never	<3	<6	<30	Never	<1	<6	Never
	Extreme-cool	Ex-cool	>1	>3	<6	>40	<1	<3	<6	Never
	Extreme-cool (moderate)	Ex-cool-mod	>1	>3	<6	>30	Never	<3	>3	Never
	Extreme-cool (eutherm)	Ex-cool-eu	>1	>3	Never	>45	>1	>3	Never	Never
	Moderate-cool	Mod-cool	>1	>3	<1	>25	Never	>1	Never	Never
Soil	Extreme-cold	Ex-cold	Never	<3	>6	>20	Never	Never	>6	Never
	Persistent cold	Per-cold	Never	<1	>6	<20	Never	Never	>6	Never
	Moderate-cold	Mod-cold	Never	<3	<6	<20	Never	Never	>3	Never
	Extreme-cool	Ex-cool	>1	>3	<6	>30	Never	<1	<6	Never
	Moderate-cool	Mod-cool	Never	>3	Never	<15	Never	Never	Never	Never
	Moderate-cool (extreme)	Mod-cool-ex	Never	>3	<3	<20	Never	never	>1	never

occur over short periods in ridge and upper slope positions as well as in exposed depressions. The seasonal variation of surface temperature dynamics is similar to that of the air, but is buffered according to isolating effects of vegetation, as well as to soil moisture and snow cover conditions. Annual variations of the soil temperatures are still slightly pronounced in well drained and less snowy ecotopes as well as wind-exposed plain depressions. Wet and snowy ecotopes show no change of the soil temperature. Finally, Figure 13.17 and 13.18 in combination with the legends in Figure 13.19 and Table 13.2 synthesise fine-scaled spatial attributes and high-resolution temporal features on different vertical layers, resulting in a complex and highly integrating abstraction of the reality in high mountain landscapes.

13.7 DISCUSSION AND CONCLUSIONS

As demonstrated, fine-scale differences of ecological conditions have to be explained through complex attributes that result from hydrologic dynamics, in particular, the formation, thickness, duration and melting of the snow cover (see also Köhler *et al*. 1994).

Figure 13.20 synthesises the results from an ecological point of view and stresses the importance of the snow cover in the Norwegian high mountain ecosystems. The specific constellation of lee-side snow accumulation on the southern exposed slopes is important. Thus, the differences between northern and southern exposures are not as extreme as in other high mountain regions. Water stagnation results from snow melting; but wet conditions are restricted to depressions, where water surplus is detected throughout the summer. The ecosystems show high soil moisture content; this affects periglacial processes such as solifluction and cryoturbation. According to snow cover thickness, frost occurred in the ground more or less intensively at the ridge and upper slope positions. Snow cover protects the ground from frost.

Snow is the most decisive ecological factor for the occurrence and distribution of arctic-alpine vegetation (Figure 13.13, Figure 13.14, and Figure 13.21). The conservative aspects of snow cover can be summed up as follows: snow prevents plant exposure to low temperature extremes, winter desiccation, ice blast and solar radiation (potentially dangerous to dormant tissue) during the cold seasons. Its adverse effects are less clear: shortening of the length of the growing season is

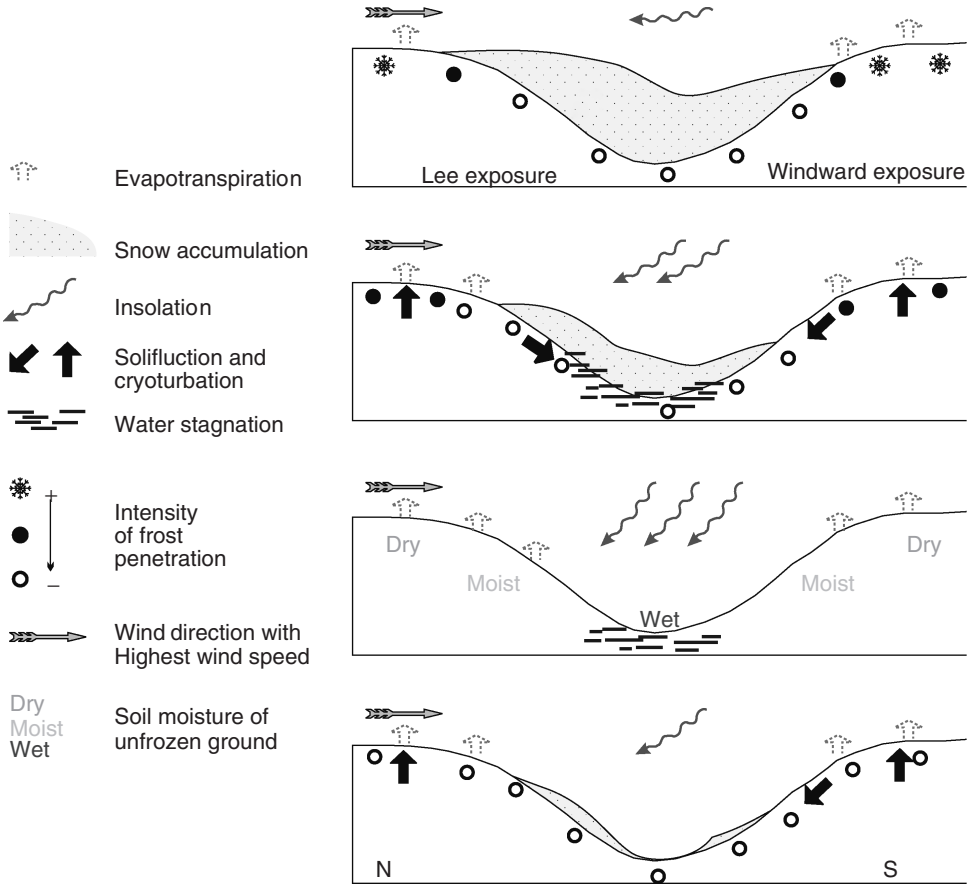


Figure 13.20 Scheme of ecological determinants in high mountain catchments. Hydrologic dynamics resulting from different seasons: winter situation from January to May, early summer situation in the middle of May, summer period from the middle of June until the end of September, autumn snow accumulation from October to December (after: Billings 1973, Köhler *et al*. 1994, Löffler 2003). Reproduced by permission of Dr Andreas Dittmann

the only obvious limitation. Others, like effects on plant respiration by elevated soil temperatures in winter, effects on microbial activity, nutrient cycling, melt water seepage and water logging, ground ice formation and possible anoxia in and above the soil, mechanical pressure and shearing effects on slopes, mechanical breaking of the vegetations structure, snow mould, and other pathogen effects or below snow rodent activity, plus effects on soils during freeze–thaw cycles are more difficult to evaluate (Körner 1999).

As a whole, snow-ecosystem studies show that feedbacks between snow, vegetation and climate are complex and occur at multiple scales (Jones *et al*. 2001). The results of this study show that the distribution of vegetation is influenced by thermal summer and winter conditions along gradients such as altitude, snow cover thickness and duration of snow cover. Figure 13.21 sums up the principles in climatic and hydrologic determination of the vegetation. During winter, extreme cold and harsh conditions occur and ecosystem functioning is primarily determined by snow cover thickness and duration of snow cover. Snow cover also determines surface and soil temperatures. Survival of plants is determined by snow during periods with low temperatures. Vegetation distribution mainly follows a pattern of spatial snow distribution. Important exceptions are given by chionophobous vegetation surviving cold winters for the sake of a longer vegetation period. On the contrary, chionophilous vegetation is more frequently found at higher altitudes where the snow cover is thicker, the vegetation period is shorter and the summers are cooler. These results are corroborated with results from

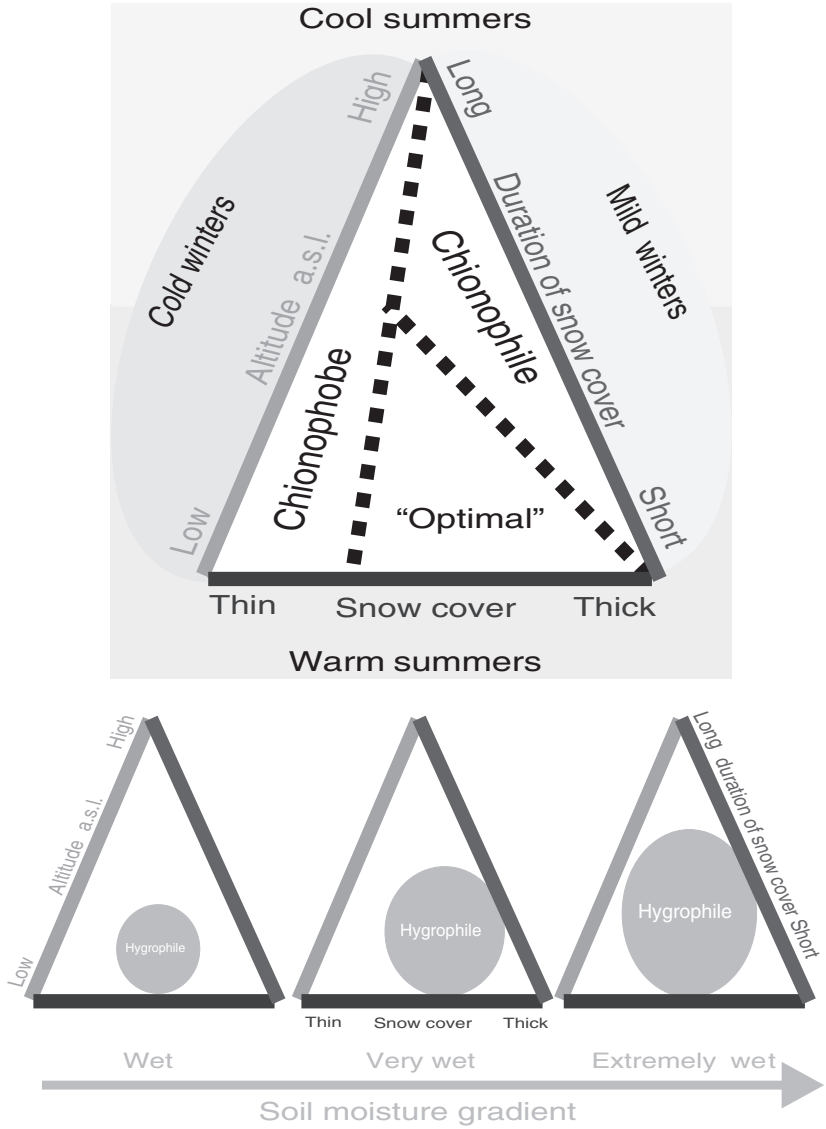


Figure 13.21 Scheme of snow cover and soil moisture influences on vegetation in the altitudinal belts (based upon Fægri 1972, modified and supplemented; Löffler 2003). Survival of plants is determined by snow during periods of lowest temperatures; vegetation distribution follows a gradient along spatial snow pack distribution. Optimal conditions are seldom found in the mountains. The most important distinction is that of chionophobes surviving cold winters for the sake of a longer vegetation period. On the contrary, chionophiles are more frequently found with altitude, where the snow cover is thicker, the vegetation period shorter and the summers cooler. Moisture gradients are contrasting: dry conditions do not occur in the mountains at any time, but near-surface wet conditions are most decisive determining species turnover and distinct vegetation changes. Wet conditions are considered to be optimal for vegetation most frequently found in low-alpine areas. With increasing moisture, chionophiles in the middle-alpine belt is also influenced superiorly, but chionophobes are not affected. Under extremely wet conditions, hygrophilous determination might occur at the exposed sites. Reproduced by permission of Dr Andreas Dittmann

the literature (Vestergren 1902, Gjærevoll 1956, Dahl 1956, Billings & Bliss 1959, Holtmeier & Broll 1992, Körner 1999, Jones *et al*. 2001) although quantitative functional data are rare. Results on moisture gradients contrast with the literature (Billings 1973, May 1976, Molenaar 1987, Isard & Belding 1989) since dry conditions do not occur in the investigated mountains at any time of the year. Near-surface wet conditions are most decisive in determining species turnover. With increasing moisture, chionophilous vegetation shows a distinct plant species turnover, while chionophobous vegetation remains unaffected. Under extremely wet conditions, hygrophilous might also occur at exposed sites (Löffler 2003). On the one hand, the alpine altitudinal gradient is characterised by a clear change in the vegetation according to the distribution of snow in the low- and middle-alpine belt as well as the absence of mire species with increasing altitude (Fægri 1972, Dahl 1986, Fremstad 1997). On the other hand, ridge and upper slope vegetation is similar at both altitudes according to a narrow range of environmental conditions. These contradictions are strengthened by two overall determinants: (i) temperature gradients responsible for altitudinal changes in snow bed species composition (Löffler 2002a) and (ii) similarities in ecological conditions at exposed sites and secondary effects of moisture gradients on low-alpine vegetation in depressions (Löffler 2005).

In summary, the new outcomes of this study are as follows.

- Soil moisture gradients do not primarily determine the distribution of alpine vegetation.
- Snow cover is important but does not explain differences in low- and middle-alpine conditions.
- Similar snow conditions correspond to different vegetation along an altitudinal range.
- Near-surface temperature conditions have secondary effects on plant species distribution.

13.8 RESEARCH PERSPECTIVES

As has been shown, altitudinal and continental-oceanic changes in high mountain ecosystem dynamics can be explained by means of hydrologic and climatologic coupling. The delineation of spatial units, the quantification of ecological processes and the registration of their temporal dynamics is based on a complex methodological concept, integrating extensive measurements and mapping routines with highest resolution. In high mountain catchments, fine-scale differences of topography determine the landscape functioning above all other structural factors. The fundamental problem of landscape ecological approaches in the chorological dimension has been the lack of process-oriented methods (Haase 1979, Leser 1997). Thus, concepts had to be developed to extrapolate local measurements from the high mountain catchments into a larger area. Current regionalisation approaches from central Europe that focus on meso-scale water matter fluxes between different ecosystems could serve as a basis for this step (Duttmann 1999, Steinhardt & Volk 2002). Moreover, Reynolds & Tenhunen (1996) ask for landscape ecological studies that integrate processes within the water and solid matter balance. In the frame of this project in high mountain landscapes, techniques are developed to facilitate measurements under extreme conditions with a spatio-temporal resolution high enough for ecosystem modelling. Functional data are generally required for high mountains to explain the current systems and scenarios for future changes in alpine environments (Gottfried *et al*. 1999).

In general, perspectives in ecosystem analysis rely on quantification of biogeochemical cycles and energy fluxes in catchments and the regionalisation of results into larger areas (Withers & Meentemeyer 1999). As an overall objective for the future, regionalisation will be extended to the macro scale. To continue high mountain research in central Norway, functional regionalisation of ecological process systems is aspired, using a fine-scale spatial resolution from remote-sensing data and a high temporal resolution for landscape ecological models. The development of those models will have to be based on intensive field measurements using automatic equipment for high temporal resolution wherever possible.

Since the methodological concept is strictly based on theoretical constructions of different spatial units, the existence of such ecotopes, ecochores and ecoregions will have to be proved. This will be done along gradients with spatial differentiation according to lateral process directions. Indicators are available in the abiotic cycle of water fluxes and correlated solid matter dynamics. Moreover, the biotic compartment promises interesting hints on the existence of spatial landscape units. From the level of mobile organisms, vectors along temperature gradients might be expected (Löffler *et al*. 2001). As snow has proved to be an integrating hydrologic factor, further investigations will be concentrated on fluxes of water and associated materials. First and foremost, within-snow hydrology will be examined by tracer experiments to detect water fluxes during the melting period. Many further research questions for alpine ecosystems remain, some of which have been summarized by Bowman & Seastedt (2001).

13.9 ACKNOWLEDGEMENTS

The authors thank their companions, collaborators and colleagues for data processing and essential discussions: Anders Lundberg (University of Bergen, Norway), Oliver-D. Finch, Roland Pape, and Dirk Wundram (University of Oldenburg); all other members of the team and ''generations'' of students for field assistance; and extend warmest gratitude to Carmen de Jong (University of Bonn) for editing their ''Germlish''.

REFERENCES

Bastian O, Schreiber K-F (eds) (1999) *Analyse und Ökologische Bewertung der Landschaft*. Spektrum, Heidelberg, Berlin, pp. 1–564.

Bastian O, Steinhardt U (eds) (2002) *Development and Perspectives in Landscape Ecology*. Kluwer, Dordrecht, pp. 1–498.

Bernes C (1993) *The Nordic Environment – Present State, Trends and Threats*, Nord 12. Nordic Council of Ministers, Copenhagen, pp. 1–212.

Billings WD (1973) Arctic and alpine vegetations: similarities, differences, and susceptibility to disturbance. *Bioscience* **23**: 697–704.

Billings WD, Bliss, LC (1959) An alpine snowbank environment and its effects on vegetation, plant development, and productivity. *Ecology* **40**: 388–397.

Billwitz K (1997) Allgemeine geoökologie. In: Hendl M, Liedtke H (eds) *Lehrbuch der Allgemeinen Physischen Geographie*. Klett-Perthes, Gotha, pp. 635–720.

Bliss L, Heal OW, Moore JJ (eds) (1981) *Tundra Ecosystems: A Comparative Analysis*, IBP 25. University Press, Cambridge, pp. 1–813.

Bowman, WD, Seastedt TR (eds) (2001) *Structure and Function of an Alpine Ecosystem: Niwot Ridge, Colorado*. University Press, Oxford, pp. 1–337.

Dahl E (1956) Rondane. Mountain vegetation in south Norway and its relation to the environment. Skr. utg. av Det Norske Vid. Akad. i Oslo. Mat.-Nat. Kl. 3. Oslo, pp. 1–374.

Dahl E (1986) Zonation in arctic and alpine tundra and fellfield ecobiomes. In: Polunin N (ed) *Ecosystem Theory and Application*. Wiley, Chichester, pp. 35–62.

Dahl E (1998) *The Phytogeography of Northern Europe (British Isles, Fennoscandia and Adjacent Areas)*. University Press, Cambridge, pp. 1–297.

de Jong C, Ergenzinger P (2002) Experimental hydrological analyses in the Dischma based on daily and seasonal evaporation. *Nordic Hydrology* **33**: 1–14.

Döbeli C (2000) Das hochalpine Geoökosystem der Gemmi (Walliser Alpen). Eine landschaftsökologische Charakterisierung und der Vergleich mit der arktischen Landschaft (Liefdefjorden, Nordwest-Spitzbergen). *Physiogeographica, Beiträge zur Physiogeographie* **28**: 1–193, Basel.

Duttmann R (1999) Partikuläre Stoffverlagerungen in Landschaften. Ansätze zur flächenhaften Vorhersage von Transportpfaden und Stoffumlagerungen auf verschiedenen Maßstabsebenen unter besonderer Berücksichtigung räumlich-zeitlicher Änderungen der Bodenfeuchte. *Geosynthesis* **10**: 1–234, Hannover.

Fægri K (1972) Geo-ökologische probleme der Gebirge Skandinaviens. In: Troll C (ed) *Geoecology of the High-Mountain Regions of Eurasia: Proceedings of the Symposium of the International Geographical Union, Commission on High-Altitude Geoecology*, November 20–22, 1969 at Mainz in connection with the Akademie der Wissenschaften und der Literatur in Mainz, Kommission für Erdwissenschaftliche Forschung, Erdwissenschaftliche Forschung 4. Wiesbaden, pp. 98–106.

Faugli PE (1994a) The Aurland river catchment area – impact of hydropower development. *Norsk Geologisk Tidsskrift* **48**: 1–2.

Faugli PE (1994b) The Aurland catchment area – the watercourse and hydropower development. *Norsk Geologisk Tidsskrift* **48**: 3–7.

Faugli PE (1994c) Watercourse management in Norway. *Norsk Geologisk Tidsskrift* **48**: 75–79.

Fortescue JAC (1980) Environmental geochemistry – a holistic approach. *Ecological Studies* **35**: 1–347, New York.

Fremstad E (1997) *Vegetationstyper i Norge*. Norsk institutt for naturforskning, Temahefte 12. Trondheim, pp. 1–279.

Gjærevoll O (1956) *The plant communities of the Scandinavian alpine snowbeds*. Det Kongelige Norske Videnskabers Selskraps Skrifter, 1. Trondheim, pp. 1–405.

Gottfried M, Pauli H, Reiter K, Grabherr G (1999) A fine-scaled predictive model for changes in species distribution patterns of high mountain plants induced by climate warming. *Diversity and Distributions* **5**: 241–251.

Haase G (1979) Entwicklungstendenzen in der geotopologischen und geochorologischen Naturraumerkundung. *Petermanns Geographische Mitteilungen* **123**: 7–18.

Haase G, Barsch H, Hubrich H, Mannsfeld K, Schmidt R (1991) Naturraumerkundung und Landnutzung. Geochorologische Verfahren zur Analyse, Kartierung und Bewertung von Naturräumen. *Beiträge zur Geographie* **34**: 1–373, Berlin.

Håland A, Faugli PE (1994) The Aurland hydropower development – its impact on nature and the environment. *Norsk Geologisk Tidsskrift* **48**: 81–84.

Holtmeier F-K, Broll G (1992) The influence of tree islands and microtopography on pedological conditions in the forest-alpine tundra ecotone on Niwot Ridge, Colorado Front Range, U. S. A. *Arctic and Alpine Research* **24**: 216–228.

Isard SA, Belding MJ (1989) Evapotranspiration from the alpine tundra of Colorado, USA. *Arctic and Alpine Research* **21**: 71–82.

Jones HG, Pomeroy JW, Walker DA, Hoham RW (2001) *Snow Ecology. An Interdisciplinary Examination of Snow-Covered Ecosystems*. University Press, Cambridge, pp. 1–378.

Kaltenborn BP (1999) *Tourism in an arctic wilderness. Mountains of the world. Tourism and sustainable mountain development*. Mountain Agenda, Berne, p. 13.

Köhler B, Löffler J, Wundram D (1994) Probleme der kleinräumigen Geoökovarianz im mittelnorwegischen Gebirge. *Norsk Geologisk Tidsskrift* **48**: 99–111.

Körner C (1999) *Alpine Plant Life. Functional Plant Ecology of High Mountain Ecosystems*. Springer, Berlin, Heidelberg, New York, pp. 1–338.

Leser H (1986) Arbeitstechnische und methodische probleme geoökologischer Forschungen in Extremklimaten – unter Bezug auf Erfahrungen in Namib, Kalahari und Arktis. *Geoökodynamik* **7**: 275–304.

Leser H (1997) *Landschaftsökologie. Ansatz, Modelle, Methodik, Anwendung*. Ulmer, Stuttgart, pp. 1–644.

Löffler J (1998) Geoökologische Untersuchungen zur Struktur mittelnorwegischer Hochgebirgsökosysteme. *Oldenburger Geoökologische Studien* **1**: 3–207, Bibliotheks-und Informationssystem, Oldenburg.

Löffler J (1999) Podsolierung als energetisch gesteuerter Translokationsprozess? Untersuchungsergebnisse aus dem mittelnorwegischen Hochgebirge. *Oldenburger Geoökologisches Kolloquium* **6**: 37–86, Oldenburg.

Löffler J (2000) High mountain ecosystems and landscape degradation in northern Norway. *Mountain Research and Development* **20**: 356–363.

Löffler J (2002a) Altitudinal changes of ecosystem dynamics in the central Norwegian high mountains. *Die Erde* **133**: 227–258.

Löffler J (2002b) Vertical landscape structure and functioning. In: Bastian O, Steinhardt U (eds) *Development and Perspectives in Landscape Ecology*. Kluwer Academic, Dordrecht, pp. 44–58.

Löffler J (2002c) Landscape complexes. In: Bastian O, Steinhardt U (eds) *Development and Perspectives in Landscape Ecology*. Kluwer Academic, Dordrecht, pp. 58–68.

Löffler J (2003) Micro-climatic determination of vegetation patterns along topographical, altitudinal, and oceanic-continental gradients in the central Norwegian high mountains. *Erdkunde* **57**: 232–249.

Löffler J (2005) Snow cover dynamics, soil moisture variability and vegetation ecology in high mountain catchments of central Norway. *Hydrological Processes* (in print).

Löffler J, Finch OD, Naujok J, Pape R (2001) Möglichkeiten der integration zoologischer Aspekte in die landschaftsökologische Untersuchung von Hochgebirgen. Methodendiskussion am Beispiel ökologischer Prozesssysteme und Biozönosen. *Naturschutz und Landschaftsplanung* **33**: 351–357.

Löffler J, Wundram D (2001) Räumliche und zeitliche Differenzierung des Temperaturhaushalts von Hochgebirgsökosystemen. *Norden* **14**: 85–102, Bremen.

Löffler J, Wundram D (2003) *Geoökologische Untersuchungen zur Prozessdynamik mittelnorwegischer Hochgebirgsökosysteme*, Oldenburger Geoökologische Studien 2. Bibliotheks-und Informationssystem, Oldenburg, pp. 3–158.

May DE (1976) The response of alpine tundra vegetation in Colorado to environmental modification. PhD thesis, University of Colorado, Boulder, pp. 1–64.

Messerli B, Ives JD (1997) *Mountains of the World. A Global Priority*. Panthenon, New York, London, pp. 1–495.

Moen A (1999) *National Atlas of Norway: Vegetation*. Norwegian mapping authority, Hønefoss, pp. 1–200.

Molenaar GJ de (1987) An ecohydrological approach to floral and vegetational patterns in arctic landscape ecology. *Arctic and Alpine Research* **19**: 414–424.

Mountain Agenda (1998) *Mountains of the World. Water Towers for the 21st Century. A Contribution to Global Freshwater Management*. Mountain Agenda, Berne, pp. 1–32.

Mosimann T (1984a) *Landschaftsökologische Komplexanalyse*. Steiner-Verlag, Wiesbaden, pp. 1–115.

Mosimann T (1984b) Methodische Grundprinzipien für die Untersuchung von Geoökosystemen in der topologischen Dimension. *Geomethodica* **9**: 31–65, Basel.

Mosimann T (1985) Untersuchungen zur Funktion subarktischer und alpiner Geoökosysteme (Finnmark [Norwegen] und Schweizer Alpen). *Physiogeographica, Basler Beiträge zur Physiogeographie* **7**: 1–488, Basel.

Mosimann T (1997) Prozess-Korrelationssystem des elementaren Geoökosystems. In: Leser H (ed) *Landschaftsökologie. Ansatz, Modelle, Methodik, Anwendung*. Ulmer, Stuttgart, pp. 262–270.

Potschin M (1996) Nährstoff- und Wasserhaushalt im Kvikkåa-Einzugsgebiet, Liefdefjorden (Nordwest-Spitzbergen). Das Landschaftsökologische Konzept in einem hocharktischen Geoökosystem. *Physiogepgraphica, Basler Beiträge zur Physiogeographie* **23**: 1–258, Basel.

Potschin M (1998) Ökologische Jahreszeiten in der Hocharktis – Kriterien der Abgrenzung. *Die Erde* **129**: 229–246.

Potschin M, Wagner R (1996) The hydrological and ecological situation of surface waters in a newly evolved terrestrial geosystem on Potter Peninsula, King George Island (Antarctica). *Heidelberger Geographische Arbeiten* **104**: 496–515, Heidelberg.

Rempfler A (1989) Boden und Schnee als Speicher im Wasser- und Nährstoffhaushalt hocharktischer Geosysteme (Raum Ny Ålesund, Brøggerhalvøya, Nordwestspitzbergen). *Materialien zur Physiogeographie* **11**: 1–159, Basel.

Reynolds JF, Tenhunen JD (eds) (1996) *Landscape Function and Disturbance in Arctic Tundra*, Ecological Studies 120. Springer, Berlin, Heidelberg, New York, pp. 1–437.

Rosswall T, Heal OW (eds) (1975) Structure and function of tundra ecosystems. *Ecological Bulletins* **20**: 1–450, Stockholm.

Steinhardt U, Volk M (2002) The investigation of water and matter balance on the meso-landscape scale: a hierarchical approach for landscape research. *Landscape Ecology* **17**: 1–12.

Vestergren T (1902) Om den olikforminga snöbetäckningens inflytande påvegetationen i Sarjekfjällen. Bot. Not. Lund

Walker DA, Billings WD, de Molenaar JG (2001) Snow – vegetation interactions in tundra environments. In: Jones HG, Pomeroy JW, Walker DA, Hoham RW (eds) *Snow Ecology. An Interdisciplinary Examination of Snow-Covered Ecosystems*. University Press, Cambridge, pp. 266–324.

Wielgolaski FE (ed) (1975) *Fennoscandian Tundra Ecosystems. Part 1: Plants and Microorganisms*, Ecological Studies Vol. 16. Springer, Berlin, Heidelberg, New York, pp. 1–366.

Wielgolaski FE (ed) (1998) *Polar and Alpine Tundra*, Ecosystems of the World 3. Elsevier, Amsterdam, pp. 1–920.

Wielgolaski FE (ed) (2001) *Nordic Mountain Birch Ecosystems*, Man and the biosphere series 27. Panthenon, New York, London, pp. 1–390.

Withers MA, Meentemeyer V (1999) Concepts of scale in landscape ecology. In: Klopatek JM, Gardner RH (eds) *Landscape Ecological Analysis*. Issues and applications. Springer, New York, pp. 205–252.

Wundram D (2003) Die Bedeutung des Temperaturhaushalts für die Prozessdynamik mittelnorwegischer Hochgebirgsökosysteme. Dissertation, Universität Oldenburg, http://docserver.bis.uni-oldenburg.de/publikationen/dissertation/2003/wunbed03/wunbed03.html, pp. 1–148.

PART IV: COUPLING METEOROLOGY AND HYDROLOGY

Climate and Hydrology in Mountain Areas. Edited by C. de Jong, D. Collins and R. Ranzi
© 2005 John Wiley & Sons, Ltd. ISBN: 0-470-85814-1

14

Runoff and Floods in the Alps: An Overview

BALDASSARE BACCHI[1] AND VIGILIO VILLI[2]
[1]Department of Civil Engineering-University of Brescia – Via Branze, 38-25123 Brescia-I, [2]CNR – Research Institute for Hydrogeological Risk Prevention – Corso Stati Uniti, 4-35127 Padova-I

14.1 INTRODUCTION

In this overview, the close links between meteorological and hydrological aspects in mountain areas are briefly discussed and state-of-the-art issues related to the influence of meteorological and surface processes on flood formation are presented. Although this paper is focused on the European Alps, most considerations could be applied to mountain areas in general.

As pointed out recently by Weingarten *et al*. (2003), mountain floods are special since they are the result of a combination of factors unique to mountain basins such as high-intensity precipitation, steep gradients and thin soils but nevertheless ''despite much research, the production of storm runoff in responsive catchment is still poorly understand''. Consequently, when coupling meteorological and hydrological models, the effect of orography and geomorphology on floods should be considered particularly closely.

14.2 PRECIPITATION AND RUNOFF FORMATION

It is well known that heavy precipitation in the Alps is reproduced when polar and North Atlantic air masses, characterised by low temperatures, interact with warm and moist air masses of oceanic or Mediterranean origin. The resulting fronts vary in size from several hundreds to more than a 1000 km and tend to move from West to East with a mean lifespan of 2–7 days. Knowledge of particular aspects of mountain precipitation was intensified under the Mesoscale Alpine Programme (Bougeault *et al*. 2003) where dynamical and microphysical processes leading to the enhancement and organisation of precipitation in alpine mountain ranges were investigated by experimental and numerical models. Summarising some of the results of the project, it appears that the effect of arc-shaped alpine relief on air movement is connected to two relevant atmospheric phenomena: the deviation of precipitation fronts in almost parallel orientation with the mountain chains (Rotunno and Ferretti 2001) and the forced convection of air masses towards the water divide. These phenomena can produce persistent and spatially diffuse rainfall contributing to areas with the highest annual precipitation and frequency of thunderstorms located along the border of the Alps. In contrast, rapid decrease of atmospheric moisture with altitude combined with the rain shadow effects in the leeside valleys of mountain ridges cause east–west-oriented inner alpine valleys to gain considerably less mean annual precipitation (Alpert 1986; Buzzi and Foschini 2000; Van Delden 2001; Frei and Schär 1998). Finally, in the summer, convection produces an abrupt cooling of warm air masses, causing frequent and localised thunderstorms particularly in the headwater areas dominated by steep slopes and thin soils.

It is important to note that in alpine catchments, meteorological, hydrological and glaciological phenomena undergo complex and highly variable interactions over short spatial and temporal scales. However, effects can be

Climate and Hydrology in Mountain Areas. Edited by C. de Jong, D. Collins and R. Ranzi
© 2005 John Wiley & Sons, Ltd. ISBN: 0-470-85814-1

perpetuated over long distances and time. Alpine slopes host many different environments: extreme mountain peaks with prevailing glacial and periglacial phenomena, lower pasture and forest zones, alluvial terraces marking the former flood plain and finally the valley bottoms bordering the river channels as relatively smooth strips of land. Along this ''section'', characterised by steep slopes and creeks, the dynamic equilibrium between form and process is continuously modified by the magnitude and frequency of hydrometeorological processes (rainfall, evapotranspiration, ice and snow melt, etc). The most significant evidence for these interactions is given by alluvial fans, which are generated by debris flows that originate from the steep tributaries of the main valleys. These impulsive phenomena together with landslides modify the landscape in combination with other slower phenomena. In the literature is still deeply debated whether alterations in surface flow, erosion and flooding are due to changing land use as a result of modified agricultural practices, deforestation and the increase of impermeable areas as a consequence of urbanisation (Ranzi *et al*. 2002, Brath *et al*. 2002).

By linking the hydrometeorological space-time domain with the characteristics of alpine valleys, the following spatial and temporal scales of hydrological processes can be identified in alpine regions.

At microscales of some square kilometers, local atmospheric instabilities prevail in the form of isolated storm cells triggered by orographic lifting. Here, the main processes controlling runoff formation are affected by the geomorphological and topographical characteristics of the basins, rainfall conditions, snowfall and ablation, soil moisture conditions, vegetation cover, land use, and so on.

At the mesoscale, widespread stratiform precipitation is induced by uplift of large-scale air masses with high equivalent potential temperatures, causing severe floods in basins of some thousands of square kilometres. Flood intensities reflect both meteorological and physiographic factors as well as the routing properties of the channels.

Floods in larger basins such as those that occurred in central and eastern Europe in 2002 are forced by synoptic scale precipitation from a combination of climatic events caused both by anomalies in upper-level circulations and sea-surface temperatures as well as other unusually intensive hydrometeorological interactions.

Following the discussion on runoff processes in alpine areas, a brief excursion will be taken into types of models used in reconstructing and/or predicting catchment response.

Infiltration is simulated according to two basic assumptions. The first one is based on the ''Hortonian'' concept of rainfall exceeding the infiltration capacity of soils with low permeability or low depth. This identifies one of the main mechanisms by which rainfall can reach drainage networks via overland flow. Many models are based on the concept of estimation of infiltration excess rate (Green and Ampt 1911; Horton 1933, 1940). Since this conceptual scheme became inappropriate in some basins, especially in areas with gentle slopes or those characterised by greater infiltration capacities, another mechanism was proposed by Dunne *et al*. (1975) on the basis of the *Variable Source Area* concept, which was first defined by Hewlett (1961). This model assumes that catchment outflow is mainly due to overland flow that originates from saturated areas close to streams. Here, the role of topography is crucial, especially that of hollows in the development of saturation. This conceptual scheme has formed the basis of many runoff generation models: the Topmodel (Beven and Kirkby 1979) and the Probability Distributed Model (Moore and Clarke 1981).

The ice-snow melting phase is often estimated by using a simplified conceptual scheme based on air temperature. This so-called ''degree-day'' method has been used in many different ways for more than 60 years. When a complete set of meteorological data is available (radiation, wind speed, air humidity and temperature, precipitation), models based on the energy-balance equation are applied. Advantages and disadvantages of distributed snow-melt models are discussed by Kirnbauer *et al*. (1994). Nevertheless, the empirical degree-day method cannot be easily replaced by more physically based methods (Martinec and Rango 1995) because the required meteorological data is often missing.

Surface runoff, especially channel flow processes, is related to the hydraulic properties of the channel network that governs flow propagation. The kinematic formula and linear reservoir methods are probably the oldest methods available to determine the hydrologic response of drainage network. The related IUH concept was introduced by Sherman (1932) and was later applied mainly to hydrological studies. In the 1950s, a conceptual model that considers the drainage basin as a cascade of linear reservoirs was introduced (Nash 1957). This model is probably most widely adopted in hydrological practice. By successively linking hydrology with quantitative geomorphology (Rodriguez-Iturbe and Valdes 1979; Valdes *et al*. 1979; Gupta *et al*. 1980; Rinaldo *et al*. 1991), attempts were made to estimate the hydrologic response of catchments. Relationships between geomorphological basin characteristics and parameters of the geomorphological IUH function were retrieved. The Nash conceptual model with the same time lag and peak height fits the resulting GIUH very well (Rosso 1984).

14.3 FLOODS AND FREQUENCY ANALYSIS

In recent years, a number of European countries experienced damaging flood events that were caused by persistently high precipitation concentrated in mountain areas. In some countries, catastrophic floods occur almost every year, damaging villages, infrastructures, cultivated areas and causing loss of lives. The most recent floods occurred in central Europe in August 2002, in the Po basin in 1994 and 2000, in Italy (Valtellina, a combined flood and landslide event) in 1987 and in Switzerland, Austria, Germany (Rhein and Meuse) and the Netherlands in 1993, 1994, 1995 and 2000, respectively. The Oder, Morava and Danube rivers experienced floods in July 1997. In the years 1998–2002, more than 200 floods occurred in Europe, leading to the loss of 700 lives. In the 2002 flood, less than 100 lives were lost but costs cumulated to 4.1 billion Euros for insurance companies.

Scientists and citizens are challenged by the question of whether such frequent and catastrophic events are due to extraordinary rainfall episodes, to changes in our climate, or instead result from increased vulnerability of territory and insufficient maintenance of river beds.

The debate also remains open because available data is contradictory. With reference to the Italian rivers, it is important to note that whereas the gauging stations of Piacenza and Pontelagoscuro in the Po river show increasing maximum annual floods in the period 1920–2000, those in the Adige river mostly measure steady or lightly decreasing floods in the period 1923–1997. In the Adige basin, the mean daily discharge shows a significant decreasing tendency by about 30% (Villi 2003), a fact observed for several other rivers in Europe too.

The costs and effectiveness of structural measures mitigating the effects of floods depends on the design flood estimates. The choice of the design peak-flood, Q_T, with a given return period, T, is of crucial importance for river training. It is based on the assumption of *level of acceptable risk*, a knowledge of river hydrology and the availability of hydrological data. In brief, with increasing potential damage the cost of protection increases parallel to an increasing design return period.

In the last 30 years, effective procedures have been established for flood estimation, including several techniques for regionalisation of flood data in a unique statistical model (Committee on Techniques for Estimating probabilities for extreme floods, 1988). The basic hypothesis assumes that time series of peak floods in a given region rescaled to an appropriate index value (e.g. the mean annual flood) represent the same dimensionless variable distributed homogeneously over each river section of the region. This hypothesis is acceptable only if the rescaled floods are spatially homogeneous.

In the Alps, a number of regional flood frequency methods have been applied. In Austria and Switzerland, the EU FRAMEWORK Program (flash flood risk assessment under the impact of land use changes and rivers engineering works) applied to the Region Of Influence (ROI) concept in addition to seasonality measures and the Gradex method. In Italy, a hierarchical-type regionalization model, the TCEV (Two Component Extreme Value) was applied on a national basis (see Rossi *et al*. 1984; Villi and Bacchi 2001).

As a final remark, this brief overview demonstrates both progress and uncertainty in our understanding of the hydrometeorological aspects of mountain floods and we hope that future research will improve our knowledge on these complex and relevant phenomena.

14.4 ACKNOWLEDGEMENTS

The manuscript benefited from comments by Roberto Ranzi and English proofreading by Carmen de Jong and it is a pleasure to acknowledge their assistance and suggestions.

REFERENCES

Alpert P., Mesoscale indexing of distribution of orographic precipitation over high mountains. *J. Appl. Meteorol.*, **25**, 532–545, 1986.

Beven K.J., Kirkby M.J., A physically-based variable contributing area model of basin hydrology, *Hydrol. Sci. Bull.*, **24**, 43–69, 1979.

Brath A., Castellarin A., Montanari A., Assessing the effects of land use changes on annual average gross erosion. *Hydrol. Earth Syst. Sci.*, **6**(2), 255–265, 2002.

Bougeault P., Houze R.A. jr., Rotunno R., Volkert H., Guest Ed., Mesoscale Alpine Programme (MAP). *Q. J. Meteor. Soc.*, **129**, 588, Part B, 2003.

Buzzi A., Foschini L., Mesoscale meteorological features associated with heavy precipitation in southern Alps. *Atmos. Phys.*, **72**, 131–146, 2000.

Committee on Techniques for Estimating probabilities for extreme floods, *Techniques for Estimating Probabilities of Extreme Floods: Methods and Recommended*. National Academy Press, Washington, DC, 1988.

Dunne T., Moore R.T., Taylor C.H., Recognition and prediction of runoff-producing zones in humid regions. *Hydrol. Sci. Bull.*, **20**(3), 305–327, 1975.

Frei C., Schär C., A precipitation climatology of the Alps from high-resolution rain-gauge observations. *Int. J. Climatol.*, **18**, 873–900, 1998.

Green W.H., Ampt G.A., Studies on physics, part I, the flow of air and water through soils. *J. Agric. Sci.*, **4**(1), 1–24, 1911.

Gupta W.K., Waymire E., Wang C.T., A representation of an instantaneous unit hydrograph from geomorphology. *Water Resour. Res.*, **16**(5), 855–862, 1980.

Hewlett J.D., *Soil Moisture as a Source Baseflow from Steep Mountain Watersheds*, (Station Paper 132). U.S. Forest Service, Southeastern Forest Experiment Station, Asheville, NC, 1961.

Horton R.E., The role of infiltration in the hydrologic cycle. *Trans. Am. Geophys. Union*, **14**, 446–460, 1933.

Horton R.E., An approach towards a physical interpretation of infiltration capacity. *Proc. Soil Sci. Soc. Am.*, **5**, 399–417, 1940.

Kirnbauer R., Blöschl G., Gutnecht D., Entering era of distributed snow model. *Nord. Hydrol.*, **25**, 1–24, 1994.

Martinec J., Rango A., Revisiting the degree-day method for snowmelt computation. *Water Resour. Bull.*, **31**(4), 657–669, 1995.

Moore R.J., Clarke R.T., A distribution function approach to rainfall-runoff modelling. *Water Resour. Res.*, **17**(5), 1367–1382, 1981.

Nash J.E., *The form of Instantaneous Unit Hydrograph*. IAHS Publication No. 42, 1379–1394, 1957.

Ranzi R., Bochicchio M., Bacchi B., Effects on floods of recent afforestation and urbanisation in the Mella River (Italian Alps). *Hydrol. Earth Syst. Sci.*, **6**(2), 239–265, 2002.

Rinaldo A., Marani R., Rigon R., Geomorphological dispersion. *Water Resour. Res.*, **27**(4), 513–525, 1991.

Rodriguez-Iturbe I., Valdes J., The geomorphological structure of hydrologic response. *Water Resour. Res.*, **15**(5), 1409–1420, 1979.

Rossi F., Fiorentino M., Versace P., Two-component extreme value distribution for flood frequency estimation. *Water Resour. Res.*, **20**(7), 847–856, 1984.

Rosso R., Nash model relation to Horton order ratios, *Water Resour. Res.*, **20**(7), 914–920, 1984.

Rotunno R., Ferretti R., Mechanism of Intense Alpine Rainfall. *J. Atmos. Sci.*, **58**, 1732–1749, 2001.

Sherman L.K., Streamflow from rainfall by the unit-graph method. *Eng. News Rec.*, **18**, 501–505, 1932.

Valdes B.J., Fiallo J., Rodriguez-Iturbe I., A rainfall-runoff analysis of the geomorphologic IUH. *Water Resour. Res.*, **15**(6), 1421–1444, 1979.

Van Delden A., The synoptic setting of thunderstorms in western Europe. *Atmos. Res.*, **56**, 89–110. 2001.

Villi V., The reduction of the daily discharges in the upper Adige River and possible causes (in Italian). *Boll. Geofisico*, **XXVI**(3–4), 73–87, 2003.

Villi V., Bacchi B., *Evaluation of Peak Flood in North-Eastern Italy*. CNR-GNDCI, Publication No. 2511 (in Italian), 2001.

Weingarten R., Barben M., Spreafico M., Floods in mountain areas-an overview based on examples from Switzerland. *J. Hydrol.*, **282**, 10–24, 2003.

15

The Use of Coupled Meteorological and Hydrological Models for Flash Flood Simulation

CHARLES A. LIN[1], LEI WEN[1], DIANE CHAUMONT[2] AND MICHEL BÉLAND[3]

[1]Department of Atmospheric and Oceanic Sciences, and Global Environmental and Climate Change Centre, McGill University, 805 Sherbrooke Street W., Montréal (Québec), H3A 2K6, Canada, [2]Ouranos Consortium sur la climatologie régionale et l'adaptation aux changements climatiques, 550 Sherbrooke Street W., Montréal (Québec), H3A 1B9, Canada, [3]Réseau québécois de calcul de haute performance, Université de Montréal, C.P. 6128, succ. Centre-ville, Montréal (Québec), H3C 3J7, Canada

15.1 INTRODUCTION

The atmosphere, ocean, and land surface are important components of the global hydrological cycle. Interactions in the coupled atmosphere–ocean–land surface system give rise to weather and climate variability. At the regional scale, the exchange of moisture and heat between the land surface and the atmosphere determines the low level atmospheric humidity and temperature fields, which in turn has an impact on regional weather and climate. The land surface is the interface between the atmosphere and the underlying hydrological regime; the latter is characterized by surface runoff, interflow, baseflow, soil moisture, and other hydrological variables. The importance of the land surface scheme (LSS) and its feedback to the atmosphere have long been recognized for regional climate. For example, Entekhabi *et al*. (1999), in their proposed agenda for land surface hydrology research, note that surface soil moisture is as important as sea surface temperature as boundary conditions for the climate system. In fact, they point out that precipitation extremes in the United States can be more strongly influenced by soil moisture fields than sea surface temperatures.

There have been less studies of the effect of LSSs on regional weather, in particular, precipitation. A reason is the perception that the atmosphere may not have enough time to react to significant surface flux changes, and thus LSSs are not as important for short-range precipitation forecasts. Recent studies show that this is not always the case. Entekhabi *et al*. (1999) report an improvement in the threat score of 36-h precipitation forecast by a weather prediction model when coupled to a more sophisticated LSS. The improvement is of the same order as a doubling of the resolution of the atmospheric model; a similar result was also obtained by Wen *et al*. (2000a). The latter evaluated the effects of two LSSs coupled to a mesoscale atmospheric model, and showed that the simulated precipitation over a 48-h period does depend on the LSS used. In addition, the

Climate and Hydrology in Mountain Areas. Edited by C. de Jong, D. Collins and R. Ranzi
© 2005 John Wiley & Sons, Ltd. ISBN: 0-470-85814-1

partitioning of the simulated sensible and latent heat flux also changes. The sensitivity of simulated short-range precipitation to LSS is important for flood prediction because the single most uncertain variable in this case is the precipitation.

In addition to improving short-range precipitation, a mesoscale atmospheric model coupled to an LSS offers the potential of a longer lead time for flood prediction compared to other means of precipitation forecast. The displacement of rain cells obtained from radars based on Lagrangian advection offer a predictability lead time of up to 3 h (Zawadzki *et al*. 1994); the use of composite radars could extend this up to 6 h (Germann and Zawadzki 2002). The predictability depends on the spatial scale considered. The predictability limit using precipitation from rain gauges is likely to be shorter than with radars because the gauge coverage is usually not sufficient. The representativeness of rain gauge data is a classic problem in hydrological applications. As an alternative, the use of precipitation from mesoscale models could extend the predictability limit to beyond several hours. For example, Wen *et al*. (2000a) showed that a reasonable 48-h simulation of precipitation is obtained with a mesoscale model coupled to an LSS when compared with observed values from rain gauges. This could potentially provide a longer lead time in flood forecast.

Other studies have examined the coupling of atmospheric and hydrological models. Georgakakos and Hudlow (1984) advocated the use of coupled cloud, soil moisture, and channel routing models for hydrological applications. They also proposed an assimilation procedure for ingesting rainfall and flow data to update the model state. The use of rainfall from such cloud models successfully extended the lead time of rainfall and flow prediction (Georgakakos 1986a, b). Operational applications have also been made (Bae *et al*. 1995; Georgakakos 2002). Vörösmarty *et al*. (1993) discuss different aspects of macroscale hydrological models, with an emphasis on linkage to atmospheric models. Some key problems in the coupling of these models are discussed and summarized in Schultz *et al*. (1995). Benoit *et al*. (2000) used one-way coupling to drive a hydrological model, with precipitation from a mesoscale atmospheric model. In this way, hydrological basins can be used as macrorain gauges to verify the precipitation from atmospheric models. Pietroniro *et al*. (2001) examined different levels of coupling, leading to a fully interactive coupled meteorological–hydrological model. Seuffert *et al*. (2002) used a coupled mesoscale atmospheric model and a land surface hydrological model to study regional weather. The atmospheric models have improved over the years in resolution and physical parameterizations, which will help improve precipitation forecast. This is important because precipitation is the single most uncertain parameter in flash flood prediction.

LSSs coupled to weather prediction models generally do not generate runoff, as lateral flow processes are not resolved in the LSS. As runoff is important for flood simulation, the LSS needs to be modified. Wen *et al*. (2000b) and Lin *et al*. (2002) did this using a field capacity threshold interflow generation in an LSS, which was subsequently coupled to a mesoscale atmospheric model. A router was then used to obtain a hydrograph. This approach would help answer the first priority science question posed by Entekhabi *et al*. (1999) in their agenda for land surface hydrology research: ''What are the mechanisms and pathways by which the coupling between surface hydrological systems and the overlying atmosphere modulate weather and climate variability?'' by determining the contributions of land–atmosphere coupling to severe precipitation and flood events.

In this paper, we report on a coupled meteorological–hydrological modelling system consisting of a mesoscale atmospheric model, a runoff-generating LSS, and a router. The system is described in Section 15.2. Each component of the system is tested in an uncoupled stand-alone mode in Section 15.3, and the coupled model is applied to the flood that occurred in the Saguenay region of Québec, Canada in July 19–21, 1996, in Section 15.4. The conclusions are presented in the final section.

15.2 DESCRIPTION OF THE MODELLING SYSTEM

The meteorological–hydrological modelling system consists of a mesoscale atmospheric model, coupled interactively to an LSS that generates runoff, and a routing module that is run off-line. We now describe each of the components and the coupling procedure.

The atmospheric model is the Mesoscale Compressible Community Model (MC2, Benoit *et al*. 1997) developed in Environment Canada. MC2 is a limited area, high-resolution 3-dimensional regional model with compressible non-hydrostatic dynamics and it uses a semi-Lagrangian treatment of advection. The treatment of physical processes includes a planetary boundary layer based on turbulent kinetic energy (Benoit *et al*. 1989), short- and long-wave radiation schemes with interactive clouds, shallow convective parameterization and Sundqvist parameterization (Sundqvist *et al*. 1989; Yu *et al*. 1998) for resolved scale condensation and Kuo's scheme for subgrid scale convection (Kuo 1974).

MC2 is a community model that is well documented in the literature; it has been used extensively in different studies in Canada and abroad. We shall describe the LSS and routing module in more detail.

An LSS is needed to provide lower boundary conditions to MC2 over land areas. The LSS is a modified version of the Canadian Land Surface Scheme (CLASS; Verseghy 1991; Verseghy *et al*. 1993), modified to generate runoff for flood simulation. The standard version of CLASS is a physically based 1-dimensional column model designed to represent the average characteristics of a grid square. It resolves three soil layers, and uses a ''mosaic'' approach to treat surface vegetation in a grid square. Each square includes up to four surface types: bare soil, snow cover alone, vegetation cover alone, and both snow and vegetation cover. The vegetation itself has four types: needleleaf trees, broadleaf trees, crops, and grass. The surface energy budget is resolved for each of the four surface types when present. The sensible and latent heat flux fed back to the atmosphere are the sums over the four surface types weighted by their area fractions. For the soil column, the depth-averaged temperature and soil moisture content are calculated at each time step for each of the three layers. The soil moisture flux between layers is obtained using Darcy's Law for a 1-dimensional fluid. The Green–Ampt method is used for infiltration, and hence for surface runoff when precipitation exceeds infiltration capacity and the surface ponding limit is reached. The soil moisture flux at the bottom of the third layer (baseflow) is calculated using the third layer hydraulic conductivity modified by a drainage parameter that depends on soil type. This is generally a reasonable approximation as the variation of the deep soil water content is small over the small time steps (less than 30 min) used in CLASS.

It is well known that interflow is important for flood events in humid and semi-humid regions like eastern Canada. However, the standard version of CLASS has no treatment of interflow, and the baseflow treatment is not appropriate for flood simulation when the soil moisture is improperly initialized. It is thus necessary to modify CLASS. The mechanisms of runoff generation in humid and semi-humid regions are relatively well understood and can in principle be modelled with great detail for a point location, hydrological element, or small experimental catchment, if all the model parameters are measured and calibrated, and initial and boundary conditions provided. However, the application of a sophisticated runoff generation method over a large catchment is strongly limited by the lack of data for initialization, calibration, and verification. This is especially true of a coupled meteorological–hydrological modelling system with a mesoscale atmospheric model, as tens of thousands of surface grid point points are involved. Another consideration is that, as these coupled models are usually run on supercomputers, the fine tuning of model parameters, common in hydrological modelling, is not readily done. We thus keep the modifications to CLASS for runoff generation as simple as possible. Any newly introduced model parameter is either defined using the existing CLASS database or obtained with minimum tuning. Finally, we wish to point out that our modification to CLASS is to improve its hydrological response to short-term rain events. At present, we do not plan to use the coupled system for long-term simulations, as the predictability of regional mesoscale atmospheric models is usually limited to a few days.

Our major modification to CLASS consists of the use of a field capacity threshold to allow for interflow generation and the introduction of a reservoir at the bottom of the third CLASS soil layer that is similar to the drainage parameterization of Dümenil and Todini (1992). The baseflow drainage in the standard version of CLASS proceeds at a rate governed by a hydraulic conductivity modified by a drainage parameter. Our numerical experiments show that this can result in a large overestimation of the baseflow if the soil moisture content is initialized at too high a value. The initialization of soil moisture is problematic in meteorological and hydrological models. We introduce a reservoir at the bottom of the third soil layer to moderate the baseflow, thus circumventing the initialization problem. For the interflow, we take it from the portion of soil moisture in the first CLASS layer that exceeds field capacity; the primary interflow mechanism is saturated and unsaturated matrix flow enhanced by macropore flow near the surface. The interflow is removed from the first layer at a rate given by the horizontal hydraulic conductivity (K_{HI}) modified by the local slope (s). According to Bear (1972), the ratio (a_r) of K_{HI} to the vertical hydraulic conductivity (K_{VI}) ranges from about 10 to 100 near the surface. K_{VI} is calculated in CLASS and thus the modified horizontal hydraulic conductivity can be obtained using a_r. The product of a_r and s is a tunable parameter. A similar approach is used by Soulis *et al*. (2000) to model interflow in CLASS. Any part of the interflow that is not removed at the end of each time step is added back to the soil moisture budget for the subsequent time step. The surface ponding limit (2 mm) in the standard version of CLASS was removed for surface runoff. The time step used in the coupled modelling system is dictated by the meteorological component, usually of the order of hundreds of seconds. Our experiments indicate that unless the precipitation rate is extremely large, the surface

ponding limit is not met when interflow is generated as described earlier.

The coupling between MC2 and the modified version of CLASS proceeds as follows. Seven atmospheric variables are needed to drive CLASS: short-wave and long-wave radiation, wind, temperature, humidity and pressure at the surface, and precipitation. These variables are provided by the atmospheric model at each time step. CLASS in turn provides the surface sensible and latent heat fluxes to the atmosphere. The latter are calculated using bulk transfer coefficients, and depend on the surface wind speed and the temperature and humidity gradients at the surface. The time step of the coupled MC2/CLASS model is dictated by the smaller time step of the atmospheric model, which is of the order of tens of seconds. The fully interactive coupling between the atmosphere and the LSS is through the sensible and latent heat fluxes.

The off-line routing module in the modelling system is the geomorphological instantaneous unit hydrograph (GUH). The GUH is simple to use; all but one parameter depend upon the geomorphology of the basin, and can be determined directly either from 1:50,000 maps or from remotely sensed data using geographic information system (GIS) methods. The remaining parameter is the mean streamflow velocity. As GUH parameter estimation is relatively independent of rainfall-runoff data, the GUH is a promising tool for calculating flows in small- and medium-sized ungauged catchments. The GUH was first introduced by Rodríguez-Iturbe and Valdés (1979) to link the catchment hydrological response given by the instantaneous unit hydrograph with its geomorphological parameters. The catchment is assumed to be drained by a perfect Horton network. Much research has been published on this subject since its introduction. The principal assumption of the GUH was examined by Wen (1991), and Rodríguez-Iturbe and Rinaldo (1997) provided a review. To make the GUH more practical, Wen *et al*. (1988) derived a generalized GUH expression for a Horton-type basin of any order. The GUH so derived is a function of Horton's bifurcation ratio, stream length ratio, stream area ratio, length of the highest-order channel, and a dynamic parameter, which is the mean streamflow velocity in the catchment. The GUH can be time varying during the course of a storm, through the time-varying streamflow velocity. The geomorphological parameters can be determined directly from the basin geomorphology, whereas the streamflow velocity can be obtained using historical data or methods appropriate for ungauged catchments (Wen *et al*. 2001).

15.3 TESTING THE MODELLING SYSTEM IN UNCOUPLED MODE

We describe in this section the numerical experiments we have conducted to test each of the components of the modelling system in an uncoupled stand-alone mode. This is a necessary step in the development of a coupled modelling system. The mesoscale atmospheric model MC2 is tested by comparing the simulated precipitation with radar-retrieved and rain gauge values. The land surface scheme CLASS is tested using observed soil moisture data from two agricultural sites in Québec, Canada, and observed sensible and latent heat flux values from the Mackenzie GEWEX Study (MAGS). Finally, the GUH is tested using data from flood events in China.

Yu *et al*. (1998) compared the precipitation simulated by MC2 with values retrieved from the McGill University radar, using two heavy rain cases in the Montréal region, Canada. The LSS used in MC2 is the force–restore scheme (Deardorff 1978), a diffusion-based scheme that is much simpler than CLASS. The goal is thus to test the atmospheric component itself. The first case (October 14–15, 1995) is used to calibrate model parameters, whereas the model is applied with no further tuning to the second case (November 8–9, 1996). The calibration takes into account uncertainty in the values of cloud parameters by varying them within reasonable ranges based on experimental measurements. MC2 is run in a self-nesting mode, with spatial resolution of 50, 18, and 6 km. The radar-retrieved precipitation is obtained from the Marshall Radar Observatory of McGill University, and is first corrected using rain gauge observations through a multiplicative factor. The mean precipitation rates for the two cases are simulated well over a domain of radius 100 km centered at Montréal, the area of coverage of the radar. The banded precipitation features are reproduced well. The model also successfully simulates the precipitation intensity, with the difference between MC2 and radar estimates being the same order as the uncertainty of the radar values, which is estimated to be about ±50%. Time correlation studies were also performed with a sliding time window. The results show that the model has phase errors, with the model precipitation taking place before or after the actual precipitation at a given location. The typical time shift increases from about ±1 to ±3 hours as the forecast lead time increases from 2 to 24 h.

MC2 with the force–restore LSS, denoted as MC2/force–restore, is then applied with no further tuning to the flash flood case that occurred in the Saguenay region of Québec, Canada during July 19–21, 1996. Initial simulations were performed at a resolution of 35 and 10 km (Yu *et al*. 1997). The simulated

48-hour accumulated precipitation is compared point by point with values from 46 stations in the Saguenay region. Regression lines from a least-square best fit show an improvement of the simulated precipitation with resolution. Qualitative evaluation of the rain distribution is performed by comparison with GOES satellite image of brightness temperature; the spatial structure compares well. Quantitative measures (mean bias and root-mean-square error) are also used to determine the quality of the simulation. The maximum accumulated precipitation over the model domain is 274.4 mm, compared with the simulated maximum of 205.0 mm at 10 km resolution. The bias improves from −23.5 to −14.3 mm as the resolution is improved from 35 to 10 km. Similarly, the root-mean-square (RMS) error decreases from 58.3 to 48.6 mm. As the precipitation system is largely topographically forced, a higher resolution improves the topography in the model, and thus the quality of the precipitation simulation. The highest topography in the Saguenay region in the model domain reaches 1086 m. Our results show the importance of model resolution in simulating precipitation in mountainous areas.

We now turn to testing the land surface scheme CLASS in a stand-alone mode. The first test (Wen *et al*. 1998) examines the CLASS soil moisture regime that is important for runoff generation, through a comparison of the simulated soil moisture content with values retrieved from two experimental agricultural sites in Québec, Canada, for the 1993 growing season (Figure 15.1). For depths of 0–0.45 m and 0–0.90 m of the soil column, the simulated values are within one standard deviation of the measured values, indicating CLASS can reproduce the soil moisture variability over a relatively large depth. Wen *et al*. (1998) present an error analysis of the soil moisture measurements. The agreement in the surface layer (0–0.15 m) is not as good, but the major features are still captured. Observed precipitation and other atmospheric parameters from a meteorological station are used to drive the column model.

The second test of CLASS (Rodgers 2002) uses data from the Mackenzie GEWEX Study (MAGS),

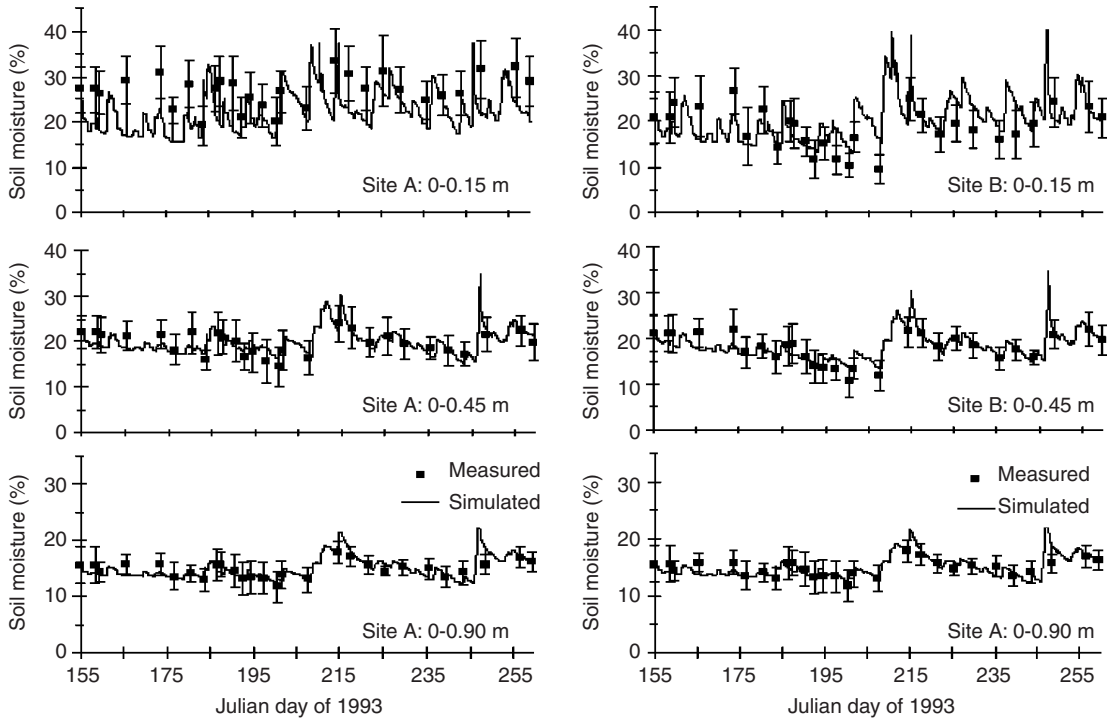


Figure 15.1 A comparison of the soil moisture content simulated by CLASS (solid line) with observed values (dots) for two agricultural sites in Québec, Canada over the 1993 growing season. The left and right panels correspond to sites A and B respectively. For each site, the comparison is done for three depths (0–0.15, 0–0.45, and 0–0.90 m) of the soil column. Taken from Wen L, Gallichand J, Viau AA, Delage Y, Benoit R (1998) Calibration of the CLASS model and its improvement under agricultural conditions. *Trans ASAE* **41**: 1345–1351. Reproduced by permission of ASAE

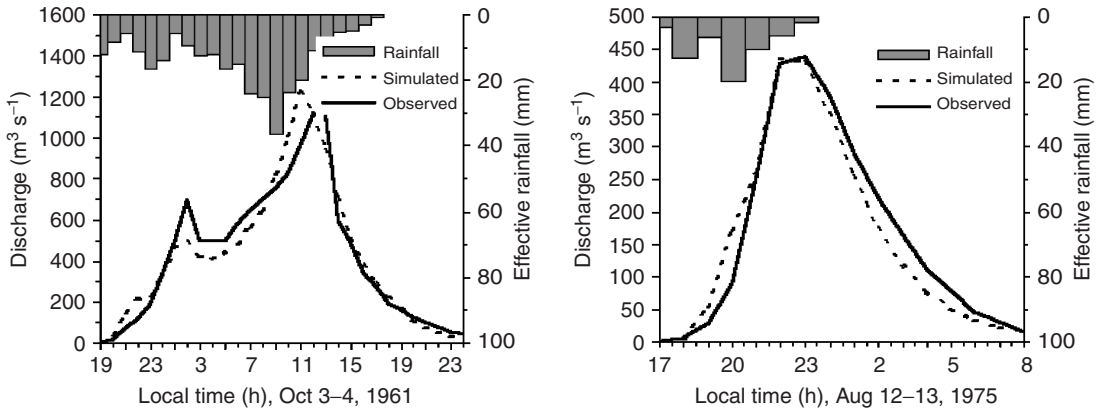


Figure 15.2 A comparison of simulated and observed hydrographs for two flood events (October 3–4, 1961; August 12–13, 1975) in the Hong Jia Ta catchment located in the Zhejiang Province of China. The rainfall is obtained from gauge measurements and the GUH is used for the simulated hydrographs

the principal Canadian contribution to the international GEWEX project. Observations taken during Canadian GEWEX Enhanced Study (CAGES) over the period July to September 1999 are used to evaluate the simulated sensible and latent heat fluxes. The field sites are located at two subarctic tundra sites in the Trail Valley Creek drainage basin in the Mackenzie River delta, Northwest Territories, Canada. CLASS is run in a stand-alone mode from July 2 to September 30, 1999, initialized with observations and driven with observed meteorological forcing variables. The simulated sensible and latent heat fluxes averaged over a diurnal cycle are compared with observed values, using different diagnostic statistics (mean bias error, RMS error, index of agreement). The CLASS forcing variables and the latent and sensible heat fluxes are all measured as part of CAGES. The results show the latent heat flux is underestimated by the model and the sensible heat flux is overestimated, with the mean bias and RMS errors of order 20–30 W/m^2 and 40–60 W/m^2 respectively. The magnitude of these errors can be reduced by at least 50% through further modifications to CLASS that take into account the organic soil nature of the site (Letts *et al*. 2000) and the local hummock hollow microtopography (Rodgers 2002). We will not focus on these modifications in this paper because they are site specific. For the purpose of coupled meteorological–hydrological modelling, we note that it may not be possible to reduce the errors in sensible and latent heat fluxes much below several tens of W/m^2 because errors in the radiative fluxes themselves in atmospheric models are of this order (Feng 2001). The major source of error is the inadequate treatment of clouds.

The final component to be tested in a stand-alone mode is the generalized GUH used for routing. To do this, we use data from 252 flood events over 25 catchments from the Zhejiang Province of China. This province is located in China's southeastern coast, and extends from 27°12′ to 31°31′N latitude, and 118° to 123°E longitude. The 25 catchments are part of the Xin An-Jiang basin and range in area from 16.3 to 330 km^2. All but one of the GUH parameters are obtained either from 1:50,000 maps or from remote sensing data using GIS methods. The remaining parameter, the mean streamflow velocity, is determined using methods discussed in Wen *et al*. (2001) for both gauged and ungauged catchments. Observed hydrographs are used only for model verification. An example of the results of a comparison of simulated and observed hydrographs is shown in Figure 15.2 for two flood events (October 3, 1961 and August 12, 1975) in the Hong Jia Ta catchment.

This is a fifth order Horton basin with a drainage area of 151 km^2. The agreement is good, and is typical of most of the 252 flood cases examined. The GUH is thus a good tool for flash flood routing.

15.4 APPLICATION OF THE COUPLED MODELLING SYSTEM TO THE 1996 SAGUENAY, QUÉBEC FLOOD

We now describe two studies that use the modelling system to study the severe precipitation and flash flood events that occurred in July 19–21 in the Saguenay region of Québec. The first (Wen *et al*. 2000a) focuses on the precipitation simulated by MC2 coupled to the standard version of CLASS. The second (Lin *et al*.

2002) uses MC2 coupled with the modified version of CLASS that allows for runoff generation as described in Section 15.2, together with the GUH run off-line to generate a hydrograph at the outlet of the Ha! Ha! Lake in the Saguenay region.

The synoptic situation that gave rise to the severe precipitation and flash flood is as follows. Heavy rain and early snowmelt in the spring of 1996 resulted in near saturated soil moisture. On July 18, 1996, a small low-pressure system with a central sea level pressure of 1002 mb, which had originated in southern Manitoba, formed and slowly deepened as it moved eastward. When the system reached the Saguenay region in Québec, the system deepened rapidly, with a pressure drop of 20 mb. Over the next 48 h (July 19–21), the low pressure stalled over the Gaspé Peninsula of Québec, resulting in intense precipitation. The observed maximum value of the 48-h accumulated precipitation was over 270 mm in the Saguenay region, several times larger than the maximum record of the past 120 years. The subsequent flooding led to a loss of life and widespread property damage.

Wen *et al*. (2000a) examined the precipitation of the Saguenay storm simulated by MC2 coupled to two LSSs: force–restore and the standard version of CLASS. As mentioned earlier, the role of LSSs in long-term climate simulations is well recognized, but its role in short-range precipitation forecasts is less clear. Our results show that the impact of LSSs can be significant for the latter as well, especially in regions of complex vegetation variations. The resolution of the coupled models is 10 and 5 km. Figure 15.3 shows a comparison of the simulated 48-h accumulated precipitation with 46 rain gauge measurements for MC2/force–restore and MC2/CLASS in the Saguenay region. The best results are obtained with the more sophisticated land surface scheme (CLASS) at the higher resolution (5 km). In addition, MC2/CLASS at 10 km resolution performs better than MC2/force–restore at 5 km. This is due to the higher effective resolution of CLASS, as it resolves surface vegetation characteristics within a grid box, which is not the case for the force–restore LSS (Wen *et al*. 2000a).

Figure 15.4 shows the sensitivity of the simulated accumulated precipitation to surface vegetation characteristics. The results for four 10-km MC2/CLASS runs (actual vegetation, uniform coniferous trees, bare soil, grass) and MC2/force–restore are shown. The difference

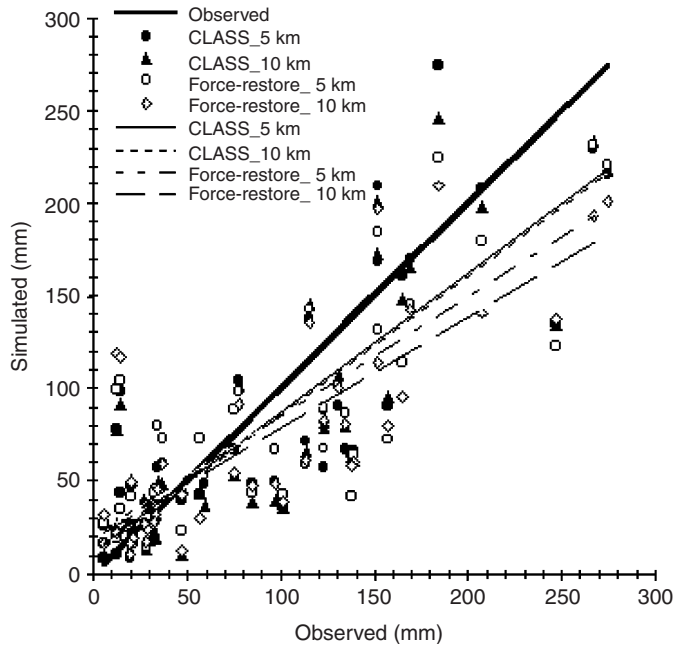


Figure 15.3 A scatter plot of the 48-h accumulated precipitation (mm) from MC2/CLASS and MC2/force–restore at 10- and 5-km resolution versus observations (45° line) from 46 rain gauges in the Saguenay region in Québec, Canada. Regression lines from a least-square best fit are also shown. From Wen L, Yu W, Lin CA, Béland M, Benoit R, Delage Y (2000a) The role of land surface schemes in short-range, high spatial resolution forecasts. *Mon Weather Rev* **128**: 3605–3617. Reproduced by permission of American Meteorological Society

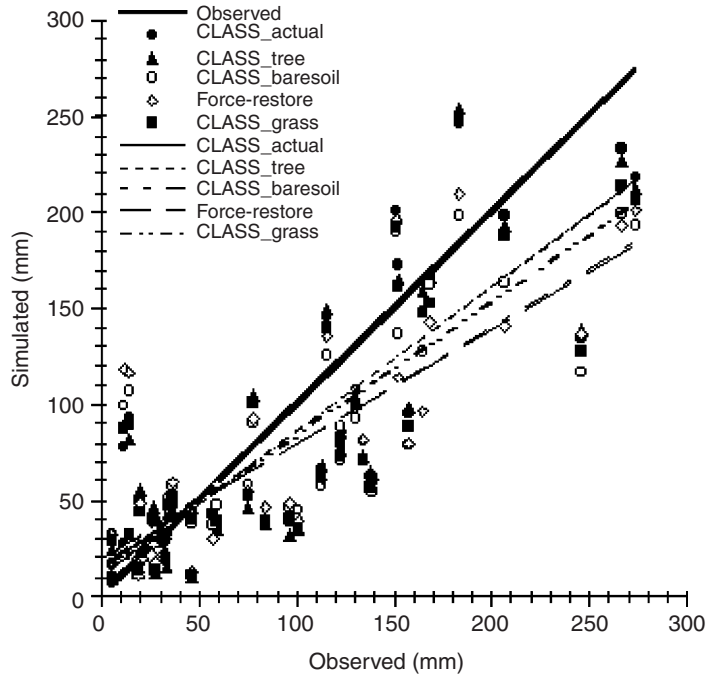


Figure 15.4 A scatter plot of the 48-h accumulated precipitation (mm) obtained with different surface vegetation conditions versus observed values from 46 gauges in the Saguenay region in Québec, Canada. Results from four MC2/CLASS runs with vegetation conditions of normal, uniform coniferous trees, grass, bare soil, and MC2/force–restore are shown. The resolution is 10 km. From Wen L, Yu W, Lin CA, Béland M, Benoit R, Delage Y (2000a) The role of land surface schemes in short-range, high spatial resolution forecasts. *Mon Weather Rev* **128**: 3605–3617. Reproduced by permission of American Meteorological Society

between MC2/CLASS with actual vegetation conditions and coniferous trees is small. This is because for the actual conditions, mixed forest consists of coniferous and deciduous trees, and the former dominates in the Saguenay region. The difference between bare soil and force–restore is also small, as there is no physically based vegetation treatment in the force–restore scheme. We see from Figure 15.4 that there is sensitivity of the simulated precipitation to surface characteristics. In fact, this sensitivity is comparable to a doubling of spatial resolution (Figure 15.3). We also note that surface characteristics have a direct influence on sensible and latent heat flux, and only indirectly affects precipitation through cloud formation. Thus, the sensitivity of precipitation to the treatment of surface characteristics is lower compared to that of heat fluxes. In fact, Wen *et al*. (2000a) showed that the partition between sensible and latent heat fluxes is quite different between MC2/CLASS and MC2/force–restore, with their sums remaining about the same.

Finally, we describe the results using MC2 coupled to the modified version of CLASS that generates runoff. The study area is the Ha! Ha! River basin with a drainage area of 567 km^2 and is located in the mountainous and forested area of the Saguenay region. The basin extends about 45 km in the north–south direction and about 14 km in the east–west direction, with the Ha! Ha! River flowing from south to north. Figure 15.5 shows the study area and Table 15.1 shows a summary of the basin characteristics. We use our modelling system to reconstruct the hydrograph at the outlet of the Ha! Ha! Lake in the southern Ha! Ha! River basin. The southern basin has an area of 250 km^2 and is covered by six 10×10 km MC2 grid points. We first examine the precipitation simulated at these six grid points, and compare them with the nearest available gauge measurement located 20 km to the south (Station No. 7043713; Figure 15.6). The initial underestimation of the precipitation is due to the spin-up of the model. The overall agreement is very good, thus giving us confidence in the subsequent hydrograph calculation.

Figure 15.7 shows the hydrograph simulated at the outlet of the Ha! Ha! Lake. The effective precipitation from the six grid points in MC2 coupled to the modified

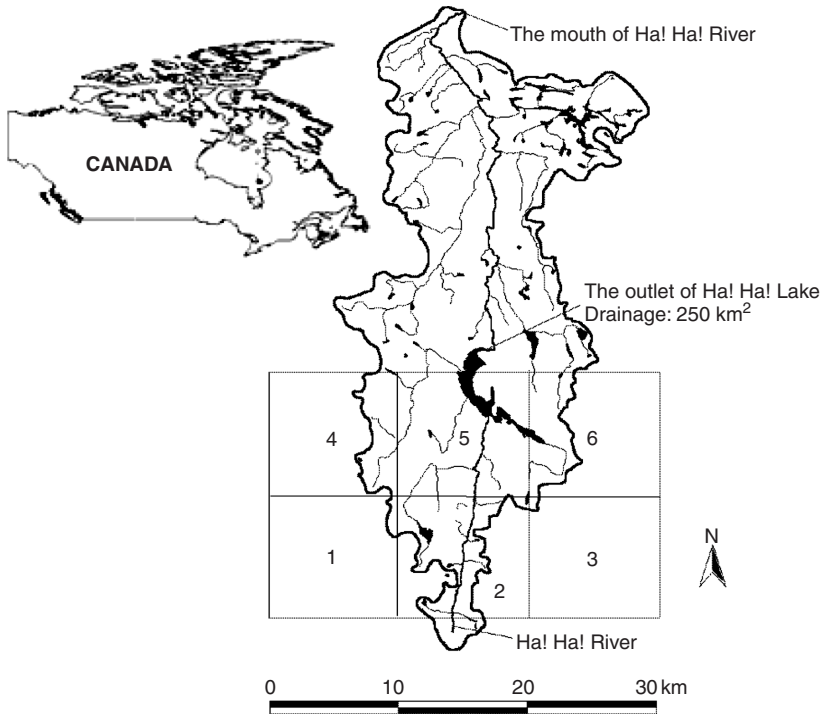


Figure 15.5 The Ha! Ha! River basin, with six model grid points (labelled 1 to 6) covering the southern basin. From Lin CA, Wen L, Béland M, Chaumont D (2002) A coupled atmospheric-hydrological modeling study of the 1996 Ha! Ha! river basin flash flood in Québec, Canada. *Geophys Res Lett* **29**: 10.1029/2001GL013827. Reproduced by permission of American Geophysical Union

Table 15.1 Physical characteristics of the Ha! Ha! River basin

	Catchment
Name of the basin/area	Ha! Ha! River basin
Mountain range	Laurentians
Elevation range of the entire catchment (m)	0–1120
Elevation range of individual sites (m)	300–1120
Latitude and longitude	48°16′N 70°52′W
Area in km^2	567
Geology	Granite and gneissic rocks
% glacierised	100
Vegetation type (dominant)	Mixed coniferous
% forested	100
Mean Q at catchment outlet (mm/year)	460

version of CLASS is used to drive the GUH routing module offline. The geomorphological parameters of the basin are obtained using GIS methods, and the streamflow velocity is determined using the method proposed by Wen *et al*. (2001) for an ungauged catchment. The total runoff at the outlet is 312 million m^3, which agrees with the runoff of 322 million m^3 of another reconstructed hydrograph obtained with a different hydrological model and source of precipitation (Lapointe *et al*. 1998). There is a significant time difference between the time of peak precipitation and peak flow in their study (over 30 h) compared to our study (about 8 h). Although the precipitation sources used are different, the peak precipitation and its timing are similar in the two studies. It is thus unclear why the time lag in Lapointe *et al*. (1998) is much longer than in Lin *et al*. (2002). However, our experience with flood events in basins in China of similar size and characteristics suggests the time lag between peak precipitation and peak flow should be much less than 30 h. There are no observed flow data available at the Ha! Ha! River basin for model verification. We chose this case for study, as it was a big flood event in Canada, ranking as the sixth most costly natural disaster event in the country. Our study, using a coupled model, offers a comparison study with Lapointe *et al*. (1998) for this case.

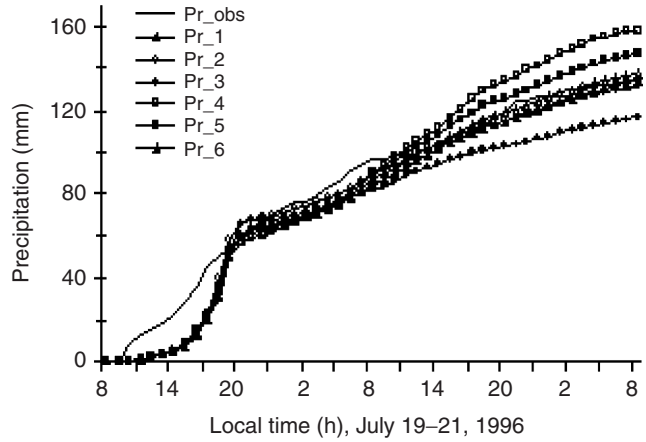


Figure 15.6 A comparison of the 48-h model precipitation from MC2/CLASS for the six grid points ($Pr_1, \ldots, Pr_6$) covering the southern Ha! Ha! River basin with observed values from the nearest gauge (No. 7043713) located 20 km to the south of the basin. From Lin CA, Wen L, Béland M, Chaumont D (2002) A coupled atmospheric-hydrological modeling study of the 1996 Ha! Ha! river basin flash flood in Québec, Canada. *Geophys Res Lett* **29**: 10.1029/2001GL013827. Reproduced by permission of American Geophysical Union

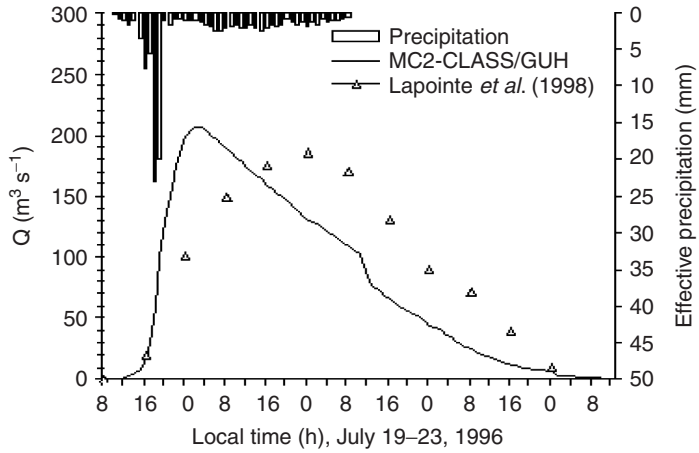


Figure 15.7 A comparison of two reconstructed hydrographs at the outlet of the Ha! Ha! Lake in the southern Ha! Ha! River basin. The solid line shows results from our coupled meteorological–hydrological modelling system, and the triangles are taken from the study by Lapointe *et al*. (1998). The simulation starts at 8 AM local time on July 19. See text for further discussion. From Lin CA, Wen L, Béland M, Chaumont D (2002) A coupled atmospheric-hydrological modeling study of the 1996 Ha! Ha! river basin flash flood in Québec, Canada. *Geophys Res Lett* **29**: 10.1029/2001GL013827. Reproduced by permission of American Geophysical Union

15.5 CONCLUSIONS

We have summarized a series of studies that were undertaken to develop, test, and implement a coupled meteorological–hydrological modelling system for flood prediction. Precipitation forecasts from high-resolution mesoscale atmospheric models are now developed to a stage where these might be sufficiently accurate to drive hydrological models for flood prediction. If this is the case, the prediction lead time can then be increased compared to other means of forecasting precipitation, such as using displacement algorithms with radar or rain gauge values. The potential increase in lead time is important as precipitation

is the single most uncertain unknown in forecasting flash floods.

The modelling system consists of a mesoscale atmospheric model (MC2) coupled to a land surface scheme (CLASS) modified to generate runoff. The GUH is run off-line as a routing module to generate a hydrograph. The LSS is the interface between the atmosphere and the hydrological regime, and the coupling between the two is through the sensible and latent heat fluxes. CLASS is driven by seven atmospheric variables (short-wave and long-wave radiation, wind, temperature, humidity and pressure at the surface, and precipitation) furnished by the atmospheric model, and it returns the sensible and latent heat flux to the atmosphere, thus providing feedback and completing the coupling.

Each component of the modelling system is first tested in a stand-alone mode. The precipitation simulated by MC2 is evaluated using values retrieved from radar and rain gauges. The results for the accumulated precipitation show that the model errors are within the errors of the radar, and there is a phase error in the timing of the precipitation. The soil moisture content and sensible and latent heat fluxes simulated by CLASS in a stand-alone mode are compared with values from two agricultural sites in Québec, Canada, and the Trail Valley Creek site in Northwest Territories, Canada. The latter is in the Mackenzie Basin, the study site of the Canadian GEWEX program. It is important to verify the accuracy of the sensible and latent heat fluxes, as they provide the feedback to the atmosphere from the LSS. These fluxes are simulated to an accuracy of several tens of W/m^2, which is the limit of accuracy of regional atmospheric models, as the radiative fluxes have errors of this order. Finally, the GUH is tested using 252 flood events over 25 catchments from the Zhejiang Province of China.

After testing the model components in a stand-alone mode, we apply the coupled modelling system to the Saguenay flood that occurred in Québec, Canada in July 19–21, 1996. A hydrograph at the Ha! Ha! Lake in the southern Ha! Ha! River basin is generated using the modelling system, which is compared with another reconstructed hydrograph published in the literature. No observed flow data during the flood are available for model verification. The precipitation used to derive the hydrograph is verified against station observations, and the results are good. We believe that the results of this proof-of-concept study of using a coupled meteorological–hydrological modelling system for flood simulation are encouraging, and the modelling system should be tested with additional flash flood cases for further verification.

REFERENCES

Bae DH, Georgakakos KP, Nanda SK (1995) Operational forecasting with real-time databases. *ASCE J Hydraulics Div.* **121**: 49–60.

Bear J (1972) *Dynamics of Fluids in Porous Media*. Dover Publisher, New York.

Benoit R, Côté J, Mailhot J (1989) Inclusion of a TKE boundary layer parameterization in the Canadian regional finite-element model. *Mon Weather Rev* **117**: 1726–1750.

Benoit R, Desgagné M, Pellerin P, Pellerin S, Chartier Y, Desjardins S (1997) The Canadian MC2: a semi-lagrangian, semi-implicit wide-band atmospheric model suited for fine-scale process studies and simulation, *Mon Weather Rev* **125**: 2382–2415.

Benoit R, Pellerin P, Kouwen N, Ritchie H, Donaldson N, Joe P, Soulis ED (2000) Toward the use of coupled atmospheric and hydrologic models at regional scale. *Mon Weather Rev* **128**: 1681–1706.

Deardorff JW (1978) Efficient prediction of ground surface temperature and moisture, with inclusion of a layer of vegetation. *J Geophys Res* **83**(C4): 1889–1903.

Dümenil L, Todini E (1992) A rainfall-runoff scheme for use in the Hamburg climate model. In: O'Kane JP (ed) *Advances in Theoretical Hydrology, A Tribute to James Dooge*. Elsevier, Amsterdam, pp. 129–157.

Entekhabi D, Asrar GR, Betts AK, Beven KJ, Bras RL, Duffy CJ, Dunne T, Koster RD, Lettenmaier DP, McLaughlin DB, Shuttleworth WJ, van Genuchten MT, Wei MY, Wood EF (1999) An agenda for land surface hydrology research and a call for the second international hydrological decade. *Bull Am Meteorol Soc* **80**: 2043–2058.

Feng J (2001) Solar radiation in the Mackenzie river basin: retrieval from satellite measurements and evaluation of atmospheric models. Ph.D. thesis, McGill University.

Georgakakos KP (1986a) A generalized stochastic hydrometeorological model for flood and flash-flood forecasting, 1 formulation. *Water Resour Res* **22**: 2083–2095.

Georgakakos KP (1986b) A generalized stochastic hydrometeorological model for flood and flash-flood forecasting, 2 case studies. *Water Resour Res* **22**: 2096–2106.

Georgakakos KP (2002) US corporate technology transfer in hydrometeorology. *J Hydroinformatics* **4**: 3–13.

Georgakakos KP, Hudlow MD (1984) Quantitative precipitation forecast techniques for use in hydrologic forecasting. *Bull Am Meteorol Soc* **65**: 1186–1200.

Germann U, Zawadzki I (2002) Scale-dependence of the predictability of precipitation from continental radar images. Part I: Description of the methodology. *Mon Weather Rev* **130**: 2859–2873.

Kuo HL (1974) Further studies of the parameterization of the influence of cumulus convection of large-scale flow. *J Atmos Sci* **31**: 1232–1240.

Lapointe MF, Secretan Y, Driscoll SN, Bergeron N, Leclerc M (1998) Response of the Ha! Ha! river to the flood of July 1996 in the Saguenay region of Québec: large-scale avulsion in a glaciated valley. *Water Resour Res* **34**: 2383–2392.

Letts MG, Roulet NT, Comer NT, Skarupa MR, Verseghy DL (2000) Parameterization of peatland hydraulic properties for the Canadian land surface scheme. *Atmos-Ocean* **38**: 141–160.

Lin CA, Wen L, Béland M, Chaumont D (2002) A coupled atmospheric-hydrological modeling study of the 1996 Ha! Ha! river basin flash flood in Québec, Canada. *Geophys Res Lett* **29**: 10.1029/2001GL013827.

Pietroniro A, Soulis ED, Snelgrove K, Kouwen N (2001) A framework for coupling atmospheric and hydrological models. In: Dolman AJ, Hall AJ, Kavvas ML, Oki T, Pomeroy JW (eds) *Soil-Vegetation-Atmosphere Transfer Schemes and Large-Scale Hydrological Models*. IAHS Publication No. 270, IAHS Press, pp. 27–34.

Rodgers D (2002) Validating Canadian land surface scheme heat fluxes under subarctic tundra conditions. M.Sc. thesis, Department of Atmospheric and Oceanic Sciences, McGill University.

Rodríguez-Iturbe I, Rinaldo A (1997) *Fractal River Basins Chance and Self-Organization*. Cambridge University Press.

Rodríguez-Iturbe I, Valdés JB (1979) The geomorphologic structure of hydrologic response. *Water Resour Res* **15**: 1409–1420.

Schultz GA, Hornbogen M, Viterbo P, Noilhan J (1995) *Coupling Larger-Scale Hydrological and Atmospheric Models*. IAHS Special Publication No. 3, IAHS Press.

Seuffert G, Gross P, Simmer C, Wood EF (2002) The influence of hydrologic modeling on the predicted local weather: two-way coupling of a mesoscale weather prediction model and a land surface hydrologic model. *J Hydrometeorol* **3**: 505–523.

Soulis ED, Snelgrove K, Kouwen N, Seglenieks F, Verseghy DL (2000) Towards closing the vertical water balance in Canadian atmospheric models: coupling of the land surface scheme CLASS with the distributed hydrological model WATFLOOD. *Atmos.-Ocean* **38**: 251–269.

Sundqvist H, Berge E, Kristjánsson JE (1989) Condensation and cloud parameterization studies with a mesoscale numerical weather prediction model. *Mon Weather Rev* **117**: 1641–1657.

Verseghy DL (1991) CLASS-a Canadian land surface scheme for GCMS, I. soil model. *Int J Climatol* **11**: 111–133.

Verseghy DL, McFarlane NA, Lazare M (1993) CLASS-a Canadian land surface scheme for GCMS, II. vegetation model and coupled runs. *Int J Climatol* **13**: 347–370.

Vörösmarty CJ, Gutowski WJ, Person M, Chen TC, Case D (1993) Linked atmosphere-hydrology models at the macro-scale. In: Wilkinson WB (ed) *Macro-Scale Modeling of the Hydrosphere*. IAHS Publication No. 214, pp. 3–27.

Wen K, Li Q, Lu WX (1988) A generalized R-V geomorphologic instantaneous unit hydrograph expression and its application (in Chinese). *J Hydrometeorol* **45**(3): 20–25.

Wen L (1991) The principle assumption of the GUH model. Master of Engineering Science Thesis, National University of Ireland, Galway.

Wen L, Gallichand J, Viau AA, Delage Y, Benoit R (1998) Calibration of the CLASS model and its improvement under agricultural conditions. *Trans ASAE* **41**: 1345–1351.

Wen L, Lin CA, Li Q, Wen K (2001) The geomorphological unit hydrograph-a practical tool for catchment flow computation. Technical Report R2001-70, CERCA (Centre de recherche en calcul appliqué), Montréal (Québec).

Wen L, Lin CA, Yu W, Béland M, Benoit B, Delage Y (2000b) Land-atmosphere coupling: a modeling study of precipitation, sensible and latent heat flux, and runoff simulations. *EOS Trans AGU* **81**(48): F30.

Wen L, Yu W, Lin CA, Béland M, Benoit R, Delage Y (2000a) The role of land surface schemes in short-range, high spatial resolution forecasts. *Mon Weather Rev* **128**: 3605–3617.

Yu W, Lin CA, Benoit R (1997) High resolution simulation of the severe precipitation event over the Saguenay, Québec region in July 1996. *Geophys Res Lett* **24**: 1951–1954.

Yu W, Lin CA, Benoit R, Zawadzki I (1998) High resolution model simulation of precipitation and evaluation with Doppler radar observation. *Water Sci Tech* **37**: 179–186.

Zawadzki I, Morneau J, Laprise R (1994) Predictability of precipitation patterns: an operational approach. *J Appl Meteorol* **33**: 1562–1571.

16

Operational Weather Radar Assessment of Convective Precipitation as an Input to Flood Modelling in Mountainous Basins

STEFAN UHLENBROOK[1] AND DOERTHE TETZLAFF[2]
[1]*UNESCO-IHE, Department of Water Engineering, Westvest 7, 2611 AX Delft,*
[2]*Department of Geography and Environment, University of Aberdeen, Aberdeen AB24 3UF, Scotland, UK*

16.1 INTRODUCTION

Floods are generated in mountainous basins by the complex interplay of precipitation input (i.e. rain as well as snow and ice melt) and temporally variable or constant basin characteristics (e.g. topography, soils, drainage network etc.). Therefore, firstly, for flood modelling, the understanding of flood runoff generation processes is crucial. In the last decade, numerous field investigations were performed, which were often coupled with model developments and applications. These studies focussed on identifying processes at the plot scale (e.g. Mosley 1982; Hornberger *et al*. 1991; Faeh *et al*. 1997), the headwater scale (e.g. McDonnell 1990; Hinton *et al*. 1994; Grayson *et al*. 1997; Anderson *et al*. 1997; Uchida *et al*. 2002), and the catchment scale (e.g. Merot *et al*. 1995; Uhlenbrook *et al*. 2002). A collection of state-of-the-art approaches is given in McDonnell and Tanaka (2001) and Uhlenbrook *et al*. (2003a). Secondly, the runoff processes need to be conceptualised adequately in the applied hydrological model. Therefore, more physically based (e.g. MIKE-SHE, Refsgaard and Storm 1996; WASIM-ETH, Schulla 1997) or more conceptual (e.g. TOPMODEL, Beven *et al*. 1995; HBV, Bergström 1992) model approaches were developed, which work in a distributed or semi-distributed manner. Each modelling approach has its strengths and shortcomings in consideration of the costs, applicability, and uncertainty, as discussed in several papers in Beven (2002). An overview of current process-oriented model developments is also given by Uhlenbrook *et al*. (2003a). Thirdly, the required input data for the model needs to be in an appropriate spatial and temporal resolution. Regarding rainfall input, this is difficult, in particular in mountainous basins, as precipitation is often very localised (e.g. Woods *et al*. 2000) and diverse along altitudinal gradients (e.g. Gurtz *et al*. 1997).

For flood modelling in heterogeneous catchments with an inadequate consideration of rainfall, variability can cause significant errors (e.g. Milly and Eagleson 1988; O'Loughlin *et al*. 1996; Koren *et al*. 1999). In many studies, an improvement of rainfall-runoff modelling owing to the use of distributed rainfall input data is shown (e.g. Schilling and Fuchs 1984; Quirmbach *et al*. 1999; Sun *et al*. 2000; Boyle *et al*. 2001). The increase of simulated runoff volumes with stronger consideration of rainfall heterogeneity was reported, for example, by Michaud and Sorooshian (1994) for a semi-arid 150-km^2 watershed and Winchell *et al*. (1998) for a medium-sized catchment with intense convective summer storm events. In contrast, Faures *et al*. (1995) found for a small catchment of some hectares a decrease in simulated

Climate and Hydrology in Mountain Areas. Edited by C. de Jong, D. Collins and R. Ranzi
© 2005 John Wiley & Sons, Ltd. ISBN: 0-470-85814-1

runoff volume with increased rainfall disaggregation. This indicates the dependence on the number and location of the rain gauges and the implications on the calculated basin precipitation for an investigated event. However, with increasing catchment size, an increased heterogeneity of precipitation can be observed, and the goodness of simulated runoff depends largely on the representation of the spatial and temporal variability of basin precipitation (Arnaud *et al*. 2002). But this variability can be crucial also for small catchments of a few hectares, in particular, in semi-arid regions (Faures *et al*. 1995; Goodrich *et al*. 1995). Obled *et al*. (1994) found that runoff simulations were more sensitive to the spatial variability compared to the temporal variability of precipitation, whereas Krajewski *et al*. (1991) showed a higher influence of the temporal aspect compared to the spatial aspect. In general, the capturing of spatially and temporally limited rain cells is difficult even with a detailed network of ground stations (Terblanche *et al*. 2001). The partly contrary results of the various studies depend on the one hand on the investigated event and catchment characteristics, and on the other hand on the applied model and scale.

For linking rainfall and runoff responses, Woods and Sivapalan (1999) developed a method for analysing the spatial and temporal patterns for both processes. This approach allows assessing the importance of dominant runoff generation processes and their spatial distribution in a catchment and, thus, the necessity of considering the spatial and temporal variability in hydrological investigations, that is, modelling.

The application of rainfall radar data seems to be a suitable method for capturing detailed rainfall information for catchment modelling. In recent years, radar data were more and more used for hydrological applications, for example, Obled *et al*. (1991) for a mountainous watershed, Winchell *et al*. (1998) for a 100-km^2 catchment with special focus on saturation excess and infiltration excess overland flow, Quirmbach *et al*. (1999) for a 4-km^2 urban catchment, Lange *et al*. (1999) and Lange (1999) for a 1400-km^2 arid catchment, Ogden *et al*. (2000) for a 25-km^2 basin with high variability of land surface parameters and for convective storm investigations, and Carpenter *et al*. (2001) for a macro-scale watershed (4100 km^2).

Radar systems do not measure rainfall intensity itself but the reflectivity of radar beams by raindrops. The reflectivity is strongly dependent on drop size and precipitation type. Thus, the parameters $\alpha_{Z/R}$ and $\beta_{Z/R}$ from the $Z_{\text{radar}}/R_{Z/R}$ relation, which relate the radar reflectivity and the precipitation intensity, can vary considerably (e.g. Smith and Krajewski 1993; Pessoa *et al*. 1993; Ciach and Krajewski 1999; Quirmbach *et al*. 1999; Lange *et al*. 1999; Haase and Crewell 2000). The applicability of rainfall radar is strongly dependent on topography, distance from radar device, characteristics of the radar and precipitation characteristics. For instance, the radar may detect echoes from non-precipitation targets' so-called ground clutters, or the occurrence of hail may make the use of radar data impossible. In addition, the intensity of echoes decreases with increasing distance from radar because of the expansion of the radar beam and attenuation effects, and mountains can block the radar beam (Andrieu *et al*. 1997; Creutin *et al*. 1997).

For a correct transformation of radar reflectivities into rain intensities, the adjustment of the signals using ground station data is necessary (Adamowski and Muir 1989; Winchell *et al*. 1998; Seo *et al*. 1999; Quirmbach *et al*. 1999). But the differences in data collection can be problematic. The radar measures stepwise, for example, every five minutes. In contrast, the rain gauges record normally cumulative values over longer time steps. Additionally, ground data represent rainfall at a certain point, while the radar data average the reflectivity of raindrops of an air volume over the ground.

There are two main foci during radar data adjustment: (i) For the volume adjustment, the totally recorded rainfall amounts of ground data and radar data are compared, and (ii) for the distribution adjustment, the temporal distribution of the intensities (rain vs radar data) is considered (Maul-Kötter *et al*. 2001). After the decision, if either the volume or the intensity distribution is used as target value, the adjustment of measured reflectivities can occur (i) by application of a standard $Z_{\text{radar}}/R_{Z/R}$ relation with spatially and temporally uniform parameters (e.g. Sun *et al*. 2000; Ogden *et al*. 2000) or (ii) by using an event- and space-dependent $Z_{\text{radar}}/R_{Z/R}$ relation (e.g. Smith and Krajewski 1993; Hirayama *et al*. 1997; Winchell *et al*. 1998).

Numerous studies examined essential improvements in radar data quality by attenuation correction, considering of drop size distribution or vertical reflectivity profile correction (e.g. Sempere Torres *et al*. 1994; Uijlenhoet and Stricker 1999; Grecu and Krajewski 2000). This information was not available for the radar product used in this study. Hence, the operational available radar data in this study could only be corrected by using the available rainfall information from the ground stations.

Applications of radar data in mountainous catchments with their special problems due to the influence of topography are published in various studies (Delrieu *et al*. 1999; Jasper *et al*. 2002). A main error source is the affection by beam blockage as shown for instance by Andrieu *et al*. (1997) and Creutin *et al*. (1997). They

corrected beam blockage by using digital terrain models and vertical profiles of radar reflectivity variability. They recommended the use of S-band radar with a wavelength of 10 cm for minimising attenuation effects in Mediterranean regions with intense rain events. The nowcasting of precipitation on the basis of radar data in an Alpine region is examined by Mecklenburg *et al*. (2000). They found improvements by removing small-scale features by using larger tracking areas.

The central objective of this study is to investigate the significance of the spatial and temporal variability of convective precipitation for flood modelling in a mountainous basin. Therefore, the use of rainfall radar data in addition to a classical precipitation network for deriving basin precipitation is examined. The following questions are addressed in further details:

1. What might be the contribution of highly resoluted radar data to capture spatial and temporal variability of convective precipitation events in mountainous areas?
2. What is the significance of the distribution of basin precipitation during convective cells for flood modelling in mountainous catchments?
3. How can operational available radar data be used within a detailed hydrological model in an appropriate way?

16.2 MATERIAL AND METHODS

16.2.1 Study site

The study was performed at the meso-scale Brugga catchment (40 km^2), located in the Southern Black Forest Mountains, southwest Germany (Figure 16.1, Table 16.1). It is a pre-alpine mountainous catchment with a mean elevation that amounts to 986 m a.s.l. The bedrock consists of gneiss and is covered by a drift of glacial and periglacial origin with varying depths (0–10 m). Brown soils have mainly developed in this drift cover material. The morphology is characterised by

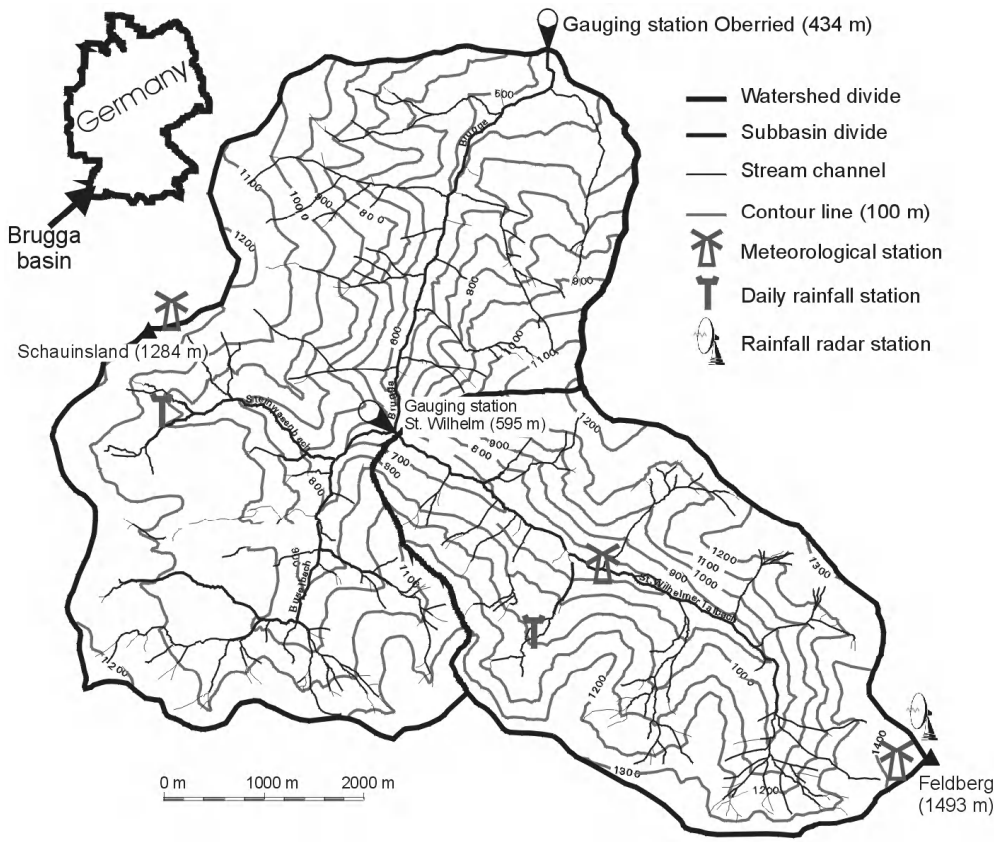


Figure 16.1 The Brugga basin with instrumentation network

Table 16.1 Basin characteristics of the Brugga basin and the sub-basin St. Wilhelmer Talbach

	Basin properties	
Name	Brugga	St. Wilhelmer Talbach
Mountain range	Black Forest Mountains	Black Forest Mountains
Elevation range	438–1493 m	633–1493
Area	40 km^2	15.2 km^2
Geology	Gneiss covered by drift	Gneiss covered by drift
Dominant vegetation type	Forest and pastureland	Forest and pastureland
% forested	71	73.4
Mean precipitation	1750 mm	1853 mm
Mean runoff	1195 mm	1301 mm
Mean evapotranspiration	555 mm	552 mm

moderate to steep slopes (75% of the area), hilltops and hilly uplands (about 20%), and narrow valley floors (less than 5%). The overall average slope is 19°, calculated with a $50 \times 50\,m^2$ digital elevation model. Owing to the strong variability of elevation, slope, and exposition caused by the deeply incised valleys, the catchment is characterised by a large heterogeneity of all climate elements, in particular, precipitation. This causes spatially and temporally very different elevation-precipitation gradients within the basin and articulated luv-lee effects. Further details about the basin can be found in Uhlenbrook (1999).

16.2.2 Database

Two runoff gauges are located at the outlets of the Brugga (40 km^2) and sub-basin St. Wilhelmer Talbach (15.4 km^2) (Figure 16.1). Two meteorological stations are situated within the basin, which record precipitation in 10-min intervals. At another two stations, the daily precipitation is measured. Additionally, nine rainfall stations from the State Institute for Environmental Protection Baden-Württemberg (Landesanstalt fuer Umweltschutz (LfU) Baden-Württemberg) are distributed around the basin, recording in temporal resolutions between 1 and 30 min. These stations are located in a circumference of maximal 30 km and at elevations between 200 and 1010 m a.s.l. Hence, for rainfall-runoff modelling, 13 rain gauges were available. For radar data calibration, the two stations with daily data were not considered because of the difficulties of comparing these data with the highly resoluted radar data.

The radar data came from a C-band Doppler radar with a wavelength of 3.75–7.5 cm. The rainfall radar station can be found near the highest point of the catchment at the peak of the Feldberg mountain (1493 m a.s.l.). The radar product is a quantitative DX product from the German weather survey. The spatial resolution is $1\,km \times 1°$ azimuth angle and has a temporal resolution of 5 min. The available data from 1998 have only coarse dBZ classes with 4-dBZ steps due to technical problems during this time period. These problems were solved in 1999, and from then on the resolution of dBZ values is 0.5. This resulted in relatively coarse rainfall intensity values for the events in 1998, which have to be considered by interpreting the results.

The radar data are operationally corrected for clutters by clutter maps by the German Weather Service (DWD). These clutter maps were compiled during a period when no precipitation echoes were relevant. There were neither distance nor vertical reflectivity profile corrections conducted. A detailed description of the DX product can be found at DWD (1997). Problems connected with these operational radar products are discussed in Lange *et al*. (2003) and Quirmbach (2003).

Three convective storm events in summer 1998 were investigated with measured maximum radar reflectivities of more than 36 dBZ at the two ground stations within the catchment. The calibrated radar data with a temporal resolution of 5 min were aggregated to hourly time steps as input for the TAC^D model. The original spatial resolution of the polar co-ordinate grid of $1\,km \times 1°$ azimuth angle was disaggregated to a $50 \times 50\,m^2$ grid as input for the TAC^D model using the GIS software Arc Info.

16.2.3 Calibration of radar data

Radar reflectivities were adjusted using corresponding ground station data. All available ground stations (see Section 16.2.1) with high temporal resolutions and different reflectivity ranges were used for radar data adjustment. The ground station data were compared with mean values of the radar data of the surrounding cells of

a 3 × 3 cells grid instead of a single cell, as the small cell size (50 × 50 m^2) could lead to wrong interpretations. In a first step, both data sets were transferred to equidistant time intervals. It became obvious that a station- and event-dependent time shift correction between 5 to 15 min was necessary. These time shifts are caused, for example, by wind drift or delayed clocks of the ground stations. Afterwards, a coefficient of determination (r^2) of at least 0.47 between both data sets was achieved.

In a next step, radar data were adjusted with an automated algorithm on the basis of the minimum squared deviation method for the cumulative curves of both data sets. By minimising the square deviation of both data sets, the temporal distributions of rainfall intensities were considered. Additionally, the minimum difference between the total precipitation amounts of both data sets was aimed. Consequently, an optimal parameter set of $\alpha_{Z/R}$ and $\beta_{Z/R}$ of the $Z_{radar}/R_{Z/R}$ relation was determined by automatically minimising both target measures of the squared deviations and the differences of total rain amounts of both data sets. This non-linear adjustment method excludes that higher rain intensities get a larger weight than lower rain intensities.

To summarize, the measured radar reflectivities were transformed into rainfall intensities using spatially averaged but event-dependent $Z_{radar}/R_{Z/R}$ relations. The resulting $Z_{radar}/R_{Z/R}$ relations differed strongly for the three investigated events (see next section). On the basis of these relations, rainfall patterns were derived by calculating the rainfall intensity for each grid cell of the whole basin.

16.2.4 Investigated scenarios for basin precipitation

To analyse the significance of the spatial and temporal variability of basin precipitation for flood modelling, three storm events during the summer of 1998 were investigated in further detail. Therefore, the following precipitation scenarios were applied:

1. *Scenario (1)*: Up to seven ground stations, located within or near the Brugga basin, were used to distribute precipitation over the basin using an 80:20 combination of the inverse distance weighting (IDW) method (80%) and an elevation gradient (20%). The IDW method is an inverse distance scheme that calculates a weighted average precipitation for each raster cell with a weight of d^{-2}, where d is the distance between the rain station and the respective raster cell. Only stations within a radius of 6 km for each raster cell were considered for the calculation. The elevation gradient is a non-linear function that considers the mean annual increase of precipitation with height (see Uhlenbrook 1999). The precipitation measurement error caused by wind was corrected according to the approach of Schulla (1997) that differentiates between liquid and solid precipitation.
2. *Scenario (2)*: For hourly time steps, aggregated rainfall radar data with an original temporal resolution of 5 min (for further details, see previous section) and in the original polar co-ordinate grid of 1 km × 1° azimuth angle were disaggregated to the 50 × 50 m^2 raster cells used by the TAC^D model. The spatial rainfall pattern for the whole catchment was derived by calculating the rainfall intensities for each grid cell on the basis of a spatially uniform, but event-dependent $Z - R$ relation. Owing to technical limitations of the radar measurement, a small area around the radar device needed to be ''filled'' with ground data measurements.

To compare the impact of the two precipitation scenarios on runoff simulations, the following procedure was performed: The model was run twice, each time with the same initialisation period (eight months), parameter values (determined during model calibration), and input data sets, but with different basin precipitation maps for each time step of the three investigated events. This has the advantage that the model is run continuously and, thus, the spatial and temporal variable soil moisture and groundwater storage is modelled reasonably before the investigated event, which is a prerequisite for process-oriented modelling. This could not be warranted if the events are modelled separately and are more independent from the previous hydrological conditions.

16.3 PREVIOUS INVESTIGATIONS AT THE BRUGGA BASIN

16.3.1 Dominant runoff generation processes

In recent years, detailed tracer investigations were performed at Brugga and the neighbouring Zastler basin: (i) hydrograph separations using the natural tracers (Hoeg *et al*. 2000; Uhlenbrook *et al*. 2002), (ii) tracer experiments with artificial tracers at different hill slopes and at the river channel system (Mehlhorn *et al*. 1998; Uhlenbrook *et al*. 2003c), and (iii) residence time determinations using environmental isotopes and CFCs (Uhlenbrook *et al*. 2002). These experimental findings led to the development of the following perceptual model of runoff generation for the study site. Three main flow systems were identified: Firstly, fast runoff components (surface and near-surface runoff) are generated on sealed or saturated areas, and on steep highly permeable

slopes covered by boulder fields. Secondly, slow base flow components (deep groundwater) originate from the fractured hard rock aquifer and the deeper parts of the weathering zone. There is no evidence that these components are important for flood formation. Thirdly, an intermediate flow system contributes mainly from the periglacial deposits of the slopes (shallow groundwater). These are mainly delayed runoff components compared to the surface and near-surface runoffs. However, they can also contribute to flood formation, depending on the antecedent moisture content.

16.3.2 Modelling investigations

Several hydrological models were used at the Brugga basin, sub-basins, and the neighbouring Zastler basin (e.g. PRMS/MMS, Mehlhorn *et al*. 1998; TOPMODEL, Güntner *et al*. 1999; HBV, Uhlenbrook *et al*. 1999). The applications of these models and the results of the experimental studies led to the development of the TAC model, the tracer aided catchment model (Uhlenbrook 1999; Uhlenbrook and Leibundgut 2002). The aim was to develop a better process-realistic model to compute the water balance on a daily mode. TAC is a process-oriented, semi-distributed catchment model, which requires a spatial delineation of units with the same dominating runoff generation processes (cf. hydrotopes or hydrological response units). This spatial delineation is based on the findings of the experimental investigations (see above). For each of the seven units, a specific runoff generation routine was developed, using linear and non-linear storage routines. The spatial variability of basin precipitation was considered using a non-linear elevation gradient for 11 elevation zones (100-m intervals). This gradient was kept constant within the basin, but varied for every modelling time step. The TAC model was applied using daily values with good success. In particular, the use of tracer data, that is, contribution of the different runoff components and the concentration of dissolved silica, showed that not only the total runoff was computed well but also the internal processes were modelled correctly.

The process-oriented TAC model was advanced to the TAC^D model with the following modifications: (i) It is still a conceptual model with a modular model structure using storage routines to conceptualise the runoff generation processes, but it was changed from the semi-distributed to a fully distributed raster model. The spatial discretisation is still based on the spatial delineation of the units with the same dominating runoff generation processes, which was converted into $50 \times 50\,m^2$ raster cells that are connected by a single flow algorithm. The distributed computation allowed using spatially and temporally variable input data much better than with the previous semi-distributed model version. (ii) The aim of the model was not only to simulate the annual water balance and the daily contributions of different runoff components correctly, but in addition that floods and its generation processes should be simulated correctly. Therefore, the modelling time step was reduced to an hourly mode. (iii) Channel routing is modelled with a kinematic wave approach (implicit, non-linear). (iv) The whole model was integrated into the GIS PC-Raster (Karssenberg 2002) and all dynamic calculations are performed within the GIS environment.

The TAC^D model was applied to the Brugga basin using the period 1.8.95–31.7.96 for model calibration (further details are given in Uhlenbrook *et al*. 2003b). It was initialised with a period of three months, which had some fillings of the different storages before. The calibrated parameter set was used for modelling the sub-basin St. Wilhelmer Talbach without re-calibration. The three events, which are investigated in further detail in this paper, are part of the model validation period (1.8.96–31.7.99). To evaluate model goodness, the model efficiency, $R_{eff}(Q)[-]$, according to Nash and Sutcliffe (1970) and the model efficiency using logarithmic runoff values, $R_{eff}(\log Q)[-]$, were used.

16.4 MODELLING RESULTS

16.4.1 Basin precipitation based on different calculation methods

For event I, the highest total precipitation for the Brugga basin occurred using the IDW-elevation method (scenario 1) (Table 16.2). Compared to event I, events II and III are characterised by higher rain amounts and higher rain intensities. For both events, the available ground stations within or near the Brugga basin did not record as high intensities as the radar data. Thus, the resulting catchment precipitation is higher using the radar data, in particular for event II (Table 16.2). The temporal distributions of the catchment rainfall values

Table 16.2 Comparison of the two catchment precipitation values (mm) of the Brugga basin for the three investigated events

	Scenario (1) IDW-elevation (80:20)	Scenario (2) Rainfall radar data
Event I (27.08.98)	25.9	22.8
Event II (22.08.98–23.08.98)	35.1	44.4
Event III (4.09.98–5.09.98)	39.1	41.1

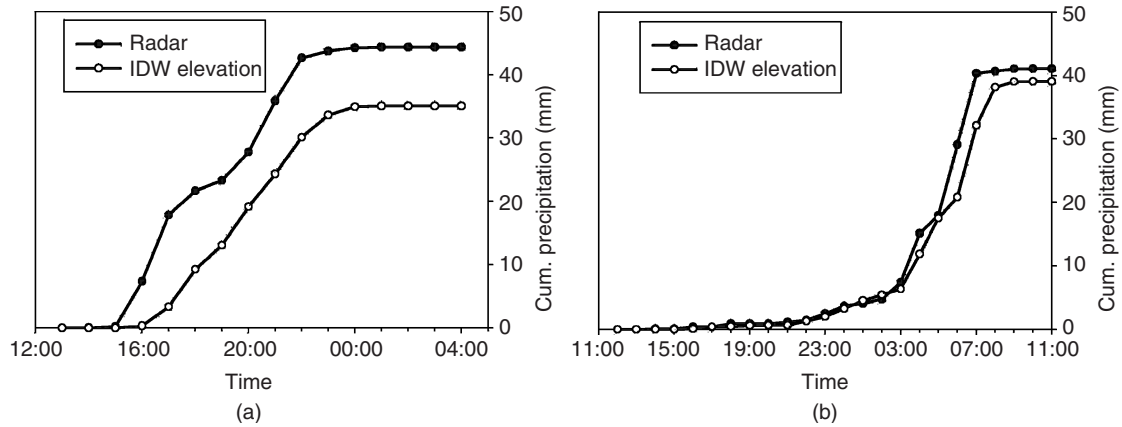


Figure 16.2 Temporal distribution of cumulative basin precipitation calculated on the basis of scenario 1 (IDW-elevation) and scenario 2 (rainfall radar data) for event II (3a) and event III (3b)

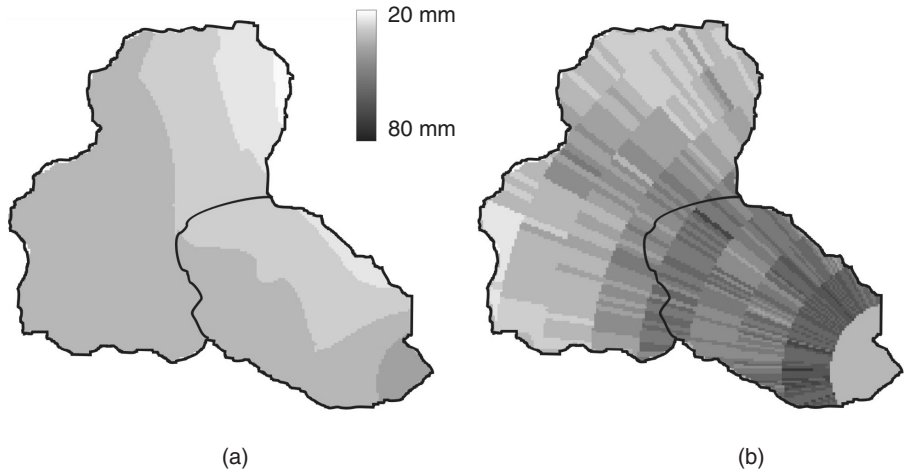


Figure 16.3 Spatial distribution of basin precipitation of event II: (a), calculated using the IDW-elevation method (scenario 1), and (b), calculated using the rainfall radar data (scenario 2)

calculated by the scenario 1, using the IDW-elevation method, and scenario 2, using radar data, are highlighted in Figure 16.2. For event II (Figure 16.2a), differences in cumulative total precipitation amounts based on both the rainfall data sets become obvious (see also Table 16.2). The larger temporal variability of the radar data became obvious by the temporal distribution in the cumulative curve, which is less regular than the ground station curve. Also, the radar data showed an earlier start of the event and higher rain intensities around 8 P.M. This indicates that the convective event II is an event with an isolated rain cell that was only partly detected by the ground stations, and consequently the IDW-elevation method calculated lower precipitation values. For event III (Figure 16.2b), precipitation of both data sets for both total amounts and temporal distributions show less differences. However, during the intense part of the event, the radar data showed somewhat higher rain intensities, which results in a higher total basin precipitation.

In Figure 16.3, the spatial patterns of the total precipitation for event II are shown. The spatial pattern of the basin precipitation of scenario 1 (IDW-elevation method, Figure 16.3a) is much more homogenous compared to scenario 2 (rainfall radar data, Figure 16.3b). The radar data showed that the convective cell was mainly at the upper parts in the northeast of the basin, within

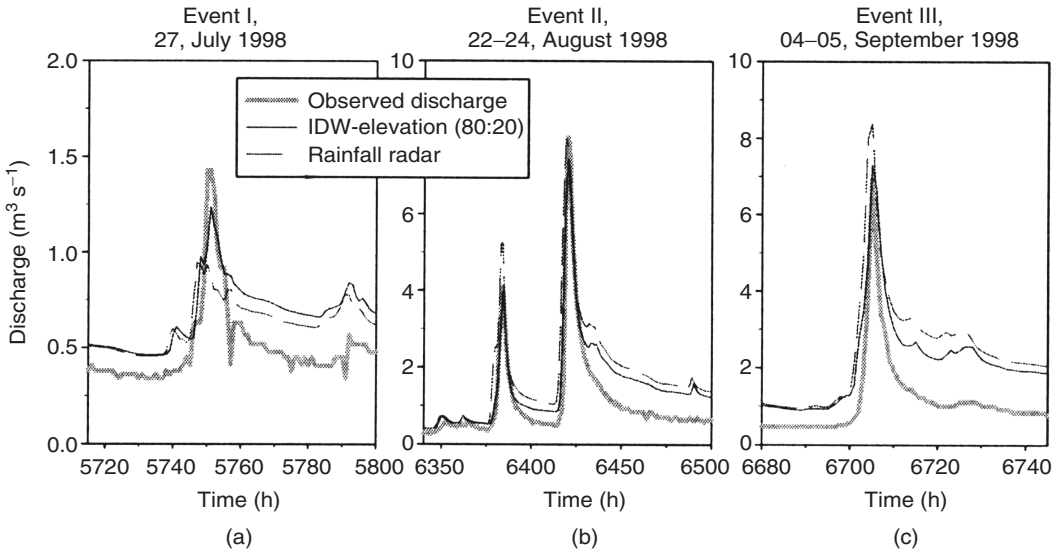


Figure 16.4 Results of simulating the three investigated events at the outlet of the Brugga basin using the TAC^D model and applying the two different precipitation scenarios

the sub-basin St. Wilhelmer Talbach. Here the highest intensities were recorded, which could not be captured correctly by the ground station network.

16.4.2 Runoff calculations using different precipitation inputs

It was possible to apply the TAC^D model with very good success: The $R_{eff}(Q)$ amounted to 0.94 and 0.85 and $R_{eff}(\log Q)$ amounted to 0.99 and 0.90 during the calibration period for the Brugga basin and the St. Wilhelmer Talbach basin, respectively. The statistical measures for the model validation period showed also clearly the suitability of the TAC^D for runoff calculation: $R_{eff}(Q)$ amounted to 0.80 and 0.85 and $R_{eff}(\log Q)$ amounted to 0.83 and 0.87 for the Brugga basin and the St. Wilhelmer Talbach basin, respectively. It is important to note that the model was calibrated and validated using ground station data. Radar data were only available for the three selected events.

Comparing the model performance for the three investigated events (Figure 16.4, Table 16.3) demonstrates the importance of the spatial and temporal distribution of the precipitation input for flood modelling. In general, the simulated discharge using the IDW-elevation method matches the observed discharge better than the simulated discharge using radar data as precipitation input data. The falling limbs are not modelled well, independent of the precipitation input. This failing in capturing accurately the falling limbs is exceptional for the three examined events from the validation period; others were modelled much better as indicated in the high statistical measures of model efficiency values of more than 0.8 (see above).

Table 16.3 Observed and simulated peak discharges of the three investigated events [$m^3 s^{-1}$]

Event	Brugga			St. Wilhelmer Talbach		
	Observed	IDW-elev.	Radar	Observed	IDW-elev.	Radar
I	1.4	1.2	0.9	0.6	0.4	0.4
II	8.0	7.4	8.0	4.2	2.9	3.2
III	6.9	7.3	8.4	2.3	2.5	3.3

Event I is a typical small event during summer times (Figure 16.4a). This type of event might occur several times during a year. The basin precipitation calculated by radar data is lower compared to that using the IDW-elevation method (Table 16.2). This resulted in a smaller simulated event (Table 16.3). Remarkable are the large differences in the timing of the simulated peak discharges. The differences in the temporal variability of rainfall cause an earlier peak discharge using radar data than the IDW method.

Event II occurred after a two-week rainless low-flow period and was followed by a second event for which no radar data were available (Figure 16.4b). The radar data had higher basin precipitation values than the IDW-elevation method (Table 16.2); this resulted in a

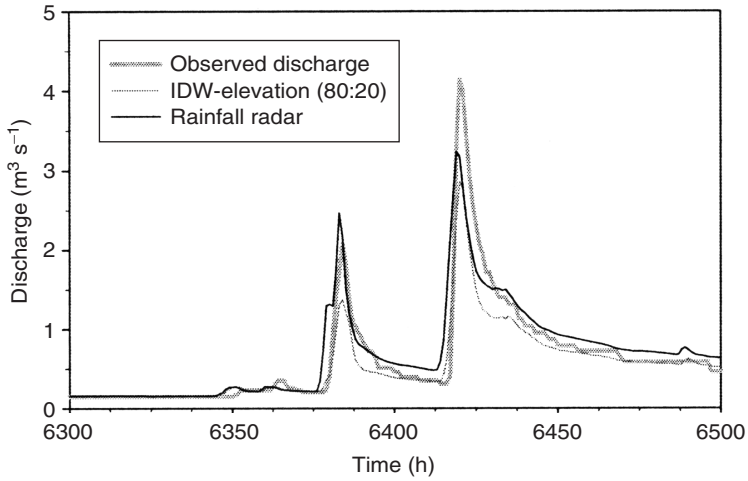


Figure 16.5 Results of simulating event II at the outlet of the sub-basin St. Wilhelmer Talbach using the TAC^D model and applying the two different precipitation scenarios

larger simulated flood. Hence, in this case, simulation results are better using radar data (Table 16.3). Also, the subsequent event is simulated differently even if the same rainfall input was applied. This is caused by the higher antecedent moisture conditions for this event during the model run using the higher radar rainfall input for the first event.

For event III, again the radar data led to higher basin precipitation that resulted in a larger simulated flood (Figure 16.4c). However, the 2 mm more precipitation using radar data (Table 16.2) could not explain the larger simulated response alone. Thus, the temporal distribution with larger intensities for the radar rainfall (Figure 16.2b) and the spatial pattern seems to be responsible for the differently simulated runoff. The radar data had much higher rain intensities in an area in the southwest of the Brugga basin with 55–75 mm for the whole of the event, compared to 45–52 mm for the precipitation input using the IDW-elevation method. At this part of the basin, a lot of fast responding areas, in particular saturated areas, are located (Uhlenbrook *et al*. 2003b), which caused the increased runoff response modelled by the process-oriented model.

The simulation of the event II at the sub-basin St. Wilhelmer Talbach (Figure 16.5) highlights the power of rainfall radar data for spatially very unequally distributed events. The largest rainfall occurred within the St. Wilhelmer Talbach (Figure 16.3b) and could not be observed adequately with the existing monitoring network (see Figure 16.1). This resulted in a significant underestimation of the flood at the outlet of the St. Wilhelmer Talbach basin. The radar observed the event much better and, consequently, the TAC^D model was able to simulate the flood discharge more closely to the observed discharge. Again, the different simulations of the second event using the two rainfall scenarios are caused by the different antecedent moisture conditions owing to the different rainfall inputs of the preceding event. Unfortunately, no radar data were available for the second peak of event II. But it is plausible that the underestimation of this convective event is also caused by an inappropriate rainfall input.

The comparison of the simulated peak discharges (Table 16.3) shows that compared to the measured peaks, both input data sets result in similar responses: either both data sets under- or overestimate the peak. When high rainfall intensities at areas with quick runoff responses (according to the spatial delineation runoff generation areas used in the TAC^D model, see Section 16.3.2) are determined (e.g. during event III), the more extreme rainfall values associated with radar data cause higher errors in peak discharge simulation. Because of the more smoothed rainfall pattern using ground station data and the IDW-elevation method for regionalisation, the deviations of the peak discharge predictions are smaller. However, if high intensity rain cells were not recorded by the ground station network, in particular, at locations with many direct runoff generation areas (the St. Wilhelmer Talbach sub-basin during event II, Figure 16.3), the simulations using radar data outperform those using the IDW-elevation method also for the whole Brugga basin (Table 16.3).

16.5 DISCUSSION

The importance of an adequate representation of the spatial and temporal distribution of convective precipitation for runoff modelling can only be examined by a well-validated process-oriented model. Owing to previous investigations (see Section 16.3), the TAC^D model is qualified to study the impact of precipitation variabilities in the mountainous Brugga basin. Its large significance was clearly demonstrated. These findings are in line with other studies in heterogeneous catchments (Woods *et al*. 2000; Ogden *et al*. 2000; Syed *et al*. 2003). However, these insights are restricted to the examined convective storm events. Events that are (partly) produced by snow melt were not considered, but a similar importance of the precipitation input (rain and snow melt) is very likely.

Small differences in total basin rainfall can cause large differences in the simulated hydrographs due to non-linear feedback mechanisms, as shown for event I. However, depending on the position and the movement of the rain cell and the runoff travel times to the basin outlet, the importance of the rain distribution can differ. This was learnt by comparing the Brugga basin and its sub-basin.

The contribution of spatial highly resoluted radar data is the ability of capturing highly localised rain cells, which are not well represented by a ground station network. This was clearly demonstrated for event II at the St. Wilhelmer Talbach basin. The rain cell was too small to be captured adequately by the gauging network, even if this can be attributed as dense with up to seven stations within or near the examined basin. However, the use of radar can also lead to runoff simulations, which are worse than the simulations using the ordinary gauging network only (see simulations for the Brugga basin, Figure 16.4). This is caused mainly by two reasons: (i) The model was not trained (calibrated) with input from radar data, but with input using the IDW-elevation method. This is caused by the fact that the model run continuously for several months and radar data were only available for the three events. (ii) Because of the technical problems in 1998 (see Section 16.2.2) the radar data resolution is relatively coarse and it tends to overestimate high rain intensities. Owing to non-linearities during flood formation processes (e.g. Grayson *et al*. 1997) and the respective mathematical description in the TAC^D model, relatively small differences in precipitation input can cause large differences for the modelled flood. The latter was shown clearly for event I.

The used radar device is located at the highest part of the catchment (Figure 16.1). However, this is not the case in many mountainous regions and the radar measurement can be affected by factors like beam blocking as demonstrated, for instance, by Andrieu *et al*. (1997). They showed that beam blocking can be corrected using digital terrain models and took into account vertical variations in radar reflectivity for providing satisfactory range-dependent corrections. But these data are not available in many studies. Thus, the comparison and adjustment of the radar data with highly resoluted ground station data is essential (e.g. Creutin *et al*. 1997). In this study, also ground stations that are not situated directly within or near the catchment were used for radar data adjustment. This made it possible to consider a wider range of rain intensities for data adjustment, and hence, made the calibration more robust.

For the used adjustment method (Section 16.2.3), only the parameters α and β were calibrated to optimise the $Z_{\text{radar}}/R_{Z/R}$ relation and no additional adjustment factor was considered. Further investigations regarding the correlation between the parameters α and β and spatial factors like the distance from radar device or the height of the radar beam above the ground did not lead to conclusive results. This seems to have been caused by the heterogeneity of the convective events. Therefore, a spatial mean but event-dependent $Z_{\text{radar}}/R_{Z/R}$ relation was used. The use of a standard $Z_{\text{radar}}/R_{Z/R}$ relation (e.g. Marshall *et al*. 1955; Dyck and Peschke 1995) without calibrating α and β would not have led to an acceptable data adjustment and consequently to large runoff modelling errors. This was also concluded by Quirmbach *et al*. (1999), who showed a significant underestimation of flood events using a standard $Z_{\text{radar}}/R_{Z/R}$ relation. This is caused by the event-dependent raindrop size distribution as well as by precipitation characteristics (e.g. Smith and Krajewski 1993; Pessoa *et al*. 1993; Haase and Crewell 2000). In general, the used method for radar data adjustment was found to be practical and efficient as it considered the total amount and the distribution of rainfall intensity during the event. It led to α-values below 100, which were lower that the α-values of the standard $Z_{\text{radar}}/R_{Z/R}$ relation of the German weather survey, but were found in the earlier literature (e.g. Hirayama *et al*. 1997).

A good overview about limitations and shortcomings connected with observation and transformation of radar data and ongoing research to improve weather radar measurements is given, for example, by Terblanche *et al*. (2001). In recent years, numerous uncertainties during data observation and transformation were investigated (e.g. Grecu and Krajewski 2000). In addition, methods for improvement of data quality were developed (e.g. Georgakakos 2000), and the precipitation rate dependence on the raindrop size distribution was examined (Uijlenhoet

and Stricker 1999). Lange *et al*. (2003) discuss the shortcomings of using C-band radar products. In general, the use of operational available radar data for hydrological applications is still controversial, also because of the labour-intensive radar data management and adjustment. But the results of this study highlight also the potential of radar data, in particular, for convective storm events with large spatial and temporal heterogeneities. However, the prerequisites to utilise these data are a reliable ground station network and a distributed, process-oriented and well-validated rainfall-runoff model.

16.6 CONCLUSIONS AND OUTLOOK

The following three questions were addressed in this study:

1. *What might be the contribution of highly resoluted radar data to capture spatial and temporal variability of convective precipitation events in mountainous areas?*

Detecting rainfall patterns in mountainous catchments is complicated because of the difficulties both in maintaining a sufficient network of ground stations and the variability of precipitation caused by luv and lee effects, and hence, difficulties in detecting highly localised intense rain cells. Highly resoluted rainfall radar data can help significantly in capturing the spatial and temporal variability of precipitation in mountainous areas, in particular, for very heterogeneous events, or if a sufficient number of good ground stations is not available, for example, in smaller sub-catchments. Additionally, higher short-term intensities are measured using radar data, which can be important for triggering certain runoff generation processes. However, the location of the radar station, the topography of the basin, the characteristics of the respective event, the specific problems of radar measurements in mountainous catchments and availability of representative ground stations at least near the catchment for radar data adjustment need to be considered regarding the potential of highly resoluted rainfall radar data. Although the quality of operational radar data can be – event dependent – low, they offer useful information about rainfall patterns and maximum intensities.

2. *What is the significance of the distribution of basin precipitation during convective cells for flood modelling in mountainous catchments?*

The importance of considering adequately the spatial and temporal variability of basin precipitation during convective cells for flood modelling has been demonstrated clearly in this study. Basin precipitation is a major order control on flood modelling in mountainous, meso-scale basins, and the errors in flood predictions can be large if incorrect basin precipitation values are used. Lumped precipitation values can lead to wrong runoff generation predictions locally and, consequently, to uncertain discharge predictions at ungauged sites or sub-basins. However, there are many site- and event-specific circumstances that make general statements regarding the impact of rainfall distributions on runoff simulations difficult.

3. *How can operational available radar data be used within a detailed hydrological model in an appropriate way?*

The results showed that an improvement of the runoff simulation by incorporating radar data is only possible if an extensive data disaggregation, correction, and adjustment is performed. Therefore, suitable ground station data are indispensable. Considering the experiences with the radar product used in this study let us conclude that a nowcasting of basin precipitation using standard $Z_{\text{radar}}/R_{Z/R}$ relations without an event-dependent adjustment of the data seems to be hazardous and will result in uncertain discharge predictions.

The results of this study suggest a number of new avenues for research. Firstly, so far the precipitation input was used in a very detailed spatial resolution ($50 \times 50\,\text{m}^2$). In a next step, different aggregations and their influence on the runoff modelling need to be examined. Therefore, the used process-based catchment model and the nested basin structure of the test site are suitable. Secondly, the parameters α and β were adjusted for each event separately but averaged spatially. It should be investigated if even better simulation results can be obtained by a ground station or better elevation-specific, and thus spatially variable, determination of these two fitting parameters. These results should be compared with calibrating the $Z_{\text{radar}}/R_{Z/R}$ relation using spatially variable adjustment factors and standard $Z_{\text{radar}}/R_{Z/R}$ relations. Thirdly, the significance of the spatial and temporal variability of precipitation for flood modelling should be compared for different magnitudes of events, different scaled basins, and different landscapes. The scale at which the basin precipitation dominates the extent of flood generation in comparison with other influences, such as the physiographic basin characteristics, should be examined.

16.7 ACKNOWLEDGEMENTS

The detailed radar data were been provided from the German Weather Service (DWD). The State Institute for Environmental Protection Baden-Württemberg

(Landesanstalt für Umweltschutz (LfU) Baden-Württemberg) made the precipitation ground station data available. In addition, the federal environmental survey (Umweltbundesamt, UBA) provided the rainfall data from the station Schauinsland. The Gewaesserdirektion Waldshut, Germany, measured the runoff data. The input of Günter Gässler during analysis of the radar data and during extensive discussions is gratefully acknowledged. Jens Lange (University of Freiburg, Germany) has provided a code for converting the radar data. Also his helpful comments are very much appreciated. Parts from the converting program from Jens Lange were combined with a reading program from Daniel Sacher, J. Lang Datenservice. We would also like to thank Daniel Sacher. The study was supported by the German Research Foundation (Deutsche Forschungsgemeinschaft, Bonn) grant no. Le 698/12-1.

REFERENCES

Adamowski K, Muir J (1989) A Kalman-filter modelling of space-time rainfall using radar and rain gauge observations. *Can. J. Civil Eng.* **16**(5): 767–773.

Anderson SP, Dietrich WE, Montgomery DR, Torres R, Conrad ME, Loague K (1997) Subsurface flow paths in a steep, unchanneled catchment. *Water Resour. Res.*, **33**(12): 2637–2654.

Andrieu H, Creutin JD, Delrieu G, Faure D (1997) Use of weather radar for the hydrology of mountainous area. Part I: radar measurement interpretation. *J. Hydrol.* **193**(1–4): 1–25.

Arnaud P, Bouvier C, Cisneros L, Dominquez R (2002) Influence of spatial variability on flood prediction. *J. Hydrol.* **260**: 216–230.

Bergström S (1992) *The HBV Model – Its Structure and Applications*. SMHI, RH, 4., Norrköping, Schweden.

Beven KJ (2002) *The future of distributed hydrological modelling*, Special Issue of the Journal Hydrological Processes, 16. John Wiley & Sons, Chichester, UK.

Beven KJ, Lamb R, Quinn P, Romanowicz R, Freer J (1995) TOPMODEL. In: VP Singh (Ed.), *Computer Models of Watershed Hydrology*. Water Resources Publications, Colorado, CO.

Boyle DP, Gupta HV, Sorooshian S, Koren V, Zhang Z, Smith M (2001) Toward improved streamflow forecasts: Value of semidistributed modeling. *Water Resour. Res.* **37**(11): 2749–2759.

Carpenter TM, Georgakakos KP, Sperfslagea JA (2001) On the parametric and NEXRAD-radar sensitivities of a distributed hydrologic model suitable for operational use. *J. Hydrol.* **253**: 169–193.

Ciach GJ, Krajewski W (1999) On the estimation of radar rainfall error variance. *Adv. Water Resour.* **22**(6): 585–595.

Creutin JD, Andrieu H, Faure D (1997) Use of weather radar for the hydrology of mountainous area. Part II: radar measurement validation. *J. Hydrol.* **193**(1–4): 26–44.

Delrieu G, Serrar S, Guardo E, Creutin JD (1999) Rain measurement in hilly terrain with X-band weather radar systems: Accuracy of path-integrated attenuation estimates derived from mountain returns. *J. Atmos. Ocean. Tech.* **16**(4): 405–416.

DWD Deutscher Wetterdienst (German Weather Service) (1997) *AKORD – Anwenderkoordinierte Organisation von Radar-Daten. Produktkatalog*. Deutscher Wetterdienst Geschäftsfeld Hydrometeorologie, Offenbach, Germany.

Dyck S, Peschke G (1995) *Grundlagen der Hydrologie*. Verlag für Bauwesen, Berlin, Germany, p. 408.

Faeh A, Scherrer S, Naef F (1997) A combined field and numerical approach to investigate flow processes in natural macroporous soils under extreme precipitation. *Hydrol. Earth Syst. Sci.* **4**: 787–800.

Faures JM, Goodrich DC, Woolhiser DA, Sorooshian S (1995) Impact of small-scale spatial variability on runoff modelling. *J. Hydrol.* **173**: 309–326.

Georgakakos KP (2000) Covariance propagation and updating in the context of real-time radar data assimilation by quantitative precipitation forecast models. *J. Hydrol.* **239**(1–4): 115–129.

Goodrich DC, Faures J-M, Woolhiser DA, Lane LJ, Sorooshian S (1995) Measurement and analysis of small-scale convective storm rainfall variability. *J. Hydrol.* **173**(1–4): 283–308.

Grayson RB, Western AW, Chiew FHS, Blöschl G (1997) Preferred states in spatial soil moisture patterns: Local and non-local controls. *Water Rescour. Res.* **33**(12): 2897–2908.

Grecu M, Krajewski W (2000) Simulation study of the effects of model uncertainty in variational assimilation of radar data on rainfall forecasting. *J. Hydrol.* **239**(1–4): 85–96.

Güntner A, Uhlenbrook S, Seibert J, Leibundgut C (1999) Multi-criterial validation of TOPMODEL in a mountainous catchment. *Hydrol. Process.* **13**: 1603–1620.

Gurtz J, Baltensweiler A, Lang H, Menzel L, Schulla J (1997) *Auswirkungen von Klimatischen Variationen auf Wasserhaushalt und Abfluß im Flußgebiet des Rheins*. Vdf Hochschulverlag AG an der ETH Zürich, Zürich, Schweiz.

Haase G, Crewell S (2000) Simulation of radar reflectivities using a mesoscale weather forecast model. *Water Resour. Res.* **36**(8): 2221–2231.

Hinton MJ, Schiff SL, English MC (1994) Examining the contributions of glacial till water to storm runoff using two- and three-component hydrograph separations. *Water Resour. Res.* **30**: 983–993.

Hirayama D, Fujita M, Nakatsugawa M (1997) The identification of optimum Z-R relation based on runoff analysis. In: BJ Braga, O Massambani (Eds.), *Weather Radar Technologies for Water Resources Management* IRTCUD/University of Sao Paulo, Brazil, South America and IHP-UNESCO.

Hoeg S, Uhlenbrook S, Leibundgut C (2000) Hydrograph separation in a mountainous catchment – combining hydrochemical and isotopic tracers. *Hydrol. Process.* **14**: 1199–1216.

Hornberger GM, Germann PF, Beven KJ (1991) Throughflow and solute transport in an isolated sloping block in a forested catchment. *J. Hydrol.* **124**: 81–99.

Jasper K, Gurtz J, Lang H (2002) Advanced flood forecasting in Alpine watersheds by coupling meteorological observations and forecasts with a distributed hydrological model. *J. Hydrol.* **267**(1–2): 40–52.

Lange J (1999) A non-calibrated rainfall-runoff model for large arid catchments, Nahal Zin, Israel. PhD Thesis, Freiburger Schriften zur Hydrologie, Band 9, University of Freiburg, Institute of Hydrology, Freiburg.

Lange J, Leibundgut C, Greenbaum N, Schick AP (1999) A non-calibrated rainfall-runoff model for large, arid catchments. *Water Resour. Res.* **35**(7): 2161–2172.

Lange J, Wagner A, Tetzlaff D (2003) Hochwassersimulation in kleinen Einzugsgebieten: Eignung von Niederschlagsradar und Auswirkung versiegelter Flächen (Flood simulation in small catchments: Applicability of rainfall radar data and effects of impervious areas). *Tag der Hydrologie 2003, ATV-DVWK*, HB Kleeberg (Ed.), Vol. 1, pp. 123–131.

Karssenberg D (2002) The value of environmental modelling languages for building distributed hydrological models. *Hydrol. Process.* **16**: 2751–2766.

Koren VI, Finnerty BD, Schaake JC, Smith MB, Seo DJ, Duan QY (1999) Scale dependencies of hydrological models to spatial variability of precipitation. *J. Hydrol.* **217**: 285–302.

Krajewski WF, Ventakataramann L, Georgakakos KP, Jain SC (1991) A Monte Carlo study of rainfall sampling effect on a distributed catchment model. *Water Resour. Res.* **27**(1): 119–128.

Marshall JS, Hitschfeld W, Gunn KLS (1955) Advances in radar weather. *Adv. Geophys.* **2**: 1–56.

Maul-Kötter B, Spies S, Einfalt T (2001) Qualitätskriterien für Radardaten in der hydrologischen Simulation. *Hydrol. Wasserbewirt.* **45**(6): 236–243.

McDonnell JJ (1990) A rationale for old water discharge through macropores in a steep, humid catchment. *Water Resour. Res.* **26**: 2821–2832.

McDonnell JJ, Tanaka T. (2001) *Hydrology and biogeochemistry of forested catchments*. Special Issue of the Journal Hydrological Processes, 15, John Wiley & Sons, Chichester, UK, pp. 1673–2055.

Mecklenburg S, Joss J, Schmid W (2000) Improving the nowcasting of precipitation in an Alpine region with enhanced radar echo tracking algorithm. *J. Hydrol.* **239**: 46–68.

Mehlhorn J, Armbruster F, Uhlenbrook S, Leibundgut C (1998) *Determination of the Geomorphological Instantaneous unit Hydrograph Using Tracer Experiments in a Headwater Basin*. IAHS Publication No. 248, pp. 327–336.

Merot Ph, Ezzehar B, Walter C, Aurousseau P (1995) Mapping waterlogging of soils using digital terrain models. *Hydrol. Process.* **9**: 27–34.

Michaud JD, Sorooshian S (1994) Effects of rainfall-sampling errors on simulations of desert flash floods. *Water Resour. Res.* **30**(10): 2765–2775.

Milly PCD, Eagleson PS (1988) Effects of storm scale on surface runoff volume. *Water Resour. Res.* **24**(4): 620–624.

Mosley MP (1982) Subsurface flow velocities through selected forest soils, south island, New Zealand. *J. Hydrol.* **55**: 65–92.

Nash JE, Sutcliffe JV (1970) River flow forecasting through conceptual models, 1. A discussion of principles. *J. Hydrol.* **10**: 282–290.

Obled C, Cluckie ID, Collier CG (1991) *Reflections on Rainfall Information Requirements for Operational Rainfall-Runoff Modelling, Hydrological Applications of Weather Radar*. Ellis Horwood, pp. 469–482.

Obled C, Wendling J, Beven K (1994) The sensitivity of hydrological models to spatial rainfall patterns: an evaluation using observed data. *J. Hydrol.* **159**: 305–308.

Ogden FL, Sharif HO, Senarath SUS, Smith JA, Baeck ML, Richardson JR (2000) Hydrologic analysis of the Fort Collins, Colorado, flash flood of 1997. *J. Hydrol.* **228**: 82–100.

O'Loughlin G, Huber W, Chocat B (1996) Rainfall-runoff processes and modelling. *J. Hydraulic Res.* **34**(6): 733–751.

Pessoa ML, Bras RL, Williams ER (1993) Use of weather radar for flood forecasting in the Sieve River basin: A sensitivity analysis. *J. Appl. Meteorol.* **32**(3): 462–475.

Quirmbach M (2003) Nutzung von Wetterradardaten für Niederschlags- und Abflussvorhersagen in urbanen Einzugsgebieten. PhD Thesis, Ruhr-Universität Bochum, Bochum, Germany, p. 178.

Quirmbach M, Schultz G, Frehmann T (1999) Use of weather radar for combined control of an urban drainage system and a sewage treatment plant. *Impacts of Urban Growth on Surface Water and Groundwater Quality, Proceedings of IUGG 99 Symposium HS5, Birmingham, July 1999*, IAHS Publication No. 259, pp. 245–250.

Refsgaard JC, Storm B (1996) Construction, calibration and validation of hydrological models. In: MB Abbot, JC Refsgaard (Eds.), *Distributed Hydrological Modelling*. Kluwer Academic, Dordrecht, Niederlande, pp. 41–54.

Schilling W, Fuchs L (1984) *A Quantitative Assessment of Uncertainties in Stormwater Modeling*. Urban storm drainage. Göteborg, Schweden, pp. 625–633.

Schulla J (1997) *Hydrologische Modellierung von Flußeinzugsgebieten zur Abschätzung der Folgen von Klimaänderungen*, Züricher Geographische Hefte, 65. ETH Zürich, Zürich, Schweiz.

Sempere Torres D, Porra JM, Creutin JD (1994) A general formulation for raindrop size distribution. *J. Appl. Meteorol.* **33**: 1494–1502.

Seo DJ, Breidenbach JP, Johnson ER (1999) Real-time estimation of mean field bias in radar rainfall data. *J. Hydrol.* **223**: 131–147.

Smith JA, Krajewski WF (1993) A modelling study of rainfall-rate-reflectivity relationships. *Water Resour. Res.* **29**(8): 2505–2514.

Sun X, Mein RG, Keenan TD, Elliott JF (2000) Flood estimation using radar and raingauge data. *J. Hydrol.* **239**: 4–18.

Syed KH, Goodrich DC, Myers DE, Sorooshian S (2003) Spatial characteristics of thunderstorm rainfall fields and their relation to runoff. *J. Hydrol.* **271**: 1–21.

Terblanche DE, Pegram GGS, Mittermaier MP (2001) The development of weather radar as a research and operational tool for hydrology in South Africa. *J. Hydrol.* **241**: 3–25.

Uchida T, Kosugi K, Mizuyama T (2002) Effects of pipe flow and bedrock groundwater on runoff generation in a steep headwater catchment in Ashiu, central Japan. *Water Resour. Res.*, **38**(7): 24–38.

Uhlenbrook S (1999) *Untersuchung und Modellierung der Abflussbildung in einem mesoskaligen Einzugsgebiet*, Freiburger Schriften zur Hydrologie, 10. Universität Freiburg, Freiburg, Germany.

Uhlenbrook S, Didszun J, Leibundgut Ch (2003c) Runoff generation processes on hillslopes and their susceptibility to global change. In: UM Huber, MA Reasoner, B Bugmann (Eds.), *2003: Global Change and Mountain Regions: A State of Knowledge Overview. Advances in Global Change Research*. Kluwer Academic Publishers, Dordrecht, Netherlands.

Uhlenbrook S, Frey M, Leibundgut Ch, Maloszewski P (2002) Residence time based hydrograph separations in a meso-scale mountainous basin at event and seasonal time scales. *Water Resour. Res.* **38**(6): 1–14.

Uhlenbrook S, Leibundgut Ch (2002) Process-oriented catchment modelling and multiple-response validation. *Hydrol. Process.* **16**: 423–440.

Uhlenbrook S, McDonnell JJ, Leibundgut Ch (2003a) *Runoff Generation and Implications for River Basin Modelling*, Special Issue of the Journal Hydrological Processes, 17, John Wiley & Sons, Chichester, UK, p. 2.

Uhlenbrook S, Roser S, Tilch N (2003b) Hydrological process representation at the meso-scale: The potential of a distributed, conceptual catchment model. Accepted by *J. Hydrol.* **291**: 278–296.

Uhlenbrook S, Seibert J, Leibundgut C, Rodhe A (1999) Prediction uncertainty of conceptual rainfall-runoff models caused by problems to identify model parameters and structure. *Hydrol. Sci. J.* **44**(5): 279–299.

Uijlenhoet R, Stricker JNM (1999) A consistent rainfall parameterization based on the exponential raindrop size distribution. *J. Hydrol.* **218**(3–4): 101–127.

Winchell M, Gupta HV, Sorooshian S (1998) On the simulation of infiltration and saturation-excess runoff using radar-based rainfall estimates: Effects of algorithm uncertainty and pixel aggregation. *Water Resour. Res.* **34**(10): 2655–2670.

Woods R, Grayson R, Western A, Duncan M, Wilson D, Young R, Ibbitt R, Henderson R, McMahon T (2000) Experimental design and initial results from the Mahurangi River Variability Experiment: MARVEX. In: V Lakshmi, JD Albertson, J Schaake (Eds.), *Land Surface Hydrology, Meteorology and Climate: Observations and Modeling. Water Science and Application*, Vol. 3, American Geophysical Union, Washington, DC, pp. 201–213.

Woods R, Sivapalan M (1999) A synthesis of space-time variability in storm response: rainfall, runoff generation and routing. *Water Resour. Res.* **35**(8): 2469–2485.

17

Geomorphological Zoning: An Improvement to Coupling Alpine Hydrology and Meteorology?

CARMEN DE JONG[1], PETER ERGENZINGER[2], MARTIN BORUFKA[3], ARNE KÖCHER[4] AND MARTIN DRESEN[5]

[1]Geography Department, University of Bonn, Germany, [2]Berlin-Bonn Environmental Research Group, Bornheim-Uedorf, Germany, [3]Institute of Geographic Sciences, Free University of Berlin, Germany, [4]Institute of Geographic Sciences, Free University of Berlin, Germany, [5]geoSYS, Berlin, Germany

17.1 INTRODUCTION

To solve complex hydrometeorological problems in mountain catchments under the impact of climate change (Price & Barry 1997), a new generation of models and tools is required. Integrated Watershed Management can benefit from coupled models through improved parameterisation of the earth's properties by geomorphological zoning. In mountain areas, investigation of energy and/or mass exchange does not require only data on incoming and outgoing radiation, precipitation, evapotranspiration (ET) and discharge for every unit of the surface but also submodels on sediment dynamics. These interrelations and processes are highly variable since, for example, radiation and water are directly linked to plant life, whereas sediment dynamics are linked to individual geomorphological and geological zones. Crosscutting models describing the dynamics of meteorology, hydrology and geomorphology in alpine valleys therefore require other parameters for describing surface and subsurface properties. It is important that one's focus should be placed on river bed changes in mountain torrents because of varying erosion and accretion. Apart from fluvial sediment transport, hillslope dynamics also needs consideration in hydrological catchment models. This demands a shift in focus on new problems and techniques such as detailed geomorphological zoning of a basin. In contrast, most meteorological models run at small scales. Mountains are described crudely as bulged terrain, an umbrella-like surface characterised by grid nodes with distances of several kilometres. Such approaches may suffice for the description of general air movement, but in situations in which, for example, a stagnating local thunderstorm triggers a large flood, the related model must be adjusted to a different spatial and temporal scale. Clearly, there is considerable contrast in scale between meteorological models on the one hand and hydrological models, including sediment transport, on the other.

Hydrological models should not be restricted to the definition of surface runoff as a function of precipitation alone but should also include regional ET and the

Climate and Hydrology in Mountain Areas. Edited by C. de Jong, D. Collins and R. Ranzi
© 2005 John Wiley & Sons, Ltd. ISBN: 0-470-85814-1

changing storage conditions of soils, regolith and aquifers (Molnar *et al*. 1990). The parameters required for the description of regional ET differ from those required for surface runoff, slope water or groundwater. This is relevant for mountain slopes where water is predominantly transported laterally. In this context, geomorphological–geological zoning is particularly important and the description of surface properties should not to be restricted to the vegetation cover, distribution of soil classes and topography alone (Duan *et al*. 2001). In addition, there is a growing demand to describe the reaction of the basin during extreme events, including the prognosis of river bed stability. This can only be modelled using more sophisticated process conceptualisations with parameters describing sediment sources, grain size, bed structure and the dynamics of river bed material.

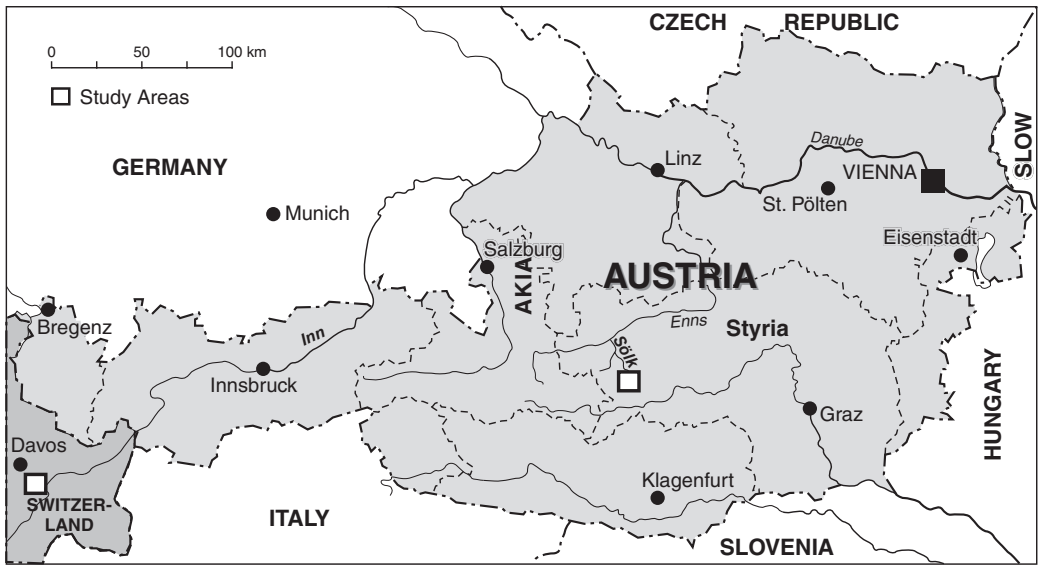


Figure 17.1 The Sölk (Austria) and Dischma (Switzerland) study areas

Table 17.1 Characteristics of study areas

Catchment	Braeualmbach/Soelktal, Austria	Dischma, Switzerland
Location	Tauern/Styria	Graubünden, E. Alps
Size (km^2)	7.8	43
Length (km)	2.6	14
Altitude (m)	1100–2600	1500–3100
Average grad. (°)	27	30
Glaciers (km^2)	None	Scaletta (0.66) Chüalp (0.3)
Geology	Slate, schist, amphibolite, marble	Mainly gneiss, some amphibolite
Soils	Regosols, brown soils, podsols	Regosols, podsols
Vegetation	Forest, dwarf pine, meadows, shrubs and alpine pasture	Mainly alpine grass, dwarf shrubs, forest (spruce, larch, and pine)
Annual aver. snow cover	205 days[a]	225 days[b]
Mean rainfall (summer/annual) (mm)	850 (April to August)/1200[a]	500 (mid-June to mid-Sept)/1200[b]
Mean annual temp. (°C)	1.6 (at 1110 m)[a]	1.1 (at 2000 m a.s.l)[b]
Mean discharge (summer/annual) (mm)	610/860[a]	800/1200[b]
Mean evapotranspiration (mm)	340 (at 1200 m a.s.l)[a]	300 (at 2000 m a.s.l)[b]

[a]BMLF (1981).
[b]Wildi & Ewald (1986).

The goal of this contribution is to recommend the importance of geomorphological zoning for future development of watershed management models dependant on hydrological, meteorological and geomorphological coupling. This approach will be discussed using case studies from the Dischma valley in Grisons south of Davos (Switzerland) and from the Sölk valleys in Styria, situated in the Tauern Mountains east of Schladming (Austria) (Figure 17.1). These valleys represent geological and geomorphological aspects typical for the metamorphic central ranges of the Alps with unstable slopes, active sediment sources and significant fluvial sediment transport (Table 17.1).

17.2 SCALES AND DIGITAL ELEVATION MODELS

It is inevitable that scales have to be shifted according to different goals. Timescales of days, weeks and years are commonly used for analysing many different regional hydrological aspects such as stage or discharge in accordance with the interests of hydrological management (Baumgartner *et al*. 1983). In contrast, forecasts of precipitation and associated floods under mountain conditions often require much higher resolution time steps of tens of minutes or at least half-hourly intervals. Since water levels in torrents and rivers rise rapidly during storm events, time intervals of approximately 10 min are preferable. When aspects such as hazard and risk analysis are mandatory, new model approaches are necessary. For this purpose, precise measurements of regional precipitation and snowmelt are required to simulate discharge and to enable detailed description of their influences on the main water storages in mountain slopes and valleys.

Corresponding spatial descriptions are equally important. For many model approaches, coarse grids (25 by 25 m) are sufficient to describe driving parameters (Grayson & Bloeschl 2001). However, when roughness and geometry of slopes and torrents have to be considered because of, for example, their influence on snow distribution or evaporation, smaller grid sizes or landscape units have to be incorporated. In the Swiss Alps, topographical plans are typically available at a scale of 1:10,000, forming a good basis for digital elevation models (DEM) with grid sizes of 5–10 m. At present, this scale is complemented by a new generation of remote sensing images such as ASTER or SPOT. Considering the stability of rivers and torrents, it is not advisable to model with a uniform spatial resolution but to apply a dual-nested approach with a higher spatial resolution for selected areas sensitive to rapid changes in surface discharge. For a daily prognosis of discharge, coarser scale models suffice.

17.3 PARAMETERISING SURFACE PROPERTIES BY GEOMORPHOLOGICAL ZONING

The traditional approach of hydrological models, where surface characteristics are described only in terms of topography, vegetation cover and soils, is not adequate for modelling in mountain terrain (Price & Heywood 1994, Duan *et al*. 2001). Parameters that are necessary for the description of surface properties, especially geomorphological zones, will be discussed for the following three types of models.

1. Evapotranspiration models
2. Slope models
3. Precipitation-runoff models and sediment transport

17.3.1 Evapotranspiration models for mountain valleys

Evapotranspiration models are of special interest for mountains in semi-arid or arid environments. Water management that relies on the role of water towers (Price & Barry 1997) requires improved hydrological models. Amongst important hydrometeorological parameters such as precipitation and ET, runoff is the only reliably measured regional hydrological component under mountain conditions (Whiting 2003). Of the remaining components, regional precipitation is even more difficult to determine (Sevruk & Martinec 1985) than ET. Therefore, it should be more accurate to solve the regional water balance from the sum of discharge and evaporation for dry pentades or decades as well as on an annual timescale (Molnar *et al*. 1990, de Jong 2002, Weingartner *et al*. 2003). However, it is not sufficient to derive evaporation from functions without any further validation. Standard procedures rely on meteorological data and parameters typically available only for the valley bottom. When regionalising these data, parameters are introduced according to assumptions supported only by linear altitudinal regressions. Apparently, all that is required is a suitable DEM and GIS (Geographical Information System) of the vegetation or land cover but when looking at the results in detail, the local water balance requires a lot of improvement and validation.

In contrast to precipitation-runoff models, which are delineated according to the extent of valleys and subbasins, evaporation models should comprise units with more or less uniform evaporation and can therefore extend across several discharge subunits. These units can be defined from areas with homogeneous vegetation cover and surface properties, including soils, aspect and topography (Hipps & Kustas 2001), as well as geomorphology in areas with, for example, glaciers

or scree slopes. One problem concerning regional ET models is that only the horizontal projection and not the actual size of slopes is treated. For example, a steep slope with approximately 75° average inclination and 200 m length is represented by only a quarter of its topographic length in a topographic map of 1:25,000. Appropriate correction functions are therefore desirable. Another handicap for evaporation models is that direct ET measurements with lysimeters in mountains cover a density of hardly 1/10,000 km^2. For validation purposes, there is a strong demand for more observations and measurements on ET and evaporation. As shown by de Jong (2002) and in Chapter 12 of this book, electronic measuring systems are relatively easy to construct and affordable.

In mountain catchments, the extent of local water bodies or areas of potential evaporation can be determined from topographical maps, air photos or satellite images. However, the quantification of the extent of lakes, ponds, mires, creeks and river surfaces is particularly problematic during phases of intense snowmelt or extreme precipitation. The parameterisation of dynamic zones with saturated soil and wet locations on slopes remains difficult. According to Dunne *et al*. (1975), the resulting saturated zones form narrow bands in steep neighbouring slopes, but they are wide in gently inclined neighbouring slopes. Under these circumstances, subsurface transmissivity and slope length can help in defining the potential zone of saturated soil. This local situation affects vegetation and the amount of organic content in the soils of the related zones.

With these large local variations, no linear decline in ET can be expected between alpine valley bottoms and peaks (de Jong 2002). The anticipated decline of ET with altitude in parallel with a decline in organic matter is typical only for the poor pasture zone lying above the steep valley troughs (usually above 2200 m). Investigations show that the valley bottom has a strong tendency towards cooling, reducing ET even during the summer. A further reduction in ET is caused by the spatial transport and distribution of humidity and condensation. Evaporation and transpiration on the lower trough slopes is more intensive than on the valley bottom or the higher slopes even where alpenrose (*Rhododendrum ferrugineum*) has replaced the former forest cover (de Jong 2002, Chapter 12 of this book). The variability of radiation with aspect induces variations in the timing of maximum transpiration rates, but the difference between the sum of daily ET on east and west sloping sites remains small.

The local topographic position of a site has a more important influence on ET. The more exposed it is to wind, the higher the ET. Special geomorphic zones such as lateral moraines encourage high ET in relation to the surrounding slopes. On the other hand, units of positive relief do not receive lateral water and are therefore the first to suffer desiccation with reduced summer rainfall. Such sites cool intensively during the winter in the absence of thick snow covers and are more prone to long-lasting soil frost. In the alpine meadow and shrub zones above the tree line (at approximately 2300 m in the Dischma), geomorphological zones can differ substantially. They can range from wet zones typical for the centres of corries or wet niches behind lateral moraines on trough shoulders to relatively dry rock faces and scree slopes (Figure 17.2). Indicators for exceptionally humid zones include mossy vegetation in moors and depressions near local moraines and lichens on boulders or on older scree particles. During snowfall and drift or during snowmelt, micro relief amplifies differences in subsurface humidity and temperature. In general, geomorphological zones that are homogeneous over large areas (see upper Dischma Figure 17.2) are easy to delineate from remotely sensed images (Figure 17.3a) or from good topographical maps.

One of the greatest restrictions for quantifying ET is the unsolved problem of defining local roughness of vegetation, rock or sedimentary surfaces. Even micro surfaces of different rocks vary immensely. They are very large for sandstones or schists but rather small for many limestones. No data is available on the potential of different rock surfaces to temporarily store surface water films. Nevertheless, climbers know that large variabilities exist between different slopes. Vegetation and its potential for interception vary significantly over time. Interactions between snow and vegetation during snowmelt typically induce high evaporation. With their unique geomorphic setting, ''Schneetaelchen'' or ''snow valleys'' (Franz 1979) are of special interest since they allow snow to persist during the short summers and most of the meltwater to evaporate at the outlet. What is typical locally is also true for whole valley slopes: periods and regions with snowmelt correspond with the largest annual evaporation rates. In contrast, rock faces and large scree surfaces evaporate most intercepted rainwater and condensated water from their wetted surface. It is therefore reasonable to assume that about 2 mm of intercepted rain or condensation will evaporate per day and that only surplus water will infiltrate into talus scree.

Evapotranspiration models should be differentiated and scaled according to these observations. Surface descriptions should not be limited to vegetation cover (e.g. different grass types, shrubs, forest or bog) or selected soil properties alone. Under alpine conditions, the properties of these surfaces must be differentiated according to geomorphological zones with dominant

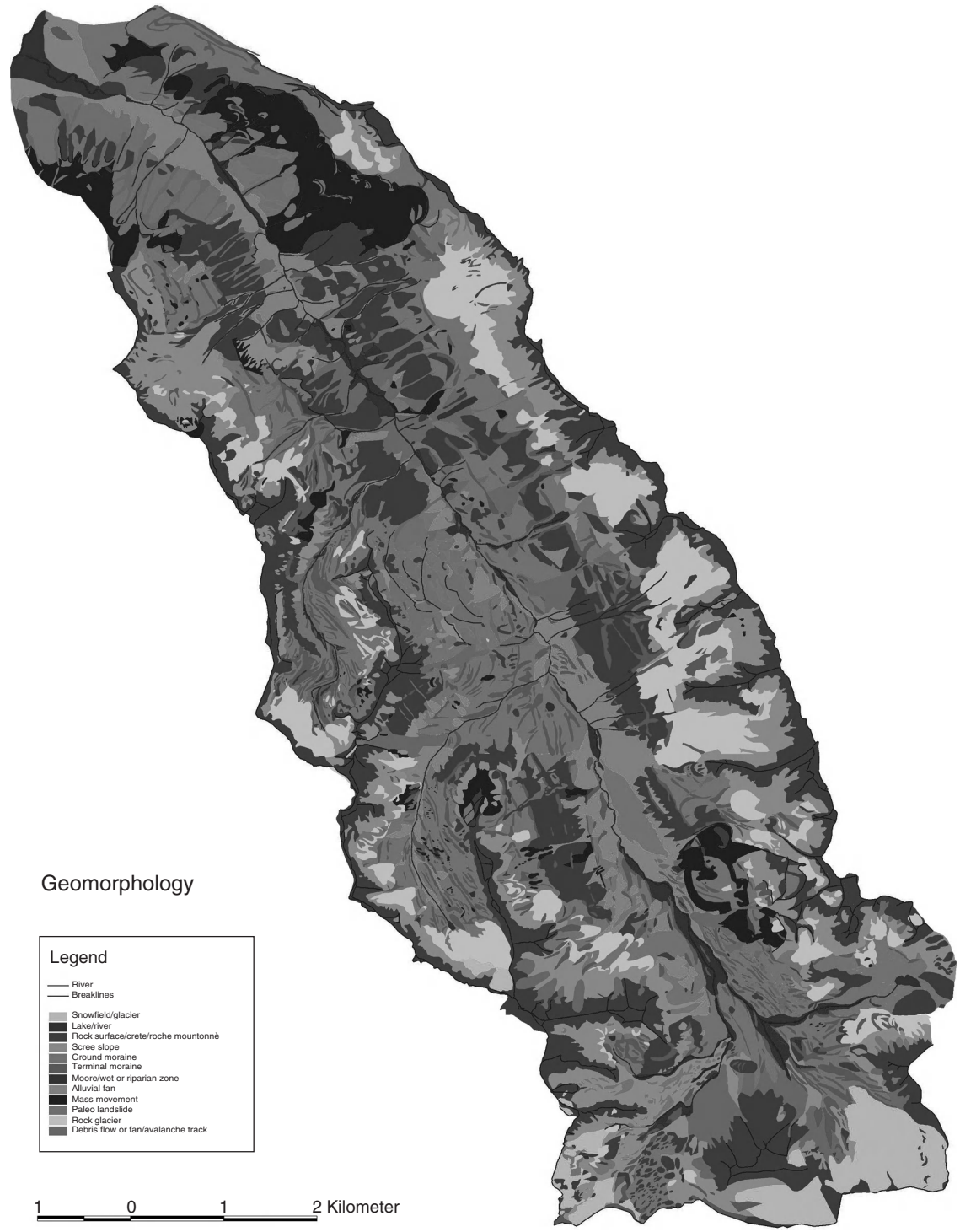


Figure 17.2 (Plate 13) Detailed geomorphological map of the Dischma divided into 14 different zones. The valley is dominated by moraines, scree slopes, rock faces, alluvial fans, glacier and snow fields

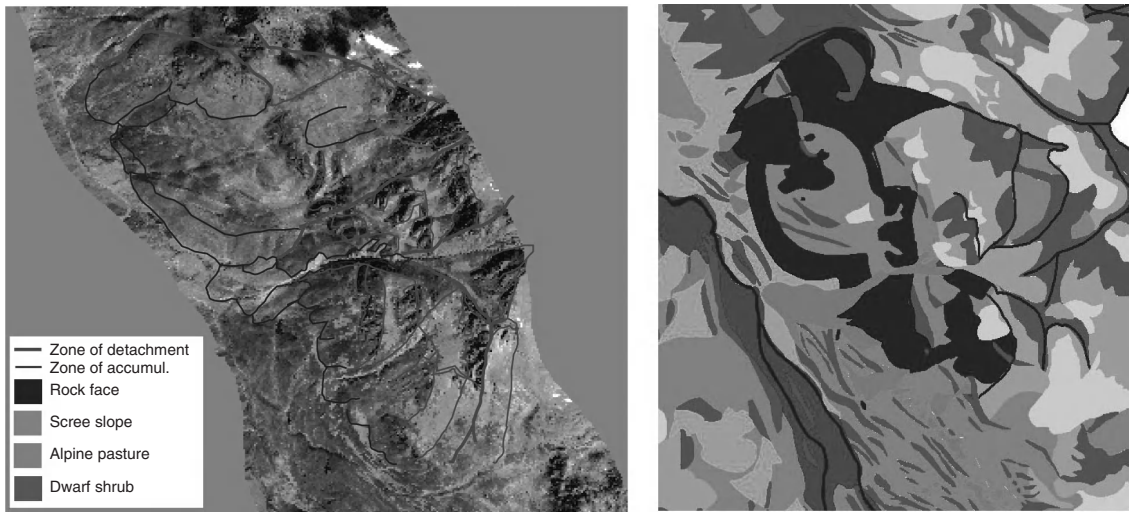


Figure 17.3 (Plate 6) (a) Remotely sensed CASI (Canadian Airborne System) image of the Duerrboden mass movement in Upper Dischma with a resolution of 5 m in the infrared canal and (b) enlargement of geomorphological map of corresponding area

units such as rock surfaces, scree slopes, trough slopes, ground moraines and terminal moraines. Spring horizons resulting from the lateral movement of interflow should be considered on the lower valley slopes or in areas where the carrying capacity of water is reduced owing to changes in the transmissivity of scree material. For similar reasons, slopes prone to mass movements are hydrologically complex and should be carefully integrated into models.

For validating the spatial and temporal distribution of ET, meteorological variables should be obtained at the regional scale by remote sensing or from infrared images. This is especially true for temperature, which should be scanned regularly to complement multiple climate station profiles and improve our knowledge on the budget of sensible and latent heat.

17.3.2 Slope models

The goal is to develop models combining surface, lateral and groundwater flow as well as geomorphological slope dynamics (Kirkby 1996). It is clear that this task is especially important for mountains. The general problem is tackled only partially by soil erosion experts (e.g. Hurni 1988) or by geologists or soil scientists dealing with landscape denudation at different scales (Montgomery *et al*. 1995, Schreier 2002).

During the last decade, more and more GIS models have been applied to describe changes in land use and/or vegetation cover in mountain regions and to speculate about the future impact of climatic or hydrological changes (Leavesley 1994). The most important parameter linked to vegetation change is ET. Only major changes have an impact on slope water and geomorphological stability. For example, the hydrological impact of reforestation of former alpine meadows is often less important than the construction of a network of forest roads on steep trough slopes (Megahan 1981). In the Soelktal, there are very serious examples of the impact of new forest roads on slope stability, but related impact studies do not exist yet.

In the Dischma and Sölk valleys, the sequences of soils from the rocky ridges to the valley bottom are comparable. The typical catena (Krause & Peyer 1986) begins with shallow silicate soils on the rocky ridges (5–15 cm), followed by humus-rock soils (10–30 cm) on alpine meadows down to the tree line. Regosoils are very typical for trough slopes. Here, no distinct horizon is detectable, and because of ongoing erosion, weathering products are rare. The thickness of these soils range between 30 and 50 cm. Brown soils and podsols are dominant in the valley bottom and the neighbouring terraces. The distribution of ‘‘moderhumus’’ is of high interest since this surface cover forms a very good buffer and storage for rainwater. Tensiometer studies at the Stillberg site, Dischma, showed that even during the summer the dominant shrub and meadow vegetation suffer no water shortage (Bednorz *et al*. 2000). Plants

will indicate water stress only when rainfall fails for more than 10 days.

The subsurface sediment and regolith must be considered in models of local slope hydrology. Here again, geomorphological zoning of slopes with different properties is very important. On the lower slopes of schist or gneiss rocks, several meters of weathered material often lie below covers of periglacial scree and deposits of morainic material. In the Tauern, schists often trigger mass movements. In the Dischma, recent and pre-Wuermian mass movements can be found even in harder gneiss rocks (Figure 17.3a and b). As shown in this example, mass movements can be clearly distinguished from high-resolution remotely sensed images. They decisively influence lateral water transport in slopes and for this reason geomorphological maps are important tools for flow routing in hydrological modelling. At the foot of mass movements, a spring horizon is common.

Both the gneiss of the Dischma as well as the schist of the Tauern are prone to mechanical weathering. Talus slopes of weathered material preferentially develop below rock faces in the corrie zone above the present tree line. As indicated for the Braeualm valley (Figure 17.4), long steep trough slopes are often covered by scree. The talus slopes in the corries are only partially covered by short grass and shrubs. These typically develop according to the Richter model (Selby 1993). During phases of intensive precipitation, the surplus of sudden infiltration water causes groundwater outbursts at the lower end of the cones and may even trigger small debris flows. Since debris flows cannot travel far because of breaks in slope on the corrie floor, these cannot feed into the main valley. For modelling purposes, talus slopes are very important since these combine impermeable rock faces with the highly permeable screes below.

The older scree and talus slopes of the trough valley south of St. Nikolai develop differently because of creep processes (e.g. east-facing slope below Mt. Scheiben, Figure 17.5). This slope is covered by large and steep debris lobes moving slowly towards the valley bottom. The lobes are delineated at their upper end by a zone of detachment with a steep rim. Creep slopes are common in the Sölk valleys and are a function of the depth of scree material and its hydrological properties. The movement of such debris creeps can continue across thousands of years but in certain zones they can suddenly accelerate to form debris flows or mass movements. Such an event occurred in the summer 1994 in the neighbouring valley of Klein Sölk (Hermann & Becker 1998). Signs for this transition can be observed from three small incised channels feeding larger debris fans below the Scheiben. Infiltration of creep slopes is reduced to moderate rates, thereby also reducing surface runoff (Figure 17.5). Zones with more intensive runoff are located at upper rim above scree slopes. Such aspects need consideration in spatially diversified hydrological models and can be integrated accordingly.

Hence, in terms of modelling sediment sources, creeping slopes are ''silent sources'' that can be activated randomly, whereas other sources are more continuously mobilised through avalanche and debris flow activity. An important geomorphological boundary exists between trough slopes and corrie areas (Figure 17.4). This boundary splits the watershed into two parts. The higher part of the basin is hydrologically active, creating high discharge rates on rock faces down to the talus. Discharge is transmitted through the corrie lakes and depressions, but coarse sediments cannot pass. Under present conditions, coarse sediments can only be transferred from the steep trough slopes into the main valley via avalanches and debris flow channels.

In principle, the corrie zone in the Dischma resembles that of the Sölk valley. Since the weathering rates of gneiss are lower than those of schist, less scree material is produced on the trough slopes and debris creep is reduced accordingly. On the other hand, the Dischma is still presently glaciated with a more intensively eroded upper valley (de Jong *et al*. 2002). This has caused a mass movement near Duerrboden mobilised on the west-facing slope (Figure 17.3). However, this material stagnated at the edges of the valley. Intensive erosion only occurs along the southern edge of the mass movement. Here, scree material is carried towards the river by debris flows. Locally, the mass movement is extremely porous. Corresponding to high rates of infiltration over this zone, a distinct spring horizon has formed at the lower end.

The importance of frozen ground for infiltration and groundwater recharge is significant in zones with rock glaciers. These occur in the Dischma at altitudes above 2400 m and in the Sölk valleys above 2250 m. Permafrost is another key factor combining local hydrology, meteorology and geomorphology in high alpine valleys and slopes (Schrott 1998). This is well documented for the Dischma (Haeberli & Beniston 1998). At the end of the winter, the distribution of permafrost is as important as temporarily frozen ground. The latter is dominant during cold winters with shallow snow cover and wind drift. Under such conditions, water from snowmelt and first rain will be transported close to the surface as long as subsurface sediments and soils are frozen.

Other geomorphological zones important for hydrological models include terminal and ground moraines in corries and at the head of the trough valleys. Morainic



Figure 17.4 Corries and zones of sediment sources, River Braeualmbach south of St. Nikolai (Grosssoelk/Tauern/Austria)



Figure 17.5 Hydrogeomorphological zoning of the trough slopes in Braeualm valley south of St. Nikolai (Grosssoelk/Tauern/Austria)

material is normally rich in silt and can even contain some clay. This causes significant differences in infiltration over short distances. Bogs are quite common amongst the Holocene terminal moraines and demonstrate a low potential both for infiltration and for throughflow. According to Parriaux & Nicoud (1990), surface runoff and/or mass movement are dominant in water lain tills and glaciolacustrine beds, whereas deep infiltration only dominates in glaciofluvial deposits, kames terraces and terminal moraines. Shallow infiltration is typical for ground moraines and many lateral moraines.

These examples cover the broad spectrum of options that can be obtained from geomorphological interpretations of slopes for regional hydrology and even more so their potential in complex ecological models, including sediment dynamics.

17.3.3 Precipitation-runoff models and sediment transport

In contrast to evapotranspiration models, precipitation-runoff models should describe both water and sediment dynamics in confined mountain valleys. Geomorphological zoning (Naef 2002) is especially important for precipitation-runoff models that comprise lateral flow on slopes and include the problem of sediment sources bed stability and coarse sediment transport.

A prerequisite for defining surface runoff is the definition of the catchment boundary. In high alpine regions, catchment boundaries usually form well-developed arêtes. Groundwater flow is more difficult to define, especially in karst regions with complex tectonics. In cristalline rocks, obscure catchment boundaries can occur where glaciers traverse the boundaries and separate water flowing subglacially to both sides (e.g. Chuealp Glacier, lower south-western edge of the geomorphological map, Figure 17.2).

In contrast to soil erosion models (e.g. Ascough *et al*. 1997), precipitation-runoff models do not explicitly include terms such as erosion, transport and sedimentation. In runoff models, sediment transport is usually superimposed via common sediment functions (Nelson *et al*. 2003). Since most of these functions are derived from and validated by laboratory experiments and only consider sediment transport under equilibrium conditions, these results cannot be readily transferred to mountain terrain. Short-term sediment transport dynamics caused by floods differ from mid- and long-term dynamics. For example, Bunte (1996) measured a decline in maximum coarse particles transport from about 430 to below 100 particles per 10 minutes during a sequence of seven snow melt floods at Squaw Creek in Montana/USA. Obviously, there was a shortage of particles because of bed armouring. The river bed was ''cleaned'' of particles by the first flood, thereby reducing the availability of particles from flood to flood. This shows that rivers require time to recover from their sediment deficit. In contrast, the Lainbach in Upper Bavaria eroded, transported and deposited so much coarse sediments during an extreme flood in 1990 (de Jong 1994) that the river bed changed from step-pool to braided. After this event, the Lainbach took two years in succeeding to re-establish its former step-pool situation by erosion and this produced higher rates of coarse sediment transport than in the years before. To model such situations, armouring has to be included as a term of erosion protection.

A similar surge in sediment transport occurred in the Buonamico in the crystalline Aspromonte Mountains in Calabria/Southern Italy (Ibbeken & Schleyer 1991). The winter of 1971–72 was very wet, with up to 2000 mm of precipitation. Several large and small landslides occurred. The largest landslide dammed the valley, creating Lake Costantino (Lago Costantino). After March 1972, the river eroded a new canyon into the landslide material, causing large amounts of accretion below the slide. In the following six years, there was very significant delta accretion into the small remaining lake above the landslide. Calculations showed that the Lago Costantino would be infilled within 25 years. Since that time, however, the filling rates of the lake declined because of a decrease in severe rainfall and an associated reduction in mass movements. Without the supply of sediment from the slopes, the transport rates of coarse sediments continued at a very low level. For such cases, the interrelation between the slope and river bed dynamics can be parameterised from a conceptual model (Ergenzinger 1992).

These examples demonstrate the importance of sediment dynamics and mass movements on mountain rivers and torrents. However, neither sediment functions nor results from different types of landslide and mass movement models (Carrara *et al*. 1977, Eisbacher & Clague 1985, van Westen 1994) can be derived from simple precipitation–runoff models. Mountain rivers should not be compared to or modelled as dynamic, water-filled pipes but should be considered as joint carriers of both water and coarse sediment (Darby & van de Wiel 2003). This not only requires adjustment of precipitation-runoff models but also the development of more sophisticated models capable of integrating sediment inputs from slopes and river banks as well as the stability and properties of the river bed. In this sense, there is still a lot to be accomplished, and the

basis for such models must involve complete sets of geomorphological and geological parameters and zones where possible.

17.4 REGIONAL PRECIPITATION AND WIND

The regional distribution of precipitation, both as snow and rainfall, is very difficult to determine (Baumgartner *et al*. 1983, Sevruk 1997, Tarboton *et al*. 2001). Regional precipitation is often underrepresented since standard rainguage networks only have a density of 1/100 km^2. In mountains, nearly all raingauges are situated near roads along the valley floor. Even in favourable situations in which climatological stations are also located at higher altitudes close to the catchment boundary, the definition of local precipitation remains problematic. For single events, linear relationships between altitude and precipitation often do not exist. This is due to the temporal and spatial influence of wind irregularities. In principle, there is more precipitation in upwind situations but less in downwind situations (Sharon & Arati 1997), therefore a well-defined regional measuring network of precipitation stations is essential. In addition, measurement of precipitation is seriously affected by wind as a site-specific factor (Sevruk & Martinec 1985). Even when the tracks of rain fields are well documented with large-scale radar or remotely sensed data, the regional distribution of rainfall is still not resolved. If precipitation continues to be measured only at one point in a catchment, the local or regional precipitation will remain poorly defined. More point measurements and additional measurements with small-scale local radar beams near the ground along the valley axis would be more appropriate.

In all hydrometeorological models, precipitation is the most important input, but modelling of ET is often neglected. In mountain regions, model validation could be improved by optimising precipitation measurements instead of deriving precipitation from the sum of discharge and poorly estimated ET. The accuracy of measuring and extrapolating precipitation in models could be enhanced by improving wind measurements and establishing high-resolution regional wind models.

17.5 CONCLUSION AND RECOMMENDATIONS

Mountain regions differ hydrologically from lowlands in two main ways as follows.

1. There is a substantial difference between hard rocks with low hydraulic conductivity and low storage capacity (excluding limestone and sandstone) and areas with high hydraulic conductivity and high storage capacity such as glacial deposits, scree and fluvial or other quaternary sediments. This leads to a high regional variability of hydrological components such as discharge.
2. Mountain rivers are developed so that they can carry water as well as sediments in large surges from the slopes down to the rivers and into the tectonic basins and forelands. This not only is part of hazard and risk analysis but it also determines the ecology of flood prone zones. The amount of bed forming load is particularly important for river bed stability (Vischer 2002).

Under these conditions, there is an urgent need to improve the coupling of hydrology and meteorology with the help of geomorphological and geological parameters and to create new models that comprise problems of sediment transport and river bed dynamics (Sieben 1997). Most existing models exclude geomorphological zones and problems of sediment dynamics that are particularly important in sustainable watershed management (Schaller 1994, Schreier 2002). For this purpose, the MMS/PRMS Model Package developed by Leavesley *et al*. (2002) is particularly suitable. In this modelling system, the programme library and source code is public and new subprograms can be added.

According to research experiences gained on ET in the Dischma, *ET models* should be based on Evaporation Response Units (ERUs) that depend on the following parameters.

- Topography and geomorphology (slope and aspect, rocks, scree, soils and roughness)
- Surface cover (vegetation, water bodies, snow, etc.)
- Meteorological variables (radiation/temperature, wind, humidity/dew point)
- Wind distribution.

A geomorphological map can help define local extremes such as localities with specific aridity or humidity. Whereas rock surfaces and bare scree slopes are dry, lakes, watercourse, moors, snow valleys and the border of snowfields are wet. The ERUs in such zones should not only consist of the horizontal area on maps but should also be corrected according to the real area of strongly inclined slopes. The scales of an ERU should lie around 1:10,000 or encompass areas of several 100 m^2.

Slope models should be included in hydrological watershed models, especially where surface runoff and sediment transport is highly productive. Soil, slope and groundwater parameters should be considered in addition to slope stability and related problems of

erosion and transport. Slopes should be differentiated according to present as well as past slope movement and development. Thus, apart from hydrological aspects, Hydrological Response Units (HRUs) have to consider geomorphological as well as geological rock and slope properties. The size of HRUs differs according to the size of slope sectors and should accommodate broad channels as well as debris flow and avalanche transport paths. The variability in size of different trough slopes according to different dynamics was demonstrated in the valley of Braeualmbach at St. Nicolai in the Tauern. The number of parameters and the scale of the HRUs must correspond to the problems in the catchment. In tectonically active regions, the risk of slope failure (Eisbacher & Clague 1985) and the occurrence of earthquakes should be integrated into slope models (Hewitt 1976).

Precipitation-runoff models should be developed as tools for watershed management in mountain regions (Schreier 2002). It is recommended that lateral flow dynamics and sediment balance should be included in regional water balance analysis. Models of catchment processes such as fluvial and slope dynamics are recently available (Downs & Priestnall 2003). Watershed management cannot succeed in the long term without including debris flows (Rebetez *et al*. 1997), mass movements and fluvial erosion, transport and sedimentation. Existing models with bed load functions (Vischer 2002) do not usually treat long-term response. Research on the regional dynamics of sediment sources remains a major challenge to science (Thornes *et al*. 1996).

Methods differentiating sediments according to different sources (avalanche, debris flow or mass movement) are not available yet. Many hints on how to solve such problems were already provided more than a decade ago by Ibbeken & Schleyer (1991). One method that can be applied to and modelled under fluvial conditions is tracer studies, for example, models of travel lengths of coarse sediment during floods (Hassan & Ergenzinger 2003, Brenda & Dunne 1997). In addition, there is potential to validate such models by applying the newest remote-sensing techniques: for example, the HRSC camera of the DLR (German Aero Space Agency) already in function on Mars. The resolution of a pixel is smaller than two decimetres and this allows the detection of coarse cobbles as well as many structures typical for gravel bed rivers during dry conditions. Comparison of HRSC data for different floods can increase our understanding of the behaviour of river beds and allow highly precise quantification. These techniques can determine the amount of erosion and accretion or bank retreat more accurately than measured discharge volumes (Ergenzinger & de Jong 2004). In the near future, the increasing demand for data sets required to validate the newly developed integrated models will grow.

Under alpine conditions, more than 100 years of sediment management by ''Wildbachverbauung'' (or mountain torrent control) combined with intensive reservoir construction has caused an immense sediment deficit in gravel bed rivers, causing widespread river instability and erosion. There is a growing demand for *watershed* and *river bed management* (Goettle 2002). New tools and models are required to simulate both discharge and regional sediment budgets in order to solve problems of river bed instability.

REFERENCES

Ascough, J.C. II, Baffaut, C., Nearing, M.A. & Liu, B.Y. 1997: The WEPP watershed model. I. Hydrology and erosion. *Transactions of the American Society of Agricultural Engineers*, **40**: 921–933.

Baumgartner, A., Reichel, E. & Weber, G. 1983: *Der Wasserhaushalt der Alpen*. Oldenbourg Verlag, München.

Bednorz, F., Reichstein, M. Broll, G., Holtmeier, F.-K. & Urfer, W. 2000: Humus forms in the forest-alpine tundra ecotone at Stillberg (Dischmatal, Switzerland): spatial heterogeneity and classification. *Arctic and Alpine Research*, **32**: 21–29.

BMLF 1981: (Bundesministerium für Land- und Forstwirtschaft) (ed.): Erläuterungen zur Bodenkarte 1:25000, Kartierungsgebiet Gröbming, Steiermark. Wien, Austria.

Brenda, L. & Dunne, T. 1997: Stochastic forcing of sediment routing and storage in channel networks. *Water Resources Research*, **33**: 2865–2880.

Bunte, K. 1996: Analysis of the Temporal Variation of Coarse Bedload Transport and its Grain Size Distribution: Squaw Creek, General Technical Report RM-GTR-288, Montana, MT, USDA Forest Service.

Carrara, A., Pugliese, C. & Merenda, L. 1977: Computer – based data bank and statistical analysis of slope instability phenomena. *Zeitschrift fur Geomorphologie*, **N.F.21**: 187–222.

Darby, S.E. & van de Wiel, M. 2003: Models in fluvial geomorphology. in: Kondolf, G.M. & Piegay, H. (eds.): *Tools in Fluvial Geomorphology*. Wiley, Chichester: 503–537.

de Jong, C. 2002: Regionale Untersuchungen zum Wasserhaushalt und speziell zur Verdunstung im alpinen Einzugsgebiet des Rheins: Dischmatal/Davos. Final report for the Deutsche Bundesstiftung Umwelt, Osnabrück.

de Jong, C. 1994: The significance of extreme events in the development of mountain river beds. in: Olive, L.J., Loughran, R.J. & Kesby, J.A. (eds.): *Variability in Stream Erosion and Sediment Transport*. IAHS Publication no. 224: 13–24.

de Jong, C., List, F.K. & Ergenzinger, P.J. 2002: Experimental hydrological analyses in the Dischma based on daily and seasonal evaporation. *Nordic Hydrology*, **33**: 1–14.

Downs, P.W. & Priestnall, G. 2003: Modelling catchment processes. in: Kondolf, G.M. & Piegay, H. (eds.): *Tools in Fluvial Geomorphology*. Wiley, Chichester: 205–230.

Duan, Q., Schaake, J. & Koren, V. 2001: A priori estimation of land surface model parameters. in: Venkataraman, L., Albertson, J. & Schaake, J. (eds.): *Land Surface Hydrology, Meteorology and Climate*, Water Science and Application 3. AGU: 77–94.

Dunne, T., Moore, R.T. & Taylor, C.H. 1975: Recognition and prediction of runoff-producing zones in humid regions. *Hydrological Sciences Bulletin*, **20**(3): 305–327.

Eisbacher, G.H. & Clague, J. 1985: Destructive Mass Movements in High Mountains. Geological Survey of Canada, Paper 84/16.

Ergenzinger, P. 1992: A conceptual geomorphological model for the development of a Mediterranean river basin under neotectonic stress (Buonamico, Calabria, Italy). in: Walling, D.E., Davis, T.R. & Hasholt, B. (eds.): *Erosion, Debris Flows and Environment in Mountain Regions*. IAHS Publication no. 209, Chengdu: 51–60.

Ergenzinger, P. & de Jong, C. 2004: Perspectives on bedload measurement. in: Bogen, J., Fergus, T. & Walling, D. (eds.): *Erosion and Sediment Transport Measurement: Technological and Methodological Advances*. International Association of Hydrological Sciences, Publication no. 283: 113–126.

Franz, H. 1979: *Ökologie der Hochgebirge*. Ulmer, Stuttgart.

Goettle, A. 2002: Profit of watershed management for lowland areas – experiences made in Bavaria. *Greminger: Mountain Watershed Management*, Lessons from the Past – Lessons for the Future. Proceedings. Environmental Documentation No. 165: 97–114. Forests. Swiss Agency for Environment, Forests and Landscape (SAEFL), Berne.

Grayson, R. & Bloeschl, G. 2001: Spatial patterns in catchment hydrology. *Observations and Modelling*. Cambridge University Press, Cambridge.

Haeberli, W. & Beniston, M. 1998: Climate change and its impacts on glaciers and permafrost in the Alps. *Ambio*, **27**: 258–265.

Hassan, M.A. & Ergenzinger, P. 2003: Use of tracers in fluvial geomorphology. in: Kondolf, G.M. & Piegay, H. (eds.): *Tools in Fluvial Geomorphology*. Wiley, Chichester: 397–423.

Hermann, S. & Becker, P.L. 1998: Rutschungs- und Erosionserscheinungen im Naturpark Soelktaeler, ausgelöst durch ein Niederschlagsereignis vom 29. Juni 1994. Mitteilungen des naturwissenschaftlichen Vereins Soelktaeler, Band 128: 5–15.

Hewitt, K. 1976: Earthquake Hazards in mountains. *Natural History*, **85**: 30–37.

Hipps, L. & Kustas, W. 2001: Patterns and organisation in evaporation. in: Grayson, R. & Bloeschl, G. (eds.): *Spatial Patterns in Catchment Hydrology. Observations and Modelling*. Cambridge University Press, Cambridge: 105–122.

Hurni, H. 1988: Degradation and conservation of soil resources in the Ethiopian highlands. *Mountain Research and Development*, **7**: 123–30.

Ibbeken, H. & Schleyer, R. 1991: *Source and Sediment. A Case Study of Provenance and Mass Balance at an Active Plate Margin (Calabria, Southern Italy)*. Springer, Berlin.

Kirkby, M.J. 1996: A role for theoretical models in geomorphology? in: Rhoads, B.L. & Thorn, C.E. (eds.): *The Scientific Nature of Geomorphology*. Wiley, Chichester: 257–272.

Krause, M. & Peyer, K. 1986: Böden. in: Wildi, O., Ewald, K. & Bosshard, W. (eds.): *Der Naturraum und dessen Nutzung im alpinen Tourismusgebiet von Davos. Ergebnisse des MAB – Projektes Davos*. Eidgenoessische Anstalt fuer das forstliche Versuchswesen, Birmensdorf: 67–78.

Leavesley, G.H. 1994: Modeling the effects of climate change on water resources: a review. in: Frederick, K.D. & Rosenberg, N. (eds.): *Assessing the Impacts of Climate Change on Natural Resource Systems*. Kluwer, Dordrecht: 179–208.

Leavesley, G.H., Markstrom, S.L., Restrepo, P.J. & Viger, R.J. 2002: A modular approach to addressing model design, scale and parameter estimation issues in distributed hydrological modeling. *Hydrological Processes*, **16**: 173–187.

Megahan, W.F. 1981: Nonpoint source pollution from forestry activities in the western United States: results of recent research and research needs. *US Forestry and Water Quality: What Course in the '80s?* Water Pollution Control Federation, Washington, DC: 92–151.

Molnar, L., Miklanek, P. & Meszaros, I. 1990: Problems of the water balance components determination in a mountainous watershed. in: Molnar, L. (ed.): *Hydrology of Mountainous Areas*. IAHS Publication no. 1990: 167–178.

Montgomery, D.R., Grant, G.E. & Sullivan, K. 1995: Watershed analysis as a framework for implementing ecosystem management. *Water Resources Bulletin*, **31**: 369–386.

Naef, F. 2002: How often do extreme events occur? *The Extremes of the Extremes: Extraordinary Floods*. IAHS Publication no. 271: 65–70.

Nelson, J.M., Bennett, J.P. & Wiele, S.M. 2003: Flow and sediment – transport modeling. in: Kondolf, G.M. & Piegay, H. (eds.): *Tools in Fluvial Geomorphology*. Wiley, Chichester: 539–576.

Parriaux, A. & Nicoud, G.F. 1990: Hydrological behaviour of glacial deposits in mountainous areas. in: Molnar, L. (ed.): *Hydrology of Mountainous Areas*. IAHS Publication no. 190: 291–312.

Price, M.F. & Barry, R.G. 1997: Climate change. in: Messerli, B. & Ives, J.D. (eds.): *Mountains of the World*. A Global Priority: 409–445.

Price, M.F. & Heywood, D.I. (eds.) 1994: *Mountain Environments and Geographic Information Systems*. Taylor & Francis, London.

Rebetez, M., Lugon, R. & Baeriswyl, P.A. 1997: Climatic change and debris flows in high mountain regions. *Climatic Change*, **36**: 371–389.

Schaller, J. 1994: Geographic information systems and ecosystem models as tools for watershed management and ecological balancing in high mountain areas: the example of ecosystem research in the Berchtesgaden area, Germany. in: Price, M.F. & Heywood, D.I. (eds.): *Mountain Environments*

and Geographic Information Systems. Taylor & Francis, London: 43–58.

Schreier, H. 2002: Mountain watershed management: scaling up and scaling out. *Greminger: Mountain Watershed Management*. Lessons from the Past – Lessons for the Future. Proceedings. Environmental Documentation No. 165: 29–42. Forests. Swiss Agency for Environment, Forests and Landscape (SAEFL), Berne.

Schrott, L. 1998: The hydrological significance of permafrost in the semiarid Andes. in: Price, M. (ed.): *Global Change in the Mountains*. Parthenon, New York, London: 199–201.

Selby, M.J. 1993: *Hillslope Materials and Processes*, 2nd Edition. Oxford University Press, Oxford.

Sevruk, B. 1997: Regional dependancy of precipitation – altitude relationship in the Swiss Alps. *Climatic Change*, **36**: 355–369.

Sevruk, B. & Martinec, J. 1985: Fehlerquellen, Genauigkeit, Korrekturmöglichkeit. in: Sevruk, B. (ed.): *Der Niederschlag in der Schweiz*. Kuemmerly & Frey, Bern: 65–86.

Sharon, D. & Arati, A. 1997: The distribution of wind – driven rainfall in a small valley: an empirical basis for numerical model verification. *Journal of Hydrology*, **2001**: 21–48.

Sieben, J. 1997: *Modelling of Hydraulics and Morphology in Mountain Rivers. Proefschridt*. Technische Universiteit Delft, Delft.

Tarboton, D., Bloeschl, G., Cooley, K., Kirnbauer, R. & Luce, C. 2001: Spatial snow cover processes at Kuehtai and reynolds creek. in: Grayson, R. & Bloeschl, G. (eds.): *Spatial Patterns in Catchment Hydrology. Observations and Modelling*. Cambridge University Press, Cambridge: 158–186.

Thornes, J.B., Shao, J.X., Diaz, E., Roldan, A., McMahon, M. & Hawkes, J.C. 1996: Testing the Medalus hill-slope model. *Catena*, **26**: 137–160.

van Westen, C.J. 1994: GIS in landslide hazard zonation: a review, with examples from the Andes of Colombia. in: Price, M.F. & Heywood, D.I. (eds.): *Mountain Environments and Geographic Information Systems*. Taylor & Francis, London: 135–165.

Vischer, D. 2002: The Tricky Question of Equilibrium. *Greminger: Mountain Watershed Management*. Lessons from the Past – Lessons for the Future. Proceedings. Environmental Documentation No. 165: 43–49. Forests. Swiss Agency for Environment, Forests and Landscape (SAEFL), Berne.

Weingartner, R., Barben, M. & Spreafico, M. 2003: Floods in mountain areas-an overview based on examples from Switzerland. *Journal of Hydrology*, **282**: 10–24.

Whiting, P.J. 2003: Flow measurement and characterization. in: Kondolf, G.M. & Piegay, H. (eds.): *Tools in Fluvial Geomorphology*. Wiley, Chichester: 323–346.

Wildi, O. & Ewald, K. 1986: Der Naturraum und dessen Nutzung im alpinen Tourismusgebiet von Davos. Ergebnisse des MAB – Projektes Davos. Eidgenössische Anstalt für das forstliche Versuchswesen. Birmensdorf, Switzerland.

PART V: CLIMATE CHANGE IMPACT AND MOUNTAIN HYDROLOGY

Climate and Hydrology in Mountain Areas. Edited by C. de Jong, D. Collins and R. Ranzi
© 2005 John Wiley & Sons, Ltd. ISBN: 0-470-85814-1

18

The Influence of Glacier Retreat on Water Yield from High Mountain Areas: Comparison of Alps and Central Asia

WILFRIED HAGG AND LUDWIG BRAUN
Bavarian Academy of Sciences, Commission for Glaciology, Marstallplatz 8, 80539 Munich, Germany

18.1 INTRODUCTION

The hydrological importance of mountains has several aspects. The orographic effect and the resulting interaction with the atmosphere produce a highly enhanced precipitation input as compared to lowland areas. Moreover, winter precipitation is stored as snow cover and glacier ice and released, seasonally delayed, in spring and summer, when the demand for irrigation is highest. Not only the water benefits mountain regions themselves but also the rivers transport the surplus of water downstream and provide lowlands with this precious resource. Mountain areas can be regarded as water towers that yield and preserve water and distribute it over time and space.

The importance of such water towers for the lowlands and the strength of the remote impact are strongly influenced by the precipitation conditions of the lowlands. When surrounded by arid regions, mountains are the only relevant water supplier to support the existence of the lowland population. In humid lowlands, the mountainous runoff regime is gradually overlaid by a pluvial one, whereas in dry regions the nival or glacial runoff character is preserved further downstream.

This shows that hydrological processes and changes in mountain areas have a greater importance in drier parts of the continents, as in Central Asia, because here highlands are not only additional water suppliers like in Middle Europe but also the most important and sometimes even the only ones.

Against a background of globally increasing demand for water, climate change and conflicts that can arise from the unequal distribution of water on the earth's surface, one can imagine what great importance international water resources management will play in the future. Regions with great differences in water supply, for example, as a result of the above-described highland–lowland interaction, will have to solve even greater problems in water supply than they already have today.

The aim of this study is to estimate the effect of deglacierisation on river runoff in different climatic regions by applying a conceptual precipitation-runoff model in Central Asia and by comparing the results with similar investigations in the Alps.

18.2 CHARACTERISATION OF THE RESEARCH AREAS

In Central Asia, three test sites with different degrees of continentality were chosen: the Tuyuksu Glacier Region in Kazakhstan, which shows moderate maritime influence, Abramov Glacier in Kyrgyzstan and the highly continental Glacier No. 1 in China (Figure 18.1).

Climate and Hydrology in Mountain Areas. Edited by C. de Jong, D. Collins and R. Ranzi
© 2005 John Wiley & Sons, Ltd. ISBN: 0-470-85814-1

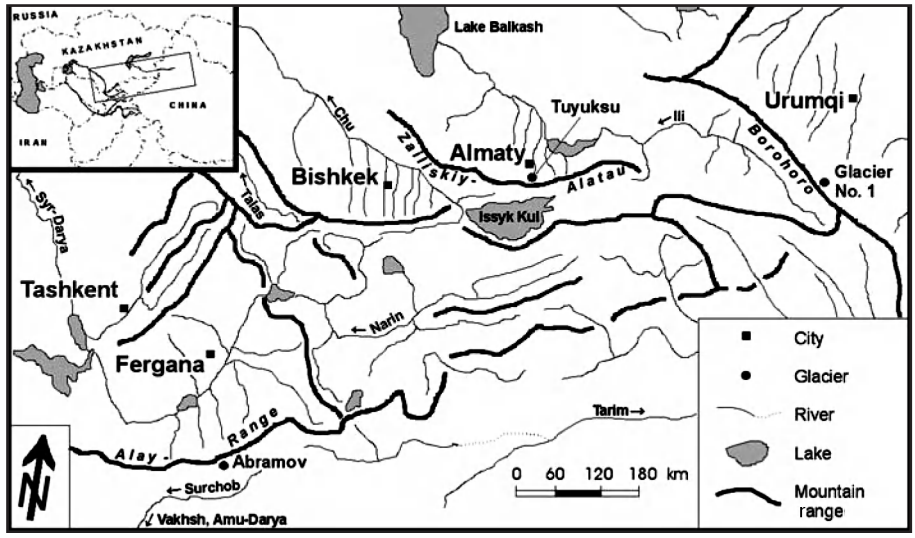


Figure 18.1 Location of the Central Asian research areas, schematic sketch after Aizen *et al*. (1995)

The Tuyuksu area is located on the northern slope of the Zailiskiy Range, which is the most humid part of the northwestern Tien Shan. The basin is drained by the Little Almatinka River, which meets the Ili River ending in Lake Balkash. The largest of the nine glaciers is Central Tuyuksu with an area of 2.5 km^2 (Kommission für Glaziologie 2001).

Abramov Glacier is located in the Pamiro-Alay, a transition zone between Tien Shan and Pamirs. The melt water feeds Koksu River, a third-degree tributary of Amu Darya, one of the main inflows of the Aral Sea. There are 10 small glaciers and Abramov glacier with an area of 26 km^2 (WGMS 1999).

Glacier No. 1 is situated in the extremely continental eastern part of the Tien Shan. From the source area of Urumqi River, it supplies the city of Urumqi and large agricultural areas with water before the river dries up in the desert. Because of the strong influence of the Siberian High in winter, precipitation is concentrated in summer months. Therefore, accumulation and ablation take part simultaneously in different elevation belts, and both reach their maximum in summer (''summer accumulation glacier type'' after Ageta & Higuchi 1984).

In the Alps, the catchment Rofenache was chosen for comparison with the Central Asian results. Here, the HBV–ETH model has been applied previously (BayFORKLIM 1999), and additional model runs have been conducted for this study. The Rofenache is located in the upper Ötztal in Austria and belongs to the Inn basin. A highly glacierised sub-basin of Rofenache is Vernagtbach, where the Commission for Glaciology of the Bavarian Academy of Sciences carries out glaciological studies on Vernagtferner and hydrometeorological measurements.

The main characteristics of all test sites are shown in Table 18.1.

18.3 MODEL DESCRIPTION

The HBV–ETH model is a further development of the HBV model, a conceptual precipitation-runoff model that was developed in the 1970s in Sweden (Bergström 1976). The worldwide applied model was expanded at the Swiss Federal Institute of Technology (ETH) in Zürich for application in glacierised regions (Braun & Renner 1992). Further improvements and the programming for operational use on microcomputers were carried out in 1997 at the Commission for Glaciology of the Bavarian Academy of Sciences (Braun *et al*. 2000). Figure 18.2 shows the structure of the current version.

As input, the model needs the distribution of the basin area by altitude and topographic aspect, where the glaciated parts have to be treated separately. For running the model, the only required data are daily means of air temperature and precipitation. Daily runoff is needed for calibration.

The snow- and glacier-subroutine calculates terms of the snow- and ice-cover distributed for different elevation belts and aspect classes; the further steps of the model are performed on a lumped basis for the whole catchment area. The aggregational state (snow/rain) of precipitation

Table 18.1 Basin characteristics

	Catchment 1	Catchment 2	Catchment 3	Catchment 4	Catchment 5
Name of the basin/area	Tuyuksu	Abramov	Glacier No. 1	Vernagtbach	Rofental
Mountain range	Tien Shan	Pamiro–Alay	Tien Shan	Alps	Alps
Elevation range of entire catchment (m a.s.l.)	2450–4219	3580–4960	3695–4486	2635–3633	1893–3772
Elevation range of glaciers (m a.s.l.)	3415–4219	3625–4960	3700–4486	2765–3628	2400–3772
Latitude and longitude	43°03′N/77°05′E	39°38′N/71°34′E	43°05′N/86°49′E	46°52′N/10°49′E	46°52′N/10°49′E
Area in km^2	28	55.5	3.34	11.4	98
Geology	Granite	Complex (limestone, granodiorite)	Para-gneiss	Para-gneiss, mica slate	Para-gneiss, mica slate
% glacierized	26	51	55	78	41
Vegetation type (dominant)	Alpine pasture	No vegetation	No vegetation	No vegetation	Alpine pasture
% forested	0	0	0	0	0
Mean Q at catchment outlet (mm)	1012	1588	504	1801	1436
Mean N (mm)	1000	730	430	1000	700

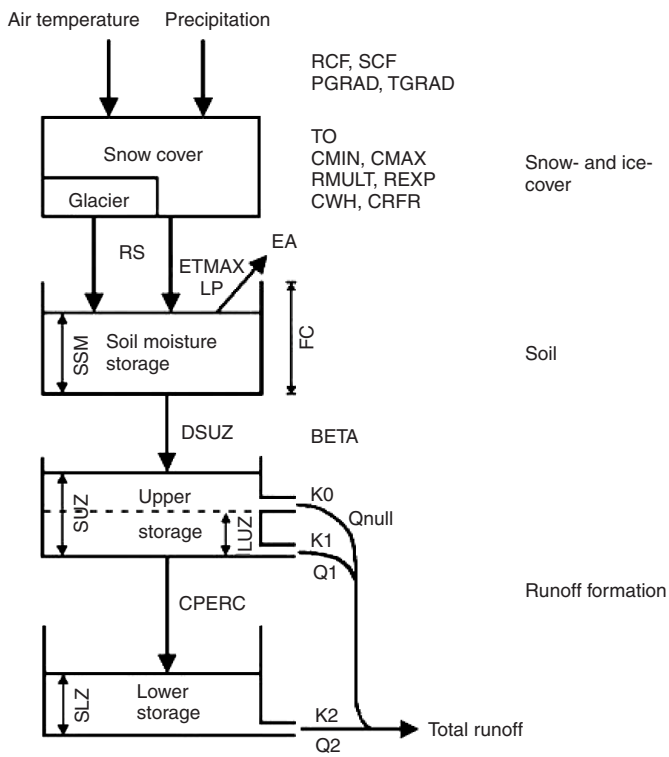


Figure 18.2 Schematic representation of the HBV–ETH model (based on Bergström 1976), (for explanations see Table 18.2)

is determined with a threshold air temperature. The melting of snow and ice is calculated with the degree-day approach using a seasonally variable degree-day factor. In addition, glacier mass balance is determined for each elevation and aspect unit.

Table 18.2 Description of the free parameters in the HBV–ETH model

Parameter	Description
RCF	Rainfall correction factor
SCF	Snowfall correction factor
PGRAD	Precipitation gradient (%/100 m)
TGRAD	Temperature gradient (°C/100 m)
T0	Temperature divider (also general temperature correction)
CMIN	Minimum degree-day factor on 21 December (mm °C^{-1} day)
CMAX	Maximum degree-day factor on 21 June (mm °C^{-1} day)
RMULT	Multiplicative factor to account for ice melt
REXP	Multiplicative factor to account for topographic aspect
CWH	Water-holding capacity of snow
CRFR	Coefficient of refreezing
ETMAX	Maximum evapotranspiration on 1 August (mm/day)
LP	Limit for potential evapotranspiration (mm)
FC	Field capacity (mm)
BETA	Coefficient to calculate outflow of soil moisture storage
k_0, k_1, k_2	Storage discharge constants

The sum of rainfall and meltwater output is then transferred to the soil moisture routine, a reservoir from which actual evapotranspiration is calculated as a function of potential evaporation and soil moisture storage.

In the last model component, the remaining water is transformed into the flow hydrograph. Three outflows with different response times are summed to yield total runoff at a daily time step. The calibration of the free parameters (Table 18.2) is done by a manual optimisation procedure, where the simulated hydrograph is compared with the measured discharge. To avoid a compensation of errors in the computation of basin precipitation by producing any desired glacier melt, it is helpful to compare calculated glacier mass balances with data observed in the field.

18.4 MODELLING RESULTS

18.4.1 Simulations under contemporary conditions

Figure 18.3 shows observed and calculated hydrographs for one hydrological year in the Abramov region, where the best results have been achieved. For the Tuyuksu area, the quality of measured discharge is insufficient (Hagg 2003), and at Glacier No. 1, the short dataset of only four hydrological years does not allow intercomparison through time.

Annual terms of the water balance in the three investigation areas, calculated by the HBV–ETH model, are shown in Table 18.3.

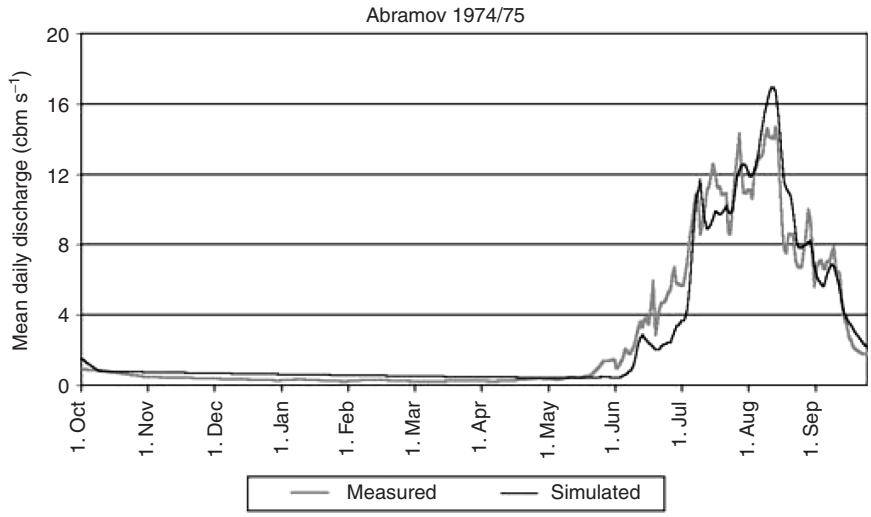


Figure 18.3 Comparison between measured and simulated daily discharge in the Abramov region

Table 18.3 Annual terms of the water balance in the three investigation areas as determined by the HBV-ETH-model (Q = runoff, P = basin precipitation, ET = basin evapotranspiration, S = storage changes) in mm/a

	Q	P	ET	$S_{glacier}$	S_{snow}	S_{ground}
Tuyuksu (1981/82–1984/85)	968	904	155	−239	6	−15
Abramov (1968/69–1987/88)	1348	1146	167	−460	57	34
Glacier No. 1 (1986/87–1989/90)	443	551	231	−135	39	−27

Numerical parameters for the goodness of fit (Table 18.4) show satisfactory values. Especially in the Abramov region, the model efficiency criterion $R_{eff}(Q)$ following Nash & Sutcliffe (1970) indicates good results. At this test site, the data series is long enough to separate a calibration period, for which the parameter values are optimised, from a validation period, in which this parameter set is tested.

Worldwide testing of conceptual models (Rango 1992) has shown that $R_{eff}(Q)$-values higher than 0.8 are above average for runoff modelling in glaciated catchments. Generally, comparison of $R_{eff}(Q)$-values between different basins has to be regarded carefully, because this statistical item is strongly influenced by runoff variability, which may explain the relatively low values at Glacier No. 1, where runoff variability is highest, due to the small size of the catchment. Furthermore, the summer maximum of precipitation introduces uncertainty in the discrimination between rain and snow on this glacier. For the investigated catchments in the Alps, the threshold temperature is a critical model parameter only in relatively few cases in spring, autumn, and cool periods in summer, but the main input of snow occurs during winter, when nearly all precipitation is solid.

To evaluate the amount of glacial meltwater and the significance of glaciation for runoff variability, all the modelling was also carried out with the glacierised parts of the catchment areas set to zero. All other parameters were left unchanged so that these model runs represent current climate conditions but without glaciers as water storages. The fractions of glacier melt in total river runoff are shown in Table 18.5 and are discussed later. Annual runoff for current conditions and no-glacier-scenarios are given in Figure 18.4. As the data series available for Glacier No. 1 are too short, this test site was omitted from the runoff variability analysis.

A main characteristic of glacier runoff is the so-called compensating effect described by Röthlisberger & Lang (1987). Ice ablation is highest in hot, dry periods and lower during wet conditions, when clouds reduce radiation, and snowfall at higher elevations increases the albedo. Glacier melt and precipitation have a negative correlation, and therefore glaciers reduce the year-to-year variation of runoff, which is of great importance for water resources management. In this context, it can be observed that annual runoff of glaciated and glacier-free catchments shows a contrary behaviour (Röthlisberger & Lang 1987). Glaciated catchments reach their highest discharge values in hot summers, when glaciers show large areas of bare ice and deliver a high basic load of meltwater. Basins without glacier cover show maximum runoff volumes in wet and cool summers. This contrasting behaviour cannot be shown in Figure 18.4, the curves for the simulations with and without glacier cover run more or less parallel.

One should bear in mind that the simulations without glaciers assume a current climate in which glaciers still exist, although they are retreating. Therefore, the ratio between snow accumulation in winter and ablation in summer is higher than in effectively unglaciated, lower basins. This means that the model builds up an

Table 18.4 Goodness of fit for the three investigation areas (Q_{diff} = accumulated difference between measured and simulated discharge in mm/a [percentage of the measured value], $R_{eff}(Q)$ = Nash–Sutcliffe criterion)

	$Qdiff_{mean}$	$Qdiff_{min}$	$Qdiff_{max}$	R^2_{mean}	R^2_{min}	R^2_{max}
Tuyuksu (1981/82–1984/85)	77 [7.6%]	10 [1%]	185 [18.3%]	0.81	0.80	0.85
Glacier No. 1 (1986/87–1989/90)	113 [21.1%]	31 [7.8%]	191 [31.6%]	0.76	0.73	0.78
Abramov (1968/69–1977/78) calibration period	226 [14.5%]	117 [8.3%]	539 [25.0%]	0.85	0.77	0.91
Abramov (1978/79–1987/88) validation period	283 [16.7%]	30 [2.7%]	566 [35.9%]	0.83	0.70	0.91

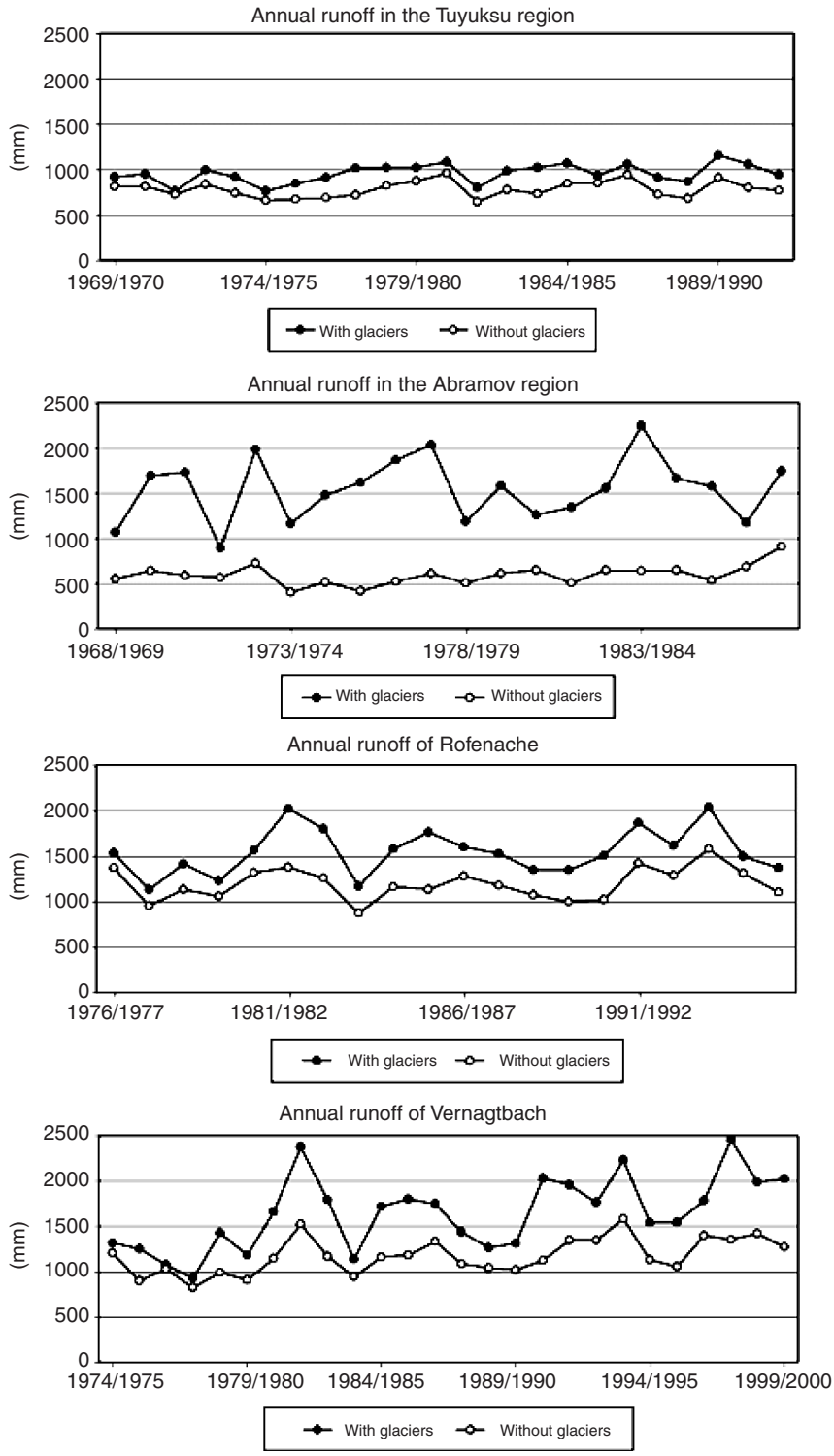


Figure 18.4 Simulated annual runoff for present climate, with and without present-day glacier cover

oversized snow pack that persists long into the ablation season and partly takes over the seasonal storage function of glaciers, which may explain why the curves are parallel instead of showing the expected contrary behaviour. In all cases, annual runoff decreases with the absence of glaciers, owing to the negative mass balances in the investigated periods. For comparison, the year-to-year variation of runoff should be related to the mean. This is accomplished by the coefficient of variation $\left(\mathrm{CV} = \frac{\text{standard deviation}}{\text{mean}}\right)$, which measures the relative dispersion.

If only July and August, the months with most intense ablation, are considered, the year-to-year variation of runoff is higher for the model runs without glaciers. Only at Vernagtbach, the coefficient of variation becomes somewhat smaller, if glaciation drops from 78 to 0%, but is relatively high in both cases. This is in good agreement with the theory of compensation, which states that the balancing effect is highest in basins with a moderate glacier cover, while runoff variation rises towards heavily glaciated and unglaciated catchments. According to Kasser (1959), the maximum compensation effect in the Alps is observed in basins with a glaciation of 30–40%. For the main ablation season, minimum variations of runoff are found in catchments with 30–60% glacier cover (Röthlisberger & Lang 1987).

In Figure 18.5, the CV-values of the period July–August are plotted against glaciation, including the simulations without glaciers. The calculated trend shows a minimum year-to-year variation at degrees of glaciation between 20 and 50%.

18.4.2 Runoff scenarios

One field of application of the HBV–ETH model is the creation of runoff scenarios for different climate and glaciation conditions by modifications of the model input. In this study, the meteorological input was not modified by applying a general shift, as usual in climate impact studies, but by changes on single days. This leads to a more realistic description of weather conditions after a climate change but requires meteorological knowledge and sensibility of the modeler (Escher-Vetter *et al*. 1998).

The meteorological input in the three basins in Central Asia was changed according to regional climate modelling with the GISS (Goddard Institute for Space Studies) model, carried out for the Tuyuksu region by the Kazakhstan Climate Change Study (KazNIIMOSK 1999). Under the assumption of the doubling of CO_2, which is expected between the years 2050 and 2075, the GISS model predicts a rise of the annual air temperature by 4.2°C and a change of annual precipitation by a factor of 1.17. The data were modified manually by adding hot days and introducing or deleting precipitation events so that the anticipated monthly changes were achieved. To avoid discussing particularities of one individual year, two reference years with differing meteorological conditions and glacier mass balances were chosen.

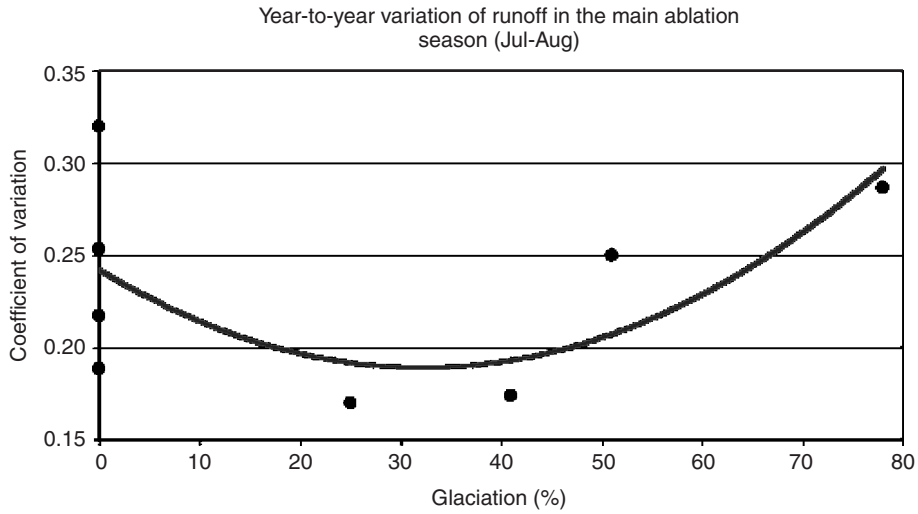


Figure 18.5 Coefficients of variation of modelled discharge in the months July and August at the test sites Tuyuksu, Rofenache, Abramov and Vernagtbach, for current glacier extent and without glaciers. Shown is the polynomic trend of second order

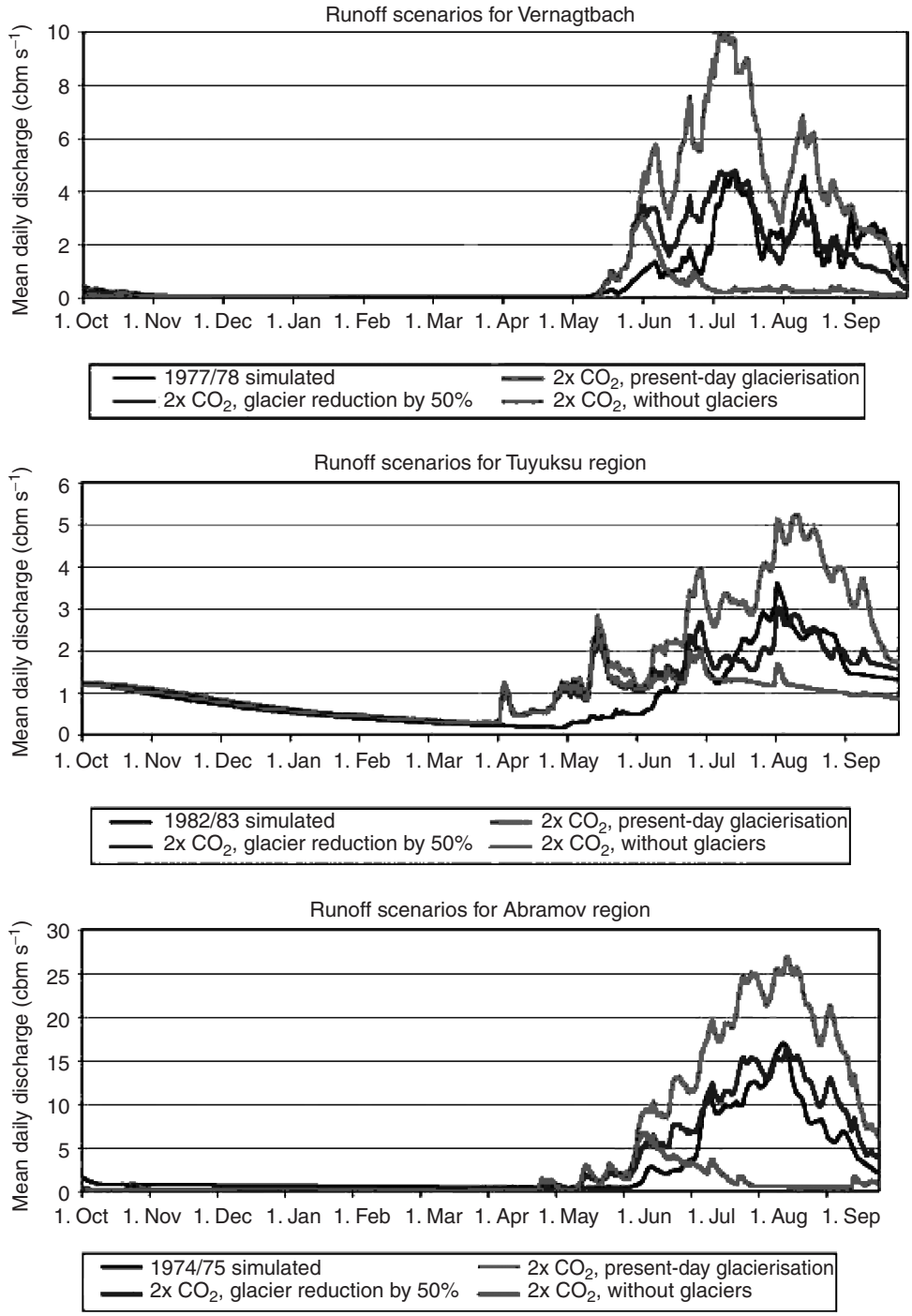


Figure 18.6 Calculated daily discharge of the reference year with substantial glacier melt and of a climate scenario after the doubling of CO_2, for three different steps of deglaciation

The effect of the climate change on river streamflow was simulated for the current glacier extent and for two stages of deglacierisation: after an areal reduction by 50% and after complete melting.

These results in Central Asia are compared with former studies in the Alps (BayFORKLIM 1999), where the same runoff scenarios, based on comparable climate changes, have been generated for the Rofenache in Austria. To assess the influence of the degree of glaciation, additional scenarios for the heavily glaciated basin of Vernagtbach, a subbasin of Rofenache, have been created for this study.

Figure 18.6 shows examples for three test sites, including the hydrographs of the reference year and the 2 × CO_2-scenarios for current glacier extent and for two steps of deglacierisation.

General effects of climate warming

The reaction of the river hydrographs follows the same principles in the Alps and in Central Asia, as the general mechanism of seasonal and long-term water storage and release are similar on every glacier.

Under current glaciation, discharge begins earlier in the year and rises towards summer, increasing the flood

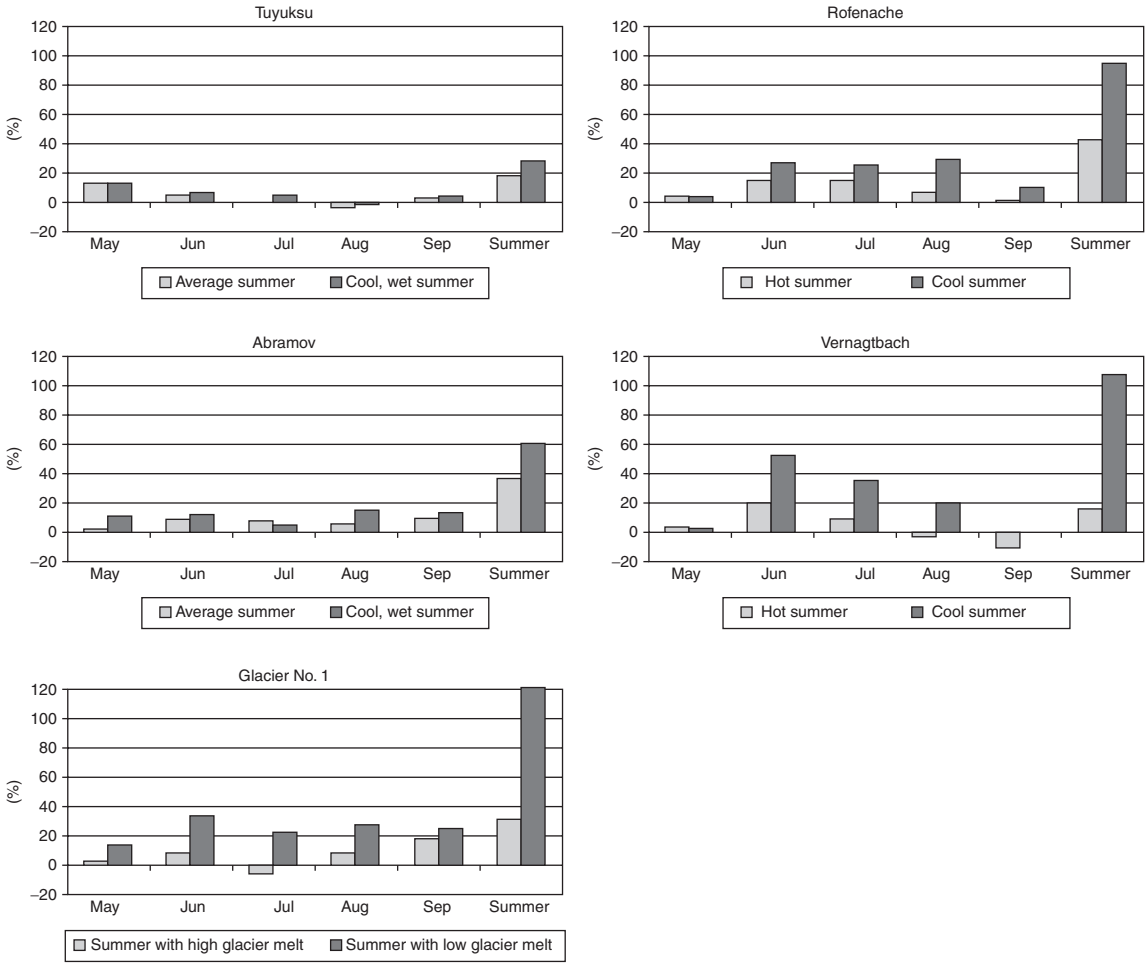


Figure 18.7 Effect of climate change (prognosed by the GISS model for the doubling of CO_2) and reduction of glaciated area by 50%, related to summer runoff of the two reference years

risk. This case has to be regarded as hypothetical because a current glacier extent is not realistic after such a climate change. If the glacierised area is reduced by 50%, snowmelt still begins one month earlier and is more intense, but the summer peaks are mostly reduced to the same level that was already observed in the reference year. The complete disappearance of glaciers yields a water shortage in summer. Under these conditions, the river hydrograph is controlled by groundwater release and rainfall events only and it drops down during dry periods.

The extent of the glacier degradation effect on river discharge varies in the different research basins. These differences are shown in Figures 18.7 and 18.8 for the two modelled steps of deglacierisation and are discussed in the following section.

Reduction of glaciated area by 50%

Figure 18.7 shows the monthly hydrological responses after climate warming and areal reduction, related to the two reference years.

In the alpine basins, there is a big discrepancy between the two model runs, which can be explained by the fact that the two reference years differ extremely in air temperature and glacier melt (Table 18.5). The scenario shows a higher increase in runoff for the cool reference year than for the hot one, where glacier melt and discharge were already high before the climate warming. The differences between the reference years are more drastic at Vernagtbach than in the larger catchment of Rofenache. This displays the influence of a higher degree of glaciation, as the same meteorological input

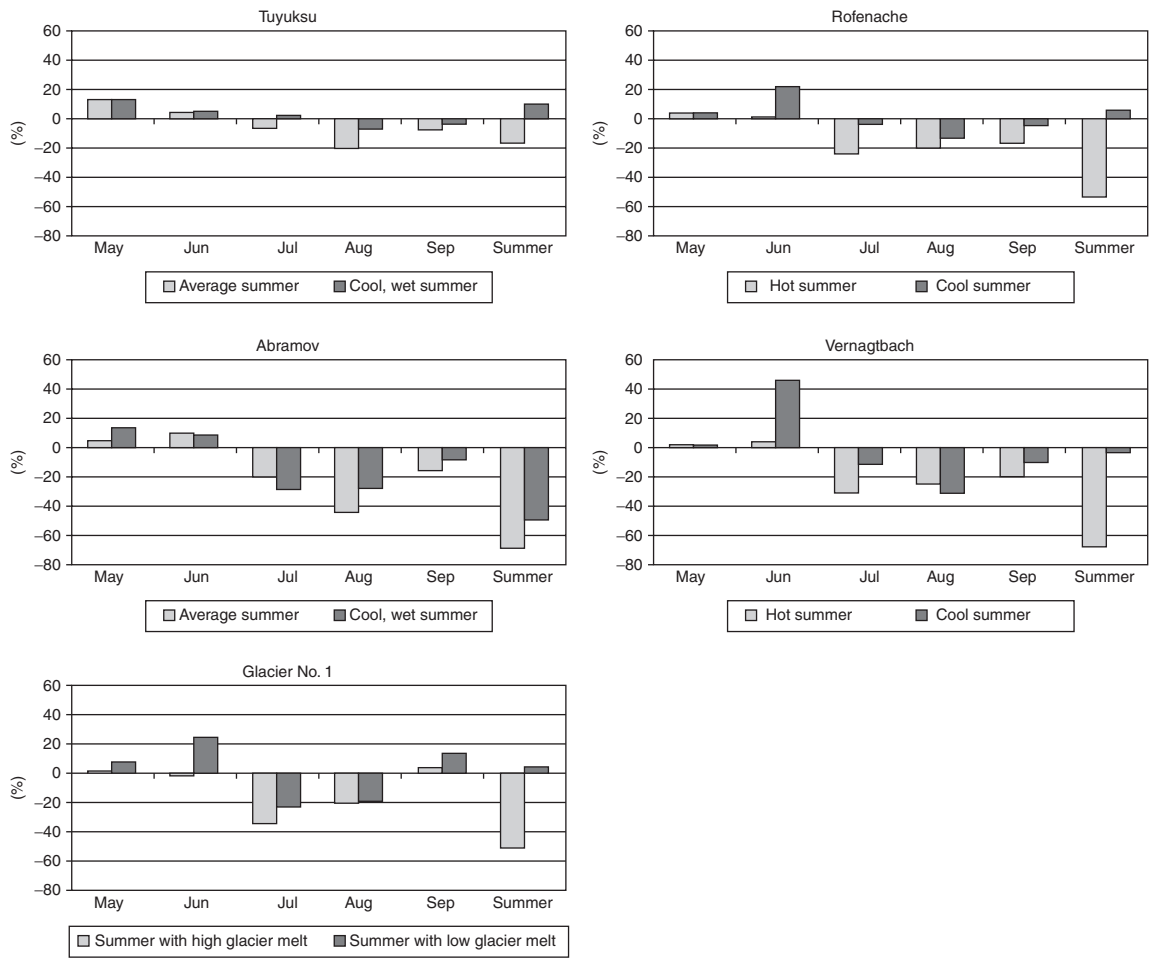


Figure 18.8 Effect of climate change (prognosed by the GISS model for the doubling of CO_2) and a complete glacier disappearance on river runoff in the investigation areas, related to summer runoff of the two reference years

was used in both cases. At Vernagtbach, even a decrease in runoff in August and September can be observed for the hot reference year, where glacier melt was so intense that its volume cannot be exceeded with half of the glacier area after the climate warming. Tuyuksu and Abramov glacier also show a stronger response for the cooler reference years, but altogether the changes are more moderate, especially in the Tuyuksu region, where the small water yield can only be explained with the low glaciation (12.5%) and the high groundwater infiltration. Also at Abramov glacier, there is only a relatively slight hydrological response for this scenario, in view of the still substantial glaciation of 25.5%. This may be attributed to the high elevation interval in which this glacier is located (highest point: 4960 m a.s.l.), which results in relatively cold temperatures at the higher parts of the glacier. At Glacier No. 1, the short dataset does not include years in which summer temperatures differ noticeably. Two years with differing mass balance behaviour, however, were chosen for illustration (Table 18.5). On this summer accumulation glacier type (50% of the annual precipitation falls in July and August), ice melt is strongly controlled by the air temperature during precipitation events, because the aggregational state of precipitation controls the albedo on the glacier. Therefore, it is highly relevant for glacier melt, whether precipitation occurs on cooler or on warmer days. Under these conditions, the mass balance can differ significantly in years with similar meteorological mean values. The basin shows a strong response for the reference year with little ice melt.

Complete melting of glaciers

The qualitative changes in monthly runoff because of a complete disappearance of glaciers are quite similar in all investigation areas, whereas there are quantitative differences (Figure 18.8). Noticeable changes begin in May or June, where all sites show an increase in runoff as a consequence of a more intense snowmelt up to the higher elevations. In the main ablation season, the absence of glacier melt leads to a remarkable reduction of discharge. In contrast to the above-described scenarios, the strongest effect is achieved for the hotter reference years with a more intense glacier melt. In the Alps, differences between the reference years are highest again, because of the large meteorological discrepancy. Monthly runoff decreases from July to September in all cases, but in the cooler reference years, this effect is compensated by the enhanced snowmelt in spring. At Rofenache, summer runoff for the scenario is even higher than in the cool reference year. The same effect can be observed at Tuyuksu glacier and Glacier No. 1. Abramov glacier shows a strong shortage of runoff in July and August for both reference years.

The hydrological effect of this glacier degradation is mainly controlled by the contribution of glacier melt to the total discharge of the reference year, and this contribution again is strongly influenced by the degree of glaciation and by the typical seasonal weather patterns, especially summer air temperature and precipitation. Table 18.5 shows the extent of water shortage in the research basins, the percentage of glacial meltwater to total discharge and the factors that control this portion.

Table 18.5 Hydrometeorological conditions of the reference years and change in discharge in the main ablation season after doubling of CO_2 and the complete melting of glaciers

Catchment Area (Glaciation)	Year	Weather conditions (Jul–Aug)		Percentage of glacier melt in total runoff [%] (long-term mean)	Glacier mass balance, related to catchment area [mm]	Change of discharge in July–August [%] (related to summer runoff)	Runoff coefficient (long-term mean)
		Temperature at mean glacier elevation [°C] (long-term mean)	Precipitation [mm] (long-term mean)				
Vernagtbach	1978	−0.1 (3.2)	181 (185)	7 (29)	238	−57 (−43)	0.64 (1.09)
11.7 km^2 (80%)	1982	4.4 (3.2)	215 (185)	41 (29)	−1139	−90 (−57)	1.65 (1.09)
Rofenache	1978	−0.1 (3.2)	181 (185)	18 (25)	−58	−25 (−16)	0.96 (1.16)
98.2 km^2 (41%)	1982	4.4 (3.2)	215 (185)	45 (25)	−679	−74 (−45)	1.61 (1.16)
Tuyuksu	1983	2.8 (3.6)	251 (244)	23 (17)	−242	−43 (−26)	1.00 (1.02)
28.0 km^2 (25%)	1972	1.2 (3.6)	315 (244)	4 (17)	1	−10 (−5)	0.75 (1.02)
Abramov	1975	4.2 (4.2)	79 (70)	70 (66)	−495	−86 (−64)	1.27 (1.18)
55.5 km^2 (51%)	1981	2.4 (4.2)	129 (70)	53 (66)	−63	−75 (−57)	0.81 (1.18)
Glacier No. 1	1988	2.0 (1.8)	250 (185)	53 (39)	−234	−70 (−57)	0.93 (0.81)
3.3 km^2 (55%)	1989	1.5 (1.8)	189 (185)	24 (39)	−7	−59 (−50)	0.58 (0.81)

The strongest shortages of discharge occur at Vernagtbach and Abramov, whereby at Abramov the same values are reached for an average reference year as at Vernagtbach for a hot year. Therefore, the decrease is most dramatic at Abramov glacier. The summers in this region are typically dry, and therefore the contribution of glacial meltwater to total runoff is very large. The hydrological effect is also very high at Glacier No. 1, even in the year with a balanced glacier mass budget, although this test site may not be comparable to the others because of its small size. The model gives best results if no groundwater storage is assumed. Without glaciers, runoff only occurs after precipitation, and with this set of model parameters no baseflow can be generated. In the Tuyuksu region, the rather slight hydrological response to glacier disappearance can be explained by the lowest degree of glaciation and by the fact that two cool reference years had to be chosen, because of problems with the quality of data.

18.5 CONCLUSIONS

The investigations have shown that the conceptual HBV-ETH precipitation-runoff model is capable of simulating runoff in the continental climate of Central Asia. This is indicated by a good agreement between modelled and measured values of runoff as well as glacier mass balance. As a consequence, the degree-day method for calculating snow and ice melt can be applied successfully under these climate conditions. In high mountain regions of Central Asia, energy for melt is predominantly supplied by radiation and therefore highly correlated with air temperature (Ohmura 2001). Moreover, the dominance of low water vapour pressure favours the occurrence of evaporation and the formation of bright ice surfaces. The constantly high albedo values of ice lead to rather stable degree-day factors.

Model runs under contemporary conditions, but without glaciers, show an increase of the year-to-year variation of runoff, if only the main ablation season is considered. This supports the theory of runoff compensation, which explains the balancing effect of a moderate glacier cover on year-to-year runoff variability.

Runoff scenarios for a warmer climate and different steps of deglaciation display a similar general behaviour in Central Asia and the Alps. The most important features are the increase of discharge during snowmelt with rising temperatures and the shortage of summer runoff with the disappearing of glaciers. Quantitative differences are mainly due to the degree of glaciation, local weather patterns and glacier mass balance behaviour in the reference period. These factors have to be taken into account if the hydrological reaction of a glaciated catchment to climate changes is to be estimated properly. Local circulation patterns and their changes with climate variations are especially important determining factors. They control water balances of smallhead watersheds and their reaction to climate changes to a higher degree than any large-scale climate parameter such as continentality. Therefore, general statements about differences between mountains in different climate zones are very difficult to make.

In contrast, there are clear differences in the consequences of the hydrological changes for the lowland areas. The greater the hydrological difference between mountains and lowlands, the more the lowlands depend on mountain runoff and the more significant are changes in mountain hydrology. This means that the shortages in summer runoff lose part of their relevance at the margin of the Alps, where high summer precipitation guarantees a minimal runoff during the vegetation period. In contrast, the dry lowlands of the Central Asian mountains depend on glacier melt to a much higher degree, and they will face a serious water deficiency if the glaciers continue to shrink at the rate observed today.

18.6 ACKNOWLEDGEMENTS

This project was funded by the German Research Foundation (DFG, project BR1622/5-3) and supported by the Bavarian Academy of Sciences. The authors thank Igor Severskiy, Felix Pertziger, Ersi Kang and their colleagues for providing essential data. The helpful comments of the reviewers are gratefully acknowledged.

REFERENCES

Ageta Y, Higuchi K (1984) Estimation of mass balance components of a summer-accumulation type glacier in the Nepal Himalaya. *Geografiska Annaler* **66A**(3): 249–255.

Aizen VB, Aizen EM, Melack JM (1995) Climate, snow cover, glaciers, and runoff in the Tien Shan, Central Asia. *Water Resources Bulletin* **31**(6): 1113–1129.

BayFORKLIM (1999) *Klimaänderungen in Bayern und ihre Auswirkungen*. Abschlussbericht des Bayerischen Klimaverbundes, München, p. 90.

Bergström S (1976) *Development and Application of a Conceptual Model for Scandinavian Catchments*. University of Lund Bulletin, Series A, p. 52.

Braun LN, Renner CB (1992) Applications of a conceptual runoff model in different physiographic regions of Switzerland. *Hydrological Sciences Journal* **73**(3): 217–231.

Braun LN, Weber M, Schulz M (2000) Consequences of climate change for runoff from Alpine regions. *Annals of Glaciology* **31**: 19–25.

Escher-Vetter H, Weber M, Braun LN (1998) Auswirkungen von Klimaänderungen auf den Wasserhaushalt

hochalpiner, teilweise vergletscherter Gebiete. *Abschlussbericht BayFORKLIM, on: CD-ROM ''Klimaerwärmung Gletscher – wie Verändern Sich die Gebirgsabflüsse''*. Kommission für Glaziologie, Bayerische Akademie der Wissenschaften, München, ISBN 3769635000.

Hagg W (2003) Auswirkungen von Gletscherschwund auf die Wasserspende hochalpiner Gebiete, Vergleich Alpen – Zentralasien. *Münchner Geographische Abhandlungen* **15**: p. 91.

Kasser P (1959) Der Einfluss von Gletscherrückgang und Gletschervorstoß auf den Wasserhaushalt. *Wasser- und Energiewirtschaft* **6**: 155–168.

KazNIIMOSK (1999) *Climate Change and a New Defence Strategy Against Mudflows and Snow Avalanches*. National report on the impact and adaptation assessment for the mountain region of South and Southeast Kazakhstan and the Kazakh part of the Caspian Sea coastal sector. Netherlands climate change studies assistance programme, Kazakhstan climate change study, Vol. 1, Kazakh Institute for Environment Monitoring and Climate, Almaty, p. 86

Kommission für Glaziologie (2001) *Gletschergebiet Tujuksu, Sailiski Alatau*. Map 1:10'000, published in: Fluctuations of Glaciers 1995–2000, Vol. VIII, World Glacier Monitoring Service, Zürich, expected in 2003.

Nash JE, Sutcliffe JV (1970) River flow forecasting through conceptual models. Part I – a discussion of principles. *Journal of Hydrology* **10**(3): 282–290.

Ohmura A (2001) Physical basis for the temperature-based melt index method. *Journal of Applied Meteorology* **40**: 753–761.

Rango A (1992) Worldwide testing of the snowmelt runoff model with applications for predicting the effects of climate change. *Nordic Hydrology* **23**: 155–172.

Röthlisberger H, Lang H (1987) Glacial hydrology. In: Gurnell AM, Clark MJ [eds.], *Glacio-Fluvial Sediment Transfer*. Wiley, New York, pp. 207–284.

WGMS (1999) *Glacier Mass Balance Bulletin No. 4*. IAHS (ICSI)-UNEP-UNESCO-WMO, compiled by the World Glacier Monitoring Service, Zürich.

19

Snowmelt Under Different Temperature Increase Scenarios in the Swiss Alps

FRANZISKA KELLER AND STÉPHANE GOYETTE
Geography, Department of Geosciences, University of Fribourg, 1700 Fribourg, Switzerland

19.1 INTRODUCTION

A paramount feature of mountainous areas in the temperate climates of Western Europe is the presence of variable snow cover during the year. Large fluctuations in snow amount and duration observed in the Alps can be related to the variability of the prevailing meteorological and physio-geographic conditions (Barry 1992). In the context of climate change, significant perturbations can be expected to the alpine snow and consequently to the ecology, hydrology, and economy of this region (Beniston 2000). The Intergovernmental Panel on Climate Change (IPCC 2001) predicts a warming of the mean global temperature of 1.9 to 5.8 K for this century with a different evolution of the minimum (T_{min}) and maximum temperatures (T_{max}). However, this global climate change scenario is likely to be different in a mountainous region such as the European Alps. According to a regional simulation done with a doubled CO_2 concentration forcing using a Regional Climate Model (RCM), the projection of the global warming in the Alps could lead to a seasonally dependent temperature rise of 1.4 to 3.9 K at the screen level (Rotach *et al.* 1997). Three-dimensional numerical climate models (i.e. Global Circulation Models (GCMs), and RCMs) are valuable tools from which to infer climate change of large areas but they use rather coarse meshes; therefore, they are inappropriate to adequately study the fine spatial and temporal variability of a particular snowpack. At fine scales, there are two main categories of snow models: conceptual index models based on the degree-day approach, which are adapted for use in large basins for operational purposes, and energy balance models. The latter are complex and require large amounts of data; they represent the physics of melting snow realistically and give more accurate representations of the spatial distribution of melt within small research basins (Williams and Tarboton 1999). Models treating the snowpack as a bulk layer are efficient tools to analyze the components of radiation, the turbulent fluxes of latent and sensible heat, and the advected heat from the precipitation to the melting of the snowpack at local scale (Tarboton and Luce 1996, Stähli and Jansson 1998). Snowmelt processes also require an accurate treatment of snow albedo and detailed thermodynamics of the snowpack, which helps to represent also midwinter melt realistically.

For more precise impact assessment of the temperature increase over snow cover at local scale in the Swiss Alps, a numerical investigation of the thermal and hydrological conditions of mountainous snow during melt at fine scale is needed. The aim of this study is to analyze the sensitivity of the snow cover to an increase of mean, minimum, and maximum temperature, in terms of snow cover duration, radiation, energy, and hydrological regimes at two Swiss meteorological stations. All these factors influence the energy state of the snowpack. Out of all physio-geographic factors, only the altitude of the study sites was considered, and it was investigated

Climate and Hydrology in Mountain Areas. Edited by C. de Jong, D. Collins and R. Ranzi
© 2005 John Wiley & Sons, Ltd. ISBN: 0-470-85814-1

if there is a discrepancy between two high-elevation stations at 1000 m and 2500 m a.s.l., according to ambient meteorological conditions. A simple numerical surface energy balance model driven by observations is used to analyze these questions.

19.2 METHOD

The time evolution of a snow cover is well described with land–atmosphere water and energy exchanges. Such processes, expressed in terms of water and energy budgets, are computed in a surface energy balance model (SEBM). A brief description of the model formulation used in this study follows emphasizing the snow component; a more thorough description is given in Goyette (2002).

19.2.1 Model description

The SEBM is similar to a land surface model formulation of intermediate complexity, such as those in GCMs and in RCMs, but it differs in details. It has a tiled surface structure including a distinct snow layer. The model is a physically based semiprognostic model, which computes explicitly the surface variables but needs atmospheric input variables in order to be run adequately. Therefore, it is driven by hourly input data of air temperature, T_{air} (K), dew point temperature, T_{d} (K), anemometer-level wind magnitude, V_{a} (m s^{-1}), precipitation rate, P_r (mm s^{-1}), and surface pressure, p_{sfc} (hPa). The model computes the radiative fluxes (incoming solar radiation, $K\downarrow$, may also be given from observations, which is the case in this study), the surface turbulent sensible and latent fluxes, as well as the heat flux in the ground and in the snowpack. Surface temperature, soil wetness, and snow mass are prognostic variables in the model.

The surface radiation budget, Q^*, may be expressed following the notation of Oke (1987, Chapter 1) as

$$Q^* = (1-\alpha)K\downarrow + L\downarrow - (1-\varepsilon_{\text{s}})L\downarrow - \varepsilon_{\text{s}}\sigma T_{\text{sfc}}^4 \tag{19.1}$$

where Q^* (W m^{-2}) is the all-wave radiation budget, $K^* = (1-\alpha)K\downarrow$ is the short-wave radiation budget. $L\downarrow$ is the incoming long-wave radiation, $\varepsilon_{\text{s}}\sigma T_{\text{sfc}}^4$ is the outgoing long-wave radiation from the surface, α is the surface albedo, ε_{s} is the surface emissivity, and σ is the Stefan–Boltzmann constant. The last two terms in Equation (19.1) represent the long-wave radiation budget (L^*). T_{sfc} is the computed snow temperature, T_{s}, if the snow covers entirely the surface, and the top ground temperature, T_{g}, if there is no snow. Otherwise, the snowpack and the ground each have their own temperature. The snow fraction at the surface, δ_{snow}, is parameterized according to Roesch *et al*. (2001):

$$\delta_{\text{snow}} = \min\left[1, \tanh\left(\frac{100 M_{\text{snow}}}{\rho_{\text{snow}}}\right)\right] \tag{19.2}$$

where M_{snow} represents the snow mass in kg m^{-2} and ρ_{snow} the snow density in kg m^{-3}. Although the empirical relation depicted in Equation (19.2) has been developed for use in coarse mesh models (e.g. GCMs), this procedure for inferring snow cover fraction appears to be satisfactory in this study. Its value equals 1 when M_{snow} exceeds $10\,\text{kg m}^{-2}$ and 0 when there is no snow.

The surface albedo, α, modulated by the snow fraction, is calculated separately for two different wavelength bands (visible (s): $0.3 < \lambda < 0.68\,\mu\text{m}$ and near infrared (nir): $0.68 < \lambda < 4.0\,\mu\text{m}$):

$$\alpha = [\alpha_{\text{s}}, \alpha_{\text{nir}}] = \delta_{\text{snow}}[\alpha_{\text{s,snow}}, \alpha_{\text{nir,snow}}] + (1-\delta_{\text{snow}})[\alpha_{\text{s,sfc}}, \alpha_{\text{nir,sfc}}] \tag{19.3}$$

where $\alpha_{\text{sfc}} = [\alpha_{\text{s,sfc}}, \alpha_{\text{nir,sfc}}]$ is the surface albedo and $\alpha_{\text{snow}} = [\alpha_{\text{s,snow}}, \alpha_{\text{nir,snow}}]$ is the albedo of snow. Its value is further modulated by snow ageing and by the presence of vegetation, according to McFarlane *et al*. (1992). Solar radiation is also allowed to penetrate into the snowpack.

Snow is modeled as an evolving one-layer pack characterized by a temperature, T_{s} (K), a mass, M_{snow}, and a density, ρ_{snow}. The surface energy budget is computed as follows:

$$Q_{\text{sfc}} = Q^* - (Q_{\text{h}} + Q_{\text{e}} + Q_{\text{snow}} + K\downarrow_{\text{snow}}) - L_{\text{f}}(M_{\text{F}}/\partial t + M_{\text{S}}/\partial t) \tag{19.4}$$

where Q_{sfc} is the heat storage term, Q_{h}, the sensible heat flux, Q_{e}, the latent heat flux, Q_{snow}, the heat flux through the snowpack, and $K\downarrow_{\text{snow}}$, the solar flux penetrating the snowpack. The last term in the equation is the energy change associated with the melting rates of frozen soil moisture ($M_{\text{F}}/\partial t$) and snow ($M_{\text{S}}/\partial t$), where L_{f} is the latent heat of fusion. The temperature of the snowpack is computed prognostically through the heat storage using a force-restore method (e.g. Stull 1988, Chapter 7, and McFarlane *et al*. 1992) as

$$Q_{\text{sfc}} = \frac{C_*}{2}\left[\frac{\partial T_{\text{sfc}}}{\partial t} + \omega(T_{\text{sfc}} - T_{\text{his}})\right] \tag{19.5}$$

where T_{his} is an historical temperature taken as a 24-h moving average of T_{g}, ω, the diurnal frequency, and C_*, the effective heat capacity of the surface. The effective heat capacity of snow, $C_{*\text{snow}}$, is fixed at $9.6 \times 10^4\,\text{J m}^{-2}\,\text{K}^{-1}$.

The surface sensible, latent, and snow heat fluxes are computed as follows:

$$Q_h = \rho_a c_p C_h V_a (T_{sfc} - T_{air}) \tag{19.6}$$

$$Q_e = L_e E_{TOT} = L_e \rho_a C_e V_a \beta_e [q_{sat,sfc}(T_{sfc}) - q_{air}] \tag{19.7}$$

$$Q_{snow} = -\lambda_{snow} \frac{\Delta T_s}{\Delta z} \tag{19.8}$$

where $\Delta T_s = T_s - T_g$, $\lambda_{snow} = 2.576 \times 10^{-6} \rho_{snow}^2$ represents the heat conductivity of snow ($W\,m^{-1}\,K^{-1}$) and $\Delta z = M_s \rho_{snow}^{-1}$ is the snow depth (m). A negative sign of Q_e and Q_h stands for a gain of energy of the snowpack, whereas the opposite is true for the other fluxes. The bulk heat and moisture transfer coefficients, C_h and C_e respectively, are parameterized according to the ideas of Benoit (1977) on the basis of the Monin–Obukov similarity theory. The air density is ρ_a, and β_e is an evapotranspiration factor, which turns 1 if the whole surface is snow covered (McFarlane *et al*. 1992). The saturation-specific humidity at the surface is $q_{sat,sfc}$ and q_{air} represents the specific humidity at the screen level in $kg\,kg^{-1}$. L_e is the latent heat of vaporization or sublimation ($J\,kg^{-1}$) according to the phase of water considered. c_p is the specific heat of air at constant pressure ($J\,kg^{-1}\,K^{-1}$).

The water budget at the surface is calculated as follows:

$$\frac{\partial W}{\partial t} = P_L - E_g + M_S - R_{off}$$

$$\frac{\partial M_S}{\partial t} = P_S - E_s - M_S \tag{19.9}$$

where W is the total soil moisture (liquid and frozen) in $kg\,m^{-2}$, P_L and P_S are the liquid and solid precipitation rates, M_S, the melting rate of snow, E_g, the ground evaporation, and E_s, the snow evaporation rate where the total evaporation rate E_{TOT} equals $E_g + E_s$.R_{off} is the total runoff, that is, surface saturation and bottom drainage, following ideas of Noilhan and Planton (1989). The partitioning of W into E_L and E_F depends on the T_{air} and is estimated as follows:

$$E_L = W,\ E_F = 0;\ T_{air} > T_{fK}$$

$$E_L = 0,\ E_F = E_W;\ T_{air} \le T_{fK} \tag{19.10}$$

where E_L is the liquid and E_F the solid part of the soil moisture. T_{fK} is the freezing point.

Precipitation is considered as solid if T_{air} is less than that of the triple point of water. Liquid precipitation on a snowpack induces snowmelt. Melted snow ($M_S/\partial t < 0$ in Equation (19.4)) goes directly into the soil as liquid moisture, latent heat is released, and energy is transferred to the surface. The surface energy budget is computed at each model time step over snow cover. The radiative and turbulent fluxes are first computed. Then, the heat storage in the snowpack is computed according to Equation (19.5). If the heat storage is positive and the snow temperature is below the melting point, the excess energy is first used to raise the temperature of the pack. Once its temperature reaches the melting point, any additional excess energy is used to melt the snow. The temperature of the snow is held below the melting point until the snow has melted. The melted snow goes directly into the ground as liquid moisture.

19.2.2 Data and experiments

Abegg and Froesch (1994) demonstrated that for Switzerland a continuous snowpack cannot be guaranteed anymore below the critical altitude of 1200 m a.s.l. Therefore, we selected two high-altitude stations representing locations above and below this threshold. Data for the winter periods of Disentis (1190 m a.s.l., 8°51′E; 46°42′N) and Säntis (2490 m a.s.l., 9°20′E; 47°15′N) were compiled from the Swiss Meteorological Service (Figure 19.1; Bantle 1989). For both stations, a snow-poor (1988–1989) and a snow-rich winter (1998–1999) were selected: at Disentis, from December 1, 1988 to March 31, 1989 (hereafter called D88–89) and from October 20, 1998 to April 30, 1999 (D98–99) and for Säntis, from September 1, 1988 to July 31, 1989 (S88–89) and from September 1, 1998 to August 31, 1999 (S98–99).

In order to infer the impact of climate change at these two stations, three temperature change scenarios are devised (Table 19.1): (1) a $2 \times CO_2$ simulation done with the ECHAM1/LSG-AOGCM-model downscaled statistically over Switzerland (Gyalistras *et al*. 1998), (2) a scenario allowing an increase of T_{min} only, inferred from an analysis of temperature changes in the twentieth

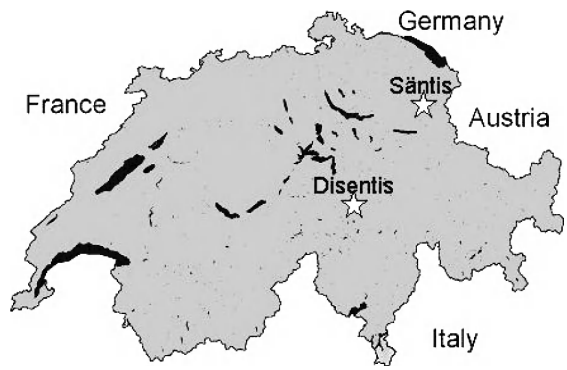


Figure 19.1 The situation of the two study sites in Switzerland

Table 19.1 Temperature increase scenarios used in this study based on the observed values (in °C). DJF stands for December to February, MAM for March to May, JJA for June to August, SON for September to November. Data taken from Gyalistras *et al*. (1998) and Weber *et al*. (1997)

	DJF	MAM	JJA	SON
First	2.10	2.30	2.20	1.80
Second	1.58	0.70	0.75	1.72
Third	1.50	0.23	0.25	2.00

century in the mountain regions of central Europe (Weber *et al*. 1997), and (3) a scenario of Weber *et al*. (1997) considering an increase of T_{max} separately. These three scenarios involve seasonal temperature changes. The two latter scenarios are projected in the future to simulate a possible temperature change for the period 2080–2100. To infer the minimum and maximum scenarios, anomalies of the observed air temperatures for both years and both stations are calculated with respect to a baseline period (1978–1998). The resulting positive (T_{max}) and negative (T_{min}) anomalies were scaled by a factor so as to obtain the required average seasonal increase rate (Figure 19.2). All other parameters are left unchanged.

For the estimation of the snow duration, a threshold value of 2.5 cm for Disentis and 5.0 cm for Säntis are applied. These thresholds were deduced from several tests about the constancy of snow cover duration. Only those days were counted where the observed and simulated snow depth exceeded these thresholds and did not fall back to zero again until the end of the investigated winter seasons.

The model's internal parameters and initial conditions of soil moisture and surface temperature were tuned for each station and year separately in comparison with the observed snow depth (Table 19.2). The following were fixed for all simulations: the surface albedo without snow to 0.285, the soil porosity to 45%, the soil drainage relaxation coefficient to 4 days, the soil hydrological depth to 500 mm, the surface emissivity to 1, the initial snow depth to 0, the surface roughness, $z_{0,sfc}$, to 0.001, the snow roughness height, $z_{0,snow}$, to 0.5×10^{-4} m and the snow masking depth to 0.07 m. There was no initial frozen soil moisture content, W_F, and the liquid soil water, W_L, was fixed at 45 kg m^{-3}.

The energy fluxes are analyzed according to the diagnostic formulation of Oke (1987) to calculate the contribution of each process to melt a volume of snow:

$$\Delta Q_m = Q^* - Q_h - Q_e - \Delta Q_s \qquad (19.11)$$

Here, ΔQ_m is the latent heat storage change due to melting or freezing and ΔQ_s represents the convergence or divergence of sensible heat fluxes within a pack; this term includes internal energy gains or losses due to variations of radiation and heat conduction. The radiation fluxes are analyzed in terms of daily and monthly

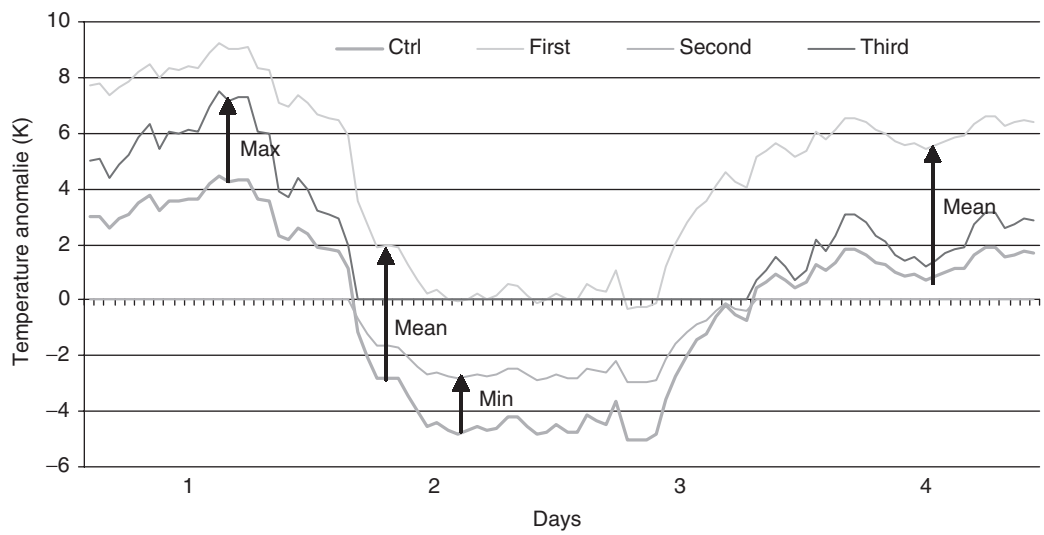


Figure 19.2 Illustration of the temperature increase scenarios. The first scenario is an increase in the mean, the second, in the minimum, and the third, in the maximum temperature

Table 19.2 Model parameters and initial conditions at D88–89, D98–99 and S88–89, S98–99. The asymptotic value of snow albedo stands for the value of the albedo after snow has aged. The duration of the snow-ageing process is determined by the snow-ageing coefficient. The extinction factor of the snowpack determines the quantity of radiation, which penetrates the pack

	D88–89	D98–99	S88–89	S98–99	Units
ρ_{snow} if $M_{snow} < 10\,kg\,m^{-2}$	50	60	220	220	$kg\,m^{-3}$
ρ_{snow} if $M_{snow} > 10\,kg\,m^{-2}$	215	225	270	220	$kg\,m^{-3}$
$\alpha_{s,snow}$	0.75	0.75	0.85	0.85	–
$\alpha_{nir,snow}$	0.65	0.65	0.65	0.75	–
Asymptotic snow α	0.5	0.55	0.48	0.45	–
Snow-aging coefficient	3	10	5	6	day
Radiation extinction factor of the snowpack	19	22	20	3	m^{-1}

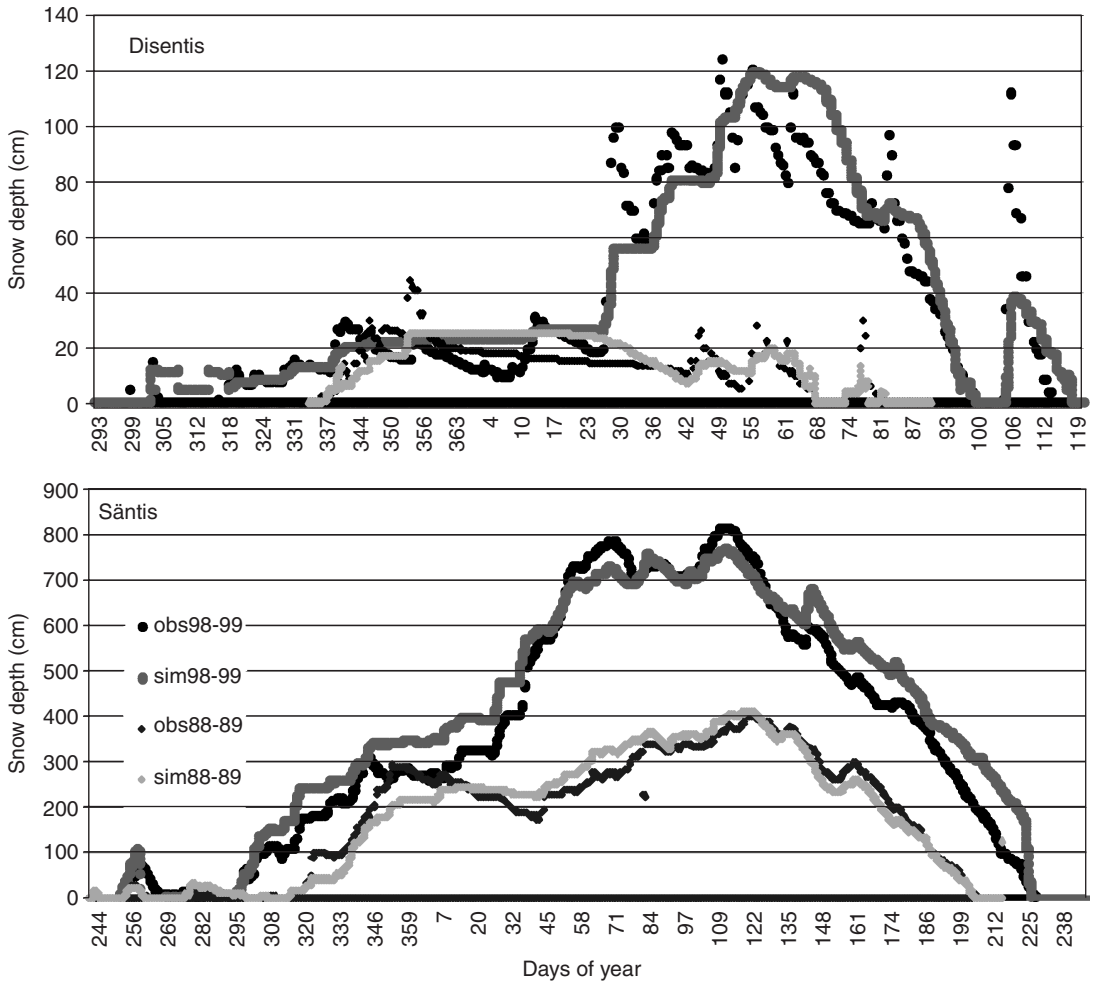


Figure 19.3 Observed (obs) and simulated (sim) snowpacks at Disentis and at Säntis for the 1988–1989 and 1998–1999 periods. Note the different scales used

averages concentrating on the melting period starting at the maximum snow accumulation.

19.3 RESULTS

19.3.1 Observations and control run

An analysis of the observed snow cover at D88–89 and D98–99 shows that the snow duration is intermittent (Figure 19.3). In 1988–1989, the maximum snow is observed in December (Days of Year (DOY): 354) and the snowpack has melted at the beginning of March (DOY: 68), whereas in 1998–1999, the maximum snow depth was reached at the end of February (DOY: 50). At S88–89, snow starts building up in December (DOY: 317) or in November at S98–99 (DOY: 291), reaches its maximum depth in April (88–89, DOY: 119; 98–99, DOY: 111) and begins to melt by the end of April. The melting is steady at a constant rate (in 88–89, 2 to 3 cm and in 98–99, 7 to 8 cm per day).

The model is first calibrated at the two stations over the two investigated periods. For the control simulations, inputs of hourly data from the Swiss Meteorological Service are used to drive the SEBM. Simulated snowpacks show generally good agreement with the observed snow depth, although it can be noted that the lack of a snow compaction parameterization in the model prevents a closer agreement (Figure 19.3). This can be seen at the Disentis station at the end of the year for both investigated periods and at S88–89 for the beginning of 1989 and at S98–99 for the end of 1998. Snowpack duration in the control run compared to the observations differed at D88–89 by two days, at D98–99 by one day, at S88–89 by two days, and at S98–99 by four days (Table 19.3).

In Figure 19.4, two days are chosen to illustrate a case with continuous melting and one day is chosen with daytime melting. The latter is described for January 31, 1989 at Disentis. The radiation input reaches nearly 150 W m^{-2} at noon. This energy is first used to warm the snowpack to T_{fK} and to increase the heat convergence (ΔQ_s); thereafter, snow starts melting, that is, ΔQ_m increases at the expense of ΔQ_s. Melt ceases when

Table 19.3 Maximum snow depth in centimeters (in parentheses the date of occurrence of the maximum snow depth), the number of snow-covered days above the thresholds of 2.5 cm for Disentis and 5.0 cm for Säntis, and the day of the year with the peak runoff. *Diff* stands for the difference in days between the respective scenario and the control run

Maximum snow depth:

	Obs	Ctrl	First	Second	Third
D88–89	**44 (20.12.)**	26 (21.12.)	14 (21.12.)	24 (21.12.)	24 (21.12.)
D98–99	**124 (19.2.)**	120 (25.2.)	92 (25.2.)	114 (25.2.)	109 (25.2.)
S88–89	**400 (29.4.)**	417 (1.5.)	319 (30.4.)	414 (1.5.)	369 (1.5.)
S98–99	**816 (21.4.)**	780 (22.4.)	640 (22.3.)	741 (22.4.)	745 (22.4.)

Number of snow-covered days:

	Obs	Ctrl	*Diff*	First	*Diff*	Second	*Diff*	Third	*Diff*
D88–89	**94**	96	*−2*	62	*−34*	95	*−1*	89	*−7*
D98–99	**146**	145	*−1*	118	*−27*	140	*−5*	139	*−6*
S88–89	**252**	250	*−2*	219	*−31*	248	*−2*	239	*−11*
S98–99	**294**	290	*−4*	239	*−51*	277	*−13*	287	*−4*

Day of year with the peak runoff:

	Ctrl	First	*Diff*	Second	*Diff*	Third	*Diff*
D88–89	68	37	*−31*	69	*+1*	42	*−26*
D98–99	99	88	*−11*	98	*−1*	96	*−3*
S88–89	202	176	*−26*	191	*−11*	191	*−11*
S98–99	221	169	*−52*	210	*−11*	219	*−2*

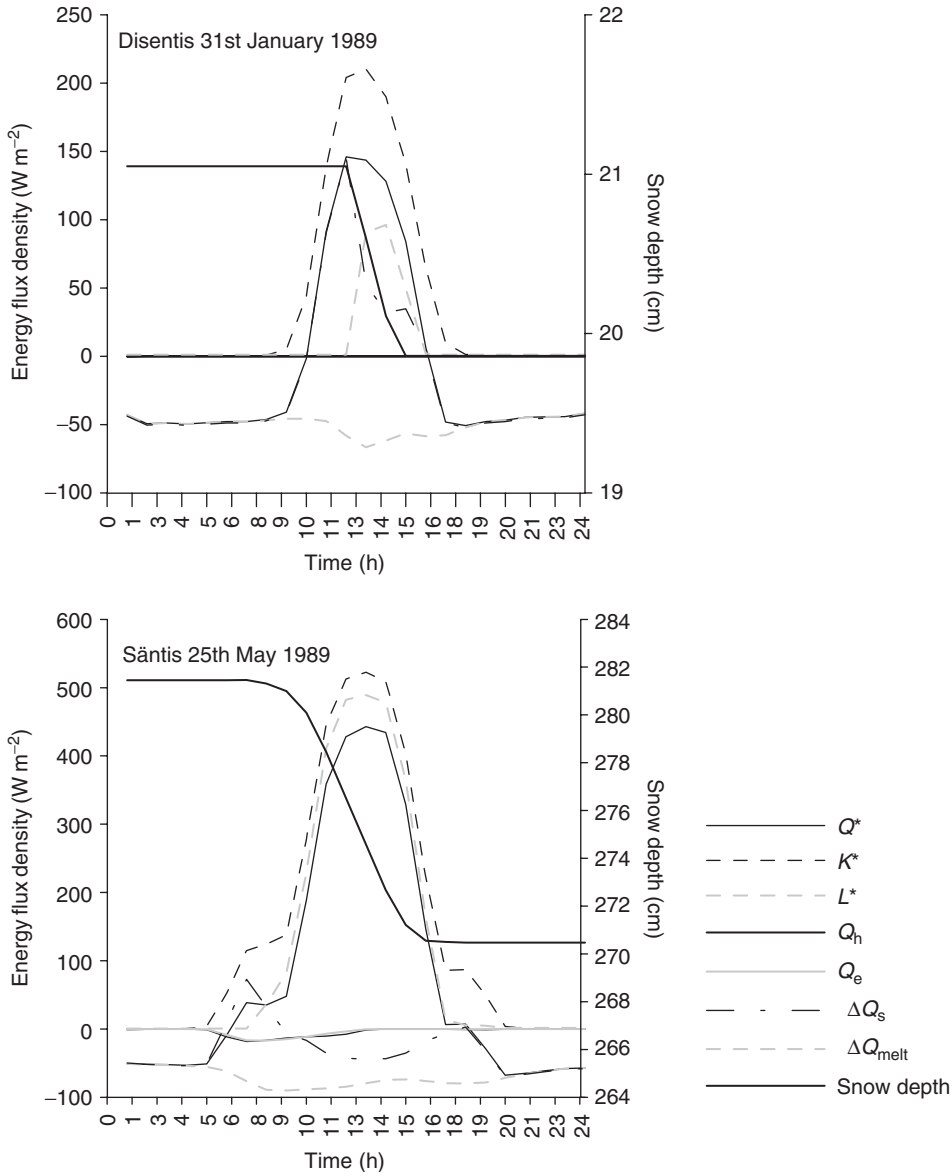


Figure 19.4 Daily evolution of radiation and energy fluxes for the January 31, 1989 at Disentis and May 25, 1989 at Säntis. Note the different vertical axes

the temperature of the pack drops below T_{fK} owing to the declining radiation input. The case of daytime melting occurs early in the year because the negative fluxes of energy and radiation during night dominate. The case of continuous melting is shown for Säntis on May 25, 1989. It happens when Q^*, Q_h and Q_e act as energy sources. Melting occurs already to a small amount during nighttime owing to the energy input of Q_e and Q_h, which increase ΔQ_s. During the day, the energy storage, ΔQ_s, increases the values of ΔQ_m beyond the radiation input.

The control runs of the two stations simulate radiation, energy, and hydrological fluxes for the two snow seasons. At D88–89, Q^* has negative daily averages because the melting begins in January. It is a daytime melting where the snowpack temperature is close to the melting

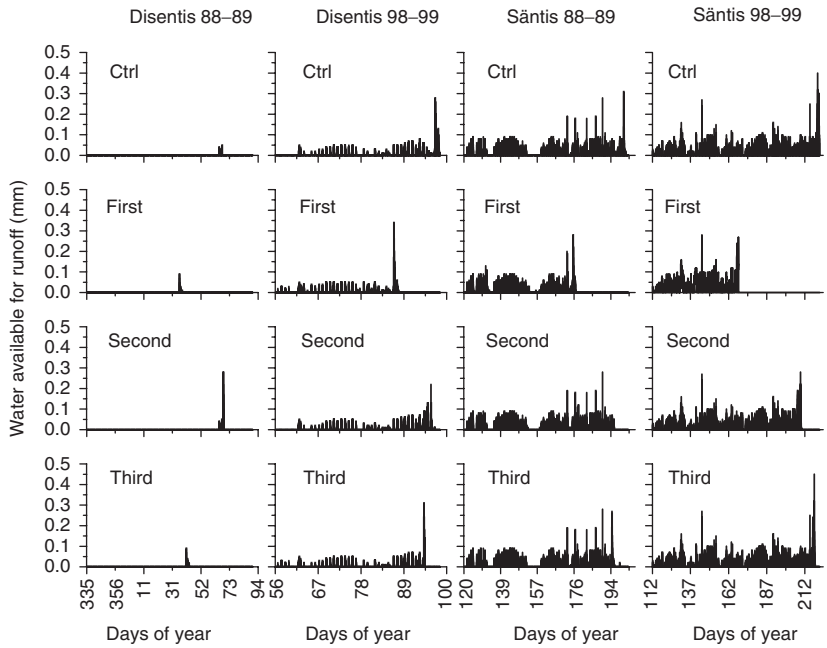


Figure 19.5 The evolution of the runoff for the two stations, the two winters, and the three scenarios. The runoff is shown during the melting period, that is, from the maximum snow depth to the end of melting. For the exact days of year, see Table 19.3

point, which is reached during the afternoons by radiative warming. Q_h, Q_e, and Q_{pcp} are about zero. The peak of runoff is concentrated at the end of the melting period at the beginning of March (Table 19.3, Figure 19.5). The situation at D98–99 differs slightly because the snow melts only at the beginning of April. The simulated radiative flux Q^* becomes positive. The energy fluxes Q_h and Q_e are weak. The timing of the peak runoff is at the beginning of April (Figure 19.5).

At Säntis, the situation is quite different. The snowpack continuously melts where Q^* is always positive and it reaches cumulated values of 150 (S88–89) to 200 MJ m^{-2} (S98–99). Q_h is negative in both years and has cumulated values of −60 (S88–89) and −50 MJ m^{-2} (S98–99). In S88–89, Q_e is positive and it becomes negative only at the end of June, whereas it has values of −25 MJ m^{-2} in S98–99. In both the periods, large runoff peaks are already simulated before the end of melting at the end of July (S88–89) and at the beginning of August (S98–99; Table 19.3, Figure 19.5).

19.3.2 First temperature scenario

The first temperature scenario is prescribed by a seasonally differentiated rise of the mean temperature (Table 19.2). The model is driven over the same period using the same overall initial conditions and the same stations as in the control integration.

At D88–89, the snow season decreases by 34 days and its maximum depth decreases by 30 cm (Table 19.3, Figure 19.6). A rise in Q^* is observed because larger values of L^* were simulated. Recalling that $Q^* = K^* + L^*$, where K^* is the net solar and L^*, the net infrared energy flux at the surface, ΔQ^* is determined by ΔL^* when there is no change in K^*. T_s also increases with the same consequences as described in Section 19.3.1. The cumulated ΔQ_m only reaches 10 MJ m^{-2}, whereas for the control run, three times more was calculated than what the much smaller snow depth can explain. The runoff peak is simulated 31 days earlier than in the control runs (Table 19.3).

At D98–99, the snow cover duration undergoes a reduction of 27 days and its depth thins by 22 cm. For the radiation and energy fluxes, the same changes are observed as for D88–89. Furthermore, a part of the precipitation falls as liquid instead of solid compared to the control run. On the one hand, this induces snowmelt (by absorption of energy by the snowpack) and on the other hand, it prevents the pack from accumulating. The runoff peak is computed for the end of March, which is 11 days before the control run (Table 19.3; Figure 19.5).

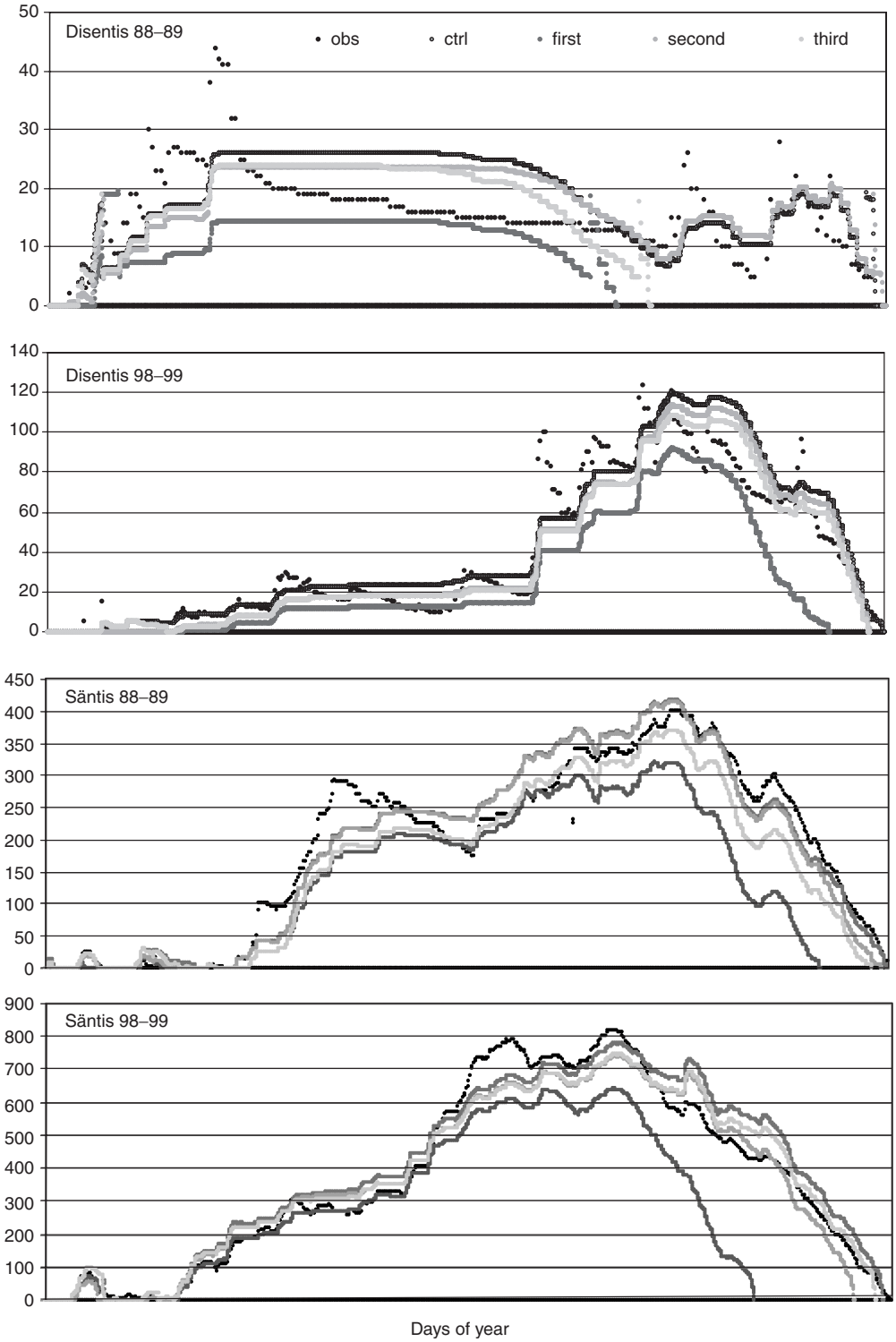


Figure 19.6 Evolution of the snowpack under the three temperature change scenarios: obs = observed snow depth. Note the different scales

At S88–89, the snow cover duration reduces by 31 days and its maximum depth decreases by 81 cm. With regard to the energy and radiation fluxes, the same changes are observed as for Disentis, but their magnitude is greater. Q^* enhances owing to a decrease of α because of more liquid precipitation, which keeps α at its lower asymptotic value (Table 19.1). If the precipitation falls as snow, α is increased, which diminishes Q^*. At this high-elevation station, the turbulent fluxes Q_h and Q_e reach cumulated values of $-45\,MJ\,m^{-2}$ and $20\,MJ\,m^{-2}$ respectively. Q_h contributes to the melting of the pack and Q_e depletes the snowpack by sublimating the snow. The runoff peaks 26 days earlier, at the end of June, compared to the control run.

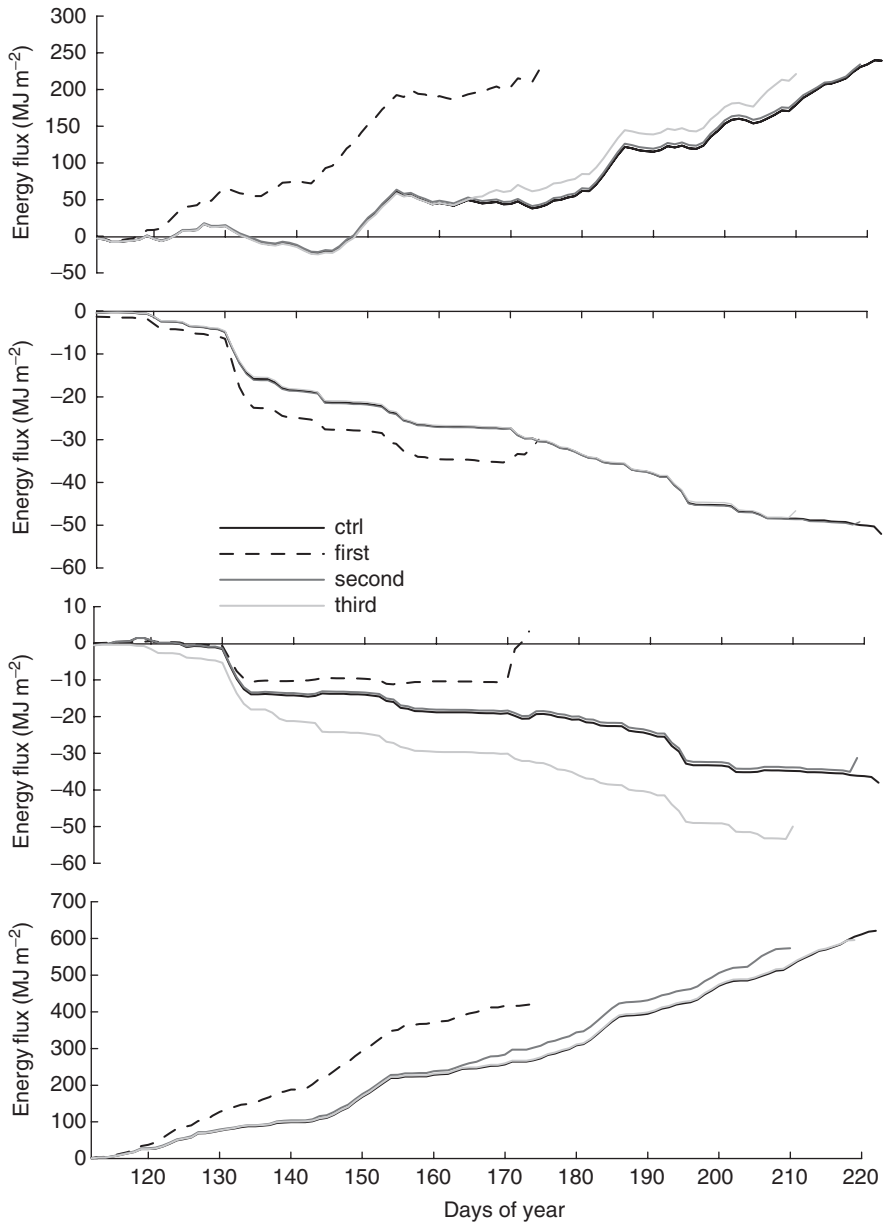


Figure 19.7 Evolution of Q^*, Q_e, Q_h, and ΔQ_m at Säntis 98–99. The curves stop when the snowpack has melted

At S98–99, the snow cover decreases by 51 days and its maximum depth decreases by 177 cm. All the above-mentioned changes of the energy and radiation fluxes are also observed except that the direction of the Q_e flux is changed and its negative sign indicates a solid condensation, which adds energy to the snow surface (Figure 19.7). The peak runoff occurs in the middle of June, 52 days earlier than in the control run (Table 19.3).

19.3.3 Second temperature scenario

The second temperature scenario is prescribed by a seasonally dependent increase in the minimum temperatures.

At D88–89, the snowpack duration is similar to the control run. Again Q^* increases in response to the rise of L^* compared to the control run. ΔQ_s has daily averages, which are more positive and therefore ΔQ_m enhanced. The peak runoff is observed one day later compared to the control runs. The peak is greatest because, at the melting, the snowpack is deepest of the three scenarios and the control run.

At D98–99, the snowpack vanishes five days earlier than in the control run. ΔQ_m only reaches higher values just before the complete melting of the snowpack. ΔQ_s increases, but T_s is smaller because of low values of T_g. On April 2, 1999, at midday, the melting of the snowpack was mainly driven by radiation (99%), but in the daily average, this percentage decreases to 56% and ΔQ_s reaches values of 42%. The peak runoff was observed one day earlier (Table 19.3).

At S88–89, the snow period was shortened by two days. The radiation fluxes are more important. The rise in T_{min} increases liquid precipitation. This happens less frequently compared to the first scenario because at S88–89, most days at which T_{min} is increased are days with very low temperatures. An augmentation in T_{min} also modifies the energy fluxes Q_e and Q_h. These tend to become more negative, that is, to add more energy to the snowpack.

At S98–99, the snowpack duration decreases by 13 days. Radiation fluxes and precipitation impacts show the same tendencies as for S88–89.Q_e achieves the most negative values of the three temperature scenarios, which indicate solid condensation, implying release of latent heat. For S88–89 and S98–99, the runoff peak is observed 11 days earlier compared to the control runs (Table 19.3).

19.3.4 Third temperature scenario

The third temperature scenario is given by a seasonal increase of the maximum temperatures. The model is run once again with the same initial and boundary conditions.

At Disentis, a rise of the maximum temperatures diminishes the snowpack duration by seven days in D88–89 and by six days in D98–99. This scenario induces similar changes as the first, especially if the melting starts early: Q^*, ΔQ_m, T_s increase, ΔQ_s becomes more positive and the snow depth declines. If differences are calculated in comparison to the control run, the fluxes of this scenario always show greater variability than the first and the second scenarios. At D88–89, the peak runoff occurs at 26 days, at D98–99, three days earlier compared to the control runs (Table 19.3).

At Säntis, the snow period decreased by 11 days in S88–89 and by four days in S98–99. In both winters, the radiation, energy, and hydrological regimes are comparable to the control runs. The impact of this scenario at this station seems to be more important during snow accumulation (Figure 19.6). At S88–89, the runoff peaks at 11 days, at S98–99, two days before the control simulations (Table 19.3).

19.4 DISCUSSION

All three temperature scenarios shorten the duration of the snow cover. The reduction of the snow season occurs mostly during the snowmelt period in spring and summer. Snow accumulation in autumn is much less sensitive. The impact of a temperature increase in all scenarios enhances more the downward than the upward long-wave radiation flux. Also, the possibility of liquid instead of solid precipitation augments the melting. For all investigated sites and years, it is noted that an increase of the mean temperature as described by the first scenario decreases the depth and duration of the snowpack most significantly. The timing of the runoff peaks follows the advancement of the snow melting, although the total amount of runoff is highest in the control runs.

The two investigated sites behave differently. The low-elevation station of Disentis shows a greater variability in the timing of its snowpack. The major contribution to melting is radiation energy. As this station shows a daytime melting pattern, the speed of melting depends on the strength of the radiation and therefore on the period of the year when melting starts. At Säntis, the building up of the snowpack and its melt are steadier. The radiation flux is important but also the turbulent energy fluxes and liquid precipitation add to the continuous melting pattern. An augmentation in the minimum temperatures has a more significant impact than a rise in the maximum temperatures. The extra heat by

the increasing temperatures is therefore used differently according to the site. At Disentis, it helps to warm the snowpack to the melting point during daytime and at Säntis, it augments the liquid precipitation amount and the turbulent fluxes.

The two sites show significant changes of their snow cover duration with a medium increase of temperature compared to the temperature rises predicted by the IPCC (IPCC 2001). Also, other studies show the same strong impacts. Hantel *et al*. (2000) calculated a decrease of the snow cover duration of up to 42 days if the European mean temperature increases by 1 K. Martin *et al*. (1997) computed a reduction of up to 66 days for the altitude of 1500 m a.s.l. in the French Alps for a doubled CO_2 experiment. Those changes are comparable to the ones estimated in this study.

Only two sites of the Swiss Alps and their sensitivity toward temperature increase scenarios are investigated in this study. It allows a temperature impact assessment at a small-scale level. To further analyze climate change impacts, more sensitivity studies of enhanced radiation, precipitation, and snow compaction parameterization need to be undertaken. Further studies are needed to better assess the model's sensitivity to ''adjustable'' parameters such as z_0 on the energy budget and on the snowpack depth and duration. With the utilization of meteorological input variables in a local model, an attempt to bridge the gap between the larger-scale studies and the smaller scale of impact assessments is shown.

19.5 CONCLUSION

A simple SEBM has been tested for two high-altitude stations in the eastern part of the Swiss Alps. It shows skill in representing the temporal variability of a snowpack during two different winter seasons. Furthermore, three temperature scenarios were applied: a rise in mean, minimum, and maximum temperatures. This study assesses the variability of snow cover duration, the radiation, energy, and runoff regimes at a local scale. The sensitivity analyses at Disentis and Säntis showed that an increase in temperature enhances the melting speed of the snowpack in the order of several days to several weeks during the snow season. Also, the runoff peaks occur earlier in the year. The maximum snow depth diminishes. At Disentis, the radiation input rises and at Säntis, the fluxes of latent and sensible heat become more dominant.

The results show that even a small temperature increase may have a significant influence on mountain snow, which has an important impact on mountain biota and other systems. To what extent this decrease in snow cover duration lies within the year-to-year variability is still to be determined. These indicate the need for future research, which will concentrate on the elaboration of more detailed climate change scenarios and sensitivity studies of further climate parameters.

19.6 ACKNOWLEDGEMENTS

The authors would like to thank E. Graham for his linguistic help and M. Verbunt for reading an earlier draft of the manuscript.

REFERENCES

Abegg B, Froesch R (1994) Climate change and winter tourism. In: Beniston M (ed): *Mountain Environments in a Changing Climate*. Routledge, pp. 328–341.

Bantle H (1989) *Programmdokumentation Klima-Datenbank am RZ-ETH Zürich*. Schweizerische Meteorologische Anstalt, Zürich.

Barry RG (1992) *Mountain Weather and Climate*, 2nd ed. Routledge, Chapman & Hall, p. 402.

Beniston M (2000) *Environmental Change in Mountains and Uplands*. Arnold/Hodder and Stoughton/Chapman and Hall Publishers, London, UK, and Oxford University Press, New York, USA, p. 172.

Benoit R (1977) On the integral of the surface layer profile-gradient functions. *J. Appl. Meteorol.* **16**: 859–860.

Goyette S (2002) *Modèle de Surface – GRENBLS*. Version 1 in French, Chap. 1. Documentation available from the author at the Department of Geosciences – Geography, University of Fribourg, Switzerland, p. 47.

Gyalistras D, Schär C, Davies HC, Wanner H (1998) Future Alpine climate. In: Cebon P, Dahinden U, Davies H, Imboden DM, Jaeger CC (eds): *Views from the Alps: Regional Perspectives on Climate Change*. MIT, pp. 171–223.

Hantel M, Ehrendorfer M, Haslinger A (2000) Climate sensitivity of snow cover duration in Austria. *Int. J. Climatol.* **20**: 615–640.

IPCC (2001) *Climate Change. The IPCC Third Assessment Report*, Volume I: The Scientific Basis. Contribution of Working Group I. Cambridge University Press, Cambridge and New York. p. 944.

Martin E, Timbal B, Brun E (1997) Downscaling of general circulation model outputs: simulation of the snow climatology of the French Alps and sensitivity to climate change. *Clim. Dyn.* **13**: 45–56.

McFarlane NA, Boer GJ, Blanchet JP, Lazare M (1992) The Canadian climate centre second-generation general circulation model and its equilibrium climate. *J. Clim.* **5**: 1013–1044.

Noilhan J, Planton S (1989) A simple parameterization of land surface processes for meteorological models. *Mon. Weather Rev.* **117**: 536–549.

Oke TR (1987) *Boundary Layer Climates*, 2nd ed. Routledge, London, p. 435.

Roesch A, Wild M, Gilgen H, Ohmura A (2001) A new snow cover fraction parametrization for the ECHAM4 GCM. *Clim. Dyn.* **17**: 933–946.

Rotach MW, Marinucci MR, Wild M, Tschuck P, Ohmura A, Beniston M (1997) Nested regional simulation of climate change over the Alps for the scenario of a doubled greenhouse forcing. *Theor. Appl. Climatol.* **57**: 209–227.

Stähli M, Jansson PE (1998) Test of two SVAT snow submodels during different winter conditions. *Agric. Forest. Meteor.* **92**: 31–43.

Stull RB (1988) *An Introduction to Boundary Layer Meteorology*, Atmospheric and Oceanographic Science Library: Volume 13. Kluwer Academic Publishers, Dordrecht, p. 680.

Tarboton DG, Luce CH (1996) *Utah Energy Balance Snow Accumulation and Melt Model (UEB)*. Utah Water Research Laboratory, Utah State University, Utah.

Weber RO, Talkner P, Auer I, Böhm R, Gajic-Capka M, Zaninovic K, Brazdil R, Fasko P (1997) 20th century changes of temperature in the mountain regions of Central Europe. *Clim. Change* **36**: 327–344.

Williams KS, Tarboton DG (1999) The ABC's of snowmelt: a topographically factorized energy component snowmelt model. *Hydrol. Process.* **13**: 1905–1920.

20

Climate Variability, Water Resources, and Hydrologic Extremes – Modeling the Water and Energy Budgets

OSMAN YILDIZ[1] AND ANA P. BARROS[2]
[1]*Faculty of Engineering, Kirikkale University, Yahsihan/Kirikkale, Turkey,*
[2]*Pratt School of Engineering, Duke University, Durham, NC, USA*

20.1 INTRODUCTION

The connections between climate, water resources, and hydrologic extremes as described by streamflow anomalies have been widely addressed in the literature (Schwarz 1977; Meyer *et al*. 1996; Kaczmarek *et al*. 1996; Hamlet and Lettenmaier 1999; and many others). However, the water resources impacts of climate variability go beyond changes in river water and indeed extend to all pathways of water in natural systems. Recently, increasing attention has been placed on the linkages between the so-called colors of water resources and sustainable development (Falkenmark *et al*. 1998). In this framework, rainfall is white water, streamflow (and groundwater) is blue water, and soil water content in the unsaturated zone is green water. Green water is the key water resource for food production (and ecosystem preservation), where irrigation is an artificial process of transferring blue water to green water. The underpinning rationale is that quantitative understanding of the dynamic balance between white, green, and blue water (i.e. the water cycle proper) is required to assess the long-term availability and resiliency of water resources at the spatial and temporal scales relevant for the human enterprise (Falkenmark 1997). Following this lead, our overarching objective is to assess the utility of hydrologic models to investigate the relationships among precipitation, vegetation, soil moisture dynamics and the intraseasonal variability of runoff production in complex landscapes. Specifically, we focus on elucidating the spatial and temporal variability of water and energy fluxes through interpretive analysis of model simulations of extreme hydrologic regimes.

Natural watersheds are characterized by high spatial heterogeneity that reflects interactions among the topographic, geomorphological, and biophysical characteristics of the landscape. The representation of spatial variability and associated nonlinear scale effects in hydrologic models remains a challenge both from the observational and from the modeling point of view (e.g. Binley *et al*. 1991; Seyfried and Wilcox 1995; Devonec and Barros 2002; among others). Our working hypothesis is that the utility of land hydrology models depends on their structural stability. By structural stability, we mean here the model's ability to simulate the onset and persistence of a hydrologic regime with consistent physics and without need for calibration (which is forcing dependent) or adjustment of model parameterizations. Structural stability implies predictive skill, and model portability or transferability (Barros 1995; Bindlish and Barros 2000; Devonec and Barros 2002). Further, we propose that structural stability can only be achieved when the spatial resolution of the model can resolve the fundamental spatial scales of the climate forcing

Climate and Hydrology in Mountain Areas. Edited by C. de Jong, D. Collins and R. Ranzi
© 2005 John Wiley & Sons, Ltd. ISBN: 0-470-85814-1

(i.e. rainfall) as well as landscape controls of hydrologic response (terrain, geology, soil, vegetation, etc).

For this work, a distributed Land Hydrology Model (LHM-3D) including soil–vegetation–atmosphere interactions, subsurface and overland flow, and streamflow (channel) routing is used for simulating warm season (spring and summer) hydrology during the 1988 drought and 1993 floods in the Monongahela River basin. The LHM-3D is a spatially distributed model that consists of three components: a one-dimensional (vertical column) Land Surface Hydrology Model (LSHM, Devonec and Barros 2002); a two-dimensional Surface Flow and River Routing Model with spatially and temporally varying routing parameters (SFRM; Yildiz 2001); and a two-dimensional Lateral Subsurface Flow Routing Model (LSFRM; Yildiz 2001). The LSHM simulates all processes involved in energy transfer between the atmosphere and the land surface (i.e. radiative fluxes, and ground, sensible and latent heat fluxes) as well as water transfers at the surface and within the unsaturated zone (snow processes, evapotranspiration, infiltration, and percolation) using spatially varying parameters and geomorphologic characteristics. Vertical and lateral subsurface flows are simulated sequentially by the LSHM and the LSFRM, respectively. Groundwater divides are assumed to correspond to DEM-derived basin boundaries. In the Subsurface Flow Routing Model (SFRM), streams are allowed to interact with the land margins and the basin's groundwater system, and therefore river reaches may function as either gaining or losing streams. A detailed description of the model can be found in Yildiz (2001).

The Monongahela basin, a tributary of the Ohio River on the western flanks of the Appalachian Mountains, USA, is characterized by complex terrain and highly heterogeneous geology and vegetation cover and therefore provides an excellent setting to meet the objectives of our study (Figure 20.1). Sensitivity of physical processes to climate forcing (drought year of 1988 vs wet year of 1993) and the structural stability of the model as a function of spatial resolution (1 km vs 5 km) were investigated through analyses of the spatial and temporal variability of water fluxes across the basin, including precipitation, evapotranspiration, and runoff. The utility of the LHM-3D for climate impact studies on water resources was assessed by investigating the consistency between observed and simulated soil moisture (green water) dynamics across the basin, runoff

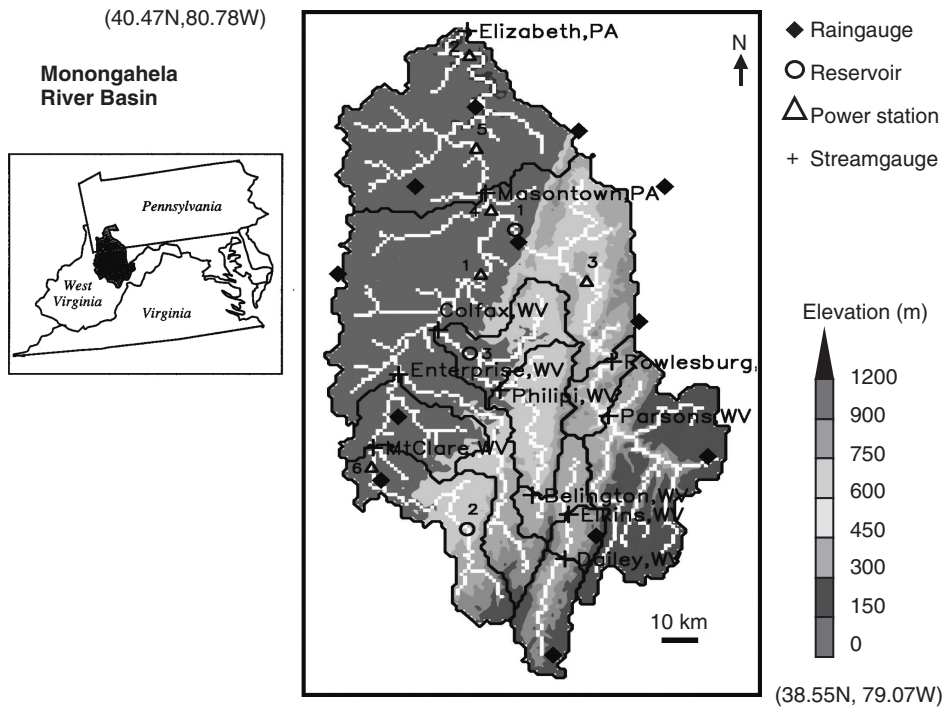


Figure 20.1 Digital Elevation Model (DEM) of the Monongahela River basin including raingauge and reservoir locations, stream network, and delineated subbasins with streamgauges at the outlets

production (blue water), and streamflow statistics, which has implications for reservoir and land management.

20.2 CASE STUDY: THE MONONGAHELA RIVER BASIN

20.2.1 Study area description

The Monongahela River basin (area = 12,875 km^2) is located on the western slopes of the Appalachian Mountains (38.56N–40.47N, 79.07W–80.76W) with portions in Pennsylvania and West Virginia, and outlet at Elizabeth, Pennsylvania, USA. The original USGS (United States Geological Survey) 3-arc second (nearly 100 m) Digital Elevation Model (DEM) data were aggregated up to 1- and 5-km for this study. The stream network was constructed using a threshold value of 25 km^2 for the minimum contributing area, and the spatial organization of streams was optimized through visual comparison with the perennial stream network from field surveys. It is recognized that a more complex and dense network could be delineated using smaller contributing areas at 1-km resolution. However, we found that the additional river reaches correspond to intermittent headwater channels, which cannot be resolved by the model. The 1-km DEM and the stream network along with the locations of raingauges, streamgauges, and major reservoirs are depicted in Figure 20.1.

As part of the Appalachian Plateau, the basin is characterized by strong spatial variability in the soil–terrain–hydrogeology system. At elevations above 500–600 m, the bedrock is highly dissected and consists of sandstone with almost flat-lying layers of shale, clay, stone, and dense limestone. The soil layers above the bedrock are very thin, and thus most of the rainfall runs off the slopes as interflow. The little amounts of water that infiltrate move vertically through fractures, and then move horizontally through sandstone or coal layers over large distances until they find another region of fractures or an unconfined flow region such as colluvium and alluvium deposits (Harlow and LeCain 1993). Accordingly, the baseflow and interflow contributions are very small during nonrainy periods, and the water levels in streams are very low. At low elevations where the land surface is nearly flat, the soil layers are relatively thicker and the productive unconsolidated alluvial aquifers ensure baseflow and interflow contributions during summer months (Harlow and LeCain 1993; Trapp and Horn 1997).

Figure 20.1 also shows the boundaries of selected catchments within the Monongahela with respect to the three major river networks, namely, West Fork River to the west, the Tygart River in the center, and the Cheat River on the eastern flank of the basin. Individual catchments are identified by the name of the streamgauge at the outlet (Table 20.1). At 5-km resolution, only the Enterprise and Dailey subbasins could be delineated separately because of spatial resolution artifacts in the watershed delineation algorithm. Consequently, the results of 5-km simulations were analyzed only for the two delineated watersheds and for the Monongahela basin proper, hereafter referred to as *Elizabeth*, the name of the outlet location.

Table 20.1 Catchments within in the Monongahela River basin (Figure 20.1)

Watershed	Area (km^2)	Tributary	Infrastructure	
			Reservoir	Power plant
Elizabeth	13,875	Monongahela	Y	Y
Masontown	10,881	Monongahela	Y	Y
Colfax	3091	Tygart	Y	
Rowlesburg	2430	Cheat		
Parsons	1785	Cheat		
Philipi	1744	Tygart		
Enterprise	1695	West Fork	Y	Y
Belington	1059	Monongahela		
Mt Clare	1021	West Fork	Y	
Elkins	715	Monongahela		
Dailey	496	Monongahela		

20.2.2 Climate forcing

The regional climate is humid to temperate, with topographic differences leading to local anomalies. The average annual temperature is about 9°C. Mean monthly temperatures range from −2 to 22°C. Average annual precipitation is 1067 mm and ranges from 940 mm in northern areas to 1524 mm in the southern mountainous areas. Precipitation during the winter is associated with the passage of frontal storms, whereas thunderstorms are responsible for most of the late spring and summer rainfall.

The drought of 1988 and the flood of 1993 were among the most severe occurrences of hydroclimatic extremes in the continental United States during the last century (Namias 1991; Kunkel *et al*. 1994). Low-flow frequency analysis performed using data from streamgauges located at Enterprise and Elizabeth for minimum flows over 7-, 14-, 30-, 60-, and 90-day periods indicate that the return periods for the 1988 drought range from 27 to 90 years at Enterprise, and from 48 to 80 years at Elizabeth.

In turn, the 1993 summer flooding in the Mississippi River Basin was produced by large rainfall anomalies such that the cumulative summer rainfall was twice as

large as the normal value (Kunkel *et al*. 1994). A flood frequency analysis using a log Pearson III distribution to fit the annual maximum streamflow records at Enterprise and Elizabeth showed that the exceedance probabilities of the 1993 floods correspond respectively to 10% (10-year of return period) and 25% (4-year of return period). Therefore, although the 1993 spring and summer seasons were characterized by wet conditions well above normal in the Monongahela, the streamflow response was not as extreme as elsewhere in the Ohio River basin where 100-year flood levels were exceeded.

The 1988 and 1993 atmospheric forcing data (i.e. air temperature, pressure, humidity, wind velocity, and short-wave and long-wave radiations) for hydrologic model simulations were obtained from two simulations for spring and summer 1988 and 1993 with the NCAR RegCM2 at 25 km spatial resolution over the Midwest United States. The RegCM2 was driven at the lateral boundaries by European Center for Medium Range Forecast (ECMWF) analyses fields (Jenkins and Barron 2000). Model outputs were produced at a temporal resolution of 6 h for the pressure and 3 h for the remaining data sets. The atmospheric forcing data (i.e. air temperature, pressure, humidity, wind velocity, and short-wave and long-wave radiation) were downscaled from 25-km to 1- and 5-km spatial resolutions using a bilinear interpolation scheme. Subsequently, these datasets were linearly interpolated to one-hour intervals for the hydrologic simulations.

Despite a close temporal correlation with the observed precipitation, the climate model simulated excessive precipitation during the entire simulation period. To remedy this problem, hourly point measurements from a total number of 13 raingauges in and around the watershed area (Figure 20.1) were used to distribute point measurements of hourly rainfall over the basin using four different interpolation methods (Dingman 1994): (i) the standard hypsometric method that results in spatially variable rainfall varying only with elevation; (ii) the arithmetic average method resulting in uniform rainfall fields; (iii) the standard Thiessen polygon method in which each Thiessen polygon is represented by a raingauge, and thus, at a given time step, rainfall is uniform over a Thiessen polygon but spatially variable over the basin; and (iv) the weighted area average method by which point measurements were weighted by the area of the corresponding Thiessen polygon. Except for the case of the hypsometric method, the rainfall fields obtained using the other three methods (2, 3, and 4) were subsequently modified to include spatially variable orographic effects. Specifically, orographic enhancement of rainfall at elevations above 400 m was imposed in the spring using the following empirical relationship derived from the climatology at the seasonal timescale:

$$P^* = P\left[1 + 0.67\frac{(Z - 400)}{700}\right] \tag{20.1}$$

where P^* is the modified rainfall with orographic enhancement, P is the rainfall estimated by any method, and Z is the local elevation in meters (Yildiz 2001). That is, the orographic enhancement corresponds to an amplification of up to 67% of the rainfall amounts estimated from the raingauge data.

20.2.3 Land-surface characterization

Soil texture (Figure 20.2(a)) and soil hydraulic properties were extracted from the database developed by the National Cooperative Soil Survey (USDA 1995). The soil column in the land surface model was divided into three, four, or five layers of various depths across the basin according to local geology and type of vegetation cover. The first layer is a thin superficial layer of 8 cm, which functions as the interface between the ground and the atmosphere for the energy balance. The second layer is an intermediate layer expanding throughout the root zone with a varying depth across the river basin as a function of land cover type. The depth of this layer is generally 50 cm for short vegetation (grass and shrubs) and 100 cm (two 50-cm layers) in forested areas, respectively. The bottom layer is a deeper layer extending between the root zone layer and the local water table, or impermeable boundary, the thickness of which varies in the watershed depending on local geology: typically, 50 cm at high altitudes and 100 cm (two 50 cm layers) at low elevations.

Land cover consists predominantly of deciduous trees in the uplands, and short grass and crops at low elevations (Figure 20.2(b)). A small area in the southeastern region of the basin is populated by coniferous, while a narrow band of nearly bare ground can be found along the northeast–southwest direction. Note that the areas identified as bare ground refer actually to agricultural fields that are intermittently cultivated. Although a vegetation dynamics model has been recently incorporated into the LSHM, in the simulations described here changes in vegetation cover are represented dynamically via direct assimilation of indices derived from remotely sensed data. Specifically, leaf area index (LAI) and fractional vegetation cover were estimated by parameterizations using NDVI (Normalized Difference Vegetation Index) data from the Advanced High Very High Resolution Radiometer (AVHRR; Tucker 1979; Jackson *et al*. 1983).

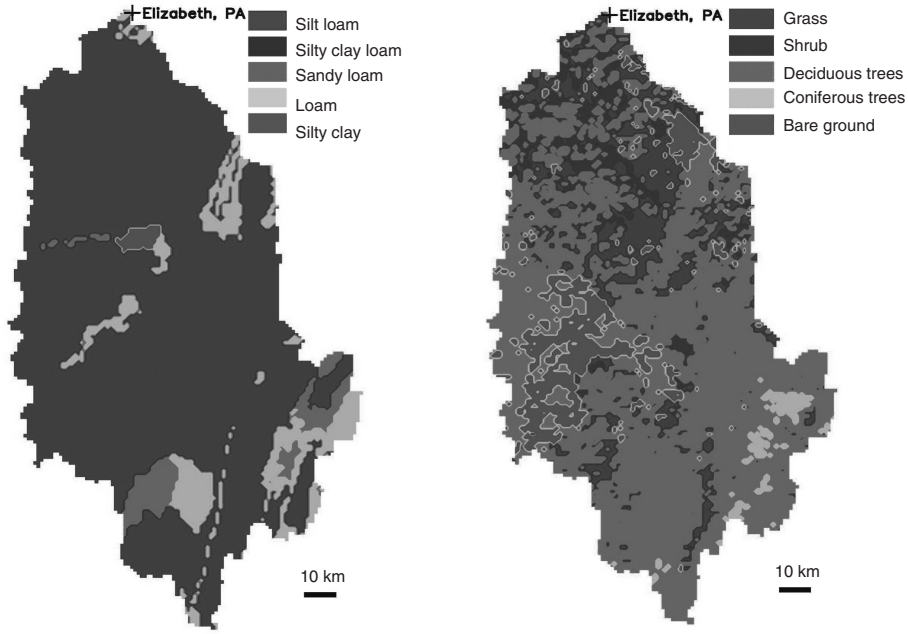


Figure 20.2 (a) Soil texture distribution at 1-km spatial resolution; (b) Landcover distribution

NDVI data were available at 8-km spatial resolution every 10 days. For use in this case study, the data were downscaled to 1- and 5-km and linearly interpolated in time down to one-hour time intervals. For grass and shrubs, LAI was derived from NDVI according to the parameterization proposed by Choudhury *et al*. (1994) [$\mathrm{LAI} = -1.81 \ln(1.36 - 2 \times \mathrm{NDVI})$]. For forested areas, Spanner *et al*. (1990) was used as reference [$\mathrm{LAI} = 0.438(\mathrm{NDVI}/0.438)^{3.77}$]. Fractional vegetation cover (F) was estimated using the relationship from Carlson and Ripley (1997) [$\mathrm{F} = (\mathrm{NDVI})^2$]. During 1988, LAI ranged from about 2 to 8 in spring and from about 4 to a maximum value of 14 at some locations in summer (Figure 20.3). LAI decreases immediately after the peak in June because of the effect of water stress on vegetation, with occasional increases of LAI at high elevations of the basin during July in response to localized thunderstorms. During 1993, LAI ranged from 2 to 10 in spring and from 4 to 16 in summer (not shown). Starting from the end of May until the end of July, LAI remains relatively high consistent with the annual cycle of deciduous trees in the basin and with the peak of the crop growing season. The space-time variability of LAI reflects the differences in the physical controls of the water cycle between the drought of 1988 and the wet summer of 1993. This indicates that LAI can be viewed as a proxy of water stress and drought conditions in the Monongahela.

Table 20.2 Surface albedo, roughness height for the atmospheric boundary layer, and Manning's roughness coefficient for overland and channel flow routing

Surface	Albedo (%)	Roughness height (m)	Roughness coefficient
Grass	22	0.1	0.1
Shrub	20	0.1	0.1
Deciduous trees	18	0.8	0.2
Coniferous trees	16	1.0	0.2
Bare ground	25	0.1	0.1
Channels			0.05

Given the soil and vegetation information, the model parameters for which there was no ancillary data (surface albedo, roughness height, and Manning's roughness coefficient) were extracted from the literature (Table 20.2). Minimum stomatal resistance, a limiting factor in the canopy resistance parameterization during the daytime, is 150 s/m for grass and shrubs and 200 s/m for deciduous and coniferous trees (Devonec and Barros 2002). Note that the parameters had the same values at both 1- and 5-km resolutions. The difference between

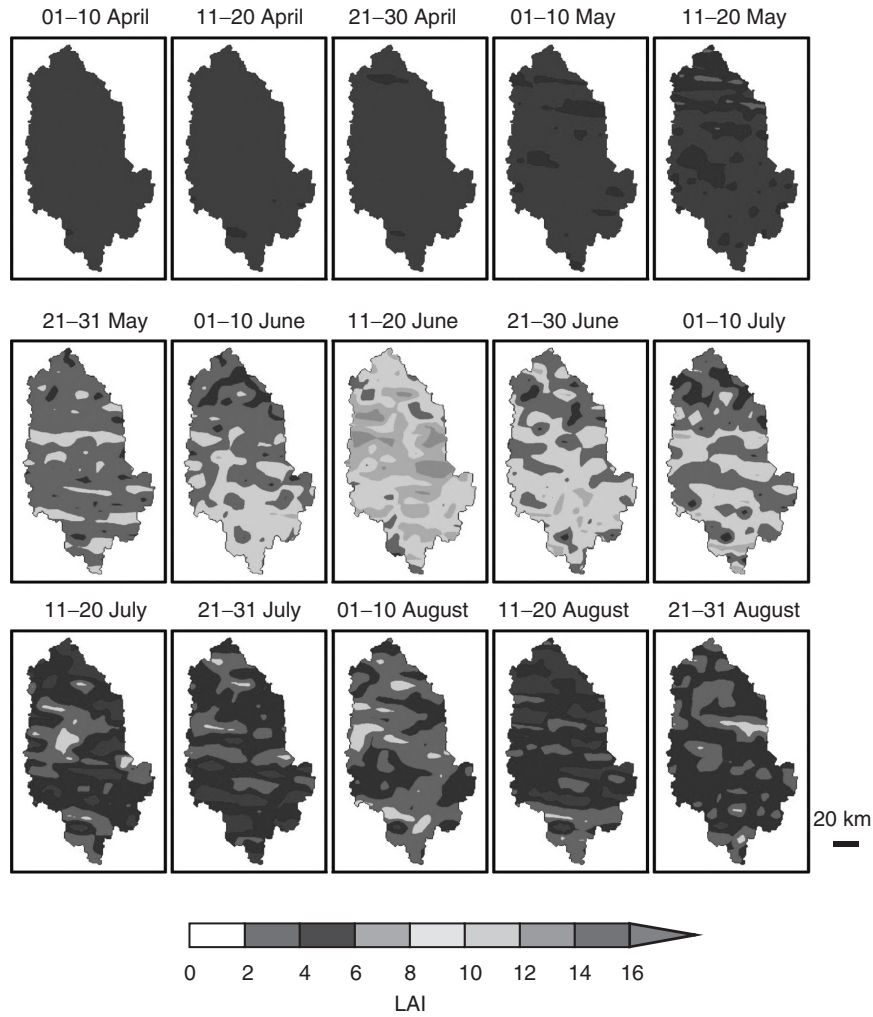


Figure 20.3 Leaf area index (LAI) distribution April through August of 1988

the model set-ups stems from the spatial resolution at which the physical processes are resolved, and from the representation of only the terrain.

20.3 MODEL RESULTS

A total of 48 model simulations (2 climate regimes × 4 rainfall interpolation methods × 2 spatial resolutions × 3 stream networks) were conducted. The hydrologic model was initialized for a period of one month (spin up period) at the beginning of each run in order to allow the state variables to reach internal equilibrium. Each model simulation was performed at one- and five-km spatial resolutions with an hourly time step for a five-month period from April through August. Following Devonec and Barros (2002), the hydrologic model was not calibrated, or specific parameters optimized. Bindlish and Barros (2000) showed that the calibration of model parameters is particularly sensitive to the underlying hydroclimatic regime and spatial resolution. Thus, any optimal set of model parameters cannot be dissociated from the conditions under which calibration took place, which goes against the structural stability requirements enunciated earlier.

Simulations of streamflow hydrographs at the outlets of subcatchments indicated in Figure 20.1 (Table 20.1) are compared against daily streamflow observations. Note that, in the ensuing discussion, the simulated streamflow

refers to total streamflow Q that comprises both overland and subsurface flows, while the simulated subsurface flow Q_s includes both interflow and baseflow.

20.3.1 Drought simulations (1988)

1. *Sensitivity to rainfall forcing* Convective storms along with orographic enhancement effects dominate spring and summer precipitation in the region, and therefore it is expected that the spatial variability of runoff production and streamflow variability closely reflect rainfall patterns within each of the subbasins within the Monongahela River basin.

Figures 20.4 and 20.5 show the simulated time-series of streamflow at Elizabeth as a function of rainfall distribution at 5- and 1-km resolution, respectively.

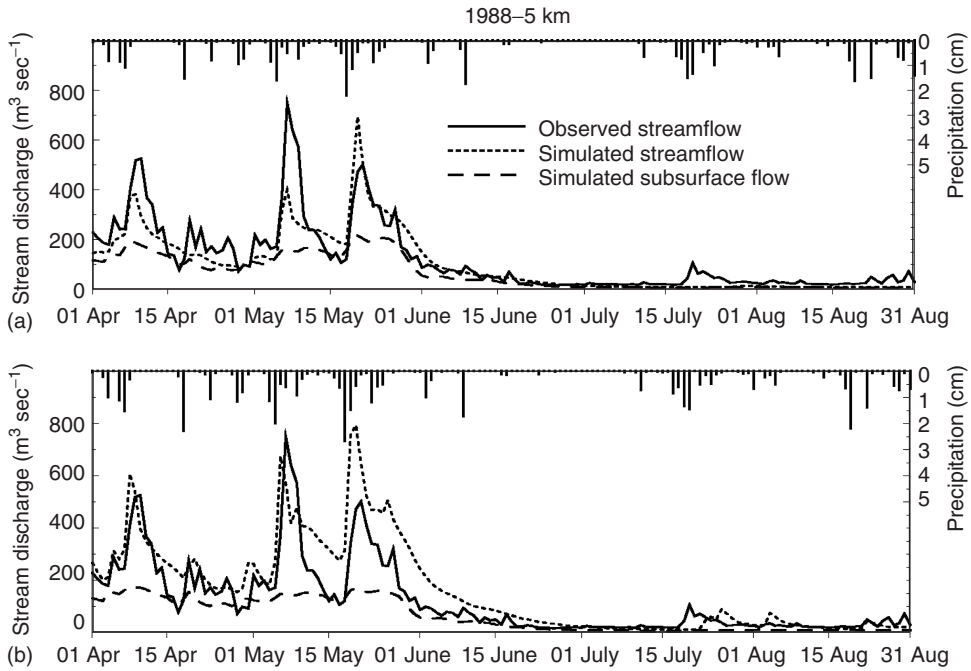


Figure 20.4 Comparison of observed and simulated hydrographs at Elizabeth, PA, between 01 April and 31 August 1988 at 5-km resolution. The model was forced with rainfall fields estimated according to: (a) the hypsometric method; and (b) the modified Thiessen polygon method

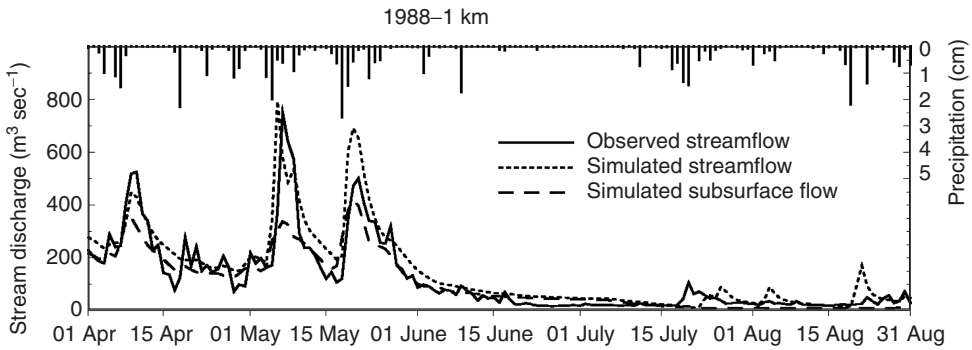


Figure 20.5 Comparison of observed and simulated hydrographs at Elizabeth, PA, between 01 April and 31 August 1988 at 1-km resolution. The model was forced with rainfall fields estimated using the modified Thiessen polygon method

The hydrographs in Figure 20.4(a) correspond to rainfall fields estimated using the standard hypsometric method, while the modified Thiessen polygon method was used for the simulation in Figure 20.4(b). Overall, the simulations are better using the rainfall fields generated by the modified Thiessen polygon method independently of the spatial resolution (compare Figures 20.4(a) and 20.4(b), and Figure 20.4(b) and Figure 20.5). This suggests that the information content provided by the existing raingauges is close to that which can be optimally described by the individual polygons.

In late spring and throughout the summer, however, the lack of adequate rainfall forcing results in poor temporal correlation between simulated and observed flows even at 1 km resolution. Because most of the warm-season rainfall is produced by small-scale thunderstorm activity (e.g. spatial scales on the order of $10-20\,\mathrm{km}^2$), the raingauge network (Figure 20.1) is too sparse to detect the occurrence of rainfall in regions of the basin where raingauges are located very far apart from each other, thus explaining the missing peaks. By contrast, if one or more of the raingauges are colocated with such events, then the total precipitation can be grossly overestimated (i.e. proportionally to the ratio between the actual area of the rainstorm and the Thiessen polygon area) such as between May 15 and June 1 (Figure 20.4(b)). Consistency between the smaller spatial scales of rainfall forcing and model resolution is therefore necessary to capture the runoff response to isolated convective storms.

Nevertheless, model statistics of streamflow closely follow the spatial patterns of those of existing observations (not shown), suggesting therefore that the model captures well the intraseasonal variability of water fluxes during the 1988 drought across the basin. The root mean square error and bias in the streamflow simulations increase with drainage area, and the coefficient of variation is usually higher in the summer than it is in the spring, and it decreases when the watershed area increases, indicating reduced variability due to spatial integrating effects of streamflow propagation.

2. *Structural stability* Comparison of the 5- and 1-km hydrograph simulations at Elizabeth (Figures 20.4(b) and 20.5) reveals important characteristics relevant to the structural stability of the LHM-3D with regard to spatial resolution. First, the relative contributions of subsurface flow (interflow plus baseflow) to the total streamflow are considerably different. While the streamflow at coarse resolution (i.e. 5 km) is produced as surface runoff (Figure 20.4(b)), the streamflow at the finer resolution (i.e. 1 km) results mostly from the contribution of subsurface flow (Figure 20.5). This implies two different control processes on runoff production: (i) vertical infiltration capacity at 1 km-vertical control; and (ii) magnitude of the lateral gradients of hydraulic head (elevation plus pressure head) and hydraulic conductivity at 5 km-lateral control.

Figure 20.6 compares the ratio of the simulated subsurface flow (Q_s) to the total simulated streamflow (Q) at Elizabeth, Enterprise, and Dailey watersheds for both 5- and 1-km resolutions using the rainfall fields estimated via the modified Thiessen polygon method. Dailey is representative of hydrologic processes in the regions of steep terrain on the eastern half of the Monongahela basin, whereas Enterprise is representative of the hydrology of the central and western catchments. The differences in (Q_s/Q) are particularly noticeable from late spring to early summer. At Dailey (top panel), the timing coincides with strong reduction in relative subsurface flow after four consecutive days of rainfall in early May that leave the shallow soil column saturated. Subsequently, soil water is quickly redistributed down slope at 1 km, and only at much slower rate at 5 km consistent with the differences in topographic slopes at both resolutions. A similar, though weaker, reduction in subsurface flow contribution takes place in response to the series of storms that occur between May 16 and May 20. After this time, the streams are maintained almost entirely by the incoming subsurface flow at 1-km resolution, while it takes almost a month for this to be the case in the 5-km simulation.

In the densely forested slopes above Dailey, evapotranspiration reaches a peak in late spring (June) during the greening season, lowering soil moisture content in the root zone, decreasing lateral hydraulic head gradients in the hillslopes, and consequently reducing subsurface flow to the streams. Vegetation is therefore a limiting factor of subsurface flow via evapotranspiration. During short-duration intense rainfall events, surface runoff production is controlled locally by the soil's infiltration capacity in the uppermost layer. After the end of June, streams are maintained by subsurface flow at either resolution. This effect is much stronger at 5-km resolution consistent with lower root zone soil moisture over larger areas (i.e. larger grid cells) and gentler topography (low hydraulic gradients).

The (Q_s/Q) time-series for Enterprise (mid panel) exhibits lower relative subsurface flow contribution at 1 km than at 5 km in contrast to what happens at Dailey. This is explained by the fact that the soils are significantly deeper and the topography generally smoother in this catchment, and therefore surface runoff is controlled by the infiltration capacity of the upper soil layers. Furthermore, the predominant vegetation types at lower elevations are characterized by shallow root systems,

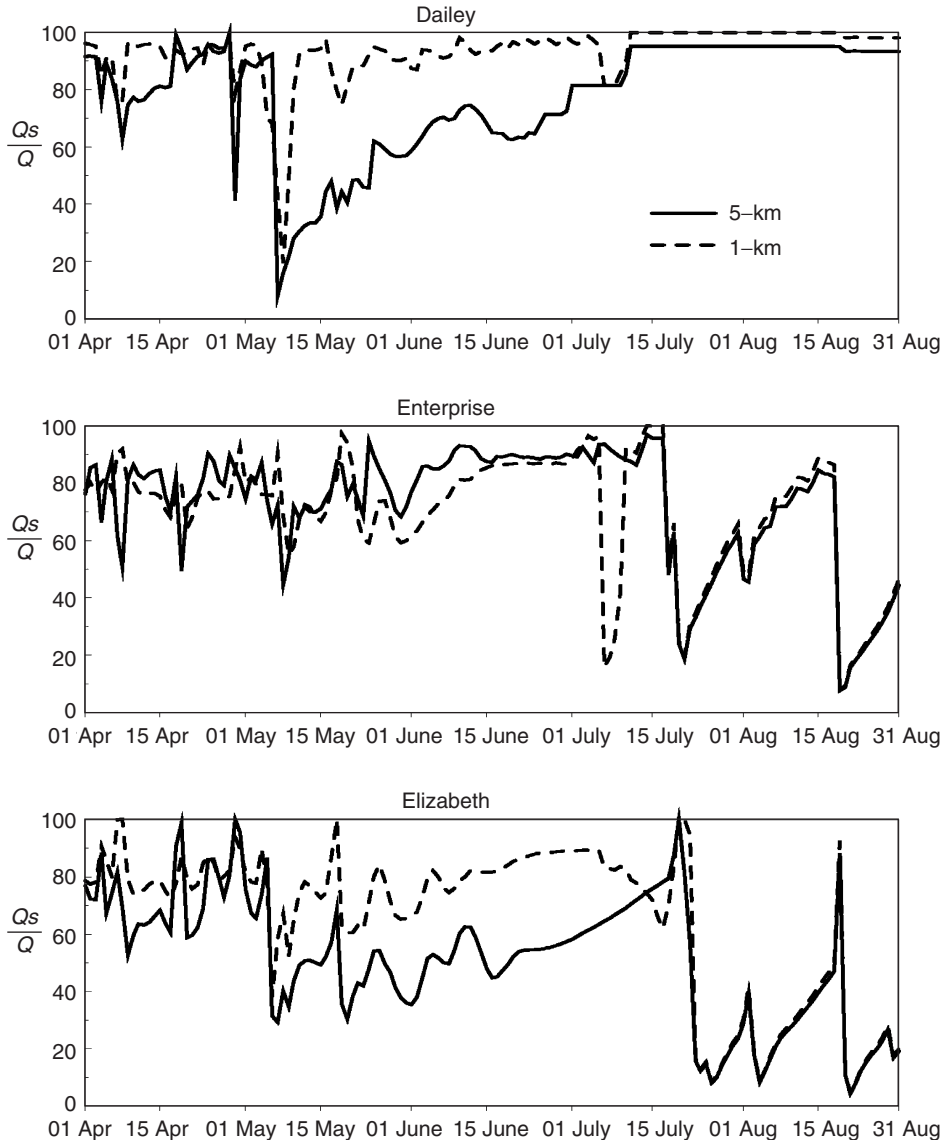


Figure 20.6 Comparison of the time evolution of the ratio of subsurface flow (Q_s) to total streamflow (Q) at 1- and 5-km resolutions km resolutions at Dailey, Enterprise, and Elizabeth in 1988

and thus increased evapotranspiration in late spring and early summer seasons predominantly affects the upper soil layers and therefore has a smaller impact on rainfall-runoff response at Enterprise than at Dailey. The Q_s/Q behavior at Elizabeth (bottom panel) reflects the integrated behavior of the Monongahela basin, which is qualitatively similar to that discussed above for Dailey, reflecting the combination of the two types of catchments in the basin.

The changes in the rainfall-runoff response due to changes in the spatial resolution of the model indicate that there is a change in governing physical processes at different resolutions, specifically infiltration capacity, evapotranspiration and root zone soil moisture, and lateral subsurface flow. These results imply therefore a dependency between model resolution and simulated physics. Although it is possible to predict streamflows with comparable skill at both resolutions, the pathways

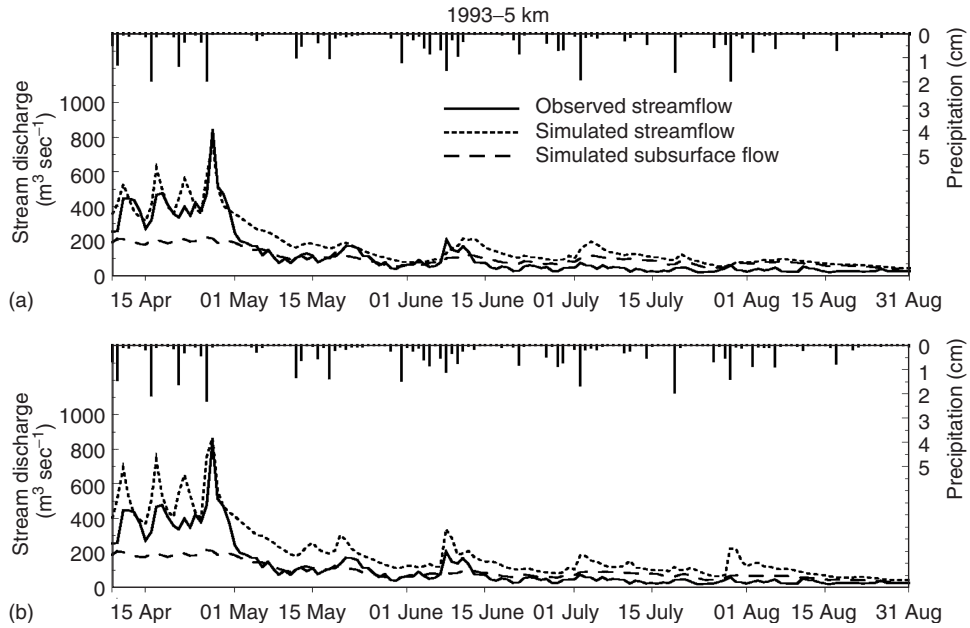


Figure 20.7 Comparison of observed and simulated hydrographs at Elizabeth, PA, between 09 April and 31 August 1993 at 5-km resolution. The model was forced with rainfall fields estimated according to: (a) the hypsometric method; and (b) the modified Thiessen polygon method

of water within the basin during drought can be quite different depending on the physiographic characteristics of individual catchments. For example, the Monongahela appears to be more resilient to drought in the 5-km simulation than in the 1-km simulation. On the basis of the observations, however, we know this is not the case (see Figure 20.4(b) and Figure 20.5). In summary, physically realistic simulations therefore require that model resolution be consistent with the spatial scale of the dominant hydrologic processes.

20.3.2 Flood simulations (1993)

1. *Sensitivity to rainfall forcing* The streamflow at Elizabeth is simulated reasonably with the rainfall fields obtained using the standard hypsometric method, especially in the case of spring peaks caused by passing frontal storms (Figures 20.7(a) and (b)). During the summer season, all simulations capture well summer peaks and low-flow variability. At Dailey (not shown), the streamflow response is generally overestimated, especially in spring and early summer. Since only dependence with elevation was used to describe orographic effects on rainfall, other factors such as ridge-valley gradients, rainshadow, and so on, were not included in the parameterization of orographic effects, and thus rainfall is overestimated at Dailey.

Although model simulations at 1 km were performed for all watersheds shown in Figure 20.1 and Table 20.1, only one of the hydrographs at Elizabeth was selected to show here (Figure 20.8). The model results and the observations match well independently of the rainfall distribution (not shown). As compared to the 5-km results, all spring peaks, except the maximum peak at the end of April, are better reproduced at 1-km resolution as expected.

2. *Structural stability* Inspection of the 5- and 1-km 1993 simulations for Elizabeth, Enterprise and Dailey reveals that the contribution of subsurface flow is much larger at 1-km resolution, especially in the spring period (e.g. Figures 20.7 and 20.8). Similar to the 1988 simulations at this resolution, the model generated streamflow is comprised mostly of baseflow and interflow. Note, however, that as opposed to what happens in 1988, the differences for the 1993 simulations are larger in early May when heavy rainstorms are more frequent, leveling off in late spring (Figure 20.9). Vegetation controls on soil moisture and subsurface flow response are not critical here, because soil water availability to plants is not a limiting factor for evapotranspiration in 1993.

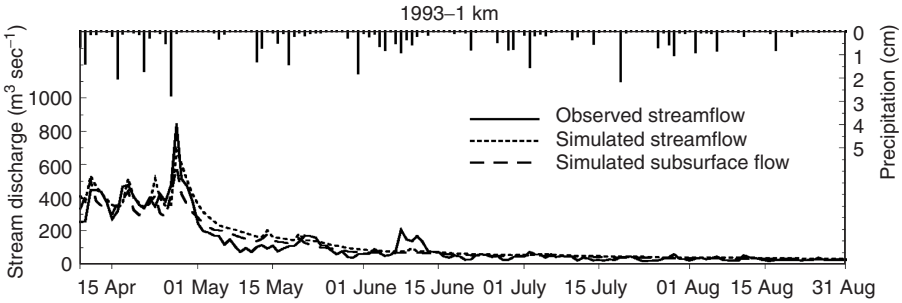


Figure 20.8 Comparison of observed and simulated streamflow hydrographs at Elizabeth, PA, between 09 April and 31 August 1993 at 1-km resolution. The model was forced with distributed rainfall estimated using the modified weighted area method

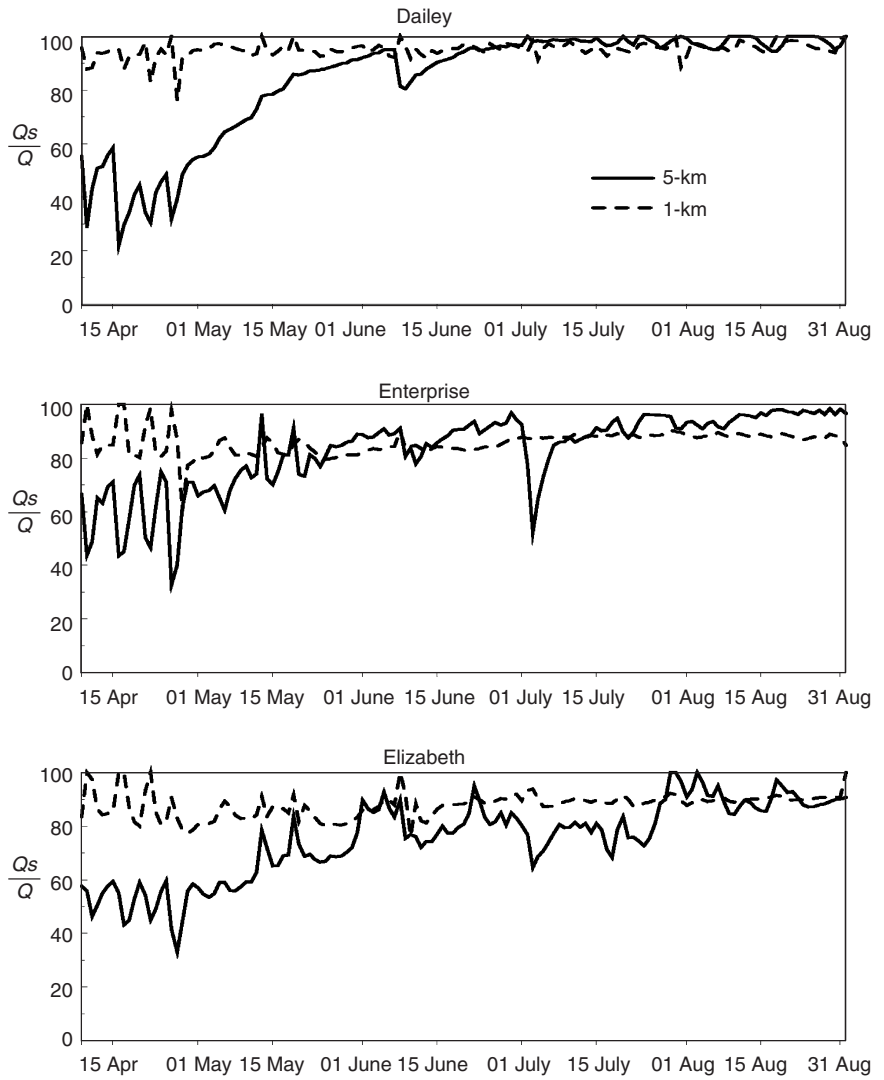


Figure 20.9 Comparison of the time evolution of the ratio of subsurface flow (Q_s) to total streamflow (Q) at 1- and 5-km resolutions at Dailey, Enterprise, and Elizabeth in 1993

Surface runoff production is overestimated at 5-km resolution as compared to the 1-km simulations, suggesting that when soils are near saturation (during April 1993), the subsurface flow response (vertical and lateral) at 5 km is ''slower'' than that at 1-km resolution. This is consistent with a longer characteristic timescale of subsurface flow: smoother topography at 5-km resolution implies lower hydraulic head gradients, and therefore reduced subsurface flow. Model calibration to replicate observed streamflows would thus lead to an ''optimal'' value of hydraulic conductivity at 5 km larger than that at 1 km. On the other hand, consistent with Bindlish and Barros (2000) who found that the optimal magnitude of hydraulic conductivity determined through calibration of a hydrologic model varies inversely with the spatial variability of rainfall, the ''optimal'' value of hydraulic conductivity at both resolutions in the summer would be smaller than that in the spring. Scale dependence of soil hydraulic properties would be therefore imposed artificially to accommodate not only changes in subsurface gradients but also in the type of rainfall forcing (i.e. frontal versus convective storms). Another interesting feature is that the differences between the two simulations quickly become very small

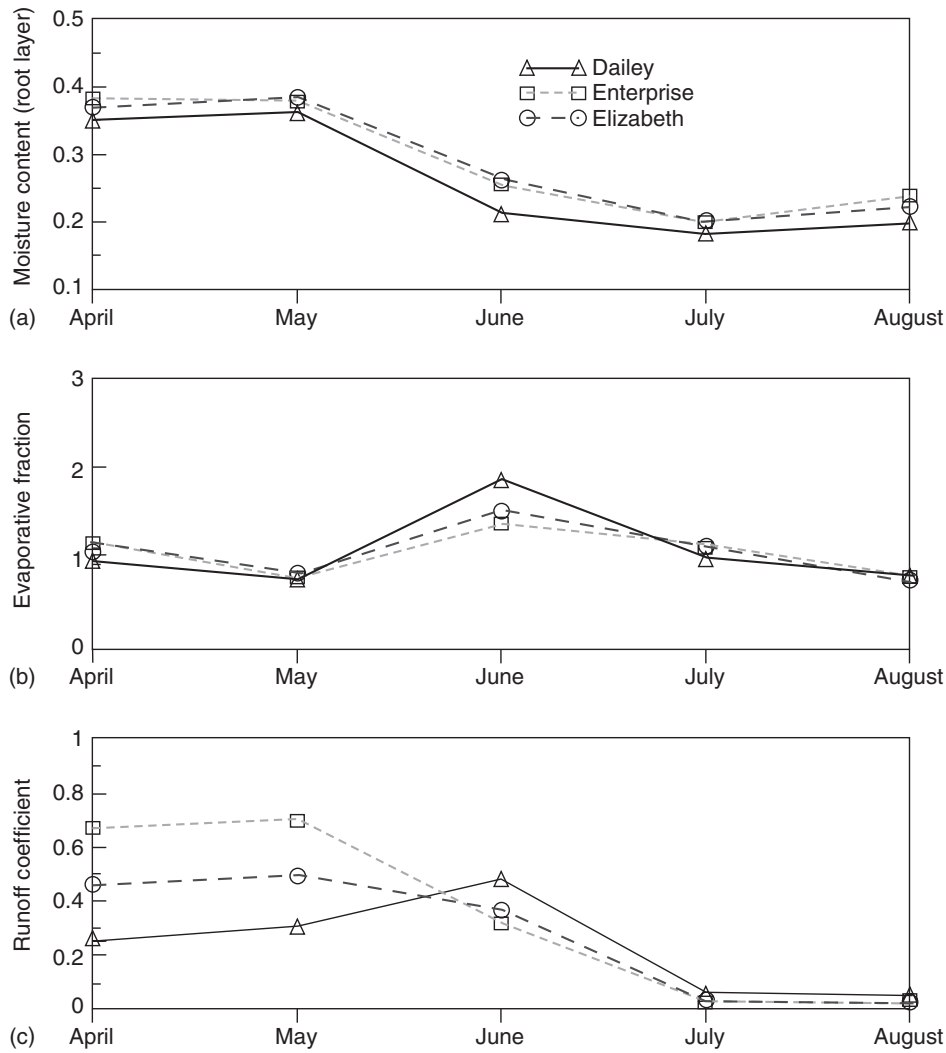


Figure 20.10 Intraseasonal variability (monthly timescale) of simulated hydrologic indices at Dailey, Enterprise, and Elizabeth in 1988: (a) volumetric soil moisture content in the root layer (θ); (b) evaporative fraction (E/P); and (c) runoff coefficient (Q/P)

in late spring and early summer, confirming our hypothesis that when soil water availability is high, evapotranspiration plays a lesser role in controlling the partitioning of surface/subsurface runoff contributions to streamflow as noted earlier in the 1988 simulations.

20.3.3 Intraseasonal variability

In the evaluation of the spatial and temporal variations of the surface energy and water budgets, we focus next on radiation fluxes, root zone soil moisture, evapotranspiration, and rainfall-runoff response within the Elizabeth, Enterprise, and Dailey watersheds at the monthly timescale.

The surface radiation budget in the LHM-3D relies on incoming short-wave and incoming long-wave radiation forcing from RegCM2 outputs, while the outgoing long-wave radiation is calculated on the basis of the simulated surface temperature. The surface fluxes including sensible, latent, and ground heat fluxes simulated by the hydrologic model must balance the net radiation. In the LHM-3D, the surface energy balance is captured virtually without discrepancy with respect to the regional model output, which indicates that energy fluxes in the LHM-3D off-line simulations are consistent with those produced in real-time RegCM2, including the surface albedo parameterization.

Figure 20.10 shows monthly values of basin averaged root zone moisture content (Figure 20.10(a)), evaporative fraction (the ratio of evapotranspiration to precipitation, Figure 20.10(b)), and runoff coefficient (the ratio of runoff to precipitation, Figure 20.10(c)) from April through August in 1988. Evapotranspiration substantially increases everywhere in June in response to rapidly increasing air temperature and LAI, thus consistent with the governing role of vegetation with respect to evapotranspiration as discussed earlier. At Dailey, in particular, evapotranspiration during June (greening phase) is almost twice the rainfall. During this period, the excess water needed to sustain the development of the canopy of the deciduous trees comes from the water stored in the deep root layer. However, there is also a simultaneous increase in the runoff coefficient that is explained by the increase in surface runoff production. In 1993, on the other hand, evapotranspiration increases significantly during the summer, especially at Dailey, because soil water is not a limiting factor (not shown).

Simulated soil water content across the Monongahela River basin exhibit strong seasonality. Monthly spatial distributions of root layer soil moisture at 1-km resolution are displayed in Figure 20.11 for 1988. In the spring, the root layer remains relatively wet across the entire river basin, especially at low elevations. In July, it dries progressively as a result of decreasing rainfall and increasing evapotranspiration. Once again, effects of spatial variability in topography, hydrogeology, and land cover on the evolution of soil moisture can be detected from these figures. Soil moisture levels are generally lower at high elevations where gradients are steep and the land surface is forested than they are at low elevations where gradients are relatively mild and the land surface is covered by short vegetation with shallow roots. In July of 1993, for example, soil moisture content is as low as $0.18\,m^3/m^3$ at high altitudes in the southern and eastern parts, and as high as $0.42\,m^3/m^3$ at low altitudes in the northern and western parts (not shown). In addition, the root zone layer at low elevations is generally wetter in the 1993 period as compared to the same zone in 1988 period as expected. However, soil moisture levels at high elevations are not significantly different in both years; that is, summertime soil water stress during drought is only anomalous at low elevations along the river valleys, in the areas typically used to grow crops. In this, the model captures the essence of the visual appearance of the landscape during drought in the region – brown fields of grass and shrubs sprinkled with green spots where trees are present.

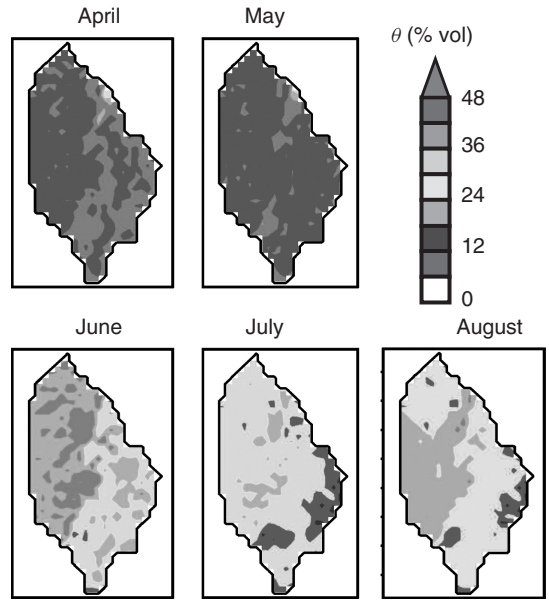


Figure 20.11 Simulated spatial distribution of monthly volumetric soil water content (θ) in the root layer from April through August of 1988

Finally, the high correlation between simulated (1 km resolution) and observed streamflow hydrographs at

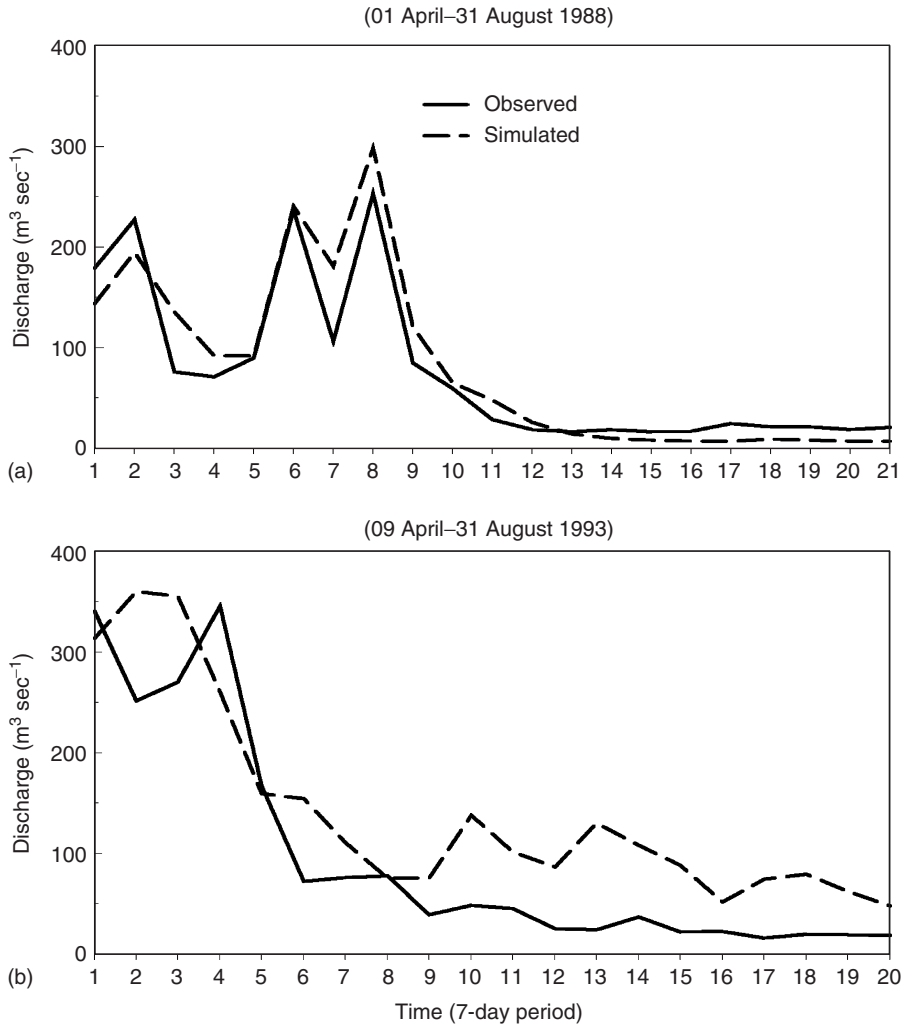


Figure 20.12 Comparison of the observed and simulated [1-km resolution] 7-day period low flows at Elizabeth between April and August: (a) 1988; and (b) 1993

Rowlesburg and Parsons suggests that the model can be an effective tool in the prediction of low flow and floods into the Lake Lynn Reservoir on the Cheat River. The same is true with regard to the Tygart River Lake on the Tygart River based on the simulations at Philipi, Belington, Elkins, and Dailey. The utility of model prognostics for water resources management is illustrated in Figures 20.12(a) and (b) for 1988 and 1993, respectively, via a comparison of the statistics of observed and simulated seven-day period low flows at Enterprise and Elizabeth, respectively. As shown in the figures, the statistics of simulated low flows are generally in agreement with observations, especially during the summer season, when low-flow management is most critical.

20.4 DISCUSSION

Hydrologic model simulations of warm season hydrology in the Monongahela River Basin were evaluated both at the basin and subbasin with an eye on elucidating the dynamics of the water cycle under extreme conditions: drought in 1988 and flooding in 1993. For each case study, the model was implemented at two spatial resolutions: a fine resolution based on the mix of ancillary data available (1 km), and a much coarser resolution

conditioned on the model's ability to preserve the terrain envelope and the stream network (5 km). Model simulations were evaluated according to a protocol of increasing complexity: (i) sensitivity to rainfall forcing as described by the streamflow response at the outlet of specific catchments; (ii) model structural stability at different resolutions as described by the physical mechanisms controlling rainfall-runoff response; and (iii) spatial and temporal variability of the coupled water and energy budgets.

First, we showed that because of landscape and river network complexity, even small differences in precipitation fields can have a significant impact depending on the physical processes that control rainfall-runoff response. By conducting simulations at different resolutions, we were able to explain how changes in the spatial resolution translate into nonlinear changes in the simulated hydrologic processes: runoff production (blue water) is controlled by hydraulic head gradients at 5 km, while infiltration capacity is the dominant control at 1 km resolution. Moreover, vegetation governs the spatial and temporal variability of root zone soil moisture (green water), especially during the greening season in June. Through evapotranspiration, vegetation also has an important role in runoff production, a role that is magnified at 5 km resolution because it acts to smooth further the steepness of hydraulic head gradients, thus reducing subsurface flow in the unsaturated zone, and consequently stream recharge. Although the streamflow simulations did not agree with observations as well for the 1988 drought as for the 1993 floods, the model was able to capture the broad space-time patterns of water and energy fluxes at both resolutions. Finally, the 1 km simulation is superior not only in matching the observed hydrographs (and associated statistics) but also with respect to the representation of hydrological processes within the basin as a whole. This implies that the model is structurally stable at 1 km resolution in the Monongahela River basin.

This research substantiates importance and necessity to our working assumptions: (i) the utility of hydrologic models for predictive studies hinges on the quality of the precipitation forcing, especially in regions of complex terrain where the space-time characteristics of rainfall combine with those of the landscape to establish highly nonlinear hydrologic regimes; and (ii) model structural stability is an essential condition of predictive ability. Furthermore, at a time when the policy paradigm in water resources has shifted toward an integrated view of land-water management and the water cycle (''a land-use decision is a water decision'', Falkenmark 2001), hydrologic modeling studies such as this provide an optimistic basis for quantitative impact assessments informed by science.

20.5 ACKNOWLEDGMENTS

This work was funded in part by a NASA Grant NAGW-5254 and NOAA GCIP Grant NA86GP0058 with the second author. We thank Drs Gregory Jenkins and Christopher Duffy for their comments and suggestions.

REFERENCES

Barros, A. P., 1995, ''Adaptive multilevel modeling of land-atmosphere interactions,'' *Journal of Climate*, **8**, 2144–2160.

Bindlish, R. and A. P. Barros, 2000, ''Disaggregation of rainfall for one-way coupling of atmospheric and hydrological models in regions of complex terrain,'' *Global and Planetary Change*, **25**, 111–132.

Binley, A. M., K. Beven, A. Calver, and L. G. Watts, 1991, ''Changing responses in hydrology: Assessing the uncertainty in physically-based model predictions,'' *Water Resources Research*, **27**(6), 1253–1261.

Carlson, T. N. and D. A. Ripley, 1997, ''On the relation between NDVI, fractional vegetation coverage, and leaf area index,'' *Remote Sensing of Environment*, **62**, 241–252.

Choudhury, B. J., N. U. Ahmad, S. B. Idso, R. J. Reginato, and C. S. T. Daughtry, 1994, ''Relations between evaporation coefficients and vegetation indices studied by model simulations,'' *Remote Sensing of the Environment*, **50**, 1–17.

Devonec, E. and A. P. Barros, 2002, ''Exploring the transferability of a land-surface hydrology model,'' *Journal of Hydrology*, **256**, 258–282.

Dingman, S. L., 1994, *Physical Hydrology*, Prentice-Hall, 646.

Falkenmark, M., 1997, ''Society's interaction with the water cycle: a conceptual framework for a more holistic approach,'' *Hydrological Sciences*, **42**, 451–466.

Falkenmark, M., 2001, ''The greatest water problem: the inability to link environmental security, water security and food security,'' *Water Resources Development*, **17**(4), 539–554.

Falkenmark, M., W. Klohn, J. Lundquist, S. Postel, J. Rockstrom, D. Seckler, H. Shuval, and J. Wallace, 1998, ''Water scarcity as a key factor behind global food insecurity: round table discussion,'' *Ambio*, **27**(2), 148–154.

Hamlet, A. F. and D. P. Lettenmaier, 1999, ''Effects of climate change on hydrology and water resources in the Columbia River basin,'' *Journal of the American Water Resources Association*, **35**(6), 1597–1623.

Harlow, G. E. Jr. and G. D. LeCain, 1993, *Hydraulic characteristics of, and ground-water flow in coal bearing rocks in southwestern Virginia*. U.S. Geological Survey Water-Supply Paper 2388, 36.

Jackson, R. D., P. N. Slater, and P. J. Pinter, 1983, ''Discrimination of growth and water stress in wheat by various vegetation indices through clear and turbid atmospheres,'' *Remote Sensing of the Environment*, **15**, 187–208.

Jenkins, G. S. and E. J. Barron, 2000, ''Regional climate simulations over the continental United States during the summer of 1988 driven by a GCM and the ECMWF analyses,'' *Global and Planetary Change*, **25**, 19–38.

Kaczmarek, Z., N. W. Arnell, and L. Starkel, 1996, ''Climate, hydrology, and water resources,'' *Water Resources Management in the Face of Climatic/Hydrologic Uncertainties*, International Institute for Applied Systems Analysis, the Netherlands, 3–29.

Kunkel, K. E., S. A. Changnon, and J. R. Angel, 1994, ''Climatic aspects of the Mississippi river basin flood,'' *Bulletin of the American Meteorological Society*, **75**(7), 811–822.

Meyer, G. K., G. T. Orlob, and C. Jokiel, 1996, ''Effects of climate change on water quality in the central valley of California,'' *Water Resources Management in the Face of Climatic/Hydrologic Uncertainties*, International Institute for Applied Systems Analysis, the Netherlands, 274–299.

Namias, J., 1991, ''Spring and summer 1988 drought over the contiguous United States-causes and prediction,'' *Journal of Climate*, **4**, 54–65.

Schwarz, H. E., 1977, ''Climatic change and water supply: How sensitive is the Northeast?'' *Climate, Climatic Change and Water Supply*, National Academy of Science, Washington, DC, 111–120.

Seyfried, M. S. and B. P. Wilcox, 1995, ''Scale and the nature of spatial variability: Field examples having implications for hydrologic modeling,'' *Water Resources Research*, **31**(1), 173–184.

Spanner, M. A., L. L. Pierce, S. W. Running, and D. L. Peterson, 1990, ''The seasonality of AVHRR data of temperate coniferous forests: relationship with leaf area index,'' *Remote Sensing of the Environment*, **33**, 97–112.

Tucker, C. J., 1979, ''Red and photographic infrared linear combinations for monitoring vegetation,'' *Remote Sensing of the Environment*, **8**, 127–150.

USDA (United States Department of Agriculture), 1995, ''State Soil Geographic (STATSGO) Data Base: Data use information,'' USDA Pub. No. 1492., 113 [ftp://ftp-fc.sc.egov.usda.gov/NCGC/products/STATSGO/statsgo-user-guide.pdf]

Yildiz, O., 2001, Assessment and simulation of hydrologic extremes by a physically-based spatially distributed hydrologic model. Ph.D. Dissertation. Department of Civil and Environmental Engineering. The Pennsylvania State University, University Park, Pennsylvania, USA, 314.

Index

Note: Page numbers in **bold** refer to tables and *italics* refer to figures.

Abramov Glacier, Kyrgyzstan 263
  annual runoff *268*
  characteristics **265**
  CV-values of modeled discharge for July–August 269
  effect of climate change and complete melting of glaciers *272*, 273–274
  effect of climate change and 50% reduction of glaciated area *271*, 272–273
  goodness of fit 267
  hydrometeorological conditions and change in discharge after doubling of CO_2 and complete melting of glaciers **273**
  location 264
  measured and simulated daily discharge 266
  runoff scenarios after doubling of CO_2 270, 271
  water balance 266, **267**
albedo, in forests 34, 36
alluvial fans 218
alpenrose (*Rhododendrum ferrugineum*) 165, 178, 250
alpine climate change, and cryospheric responses 1–4
Alps
  floods and frequency analysis 219
  hydrological processes 218
  runoff and floods 217–220
  slope environments 218
  see also Austrian Alps, French Alps, Italian Alps, Swiss Alps
Andes
  climate of Chilean 17–18
  surface energy balance of high altitude glaciers 15–27
  see also Argentinian Andes, Chilean Andes, Dry Central Andes
Appalachian mountains *xx*, 292, 293
Archie's law 61
Argentinian Andes 25
atmospheric models 222
Austrian Alps 130, **131**
  water balance modeling with fuzzy parameterizations 125–146

Black Forest Mountains, Germany 235, **236**
boreholes, total temperature difference per day 67, *69*
Bowen ratio method 161–162
Bowen ratio stations 161, **166**, 168, 180
Bowen ratios 156, *157*, 158, 165
Braeualm valley
  hydrogeomorphological zoning of trough slopes 253, *255*
  sediment sources 253, *254*
Brooks and Corey's parameters
  plotted against ASTM grain size classification 113, *115*
  plotted against organic matter content 113, *115*
Brugga catchment, Black Forest
  basin precipitation based on different calculation methods 238–240
  characteristics **236**
  comparison of model performance of Wilhelmer Talbach basin and 240–241
  comparison of two catchment precipitation values for investigated events **238**
  dominant runoff generation processes 237–238
  hydrological models 238
  location 235
  modeling results 238–241
  precipitation databases 236
  precipitation scenarios 237
  rainfall radar data 236
  runoff calculations using different precipitation inputs 240–241
  spatial distribution of basin precipitation 239
  temporal distribution of cumulative basin precipitation 239

Canadian GEWEX Enhanced Study (CAGES) 226
Canadian Land Surface Scheme (CLASS) 223, 231
  baseflow drainage 223
  coupling between MC2 and modified 224, 227, 228–229, *230*
  modifications for runoff generation 223
  testing in uncoupled mode 224–226
Cascade mountains *xx*, 148, **149**

Climate and Hydrology in Mountain Areas. Edited by C. de Jong, D. Collins and R. Ranzi

© 2005 John Wiley & Sons, Ltd.

ISBN: 0-470-85814-1

catchment boundary, definition 256
Central Asian research sites 263, *264*
Chilean Andes *xx*, 17–18
  study site location *16*
chionophilous vegetation 209, 211
chionophobous vegetation 209, 211
climate change
  evidence for changes in mountain regions 1–2
  impact and mountain hydrology 261–306
  impact on snow covered areas 52
climate warming, general effects on glaciers 271–272
climatologic and hydrologic coupled investigations in Norwegian high mountains
  aims and objectives of research program 185
  discussion and conclusions 208–211
  meteorological results 194
  results of 194–199
climatologic and hydrologic coupling, in the ecology of Norwegian high mountain catchments 185–214
climatologic and hydrologic dynamics 194
  Norwegian continental middle-alpine ridges and depressions 199
  Norwegian continental middle-alpine slopes 199
  Norwegian continental and oceanic lower alpine ridges and depressions 197–199
  spatial patterns 199–208
clutter maps 236
CNR-VAPI RIVERS project 106
conceptual index models 277
condensation, definition 162
condensation and evapotranspiration measurements, comparison between Giant Mountains and Alps 161–183
convective precipitation, assessment using operational weather radar for flood modeling in the Black Forest, Germany 233–246
COUP model *74*, 77–78, 79, 81
creep slopes 253, *255*
CROCUS snow model 30–31, 34, 42
cryosphere, responses to climate change 2–3, 59
cumulative degree-days (CDD) 47
  relationship between snow cover depletion and 48, *49*
  trend at Kalpa (W. Himalayas) 48

Dailey catchment, Monongahela River basin 293, 298
  evaporative fraction intraseasonal variability *302*, 303
  intraseasonal variability *302*, 303–304
  ratio of simulated subsurface flow to total simulated streamflow 298, *299*
  root zone moisture content intraseasonal variability *302*, 303
  runoff coefficient intraseasonal variability *302*, 303
  time evolution of ratio of subsurface flow to total streamflow 300, *301*
Darcy's method 103, 108, 109, **110**, 112, 118
DC resistivity tomography system 60
  key results 69–70
  miniature 63, *64*
degree-day factors 7, 8
degree-day method 8, 10–12, 13, 218, 274
diffusion equation 92–94
digital elevation models (DEM) 19, 21, 22
  results for Monongahela River basin 296–304
  timescales 249
digital terrain model, Upper Durance catchment 32–33
dimensionless diffusivity, behaviour of 93, 94, *95*
discharge, Upper Enns catchment 130, 135, 139, 140, 143
Dischma Valley, Grisons, Switzerland
  characteristics **162**, 164, **248**, 249
  climate 164
  evapotranspiration and condensation daily and weekly variations 178–180
  evapotranspiration and condensation measuring test sites with meteorological stations 165, **166**
  evapotranspiration and evaporation hourly variations 171–178
  geomorphological map 250, *251*, *252*, 253
  gneiss rocks *252*, 253
  location 164, *165*, *248*, 249
  meteorological variables 179
  slope models 252–256
  soil sequences 252
Disentis, Switzerland
  day of year with peak runoff **282**, 284
  evolution of the runoff 284
  location 279
  maximum snow depth **282**, 284
  maximum temperature rise scenario 287
  mean temperature rise scenario 284–287
  minimum temperature rise scenario 287
  number of snow-covered days **282**, 284
  observed and simulated snowpacks *281*, 282
  radiation and energy fluxes daily evolution 282, *283*
  sensitivity to temperature increase scenarios 288
  snow cover variability 288
  snow duration estimation 280
  snowpack evolution under temperature change scenarios *285*
  variability in timing of snowpack 287
drainage characteristics, Upper Enns catchment 135
drop collectors 164, 168
drought simulations (1988), Monongahela river basin 297–300
Dry Central Andes 15, 18, 26
dye tracer experiment 79–81
  depth profiles of areal coverage of pixels stained *80*
  infiltration pattern *80*

eastern Norwegian high mountains, vertical temperature profiles 195, *196*
ecochore concept *188*, 189
ecological base stations 192
  spatial organization of measurements and use of technical equipment 192, *193*
ecological research, hierarchy of models for high mountain research 189, *192*

econ concept 186, *188*, 189
ecotope concept *188*, 189
ecotopes *188*, *189*
  characterization 203
  legend for landscape ecological maps and profiles 203, *207*
Elizabeth, PA
  comparison of observed and simulated hydrographs *300*
  comparison of observed and simulated 7-day low flows at Enterprise and 304
  comparison of observed and simulated streamflow hydrographs 300, *301*
  evaporative fraction intraseasonal variability *302*, 303
  intraseasonal variability *302*, 303–304
  root zone moisture content intraseasonal variability *302*, 303
  runoff coefficient intraseasonal variability *302*, 303
  sensitivity to rainfall forcing 300
  simulated time-series of streamflow as function of rainfall distribution 297
  structural stability 300
  time evolution of ratio of subsurface flow to total streamflow 298, *299*, *301*
energy balance, comparison between ground temperature, resistivity evolution and 67–69
energy balance models 19–21, 277
energy flux, through snow cover 68, *69*
Enns river basin, soil properties 134
Enterprise 293
  comparison of observed and simulated 7-day low flows 304
  evaporative fraction intraseasonal variability *302*, 303
  intraseasonal variability 303–304
  root zone moisture content intraseasonal variability *302*, 303
  runoff coefficient intraseasonal variability *302*, 303
  time evolution of ratio of subsurface flow to total streamflow 298, *299*, *301*
equifinality, of model structures and parameterizations 125
evaporation 85
  of snow in forests 36
  transpiration and measured water flux (simulated), from eddy-covariance (EC) system 153, *154*
evaporation pans 166, *167*
evaporation rates, in Norwegian high mountain catchments 195
evaporation response units (ERUs) 257
evapotranspiration 131, 134
  and water balance 123–214
  comparison between condensation measurements and 161–183
  conversion from potential to actual 136
  in mountain areas 180, 181
  influence of topographic position on 250
  validating spatial and temporal distribution 252
evapotranspiration data, in mountain areas 161
evapotranspiration models
  differentiation and scaling 250
  disadvantages 250
  for mountain valleys 249–252
  research recommendations 257
external-drift-kriging procedure 133

fixed-electrode arrays 60, 62–63
flash flood simulation, coupled meteorological and hydrological models for 221–232
flood modeling
  basin precipitation variability 243
  convective precipitation using operational weather radar 233–246
  in heterogeneous catchments 233
flood runoff generation processes 233
floods
  and frequency analysis 219
  in Central Europe 219
  comparison of simulated and observed hydrographs for 2 flood events 226
  simulations at Monongahela river basin 300–303
floods in the Alps, runoff and 217–220
flow processes, analytical solutions 91–99
fog deposition, in Giant Mountains 162
Föhn winds 164
Fokker–Planck's equation 102
forecasts of snowmelt runoff, improving 29–44
forest canopy temperatures 35
forest canopy, water balance and 35
forest climate model 34–36
  application 36–37
forest harvests, impact on annual water yields 147–148
forest humidity 35
forest water-balance investigation
  methods 148–151
  modeling program 151
  objectives 148
  results and discussion 152–157
French Alps 31, *32*, 34, 288
frozen soil, effects on groundwater recharge in Alpine areas 73–83
fuzzy arithmetic, basic rules 144
fuzzy logic, application to Upper Enns catchment 126
fuzzy membership functions 126, 129–130, 137–138, *139*
fuzzy numbers 129, 130
  comparison of 145
fuzzy parameterizations, water balance modeling with 125–146
fuzzy parameters, estimation of inputs and 132–135
fuzzy sets 129
fuzzy water balance models 126

GA method 104, 109
Gd St Bernard
  discharge measurements 79
  local scale measurements for experiments 75–77
  location *75*
  relation between snow cover and soil frost 82–83
  site description 75
geoelectrical monitoring 66–67
geomorphological instantaneous unit hydrograph (GUH) 224, 226, 231
geomorphological zoning 247–260
  parameterizing surface properties 249–257
geophysical measurements 60
geophysical methods, applications 67

Giant Mountains, Poland 163–164
characteristics **162**
evapotranspiration and condensation measuring test sites and meteorological stations 164, **166**
fog deposition 162
soils 164
vegetation 164
wind systems 164
GISS model 269, *271*, *272*
glacier ablation
fractions in total river runoff 267, **273**
in Nepalese Himalayas 7–14
Glacier No. 1, China 263
characteristics **265**
effect of climate change and complete melting of glaciers *272*, 273–274
effect of climate change and 50% reduction of glacier *271*, 272–273
goodness of fit 267
hydrometeorological conditions and change in discharge after doubling of CO_2 and complete melting of glaciers **273**
location 264
glacier and rocky areas, calculation of monthly snow and ice melt 11
glacier runoff
compensating effect 267, 269
simulated for present climate with and without present-day glacier cover 267, *268*
variability 267
glaciers
effect of 50% reduction 272–273
general effect of climate warming 271–272
influence of g. retreat on water yield from high mountain basins in Alps and Central Asia 263–275
surface energy balance of high altitude 15–27
global circulation models (GCMs) 277, 278
global warming 277
effects on the cryosphere 2–3
ground substrate, spatial differentiation 199, *202*
ground temperatures, monitoring in mountain regions 2

Ha! Ha! River basin
characteristics 228, **229**
comparison of two reconstructed hydrographs 228, *229*, 231
location 228, *229*
Hannigalp 74–78
COUP-model 77–78, 79
discharge measurements 78–79
location *75*
relation between snow cover and soil frost 82–83
site description 75
water balance measurements 74, 75–77
Haut Glacier d'Arolla, solar radiation, turbulent fluxes and snow ablation *23*
HBV-ETH model
description 264–266
results 266–274
runoff scenarios 269–274
structure *265*
high mountain catchments
ecological determinants 208, *209*
future ecological research 211
high mountain landscape ecological research, hierarchy of models 189, *192*
Himalayas, calculating snow and ice melt 7–14
''Hortonian'' concept 218
HYCYMODEL 7–8
hydrological modeling, sources of uncertainty 127–129
hydrological models
definition 247
incorporation and prediction of uncertainty in 125–126
relationships between precipitation, vegetation, soil moisture dynamics and runoff production in complex landscapes variability 291
hydrological models for flash flood simulation, coupled meteorological and 221–232
hydrological response units (HRUs) 258
hydrology and meteorology coupling 215–260
using geomorphological zoning to improve 247–260
hydrology models, structural stability of 291
hypsometric method 294, *297*, 298, 300

ice melt, snow and 5–55
ice melt under debris layers, calculation of 11–12
ice-snow melting phase, estimation 218
infiltration capacity, of soils 101, 218
infiltration tests 107–108
integrated watershed management 247
interval of confidence 129
inverse distance weighting (IDW) method 237
ISBA SVAT (soil-vegetation atmosphere transfer) model 30
Italian Alps 102, 105, 107, 113, 117, 118, 219
IUH concept 218

Juncal Norte glacier 15, *16*
climate 17
main characteristics **16**
meteorological data collection 18–19
short-wave radiation and derived albedo **23**

kriging procedure 133

Lago Maggiore 86
land hydrology model (LHM-3D) 292
structural stability 298–300
land surface hydrology model (LSHM) 292
land surface scheme (LSS) 231
coupled to weather prediction models 222
effect on regional weather 221–222
importance to climate 221
role in climate simulations 227
landscape ecological investigations 186
landscape ecological synthesis, spatio-temporal 202–208
landuse map, Upper Durance catchment 37
Langtang Khola Basin 8, *9*
data for verifying calculated discharge 8
main physical characteristics **9**
observed and calculated monthly discharges *12*, 23
precipitation 10

variation in observed mean air temperature, total precipitation and calculated discharges *13*
lapse rates 1, 2
lateral subsurface flow routing model (LSFRM) 292
Laurentian highlands *xx*, **229**
leaf area index, Monongahela river basin 295, *296*
levels of presumption 129, 138, *140*
linearised Richards equation 86
Lirung glacier, relation between degree-day factor and debris thickness 11
Lirung Khola Basin 8, *9*
data for verifying calculated discharge 8
main physical characteristics **9**
observed and calculated monthly discharges *12*, 13
variation in observed mean air temperature, total precipitation and calculated discharges *13*
Loma Larga glacier 15, *16*
climate 17
energy fluxes 20
main characteristics **16**
meteorological data collection 18–19
short-wave radiation and derived albedo **23**
long-wave radiation 21
low flows, comparison of observed and simulated at Enterprise and Elizabeth 304
lower alpine belt, spatial differentiation of temperature dynamics 204, *205*
lowlands, dependence on mountain runoff 274
lysimeters *167*, 168

MAP programme 85–86
MC2 coupled to modified CLASS, results from Ha! Ha! River basin 228, *230*
Mella River basin 102, 105
characteristics **106**
CNR-VAPI RIVERS project 106
infiltration tests and areal frequency **107**
location *106*
preliminary analysis 107
sensitivity of bubbling pressure of soils to organic matter content and grain size distribution 117
Mesoscale Alpine Programme 217
Mesoscale Compressible Community Model (MC2) 222, 223
application to Saguenay flood of coupled modified CLASS and 226–229
coupling between modified CLASS and 224
evaluation 231
testing of 224
meteorological and hydrological coupled models, for flash flood simulation 221–232
meteorological data sources, Upper Durance catchment 31–32
meteorological–hydrological modeling system, description 222–224
meteorological profile stations 168
meteorology, and hydrology coupling 215–260
Metolius FLUXNET site, turbulent flux trends 157
middle alpine belt, spatial differentiation of temperature dynamics 203, *206*
modified Thiessen polygon method *297*, 298, *300*
Monin–Obukhov similarity theory 21
Monongahela river basin catchments **293**
climate forcing 293–294
digital elevation model *292*
digital elevation model results 296–304
drought simulations (1988) 297–300
flood simulations (1993) 300–303
hydroclimate extremes 293
hydrologic model simulations 294
landcover distribution 294, *295*
land-surface characterization 294–296
leaf area index 295, *296*
location 292
sensitivity to rainfall forcing 297–298
simulated soil water content 303
soil texture distribution 294, *295*
study area description 293
surface albedo, roughness height for atmospheric boundary layer and Manning's roughness coefficient **295**
mountain basins, measuring and modeling the hydrology and ecology of 185–214
mountain floods 217
mountain hydrology, climate change impact and 261–306
mountain regions, and lowlands hydrological differences 257
mountain rivers 257
mountain snow, socioeconomic effects of changes in 3
mountains, as important water source for lowlands 263
Mumlava wind system 164

Nash conceptual model 218
Nash–Sutcliffe efficiency 40
Nepalese Himalayas 7, 10
Norway
future high mountain research in Central 211
measuring and modeling the hydrology and ecology of mountain basins in 185–214
snow cover in continental eastern 199, *200*
vegetation distribution in continental 200, *203*
Norwegian continental and oceanic lower alpine ridges and depressions, climatologic and hydrologic dynamics 197–199
Norwegian continental and oceanic lower alpine slopes, climatologic and hydrologic dynamics 196–197
Norwegian continental middle-alpine ridges and depressions, climatologic and hydrologic dynamics 199
Norwegian continental middle-alpine slopes, climatologic and hydrologic dynamics 199
Norwegian Scandes
ecology data 185–186
hydrology data 186
location of study site 189, *190*
photos of catchments *190*
study site basin characteristics **191**
topography of study sites *191*

numerical weather predictions (NWP) 85, 99

open lysimeters 76, *77*
Oppland Mountains 189, *190*, *191*

parameter uncertainty 127–128
penitentes 22, 24–26
  effect of snow 15
  energy balance partition for flat snow and **24**
  factors affecting formation of 25
  insolation *24*
  sensitivity of energy balance 24–26
permafrost
  definition 59
  distribution 253
  geophysical measurements 60
  monitoring in high mountain areas 59–71
  monitoring programs 59
  soil water and 57–122
point observations 125, 128, 133
pore-size distribution index 119
positive degree-day method 8
positive degree-day sum, calculation of 10–11
positive degree-days, monthly 10, **11**
precipitation
  and runoff formation 217–218
  in alpine mountain ranges 217
  daily depth 136
  differentiating between forms of 134
  estimation of snowfall during 10
  increase with altitude 10
  regional distribution 257
  sensitivity of simulated precipitation to surface characteristics 228
precipitation data, triangular fuzzy numbers for 133
precipitation-runoff models 249
  and sediment transport 256–257
  recommendations 258
process-correlation models 186, *187*

radiation, at energy balance stations 68, *69*
rain gauges 234
rain, interception in forests 36
rainfall, detecting patterns in mountainous catchments 243
rainfall radar data 234–235, 242–243
  beam blockage 234–235, 242
  calibration 236–237
  use within hydrological models 243
random errors, in observations 128
RE method 105, 108, 109, 118
regional climate models (RCMs) 277, 278
remote sensing, for obtaining snow data 46
resistivity
  cumulative differences per day *66*, 67
  DC surveys 60
  dependence on temperature 61, 63, 64, *65*
  estimation of unfrozen water content from measurements of 61
  measurements using fixed-electrode arrays 62–63
resistivity–temperature relationships 63, 65, 67, *68*, 70
Richard's equation 86, 92
  and constitutive laws 102–103
Rofenache
  annual runoff *268*
  characteristics **265**
  CV-values of modeled discharge for July–August 269
  effect of climate change and complete melting of glaciers *272*, 273
  effect of climate change and 50% reduction of glacier *271*, 272–273
  hydrometeorological conditions and change in discharge after doubling of CO_2 and complete melting of glaciers **273**
  location 264
runoff and floods, in the Alps 217–220
runoff formation, precipitation and 217–218
runoff generation models 218
runoff production, control of 305

Saguenay, Québec flood
  application of MC2 coupled to CLASS model 226–227
  scatter plot of 48-h accumulated precipitation *227*
  scatter plot of 48-h accumulated precipitation and sensitivity to surface vegetation *228*
Saguenay region, location 228, *229*
Säntis, Switzerland
  day of year with peak runoff **282**, 284
  energy and radiation fluxes evolution *286*, 287
  location 279
  maximum temperature rise scenario 287
  mean temperature rise scenario 284–287
  minimum temperature rise scenario 287
  number of snow-covered days 282
  radiation and energy fluxes daily evolution *283*
  runoff evolution 284
  snow cover duration 286, 288
  snow depth 282
  snowpack variability 287, 288
sap flux, from Douglas-fir trees 153
Satluj river basin
  depletion of SCA 48
  depletion of SCA under different climatic scenarios 52, *53*
  depletion of SCA with time *50*
  increase in melting area with increase in mean temperature over the melt period 52, *53*
  location map *47*
  main physical characteristics **47**
  study period and data used 48
saturated conductivity, in upper soil layers 112, *113*
saturated conductivity of Toce River basin soils
  comparison of estimates after field and laboratory data 109, *111*
  comparison of estimates after field data 109, *111*
  dependency on altitude 113, *114*
saturated hydraulic conductivity, and water retention relationships for Alpine mountain soils 101–121
saturation excess runoff 136
Schilthorn, Swiss Alps
  2-D geophysical ground monitoring 60
  annual precipitation 62
  calculating unfrozen water content 64
  characteristics of the field site **61**

- geoelectrical monitoring 66–67
- laboratory experiments 63–66
- location 61, *62*
- mean annual air temperature (MAAT) 62
- resistivity, temperature and unfrozen water content plotted against time *65*
- resistivity–temperature curves for saturated and dry material 63, *65*
- results 63–67
- seasonal variation of vertical temperature profile *63*
- temporal evolution of temperature *63*

sediment sources, modeling 253
sediment transport, and precipitation-runoff models 256–257
sediments, differentiating according to sources 258
short-wave radiation model 20–21
simulated annual site water balance summary 154
simulated seasonal water flux trends 154–157
simulated subsurface flow, comparison to total simulated streamflow at Elizabeth, Enterprise and Dailey watersheds 298, *299*
simulated water balance trends 154, *155*, *156*
simultaneous heat and water (SHAW) model 148, 151, 157
- conceptual diagram *151*
- validation 153–154

single ring infiltrometer method 102, *104*, 105–109, 118
slope models 252–256, 257–258
snow
- and ice melt 5–55
- effects on vegetation occurrence and distribution 208–209
- evaporation in forests 36
- socioeconomic effects of change in mountain 3

snow and ice melt 5
- from glacier and rocky areas 11
- methods for calculating 7–14

snow and ice penitentes 18
snow cover
- analysis at Disentis and Säntis *281*, 282
- effects on vegetation on soil moisture and 209, *210*
- height at Schilthorn 67, *69*
- in continental eastern Norway 199, *200*
- in Scandes Norwegian mountains 186
- relationship between cumulative degree-days and depletion of *51*
- runoff from melt of 2, 3
- spatio-temporal distribution 199, *201*

snow cover maps 46
snow cover patterns, future investigation improvements 42
snow covered areas
- application of 54
- application for snow melt modeling studies 45
- assessment using air temperatures during melt in a mountainous basin 45–55
- depletion in Satluj basin under different climatic scenarios *53*
- impact of climate change on 52
- interpolation of 50
- methods for measuring 46–47
- relationship with CDD 54
- satellite data 46
- Satluj River basin study period and data used 48
- simulation of 50–52
- variation in 45

snow depth, measured and simulated at Grächen 81
snow melt
- computation 136
- discharge measurements at Hannigalp 78–79
- prediction of melt in Himalayan rivers 45
- under different temperature increase scenarios in the Swiss Alps 277–289

snow melt models 46, 277
snow melt runoff
- improving forecasts of 29–44
- socioeconomic consequences in changes to 3

snow melt runoff model (SRM) 29, 45
snow melt simulation, resolution impact investigation 29
snow packs
- evolution of 30
- observed and simulated at Disentis and Säntis *281*, 282

snow packs in forest canopy, conditions affecting 33–34
snow penitentes 15, 18
soil depths, estimates made by experts 129
soil frost 73
- effect on aquifer recharge at snowmelt 81–82
- and groundwater recharge numerical modeling 77–78

soil hydraulic properties 101
soil moisture
- during dry event at Pallanzeno 97, *98*
- during wet event at Pallanzeno 97–99
- effects on vegetation of snow cover and 209, *210*
- restricting fuzziness of modeled 136
- spatio-temporal variability 200, *204*
- TDR measurement 86
- uncertainty of simulated 136
- variability in E. Norwegian mountains 194

soil moisture content, comparison between simulated CLASS and observed data in Québec, Canada 225
soil moisture profiles, behaviour of 96
soil pore-size distribution sensitivity, Mella River basin *116*, 117
soil properties, Enns river basin 134
soil saturated conductivity 118
- after field data 103–105
- and water retention relationships 102
- estimates comparison for pedogenetic and land-use classes of Toce River Basin *112*
- measurement of 102

soil saturated conductivity map, Toce river basin 108, **109**
soil texture, for Monongahela river basin 294, *295*
soil water, and permafrost 57–121
soil water content
- daily mean values 88, *89*
- simulated and measured 154, *155*

soil water flow 73

soil water retention relationships
estimation of 105
of Toce River basin soils 113, *114*
soil water transfer models 73
soil-vegetation-atmosphere transfer (SVAT) schemes 73
soils, sensitivity of bubbling pressure to organic matter content and grain size distribution at Mella River basin 117
solid precipitation, in forests 35
Sölk (Austria) study area 249
characteristics **248**
location *248*
slope model 252
soil sequence 252
sorptive number 103
Southern Black Forest 235
streamflows, annual and monthly simulated vs observed discharge 138–139, *140*
structural stability 300
structural uncertainty 127
subgrid parameterization methods 30, 33–37
of forest climate 33–34
of topography 33, *34*
subgrid parameterizations
comparison of simulated discharges 37–40
quantitative validation of simulated results 40–41
subsurface flow routing model (SFRM) 292
surface energy balance model (SEBM)
description 278–279
observations and control run 282–284
results 282–287
temperature increase scenarios **280**, 284–287
surface microtopography modeling 21–22
surface properties, parameterizing by geomorphological zoning 249–257
surface runoff 101
at Hannigalp *79*
schematic instrumental setup for collecting *76*
surface sea level pressure, South America 17
surface soil saturated conductivity, Mella River Basin 108, **110**
surface soil, water balance in 85–100
SVAT (soil-vegetation atmosphere transfer) model ISBA 30
Swiss Alps 60, 162, 163, **248**, 249
snowmelt under different temperature increase scenarios 277–289
southern 74
system state uncertainty, carry-over from time t to $t + 1$ 145
systematic errors 128
Szrenica study site
evapotranspiration and condensation daily and weekly variations 178–179
evapotranspiration and condensation hourly variations 169–171
experimental design 164
fog 163
location *163*
meteorological variables comparison *174–175*
precipitation 163
results and discussion 169–171
transpiration, evaporation and condensation comparison *176*

TAC model 238
TAC^D model 238, 242
talus slopes 253
Tauern, schist rocks 253
temperature
point measurements of 133
snowmelt under different temperature increase scenarios 277–289
temperature dynamics
classification **208**
lower alpine belt spatial differentiation 203, *205*
middle alpine belt spatial differentiation 203, *206*
Ticine–Toce watershed 86
Tien Shan, Pamir 264, **265**
time domain reflectometry (TDR) 86, 89–91
Toce River basin 102, 105
characteristics **86**, **106**
comparison between moisture of sieved, bulk or crumbled soil samples 117, *118*
infiltration tests and areal frequency **107**
location *87*, *106*
preliminary analysis 107
soil hydraulic characteristics 87, **88**
surface soil saturated conductivity map **108**
Toce Valley, analytical solutions of flow equations and measurements in 85–100
total resistivity, at borehole location 68, *69*
transpiration, from Douglas-fir trees 153
triangular fuzzy numbers 130
triangular membership functions 132
trough slopes and corrie areas, geomorphological boundary 253, *254*
turbulent fluxes *20*, 24
calculation 21
turbulent heat flux, partitioning during dry season weekly average 156, *157*
Tuyuksu Glacier region, Kazakhastan 263
annual runoff *268*
characteristics **265**
CV-values of modeled discharge for July–August 269
effect of climate change and complete melting of glaciers *272*, 273–274
effect of climate change and 50% reduction of glaciated area *271*, 272–273
goodness of fit 267
hydrometeorological conditions and change in discharge after doubling of CO_2 and complete melting of glaciers **273**
location 264
runoff scenarios after doubling of CO_2 270, 271

uncertainty in hydrological modeling, sources of 127–128
unfrozen water content, evolution of 68, *69*, 70
Upper Durance catchment 31–37
basin characteristics **31**
daily discharges *38–39*
digital terrain model 32–33
indices that characterise the different datasets and experiments **39**
landuse map 37
location *32*
mean annual water balance 41–42

meteorological data 31–32
soil and vegetation maps 31
Upper Enns catchment
characteristics 130, **131**
climate 130
drainage characteristics 135
hydrology 130
location 130, *131*
soil properties 134
water balance model 131–132
USDA soil texture classification 87
used adjustment method 237, 242

variable source area concept 218
vegetation
distribution in continental Norway 200, *203*
distribution in Norwegian high mountains 209
effects of snow cover and soil moisture on 209, *210*
input data in upper Durance catchment 31
root zone soil moisture and 305
spatial differentiation of types in lower alpine catchment 200, *203*
Vernagtbach
annual runoff *268*
CV-values of modeled discharge for July–August 269
effect of climate change and complete melting of glaciers *272*, 273–274
effect of climate change and 50% reduction of glaciated area *271*, 272–273
hydrometeorological conditions and change in discharge after doubling of CO_2 and complete melting of glaciers **273**
Rofenache sub-basin 264, **265**
runoff scenarios after doubling of CO_2 270, 271
vertical landscape structure analysis *188*, 189
vertical temperature dynamics 195, *196*, *197*, *198*
vertical water fluxes 194, *195*
water and energy budget models, in Appalachian mountains under climate variability and hydrological extremes 291–306
water balance equations 135
water balance modeling, with fuzzy parameterizations in Austrian Alps 125–146
water balance models
accuracy and sensitivity to fuzzy parameters and climatic inputs 139–141
criteria of uncertainty and measures of accuracy for basic and alternative 143
important parameters 144
magnitudes of system state variables 136
mathematical formulation 135–137
performance of alternative *142*, 143
performance with fuzzy input data but crisp estimates for model parameters 139, *141*
performance with fuzzy parameters and climatic inputs 137–139
precipitation and potential evapotranspiration fuzzy climatic input variables 137, *138*
reducing model complexity 141–143
simulated daily discharge parameters and input variables 140
Upper Enns catchment 131–132
water balance, upper Durance catchment mean annual 41–42
water balances
annual and monthly 137–143
evapotranspiration and 123–214
in Norwegian middle-alpine ridges 195
in surface soil 85–100
for Tuyuksu, Abramov and Glacier No. 1 266, **267**
water fluxes, measurement 180
water holding capacity of soil 137, *138*
water, influence of glacier retreat on yield 263–275
water mass balance 91
water relations, of an old-growth Douglas Fir stand 147–159
water resources
colors of 291
impact of climate variability 291
water retention curves 88
water retention relationships 102, 103, 113–117
estimation of 105
of Toce River basin sandy soils *116*, 117
with saturated hydraulic conductivity for Alpine mountain soils 101–121
watersheds
characterization 291
intraseasonal variability 303–304
water-table, rise during snowmelt at Grächen vs. winter precipitation 81, *82*, 83
West Himalayas (India) 47, 52, 54
western Norwegian high mountains, vertical temperature profiles 195, *197*
Wilhelmer Talbach sub-basin
characteristics **236**
modeling investigations 238
observed and simulated peak discharges 240, 241
precipitation 236, 240
runoff calculations 240
wind
influence on transpiration 180
and precipitation measurements 257
Wind River Canopy Crane Research Facility (WRCCRF) *150*
characteristics 148, **149**
climate 150
experimental measurements 150–151
location 148, *149*
soil 150
vegetation 149–150
wind speed, in forest canopy 35
wind systems, in Giant Mountains 164